**PhD Thesis**

# Concrete façade panels with enhanced thermal energy storage capacity

**Dervilla Niall**

**Candidate No. 88187349**

Supervisor: Professor Roger P. West

Department of Civil, Structural and Environmental Engineering

Trinity College Dublin, the University of Dublin

**2024**

## DECLARATION

I hereby declare that this PhD thesis is entirely my own work and that it has not been submitted as an exercise for a degree at this or any other university.

I agree to deposit this thesis in the University's open access institutional repository or allow the library to do so on my behalf, subject to Irish Copyright Legislation and Trinity College Library conditions of use and acknowledgement.

I consent to the examiners retaining a copy of the thesis beyond the examining period, should they so wish (EU GDPR May 2018).

_____

Dervilla Niall

## ABSTRACT

The escalating global climate change crises is motivating governments to seek solutions for reducing non-renewable energy consumption. Buildings are responsible for more than 40% of the total global energy consumption and over 30% of greenhouse gas emissions, and hence the improvement of the energy efficiency of buildings, particularly during their operational phase, is an active area of research. One of the commonly proposed methods of enhancing the energy performance of a building is to use the mass of the building envelope as a thermal energy storage system. The absorption and storage of heat during the day can reduce overheating of the internal environment in a building and hence reduce the energy demand of the air conditioning system. The stored heat is then dissipated into the internal environment at night when the temperature of the building naturally reduces.

The thermal energy storage capacity of a building material can be enhanced by incorporating phase change materials (PCMs), which are materials that absorb or release a high amount of heat energy while changing phase from solid to liquid or vice versa while remaining at the same temperature. Previous laboratory research by the author has shown that the incorporation of PCMs into concrete enhances its thermal storage capacity by up to 50%. However, it cannot be assumed that this thermal mass benefit will be replicated in a full-scale actual scenario. There is a scarcity of full-scale research studies in the literature as previous studies were largely on numerical studies validated by laboratory experiments. To address these gaps in the research this study, after initial laboratory investigations to develop an appropriate PCM-concrete composite material, manufactured precast cladding sandwich panels with a PCM-concrete inner leaf. The panels were tested thermally and structurally in the laboratory. Three full-scale demonstration huts were constructed using the panels and instrumented to record both internal thermal data and local climate data over an 18 month period. Analysis of this data showed that when the internal air temperature fluctuated above and below the phase change temperature of the PCM within a 24 hour period, the PCM-concrete composite was effective at reducing the air temperature in the huts by up to 16% if overnight ventilation was provided and up to 12% without overnight ventilation in a temperate climate.

The potential of the PCM-concrete composite to provide a beneficial thermal mass effect in a building depends on many variable factors including geographical location, the local climate, building geometry and use of the building. As all buildings differ, each building

will require a unique optimal solution for the application of a PCM composite material as a thermal energy storage system. For this reason, the development of numerical simulation tools is necessary to achieve a practical and economic application of this technology. In this study, a 3D finite element model was developed using COMSOL Multiphysics which replicates the thermal behaviour of the PCM-concrete composite in the full-scale huts. The model was validated by comparing the simulated temperatures in the model with the actual temperatures recorded in the huts. The validated model was used to investigate the influence of geographical location, that is, latitude, on the performance of the PCM-concrete composite. This 'scenario' modelling concluded that during the summer in the Northern hemisphere, the PCM-concrete provided more beneficial thermal mass effect at higher latitudes. It was also demonstrated that the PCM-concrete was more effective when placed in a floor rather than a North wall under summer conditions. In contrast, in winter conditions the PCM-concrete composite was more effective in lower latitudes when positioned in the walls.

## ACKNOWLEDGEMENTS

Firstly I would like to acknowledge the positive encouragement and generosity of time of my supervisor Prof Roger West throughout the entire course of this project. His advice, attention to detail and continued support was greatly appreciated.

I would also like to thank all the technical staff and in particular Michael Grimes and Dave McAuley. It was a privilege to carry out my laboratory work in such a professional, supportive and pleasant environment. The assistance and advice given to me during the course of the project was invaluable.

I would like to acknowledge the support of my colleagues in Technological University Dublin and the efforts that were made to provide me with sufficient time to engage with my research. It would not have been possible to complete this thesis without such support.

I wish to acknowledge the financial support of the European Horizon 2020 Framework Programme that funded the IMPRESS project (http://www.project-impress.eu) which this research project formed part of. I would also like to acknowledge the assistance provided by the IMPRESS partners, in particular Techrete Ltd who facilitated the manufacture of the panels and construction of the huts, Sirus International who provided the monitoring equipment in the huts and IMPRESS project leader Dr. Oliver Kinnane of UCD.

I would like to thank my friends for their encouragement and empathy and for all the various ways in which they have helped myself and my family over the long course of this research project.

Most of all I would like to express my love and gratitude to my husband Russell and my daughters Isabelle, Charlotte and Sophia. I deeply appreciate their unconditional support and all the sacrifices and extra efforts that they made to help me succeed in completing this project. It will never be taken for granted.

**TABLE OF CONTENTS**

## APPENDICES

# LIST OF FIGURES

## LIST OF TABLES

.

## NOMENCLATURE

BS Butyl Stearate

CA Capric acid

CFD Computational fluid dynamics

CFRP Carbon fibre reinforced polymer

CO Cloud Opacity

DA Decanoic acid

DI Diffuse irradiance

DSC Differential Scanning Calorimetry

EPS Expanded polystyrene

FEA Finite element analysis

FEM Finite element modelling

FRP Fibre reinforced polymer

GGBS Ground granulated blast furnace slag

GHGs Greenhouse gases

GI Global irradiance

HDPE High-density polyethylene

HPFRC High performance fibre reinforced concrete

LA Lauric acid

LWA Lightweight aggregate

MA Myristic acid

ME Microencapsulated

OPC Ordinary Portland cement

PAR Paraffin wax

PEG Polyethylene glycol

PCM Phase Change Material

SEM scanning electronic microscopy

SF Slump flow

SP Superplasticiser

TES Thermal Energy Storage

TM Thermomass connector

XPS Extruded polystyrene

# Chapter 1. Introduction

## 1.1 Background

It is generally accepted globally that climate change is a real threat to the environment. Climate change is driven by an increase in concentration of greenhouse gases (GHGs) in the earth's atmosphere. To address the threat of global climate change, in December 2015, 195 countries committed to the Paris Agreement – a legally binding global climate deal aimed at reducing GHGs. To enable the European Union (EU) to move towards a low-carbon economy and implement its commitments under the Paris Agreement, the 2030 Climate and Energy framework was derived, which includes EU-wide targets and policy objectives for the period from 2021 to 2030. The key targets for 2030 were:

- At least 40% cut in GHG emissions (from 1990 levels)
- At least 32% share for renewable energy
- At least 32.5% improvement in energy efficiency

In December 2023, during the 28$^{th}$ Conference of the Parties (COP28), which brings together world leaders annually to discuss and agree strategies to address the climate crisis, it was highlighted that governments are not on track to achieve the targets of the 2015 Paris agreement. To address this delay in progress 130 national governments endorsed the Global Renewables and Energy Efficiency Pledge which stipulates that the signatories commit to work together to triple the world's renewable energy generation capacity to at least 11,000 GW by 2030 and to double the global average annual rate of energy efficiency improvements from 2 % to over 4 % every year until 2030. The participants also committed to working together with the aim of reducing cooling-related emissions across all sectors by at least 68 % globally relative to 2022 levels by 2050.

New, more aggressive targets were set as summarised by the December 2023 Implementation Roadmap, published by the UN Climate Change High-Level Champions (HLCs) and the Marrakech Partnership for Global Climate Action. Some of the key targets are as follows:

- Solar and wind power to contribute at least 46%, and all renewables to contribute at least 68% of global electricity generation by 2030
- Electricity consumption for cooling of buildings to be reduced by approximately 30% by 2030
- 100% of building projects completed in 2030 or after to be net zero carbon in operation

The International Energy Agency (IEA) states that buildings are responsible for 30 % of global energy consumption, with space heating and cooling consuming 33 % of this energy, increasing to 50 % in cold climates (https://www.iea.org/energy-system/buildings). By transforming the built environment to be more energy-efficient, the building sector can play a major role in reducing the threat of climate change. With the publication of the Energy Performance of Buildings Directive (EPBD, 2018) and the legal requirement to increase energy efficiency, the need to reduce the overall energy usage of buildings has become a focus of government policy in European countries.

The use of renewable energy sources is increasing due to the drive to reduce the threat of climate change and secure energy supply. Solar energy is a major renewable heat energy source however its intermittent nature means that its effectiveness is dependent on the inclusion of an efficient thermal energy storage system. As noted by Fenollera et al. (2013), as the main consumer of material resources and energy, the construction industry has great potential to develop new efficient materials to reduce energy consumption in buildings and enhance the utilization of renewable energy sources.

According to the World Business Council for Sustainable Development's publication, 'Energy Efficiency in Buildings – Transforming the market' (2009), over half of Europe's building stock – circa 80 million buildings - was constructed between 1950 and 1975. In this period efficient energy performance was not a critical design factor. Often these buildings are fit for purpose structurally however their energy performance is very poor. In order to achieve an improved energy performance while minimising associated material consumption, a proposed solution is to retain the loadbearing structure but replace the non-loadbearing façade of the building with a modern, energy efficient building envelope. Improving the energy performance of building envelopes is a critical strategy for achieving the required reduction in space heating and cooling energy demand necessary - at least 25 % - 35 % from current values - to achieve the net zero carbon target for 100% of building by 2030 (IEA 2023).

One method that can be employed to improve the energy performance of a building envelope is to use the mass of the envelope to store thermal energy. Thermal energy storage (TES) in buildings is a building-integrated renewable technology that is proposed as one of the most effective approaches to reducing energy consumption of buildings. A TES system can be used to absorb and store both solar energy and excess heat due to use and occupancy during the day which can then be released to the internal environment when the room temperatures fall at

night. In this way, a TES system provides a potential for improved indoor thermal comfort for occupants by moderating internal temperature fluctuations and reducing the overall energy consumption of the building due to load reduction while shifting electricity consumption to off-peak periods. An area of research that is gaining attention is the enhancement of TESs through the addition of phase change materials (PCMs) due to their high energy storage density capabilities and their ability to store thermal energy in a constant temperature phase transition process, that is, PCMs provide a latent heat capacity (Figure 1-1).

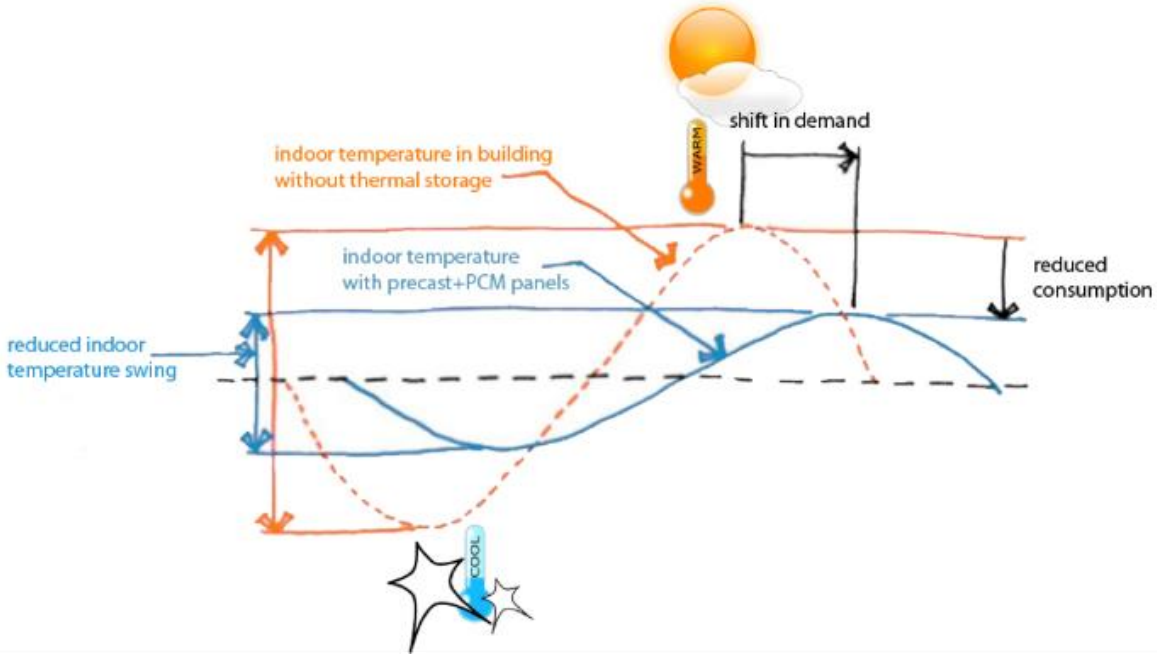


**Figure 1-1 Impact of increased thermal mass provided by PCM-concrete panels on internal temperatures. (Adapted from image on Autodesk Sustainability Workshop)**

This PhD research project aims to design, manufacture and carry out full-scale monitoring of a non-loadbearing precast concrete cladding panel with enhanced thermal storage capacity. This research was part of a European funded Horizon 2020 project entitled IMPRESS (http://www.project-impress.eu). The overall aim of IMPRESS was to develop innovative precast products for the renovation of existing building stock, thereby improving the performance and energy efficiency of European buildings. Both over-cladding and re-cladding façade panels have been investigated in the IMPRESS project. Re-cladding includes the removal and replacement of the existing façade whereas over-cladding involves the installation of a new cladding placed on top of the existing façade. This PhD research project focuses on a solution for the recladding option. To re-clad an existing building the existing façade must be removed without compromising the structural integrity of the building hence the existing and replacement cladding must be non-loadbearing.

It was the intent of the IMPRESS project to use the developed panel to re-clad a section of a school building in Coventry, England which was shown to have an over-heating problem through the collection and analysis of thermal data. Re-cladding a number of the classrooms in the school would allow the performance of the new panel to assess it in a real setting. However, the school pulled out of the IMPRESS project after the Grenfeld fire event due to the inability to fire safety test the novel PCM-concrete material withing the timescale and budget of the IMPRESS project. For this reason full-scale test huts were constructed instead to enable the thermal behaviour of the panels to be assessed in a real scenario.

### 1.2 Phase change materials

This project concerns the development of a pre-cast concrete sandwich cladding panel with thermo-physical properties that will enhance passive heating and cooling. Using the mass of a building to store heat and/or cold can reduce the demand on the auxiliary heating and/or cooling systems and hence reduce the overall energy demand of the building.

The ability of a material to store and release heat is a function of its specific heat capacity and the mass of the material and is commonly referred to as thermal mass. Materials of different conductivities will absorb and release heat at different rates to the environment. For a building material to provide suitable thermal mass an appropriate balance between the conduction of heat through it and the inertia to temperature change is required, that is, between its heat release and storage tendencies. Concrete is a building material that combines a high specific heat capacity and high density with a thermal conductivity that is appropriate for the diurnal heating and cooling cycle of buildings and hence it has good thermal mass characteristics. Previous research (Niall et al., 2016, Niall et al., 2017) has shown that the thermal mass behaviour of concrete can be enhanced by incorporating PCMs into the concrete which provide an additional latent heat capacity and hence increase its overall thermal storage capacity.

PCMs are materials that absorb and release high quantities of heat energy at specific temperatures as they change phase, that is, from solid to liquid and from liquid to gas. When incorporating a PCM into a building material it is only feasible to consider the solid-liquid phase change. The temperature of the PCM remains relatively constant during phase change hence the PCM provides a high latent heat capacity. There are many different types of PCMs available so the selection of a PCM for a given application requires consideration of the properties of the PCMs and a weighing up of their particular advantages and disadvantages in order to reach an acceptable compromise. Primarily the selection of a PCM should ensure that

the melt temperature range of the PCM is suitable for the intended application. Kosny et al. (2013) carried out an overview of the potential applications of PCMs in building envelopes which depend largely on local climate conditions and the melt temperature range of the proposed PCM.

Niall et al. (2016 and 2017) carried out laboratory research to determine the properties and observe the thermal behaviour of PCM-concrete composites. Two methods of incorporating PCMs into concrete were used to form PCM-concrete composite panels. The first type of panel was formed by adding a microencapsulated paraffin to fresh concrete during the mixing process. The second panel was formed by vacuum impregnating a fatty acid - butyl stearate - into lightweight aggregate which was then included in the concrete mix. Both types of panels containing PCM displayed significantly greater thermal storage capacity - up to 50 % - despite having reduced thermal conductivity and density. The study concluded that the panel containing a lightweight aggregate PCM composite was more effective at providing additional thermal storage, particularly within the first 100mm of depth of an element of structure. However evidence of leakage of the butyl stearate was observed on the surface of the panels so further research was required in order to investigate a potential solution to this issue prior to using it in a real life application.

This previous research also highlighted the fact that the effectiveness of the PCM in increasing the overall thermal storage of the concrete panels reduced with depth into the panel. This is due to the fact that the PCM absorbs the heat as it changes phase and hinders the penetration of heat deeper into the panel. The overall thermal storage of a panel will increase as the amount of heat energy transferred to the panel increases. In a real application where a PCM-concrete composite material is used in a building to store thermal energy, the effective depth of the PCM will depend on the temperature profile of the internal environment.

For the PCM to be effective it is critical that the temperature of the environment in which the PCM is located varies above and below the melt temperature range of the selected PCM within a diurnal period. If this range of temperature fluctuation does not occur then the PCM will not discharge latent heat energy and will not have the capacity to absorb more heat the following day. The fluctuation in the indoor temperature depends on both the local climate and the level of insulation in a building. Modern buildings that are well insulated may hinder the performance of a PCM’s thermal energy storage element. For this reason, the use of PCM-concrete

composites for enhanced thermal mass behaviour is more suitable for the refurbishment of buildings that have poor levels of insulation and air-tightness.

This PhD research aims to design a precast concrete sandwich panel, suitable for the recladding of existing buildings, with enhanced thermal mass properties that will enable passive heating and cooling behaviour to improve the energy performance of the building. The core innovative technology is the incorporation of PCMs within the concrete to form a PCM-concrete composite material which has an increased thermal storage capacity. This composite material is used in the inner leaf of the sandwich panel and it is expected that the presence of the PCM will reduce overheating effects in any environment in which it is placed.

### 1.3 Objectives of thesis

As stated in Section 1.2, the principal aim of this research project is to design and develop an innovative precast concrete cladding panel with enhanced thermal mass properties that can be used for recladding existing buildings and thereby enhance their energy performance. It is proposed to achieve this aim by completion of the following set of objectives:

- Previous research carried out by the author concluded that a fatty acid PCM was more effective than microencapsulated paraffin at enhancing thermal mass behaviour. For this reason, the first objective of the research is to create a eutectic fatty acid PCM to be vacuum impregnated into lightweight aggregate. Different methods to seal the PCM into lightweight aggregate in order to prevent leakage will be tested and evaluated. The results of this investigation will inform the decision on which type of PCM will be used in the cladding panel.
- Previous research also demonstrated that the addition of PCM to concrete reduces its thermal conductivity. Having a lower thermal conductivity can hinder the utilization of the PCM because the heat energy is slower to reach the PCM deeper within the wall panel. The second objective of this research is to complete a laboratory investigation to assess different methods of improving the thermal conductivity of a PCM-concrete composite.
- Using the results of the studies from objectives one and two, a full-scale precast concrete panel will be designed. The third objective of the project is to ensure that the panels have sufficient strength to withstand lateral wind loads, and also to determine the thermal characteristics of the panel. This objective will be achieved through a laboratory investigation in which test panels will be subjected to thermal testing followed by a

structural testing regime to evaluate and compare the composite structural behaviour of the two layers of the sandwich panel under different connectivity scenarios.

- As the thermal behaviour of a PCM-concrete material is complex and depends on the environmental conditions in which it is placed, the fourth and primary objective of this research is to construct three full-scale huts using the PCM-concrete panels and instrument them to record thermal and environmental data. Thermal data will be recorded over an 18 month period so that the thermal behaviour and impact of the PCM-composite in a full-scale scenario can be analysed.
- The fifth objective of this research project is to develop a software model that can accurately simulate the thermal behaviour of the PCM-composite panels in various full-scale environmental conditions. The environmental data collected at the huts will be used to validate the model whereupon parametric simulations will allow optimum designs to be proposed.

The fulfillment of these five objectives will further the knowledge in this field of research through the provision of a thermal data set collected within a 'real', full-scale form of construction, throughout all seasons which enables the impact of this form of technology to be realistically assessed. The data set will also facilitate the development of a simulation model that is validated using data recorded in a full-scale 'real' scenario. The model will enable bespoke solutions for PCM-concrete composites to be assessed and optimised for any geographical location and building geometry which will make further research into this form of technology more accessible and enhance its potential applications. The design and manufacture of the full-scale PCM-concrete panels will provide evidence that PCM -concrete can be successfully up-scaled for use in real construction projects using standard manufacturing methods.

### 1.4 Scope of thesis

This PhD thesis comprises nine individual chapters. The following is a brief outline of Chapters 2 to 9.

**Chapter 2: Literature review**

Chapter 2 provides a summary of previous research on topics relevant to the development of a PCM-concrete composite material for use as a thermal energy storage unit in a building envelope. The topics discussed include the behaviour and classification of PCMs and methods for incorporating PCMs into concrete. The impact that the incorporated PCMs may have on

the properties of concrete are discussed. Previous research that investigated the use of PCM-composites in building envelopes is also reviewed. The conclusion to this chapter summarises how the key findings of research carried out to date informs the methodology for this project.

**Chapter 3: Methodology**

Chapter 3 details the methodology for achieving the objectives of the research project including the experimental design for the laboratory investigations and the design and instrumentation of the full-scale huts.

**Chapter 4: Initial laboratory investigations**

Chapter 4 presents the results of the initial laboratory studies including characterization of the PCMs, sealing of the PCM into a lightweight aggregate and enhancement of thermal conductivity of the PCM-concrete composites. The results are discussed which leads to the final selection and design of a PCM-concrete composite to be used in the latter parts of the research.

**Chapter 5: Thermal testing of cladding panels**

Chapter 5 describes the manufacture of a number of test cladding panels which are then subjected to thermal testing in an adjusted hot plate apparatus. The results of the tests are analysed and the resistivity and U-values of the panels are derived under steady-state conditions.

**Chapter 6: Structural testing of cladding panels**

Chapter 6 describes the structural testing of the test cladding panels, with and without PCMs. The structural response of the panels to an applied displacement is observed and recorded for different types of connectivity between the wythes of the cladding panel. The results are analysed and the degree of composite action is quantified. The load capacity of each panel is confirmed.

**Chapter 7: Analysis of data from huts**

In Chapter 7 the design, manufacture and instrumentation of the full-scale huts are detailed. An extensive analysis of the thermal data recorded in the huts over an 18 month period is carried out and discussed. Key conclusions regarding the thermal performance of the PCM-concrete composite are made.

**Chapter 8: Modelling**

Chapter 8 details the development of a simulation model which is then validated using the data collected at the full-scale huts. The validated model is then used to explore the impact of geographical location on the thermal performance of the PCM-concrete composite.

**Chapter 9: Conclusions and recommendations**

In Chapter 9 the objectives of the research study are reiterated and the achievement of the objectives is discussed. The principal conclusions of the research are summarised and a number of recommendations for further work are presented.

# Chapter 2. Literature Review

This chapter presents a comprehensive overview of thermal behaviour of PCMs together with a state-ot-the-art analysis of previous research into application of PCMs to thermal energy storage systems in buildings. Initially the theoretical methods of heat transfer are explained and the strategy of using thermal energy storage (TES) systems to improve the energy performance of buildings is discussed. The thermal behaviour of PCMs is examined including the criteria for their selection, their thermophysical properties and the techniques for characterisation, along with problematic issues associated with PCMs including thermal hysteresis behaviour and supercooling. This analysis informs both the selection of PCMs for this study and highlights critical thermal behaviour characteristics for simulation modelling.

Several techniques for incorporating PCMs in construction materials have been investigated in previous research studies. This chapter reviews these techniques and evaluates the impact that each method has on the thermal and mechanical properties of concrete leading to the selection of appropriate proposals for PCM-concrete composite materials.

The optimisation of integrating PCMs within passive latent heat TES systems and the optimal integration of these elements within a building is very complex and depends on many variables. This chapter presents and evaluates prior full-scale studies that explored the use and impact of PCMs in building envelopes. The modelling techniques employed to simulate the behaviour of PCMs in buildings are also assessed and compared.

Finally, the chapter describes the structural behaviour of concrete sandwich panels and reviews research on the influence of shear connector type and insulation stiffness on achieving composite action between panel layers. The findings of these research studies inform the thesis objectives and the experimental design for the structural testing of the proposed panels. The chapter concludes with a summary of the findings drawn from the literature and identifies gaps in the research that lead to the design of the objectives of this thesis

## 2.1 Heat energy transfer

The transfer of energy as heat occurs when a temperature differential exists between two mediums. Heat energy is always transferred from the hotter medium to the colder medium. Heat transfer stops when the two mediums reach the same temperature and hence are in thermal equilibrium. There are three distinct mechanisms of heat transfer, namely convection, conduction and radiation.

### 2.1.1 Conduction

Conduction is a heat transfer mechanism in which the heat is carried through a body of material. When the surface of a material is exposed to an increase in temperature the molecules at the surface start to vibrate and in turn excite the adjacent molecules. In this way the heat is transferred through the body of the material, reducing the thermal differential in the material until thermal equilibrium is reached. The rate at which heat energy is transferred through a material depends on the molecular structure of the material and is termed the thermal conductivity, k, (W/mK).

Considering a body of material with a surface area of 'A' and thickness 'd' subjected to a high temperature '$T_h$' on one side and a lower temperature '$T_c$' on the other side (Figure 2-1), the thermal energy conducted through the material is proportional to the area, the difference in temperature, ($T_h$ - $T_c$) and time. The larger the area, the greater the temperature differential and the longer the time, the more thermal energy is transmitted (Nolan, 2012).

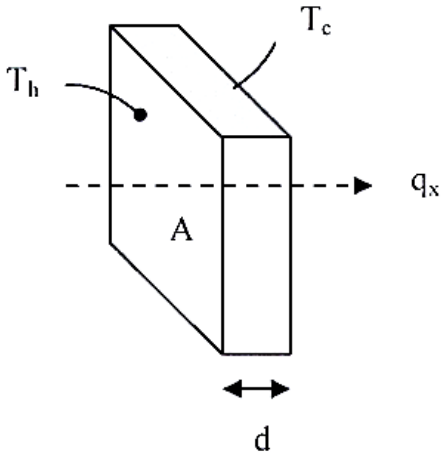


**Figure 2-1 Heat conduction through a body of material (Nolan, 2012)**

The amount of heat energy transferred by conduction, q, in Joules, is given by the following equation (Çengel and Ghajar, 2015):

$$q = \frac{kA(T_h - T_c)t}{d} \quad \text{(Joules)} \qquad \textbf{(2-1)}$$

where:

k = thermal conductivity (W/mK)

A = surface area ($m^2$)

d = depth of material (m)

t = time (seconds)

$T_h$ = higher temperature (K)

$T_c$ = lower temperature (K)

It can be noted that the heat energy transmitted through a medium is directly proportional to the temperature differential, ($T_h$ - $T_c$), and inversely proportional to the depth of the material.

### 2.1.2 Convection

Convection is the mechanism of heat transfer through a fluid and between a solid and a fluid in the presence of bulk fluid motion. If the fluid motion is caused by mechanical or external means such as a fan, a pump, or atmospheric wind, it is called forced convection. In the absence of forced convection, for natural (free) convection the motion is induced by buoyancy forces in the fluid that arise from density variations caused by temperature variations in the fluid. Convection requires the presence of fluid motion. Heat transfer through a fluid is by convection in the presence of bulk fluid motion and by conduction in the absence of it.

Heat transfer by convection is also achieved by the movement of a fluid past a solid, for example movement of warm air in a room may transfer heat to the walls and floors. Initially heat is transferred to a thin layer of air adjacent to the solid by conduction. This heat is then carried away from the surface of the solid by convection, that is, by the bulk motion of the air which removes the heated air near the surface and replaces it with cooler air. The faster the fluid motion, the greater the convection heat transfer. If the fluid is stationary, the heat transfer between the solid and fluid is by conduction only. The presence of bulk motion of the fluid enhances the heat transfer between the solid surface and the fluid.

The rate of convective heat transfer, $q_{c,}$ between a solid and a fluid, is governed by Newton's law of cooling which states that the heat transfer from a solid surface to a fluid is proportional to the difference between the surface and fluid temperatures, and the surface area and is expressed by the following equation (Figure 2-2) (Ghoshdastidar, 2012):

$$q_c = hA(T_s - T_\infty) \text{ (Watts)} \qquad \textbf{(2-2)}$$

where:

- h = the convection heat transfer coefficient ($W/m^2K$)
- $T_s$ = is the temperature of the solid (K)

- $T_\infty$ = is the temperature of the fluid body, at a distance from the solid surface (K) (At the surface, the fluid temperature equals the surface temperature of the solid)
- A = surface area ($m^2$)

The convective heat transfer coefficient is not a property of the fluid. It is an experimentally determined parameter whose value depends on all the variables influencing convection such as the surface geometry and roughness, the nature of fluid motion, the bulk fluid velocity and properties of the fluid including thermal conductivity, density and specific heat capacity.

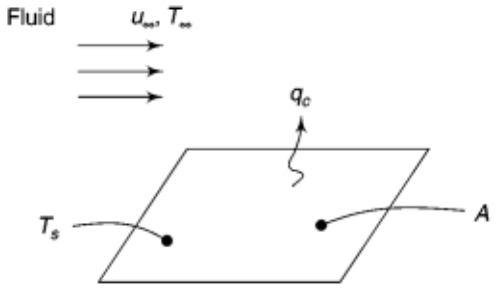


**Figure 2-2 Convection from surface area A at $T_s$ to cooler flowing fluid at $T_\infty$ (Ghoshdastidar, 2012)**

### 2.1.3 Radiation

Radiation is an energy transfer mechanism in which the energy is transferred by the emission or absorption of electromagnetic waves, for example solar radiation. Unlike conduction and convection, the transfer of heat by radiation does not require the presence of an intervening medium. Any object emits radiant thermal energy in all directions unless its temperature is absolute zero. The higher the temperature, the greater is the amount of energy radiated. If two objects at different temperatures are placed so that the radiation from each object is intercepted by the other, then the body at the lower temperature will receive more energy than it radiates, and hence its temperature will increase. In conjunction with this, the internal energy of the object at the higher temperature will decrease.

Thermal radiation has significant energy in the range of wavelength between $2 \times 10^{-7}$ to $10^{-3}$ which includes the visible range, infrared range and a portion of the ultraviolet range. However for low to moderate temperature applications, thermal radiation is generally within the infrared wavelength (Kaviany, 2011)).

If radiated energy strikes another medium, it may be absorbed, reflected or transmitted through the medium. The fractions of the radiation absorbed, reflected and transmitted are called the absorptivity, reflectivity and transmissivity respectively. The absorptivity, the reflectivity and

the transmissivity must add up to one. A body that absorbs all radiation striking it is called a blackbody. For a blackbody the reflectivity and the transmissivity are zero and the absorptivity is one (Dincer and Rosen, 2001). The total thermal energy radiated from a blackbody, $E_b$ ($W/m^2$) at temperature 'T' (K) can be determined from the following equation:

$$E_b = \sigma T^4 \quad (W/m^2) \tag{2-3}$$

where σ is known as the Stefan-Boltzmann constant and is equal to 5.669 x $10^{-8}$ $W/m^2K^4$. Equation (2-3) is known as the Stefan-Boltzmann law.

Radiation is a volumetric phenomenon, and all solids, liquids, and gases emit, absorb, or transmit radiation to varying degrees. However, for opaque solids such as concrete, metals and wood, radiation is considered to be a surface phenomenon since the radiation emitted by the interior regions of such material can never reach the surface, and the radiation incident on such bodies is usually absorbed within a few microns from the surface. To take into account the non-black nature of such surfaces, the definition of 'emissivity', ε, which relates to the radiation from a non-black surface, E, to that of a blackbody, is introduced:

$$\varepsilon = E/E_b \tag{2-4}$$

The emissivity of a surface is a value between zero and one. The energy emitted by a non-blackbody is:

$$E = \varepsilon \sigma T^4 \quad (W/m^2) \tag{2-5}$$

Another radiation property of a surface is its absorptivity, α, which is the fraction of the radiation energy incident on a surface that is absorbed by the surface. Like emissivity, its value is in the range of zero to one. A blackbody absorbs all the incident radiation so that $\alpha = 1$. Both ε and α of a surface depend on the temperature of the surface and the wavelength of the radiation. Kirchhoff's law of radiation states that the emissivity and the absorptivity of a surface at a given temperature and wavelength are equal.

### 2.2 Thermal energy storage

As discussed in Section 1.1, with increasing global focus on mitigating climate change governments are committed to reducing $CO_2$ emissions by transitioning to the use of renewable energy sources. One of the main challenges associated with renewable energy sources, such as solar and wind, is that the energy supply is intermittent. For example, solar energy is dependent on daylight availability which may lead to a mismatch between the generation of renewable

energy and the varying energy demands of buildings during the day. To address this disparity, energy storage systems can be used to bridge the gap between energy supply and demand and hence reduce dependence on non-renewable energy sources. As the heating and cooling of buildings consume a large proportion of total energy use, the integration of thermal energy storage systems can play an important role in enhancing the energy efficiency of buildings.

A thermal energy storage system can utilise sensible heat storage, latent heat storage or a combination of both. Sensible heat storage involves the use of materials with high specific heat capacities to store and release heat without undergoing a phase change. Latent heat storage utilises PCMs to store and release thermal energy during phase transitions while maintaining relatively constant temperatures.

### 2.2.1 Sensible heat storage

In sensible heat storage systems, energy is stored in a material by increasing the temperature of the material. The capacity of a material to store energy depends on its specific heat capacity, $C_{p,}$ which represents the amount of energy required to change the temperature of a unit amount of the material. The thermal storage capacity of a sensible heat system can be determined using the following equation (Sharma et al., 2009):

$$Q = \int_{T_i}^{T_f} mC_p \, dT = mC_{ap}(T_f - T_i) \quad \text{(Joules)} \qquad \textbf{(2-6)}$$

where:

$Q$ = quantity of heat stored (Joules)

$T_f$ and $T_i$ = final temperature and initial temperature respectively (K)

$m$ = mass of heat storage material

$C_p$ = specific heat capacity of material (J/kgK)

$C_{ap}$ = average specific heat between $T_i$ and $T_f$ (J/kgK)

Equation (2-6) illustrates that if two bodies of equal mass but different material are exposed to an equal amount of heat energy, the material with a higher specific heat capacity will remain cooler.

In buildings, a sensible heat storage system can be provided by using the mass of the building as the storage unit. The ability of a material to store heat is referred to as its *thermal mass* and is determined by multiplying the mass of the material by its specific heat capacity (equation 2-7).

$$\text{Thermal mass} = \text{mass} \times \text{specific heat capacity} \qquad \textbf{(2-7)}$$

For a material to provide good thermal mass it requires three properties:

1. A high specific heat capacity, $C_p$ (J/kgK)
2. A high density, ρ (kg/m$^3$)
3. An appropriate thermal conductivity, k, that suits the required storage period (W/mK)

Another important thermal property of a material is thermal diffusivity, δ, which relates the ability of a material to conduct heat to its ability to store heat (equation 2-8).

$$\delta = \frac{k}{\rho C_p} \quad (m^2/s) \qquad \textbf{(2-8)}$$

Thermal diffusivity indicates the rate at which temperature changes occur in a material. Materials with higher values of thermal diffusivity will reach temperature equilibrium with the environment quicker.

Table 2-1 presents the thermal properties of common construction materials (Dincer and Rosen, 2001 and The Concrete Centre, 2012). These values were used to calculate the corresponding values for thermal diffusivity.

**Table 2-1 Thermal properties of common construction materials (The Concrete Centre, 2012 and Dincer and Rosen, 2001)**

| Building Material | Specific heat capacity (J/kgK) | Density (kg/m$^3$) | Thermal conductivity (W/mK) | Thermal diffusivity (m$^2$/s) |
|---|---|---|---|---|
| Concrete | 880 | 2300 | 1.4 | 0.69 x 10$^{-6}$ |
| Timber | 2300 | 550 | 0.13 | 0.10 x 10$^{-6}$ |
| Steel | 470 | 7800 | 48.0 | 13.0 x 10$^{-6}$ |
| Brick | 1000 | 1750 | 0.77 | 0.44 x 10$^{-6}$ |
| Sandstone | 1000 | 2300 | 1.8 | 0.78 x 10$^{-6}$ |
| Water | 4190 | 1000 | 0.62 | 0.15 x 10$^{-6}$ |

As can be noted from Table 2-1, timber has a high specific heat capacity, however its low conductivity limits the rate at which it can absorb and release heat and as a result, timber has a relatively low thermal diffusivity. This makes timber more of an insulating material than a thermal storage material. Steel, on the other hand, has a relatively high thermal conductivity which results in fast absorption and release of heat, making it unsuitable for use as a thermal storage material in a space heating application. Concrete provides a combination of high specific heat capacity and an appropriate thermal conductivity which makes it a suitable thermal storage material for the diurnal heating and cooling cycle of buildings.

The walls and floors of buildings, excluding lightweight buildings, are typically constructed with concrete. They provide a large surface area for absorbing heat energy from both direct solar radiation and from internal heating systems via convection and/or conduction. The thermal energy stored in the concrete mass during the day is then released back into the interior space during the night as the internal environment cools. Hence the thermal mass of the concrete moderates the extreme diurnal internal temperatures and delays the time at which peak temperatures occur, that is, it provides thermal inertia (Figure 2-3).

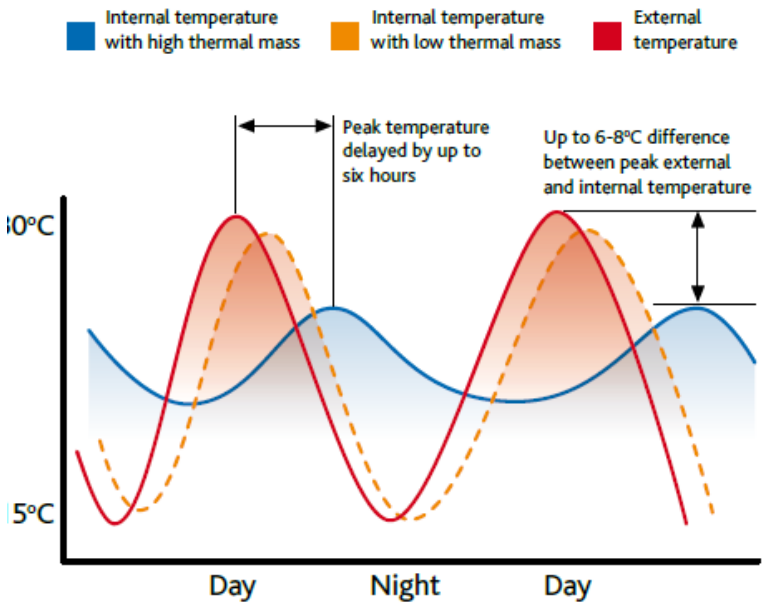


**Figure 2-3 Stabilising effect of thermal mass on internal temperature (The Concrete Centre, 2012)**

The thermal inertia of a material, denoted 'I', quantifies the responsiveness of a material to temperature variations and is defined as the square root of the product of thermal conductivity and volumetric heat capacity. The volumetric heat capacity of a material is the product of density and specific heat capacity. Hence thermal inertia can be determined using equation (2-9) (Pomianowski et al., 2012).

$$I = \sqrt{\rho\, C_p k} \qquad (J/(m^2K\sqrt{s})) \tag{2-9}$$

where:

$\rho$ = density ($kg/m^3$)

k = thermal conductivity (W/mK)

$C_p$ = specific heat capacity (J/kgK)

A high thermal inertia characterises materials with high thermal mass and high thermal conductivity (Pomianowski et al., 2012). Such materials will display small changes in

temperature throughout the diurnal cycle. Referring to equation (2-8) for thermal diffusivity, δ equation (2-9) can also be written as follows:

$$I = \frac{k}{\sqrt{\delta}} \qquad (J/(m^2K\sqrt{s})) \qquad \textbf{(2-10)}$$

It can be noted from equation (2-10) that the higher the thermal diffusivity of a material the lower the thermal inertia. Hence for a building material to provide good thermal mass it requires an appropriate balance between thermal diffusivity and thermal inertia.

Using the mass of a building as a sensible heat storage system can reduce the demand on the auxiliary heating and/or cooling system and hence reduces the overall energy consumption of a building. The selection of building materials with appropriate thermal properties is essential for optimising sensible heat storage. Thermal properties, including thermal conductivity, specific heat capacity, density and thermal diffusivity, influence the characteristics of heat storage and release within a building. The performance of a sensible heat storage system depends mainly on density and specific heat capacity of the material and hence the volume of material provided is critical (Fernandez et al., 2010). A disadvantage of sensible heat storage systems is that they have a low heat storage density, that is, they require a relatively large volume of material to store heat. A large storage volume can lead to increased cost in a building (Alkan, 2023). Another disadvantage of sensible heat storage is that the storage material changes temperature through the absorption and release of heat energy which may impact the overall thermal environment of the building.

### 2.2.2 Latent heat storage.

The overall thermal storage capacity of a system can be enhanced by the addition of latent heat storage. Latent heat storage utilises the energy absorbed by a material as it undergoes phase transitions from solid to liquid or from liquid to gas. Latent heat storage has a higher energy density than sensible heat storage so a smaller volume of material can store more heat energy. PCMs can store 5 to 14 times more latent heat than sensible heat (Sharma et al., 2009). Also the temperature variation across the heat storage operation is low as phase change occurs over a small temperature range.

The storage capacity of a latent heat system is given by equation (2-11) (Sharma et al., 2009):

$$Q = \int_{T_i}^{T_m} mC_p\, dT + ma_m\Delta h_m + \int_{T_m}^{T_f} mC_p\, dT \ (J)$$

or

$$Q = m[C_{sp}(T_m - T_i) + a_m\Delta h_m + C_{lp}(T_f - T_m)] \quad (J) \qquad \textbf{(2-11)}$$

where:

$C_{sp}$ = average specific heat between $T_i$ and $T_{m.}$ (J/kgK)

$C_{lp}$ = average specific heat between $T_m$ and $T_{f.}$ (J/kgK)

$T_m$ = melting temperature. (K)

$a_m$ = fraction of material melted

$\Delta h_m$ = heat of fusion per unit mass, that is, the amount of heat required to convert a solid mass to a liquid without an increase in temperature (J/kg)

PCMs are substances which absorb a significant amount of energy during phase transitions, that is, they have a high latent heat capacity which is utilised in latent heat storage systems. Solid-gas and liquid-gas phase changes typically have very high latent heats however they are generally avoided in energy storage systems due to the large volumes that gases tend to occupy, which can make the storage system large and impracticable (Regin et al., 2008). Solid-liquid phase transformations have comparatively smaller latent heats of phase transition, however these phase changes involve relatively small volume changes in the order of 10% or less (Sharma et al., 2009). The phase transition occurs across a specific narrow temperature range referred to as the phase change temperature range.

Cabeza et al. (2011) provided a classification of phase change substances used for latent thermal energy storage, as shown in Figure 2-4, where melting enthalpy is defined as the quantity of heat energy absorbed during a solid to liquid phase change.

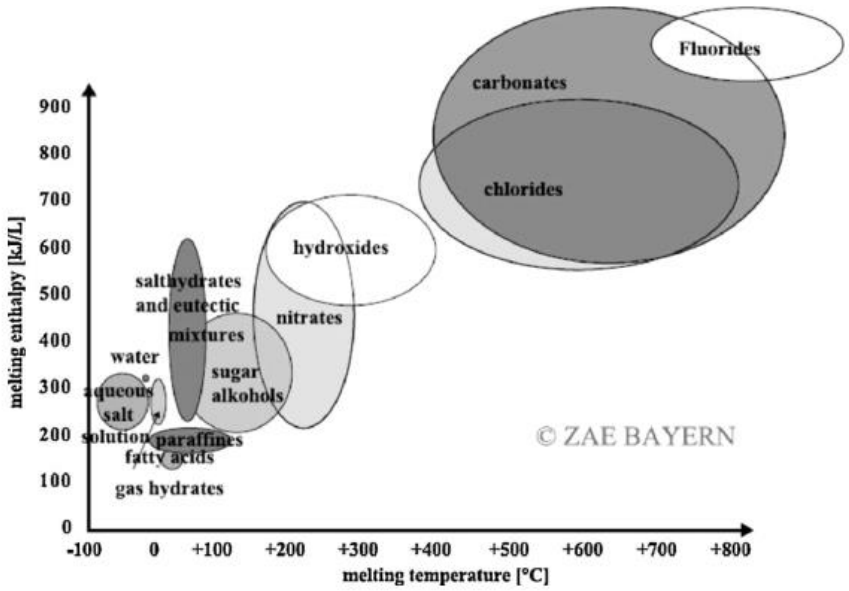


**Figure 2-4 Classification of phase change substances (Cabeza et al., 2011)**

A number of authors who have presented review studies on the use of PCMs in thermal storage systems (Sarath et al., 2023, Zeng et al., 2017, Jelle and Kalnæs, 2017, Kenisarin and Mahkamov, 2016, Osterman et al., 2015, Cui et al., 2015b, Memon et al., 2015, Cabeza et al., 2011, Sharma et al., 2009) outlined the desirable properties governing the selection of a PCM for use in a latent heat storage system, which may be summarised as follows:

**Thermal-physical properties:**

- Phase change temperature must be suitable for building application
- It has a high latent heat of fusion per unit volume
- It has a high thermal conductivity to assist in charging and discharging of the PCM within the limited time frame
- It has a high specific heat so that additional energy in the form of sensible heat is available to the thermal energy storage system
- There is a small volume change during phase transition and small vapour pressure at operating temperature
- The PCM should melt completely (that is, congruent melting) during phase transition so that the solid and liquid phases are homogenous
- It must be thermally reliable (that is, cycle stability) so that the PCM is stable in terms of phase change temperature and latent heat of fusion in long term applications

**Kinetic properties**:

- It has a high rate of crystal growth so that heat recovery from the storage system is optimum
- It has a high rate of nucleation so as to avoid supercooling of the PCM in liquid phase

**Chemical properties**:

- It is chemically compatible with construction/encapsulated materials
- There is no degradation after a large number of thermal (freeze/melt) cycles so as to assure long operation life
- It is non-toxic, non-flammable and non-explosive so as to assure safety
- It is corrosion resistant to construction/encapsulated materials

**Economic properties**:

- It is cost effective
- It is commercially available

**Environmental properties:**

- It has a low environmental impact and is non-polluting during its service life
- It has recycling potential

There is no one PCM that will satisfy all of the above desirable characteristics, hence the selection of a PCM for a given application requires consideration of the properties of the PCMs and a weighing up of their particular advantages and disadvantages in order to reach an acceptable compromise for the application.

Depending on the application, PCMs should first be selected based on their melting temperature. For example, materials that melt below 15$^{o}$C are used in air conditioning systems for cooling spaces while materials that melt above 90$^{o}$C are used for absorption refrigeration (Farid et al., 2004). For a space heating application in a building, PCMs with a melting temperature within the range of human comfort temperature (18 – 22 $^{o}$C) can be deemed suitable (Pasupathy et al., 2008). For a space cooling application the appropriate melt temperature range is higher at 19 – 24 $^{o}$C (Waqas and Ud Din, 2013).

Kousksou et al. (2014) carried out a review of the challenges and applications of TES systems. The authors concluded that while sensible heat storage systems are in an advanced stage of development, latent heat storage systems which utilise PCMs are still a developing technology. Although the principle of PCM's usage is straightforward, evaluating the effective contribution of the latent heat for the enhancement of the energy performance of the whole building is challenging.

The optimisation of integrating PCMs within passive latent heat TES systems and the integration of these systems within the building is complex due to the many influencing factors. These factors include the phase-change temperature range of the PCM, its latent heat capacity and its position within the TES system and/or, the position of the TES system within the building. The optimal values for these parameters vary according to the use, geometry and form of construction of a building and also climatic conditions at the building's geographical location. For a specified geometry and geographical location, the indoor air temperature of a building is closely related to the thermal resistance and specific heat capacity of the building envelope. Increasing the thermal storage capacity of the building envelope is an effective strategy for improving the thermal energy performance of a building.

Soares et al. (2013) presented an overview of how latent heat thermal energy storage systems are related to the energy performance of a building. The study included a review of research trends for this topic and concluded that passive TES systems with PCMs can contribute to the following:

- Increased indoor thermal comfort due to reduction in diurnal temperature fluctuations
- Improved thermal resistance and heat capacity of the envelope of the building
- Decreased energy demand for heating and cooling
- Utilisation of renewable energy sources such as solar thermal energy
- Reduced cost of operational phase energy
- Reduction of $CO_2$ emissions associated with heating and cooling.

In addition Soares et al. (2013) identified several research gaps and provided recommendations for future work, such as:

- The design of passive TES systems to take advantage of solar thermal energy
- Validation of numerical predictions using appropriate experimental data
- Inclusion of the effects of thermal hysteresis and supercooling phenomena in numerical simulations of solid to liquid phase-change which are discussed presently.

## 2.3 Phase change materials

### 2.3.1 Theory of phase change materials

For practical reasons it is only feasible to use the solid-liquid PCM when incorporating a PCM into a building component. A PCM can be a pure material, a eutectic mixture or a non-eutectic mixture. A eutectic mixture is a particular combination of chemical compounds or elements that will solidify at a lower temperature than any other combination. The temperature at which the eutectic mixture solidifies is known as the eutectic temperature. On a phase diagram the intersection of the eutectic temperature and the eutectic composition gives the eutectic point (Figure 2-5).

A pure substance and a eutectic mixture will both have a constant phase change temperature, $T_e$, however a non-eutectic mixture will change phase within a temperature interval, that is, the melting temperature, $T_m$ and solidification temperature $T_s$ are different, as shown in Figure 2-5.

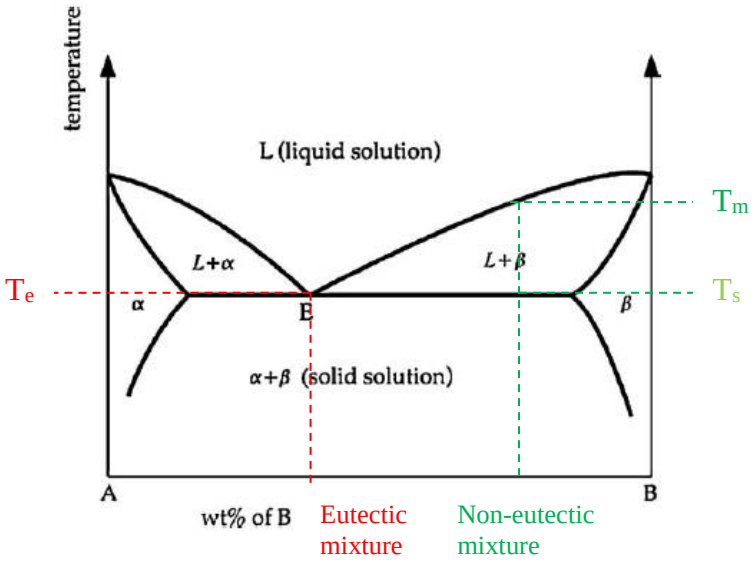


**Figure 2-5 Phase diagram for eutectic mixture of materials $\alpha$ and β - eutectic point E (Kuznik et al., 2011)**

The thermodynamic parameters of a material are temperature, pressure and volume. If the volume of a pure material is fixed then the phase state of the material at any pressure and temperature can be shown on a phase diagram (Figure 2-6).

When using PCMs in building applications, atmospheric pressure can be assumed to be constant. The temperature at which atmospheric pressure coincides with the solid-liquid boundary is known as the fusion (melting) temperature, $T_f$. If $T < T_f$ the material will be solid and if $T > T_f$ the material will be liquid.

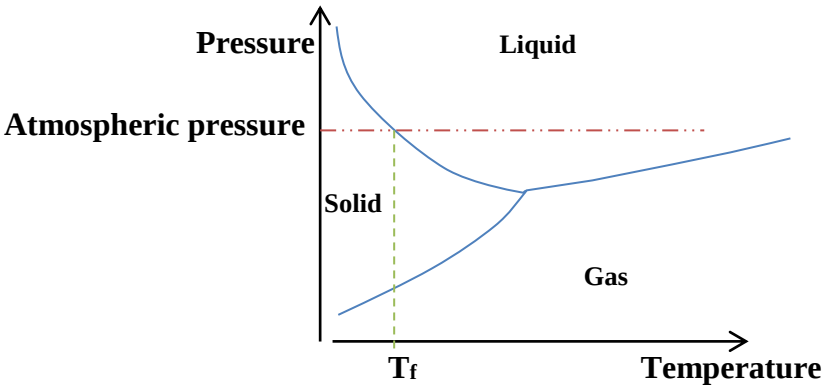


**Figure 2-6 Phase change diagram showing atmospheric pressure (Kuznik et al., 2011)**

If a material is subjected to a temperature change, it will take a period of time for the material to reach thermal equilibrium with the environment. The rate at which the heat is exchanged between the material and its environment is known as the heat flux, q. In Figure 2-7, Kuznik et al. (2011) show the time evolution of temperature and heat flux for a pure material subjected to a stepped temperature change ΔT that causes solidification.

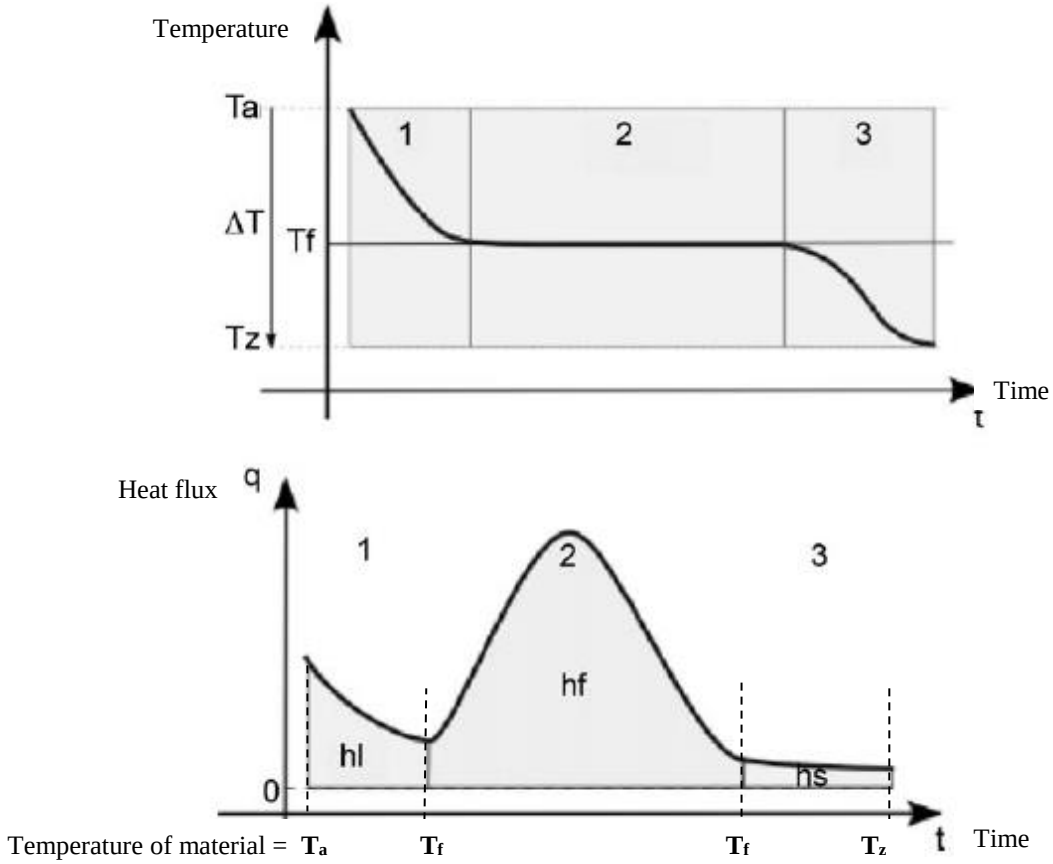


**Figure 2-7 Time evolution of temperature and heat flux for a pure material subjected to a temperature change ΔT (Kuznik et al., 2011)**

There are three stages in the solidification:

1. The liquid releases sensible heat as it cools down to the temperature of fusion. The heat energy released, $h_l$ is given by the area under the heat flux curve and is equal to:

$$h_l = C_{pl}\int_{T_f}^{T_a} dT \qquad (J/kg) \qquad \textbf{(2-12)}$$

   where $C_{pl}$ is the specific heat capacity of the liquid material. The rate at which heat is released reduces as the temperature of the material approaches the temperature of fusion.
2. Latent heat is released from the material as it changes from a liquid to a solid at a constant temperature. The rate at which the latent heat is released increases as the liquid solidifies due to the increasing rate of nucleation. When the solidification process reaches a point at which the proportion of solid material is greater than the proportion of liquid, the rate of heat release reduces due to the reduced nucleation activity.

3. When all the material is solid it continues to cool and releases sensible heat until its temperature is in equilibrium with the temperature of its environment. The heat released, $h_s$, is equal to:

$$h_s = C_{ps}\int_{T_z}^{T_f} dT \qquad (J/kg) \qquad \textbf{(2-13)}$$

where $C_{ps}$ is the specific heat capacity of the solid material. The rate of heat release slows as the temperature difference between the material and the environment reaches equilibrium.

Figure 2-7 denoted a step change in temperature, however a change in temperature can also occur over a period of time hence the heat flux curve will be a function of the rate of change of the external temperature (Figure 2-8).

The characteristic temperatures that describe a heat flux curve are:

- $T_i$ and $T_f$ which are the initial and final temperatures respectively at the beginning and end of the deviation from the sensible heat curve
- $T_p$ is the peak temperature at the maximum heat flux
- $T_o$ and $T_e$ are the temperatures that coincide with the intersection between the tangents drawn at the inflexion points of the curve either side of the maximum heat flux point and the base of the curve, referred to as the onset temperature $T_o$ and the end temperature $T_e$

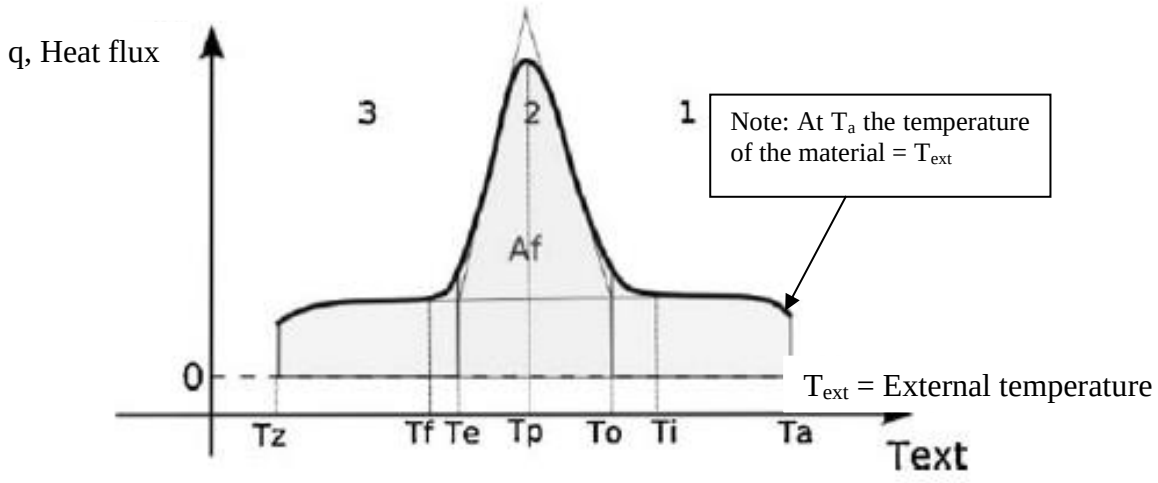


**Figure 2-8 Heat flux curve in response to a change in temperature over time (Kuznik et al., 2011)**

The latent heat of the material is obtained from the area under the curve, $A_f$ and the rate of change of the external temperature, $V_{T,ext}$ and is given by (Kuznik et al., 2011):

$$h_f = \int_{t_1}^{t_2} q(t)dt = \int_{T_e}^{T_o} q(T_{ext}) \frac{\delta t}{\delta T_{ext}} dT_{ext} = A_f / V_{T,ext} \quad \text{(J/kg)} \qquad \textbf{(2-14)}$$

Referring to Figure 2-8, the parameters most commonly used to describe a PCM are $T_p$, that is the temperature coinciding with the peak of the heat flux curve, and $\Delta T = (T_o - T_e)$, that is, the width of the peak (Kuznik et al., 2011).

### 2.3.2 Supercooling and thermal hysteresis

In an ideal situation, the enthalpy-temperature curve should be the same during the reversible melting and solidification cycles. Supercooling and thermal hysteresis are two problematic phenomena that result in a difference in the melting and solidification phase change behaviour which can reduce the effectiveness of PCMs, particularly salt hydrates. Supercooling and hysteresis are similar but distinct phenomena. Figure 2-9 provides simplified diagrams of an enthalpy curve and cooling curve of an PCM material that highlight the difference in the two phenomena (Que et al., 2021).

The solidification of a PCM commences with nucleation, that is, the formation of initial crystals called nuclei. The crystals then propagate in the material to form the solid phase. The nucleation rate of a material is its ability to produce nuclei when the temperature decreases below the fusion temperature, $T_M$ in Figure 2-9. Supercooling can occur during solidification and is caused when the rate of nucleation is slow and hence the material does not solidify at the fusion temperature. The material only starts to solidify at a temperature below the fusion temperature, $T_N$. When solidification does commence, the temperature of the material rises rapidly to the fusion temperature due to the heat energy released by nucleation and hence absorbs a small portion of the latent heat released (Solomon et al., 2013). Solidification continues, following the normal phase change enthalpy curve until all the material is solid. Supercooling is also referred to as the crystalisation driving force, which is the additional energy required to cause a liquid to crystallise (Hua et al., 2023). If supercooling occurs the benefit of the material as a heat storage material is reduced as the heat stored is not released effectively (Dincer and Rosen, 2001).

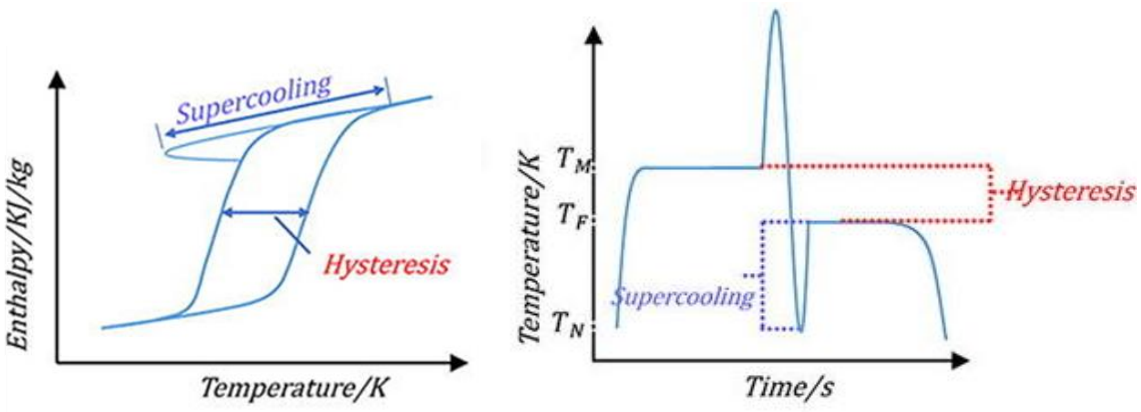


**Figure 2-9 (a) Enthalpy curve and (b) Step cooling curve of PCMs indicating supercooling and hysteresis behaviour (Que et al., 2021)**

Thermal hysteresis behaviour occurs when the melting enthalpy curve is different to the solidification enthalpy curve, that is, there is a difference in temperature between the onset of solidification and the completion of melting of a PCM, hence the melt temperature range is different from the solidification temperature range. Figure 2-10 provides a plot of enthalpy as a function of temperature for an idealised PCM material. When the material is in the solid state and is being heated, the enthalpy is given by the bottom blue curve. As the material passes the melting temperature, it becomes completely liquid. When this material is subsequently cooled in the liquid state, it will follow the red curve, thus the material remains liquid at temperatures below the melting temperature. Once the freezing temperature is reached, the material becomes solid. If the material is then heated again, it will follow the blue curve again. In the completely liquid or completely solid state, the two enthalpy curves overlap. With thermal hysteresis, in the absence of supercooling, there is little difference between the latent heats of solidification and melting.

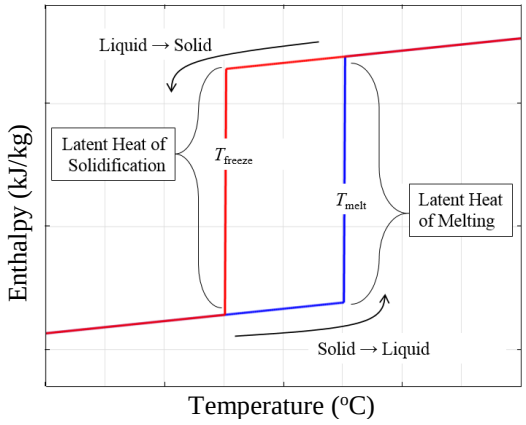


**Figure 2-10 Enthalpy versus temperature for an idealised PCM material (COMSOL Heat Transfer Module User's Guide, 2018)**

Both supercooling and thermal hysteresis behaviour add complexity to the development of numerical models for simulating the thermal behaviour of PCMs. A number of researchers have carried out experimental work and modelling studies to gain an insight into the impact of supercooling and hysteresis in simulation models (Que et al., 2021, Khan et al., 2020, Kuznik et al., 2016, Mandilaras et al., 2015). All these studies concluded that the hysteresis effect must be considered in modelling to achieve accurate prediction of the thermal behaviour of PCMs.

### 2.3.3 Classification of phase change materials

PCMs are broadly classified into three categories based on their chemical composition (Lamrani et al., 2021), organic, inorganic and eutectics. These categories are subdivided further based on the chemical components forming the PCM, as shown in Figure 2-11. These are discussed in some detail here.

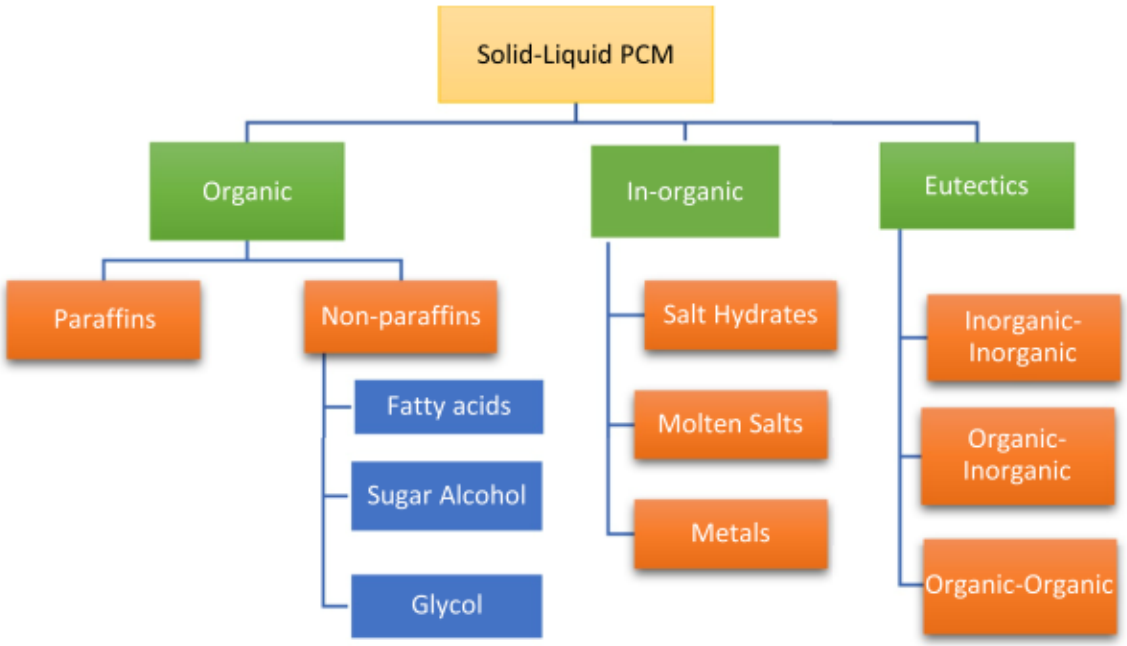


**Figure 2-11 Generalised categories of PCMs (Zeinelabdein et al., 2018)**

#### *2.3.3.1 Organic phase change materials*

Due to a melting temperature range of 0 – 150 $^{o}$C, organic PCMs are the most commonly used in thermal storage applications (Cabeza et al., 2011). The chemical properties of organic PCMs display good stability, high latent heat capacity, they are non-corrosive, non-toxic and do not undergo supercooling during solidification as they have a good nucleation rate (Kalnæs and Jelle, 2015). Organic PCMs are further divided into paraffin and non-paraffin types.

**Paraffin**

Paraffin wax (PAR) is a hydrocarbon with a chemical structure $C_nH_{2n+2}$. Paraffins typically have melting temperatures ranging between 20°C and 70°C. The higher the number of carbon atoms in the chain the higher the melting temperature (Sharma et al., 2009). Paraffins are the most widely available organic PCM, however they have some limitations such as low thermal conductivity (circa 0.2W/mK), high cost and they undergo volume change during phase change (Souayfane et al., 2016).

**Non-Paraffin**

Non-paraffin is the largest group of PCMs and includes esters, alcohols and glycols, however the majority of this group are fatty acids. The melting point of the fatty acids is similar to PAR and varies from 40 -150 °C. Fatty acids also have good melting and freezing properties however they are more expensive than PAR (Ben Romdhane et al., 2020).

The melting temperature range of fatty acids is outside the suitable range for thermal energy storage applications in buildings. However, fatty acids can be combined to form a eutectic with a lower melting temperature, without compromising the stability of the PCM (He et al., 2013). Yuan et al. (2014) carried out a comprehensive review of fatty acids as PCMs in energy storage systems which demonstrated how particular melt temperatures of fatty acid eutectics can be achieved by varying the mass ratio of the individual components. The study concluded that fatty acid eutectics displayed good thermal reliability, that is, the thermal properties of the eutectics did not change with repeated freeze/melt cycles.

Table 2-2 shows a summary of commonly used organic PCMs with melting temperatures that make them suitable for use in a building space heating application.

**Table 2-2 Organic PCMs with potential for use in space heating applications (Tyagi and Buddhi, 2007)**

| Compound | Melting point (°C) | Heat of fusion (kJ/kg) |
|---|---|---|
| Butyl stearate | 19 | 140 |
| Paraffin $C_{16}$–$C_{18}$ | 20–22 | 152 |
| Capric–Lauric acid | 21 | 143 |
| Dimethyl sabacate | 21 | 120 |
| Polyglycol E 600 | 22 | 127.2 |
| Paraffin $C_{13}$–$C_{24}$ | 22–24 | 189 |
| (34% Mistiric acid + 66% Capric acid) | 24 | 147.7 |
| 1-Dodecanol | 26 | 200 |
| Paraffin $C_{18}$ (45–55%) | 28 | 244 |
| Vinyl stearate | 27–29 | 122 |
| Capric acid | 32 | 152.7 |

*2.3.3.2 Inorganic*

Inorganic PCMs are salt hydrates and provide melting temperatures between 100 $^{o}$C and 1000 $^{o}$C. Salt hydrates are alloys of inorganic salts and water. They have high latent heats per unit mass and volume. They also have high conductivity, almost double that of paraffin (Lin et al., 2018). They are non-flammable and inexpensive relative to organic PCMs. However salt hydrates have particular problems of corrosion, incongruent melting and supercooling. At their melting point the salt hydrates melt to a salt hydrate with fewer moles of water. Incongruent melting is caused when the water that is released during the crystallisation is insufficient to dissolve all the solid phase that is present, so some solid material remains and the energy absorbed is limited. Also salt hydrates are susceptible to supercooling as described in Section 2.3.2, which reduces the efficiency of the heat transfer (Akeiber et al., 2016).

Table 2-3 shows a summary of commonly used inorganic PCMs with melting temperatures that makes them suitable for use in a building space heating application.

**Table 2-3 Inorganic PCMs with potential for use in space heating applications (Tyagi and Buddhi, 2007)**

| Compound | Melting point (°C) | Heat of fusion (kJ/kg) |
|---|---|---|
| $KF \cdot 4H_2O$ | 18.5 | 231 |
| $Mn(No_3)_2 \cdot 6H_2O$ | 25.8 | 125.9 |
| $CaCl_2 \cdot 6H_2O$ | 29 | 190.8 |
| $LiNO_3 \cdot 3H_2O$ | 30 | 296 |
| $Na_2SO_4 \cdot 10H_2O$ | 32 | 251 |

*2.3.3.3 Eutectics*

As described in Section 2.3.1 a eutectic mixture is a combination of chemical compounds or elements that at a particular combination will solidify at a lower temperature than any other combination. They can be inorganic-inorganic mixtures, organic-inorganic mixtures or organic-organic mixtures. Eutectics nearly always melt and freeze without segregation. On melting both components liquefy simultaneously hence eutectics do not display supercooling or incongruent melting. A particular benefit of eutectics is that their melting points can be adjusted by combining different weight percentage of components (Atinafu et al., 2018).

Table 2-4 shows a summary of commonly used eutectics with melting temperatures that make them suitable for use in a building space heating application.

**Table 2-4 Eutectics with potential for use in space heating applications (Tyagi and Buddhi, 2007)**

| Compound | Melting temperature (°C) | Heat of fusion (kJ/kg) |
|---|---|---|
| 66.6% $CaCl_2 \cdot 6H_2O + 33.3\%$ $Mgcl_2 \cdot 6H_2O$ | 25 | 127 |
| 48% $CaCl_2 + 4.3\%$ $NaCl + 0.4\%$ $KCl + 47.3\%$ $H_2O$ | 26.8 | 188 |
| 47% $Ca(NO_3)_2 \cdot 4H_2O + 53\%$ $Mg(NO_3)_2 \cdot 6H_2O$ | 30 | 136 |
| 60% $Na(CH_3COO) \cdot 3H_2O + 40\%$ $CO(NH_2)_2$ | 30 | 200.5 |

Pasupathy et al. (2008) summarised the advantages and disadvantages of each category of PCM as shown in Table 2-5. As this study is focusing on reducing the overheating effects in a building, the primary requirements for the PCM are:

- Fusion temperature around the human comfort temperature 19°C and 24°C
- Chemical compatibility with concrete, steel and timber (formwork)
- Low volume change during phase change

From the summary review of the various types of PCMs, an organic PCM can be deemed as the most suitable for use with a construction material. Organic PCMs, both paraffin and non-paraffin types, have been successfully combined with concrete in previous research which is discussed in further detail in Section 2.4.

**Table 2-5 Advantages and disadvantages of class of PCM (Pasupathy et al., 2008)**

| Class of PCM | Advantages | Disadvantages |
|---|---|---|
| **Organics** | 1.Availability in a large temperature range<br>2.Freeze without much supercooling<br>3.Ability to melt congruently<br>4.Self nucleating properties<br>5.Compatibility with conventional construction materials<br>6.No segregation<br>7.Chemically stable<br>8.High heat of fusion<br>9.Safe and non-reactive<br>10. Recyclable | 1. Low conductivity in their solid state<br>2. High heat transfer rates are required during the freezing cycle<br>3.Volumetric latent heat storage capacity is low<br>4.Flammable<br>5.Due to cost considerations only technical grade paraffin may be used which are essentially paraffin mixtures and are completely refined of oil |
| **Inorganics** | 1.High volumetric latent heat storage capacity<br>2.Low cost and easy availability<br>3.Sharp melting point<br>4.High thermal conductivity<br>5.High heat of fusion<br>6.Low volume change<br>7.Non-flammable | 1.Change of volume is very high<br>2.Supercooling is a major problem in solid-liquid transition<br>3.Nucleating agents are needed and they often become imperative after repeated cycling |
| **Eutectics** | 1.Eutectics have a sharp melting point similar to pure substance<br>2.Volumetric storage density is slightly above organic compounds | 1.Only limited data is available on thermos-physical properties as the use of these materials is new to thermal storage application |

A number of researchers (Eddhahak-Ouni et al., 2014, Fenollera et al., 2013, Baetens et al., 2010, Hunger et al., 2009, Cabeza et al., 2007) have carried out thermal energy storage studies that combined paraffin with concrete. The paraffin is micro-encapsulated in thin polymer shells which are then added to fresh concrete towards the end of the mixing process. The microcapsules provide a large surface area for heat transfer and also resist volume change during the phase transition. However paraffin has a relatively low conductivity and the capsules also adversely affect the mechanical properties of the concrete (Ling and Poon, 2013).

Cabeza et al. (2007) constructed two full size cubicles with windows incorporated in each wall, one with ordinary concrete and the other with a concrete which contained 5 % by weight micro-encapsulated paraffin. The study successfully demonstrated an increase in thermal storage capacity and increase in thermal inertia for the PCM-concrete composite. Generally from the review of studies that considered PCM-concrete composites, paraffin appears to be the most common choice of PCM as it is inactive in an alkaline medium, chemically stable and relatively inexpensive.

Non-paraffins have also been combined with concrete to create a thermal storage system. Yuan et al. (2014) carried out an extensive literature review of studies in which fatty acids were used as PCMs in thermal energy storage systems. Many of the studies reviewed successfully combined fatty acids with both concrete and gypsum for use in buildings. A number of studies used eutectic mixtures of fatty acids and concluded that they have better thermal reliability than the corresponding fatty acids.

Zhang et al. (2004) carried out a study to assess the suitability of using a fatty acid called Butyl Stearate (BS) with concrete. BS was selected as it is an industrial product and hence it is less expensive than the other alternatives. The BS was vacuum impregnated into different types of porous aggregate which was then added to the concrete mix. The thermal energy storage capacity of the concrete samples were assessed using differential scanning calorimeter tests and it was found that the energy absorbed by the PCM-concrete composite samples increased almost linearly with the volume fraction of PCM in the concrete.

Cellat et al. (2015) combined eutectic mixtures of bio-based fatty acids - which are readily found in nature, such as capric acid (CA), myristic acid (MA) and lauric acid (LA) - with concrete. Bio-based PCMs are reported to be significantly less flammable than paraffins (Jeong et al., 2013) and also have the benefit of being derived from vegetables and animals as opposed

to fossil fuels. Cellat et al. (2015) concluded that CA:LA and CA:MA eutectics with a 75:25 mass ratio had a melt temperature range and latent heat capacity of 22 - 25 $^{o}$C and 135 - 140J/g respectively, which is within the optimum range for a space heating application as found by Ascione et al. (2014) and Waqas and Ud Din (2013). These eutectics are also thermally stable in temperatures up to 120 $^{o}$C and are chemically compatible with concrete.

### 2.3.4 PCM characterisation

To achieve an accurate assessment of the performance of a thermal energy storage system that utilises PCMs, it is essential to have accurate values for the thermo-physical properties of the phase change behaviour. Often properties provided on product data sheets lack the required precision and can be over optimistic as reported by a number of researchers (Soares et al., 2023, Memon, 2014, Tyagi and Buddhi, 2007) therefore reliable characterisation of PCMs is essential, particularly for successful numerical simulations. Thermal analysis of PCMs is especially challenging due to the change in phase in response to temperature variation. Additionally, conventional methods for thermal characterisation are typically designed for assessing small samples of homogenous, pure materials that do not display supercooling, hysteresis or variation in thermal conductivity with temperature or temperature changes with solid to liquid phase transitions. As most PCMs that are commercially available are not 100% pure, because pure substances would be prohibitively expensive, the measurement uncertainty associated with characterising PCMs is an actively researched area. Cabeza et al. (2015) conducted a review of conventional and unconventional technologies available for the thermo-physical characterisation of PCMs. The study described the various methods and equipment used to evaluate the primary properties of the PCMs, including specific heat, latent heat, phase change temperature range, the enthalpy-temperature curve, as well as thermal conductivity and diffusivity. Presently the most commonly used techniques for determining the thermo-physical properties of PCMs are Differential Scanning Calorimetry (DSC) and the T-history method, as now described.

#### *2.3.4.1 Differential Scanning Calorimetry (DSC)*

Differential Scanning Calorimetry is the most prominent method use for characterisation of PCMs. Kuznik et al. (2011) provided an explicit explanation of the test name, Differential Scanning Calorimetry, as follows:

- *Calorimetry:* is the measurement of the quantity of heat that is absorbed or released by a body when it changes temperature

- *Differential:* the test utilises two different samples in identical conditions. The thermal reaction of the sample that is being characterised is obtained by comparison with the thermal reaction of the reference sample of known properties
- *Scanning:* the thermal excitation is a ramp of temperature. The rate of temperature change applied is a critical factor in achieving accurate results.

In DSC tests the difference in the amount of heat required to increase the temperature of a sample and a reference sample is measured as a function of temperature (Hohne et al., 2003). The test uses a scanning mode of heating and cooling segments which cause the sample to change phase. During the phase transition more or less heat will be required by the PCM compared to the reference material to maintain both samples at the same temperature. For example, during melting more heat will flow to the PCM sample to increase its temperature at the same rate as the reference material due to the additional latent heat required by the phase transition. In this way the DSC test determines the enthalpy- temperature relationship.

There are different scanning modes that can be used in DSC testing, however the two most commonly applied are the 'dynamic' method, which applies a constant heating rate and the 'stepped' method which applies a heat rate which varies in equal steps. Figure 2-12 (a) and (b) shows typical heat flow and temperature evolution for a dynamic DSC and a stepped DSC respectively, carried out on the same material (Barreneche et al., 2013). In Figure 2-12 (a) the peaks indicate a strong thermal effect at corresponding temperatures. In Figure 2-12 (b) the different peaks indicate different amounts of heat transferred in the respective temperature interval.

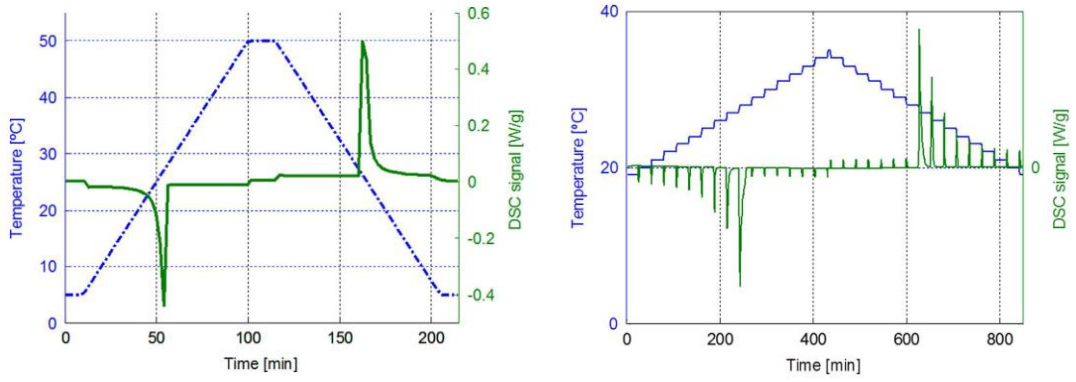


(a) (b)

**Figure 2-12 Heat flow and temperature evolution for a (a) dynamic and (b) stepped DSC test (Barreneche et al., 2013)**

The dynamic scanning mode is the most commonly used for the determination of melting enthalpies. In heat storage applications both latent and sensible heat capacities are of interest

hence sensitivity to small signals in the test is necessary. The DSC software provides the heat flux as a function of temperature and the enthalpy is determined by integration of the heat flux curve.

In the stepped scanning mode, small heating ramps are applied followed by periods during which the temperature of the samples is maintained constant to allow each sample to reach thermal equilibrium. The size of the steps must be long enough to ensure thermal equilibrium is reached in each sample. From the sample heat flux signal the enthalpy is determined by integration of every peak.

From a review of literature involving PCMs it can be noted that the dynamic method is the most widely used. Castellón et al. (2008), in a study that compared the accuracy of both scanning modes, highlighted that the dynamic scanning mode can lead to errors in the resulting enthalpy-temperature relationship due to the use of heating rates that are too high which leads to a temperature gradient across the sample. This effect is illustrated in Figure 2-13 (Castellón et al., 2008).

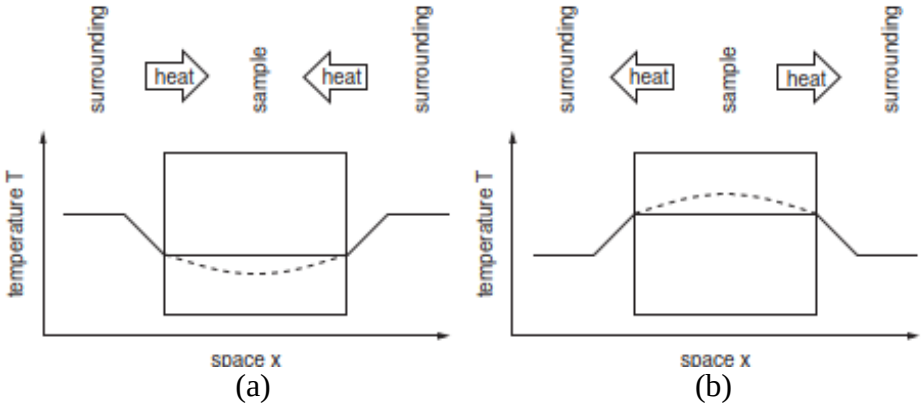


**Figure 2-13 Diagram showing assumed (solid line) and actual (dashed line) temperatures of sample during (a) heating (b) and cooling (Castellón et al., 2008)**

When calculating the thermal effect, the temperature of the material is assumed to be the same throughout the sample, however if the heat rate of the test is too high a temperature gradient can occur across the sample. This effect is also influenced by the thermal conductivity and mass of the sample. This problem is compounded for PCM samples due to their low conductivity and high heat capacity. A smaller sample size and lower heating rate result in more accurate temperature results in dynamic DSC tests, however they can also lead to lower precision in the enthalpy measurement. The heating rate does not influence the accuracy of the stepped scanning method as the sample is given time to reach equilibrium at each step.

Barreneche et al. (2013) carried out a study to determine the most appropriate scanning mode to use in a DSC test for both organic and inorganic types of PCM. The authors carried out DSC tests using both modes and varying heat rates on paraffin and a salt hydrate. The investigation highlighted the additional time in the stepped scanning mode due to the fact that the sample cannot be analysed immediately after each cycle. It also involves increased complexity in evaluating the curves which leads to longer analysis time. The study concluded that a slow dynamic mode is recommended when analysing salt hydrates with DSC. No significant differences between the accuracy of the results from the two DSC modes were observed for paraffin.

Figure 2-14 shows a typical heat flow curve output from a DSC test (Memon, 2014). The key temperature information to be derived from the curve is the temperature at the onset of melting and the temperature at completion of melting, together with the temperature coinciding with the maximum heat flow, which is referred to as the peak melt temperature of the PCM. The onset and final temperatures are the temperatures coinciding at the intersection of the extrapolation of the baseline and the tangents to the DSC curve drawn at the inflexion points.

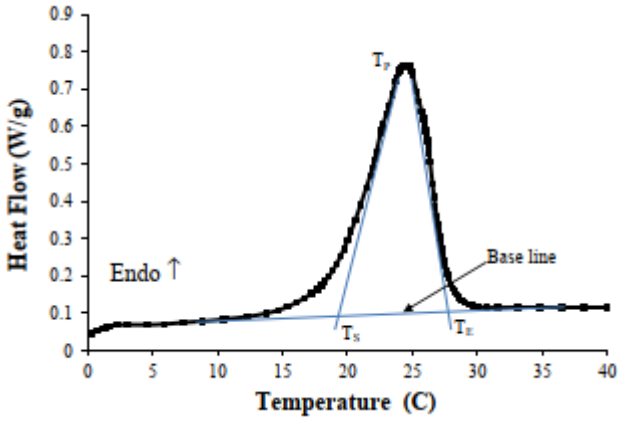


**Figure 2-14 Typical heat flow curve from a DSC test (Memon, 2014)**

The peak temperature is the temperature coinciding with the peak point of the heat flow curve. The thermal heat stored in a unit weight of PCM is obtained by dividing the integrated area between the baseline and the DSC curve with a temperature rising rate in the DSC rate. These values are calculated automatically by the DSC equipment software.

The main limitation of DSC testing is the conditions the sample must fulfil, that is, it should be small and homogeneous. The recommended sample weight is between 5 and 20mg (Barreneche et al., 2013). This is a limitation because there are many samples that cannot achieve

homogeneous conditions at such low weights as they are a composite material or a mixture of different components.

*2.3.4.2 T-history method*

For testing of larger samples Yinping et al. (1999) proposed the T-History method which involves comparing temperature-time curves of a PCM material with a temperature-time curve of a reference material. Several samples can be tested at the same time and the test also provides information on thermal conductivity of the sample. In the T-history test, the samples and reference material are placed in separate test tubes. The temperature of each sample is measured with a thermocouple placed at the centre of the tube. A schematic of the test set-up is provided in Figure 2-15 (Yinping et al., 1999).

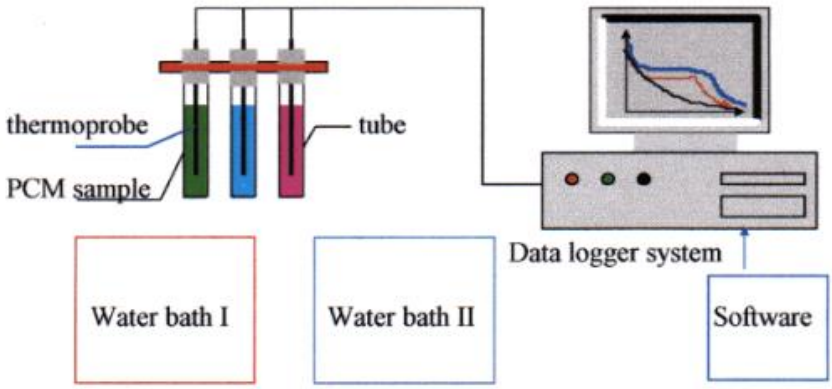


**Figure 2-15 Schematic of T-history test set-up (Yinping et al., 1999)**

At the start of the test all samples are in a liquid phase. The tubes are immersed into a controlled environment, usually water, in which the temperature is regulated and is lower than the fusion temperature of the PCM samples. The temperature within each tube is monitored against time. Figure 2-16 shows a typical T-history temperature curve (Marin et al., 2003). There are three stages identified from the temperature curve; the cooling of the liquid phase, the solidification of the PCM and the cooling of the solid phase. The latent heat of the sample and the specific heat capacity of the solid and liquid phases are obtained by calculation of the areas between the sample temperature curve and the temperature curve for the environment in which the tubes are placed (I1, I2 and I3, Figure 2-16). The thermal conductivity is derived by using an inverse method on the total solidification time. Marin et al. (2003) improved the T-history method to enable the enthalpy-temperature curves to be obtained from the test which also allowed any supercooling or hysteresis behaviour to be observed.

Cabeza et al. (2015) proposed the advantages of the T-history method compared to the DSC as follows:

- Larger sample mass can be tested as the test is not sensitive to a particular heating rate
- Supercooling and thermal hysteresis behaviour can be observed and studied

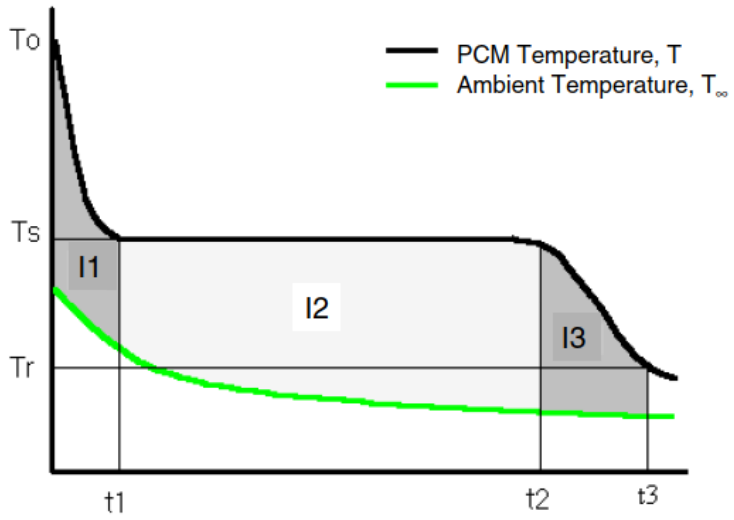


**Figure 2-16 Typical T-history temperature curve (Marin et al., 2003)**

## 2.4 Methods of incorporating PCMs into concrete

Navarro et al. (2016b) described six methods of incorporating PCMs into construction materials, namely, immersion, direct incorporation, vacuum impregnation, encapsulation, shape-stabilisation and form-stable composites. These methods are now described but with a focus on the three predominant methods that are used for incorporating PCMs into concrete, immersion, vacuum impregnation and encapsulation.

### 2.4.1 Immersion

In the immersion technique porous construction elements (concrete blocks, gypsum wall board, porous aggregate, timber) are immersed in a container that is filled with a liquid PCM. The PCM is absorbed by capillary action. The time required for effective absorption of the liquid PCM depends on three criteria; the absorption capacity of the construction element, the temperature of the PCM and the viscosity of the PCM. The immersion process normally takes a number of hours (Ling and Poon, 2013).

Hawes and Feldman (1992) studied the absorptivity of PCMs into autoclaved concrete blocks and regular concrete blocks at a temperature of 80 $^{o}$C. The time required to fully soak the autoclaved concrete blocks with butyl stearate and paraffin was between 40 mins and 1 hour. The regular concrete blocks required an immersion time of 6 hours to be fully soaked with

paraffin. The study concluded that the autoclaved blocks were a better choice for immersion due to their higher porosity and also the higher the temperature of the PCM the higher the rate of absorption.

Lee et al. (2000) also incorporated butyl stearate and paraffin into autoclaved and regular concrete blocks. However they observed that some of the paraffin leaked out during the heating cycles resulting in a thin film of paraffin remaining on the surface of the regular concrete blocks.

Bentz and Turpin (2007) investigated a number of applications for PCM/concrete applications. One of the methods that they adopted to incorporate the PCM into the concrete was to immerse a porous aggregate (expanded shale, 3mm dia.) in liquid paraffin. The aggregate was first dried at 40 $^{o}$C and then soaked in the liquid paraffin for a minimum of 24 hours. They obtained an absorption of 13.8 % by mass of dry aggregate. This PCM aggregate was then used in a concrete mix for a number of applications. An interesting finding of their study was that the heat transfer between the concrete matrix and the PCM was better in the concrete samples that were made with the PCM aggregate compared to the samples made by direct mixing of the PCM into the fresh concrete (as described in Section 2.4.2). Paraffin has a low conductivity, however embedding it in a more thermally conductive material enhanced the heat transfer between the PCM and concrete matrix.

Aguayo et al. (2017) investigated the influence of pore structure of four different types of lightweight aggregates (pumice, perlite, expanded shale/clay, and expanded slate) on the thermal conductivity of the combined PCM composite. The study concluded that porosity and pore diameter can affect the PCM absorption capacity of these materials and hence the thermal conductivity of the composite. The incorporation of 5 % of PCMs by total volume of the cementitious system reduces the composite thermal conductivity by more than 10 %. Kheradmand et al. (2016) and Kheradmand et al. (2015) indicate that the aggregate size can impact the PCM absorption capacity as their studies concluded that the absorption capacity of the smaller aggregates was higher.

Due to the high density of regular concrete, immersion is not considered to be an effective method of incorporating a PCM into concrete in this study. As Bentz and Turpin (2007) demonstrated, the immersion technique could be used to impregnate porous aggregate with a PCM which can then be used in the concrete mix, however the vacuum impregnation method as described in Section 2.4.3 is considered to be a more effective method of incorporation.

### 2.4.2 Direct incorporation

Direct incorporation is a relatively simple method in which the liquid or powder PCM is added directly to a wet mix of the construction material, for example, concrete or mortar, during production. Cunha et al. (2016) incorporated free PCM in mortar and evaluated its thermal behaviour at different temperatures, in order to observe the PCM behaviour in both liquid and solid states. The authors concluded that the incorporation of non-encapsulated PCM caused a decrease in the amount of water added to the mixture, in order to maintain the same workability. However, the ratio liquid material/binder of the mortars is similar. The study also concluded that the incorporation of non-encapsulated PCM did not cause significant changes in the flexural and compressive strengths of the mortars. However more extensive research in this area is required prior to acceptance of this conclusion.

To successfully use this method with concrete it is important to ensure that the PCM does not:

i. interfere with the hydration process
ii. adversely affect the bond between the aggregate and the cement
iii. adversely affect the mechanical properties of the concrete
iv. adversely affect the durability of the end product.

There appears to be a scarcity of research studies in which a PCM was directly added to concrete without being encapsulated in some form prior to incorporation. When the PCM is directly added to the concrete mix there is no barrier between the two materials and hence there is a higher risk of the PCM having an adverse effect on the concrete properties. For this reason direct mixing will not be used as a method for incorporating a PCM into concrete in this study.

### 2.4.3 Vacuum impregnation

The vacuum impregnation method involves firstly evacuating the air from porous aggregates using a vacuum pump. The porous aggregates are then soaked in a liquid PCM under vacuum. Finally the PCM soaked aggregate is added to the concrete mix. Figure 2-17 provides a schematic of the vacuum impregnation set up by Zhang et al. (2005).

Zhang et al. (2004) studied the ability of different types of porous aggregate to absorb butyl stearate. The three aggregate types investigated were expanded clay (C1), normal clay (C2) and expanded shale (S). The evacuation process for each aggregate took about 30 minutes at a vacuum pressure of 88.1kPa. Before the vacuum pump was stopped the valve was opened to allow the PCM cover the aggregate. The vacuum pump was then switched off and air was

allowed to enter the flask to drive the butyl stearate into the pores of the aggregate. After about 30 minutes the aggregates were removed from the flask. Table 2-6 shows the PCM absorbing capacity for the porous aggregates.

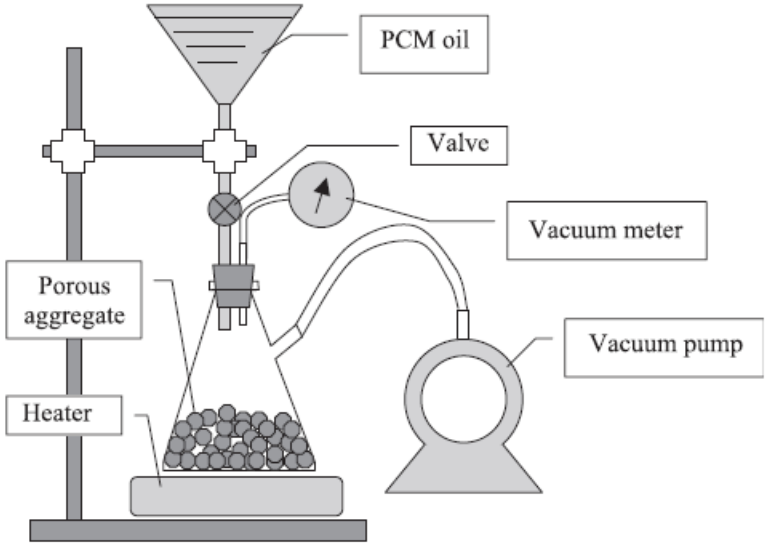


**Figure 2-17 Schematic of the vacuum impregnation set up by Zhang et al. (2004).**

**Table 2-6. PCM absorbing capacity for the porous aggregates (Zhang et al., 2005)**

| Notation | Density ($g/cm^3$) | Porosity (%) (MIP) | Water-absorbing capacity by simple immersion (%) | Water-absorbing capacity by vacuum impregnation (%) | PCM-absorbing capacity (ml) per 1 g of porous aggregate |
|---|---|---|---|---|---|
| C1 | 0.76 | 75.6 | 11.0 | 72.5 | 0.876 |
| C2 | 1.25 | 41.9 | 5.9 | 42.5 | 0.176 |
| *S* | 1.39 | 33.8 | 4.1 | 15.0 | 0.081 |

It can be seen that the porous structure of the aggregate affects the volume of PCM that is absorbed. These aggregates were subsequently used to make concrete samples and it was shown, as would be expected, that the heat storage capacity of the PCM concrete composite sample during phase change increased linearly with the volume fraction of the PCM in concrete, noting that the presence of lightweight aggregate also has an influence on the heat storage capacity.

In a later study, Zhang et al. (2005) carried out similar experiments on expanded perlite (PE), two types of expanded clay (SZ and SL) and expanded fly ash granules (FL) and they used a range of organic PCMs all of which had a viscosity between 2 and 10 MPa. They used both the

vacuum impregnation method and immersion method to incorporate the PCM into the aggregates. For the vacuum impregnation method it was found that an immersion time of 30 minutes at a temperature of 30 $^{o}$C above the melting temperature of the PCM optimises the absorption of PCM. In the natural immersion method the aggregates were soaked for 1 hour. A comparison of absorption volumes for each method is summarised in Figure 2-18 from which it can be concluded that the vacuum impregnation method is a significantly more effective method for forming a lightweight aggregate-PCM composite.

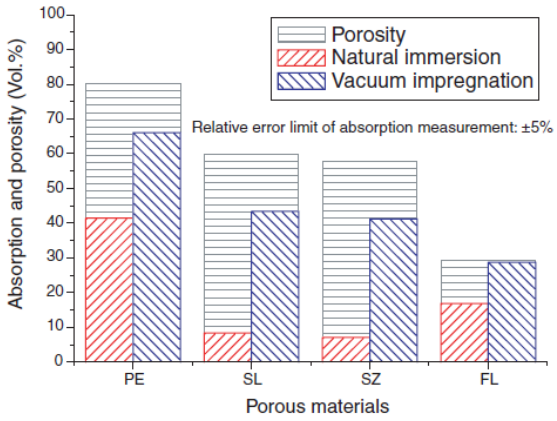


**Figure 2-18 Comparison between vacuum impregnation and natural immersion (Zhang et al., 2005)**

More recently Sani et al. (2021) assessed the feasibility of impregnation of four different types of PCMs into two different types of lightweight aggregates (LWAs) – fly ash (FA) and glass aggregates (GA)- using both simple immersion and vacuum impregnation. To prevent leakage and avoid coalescing of the aggregates, the PCM impregnated LWAs were coated with a primer epoxy resin, followed by graphite powder prior to adding to the concrete mix. In the simple immersion method, the FAs and GAs had a maximum percentage of absorption of 5.8 % and 12.9 %, respectively, whereas in vacuum impregnation, a maximum percentage of about 18.6 % and 30.7 % were observed for the FAs and GAs. PCM leakage was prevented by sealing the PCM impregnated LWAs with primer epoxy resin solution.

### 2.4.4 Encapsulation of phase change materials

PCMs can be encapsulated prior to incorporating them into construction elements. Regin et al. (2008) state four primary functions of the containment capsule:

i. Meet the requirements of strength, flexibility, corrosion resistance and thermal stability
ii. Act as a barrier to protect the PCM from harmful interaction with the environment
iii. Provide sufficient surface for heat transfer
iv. Provide structural stability and easy handling.

There are two forms of encapsulation, macro-encapsulation and micro-encapsulation.

*2.4.4.1 Macro-encapsulation*

In macro-encapsulation the PCMs are packaged into containers such as tubes, spheres or panels (> 10mm in diameter/thickness (Cabeza et al., 2011)), which are then incorporated into building elements (Figure 2-19).

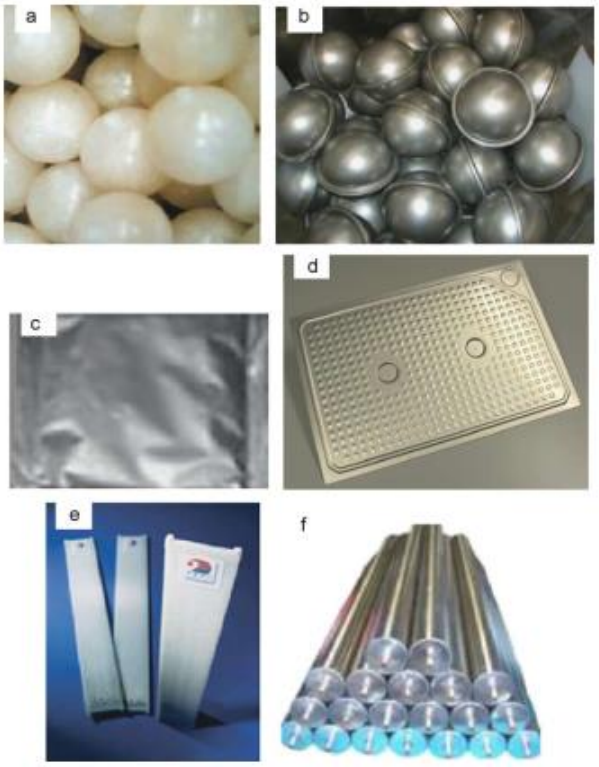


**Figure 2-19 (a) Metal ball encapsulate (b) Spherical PCM balls (c) PCM in aluminum (d) PCM in aluminum panels (e) PCM in Polypropylene flat panel (f) PCM tube encapsulation (Kenisarin and Mahkamov, 2016, Raj and Velraj, 2010)**

In this technique it is possible to incorporate a significant amount of PCM, that is, several litres, into a single container. The advantages of this technique are the easy transport and handling, the possibility of the encapsulation being designed specifically for the intended application and better compatibility with the material and the mitigation of issues with volume change of the PCM during phase change. The thermal and geometrical parameters of the container have a direct influence on the heat transfer characteristics of the PCM and they affect the melt time and performance of the PCM element. The capsule should be designed to optimise the heat transfer rate and also to eliminate leakage, corrosion and problems of change in volume of the PCM (Soares et al., 2013). Another advantage of this technique is that the PCM is not mixed in with the construction materials (concrete, mortar etc) so it does not interfere with their mechanical properties.

Previous research with macro-encapsulation failed due to poor conductivity of the PCM. When the heat energy is being released from the PCM capsule it solidifies around the edges of the capsule and prevents effective heat transfer (Khudhair and Farid, 2004). Also the heat transfer from the PCM is limited by the surface area of the capsules and hence it can be difficult to achieve sufficient area for the required heat transfer.

However more recent research carried out using reduced scale experimental procedures (Young et al., 2018, Marani and Madhkhan, 2018) concluded that including macro-encapsulted PCMs in a wall element of a building has good potential for improving the energy performance of the building. Also, several numerical investigations have been conducted to assess the effect of including macroencapsulated PCM components on the energy consumption of buildings. Shi et al. (2014) incorporated steel containers of PCMs in concrete sandwich panel walls. Their results indicated that integrating a PCM layer into the walls of a model room reduced the maximum indoor temperature and increased the minimum indoor temperature. Thus, the diurnal indoor temperature variations were significantly flattened.

Navarro et al. (2015) examined the thermal performance of PCM macro-capsules in a hollow core concrete slab. It was concluded that the proposed PCM-concrete slab could perform the charge/discharge process of PCM in almost 70% of summer and winter days. Royon et al. (2014) used a PCM-polymer composite to fill the cavity of hollow core slabs in order to provide TES. Their results indicate that PCM incorporation would regulate the indoor temperature and such a floor system could perform as a passive thermal conditioner during hot days. In a different application, Farnam et al. (2017) used a paraffin oil macro-encapsulated in metal pipes and embedded in concrete pavement slabs. Their results demonstrated the feasibility of using PCMs to prevent the build-up of melt ice and snow on concrete pavements by discharging the heat retrieved during the warmer stage of the day.

Figure 2-20 provides a schematic of some of the macro-encapsulation techniques employed in recent research, (Marani and Nehdi, 2019). Although research has demonstrated the potential benefits of these applications there are some practical disadvantages of using macro-encapsulated PCMs in buildings. There is a risk that the capsules could get damaged during the use of the building, for example, drilling nails into walls, and also there is additional work required on site to integrate the capsules into the structure. Also, the capsule replaces a certain volume of structural material so the size of structural elements may need to be increased and

the location of the capsules must be carefully co-ordinated with the structural design of the building.

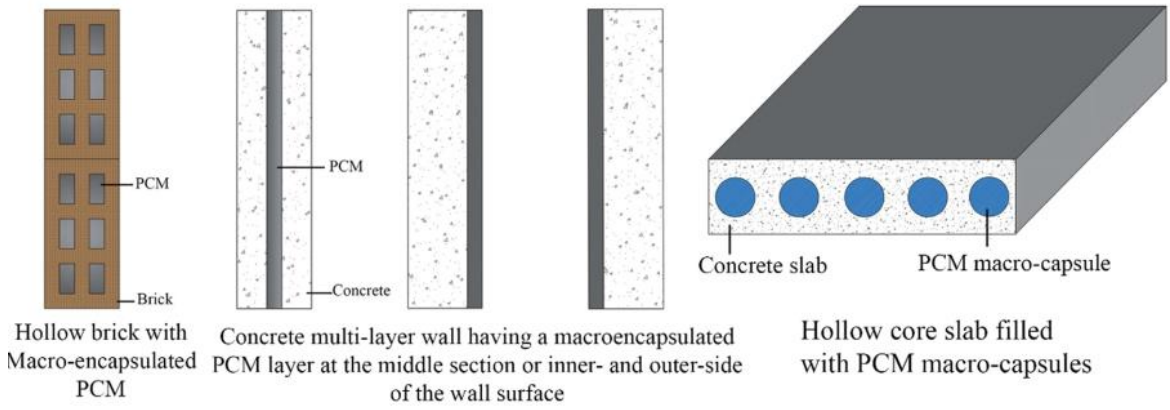


**Figure 2-20 Schematic of PCM macro-encapsulated wall and floor configuration (Marani and Nehdi, 2019)**

*2.4.4.2 Micro-encapsulation*

Walls and floors of buildings provide large surface areas to facilitate heat transfer. The most widely used method for incorporating PCMs into construction materials is micro-encapsulation, where small PCM particles (1μm to 1000μm) are encapsulated in a thin solid shell which is made from natural and synthetic polymers. These microcapsules can then be directly added to the construction material, for example, concrete or plaster, during the mixing process. This method facilitates the provision of a relatively large surface area of PCM throughout the construction material and hence it has the advantage of a high heat transfer rate per unit volume. Other advantages are that the capsules prevent leakage and resist volume change during phase change. They also have improved chemical stability and thermal reliability as phase separation during transition is limited to microscopic distances (Alkan et al., 2009). However the microcapsules can affect the mechanical properties of concrete and they are also relatively expensive (Memon, 2014).

It is important that the capsule itself is physically and chemically stable within the concrete matrix. Various studies highlighted evidence of damaged capsules within the hardened PCM-concrete composite using SEM images (Aguayo et al., 2016, Lecompte et al., 2015). The capsule needs to be hard and durable to avoid being damaged during the concrete mixing and casting process. Tyagi et al. (2011) discussed the use of zeolite and zeocarbon that some researchers have used for reinforcing microcapsules to enable them to withstand high friction and impact during the concrete mixing process. Some researchers (Hunger et al., 2009) suggested that to reduce the occurrence of mechanical damage of PCM microcapsules during the mixing process, it should be added to the fresh concrete as late as possible. More recently,

researchers have produced more resilient PCM additives by using an emulsion polymerization technique (Stritih et al., 2018, D'Alessandro et al., 2018).

A number of researchers have carried out studies using micro-encapsulated PCMs in concrete. Hunger et al. (2009) investigated the behaviour and properties of self-compacting concrete mixes that contained 1 %, 3 % and 5 % of microencapsulated PCM by mass of concrete. A self-compacting concrete mix was used to mitigate damage to the microcapsules during compaction. Also the PCM was added to the mix at the latest possible moment to reduce its exposure to the mixing process. The primary aim of their research was to demonstrate a reduction in the peak temperature of hydration so a high dosage of cement was used to ensure that the heat of hydration was significant (450 kg/m$^3$). It is noted that in order to maintain similar workability in each mix an additional 5 % and 20 % of water was added to the 3 % and 5 % PCM mixes, relative to the reference mix.

This study yielded a number of findings as follows:

- An increasing amount of PCM results in a lower peak hydration temperature as the heat of hydration is absorbed by the PCM when it changes phase but does not increase in temperature.
- The compressive strength of this specific mixture reduces by 13 % for each additional percentage of PCM however concrete strengths of 21.4 MPa were achieved with a 5 % PCM content (and additional added water as noted) which is acceptable for non-loadbearing construction purposes. However if cement content is 450 kg/m$^3$, which is a relatively high cement content, there is an economic and environmental cost.
- The concrete density reduces and the porosity increases with increasing PCM content. This can be explained by the low density of the PCM (0.915 g/cm$^3$). Also as the water content was increased with PCM content to maintain similar workability in the mixes, this will contribute to an increase in porosity.
- The addition of the PCM particles reduces the thermal conductivity of the concrete. This was explained by an increased air content in the sample due to increased porosity and the lower conductivity of the paraffin.
- With increasing PCM content the thermal mass of the sample increases significantly despite the increased porosity and decreased density. This is caused by the increase of the specific heat capacity of the sample within the melting temperature range of the PCM. However the thermal mass appeared to be bound by a maximum of

approximately 6800 J/K at 4-5 % PCM. An explanation for this upper limit was not provided by the author however a possible reason may be that the reductions in density and conductivity for samples with PCM content greater than 3 % start to counteract the additional heat storage capacity provided by the PCM.

Finally the study concluded that including 5 % PCM into a concrete mix could yield up to 12 % of an energy saving, however the context of this statement was not given. The authors also recommended that stronger shells for the micro-encapsulated PCM are used in future applications to ensure that the capsules can withstand the high alkaline environment and mechanical impact during mixing.

Eddhahak-Ouni et al. (2014) investigated Portland cement concrete samples incorporated with 1%, 3% and 5% by volume of concrete micro-encapsulated paraffin PCM. The specific heat capacity and thermal conductivity of the samples were compared. Also in order to test the stability of the PCM behaviour, the samples were subjected to artificial ageing in a climate test chamber for 50 days. The thermal conductivity of the samples was retested and again they found that the heat storage capacity of the PCM concrete was significantly improved. The compressive strength of the samples decreased as the percentage of PCM increased. There was a 32 % decrease in compressive strength between the reference sample and the sample with 5 % PCM. The thermal conductivity did not appear to be affected by the PCM. The aged samples displayed the same thermal behaviour as the non-aged samples which indicated a stabilised thermal behaviour in the long term. To compare these results with the results from Hunger et al.'s study the quantity of PCM added by volume of concrete must be correlated to an equivalent amount of PCM as a proportion of the weight of concrete as used by Hunger et al. (2009). Due to the low bulk density of micro-encapsulated PCM, circa 350 kg/m$^3$, 5 % by volume of concrete is equivalent to approximately 17.5 kg. Whereas 5 % by weight of concrete is equivalent to 120 kg of micro-encapsulated PCM hence the concrete samples in Hunger et al's study contained significantly greater quantities of PCM.

Another study in which a micro-encapsulated, high purity paraffin PCM in an aqueous dispersion was added to self-compacting concrete, was carried out by Fenollera et al. (2013). PCM dosages of 5 %, 10 %, 15 %, 20 % and 25 % of mass of cement were added to a self-compacting concrete mix and the slump, compressive strength and density were compared in order to find an optimum combination. For comparison purposes it should be noted that a 5% by weight of cement PCM content is similar to a 1 % by weight of concrete PCM content.

This study found the following:

- As the percentage of PCM increases the flowability of the fresh self-compacting concrete decreases as well as the concrete viscosity and cohesion.
- As the percentage of PCM increases the density of both the fresh and hardened concrete decreases. There was a large decrease in the density of the sample with 25 % PCM (2370 kg/m$^3$ to 1965 kg/m$^3$)
- The compressive test results are shown in Table 2-7.

**Table 2-7 Compressive strength test results of Fenollera et al. (2013)**

| Specimen Breakage | Percentage of PCM | | | | | |
|---|---|---|---|---|---|---|
| | 0% | 5% | 10% | 15% | 20% | 25% |
| | Compressive strength (N/mm2) | | | | | |
| 7 days | 50.02 | 47.70 | 43.65 | 36.40 | 32.20 | 12.10 |
| 28 days | 54.70 | 51.00 | 48.65 | 43.25 | 38.85 | 20.10 |
| 60 days | 60.10 | 55.00 | 51.20 | 48.60 | 42.05 | 20.20 |

The strength decreases by 7 % for each 5 % of PCM added with a further decrease for the sample with 25% PCM. The viability of the samples with 20 % and 25 % was discarded due to their low compressive strengths and also poor homogenization of the mixtures.

- Thermal conductivity decreased by 25 % in the sample with 10 % PCM. The decrease in thermal conductivity is to be expected due to the decrease in density and also the low conductivity of paraffin.

From the above two studies it can be concluded that circa 20 % by weight of cement, or 5 % by weight of concrete, is the maximum practical content of micro-encapsulated PCM to be used in a concrete mix application.

### 2.4.5 Shape-stabilisation and form-stable

In the shape-stabilising technique a supporting material such as high density polyethylene (HDPE) is melted with a PCM and they are mixed at high temperature. The mixture is then cooled below the glass transition temperature of the supporting material until it becomes solid. This method allows a PCM content of up to 80% by mass. Marani and Nehdi (2019) noted that this method prevents leakage of the PCM and produces a composite material with a high specific heat and an appropriate thermal conductivity that is thermally reliable over a long time period. The authors also noted that the integration of a supporting material with a PCM may impact the thermo-physical properties of the PCM. Therefore, characterising the fabricated shape-stabilised PCM composite is critical. In addition it is necessary to experimentally

evaluate the effects of shape stabilised PCMs on the thermal and mechanical properties of the construction material to which it will be added.

Another type of composite PCM is known as a form-stable composite PCM. A form-stable composite PCM retains an optimum percentage of PCM with no leakage above its melting temperature. The terms 'form-stable' and 'shape stabilised' appear to be used interchangeably in some research, however with form-stable composites it is not necessary for the supporting material to melt. Form–stable composites use immersion and vacuum impregnation methods to incorporate the PCM into the supporting materials.

Memon (2014) presented a detailed summary of research carried out using form-stable PCMs. Most of the research studied the formation of form-stable PCMs however there appears to be a lack of research on the application of these composite materials. The type of supporting materials used included diatomite, expanded perlite, expanded graphite, silica fume and ground granular blast furnace slag (GGBS). GGBS is commonly used as a partial cement replacement in concrete so its use as a supporting material for a form-stable PCM composite is of interest. In Memon et al. (2013) a PCM, dodecyl alcohol (DA), was incorporated into the GGBS using vacuum impregnation. The maximum percentage of PCM retained without leakage was 11 % by weight. The composite had a melting temperature of 21.2 $^{o}$C and a latent heat of 22 J/g. Further research is required to establish if this composite can be successfully used to effectively increase the thermal energy storage of a building. As the amount of GGBS that can be used as a cement replacement in concrete is usually limited to a maximum of 70 % of total cement content in Ireland it may not be feasible to incorporate a sufficient amount of PCM into the structure to make an effective difference to the thermal storage capacity of the building.

Although Marani and Nehdi (2019) and Memon (2014) have provided a detailed overview of the research carried out on shape-stabilised and form-stable PCMs and both forms of PCM composites display good thermal storage characteristics, there is a scarcity of literature on the incorporation of these forms of PCM into concrete and the effects that they may have on the properties of concrete. Given the scarcity of previous research on these types of PCM composites it is not proposed to use this form of PCM composite in this study.

## 2.5 Effect of the type of PCM and method of incorporation on the properties of concrete

### 2.5.1 Properties of fresh concrete

*2.5.1.1 Workability*

As noted in Section 2.4.4.2, Hunger et al. (2009) investigated the effect of micro-encapsulated PCM on the slump of a self-compacting concrete and found that all three PCM composites, 1 %, 3 % and 5 % by mass, had similar flow diameters of 740 mm to 770 mm which are within the appropriate range of 550mm to 850 mm for a self-compacting concrete. The 3 % and 5 % mixes exhibited a slightly higher viscosity however the self-compacting properties were not compromised. It should be noted though that the authors added an additional 5 % and 20% water into 3 % and 5% mixes in order to maintain similar workability in the mixes.

Fenollera et al. (2013) also studied the effect of micro-encapsulated PCMs on the slump flow of a self-compacting concrete. The dosages of micro-encapsulated PCM were 5 %, 10 %, 15 %, 20 % and 25 % by weight of cement. An addition of 5 % by weight of cement is approximately equivalent to an addition of 1 % by weight of concrete. The slump flow test results are shown in Table 2-8.

**Table 2-8 Results of slump flow tests (Fenollera et al., 2013)**

| Test | Parameter | Percentage of PCM in the Mix | | | | | |
|---|---|---|---|---|---|---|---|
| | | 0% | 5% | 10% | 15% | 20% | 25% |
| Slump flow test | $T_{50}$ (s) | 8 | 7 | 8 | 6 | 8 | – |
| | $d_f$ (mm) | 690 | 650 | 640 | 640 | 530–520 | Cone 22 cm |
| Classification according to EFNARC | Viscosity | VS2 | VS2 | VS2 | VS2 | VS2 | – |
| | Slump flow | SF2 | SF1 | SF1 | SF1 | – | – |

As noted previously, for a self-compacting concrete the allowable flow diameter, $d_f$ range is 550mm to 850mm, hence it can be noted that the 20 % and 25 % PCM mixes do not comply with the requirements.

Snoeck et al. (2016) also assessed the impact of microencapsulated paraffin on the workability of concrete and concluded the 5 % by mass of concrete is the maximum amount of PCM that can be added to achieve good workability. To mitigate the loss of workability the authors suggested incorporating the encapsulated PCM towards the end of the concrete mixing process. Pomianowski et al. (2012), although not investigating workability, indicated that one of the mixes they were using that contained 6% micro-encapsulated PCM showed poor workability despite the use of a plasticiser and the mix was excluded from further investigation

Generally, the research results on this topic concur that when adding microencapsulated PCM the workability and the flow values of concrete mixtures are reduced. To mitigate this negative effect, various authors suggested to increase the water content or to add an appropriate amount of superplasticiser to the PCM-concrete mixture content, however additional water would have an adverse effect on concrete strength. (Snoeck et al., 2016, Lecompte et al., 2015, Pomianowski et al., 2013).

*2.5.1.2 Heat of hydration*

Drissi et al. (2019) reviewed the literature on how the hydration properties of cementitious materials are impacted by the addition of PCMs. Various studies demonstrated that the incorporation of PCMs into concrete reduces the peak temperature of hydration by absorbing the heat released during hydration. Kim et al. (2015) demonstrated a reduction in peak hydration temperature of 3 $^{o}$C when microencapsulated Barium was added to concrete. Hunger et al. (2009) also concluded that an increasing amount of PCM results in a lower peak temperature of hydration. The research found that the peak hydration temperature could be reduced up to 28 % by increasing PCM content to 5 % by weight of concrete. However the heating rate did not change hence the emission of heat from the sample will continue for a longer time when the PCM content is higher.

Bentz and Turpin (2007) incorporated both a paraffin (PAR) and a polyethylene glycol (PEG) into a LWA (expanded shale) by immersion. These aggregates were then used to make mortar samples. Another PCM-mortar composite sample was made by direct mixing paraffin wax particles (1mm) into the cement paste, replacing a portion of the sand. Thermocouples were placed in the centre of the samples and the temperature of hydration was monitored over a couple of days. It was found that the PEG sample substantially retarded cement hydration thus it was concluded that to use a PEG in a concrete application the PEG would require encapsulation. For the remaining two samples, a reduction in peak temperature of 8 $^{o}$C and a delay in reaching peak temperature of 1 hour were observed. It was proposed that if 20 % of the aggregate mass of a typical concrete mix could be replaced with a lightweight aggregate impregnated with paraffin wax, the peak temperature of hydration could potentially be reduced by 25 %. It should be noted though that this proposal is subject to the porosity of the lightweight aggregate used and hence how much PCM can be incorporated into it.

More recently, Sharifi and Sakulich (2015) used an expanded shale LWA as a carrier for three different types of PCM. It was shown that the expanded shale could absorb the PCM by up to

30% by weight to form a LWA-PCM composite. The LWA-PCM was used in a concrete mix and calorimetry methods were used to measure the heat of hydration. The results showed a reduction of the heat of hydration of up to 4% and a delay in occurrence of peak temperature of 45 minutes.

### 2.5.2 Properties of hardened concrete

*2.5.2.1 Compressive strength*

All the literature reviewed that considered micro-encapsulated PCMs in concrete recorded a reduction in compressive strength of the PCM-concrete composite. As noted in Section 2.4.4.2, Figure 2-21 shows a reduction in compressive strength of 7 % for each 5 % increase in micro-encapsulated PCM (by weight of cement) in a self-compacting concrete mix observed by Fenollera et al., 2013.

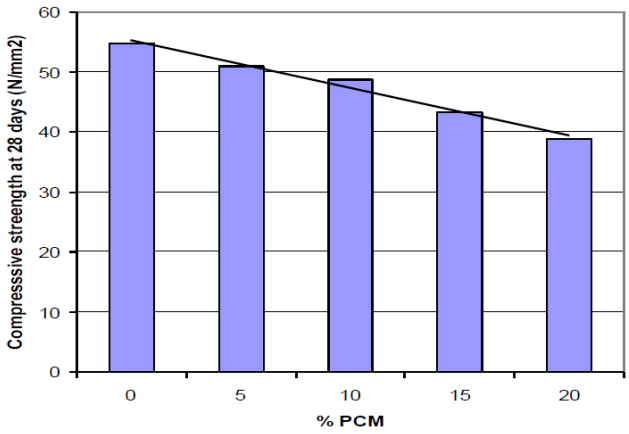


**Figure 2-21 28 day strengths for micro-encapsulated PCM-concrete composite (Fenollera et al., 2013)**

Also, as described in detail in Section 2.4.4.2, Hunger et al. (2009) reported a 13 % decrease in compressive strength for every 1 % (by weight of concrete – approximately equivalent to 5 % by weight of cement)) increase in the micro-encapsulated PCM content. These findings are to be expected as there is a significant difference between the intrinsic strength of the microcapsules and the other constituents of the concrete such as aggregates and cement. Through the use of scanning electron microscopy (SEM) the authors also revealed a porous microstructure and spherical voids in the PCM-concrete samples. The study attributed the reduction in compressive strength to breakage of the PCM capsules during the mixing process and subsequent PCM leakage which interfered with the strength development of the matrix material. Breakage of PCM capsules is a common finding in the research due to the low intrinsic strength of the capsules. Similar conclusions were also made by Eddhahak-Ouni et al. (2014) and Wei et al. (2017). This can be partly solved by the late addition of the PCM

during concrete mixing. Differences in the magnitude of strength reduction due to equivalent PCM contents can also be attributed to variations in water/cement ratios used in the studies.

SEM images were also used by Cao et al. (2017) and Pilehvar et al. (2017) to determine the cause of strength reduction in normal concrete and geopolymer concrete respectively, both of which contained varying percentages of microencapsulated PCM up to a maximum of 3.2 %. Both studies showed weak connections and air voids between the PCM capsules and the matrix material. The authors also highlighted that the capsule material lacked sufficient strength which was also a contributing factor to the reduction in strength of the PCM-concrete composite.

Cellat et al. (2017) carried out a study to develop and test stronger capsules for PCM materials. A novel microencapsulation of PCM was carried out with polystyrene as the shell material using an emulsion polymerization method. A relatively high quantity of microencapsulated PCM, 10 % by weight of concrete, was added and the average loss in concrete strength was 38 %. However concrete strengths up to 40 MPa were achieved which would be suitable for many structural applications. The study concluded that the production of robust microencapsulated PCMs could be a potential solution for reducing the loss of compressive strength, and thus increasing the thermal energy storage capacity of PCM-concrete composites.

Previous research carried out by the author (Niall et al., 2017) was included in a review study by Berardi and Gallardo (2019). Figure 2-22 provides a summary of results on the impact of micro-encapsulated PCM on the strength of concrete as compiled by this review study.

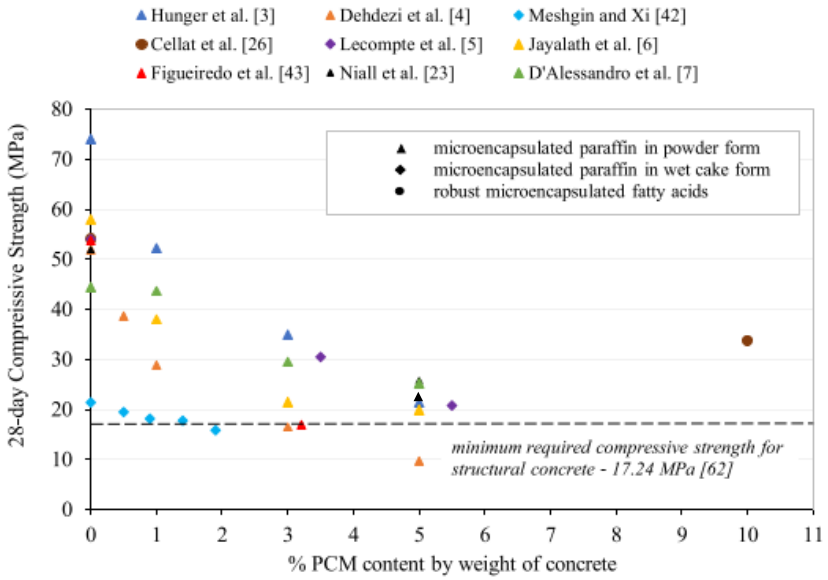


**Figure 2-22 Concrete strengths achieved with various micro-encapsulated PCM content, (Berardi and Gallardo, 2019)**

It can be concluded from this review that the limit to the quantity of micro-encapsulated PCM that can be incorporated into concrete while still achieving strengths that are suitable for structural applications is 5% by weight of concrete. It is also important to note that the use of higher water to cement ratios to compensate for the loss of workability due to the addition of PCM micro-capsules would also lead to lower 28 day concrete strengths. In order to avoid compounding the strength loss caused by the addition of micro-encapsulated PCM, the use of a superplasticiser is a better strategy for counteracting loss of workability.

The second most common method in the literature for incorporating PCM into concrete is by vacuum impregnation into porous LWAs which are then included in the concrete mix, as discussed in Section 2.4.3. It is expected that concrete containing LWA would have a lower strength than concrete with normal aggregates. Most research studies have shown that the inclusion of PCM into the LWA (LWA-PCM) reduces the strength of the concrete mix further. In research by the author (Niall et al., 2017) a particular quantity of latent heat capacity was added to concrete by incorporating 13 % LWA-PCM by volume of concrete. The LWA-PCM was created by vacuum impregnating butyl stearate into a LWA. The LWA-PCM was used as aggregate in two different concrete mixes, one with 100 % ordinary Portland cement (OPC) and one in which 50 % of the OPC was replaced with GGBS and the volume of regular coarse aggregate was reduced accordingly. The results showed that the addition of LWA-PCM had an adverse effect on the strength of the concrete panels. When replacing 13% of regular aggregates with LWA-PCM by volume, both types of PCM panels only achieved strengths in the order of 25 MPa after 28 days. LWA-PCM composite panels with 100 % OPC and 50 % GGBS had a strength reduction of 50 % and 37 %, respectively. According to the authors, one reason for the loss of strength of LWA-PCM-concrete composites was due to leaked PCM at the surface of the LWA which interferes with the bond between the aggregate and cement paste.

Cui et al. (2015a) presented a solution to the leakage problem by coating the LWA-PCM with an epoxy and modified cement paste. The results of the study showed that the compressive strength of concrete mixtures with epoxy and modified cement paste coated LWA-PCM was around 30 MPa and 32 MPa, with an average loss of compressive strength, with respect to control concrete, of around 15 % and 9 %, respectively.

Memon et al. (2015) presented a study in which LWA-PCM was coated with an epoxy resin adhesive and hardener to prevent leakage. In addition, graphite powder was used to improve thermal conductivity and silica fume was used to prevent agglomeration of the LWA-PCM

particles. The results of the strength tests showed that the concrete samples containing LWA-PCM was higher than the control mixture which contained uncoated LWA aggregates. The compressive strength of the control mixture and of the mixes containing 50 % and 100 % LWA-PCM was 15 MPa, 16 MPa, and 17 MPa, respectively. Authors suggested that the higher strength of the coating materials helped to avoid a reduction in the compressive strength of the PCM-concrete. However given the variability in the nature of the raw materials and manufacturing process on concrete the difference in the strength results cannot be considered significant.

*2.5.2.2 Density*

A reduction in density is expected when a quantity of micro-encapsulated PCM is added to concrete as a proportion of the concrete volume is being replaced by a lower density material. For example, the bulk density of Micronal, a microencapsulated paraffin used in previous research by the author, is 350 kg/m$^3$. Hunger et al. (2009) observed a decrease in the density of a self-compacting concrete incorporated with micro-encapsulated PCM by weight of concrete (Figure 2-23).

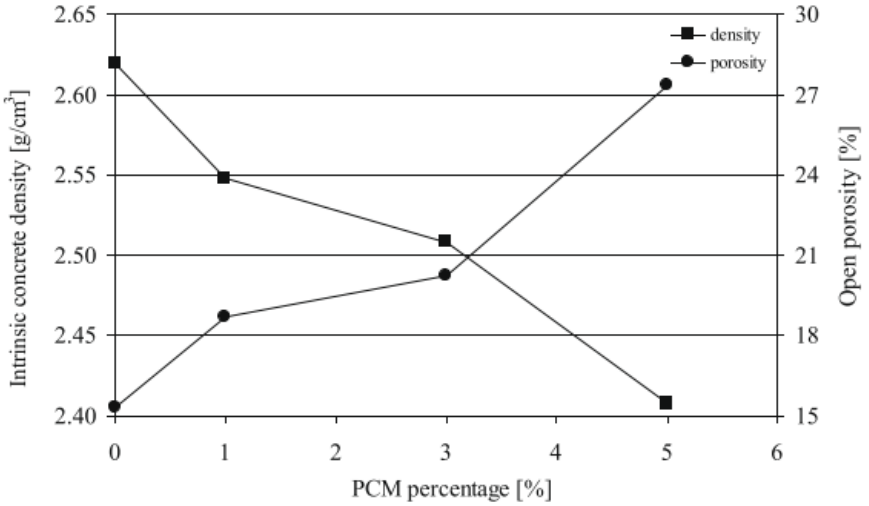


**Figure 2.23 Density and porosity versus % of PCM content (Hunger et al., 2009).**

The decrease in density is accompanied by an increase in porosity, which indicates that the microcapsules are altering the concrete packing density. Although an addition of 5 % micro-encapsulated paraffin resulted in an 8.5 % reduction in density, it is noted that the control concrete has a higher density (2.62 g/cm$^3$) than a typical structural concrete (2.45 g/cm$^3$) and that the density of the concrete which incorporates 5 % micro-encapsulated PCM is similar to that of a typical concrete mix.

Fenollera et al. (2013) also observed a reduction of 1.1 % in density for every additional 5 % (by weight of cement) of microencapsulated PCM. To facilitate a comparison of these results it is approximated that 5 % by weight of cement is equivalent to 1 % by weight of concrete (assuming a cement content of 450 kg/m$^3$ as used by Hunger et al.). Comparing the results using this approximation, Fenollera et al.'s results indicate a 5.5 % reduction in density for a 5 % addition of micro-encapsulated PCM by weight of concrete. Other research studies that investigated the density of concrete with micro-encapsulated PCMs concluded similar results (Figueiredo et al., 2016, Aguayo et al., 2016).

With regard to the density of concrete containing LWA-PCM, there are very few investigations found in the literature that reported on this topic. However given that the PCM is replacing air in the aggregates it is expected that the density would be greater than a non-PCM concrete made with the same type of lightweight aggregate. Previous research by the author (Niall et al., 2017) found that the density of concrete, in which 13 % volume of normal aggregate was replaced with LWA-PCM aggregate, was 10 to 12 % lower than concrete made with 100 % normal aggregates.

A reduction in density would lead to a reduction in thermal mass of a non PCM material (equation (2-7)). However for a PCM-concrete composite material the loss in thermal mass due to reduced density is counteracted by the additional thermal storage provided by the latent heat capacity of the PCM. All the literature reviewed found that there is a significant net benefit in thermal storage achieved by incorporating PCM into concrete. However it must be noted that a phase change must occur for this benefit to be gained otherwise there will be an overall loss in thermal mass. Hence the selection of the PCM must involve careful consideration of the requirements of the application.

*2.5.2.3 Thermal conductivity*

As concluded in Section 2.3.3, organic PCMs are the most appropriate class for use with a construction material. However one of the disadvantages of organic PCMs is that they have low thermal conductivity which can hinder their activation and hence reduce the efficiency of their application. The thermal conductivity of some PCMs can be improved by mixing the PCM with a highly conductive material so that the heat transfer rate between the PCM and the concrete matrix is increased. Li et al. (2013) made a form-stable PCM by using expanded graphite as a supporting material for paraffin. They found that the latent heat of the form-stable PCM was less than that of pure paraffin due to the fact that the mass fraction of paraffin in the

composite was 85 % and the latent heat of the form-stable PCM is provided by the paraffin. However the heating and cooling rate of the form-stable PCM was greater than that of paraffin showing an increased conductivity.

The increased porosity associated with an increase in microencapsulated PCM content noted in Section 2.5.2.2, would lead to a decrease in thermal conductivity of a PCM-concrete composite. The relatively low conductivity of the PCM also contributes to a decrease in thermal conductivity of the composite. Both Fenollera et al. (2013) and Hunger et al. (2009) observed a linear decrease in conductivity with an increase in content of microencapsulated PCM (Figure 2-24).

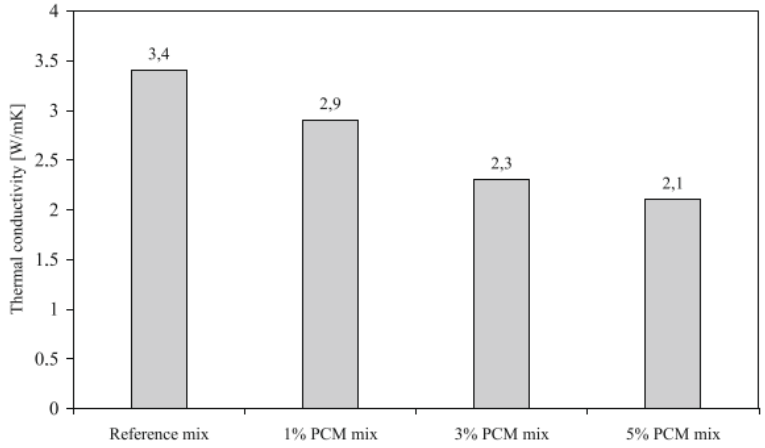


**Figure 2-24 Thermal conductivity of PCM-concrete composite (Hunger et al., 2009)**

In various studies, the thermal conductivity of PCM-concrete samples was determined at temperatures below and above the melting range of microencapsulated PCM. Research results showed that the thermal conductivity of PCM-concrete is higher when the PCM is in a solid state than when the PCM is in a liquid state (Cao et al. 2017). Both Jayalath et al. (2016) and Hunger et al. (2009) carried out thermal conductivity tests on concrete with micro-encapsulated PCM (ME PCM) while the PCM was in a liquid state. Hunger et al. (2009) investigated the thermal conductivity of self-compacting concrete containing 1 % , 3 % and 5 % of ME PCM by mass of concrete. The tests were carried out at 30 $^{o}$C, which was above the melt temperature range of the PCM. The results confirmed the thermal conductivity of the sample containing 5 % ME PCM was 2.1 W/mK reduced from 3.4 W/mK for the non-PCM sample (Figure 2-24), representing a 38 % reduction. Although as noted previously, the reference concrete in Hunger et al.'s study had a higher than typical density which results in a high thermal conductivity value. Similarly, in the research carried out by Jayalath et al. (2016), the thermal conductivity of concrete samples with 5 % microencapsulated PCM by mass of concrete was reduced by approximately 45% compared to the control mix without PCM.

Berardi and Gallardo (2019) summarised the results of a number of studies that investigated the impact of ME PCM on the thermal conductivity of concrete, as shown in Figure 2-25. It can be concluded that with a 5 % concentration of PCM by mass of concrete, the thermal conductivity of PCM-concrete composites is reduced from about 25 to 45 %.

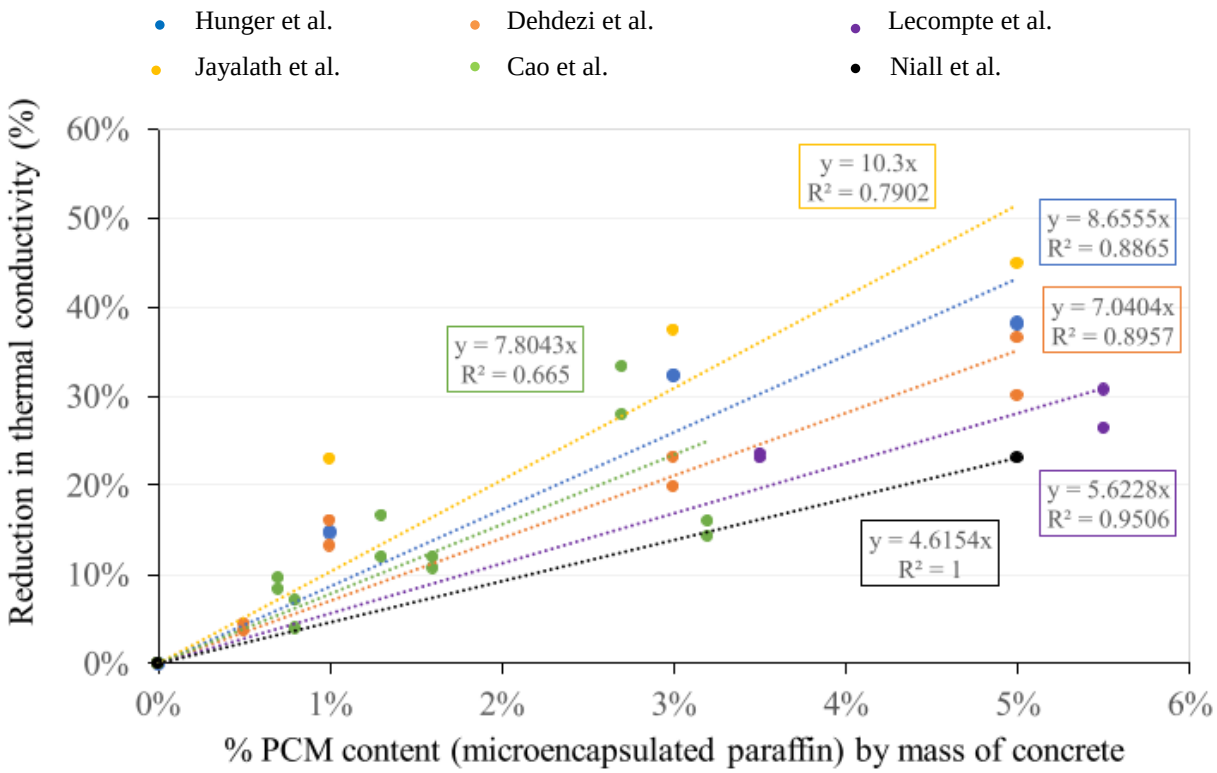


**Figure 2-25 Reduction in thermal conductivity of concrete containing micro-encapsulated paraffin (Berardi and Gallardo, 2019)**

With respect to the thermal conductivity of concrete containing LWA-PCM, Cui et al. (2015a) compared the thermal conductivities of concrete samples containing LWA-PCM that had been coated with either an epoxy or a modified cement mix. The concrete with the epoxy coated LWA-PCM and the cement paste coated LWA-PCM displayed thermal conductivities of 0.62 W/mK and 0.74 W/mK respectively, both lower than the control reference sample which had a thermal conductivity of 0.82 W/mK . The results indicate that the material used to coat the LWA-PCMs has an influence on the thermal conductivity of the PCM-concrete composite. The low thermal conductivity of the control reference sample, made with just LWA, is also notable. This result can be attributed to the low density of this LWA concrete which was reported as 1390 kg/m$^3$.

Another study carried out by Wang et al. (2018) measured the thermal conductivity of concrete containing LWA-PCM. Similarly to the study performed by Memon et al. (2015), the authors found that the incorporation of 1 %, 3 %, 5 %, 7 % and 9 % graphite powder increases the thermal conductivity of LWA-PCM by 17 %, 34 %, 55 %, 119 %, and 193 % respectively. However, the thermal conductivity of concrete containing LWA-PCM decreases with an increase of LWA-PCM content, due to the low thermal conductivity of PCM filled in the pores of LWA.

The author also carried out previous research (Niall et al., 2017) in which an adjusted hot plate apparatus was used to measure the thermal conductivity of LWA-PCM-concrete composite, in which 13 % volume of normal aggregates were replaced with LWA-PCM. The panels included either 100 % OPC or 50 % OPC and 50 % GGBS. The results of the study demonstrated that both the OPC panel and the OPC/GGBS panel displayed thermal conductivities that were reduced by 47 % and 43 % respectively relative to the control sample made with 100 % normal aggregates. The thermal conductivity of the LWA-PCM samples made with OPC/GGBS was 10 % higher than the sample made with 100 % OPC. This result was attributed to the slightly higher density of the OPC/GGBS samples. The study also concluded that lower conductivity and higher heat storage capacity of the PCM panels result in reduced thermal diffusivity, which in turn reduces the effectiveness of the PCM as depth increases as the heat takes longer to reach the PCM.

A reduced thermal conductivity is not necessarily a problem as the desired conductivity of the PCM composite depends on the application. In a thermal storage system for a space heating application it is required that the heat is absorbed and released gradually over a 24 hour period. Hence it is important that the heat flux characteristics of the composite are appropriate to achieve the desired thermal storage behaviour and thermal inertia. It has been shown by a number of researchers (Tang et al., 2018, Memon et al., 2014) that the range of thermal conductivities of PCM-concrete composites is suitable for a diurnal thermal storage period.

*2.5.2.4 Specific heat capacity and thermal mass*

The literature reviewed consistently reported that the heat storage capacity of a PCM-concrete composite is significantly increased, which is expected due to the addition of latent heat capacity of the PCM. However the majority of studies reviewed used DSC testing to determine the heat capacity of the PCM-concrete composites. Due to the very small sample size required for accurate DSC testing, (5 – 20 mg), as discussed in Section 2.3.4.1, it is questionable

whether such a small sample of PCM-concrete can be considered homogenous hence DSC testing may not be an appropriate method for determining the heat capacity of PCM-concrete.

Hunger et al. (2009) developed an alternative method for determining the heat capacity of concrete incorporated with 1 %, 3 % and 5 % micro-encapsulated PCM, by mass of concrete. The heat capacity and thermal mass of the samples were calculated from temperature and heat flux measurements of the samples placed between two thermo-regulated plates using the following formulae:

$$C_p = \frac{A\dot{q}}{m(\frac{dT}{dt})} \quad \textbf{(2-15)}$$

$$M = mC_p \quad \textbf{(2-16)}$$

where:

- $C_p$ = heat capacity (J/KgK)
- A = heat transfer surface area of the sample ($m^2$)
- $\dot{q}$ = heat flux per square meter ($W/m^2$)
- m = mass of sample (Kg)
- T = temperature of the sample (K)
- t = time
- M = thermal mass

The authors found increased improvement in thermal mass behaviour and specific heat capacity storage with increased PCM content, as shown in Figures 2-26 and 2-27. The specific heat capacity of the samples increased by factors of 1.7, 3.0 and 3.5 with the increase in PCM content of 1 %, 3 % and 5 % respectively. However, as noted in Section 2.4.4.2, there appears to be an upper limit to the improved thermal mass behaviour. This can be attributed to the decrease in concrete density with increasing PCM content which offsets the beneficial effect of the increased specific heat capacity.

Pomianowski et al. (2014) used a similar experimental technique as Hunger et al. (2009) to determine the heat capacity of concrete incorporated with micro-encapsulated PCM. The authors compared the experimental results with values obtained from four different numerical methods, described as the ‘theoretical method’, ‘simple method’, ‘numerical simple method’ and ‘inverse method’.

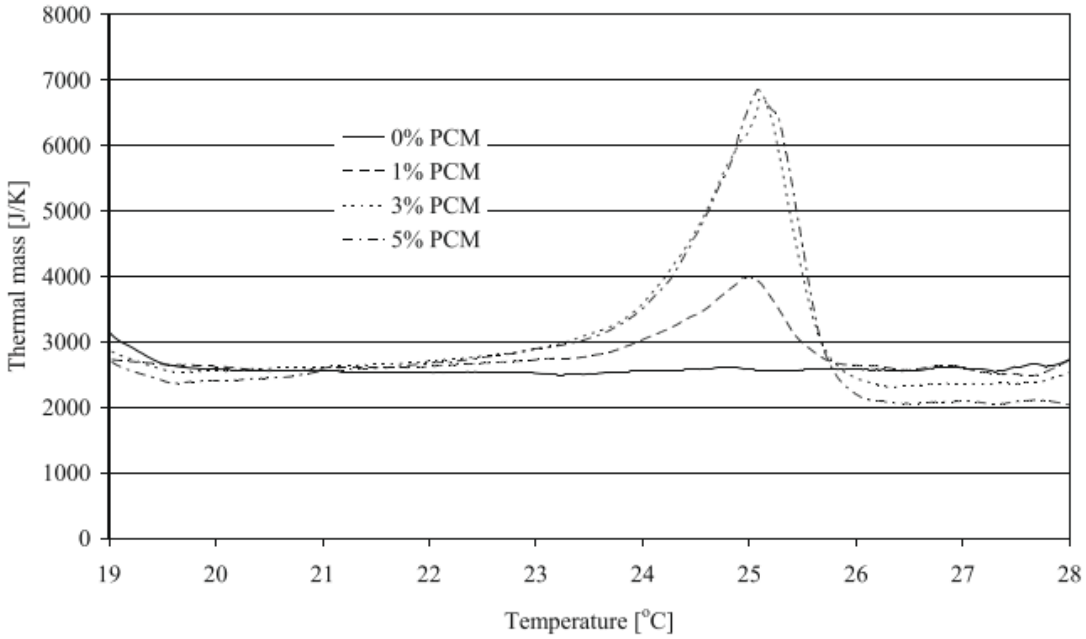


**Figure 2-26 Specific heat capacity of PCM-concrete composite versus temperature (Hunger et al., 2009)**

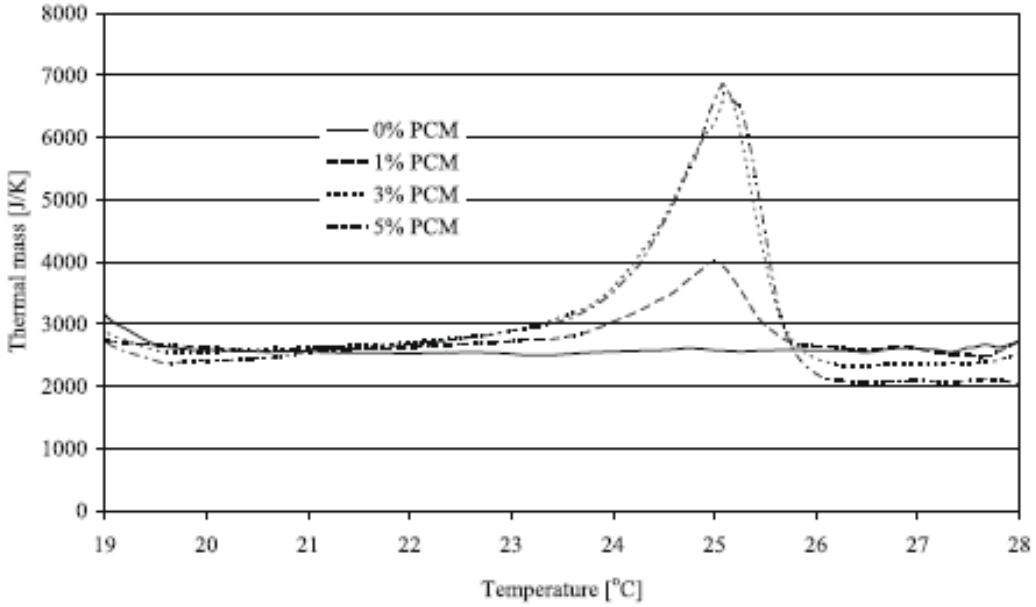


**Figure 2-27 Thermal mass of PCM-concrete composite versus temperature (Hunger et al., 2009)**

The 'simple method' is similar to the method used by Hunger et al. (2009) and utilises equation (2-15) to determine the heat capacity of the sample. The 'theoretical method' uses a weighted average of the specific heat capacity of each individual component of the composite material, which are determined using DSC. The heat capacity is then determined from the following equation:

$$C_{composite} = C_{PCM}.X_{PCM} + C_{matrix}(1- X_{PCM}) \quad \textbf{(2-17)}$$

where:

- $C_{composite}$ = the specific heat capacity of the PCM-concrete sample
- $C_{PCM}$ = the specific heat capacity of the microencapsulated PCM
- $X_{PCM}$ = the weight ratio of the PCM to the composite
- $C_{matrix}$ = the specific heat capacity of the matrix material

The 'numerical simple method' proposed a finite difference method to solve the 1-D unsteady heat conduction problem, using the following equation:

$$\frac{\partial T}{\partial t} = \alpha \frac{\partial^2 T}{\partial X^2} \quad \textbf{(2-18)}$$

where:

- T = temperature ( ◦C)
- t = time (s)
- X = length (m)
- α = the thermal diffusivity ($m^2/s$)

The 'inverse method' uses a non-linear constrained optimization method to calculate the specific heat capacity as a function of temperature. The authors concluded that while all methods produced good results the 'numerical simple method' and 'inverse method' were more appropriate as they yielded conservative estimates of heat capacity.

All the literature reviewed that investigated the heat capacity of LWA-PCM-concrete composites used DSC testing to determine the heat capacity of the composite (Ma and Bai, 2018, Min et al., 2017, Kastiukas et al., 2016).

Zhang et al. (2004) use the vacuum impregnation method to incorporate butyl stearate into three different types of LWAs, superlite clay aggregate (OC1), normal clay aggregate (OC2) and shale aggregate (OS). These aggregates were then used in equal quantities in three different concrete mixes. Samples of the normal concrete and the LWA-PCM-concrete composites were crushed to coarse powders and tested using DSC analysis to evaluate their thermal energy storage capacity. The DSC sample weight was around 70 mg which is higher than the recommended amount as discussed in Section 2.3.4.1. As each type of aggregate absorbed different volumes of butyl stearate each concrete sample contained different volumes of PCM. The observed thermal storage behaviour is shown in Figure 2-28.

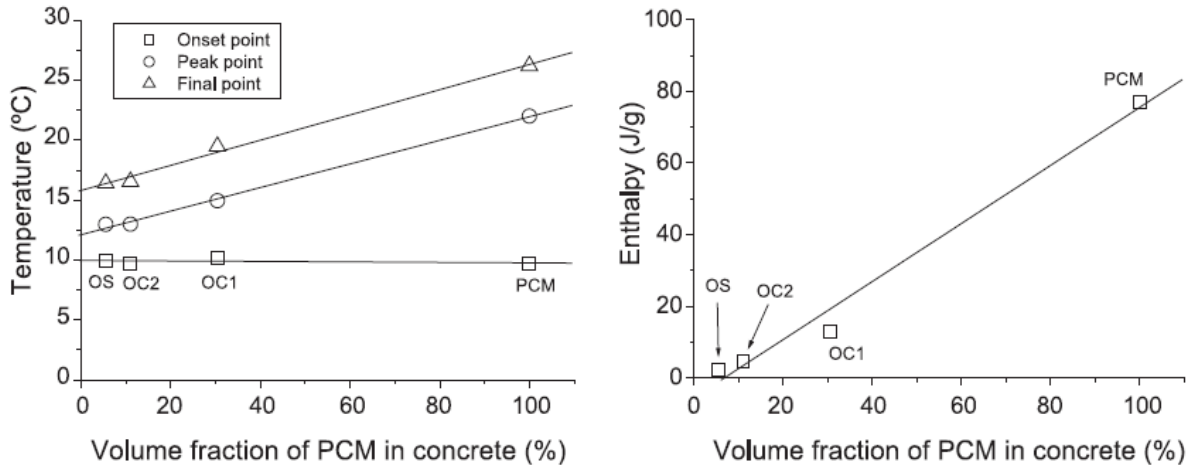


**Figure 2-28 Thermal behaviour versus volume fraction of PCM (Zhang et al., 2004)**

It was concluded that the phase changing behaviour of the composite is significantly influenced by the volume fraction of PCM in the concrete. The peak and ending temperatures and the enthalpy of the phase change increase linearly with the volume fraction of PCM, however the onset temperature of the phase change does not appear to be affected.

The author (Niall et al., 2016) carried out research in which two methods were used to incorporate different PCMs into concrete to form PCM-concrete composite panels. Firstly microencapsulated paraffin (Figure 2-29) was added to fresh concrete during the mixing process. In the second method, a fatty acid, butyl stearate, was vacuum impregnated into a LWA which was then included in the concrete mix design (Figure 2-30). The thermal behaviour of both PCM-concrete composite panels displayed significantly greater thermal storage capacity despite having reduced thermal conductivity and density.


**Figure 2-29 Images of microencapsulated paraffin - Micronal DS 5040 X**

**Figure 2-30 LWA-PCM composite material**

The study concluded that the panel containing a LWA-PCM composite was more effective at providing additional thermal storage, particularly within the first 100mm of depth of an element of structure. One of the reasons for this was that the temperature range for the solid–liquid phase change in the butyl stearate was narrower than that for the microencapsulated paraffin so the additional latent heat capacity was achieved over a smaller temperature differential. So for a given heat load, the butyl stearate PCM was engaged faster and hence more of the PCM was utilised. Also the butyl stearate provides nearly twice the latent heat capacity (172 J/g) relative to the microencapsulated paraffin (97 J/g).

*2.5.2.5 Thermal diffusivity*

As discussed in Section 2.2.1 and denoted by equation (2-8), thermal diffusivity of a material increases with thermal conductivity and decreases with increased heat capacity. As the addition of PCM to concrete reduces thermal conductivity and increases heat capacity, it also has the effect of reducing the thermal diffusivity. This effect was highlighted in previous research by the author (Niall et al., 2016) and it was concluded that the reduced diffusivity results in reduced effectiveness of the PCM as the heat takes longer to progress deeper into the thermal storage unit, hence less PCM is engaged. Similar conclusions regarding the reduction of thermal diffusivity were made by Jayalath et al. (2016) and Haurie et al. (2016).

### 2.5.3 Fire safety

All materials used in the structure of a building must be able to maintain its mechanical properties for a minimum time period that matches the fire rating of the particular building. The fire rating depends on the use and layout of a building and typically ranges between 1 hour and 4 hours. It is critical that any PCM-concrete composite material can provide the required fire resistance if it is to be successfully used in a building application. There appears to be a scarcity of research on this issue. Ling and Poon (2013) reported on a PhD thesis carried out by Hawes entitled ‘Latent heat storage in concrete’ in which the fire resistance of concrete

blocks that had been incorporated with PCM using the immersion technique was investigated. The samples were 200 mm x 200 mm x 30 mm and they were subjected to a 700 $^{o}$C flame for 10 minutes. A reduction in the mass of PCM was observed.

PCM-concrete composites could become flammable if the PCM that is used is flammable, for example, paraffin. Micro/Macro encapsulation may be a possible solution for increasing the fire resistance of a PCM-concrete composite. Some studies have proposed introducing a stabilising material with flame retardant properties, such as magnesium hydroxide and silica, (Cabeza et al. 2011, Song et al. 2010) however further research is required to gain an understanding of how a PCM-concrete composite will behave under fire conditions.

## 2.6 Use of PCM thermal storage systems in building envelopes

### 2.6.1 Previous research on use of PCMs in building envelopes

To enable governments to comply with the European Directive 2010/31/EU on the energy performance of buildings, strategies are required to improve the energy efficiency of buildings. Using the mass of a building to store or dissipate heat can reduce the demand on the auxiliary heating and/or cooling systems and hence reduce the overall energy demand of the building. As discussed in Sections 2.4 and 2.5, previous research has shown that the incorporation of PCMs into concrete enhances its thermal storage capacity by up to 50 %.

Given that heat transfer into and out of a building occurs through the building envelope, one of the most commonly proposed methods of enhancing the energy performance of a building is to use the mass of the building envelope to store thermal energy temporarily. Typically a building will lose 55 % of its heat energy through the building envelope including 25 % through the walls of the envelope (Nair et al., 2022). The absorption and storage of excess heat during the day can reduce overheating of the internal environment and hence reduce the energy demand of the air conditioning system. The stored heat can then be dissipated into the internal environment at night when the temperature of the building naturally reduces. According to the IEA's 2013 publication, Technology Roadmap Energy Efficient Building Envelopes, improving the energy performance of building envelopes can reduce the total energy consumption of the building sector by 20 %.

There are many studies in the literature which review the use of PCMs in building envelopes (Sharshir et al., 2023, Nair et al., 2022, Lamrani et al., 2021, Faraj et al., 2021, Navarro et al., 2016a, Kosny et al., 2013). All studies reported enhanced thermal mass behaviour when PCMs

are incorporated into the building envelope, however potential applications of PCMs in building envelopes depend largely on local climate conditions, melt temperature range of the PCM, the amount of PCM used, its thermo-physical properties, the encapsulation method and the placement location of the PCM within the building (Souayfane et al., 2016).

The majority of studies within the body of research into PCM enhanced building envelopes investigate the use of PCM integrated wallboards internally in buildings, particularly in a lightweight construction scenario. The use of PCMs in lightweight construction provides a proportionally greater enhancement of thermal mass due to the low baseline thermal mass of lightweight construction. PCM enhanced wallboards require less space and can also be easily used in retrofitting buildings (Nair et al., 2022). In the context of research studies, the costs and logistics of investigating PCM-concrete composites in a full-scale setting can be a significant obstacle to the exploration of the thermal performance of PCM-concrete.

Kosny et al. (2013) carried out an overview of the potential applications of PCMs in building envelopes. The two main measures of performance for PCM enhanced walls are reduction in peak air temperature during the day and a shift in the time that the peak temperature occurs. For a PCM to have an impact on the internal air temperature it must go through a complete phase transition during a 24 hour time period. Hence it is critical that the temperature of the environment in which the PCM is located oscillates above and below the PCM's melting and freezing temperature range. The effectiveness of a PCM in improving thermal mass behaviour is also influenced by the mass of PCM used, the geometry of the space, that is, floor to wall ratios and the amount and orientation of glazing. Xiao et al. (2009) carried out a theoretical analysis to find the optimal PCM melting temperature for a space heating application in a climate similar to that found in Beijing, China. The study found that the optimal melting temperature depends on the average indoor air temperature and increases with the increase in solar radiation absorbed by the PCM panels. It also concluded that the amplitude of the indoor air temperature decreases with the increase of the product of the surface heat transfer coefficient and the surface area of the panels, where the surface heat transfer coefficient is a combined value of the convective and radiative heat transfer coefficients.

As discussed in Ascione et al. (2014) the technological solution for any building application for PCM depends on both the intensity and duration of the solar radiation as well as the local climatic conditions. Hence the potential benefit of incorporating a PCM into a building is seasonal and influenced by the latitude of the location. For example, during the heating season,

if the mass of PCM used is too high then the time required for heat penetration into the PCM-concrete could be longer than the daylight period and hence not all the PCM melts. In the summer season, if the mass of PCM used is too high then the time required to discharge the heat from the PCM-concrete could be longer than the low temperature period, that is, night-time. Ascione et al. (2014) concluded in their study that for the Mediterranean climate, the optimal melting temperature range for the winter period is 18 $^{o}$C - 22 $^{o}$C while in the summer season the optimum temperatures are 25 $^{o}$C - 30 $^{o}$C. The difference in these optimal ranges highlights that there is no PCM that will provide thermal mass benefits across all seasons. Hence, the selection of PCM must take local climate and geographical location into consideration.

Diaconu and Cruceru (2010) developed a model to simulate the performance of a PCM enhanced wallboard. The study concluded that the occupancy pattern influences the value of the PCM melting point for which maximum energy savings can be achieved. Also the pattern of ventilation reduced the relative value of the energy savings.

It is clear from a review of the research studies carried out on the application of PCMs for thermal energy storage in buildings that the ability of the PCMs to reduce the operational energy consumption in a building depends on many variables. For this reason, the impact that a PCM has on the thermal mass behaviour of a panel in the laboratory is not necessarily replicated in a full-scale 'real life' scenario, hence full-scale testing under real weather and internal environmental conditions, through all seasons is an essential tool in the investigation into the potential of this technology as concluded by Nair et al. (2022), Faraj et al.,(2021) and Lamrani et al. (2021).

Kenisarin and Mahkamov (2016) provided a state-of-the-art review of research which included fifteen studies that used full-scale testing of PCM thermal energy storage applications in buildings. The majority of these research studies involved lightweight construction which has a low thermal mass. In most cases thermal mass was increased by adding PCMs to gypsum plaster or wallboards and using it in the construction. The projects were carried out in different climatic zones, in both regions with dominant heating loads (Canada, Germany, France and China) and cooling loads (Spain, Portugal, Greece, Japan, Brazil and New Zealand). However the period of testing did not exceed two weeks so the performance of the PCMs was not measured in all seasons. Also the geometry and form of construction differed in each case so it is difficult to compare the results of the projects quantitatively. Generally the overall outcome

of these studies is that the PCM heat storage systems decrease the air temperature in test rooms by 1- 4 $^{o}$C and that the maximum air temperature occurs 2-3 hours later than in the control rooms.

Of the research studies reported on in the review of existing literature only one study involved an in-situ PCM-concrete composite (Cabeza et al., 2007). A reason for this gap in the research may be the additional equipment, space and cost resources required to construct and de-construct full-scale concrete test cubicles. Cabeza et al. (2007) carried out a full-scale study to investigate the thermal mass performance of a PCM-concrete composite. The PCM used was a commercial micro-encapsulated PCM called Micronal which is manufactured by BASF. Micronal has a melting point of 26 °C and phase change enthalpy of 110 J/g. The composite was formed by adding the Micronal (5 % by weight of concrete) to the fresh concrete. Two concrete cubicles were constructed using six, single leaf panels in each, four walls, roof and floor. The cubicles had identical geometry and were 2 m x 2 m x 3 m. The thickness of the single leaf, uninsulated panels was 120 mm. One cubicle was formed with conventional concrete and the other cubicle contained the PCM-concrete composite in three of its panels – South and West walls and roof. The locations of the windows were as follows: one window of 1.7 m x 0.6 m in the East and West walls, four windows of 0.75 x 0.4 m in the South wall and a glazed door in the North wall. The cubicles were not insulated in order to test the effect of the PCM incorporation only (Figure 2-31).

The walls were instrumented with thermal sensors and internal air temperature was recorded. External climate conditions and irradiation were also monitored. Three tests, each lasting one week, were carried out under different conditions. The first test was carried out at the end of March and the windows were kept closed. The second test was carried out at the end of June and the windows in the South wall were left open. The third test was carried out in July and the windows in the South wall were closed during the day and opened at night.

The recordings of the temperature profile of the South facing wall were analyzed for the first test. It was found that the cubicle without PCM had the maximum and minimum temperatures which were 1 °C higher and 2 °C lower than that of the cubicle with the PCM. It took an additional 2 hours to achieve the maximum temperature in the wall with the PCM which demonstrates that such a wall had a greater thermal inertia. In the second and third test where the windows were open during the period when the PCM was solidifying (night-time) both huts

cooled down at the same rate so the thermal inertia provided by the PCM was not obvious in the cooling phase.

**Figure 2-31 Full-scale test huts, Cabeza et al. (2007)**

It is important to note that in Cabeza et al.'s research project there was no layer of insulation around the outside of the cubicles. This meant that at night the wall could release the heat on both sides facilitating the solidification of the PCM and ensuring that the PCM was ready to absorb heat the following day. One of the challenges of using PCMs to reduce overheating in insulated buildings is that during the summer months when the temperatures are high, the night-time temperature does not drop low enough for sufficient time to allow the PCM to fully solidify. In a 'real life' application, a panel forming the building envelope will have an insulation layer outside the internal layer and also an outer layer of some form. This means that an inner layer containing PCM can only release heat from one side during the night, that is, back into the internal environment and hence there is an increased risk that the PCM will not solidify.

Cabeza et al. (2020) carried out a follow up study 10 years later to review the long-term thermal performance of the PCM-concrete. The thermal performance of the cubicles was measured and the obtained results were compared with those recorded during the summer period of 2005. The same thermal response was observed. From this study, it is confirmed that the micro-encapsulated PCM integrated into concrete preserves the same thermal response without degradation and successfully contributes to the reduction of the indoor air fluctuations 10 years after its installation.

### 2.6.2 Summary of literature on use of PCMs in building envelopes

In the research studies that carried out full-scale tests in rooms constructed with PCM composites (both gypsum and concrete), it was found in all cases that the peak and trough daily temperatures were reduced and increased respectively and also the time taken to reach the peak and trough temperatures was increased. Passive cooling applications were shown to be most effective when the diurnal temperature variations are large (up to 15 $^{o}$C) (Souayfane et al. 2016). Hence the incorporation of PCMs into the construction elements of a building improves the stabilising effect of the thermal mass on internal temperatures.

The majority of studies reviewed in the literature investigated the incorporation of PCMs into lightweight forms of construction such as wallboards, gypsum plaster and mortars. Encapsulated paraffin was the most widely used PCM however fatty acids and salt hydrates also featured. Most of the commercially available PCMs are paraffin based (Faraj et al., 2021).

Some authors reported that high PCM melting temperatures are more effective in warmer climates, while low PCM melting temperatures are more suitable for colder climates. Other authors emphasised the importance of selecting a PCM melting temperature within the human comfort range (18 – 20 $^{o}$C). Further research is required to confirm the appropriate approach to selection of PCM properties for thermal energy storage in buildings. Another area of interest for further research is the incorporation of different PCM materials with different melting temperatures and possibly different locations within the building envelope in order to improve the building performance in both cooling and heating seasons.

A number of studies also highlighted that for a specified amount of PCM, the effectiveness of the PCM decreases as the thickness of PCM layer increases and surface area of the PCM layer decreases (Souayfane et al., 2016). Further research into the optimisation of surface area to air volume and thickness of PCM layer may provide a useful tool in the design of PCM applications in building envelopes, however such optimisation would require accurate numerical modelling tools. More than half of the studies reviewed in the literature were numerical modelling exercises which were validated using small scale laboratory experiments (Lamrani et al., 2021). To investigate the potential of PCM-concrete composite materials further research is required in which full-scale tests are carried out using a PCM-concrete composite and in which ‘real’ conditions are replicated as much as reasonably possible. Data collected during full-scale experiments can provide more accurate data for the validation of numerical models. Another scarcity found in the literature is the lack of experimental data from

year long duration tests which is required to enable the performance of the PCM-composites to be assessed in all seasons. Further full-scale research investigations should monitor the total energy consumed in test rooms during all seasons in order to enable an accurate assessment of the annual economic viability of the application of a passive PCM thermal storage system.

## 2.7 Theory of heat energy transfer through the building envelope

### 2.7.1 Thermal characterisation of cladding panels

Thermal behaviour of cladding panels for buildings is typically described by industry in terms of thermal transmittance, or a U-value. A U-value describes the ability of a single or multi-layered wall to transmit heat from a warm space to a colder space in units of W/($m^2$K).

For a unit area of wall, its U-value is equal to the inverse of the total thermal resistance of the wall, its $R_{TOT}$ value.

$$U = \frac{1}{R_{TOT}} \quad (W/(m^2K)) \qquad \textbf{(2-19)}$$

The thermal resistance, R, of a unit area of a plane uniform wall is inversely related to the thermal conductivity, k, of the wall.

$$R = \frac{d}{k} \quad (m^2K/W) \qquad \textbf{(2-20)}$$

where:

- d is the thickness of the wall (m)
- k is the thermal conductivity of the wall (W/(mK))

Under steady-state conditions the rate of heat transfer into a wall equals the rate of heat transfer out of the wall, that is, the rate of heat transfer through the wall is constant. For one dimensional steady-state heat conduction through a wall, Fourier's law of heat conduction is expressed as (Long, 1999):

$$\dot{Q} = kA\frac{dT}{dx} \quad (W) \qquad \textbf{(2-21)}$$

where:

- $\dot{Q}$ is the rate of heat transfer through the wall (Watts)
- A is a unit area of wall ($m^2$)
- $\frac{dT}{dx}$ is the temperature differential across a thickness of wall 'dx'

As $\dot{Q}$ and A are constant, $\frac{dT}{dx}$ must also be constant meaning that the temperature distribution through the wall is linear (Figure 2-32) (Cengel and Ghajar, 2015).

Integrating equation (2-21) between the boundary conditions of the temperatures at each surface of the wall provides equation 2-1, as noted in Section 2.1.1.

Equation (2-1) can be rearranged and written in terms of the thermal resistance of the wall (Figure 2-32):

$$\dot{Q} = \frac{T_1 - T_2}{R} . A \ (W) \qquad \textbf{(2-22)}$$

where $T_1$ is the higher and $T_2$ the lower temperature.

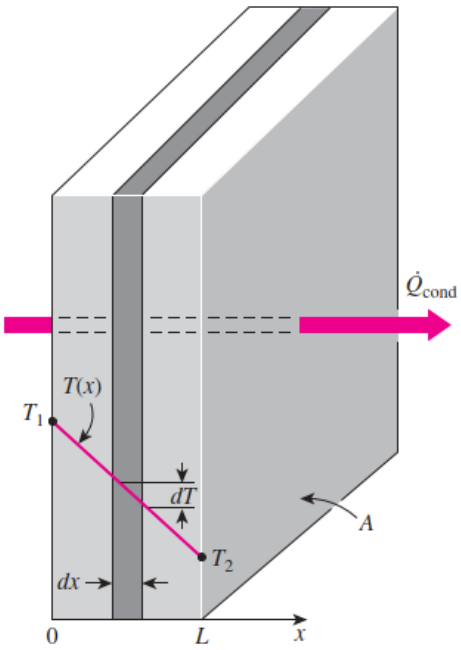


**Figure 2-32 Under steady-state conditions the temperature distribution in a plane uniform wall is linear (Cengel and Ghajar, 2015)**

For a composite cladding panel, heat transfers to the internal surface from the warm air by convection and radiation, through the panel by conduction and from the external surface to the colder air on the outside by convection and radiation. The total resistance of a wall panel, $R_{TOT}$, includes the convective and radiation resistance at the external ($R_{ex,surf}$ ) and internal surfaces ($R_{int,surf}$ ).

$$R_{TOT} = R_{ex,surf} + R_{wall} + R_{int,surf} \qquad \textbf{(2-23)}$$

The surface resistance due to convection, $R_c$, can be determined from Cengel and Ghajar (2015):

$$R_c = \frac{1}{h_c A} \quad \textbf{(2-24)}$$

where:

- $h_c$ is the convective coefficient.

The convective coefficient $h_c$ can be determined using the equation:

$$h_c = \frac{\dot{Q}_{conv}}{T_s - T_A} \quad \textbf{(2-25)}$$

where:

- $\dot{Q}_{conv}$ is the heat transfer due to convection
- $T_s$ is the temperature of the surface
- $T_A$ is the temperature of the surrounding air

It is difficult to accurately determine $\dot{Q}_{conv}$ as $h_c$ has many site specific variables, such as wind speed, surface roughness and the geometry of surrounding buildings. I.S. EN ISO 6946:2017 advises that for external surfaces, $h_c$ can be approximated as 4 + 4v, where 'v' is the wind speed adjacent to the surface (m/s). However research by Ohlsson et al. (2016) highlighted the high levels of variability in the empirical prediction models that correlate $h_c$ to v. Mirsadeghi et al. (2013) carried out a review of research that investigated the influence of $h_c$ on building energy performance and found that the choice of model used for determining $h_c$ can lead to as much as 30% variability in predicted energy performance of a cladding system. This is understandable as wind speed is a highly variable parameter. This should be allowed for in energy performance studies by considering a range of values for 'v' rather than a single value.

The surface resistance due to radiation, $R_r$ can be determined from:

$$R_r = \frac{1}{h_r A} \quad \textbf{(2-26)}$$

where:

- $h_r$ is the radiative coefficient.

I.S. EN ISO 6946:2017 provides the following equation for determining $h_r$:

$$h_r = \varepsilon h_{ro} \quad \textbf{(2-27)}$$

where:

- $\varepsilon$ is the emissivity of a surface
- $h_{ro}$ is the radiative coefficient of a black surface

$h_{ro}$ depends on the temperature of the surface and the surrounding air and can be determined from:

$$h_{ro} = 4\sigma T_{mean} \quad \textbf{(2-28)}$$

where:

- $\sigma$ is the Stefan-Boltzmann constant ($5.67 \times 10^{-8}$ W/($m^2K^4$))
- $T_{mean}$ is the mean temperature of the surface and the surrounding air

In the context of heat transfer through a typical wall construction, the heat transfer due to radiation is often assumed to be negligible so the thermal resistance at the external and internal surfaces of the wall are determined using the external and internal convection coefficients respectively. If there is insufficient data to allow $h_c$ to be determined, I.S. EN ISO 6946:2017 suggests that the surface resistance for an internal surface of a cladding wall can be taken as 0.13 $m^2K/W$ and 0.04 $m^2K/W$ for an external surface. The external surface resistance is lower than the surface resistance for an internal surface as the external air is less likely to be still. The movement of air adjacent to the external surface of the wall enhances the convective heat transfer between the wall surface and the air and hence the resistance to heat transfer at this surface is lower.

In the context of this thesis, R-values and U-values will be determined for the proposed cladding panels to facilitate comparison of thermal performance with other typical forms of cladding construction under steady-state conditions.

### 2.8 Modelling of thermal mass behaviour of PCM-composite materials

As discussed in Section 2.3.4 the commonly used techniques for characterising PCMs are not suitable for PCM-composite materials due the requirement for very small sample size and homogeneity. The thermal properties of various PCM-composite materials have been investigated experimentally in laboratory settings, however the thermal mass behaviour of such materials in a full-scale setting depends on many variables including geographical location and local climate together with building specific variables such as geometry, fenestration, orientation and form of construction. Different building types will require bespoke optimal solutions for the application of a PCM composite material as a thermal energy storage system. For this reason the development of numerical simulation tools is necessary to achieve a practical and economic application of this technology. One of the main challenges of developing models for PCM composite materials is defining the dynamic thermal properties of the material during the phase change transition.

### 2.8.1 Modelling of PCMs

*2.8.1.1 General formulation of the phase change problem*

The main feature of phase change problems is the moving boundary where the Stefan condition must be met. The Stefan condition expresses the local velocity of a moving boundary as a function of quantities evaluated at both sides of the phase boundary, and is usually derived from a physical constraint. In problems of heat transfer with phase change the physical constraint is that of conservation of energy, and the local velocity of the boundary depends on the heat flux at the boundary. For pure materials there is a clear distinction between the solid and liquid phases separated by a definite moving boundary and melting occurs at a constant temperature. For conduction-dominated heat transfer, as would be typical in a building application, the governing equations can be written for the solid and liquid phases respectively, which have to be satisfied by the Stefan condition as set out by Voller (1997):

Heat transfer in the solid phase:

$$\rho . C_s . \frac{\partial T_s}{\partial t} = \frac{\partial}{\partial x} \left(k_s . \frac{\partial T_s}{\partial x}\right) \quad \textbf{(2-29)}$$

Heat transfer in the liquid phase:

$$\rho . C_l . \frac{\partial T_l}{\partial t} = \frac{\partial}{\partial x} \left(k_l . \frac{\partial T_l}{\partial x}\right) \quad \textbf{(2-30)}$$

The Stefan condition that enforces the heat balance at the solid–liquid interface is:

$$\frac{\partial}{\partial x} \left(k_s . \frac{\partial T_s}{\partial x}\right) - \frac{\partial}{\partial x} \left(k_l . \frac{\partial T_l}{\partial x}\right) = \rho . L.v \quad \textbf{(2-31)}$$

where:

$\rho$ = density of the PCM

$C_s$ and $C_l$ = specific heat capacity of the PCM in the solid and liquid state respectively

$T_s$ and $T_l$ = temperature of the solid and liquid PCM respectively

t = time

x = distance

$k_s$ and $k_l$ = thermal conductivity of the solid and liquid PCM respectively

L = latent heat of fusion of PCM

v = velocity of phase change boundary

Numerical methods have been developed to model heat transfer during the solid – liquid phase change. The two most commonly used methods are the enthalpy method and the apparent heat capacity method.

*2.8.1.2 Enthalpy method*

The enthalpy method was proposed by Eyres et al. (1946) to deal with variations of thermal properties with respect to temperature. In the enthalpy method the latent heat and specific heat are combined into a single governing equation. It consists of solving the transient heat conduction equation expressed in terms of temperature and enthalpy, H(T) (Zhang et al., 2007). For conduction dominated heat transfer, equations (2-29) to (2-31) are rewritten into one equation where the latent heat is absorbed into the enthalpy term as follows:

$$\rho \frac{\partial H(T)}{\partial t} = \frac{\partial}{\partial x}\left(k \frac{\partial T}{\partial x}\right) \quad \textbf{(2-32)}$$

where H(T) represents the total energy of the material including sensible and latent forms of energy. The enthalpy of a PCM can be determined as a continuous function of temperature by using DSC testing (Castellon et al., 2008). Alternatively, a piecewise enthalpy function H(T) may be defined in terms of the latent heat of fusion 'L' and the phase change temperature window $\Delta T_{pc}$ (Voller and Cross, 1981, Darkwa and Su, 2012, Gowreesunker et al., 2012).

*2.8.1.3 Apparent heat capacity method*

The apparent heat capacity method was introduced by Hashemi and Sliepcevich (1967) to solve a one dimensional heat transfer with phase change in a 'mushy region', that is the phase change occurs over a temperature range so there is a region that is a mix of solid and liquid phases. The apparent heat capacity method consists of solving the transient heat conduction equation 2-32 expressed in terms of temperature and specific heat $C_p(T)$.

$$\rho C_p(T) \frac{\partial (T)}{\partial t} = \frac{\partial}{\partial x}\left(k \frac{\partial T}{\partial x}\right) \quad \textbf{(2-33)}$$

To account for the latent heat stored during phase change, the specific heat is defined as a piecewise function of temperature as expressed by (Lamberg et al., 2004):

$$C_p(T) = \begin{cases} C_s & \text{For } T < (T_{pc} - \Delta T_{pc}/2) \\ C_s + L/\Delta T_{pc} & \text{For } (T_{pc} - \Delta T_{pc}/2) < T < (T_{pc} + \Delta T_{pc}/2) \\ C_l & \text{For } T > (T_{pc} + \Delta T_{pc}/2) \end{cases}$$

where

- $T_{pc}$ = peak phase change temperature
- $\Delta T_{pc}$ = phase change temperature range

Lamberg et al. (2004) experimentally studied heat transfer through a homogeneous paraffin PCM block contained in a rectangular aluminum enclosure. The PCM temperature was measured using thermocouples placed at various locations in the enclosure. The authors compared the measured temperatures to numerical predictions obtained by implementing both the enthalpy and the heat capacity methods using COMSOL multi-physics software. They concluded that both numerical methods provided a ‘‘good estimation’’ of melting and freezing processes but that the heat capacity method agreed more closely with experimental data.

PCMs for building applications, such as paraffin, melt or freeze over a temperature range compared to pure materials where phase change occurs at a fixed temperature. This property makes the heat capacity method an attractive approach to simulating PCM in building applications. A number of researchers has successfully used this method to model PCMs in building applications (Mazo et al., 2012, Chen et al., 2008, Pasupathy and Velraj, 2006, Lin et al., 2004).

### 2.8.2 Modelling of PCM-concrete composites

One of the challenges in modelling a PCM-composite material is characterising the thermos-physical properties of the PCM composite correctly. Usually DSC is used to characterise a pure PCM. However for DSC the sample size is very small, between a milligram and one gram, depending on the calorimeter. For the type of PCM composites that are used in building walls such a small sample size would not be representative of the large scale material behaviour. When mixed with other materials, such as gypsum, mortar and concrete, the representative volume must be at least 10 times higher than the largest component size so DSC is not an appropriate method for characterising the thermo-physical properties of such PCM composites (Dumas et al., 2014).

The apparent heat capacity method and enthalpy method are straightforward to apply to one dimensional scenarios, however developing the models for 2 or 3 dimensional situations is complicated and difficult to generalise for different physics, geometries and applications. Hence when attempting to model 2 or 3 dimensional scenarios researchers have applied these methods in existing finite element modelling (FEM) software packages such as COMSOL. However these modelling packages have not being fully explored for heat transfer in PCM composite materials such as the PCM-concrete composite under study in this research project.

Baghban et al. (2010) used both COMSOL and another well-established numerical modelling system (WUFI-5) to study a three layer building envelope system including two layers of lightweight concrete incorporating PCMs and a layer of silica aerogel. The numerical results from COMSOL and WUFI-5 were compared and found to be similar however the authors concluded that COMSOL provides further facilities for defining different functions, such as thermal hysteresis and convective heat transfer. COMSOL is also flexible in modeling multi-physics within irregular and complex geometries. For example, Hasse et al. (2011) used COMSOL to model honeycomb wallboards with PCM in a 3D domain using the heat capacity method. The simulation results showed a very good agreement with experimental results.

Al-Saadi and Zhai (2013) categorised the various numerical models available for modelling PCMs in buildings, into *'Simplified'* models (suitable for steady state applications), *'Intermediate'* models – such as the enthalpy and apparent heat capacity methods, and '*Sophisticated'* numerical packages such as COMSOL, and carried out a comparative study of applications and validation methods. They found that the intermediate models are commonly used but are developed for specific applications to investigate explicit envelope designs. Hence, they lack flexibility in analysing design alternatives to enable the selection of optimal designs. Sophisticated models offer flexibility in solving complex and multi-physics problems but are not fully explored for modelling PCMs. They also demand a considerable amount of detailed data inputs, lengthy model set-up and validations. COMSOL will be used for modelling in this thesis.

### 2. 9 Structural aspects of concrete cladding panels for building envelopes

Precast concrete sandwich panels, comprising of two wythes - an inner and outer layer of concrete with a layer of insulation in between – are well established products for use as building envelopes. Together with providing protection from the external environment and a thermal buffer layer, they can also provide a structural function. The panels may be categorised as 'load-bearing' if the inner leaf of the panel is required to support vertical loads from the floors and walls above, or 'non-loadbearing' if the panel is only required to support its own self weight. However both categories of panel must be capable of resisting any horizontal loads, such as wind loads, that may be applied to it. The structural efficiency of the panel at resisting horizontal loading can be enhanced by connecting the two concrete wythes together so that the two wythes act compositely as one single element to resist the lateral loading rather than two separate thinner concrete layers acting independently.

### 2.9.1 Composite action

A two wythe sandwich panel can be designed as either fully composite, in which the two concrete wythes act together structurally, or non-composite in which each concrete wythe acts independently and the applied load is distributed to each wythe in accordance to their relative stiffnesses. The equations for calculating the second moment of area, I, of a composite and non-composite panel are provided in Table 2-9 with the dimensions defined in Figure 2-33, (O'Hegarty et al., 2019). Figure 2-33 also shows indicative strain profiles for full, partial and non-composite elastic behaviour.

**Table 2-9 Equations for determining the second moment of area of a non-composite and fully composite two wythe panel (O'Hegarty et al., 2019)**

| Non-composite panel | | Fully composite panel | |
|---|---|---|---|
| $I_1 = \frac{b_1 t_1^3}{12}$ | Eq (2-34) | $A = b(t_1 + t_2)$ | Eq (2-37) |
| $I_2 = \frac{b_2 t_2^3}{12}$ | Eq (2-35) | $c_1 = \frac{[0.5bt_1^2 + bt_2(h - 0.5t_2)]}{A}$ | Eq (2-38) |
| $I_{nc} = I_1 + I_2$ | Eq (2-36) | $I_c = \frac{bt_1^3}{12} + bt_1 y_1^2 + \frac{bt_2^3}{12} + bt_2 y_2^2$ | Eq (2-39) |

To quantify the percentage of composite action that occurs in a concrete sandwich panel elastically under flexure, k (%), Pessik and Mlynarczyk (2003) proposed the following equation:

$$k = \frac{I_{exp} - I_{nc}}{I_c - I_{nc}} \times 100 \qquad \textbf{(2-40)}$$

where:

- $I_c$ = second moment of area of the panel assuming it is fully composite
- $I_{nc}$ = second moment of area of the panel assuming it is non-composite
- $I_{exp}$ = second moment of area of the test panel determined experimentally

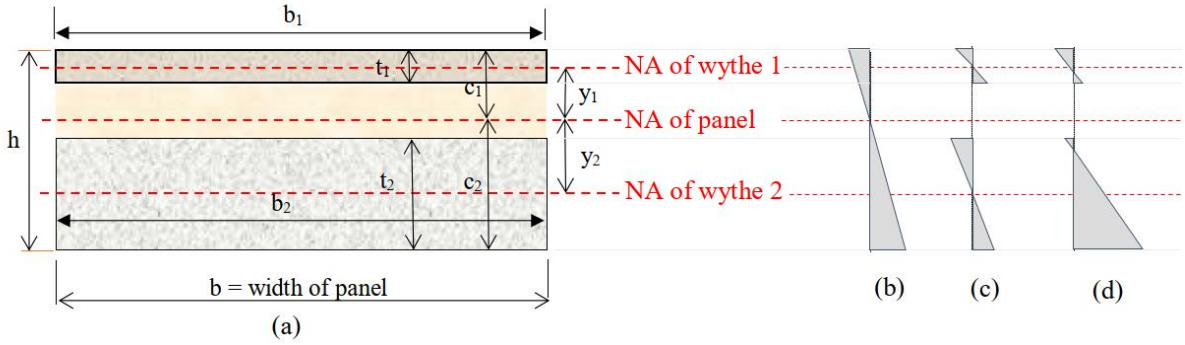


**Figure 2-33 (a) Definition of dimensional parameters for sandwich panel, and strain profiles for (b) fully composite, (c) non-composite and (d) partially composite action (O'Hegarty et al., 2019)**

The initial flexural stiffness of the panel $E_c I_{exp}$ (in N.mm$^2$), where $E_c$ is Young's modulus of the concrete (MPa), can be determined using mid span deflections (δ) measured during the linear elastic behaviour stage of a 3 point bending simply supported test and using :

$$E_c I_{exp} = \frac{PL^3}{48\delta} \quad \textbf{(2-41)}$$

where:

- P = point load applied at mid-span (N)
- L = distance between supports (mm)

From equation (2-41) $I_{exp}$ can be determined if $E_c$ is known.

It can be noted from equations (2-36) and (2-39) that the second moment of area of a composite panel $I_c$ is significantly greater than that of a non-composite panel $I_{nc}$ because $I_c$ has additional terms which include the distance between the neutral axis and the centroid of each wythe squared. Hence the greater the distance between the wythes the greater the stiffness of the panel. However the further apart the wythes are the more challenging it is for the connectors to achieve composite action through lateral shear transfer so there is a balance to be achieved in the design of sandwich panels.

In both composite and non-composite panels the insulation and/or connectors must be stiff enough to transfer the applied lateral load from the outer wythe to the inner wythe without crushing or buckling to facilitate load sharing. For composite action to occur the connectors must also be capable of transferring the longitudinal shear that occurs parallel to the wythes at each interface as a result of bending action (Figure 2-34). The bond between the insulation and the concrete wythes also contributes to the transfer of longitudinal shear in the panel.

(a)

(b)

**Figure 2-34 Depiction of (a) full composite action when connectors can transfer longitudinal shear between the wythes and (b) non-composite action resulting in relative slip between the layers**

### 2.9.2 Influence of shear connectors and insulation on composite behaviour

Initially, when two wythe wall panels were introduced in the 1960s, solid concrete zones were used to connect the two layers of concrete. However these solid concrete zones bridged the insulation layer and compromised the thermal performance of the panels. In an effort to improve the thermal performance, steel ties and steel wire trusses were used as connectors, which improved the thermal performance due to the smaller cross sectional area of the connector, however the highly conductive steel still acted as a thermal bridge. In 1997 Salmon et al. introduced the use of fibre-reinforced polymer (FRP) connectors formed in a truss pattern. Tests demonstrated that the FRP truss connector achieved a high level of composite action while mitigating the thermal bridge effect due to the very low thermal conductivity of the FRP material. This concept led to further development of non-metallic connectors including the carbon-fibre-reinforced polymer (CFRP) C-Grid continuous longitudinal shear connector (Figure 2-35 (a)) and the FRP Thermomass discrete pin connector (Figure 2-35 (b)). Previous research (O'Hegarty et al., 2021, O'Hegarty and Kinnane, 2020, O′Hegarty et al., 2019, Choi et al., 2016, Sennour et al., 2013, Frankl et al., 2011) has shown that the use of FRP ($^{TM}$Thermomass) pin connectors and CFRP C-Grid connectors results in the achievement of partial composite action in concrete sandwich panels.

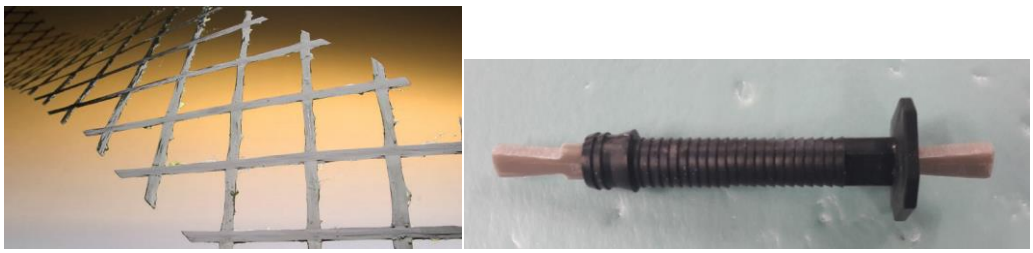

**(a) C-Grid connectors** **(b) Thermomass connectors**

**Figure 2-35 Non-conductive connectors used in panels for structural testing**

The C-Grid truss connector is a linear continuous connector formed by cutting a CFRP grid at a 45 degree angle. Continuous strips of C-Grid are embedded in the concrete wythes on either side of the insulation wythe of a panel (Figure 2-36). The C-Grid connector is very thin and has no out-of-plane stiffness so it will buckle under axial compression. Hence these connectors rely on the compressive strength and stiffness of the insulation wythe to transfer the lateral load between the two concrete wythes. However the truss profile of the grid allows it to resist longitudinal shear through axial tension in the alternate diagonal members together with the insulation acting as a compression member. Thus the compressive strength of the insulation is a significant factor contributing to the degree of composite action achieved in panels with C-Grid connectors post cracking.

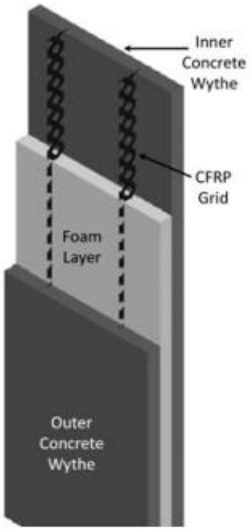


**Figure 2-36 Schematic depicting concrete sandwich panel with C-Grid connector (Sennour et al., (2013))**

The two main types of rigid foam insulation that are commonly available are Expanded Polystyrene (EPS) and Extruded Polystyrene (XPS). Shukla (2019) found that the initial stiffness of XPS insulation is circa 5 times the stiffness of EPS. Table 2-10 provides the relevant properties for XPS and EPS taken from literature and manufacturer's data.

**Table 2-10 Properties for XPS and EPS insulation**

| Insulation type | Thermal Conductivity W/mK | Compressive strength MPa | Stiffness MPa |
|---|---|---|---|
| EPS | 0.035 | 0.09[1] | 6.9[2] |
| XPS | 0.033 | 0.3[1] | 24.3[2] |

[1]Source manufacturer's data sheets; [2]Source Shams et al. (2014)

Frankl et al. (2008 and 2011) carried out extensive investigations into concrete sandwich panels connected with C-Grid using both XPS and EPS rigid foam insulation. With both types of insulation a high degree of composite behaviour was achieved (greater than 90%). Other researchers have also achieved high levels of composite action in flexural tests of concrete sandwich panels with C-Grid connectors (Sopal, 2013, Sennour et al., 2013, Bunn, 2011). In all of these investigations it was found that the EPS insulation provided a slightly better composite action than XPS insulation despite the higher stiffness of XPS insulation. This was attributed to the superior bond between EPS and the concrete wythes which provided resistance to lateral shear between the insulation and the concrete wythe.

Naito et al. (2012) investigated the performance of fourteen different types of connectors including C-Grid and Thermomass and determined that the shear strength of the C-Grid connector was improved by 21 % when used with EPS insulation over XPS insulation. This improvement was again attributed to the greater surface roughness of the EPS insulation. Pessik and Mlynarczyk (2003) found that, in the absence of connectors, the bond between EPS insulation and the concrete provided 5% composite action. However other researchers (Choi et al., 2015, Kim and You, 2015) have found opposing results under similar test conditions in which the XPS insulation provided more composite action. From the variance in the results of these research studies with regard to the contribution of EPS and XPS to composite behaviour it can be concluded that the concrete-insulation bond should not be relied on in the design of concrete sandwich panels.

O'Hegarty et al. (2019) carried out flexural tests on four concrete sandwich panels connected with C-Grid and including EPS insulation. This study concluded that an insignificant level of composite action was achieved in the panels (less than 5 %). A complimentary FEA analysis of the panel behaviour showed that as the elastic modulus of the insulation is reduced, the overall stiffness of the panel with C-Grid connectors approaches that of a panel with no connectors. However the modelling also showed that if the insulation layer has an elastic modulus greater than 5 MPa then the C-Grid type connector can achieve high levels of composite action, as reported in other research studies. The variance in the results of previous research studies may indicate that the achievement of composite action is sensitive to construction methods and quality control and hence the assumption of composite action in the design of concrete sandwich panels with CFRP Grid connectors may not be reliable.

Thermomass connectors, as shown in Figure 2-35 (b), are discrete pin connectors which are not normally designed to transfer longitudinal shear between the concrete wythes during bending. However they display good resistance to buckling and hence they are more effective at transferring load from the outer wythe to the inner wythe in the transverse direction. As a result, the load is distributed to each wythe in accordance to their individual stiffnesses rather than the wythes acting compositely through longitudinal shear resistance. The fiber composite core of the connector is supplied with dovetail ends that act as wedge anchors in the concrete and thus only thin wythes are required for anchorage. The polymer collar includes a restraining flange, which rests at the insulation face, as well as corrugations, which wedge inside the

insulation (Figure 2-37). The connectors come in various serial sizes to accommodate different insulation depths while always achieving sufficient embedment into the concrete wythes.

Previous research by O'Hegarty et al. (2021) into composite behaviour in sandwich panels connected with Thermomass pins has found that the pin connectors can provide partial composite behaviour (13 %). Shams et al. (2014) investigated the load bearing behaviour of Thermomass pin connectors in the context of flexural behaviour of concrete sandwich panels and concluded that the pin connector did not increase the overall stiffness or bending capacity of the panel however it did achieve a more ductile failure mechanism relative to a panel without connectors.

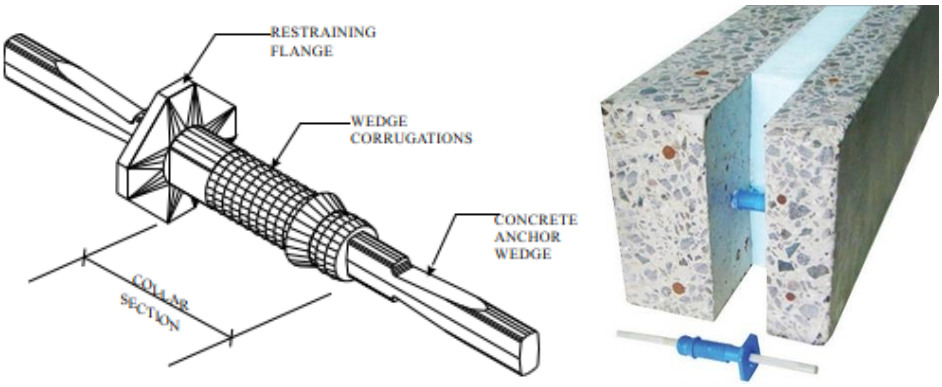


**Figure 2-37 (a) Schematic of Thermomass connector, (b) Thermomass connector in position (Source: https://www.compositeglobal.com)**

Although composite action has many advantages, it does present the disadvantage of bowing. With composite behaviour the differential strain between the wythes, caused by temperature or humidity differences in between the wythes, results in bowing of the panel which can lead to secondary bending effects (Losch, 2003). Non-composite panels typically do not experience this thermal bowing because thermal strain in the outer concrete wythe is not transferred to the inner wythe. Due to the low levels of composite action achieved with the use of Thermomass, connectors these connectors are considered advantageous in mitigating bowing effects in panels. Thermomass connectors also have the advantage of being well established in the concrete sandwich panel industry and the connectors have undergone rigorous testing, including fire testing and fatigue testing to obtain industry approval. However, as there are many factors that can potentially influence the contribution, if any, of the Thermomass connectors to composite behaviour in a panel, such as the strength of the wythes, thickness of

the wythes and the stiffness of the insulation layer, it is important to investigate how the Thermomass connector will affect the structural behaviour of the novel concrete cladding panel designed for this research project which includes a thin, high-strength concrete outer wythe and a thicker inner wythe composed of the relatively weaker PCM-concrete composite. As the stiffnesses and material strengths of each wythe is different it is difficult to predict in which wythe the first crack will occur and which wythe will control ultimate failure.

## 2.10 Conclusions

It is the overall aim of this research to design and manufacture a precast concrete sandwich cladding panel with enhanced thermal mass properties achieved through the incorporation of PCMs into the concrete. With the incorporation of PCMs, the cladding panel can provide both sensible and latent heat storage capacity and hence reduce the demand on auxiliary cooling systems, improving the overall energy performance of a building. The literature reviewed concurs that the inclusion of PCMs into the building envelope of a building shows good potential for reducing the energy demand of a building however there are many different factors which influence the efficacy of the PCM-composite materials.

There are many PCMs available however there is no one material that meets all of the desired characteristics of a PCM, as noted at the end of Section 2.3.3, so an acceptable compromise must be reached. The primary requirement for a PCM that is to be used in a thermal storage application is a suitable melting temperature. The context for this research project is to develop concrete cladding panels that will reduce overheating in buildings. From the review of the literature, a PCM with a melt temperature range circa 19 – 24 $^{o}$C would be appropriate for a space cooling application.

The PCM must also be chemically compatible with the material with which it is to be combined. From the literature review it can be concluded that organic PCMs are the most suitable for mixing with a building material. Paraffin and various fatty acid eutectics have been successfully combined with concrete in previous research and have appropriate melt temperature ranges for space cooling applications, hence it is proposed to investigate both of these types of PCMs for use in this study.

In this study it is proposed to incorporate the PCMs into concrete. A large proportion of the research that has been carried out on PCMs incorporated into concrete has used micro-encapsulated organic PCMs. The distribution of the small PCM containing capsules provides a large heat exchange surface. The capsule shell also prevents any chemical interaction between

the PCM and the concrete matrix and mitigates any issues with volume change of the PCM material during phase change. The microcapsules are relatively easy to incorporate into the construction material during the mixing process and there is no additional site work required. There is also no need to protect the PCM capsules from destruction such as from post fixed nails etc.

The second most common method in the literature for incorporating PCM into concrete is by vacuum impregnation into porous LWAs which are then included in the concrete mix. All combinations of the LWA-PCM composites in the studies described were found to be chemically compatible, non-toxic and had a large thermal energy storage density. As the PCM-aggregate is combined with the concrete in the same way as a normal aggregate would be, a reasonably even distribution of the PCM throughout the depth of each sample can be achieved.

Both micro-encapsulated paraffin and a LWA-PCM formed with a fatty acid, butyl stearate, have been successfully combined with concrete in previous research by the author. Both methods of incorporation produced PCM-concrete composite material that displayed enhanced thermal mass properties. The LWA-PWC displayed higher thermal storage capacity due to the greater latent heat capacity and narrow melt temperature range of the butyl stearate. However the melt temperature range of the butyl stearate is too low for a space heating application. For this reason, the first objective of this research study is to create a fatty acid eutectic that has a melt temperature range between 19 – 24$^{o}$C, which can then be vacuumed impregnated into a LWA for incorporation into a concrete mix. A problem that was evident from the previous research study was that some of the butyl stearate leaked from the LWA and stained the surface of the concrete. In order to use the LWA-PCM in the proposed concrete cladding panel this issue needs to be resolved. Hence the first objective of the study is to investigate methods to prevent leakage of the PCM from the LWA. These initial investigations will inform the final selection of PCM and method of incorporation into concrete to form the PCM-concrete composite material to be used in the inner leaf of the concrete sandwich cladding panels which will also include an insulation layer and a concrete outer layer.

Extensive research has been carried out on the impact of the addition of PCM on the fresh and hardened properties of concrete. With regard to the properties of fresh concrete, it is clear from previous research that the incorporation of a PCM by any method will reduce the heat of hydration and hence slow down the early strength gain of the concrete panels. This effect must be taken into consideration particularly in the manufacture of the full-scale precast cladding

panels as the concrete in the panels must achieve sufficient strength to support the self-weight of the panel before they are lifted off the casting tables, which typically occurs around eighteen hours after casting in a precast factory.

It is also clear from the literature review that the addition of micro-encapsulated PCM reduces the workability of concrete. Most studies concluded that the maximum quantity of micro-encapsulated PCM that can be added to concrete while still achieving an acceptable workability is 6 % by weight of concrete. In this study it is proposed that a superplasticiser will be included in the concrete mix design to reduce the adverse effect of micro-encapsulated PCM on the workability of the fresh concrete, without compromising the mix's water-cement ratio.

Concrete strength is the most important property for concrete that is to be used in a building element. It is clear from the literature that there is a limit to the quantity of PCM that can be incorporated into concrete due to the negative effect that it has on the material strength. With regard to micro-encapsulated PCMs, there is consensus in the literature that 5 % by weight of concrete is the maximum amount that can be incorporated into concrete while still achieving compressive strengths within the range suitable for use in building structures (greater than 20 MPa characteristic). For these reasons the use micro-encapsulated PCMs in concrete will be limited to 5% by weight of concrete. The literature review also reported that the inclusion of LWA-PCMs in concrete normally has an adverse effect on the strength, however Berardi and Gallardo's (2019) summary of compressive strength results from previous research studies that investigated LWA-PCM-concrete demonstrated the feasibility of achieving strengths suitable for structural applications.

One of the disadvantages of organic PCMs is that they have a low thermal conductivity. As discussed in Section 2.5.2.3, this leads to a reduction in the thermal conductivity of concrete that incorporates organic PCMs. The reduced thermal conductivity of the PCM-concrete composite may result in reduced efficacy of the PCM as it takes longer for the heat to penetrate deeper into the material and engage the PCM deeper in the element. For this reason, the second objective of this research study is to explore some simple methods of improving the thermal conductivity of the proposed PCM-concrete composite through the addition of GGBS and steel fibres.

To facilitate the prediction of PCM behaviour in a thermal storage element it is essential to have accurate information on the thermal properties of the PCM, particularly the phase change properties. As discussed in Section 2.3.4 the most commonly used techniques for determining

the thermo-physical properties of PCMs are Differential Scanning Calorimetry (DSC) and the T-history method. When considering an overview of the literature reviewed in which PCMs were characterised as part of the study, dynamic DSC testing appears to be the most widely used (Klimeš et al., 2020). The test procedure is more straightforward than the T-history method and is not as time consuming. For this study, a dynamic DSC test will be used to characterise the proposed PCM materials. Small, homogenous sample sizes, less than 20mg, will be used along with a low heat rate regime as recommended by Memon et al. (2015), Eddhahak-Ouni et al. (2014) and Barreneche et al. (2013).

A fundamental requirement for the design of a cladding panel for a building is that it is capable of withstanding any applied forces, in particular wind forces. As discussed in Section 2.9 the structural strength and stiffness of a two wythe concrete sandwich panel is greater if the two wythes act compositely in response to applied loading. A review of the literature on this topic has confirmed that the ability of the cladding panel to act compositely is influenced by the type of shear connectors used to connect the two wythes, the stiffness of the insulation layer and the bond between the insulation and concrete. The third objective of this PhD research study is to ensure that the proposed PCM cladding panels have sufficient strength and stiffness to withstand typical wind loads. To achieve this a structural test will be carried out on a number of sample panels with varying types of connectivity between the wythes. In addition the sample panels will undergo thermal testing to determine overall thermal conductivity values, R-values and U-values

A significant body of research has studied the use of a building envelope as a thermal energy storage unit and all studies report enhanced thermal mass behaviour and improved overall energy performance when PCMs are incorporated into the construction material of the building envelope. However the potential benefits of a PCM-enhanced building envelope are subject to many variables including building specific variables and variables of geographical location, as discussed in Section 2.6. For this reason, the thermal storage behaviour of a PCM-concrete composite as derived in a laboratory setting cannot be assumed to be replicated in a full-scale setting. Hence full-scale testing is an essential tool in the investigation into the potential of this technology. There is a scarcity of full-scale research studies into the performance of PCM-concrete enhanced building envelopes in the literature and most studies that investigated PCM-composites in a full-scale scenario were numerical simulation studies in which the model was validated using data from a laboratory study. There is a lack of modelling studies that have

been validated against results from full-scale experiments constructed using multiple layered walls and typical construction details. Another gap identified in the literature review is the lack of experimental data from year-long duration full-scale tests which is required to enable the performance of the PCM-composites to be assessed in all seasons. In order to address these noted gaps in the research, the fourth and primary objective of this PhD research project is to construct three full-scale huts using the designed concrete sandwich cladding panels with and without a PCM-concrete composite inner leaf. In contrast to the previous study by Cabeza et al., (2007) as described in Section 2.6.1, the proposed huts include a layer of insulation. The huts are instrumented to record both internal thermal data and local climate data. Also in contrast to Cabeza's previous study, the data is recorded over an 18 month period to ensure that the thermal performance of the panels can be assessed across all seasons. Thermal data is also recorded throughout the depth of the wall which enables the effective depth of the PCM to be determined under the varying daily and seasonal thermal conditions.

As reported widely in the literature there is a significant number of variables that impact the potential for a PCM-composite material to provide a beneficial thermal mass effect. Each individual building requires a bespoke design and hence the development of numerical simulation tools is necessary to enable practical and efficient solutions to be derived. However, as noted previously, there is a scarcity of simulation studies in the previous research studies that have been validated with data from 'real' full-scale experiments. It is proposed to use COMSOL in this study to achieve the fifth objective of this PhD research project which is to develop an accurate, experimentally verified, mathematical model for prediction of the dynamic thermal environment of buildings which contain PCM-concrete composite material and which accounts for different types of climate and daily and seasonal variations in outdoor conditions. Thermal data recorded at the full-scale huts will be used to validate the model.

# Chapter 3. Methodology

## 3.1 Introduction

The following chapter describes the methodology adopted to achieve the objectives of this research project as noted in Section 1.3. A schematic of the outline methodology is provided in Figure 3-1.

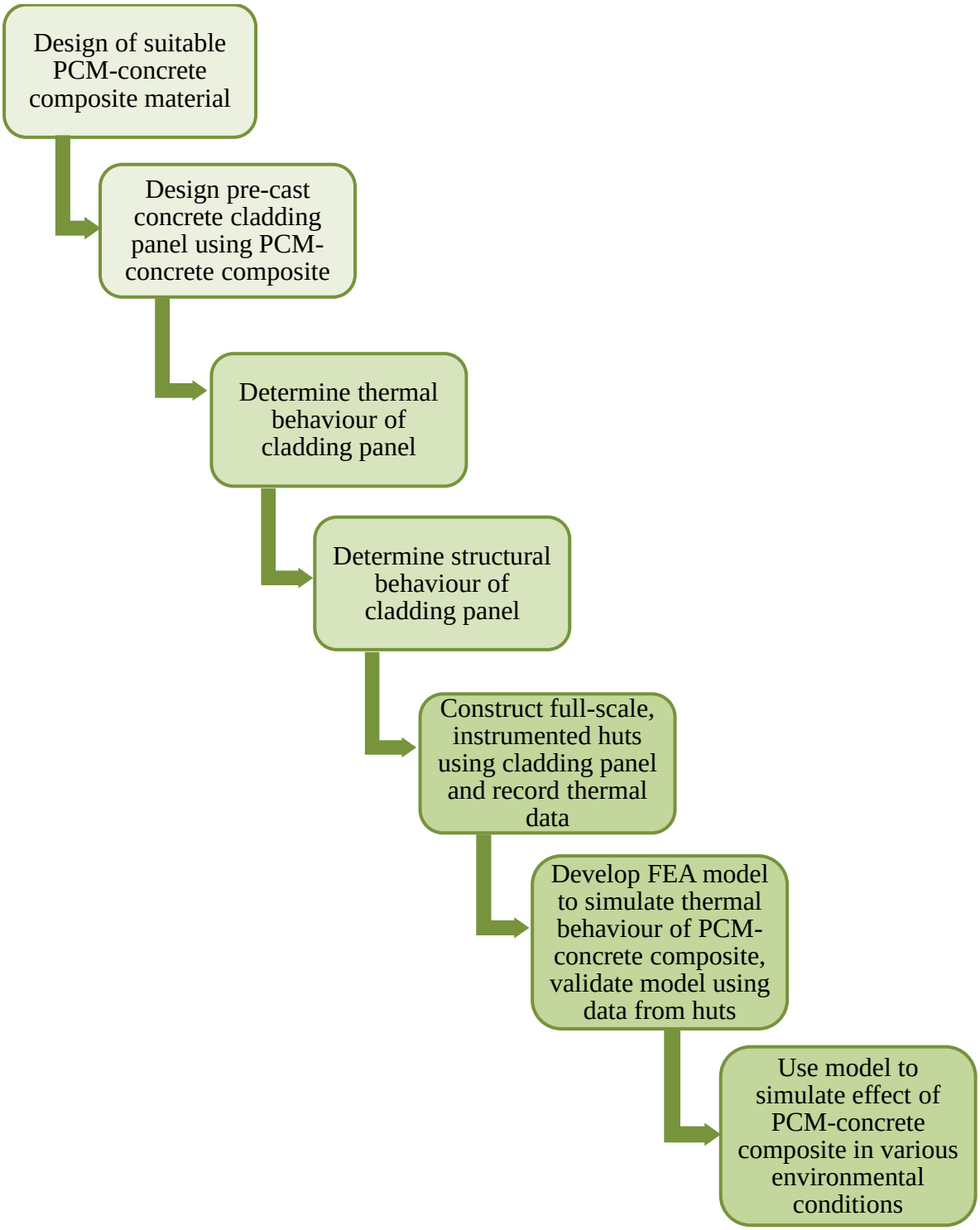


**Figure 3-1 Schematic of experimental design**

As Figure 3-1 shows, this chapter describes a laboratory experimental regime to explore the design and manufacture of a PCM-concrete composite. This laboratory exploration led to the final design mix for a PCM-concrete composite material for use in the inner leaf of the pre-cast concrete cladding panel. Further laboratory work was carried out on sample-sized pre-cast concrete cladding panels, constructed with the PCM-concrete composite, to determine the thermal conductivity and structural behaviour of the panel prior to manufacture of the full-scale panels for the test huts.

This chapter also describes the rationale for the full-scale test huts constructed with the non-loadbearing concrete cladding panels. Thermal data from the huts was recorded and used to validate a FEA simulation model which was then used to predict the impact of a PCM-concrete composite material on the internal thermal environment of a building.

The results of all tests referred to in the laboratory experimental regime are presented and discussed in Chapters 4, 5 and 6. The design, instrumentation and manufacture of the full-scale test huts are described in Chapter 7 along with an analysis and discussion of the data collected. Chapter 8 details the development of the FEA model and the simulations carried out are discussed.

### 3.2 Objectives of experimental work

The objectives of the experimentation work are as follows:

1. To manufacture a suitable fatty acid eutectic PCM to be vacuum impregnated into lightweight aggregate and incorporated into concrete
2. To find a viable method of preventing leakage of PCM from lightweight aggregate
3. To enhance the thermal conductivity of concrete by including steel fibres/GGBS in the mix
4. To design a PCM-concrete composite to be used in the inner leaf of a non-loadbearing precast concrete sandwich cladding panel
5. To determine the thermal conductivity of the PCM-concrete composite cladding panels
6. To investigate the structural behaviour of the PCM-concrete composite cladding panels
7. To design the layout and thermal monitoring regime of full-scale test huts constructed with the PCM-concrete composite, non-loadbearing cladding panels and to monitor their thermal performance

### 3.3 Assessment of PCM materials

#### 3.3.1 Manufacture of fatty acid eutectic

As discussed in Section 2.5.2.4 previous research carried out by the author found that concrete containing a lightweight aggregate-butyl stearate composite acted as an effective thermal storage material however there are some disadvantages with butyl stearate that deemed it unsuitable for this research project. One is that the melt temperature of the butyl stearate, at 15-17 $^{o}$C, is too low for an over-heating building application. For this reason, an initial aim of the project is to investigate an alternative fatty acid PCM which has a higher melt temperature range, circa 20 – 24 $^{o}$C that can be vacuum impregnated into LWA. The results of this investigation will inform which type of PCM is used in the wall, either a fatty acid eutectic vacuum impregnated into a LWA or a micro-encapsulated paraffin, which is a product readily available on the market.

From a review of the literature on the use of fatty acids as PCMs in space heating applications, as detailed in Section 2.3.3 it was concluded that a eutectic made up of Capric acid (CA) – also known as Decanoic acid (DA) - and Myristic acid (MA) with a 75:25 mass ratio would be suitable for this research project as it had an expected melt temperature range of 22-25 $^{o}$C and a relatively high latent heat capacity of 135-140J/g.

For this reason the first objective of the experimental work is to manufacture a CA-MA eutectic fatty acid PCM with a mass ratio of 75:25 that can be vacuum impregnated into LWA and then included in a concrete mix to form a potential PCM-concrete composite material for use in the cladding panels.

Capric acid ($C_{10}H_{20}O_2$) and Myristic acid ($C_{14}H_{28}O_2$) were supplied by Sigma Aldrich Ireland. In total 2 litres of a eutectic mixture of the fatty acids was prepared in half litre batches. First, the two components were fully melted and then placed together in a sealed beaker in the stated proportions, that is, 75:25 Capric acid:Myristic acid by weight. The beaker was placed in the oven at 70 $^{o}$C for 2 hours to ensure that the fatty acids were completely melted. The mixture was then placed in a ventilated chamber over a heat set at 30 $^{o}$C and constantly stirred using a magnetic stirrer for 1 hour at 400 rpm to ensure a homogenous mixture was formed (Figure 3-2). The eutectic was then allowed to cool slowly to ambient room temperature.


**Figure 3-2 Formation of the fatty acid eutectic PCM**

### 3.3.2 Characterisation of PCMs using Differential Scanning Calorimetry

In order to assess and compare the two types of PCM under investigation, that is, the microencapsulated paraffin and the fatty acid eutectic, it was necessary to determine the thermal characteristics of the materials. The thermal properties of interest for this research, as explained in Section 2.3.1 are as follows:

- Temperature at the onset of melting
- Temperature at the onset of solidification
- Peak melt temperature
- Latent heat capacity

As detailed in Section 2.3.4 DSC is widely considered to be a suitable method for determining the thermal properties of PCMs. It was concluded from the literature review that the proposed PCMs for this research project would be characterised using a dynamic DSC test using a low heat rate regime as described in Section 2.3.4.1. The instrument used to carry out the DSC analysis is a power compensation DSC8000 from PerkinElmer (Figure 3-3).

**Figure 3-3 Image of DSC8000 Perkin Elmer instrument**

In this type of DSC each sample has a separate heater and the temperatures of the two materials are controlled separately. The temperatures of the samples are kept the same by compensating for the heat flow into the PCM sample. The compensating heat power required to keep the temperature of the PCM and reference material the same is a measure of the change in enthalpy.

The reference material used in the DSC testing was indium. The same method was used to test each PCM and is described as follows (Eddhahak-Ouni, 2014, Memon, 2014):

1. A sample of the PCM (7 mg CA-MA, 10 mg Micronal) and of the reference material was placed in two separate 50µl sample pans and sealed with a lid which had a 50 micron hole.
2. In the DSC test a constant heating rate of 5 $^{o}$C/min was applied for a temperature range of -10 $^{o}$C to 40 $^{o}$C. The heating rate is set to ensure that no temperature gradient occurs within the sample. The temperature range for the DSC test is selected to encompass the solid and liquid phases of the PCM including the phase change temperature range.
3. The amount of heat absorbed or released by the sample as it is heated, cooled and held at a constant temperature was measured.
4. The DSC was set to apply the following heating/cooling regime:
    - Set the temperature of sample to -10 $^{o}$C and hold at that temperature for 5 minutes to ensure thermal equilibrium across the sample
    - Heat the sample to 40 $^{o}$C at a rate of 5 $^{o}$C per minute
    - Hold the temperature at 40 $^{o}$C for 5 minutes to ensure thermal equilibrium across the sample
    - Cool the sample to -10 $^{o}$C at a rate of 5 $^{o}$C per minute
5. This cycle was repeated 4 times to ensure the results were re-producible.

The results of the DSC tests are presented in Section 4.1.

### 3.3.3 Methods of preventing leakage of PCM from LWA

As noted in the research by Niall et al. (2016), although the LWA-PCM composite performed well in terms of heat storage, there was clear evidence of leakage of the butyl stearate on the surface of the panels. It was concluded that this leakage occurred as a result of the heat of hydration melting the butyl stearate prior to the hardening of the cement matrix and sealing of the butyl stearate into the LWA. For this reason, another initial aim of this research project was to explore different methods to try to seal a fatty acid PCM into LWA so that leakage does not occur.

Initially three methods were investigated to try to prevent the leakage:

1. Sealing the surface of the LWA-PCM composite prior to adding it to the concrete mix. Two different types of sealant were used – Sikagard 700S sealant and Sikabond SBR sealant
2. Cooling the LWA-PCM composite in a refrigerator prior to adding it to the concrete mix so that the LWA-PCM composite is at a low temperature when added to the concrete mix – circa 5 $^{o}$C. The aim was to investigate if the temperature of the PCM remains below the onset melt temperature until the hydration of the cement was complete and leakage of the PCM from the LWA was prevented by the hardened cement matrix.
3. Curing the concrete samples at a low temperature, 0-5 $^{o}$C with the aim of maintaining the PCM in a solid phase until the cement had fully hydrated and the cement matrix had hardened around the LWA preventing leakage of the PCM.

The LWA-PCM composite was made with the CA:MA eutectic using the method as described by the author in Niall et al. (2016). This composite was divided into three samples. One sample was treated with SIKAgard sealant, another sample was treated with SIKAbond sealant and the remaining sample was left untreated. The two sealant products, were selected after discussions with Sika's technical representative. Sikagard 700S is a water repellent Siloxane-based compound designed for absorbent cementitious substrates. It penetrates into the open pores of the substrate and provides a water repellent film. Sikabond SBR is a water resisting bonding agent which provides a water resistant layer which also improves the bonding properties of cementitious substrates. The data sheets for these product are provided in Appendix A.

The outline procedure used to seal the LWA-PCM composite using both proposed types of sealant was as follows:

1. Weigh a flat container.
2. Place the LWA-PCM composite aggregate into the flat container and weigh.
3. Pour a small amount of the sealant over the aggregate and move the aggregate around with a paint brush to ensure that all particles are fully coated.
4. Sieve the aggregate to remove any excess sealant.
5. Clean and dry the flat container and place the aggregate back in to it.
6. Weigh the aggregate and container.
7. Leave the aggregate to dry for 2 hours and then repeat steps 1 -7 once only.

To check the sealing performance of Sikagard 700S and Sikabond SBR the following was undertaken:

1. Weigh the dried sealed aggregate.
2. Place it in a dessicator and apply a vacuum for 1 hour.
3. Reweigh the sample and note any difference in weight.

Half of each sample of treated LWA-PCM composite was then placed in a refrigerator for a number of days prior to pouring the samples. The other half of the treated LWA-PCM composite was stored at room temperature, 18 $^{o}$C, +/-1 $^{o}$C (Figure 3-4). The purpose of cooling the aggregate prior to adding to the concrete mix was to investigate if leakage can be prevented by limiting the melting of the PCM during hydration and to determine if leakage occurs during the hydration stage.


**Figure 3-4 Image of LWA-PCM composite after sealing with Sikagard 700S**

Using the LWA-PCM composite, six concrete pours were carried out, each pour providing two concrete samples (100 x 100 x 100 mm) (Figure 3-5). A type K thermocouple was cast into the centre of each of the 12 no. cubes. Thermocouples were also placed on the surface of each cube. One sample from each pour was placed in a curing tank that was kept at a constant temperature of 20 $^{o}$C, +/-1 $^{o}$C – so called warm curing. The second sample was placed in a curing tank that was maintained at a temperature of less than 5 $^{o}$C – so called cold curing. Thermocouples were also placed in the curing tanks to monitor the temperatures. The purpose of using two different curing temperatures was to investigate if leakage occurs during curing and hence can leakage be prevented by keeping the PCM in a solid state during the curing process.

The samples were left in the curing tanks for 28 days and all temperatures were monitored during this time using a National Instruments logger and chassis (NI-cRIO-9024 & NI-cRIO-9114 ) along with three National instruments thermocouple modules (2 no. NI-9211 4- and 1 no. NI-9213 16), to which the thermocouples are connected (Figure 3-6).

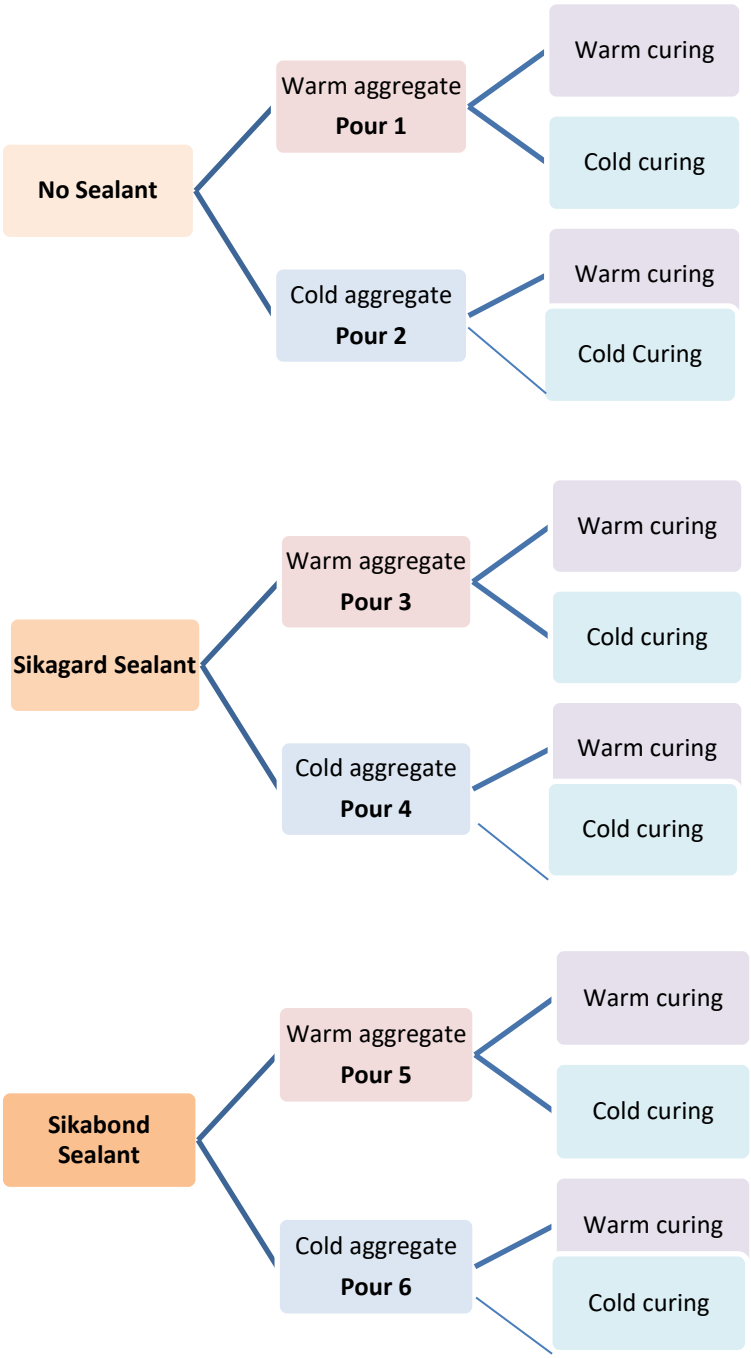


**Figure 3-5 Test samples for investigating cause and prevention of leakage of PCM from LWA**

**Figure 3-6 Images of National Instruments logger and thermocouple modules**

A second investigation was carried out in order to find a method of sealing the PCM into the LWA. This investigation focused on preventing/limiting the migration of water within the concrete and hence reduce the migration of the PCM to the surface of the concrete. A water resisting additive called Conplast WP402 was added to the fresh concrete mix during the mixing process. This additive reduces the porosity of concrete and hence reduces the permeability and diffusion coefficient of the concrete. In addition a superplasticiser called Auramix 200 was used as it allows the reduction of water in the concrete mix without loss of workability and hence reduces the permeability of the hardened concrete. Five pours were carried out to make test samples as per Figure 3-7. Two 100mm cubes were made from each pour and cured in a water tank that was kept at 20 $^{o}$C +/-1 $^{o}$C.

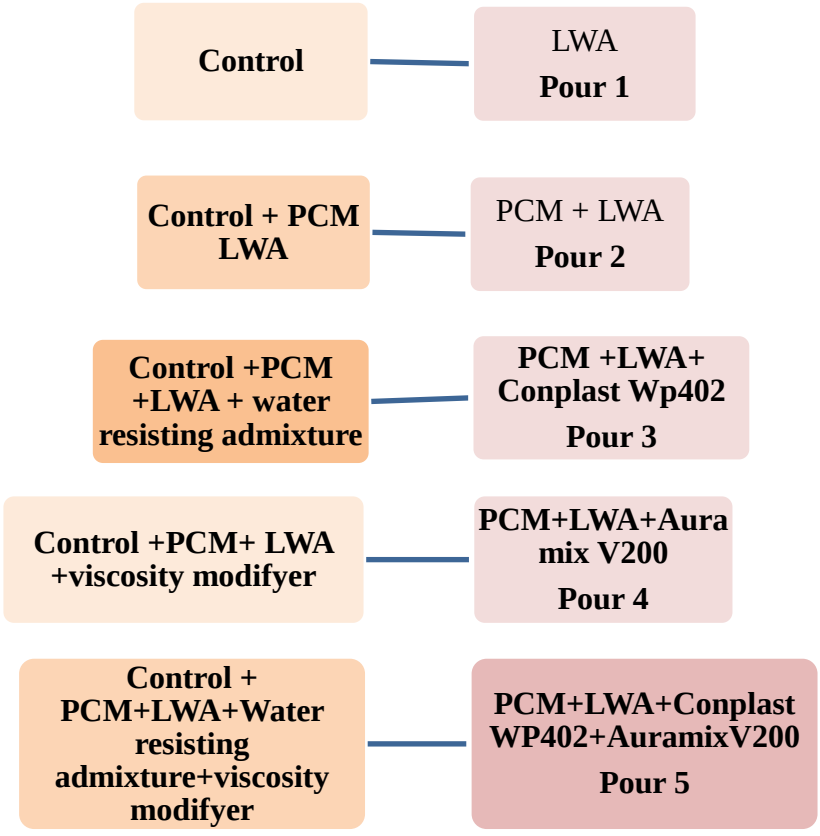


**Figure 3-7 Test samples for investigating a method for preventing leakage of PCM from LWA**

The results of these investigations informed which type of PCM was used in the wall, either a fatty acid eutectic vacuum impregnated into a LWA or a micro encapsulated paraffin which is a product readily available on the market. The results of the sealing tests are presented in Section 4.2.

### 3.4 Enhancing thermal conductivity of concrete

The thermal conductivity of the inner leaf of the cladding panel is a critical parameter for this study as once the heat is absorbed at the surface of the panel, the conductivity of the panel material will directly influence the heat flux through the wall and hence the thermal mass behaviour. As reported in Section 2.3.3 one of the disadvantages of organic PCMs is that they have low thermal conductivity which can hinder their activation and hence reduce the efficiency of their application. The thermal conductivity of some PCMs can be improved by mixing the PCM with a highly conductive material so that the heat transfer rate between the PCM and the concrete matrix is increased. The relatively low conductivity of the PCM also contributes to a 25 to 50 % decrease in thermal conductivity of the PCM-concrete composite (Niall et al., 2017, Fenollera et al., 2013, Hunger et al., 2009).

In a real application where a PCM-concrete composite material is used in a building to store thermal energy, the amount of PCM that changes phase and hence stores heat depends on the depth to which sufficient heat energy penetrates into the wall, that is, the effective depth of the PCM. This depth depends on the thermal conductivity of the PCM-concrete composite and also on the local internal and external environmental conditions of the building. As the PCM absorbs heat energy during phase change it slows the progression of heat energy deeper into the wall hence the PCM may become less effective with increasing depth. However, if the effective depth of the PCM could be improved by increasing the thermal conductivity of the PCM–concrete composite, the rate of heat penetration into the wall is increased and more of the PCM is activated. The third objective of this experimental investigation was to explore if the thermal conductivity of the PCM-concrete composite can be improved using established technologies that would not add undue complexity to the manufacture of the panels.

#### 3.4.1 Experimental design

In order to improve the effectiveness of the PCM within the concrete mix it was decided to explore some simple sustainable methods of improving the thermal conductivity of a PCM-concrete composite. Thermal conductivity of concrete has been found to be a function of its density (Bentz et al., 2011). It is generally understood that the use of ground granulated blast-

furnace slag (GGBS) as a partial cement replacement results in a denser cement paste. The testing regime set out to investigate if the use of 50% GGBS influences the thermal conductivity of concrete.

The inclusion of steel fibres in a concrete mix has been shown to increase the thermal conductivity of concrete (Cook and Uher, 1974). However other research studies have found that increasing the volume of fibres in the concrete mix does not necessarily increase the thermal conductivity of the concrete as the presence of fibres can increase the porosity of the concrete and hence reduce the density (Nagy et al. 2015). The testing regime sets out to investigate the effect of including a high dosage (100 kg/m$^3$) of steel fibres on the thermal conductivity of concrete.

The type of aggregate used in concrete has been shown in literature to influence the thermal conductivity (Howlader et al., 2012, Wadso et al., 2012). All the panels in this testing regime included the same type of limestone aggregate, which was sourced from an Irish precast manufacturer Techrete Ltd, and is the type of aggregate typically used in their panel manufacturing. Two of the panels also included the type of cement that is typically used by Techrete Ltd in their panel manufacturing – namely CEM I (Rapid Hardening). The other panels used CEM II A-L cement which was readily available in the TCD laboratory.

Seven panels were manufactured as follows:

1) **Control**: CEM II A-L + Limestone aggregate – *which is the control sample*
2) **GGBS**: CEM II A-L 50% + 50% GGBS + Limestone aggregate – *compared to the control panel indicating the influence of GGBS*
3) **Steel Fibres**: CEM II A-L + Limestone aggregate + steel fibres [100 kg/m$^3$ 35mm steel fibres] - *compared to the control panel indicating the influence of steel fibres*
4) **LWA control**: CEM II A-L + LWA - *compared to the control panel indicating the influence of LWA*
5) **LWA-PCM**: CEM II A-L + LWA + PCM - *compared to the LWA control panel indicating the influence of PCM*
6) **Control**: Techrete's CEM I Rapid Hardening + Limestone aggregate
7) **Micronal**: Techrete's CEM I Rapid Hardening + Limestone aggregate + 5% Micronal PCM - *compared to the control panel indicating the influence of Micronal*

### 3.4.2 Manufacture of test panels

Each test panel was 250 x 250 x 100 mm deep to reflect the typical depth of a wall within a building. Two thermocouples were cast into each panel at equal intervals of 33mm from the plan surfaces and thermocouples were also located on the front and rear faces. After casting the concrete, panels were cured for 28 days in accordance with I.S. EN 12390-2, as were all concrete test samples. As moisture content can significantly influence the thermal conductivity of concrete, the panels were allowed to dry out in the laboratory for a further 28 days during which moisture content was monitored. The average air temperature in the laboratory is 19 $^{o}$C and the average relative humidity is 55%. All panels had a moisture content less than 4% prior to conductivity tests being carried out.

### 3.4.3 Determining thermal conductivity of test panels

The panels were then placed in an adjusted hotplate apparatus to determine the thermal conductivity. The hotplate rig was constructed in the Trinity College laboratory for use in a previous research study (Byrne et al., 2017). The hotplate was formed from two 900 mm x 900 mm aluminium plates which had channels machined into the surface. The plates were then fixed together so that the machined channels formed a pipe network for temperature controlled water to pass through. A PVC plate is fixed to the back of the aluminium plate. A layer of high performance insulation is also attached to the back of the plate and around the perimeter. The plate and insulation is fitted into a timber frame which is fixed to a chassis with wheels. A heat mat is attached to the aluminium plate to assist the even distribution of heat to the sample (Figure 3-8).

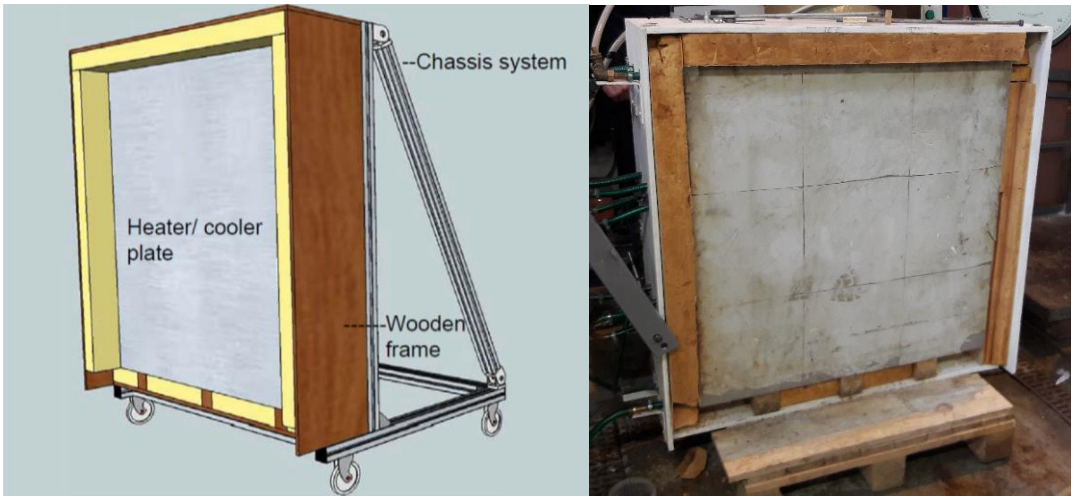


**Figure 3-8 Schematic (Byrne et al., 2017) and photograph of adjusted hot plate apparatus**

The concrete panels were heated in the hot plate rig until a steady state condition was confirmed, that is, until deviations between successive temperatures over a period of 4 hours have diminished to less than 0.5 $^{o}$C (Aviram et al., 2001). $T_c$ is the temperature at the front of the panel where a heat flux pad was placed, typically around 20 $^{o}$C. $T_h$ is the temperature of the panel surface that was in contact with the hot plate, typically around 40 $^{o}$C. The heat flux, q, (W/m$^2$) exiting the front face of the concrete panel was measured by placing a Hukseflux HFP01 heat flux pad of area A (specification provided in Appendix B), on the surface of the concrete. The heat flux measurement is given in W/m$^2$ which is equivalent to Joules/(sec m$^2$), that is, flux is given by q/At where 't' is time in seconds. The depth of the samples, d, is known and hence the thermal conductivity, k, can be calculated by rearranging equation (2-1) as follows (Sweeney, 2014):

$$k = \frac{q}{A.t} \cdot \frac{d}{(T_h - T_c)} \quad \text{(W/mK)} \qquad \textbf{(3-1)}$$

To minimise the test periods two panels were tested in the hot plate apparatus simultaneously. The procedure for determining the thermal conductivity of panels was as follows:

1. One face of each sample was grinded locally at the location where the heat flux pads were to be positioned to ensure that a smooth surface was available for contact between the pad and concrete
2. 14 no. thermocouple wires, two for each of the seven samples, were prepared and placed on the front and rear surface of each of the panels
3. 2 no. 250 mm square openings were cut into 1.0 x 1.0 x 0.13 m deep EPS insulation panels (which have a thermal conductivity of 0.035 W/mK) to suit the test panel size and ensure that there is no heat loss from the perimeter of the panel.
4. 2 no. panels were pushed into the opening in the insulation and positioned upright, tight against the hotplate apparatus and secured in place with bars (Figure 3-9).
5. Thermocouples were connected to a data logger including a thermocouple to record air temperature in the laboratory.
6. Heat flux pads were positioned on the front of each panel, fixed in place and connected to the data logger. Connectivity was assisted by the use of thermal paste.
7. The data logger was set to record the temperatures and heat flux every minute.
8. The panels were heated up until a steady state temperature differential across the concrete samples, $(T_h - T_c)$ was reached [that is, $\Delta T < 0.5$ $^{o}$C for 4 consecutive hours].
9. Panels were left in place recording data for a further 24 hours.

The thermal conductivity was determined using equation (3-1):

This process was repeated to obtain two values of thermal conductivity for each panel. The testing took place in the basement of the structures laboratory in Trinity College Dublin as there is minimal fluctuation of the surrounding air temperature in the space (18 $^{o}$C +/- 1 $^{o}$C). The results of the thermal conductivity tests are presented in Section 4.3.

**Figure 3-9 Photograph of thermal testing of sample panels**

## 3.5 Thermal and structural testing of proposed precast concrete cladding panel

### 3.5.1 Composition of cladding panel

Using the results of the experimental investigations described in Sections 3.1 to 3.4, a PCM-concrete composite material was selected and designed for use in the inner leaf of the proposed precast concrete sandwich panel.

A precast concrete sandwich cladding panel typically comprises of a relatively thin concrete/stone outer layer, a layer of insulation and a 100 mm to 200 mm thick inner layer. Generally if the inner layer is acting as a load-bearing wall in a building it would be in the order of 200 mm thick and reinforced. However if the inner leaf is only supporting its own self weight its thickness can be reduced to circa 100 mm, assuming that the height of the panel is within the normal range of floor to floor heights, that is, 3.0 m to 3.5 m. In the context of this research project the cladding panel will be non-loadbearing as the intent is that it will be used to re-clad a building so the structural frame to which it is applied is providing the vertical loadbearing function.

For this reason it was decided to make the inner leaf of the proposed precast panel 125 mm thick, slightly over 100 mm to allow for the expected reduced strength of concrete due to the inclusion of PCM in the mix as discussed in Section 2.5.2.1. The outer layer of the re-cladding panel does not impact the thermal behaviour of the inner layer of the panel due to the presence of thermal insulation between the layers (Figure 3-10).

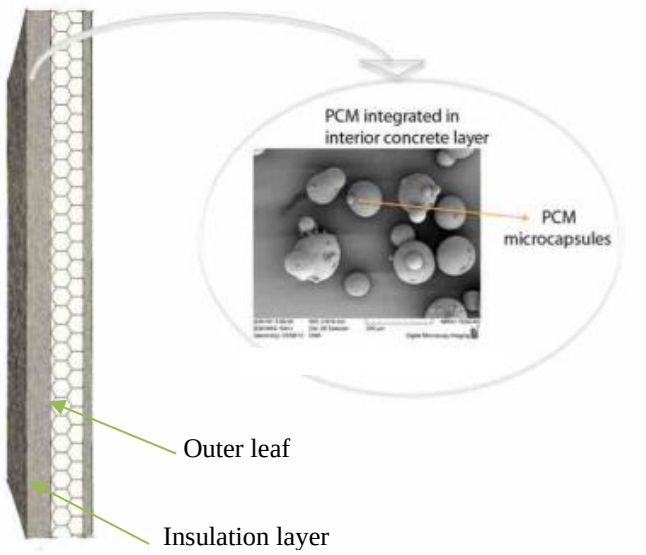


**Figure 3-10 Precast concrete sandwich panels containing PCMs**

As the IMPRESS project included a parallel study of the use of a high performance fibre reinforce concrete (HPFRC) in a thin over-cladding panel it was decided to use HPFRC in a 20 mm outer layer for these test panels to facilitate further observation of its thermal and structural behaviour without impacting on the thermal behaviour of the PCM-concrete composite. The insulation layer comprised of 60 mm XPS insulation which has a thermal conductivity of 0.033 W/mK. Details of the design and manufacture of the test panels are provided in Chapter 5.

### 3.5.2 Laboratory thermal tests on proposed cladding panel

Prior to manufacturing the cladding panels for the full-scale huts it was necessary to carry out laboratory investigations to observe the overall thermal conductivity behaviour of the three layers of panel. To facilitate using the same panels for both the thermal tests and the structural tests, five separate panels were made including panels with and without PCM in the inner leaf. Two of the panels included two different types of non-conductive connecters, C-Grid and Thermomass, connecting the inner and outer leaves of the panel together and three of the panels had no connectors. One of the aims of the thermal tests on the panel was to observe and compare any thermal bridging effect at the location of the connectors. Details of the connectors are provided in Chapter 5.

Thermocouples were cast into the concrete sandwich panel at each interface and thermocouples were also placed on the inner and outer surfaces. Each panel was placed in the adjusted hotplate apparatus as described in Section 3.4.3. Heat flux sensors were positioned on the face of the panel, one was positioned centrally and, in the panels where connector ties were used, one additional heat flux pad was located at the position of the connectors (Figure 3-11).

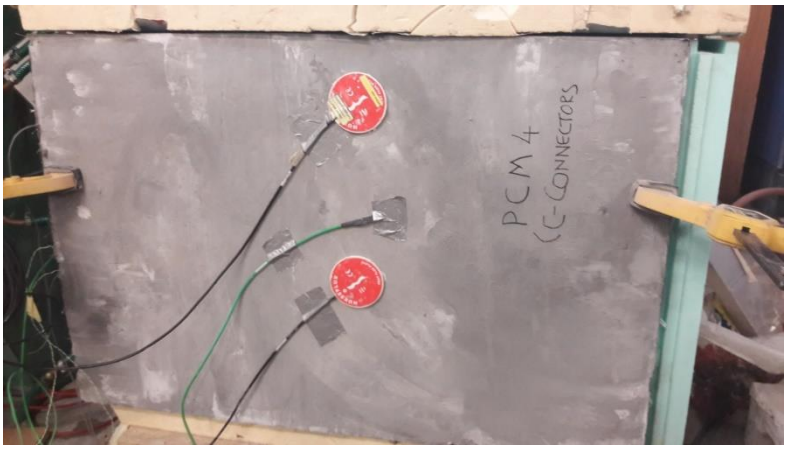


**Figure 3-11 Photograph of panel placed in the hot plate apparatus**

Details of the experimental set up for these thermal tests and the analysis of the results are provided in Chapter 5 of this dissertation.

### 3.5.3 Laboratory structural tests on proposed cladding panel

The cladding panels proposed for use in the full-scale huts must have sufficient strength and stiffness to withstand lateral wind loads as is required of all cladding panels. To achieve this objective an investigation was carried out in the laboratory which explored the composite structural behaviour of the two layers of the sandwich panel. Five separate panels were made with varying degrees of connectivity between the two layers. Each panel was subjected to loading and the structural response was recorded and analysed (Figure 3-12). The experimental regimes and the results of these structural tests are detailed in Chapter 6.

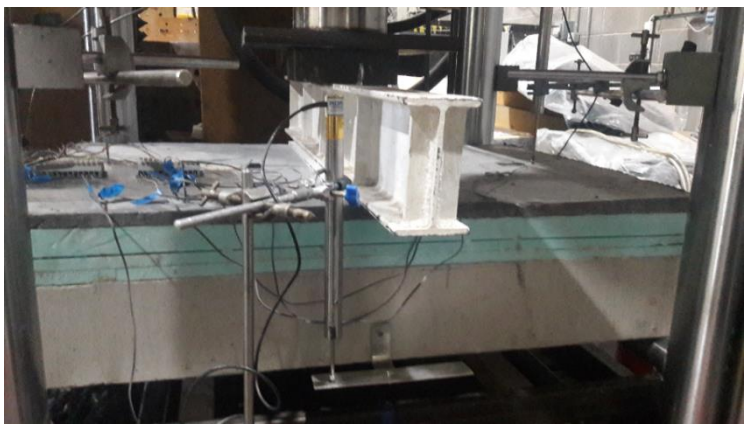

**Figure 3-12 Structural testing of cladding panels**

### 3.6 Design of the full-scale huts and their instrumentation

Although previous laboratory studies had shown that a PCM-concrete composite can provide significantly enhanced thermal storage capacity (Eddhahak-Omni et al., 2014, Pomianowski et al., 2014, Cabeza et al., 2007), in a real application the effectiveness of the PCM depends on many variables, including the form of construction, building use and local climate. For this reason it was decided to use the PCM-concrete to form precast concrete cladding panels and construct three full-scale demonstration huts - one control hut which does not contain any PCM and two huts containing the PCM-concrete composite - in order to monitor and observe the performance of the PCM-concrete composite in a real life scenario over a long duration that included all seasons. The primary objective of the PCM-concrete panel phase of the research was to demonstrate the reduction in overheating effects in the huts.

The three full-scale test huts, with internal dimensions of 1990 x 1990 x 1800 mm, were manufactured and located in the precast manufacturing plant of Techrete Ltd., Balbriggan, County Dublin. Each of the three huts were constructed with different types of panels. Each panel comprised of a 70 mm thick concrete outer leaf, 120 mm insulation and a 125 mm thick inner leaf, which varied in composition. For the Control hut, the inner leaf is constructed without the inclusion of PCM. For the second hut, the inner leaf is formed using the PCM-concrete composite through the full thickness. This hut is referred to as the Full-PCM hut. In the third hut the inner leaf is made up of two layers: the inner 60 mm comprises of the PCM-concrete composite and the outer 65 mm of the inner leaf, adjacent to the insulation layer, comprises of normal concrete without any PCM content. This hut is referred to as the Partial-PCM hut. The purpose of this hut is to enable the effective depth of the expensive PCM to be assessed. The amount of PCM that will melt during a diurnal period will depend on the intensity of heat in the environment where the panel is located. As the PCM absorbs heat and melts, it slows the penetration of heat deeper into the panel by absorbing heat energy so the PCM becomes less effective with increasing depth (Niall et al., 2016). In a real building the level of exposure to a heat source depends on both local climate and the exposure of the wall surface to daylight, together with building use and artificially applied heat loads. So the effective depth of the PCM will depend on the proposed location of the composite material. The incorporation of PCM into a panel increases the cost of the panel so it is important not to include PCM in locations where it will not provide any benefit.

The designed panels were manufactured with the assistance of Techrete Ltd at their manufacturing facility in Balbriggan, Co. Dublin and the demonstration huts were also

assembled at this facility. In order to ensure that the data from each of the huts was comparable, all of the huts had identical design parameters including dimensions, level of insulation, air tightness, glazing, orientation and artificial heating system. In order to ensure that planning permission was not required for the huts they had to be designed so that they could be categorised as uninhabitable and demountable. This means that the internal headroom was limited to 1800 mm. The clear internal plan dimensions of the hut were 1990 mm x 1990 mm. In order to capture solar radiation the southern façade of each hut was fitted with full width double glazed sliding doors. As this research study aims to investigate the thermal mass behaviour of the walls of the huts, the roof slab and floor slab were thermally isolated by placing 50 mm of rigid insulation on the inner surface. This ensured that the concrete roof slab and floor slab provided practically no thermal storage capacity in the hut. The junctions between the roof/floor and the cladding panel were designed to omit any thermal bridging effects. Figure 3-13 provides drawings of the hut design and Figure 3-14 shows the completed huts in position. The huts were positioned in an open area on the site to mitigate any overshadowing.

The huts were instrumented to record both internal thermal data and local climate data. Thermocouples were located at 30 mm, 60 mm 90 mm and 125 mm from the interior surface of the walls and also between the outer leaf and insulation layer. Internal and external air temperatures were recorded and solar irradiance at the site was recorded using a pyronometer. A convection heater was installed in each hut to enable a heat load pattern to be applied to the huts that replicates a particular scenario, for example, the heat load pattern of a classroom that has an overheating problem. A convection heater was selected so that the internal air of the hut would be heated. A heater was placed centrally on the floor of each hut to ensure equivalent distribution of heat in each direction.

To ensure that the thermal performance of the panels could be assessed across all seasons, the data was recorded over an 18 month period. Thermal data was recorded by the thermocouples placed within the wall which enabled the effective depth of the PCM to be determined under the varying daily and seasonal thermal conditions from which an optimal depth of PCM composite can be determined for a particular scenario. Details of the manufacture of the full-scale panels and instrumentation of the huts together with an analysis of the recorded data are presented in Chapter 7.

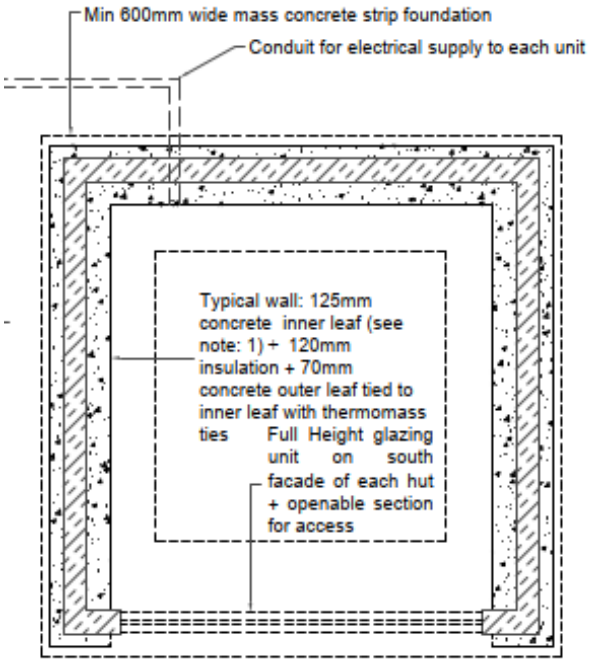


(a) Typical plan layout of huts

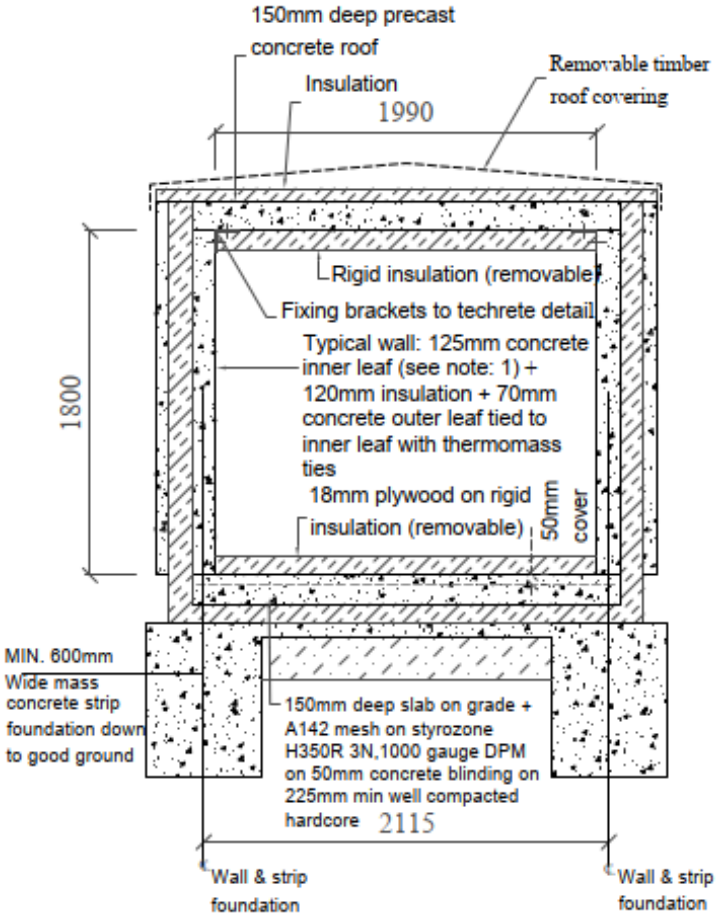


(b) Typical section through the huts

**Figure 3-13 Drawings of the hut design**

**Figure 3-14 Demonstration huts located in Techrete Ltd**

### 3.7 Development of model to simulate thermal behaviour of PCM-concrete composite

As reported in Section 2.6.1, for the PCM to have a positive effect on reducing the energy use in a building it is critical that the air temperature in the location where the PCM is located fluctuates sufficiently within a 24 hour period to ensure that the PCM material changes phase twice, once on heating and once on cooling. Many factors influence this requirement including the thermo-physical properties of the PCM and the material it is embedded in, along with the local climate, building geometry and use of the building. As all buildings differ, each building will require a unique optimal solution for the application of a PCM composite material as a thermal energy storage system. For this reason the development of a numerical simulation tool was necessary to achieve a practical and economic application of this technology. Coinciding experimental data was required to validate the PCM numerical model.

The final and fifth objective of this research was to develop a software model that could accurately simulate the thermal behaviour of the PCM-composite panels in various environmental conditions in real structures. To achieve this objective, a model of the PCM-concrete composite panel was created using COMSOL multi-physics software package. As discussed in Section 2.8.3 COMSOL has been used by other researchers to successfully model the thermal behaviour of PCMs. COMSOL also facilitates the modelling of thermal hysteresis behaviour by allowing the user to define functions for particular thermal behaviour. The environmental data collected at the huts was applied to the panels in the model and the results of the analysis were compared to the actual thermal data collected at the huts. The model was developed until it accurately simulated the actual thermal behaviour of the PCM-concrete composite material in the huts. The model was then used to investigate the effect of using the PCM-concrete composite materials in hypothetical buildings subjected to various environmental conditions. The development of the model and results of simulations are presented in Chapter 8 of this dissertation.

# Chapter 4. Results of Initial Laboratory Work leading to Design of Final PCM-Concrete Composite

This chapter presents the results of the initial laboratory tests that led to the final selection and design of the PCM-concrete composite that was used in the pre-cast concrete cladding panels. These tests included the characterisation of two types of PCM - a fatty acid eutectic and microencapsulated paraffin - using DSC, an investigation to find a method of sealing PCMs into LWA and an investigation into methods to improve the conductivity of concrete. The methodology of these tests is described in Chapter 3. This chapter also details the refinement of the final mix design of the PCM-concrete composite by carrying out trial mixes.

## 4.1 Characterisation of PCMs using DSC

The regime used in the DSC testing for this research project is described in Section 3.3.2. DSC testing was carried out on both PCMs that were under consideration - a microencapsulated paraffin product called Micronal and a fatty acid eutectic comprising of a blend of capric acid and myristic acid (CA:MA). The onset melt and solidification temperatures, the latent heat capacity and the peak melt temperature were determined as described in Section 2.3.4.

### 4.1.1 Results of DSC test on CA:MA fatty acid eutectic

Figures 4-1 and 4-2 show the output of one heating and cooling cycle respectively from the DSC test on the CA:MA fatty acid eutectic. The plots of all four heating and cooling cycles are provided in Appendix C. The results from each of the four cycles of the DSC testing are tabulated in Tables 4-1 and 4-2. The results of the DSC test showed that the eutectic had a melt temperature range of 22.7 $^{o}$C to 27.7 $^{o}$C and a latent heat capacity of 133 J/g.

It can be noted from the results of the cooling cycle that thermal hysteresis occurred in this eutectic, that is, during the cooling cycle the onset solidification temperature was 6.1 $^{o}$C lower than the temperature at which melting completes (27.7 $^{o}$C), indicating that the PCM needs to be cooled below its freezing point to initiate solidification. The hysteresis phenomenon is described in Section 2.3.2. This characteristic reduces the beneficial effect of the PCM as a heat storage material as the temperature of the environment in which the PCM is located must drop to a lower temperature to ensure that the PCM solidifies fully and the stored heat is released effectively and hence the PCM is ready to absorb heat again when the environment overheats (Dincer and Rosen, 2001).

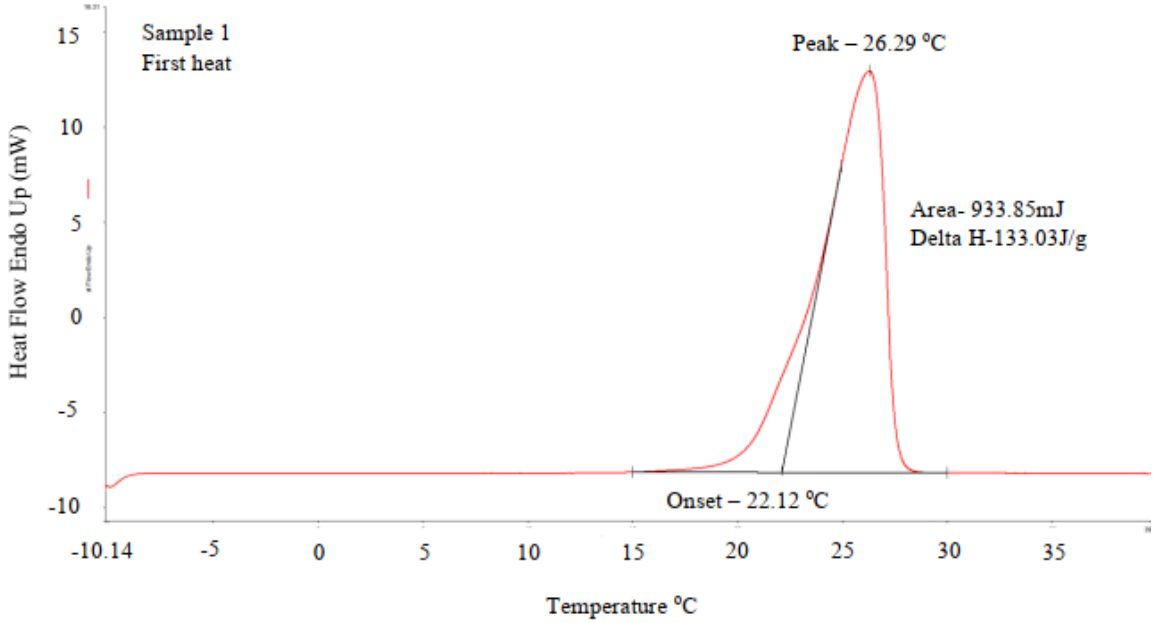


**Figure 4-1 Heating cycle enthalpy curve for CA:MA measured by DSC**

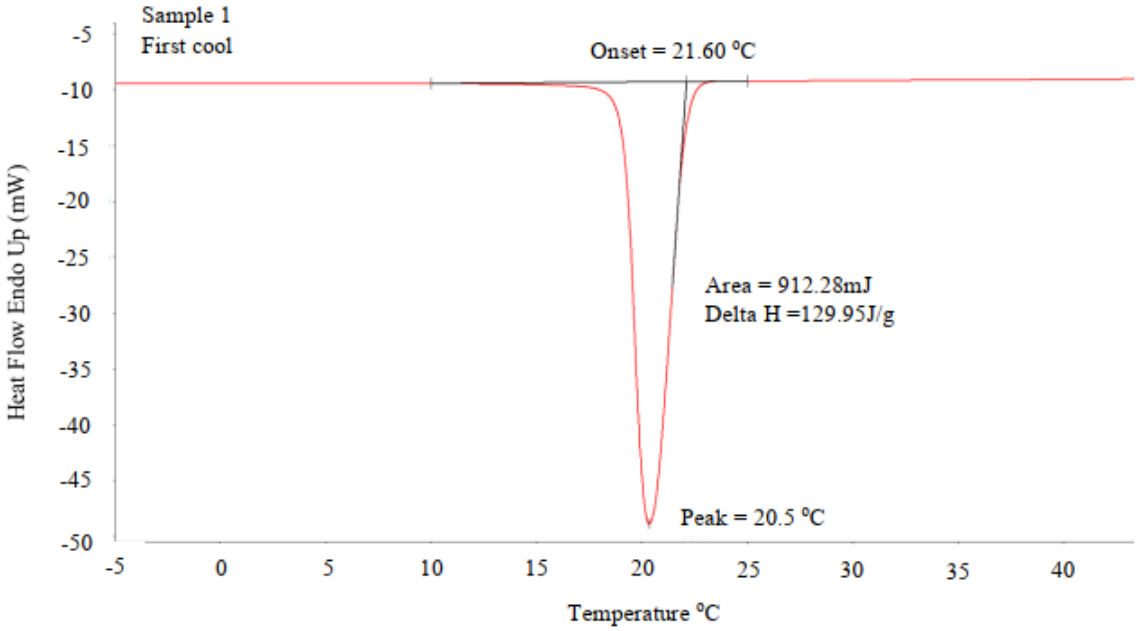


**Figure 4-2 Cooling cycle enthalpy curve for CA:MA measured by DSC**

**Table 4-1 Results of the DSC analysis of the CA:MA fatty acid eutectic- Heating cycle**

| **Heating Cycle No.** | Onset melt temperature, °C | *Peak melt temperature, °C | Melt temperature range, °C | Latent heat capacity, J/g |
|---|---|---|---|---|
| **1** | 22.1 | 26.3 | 22.1–27.5 | 133.0 |
| **2** | 22.8 | 26.5 | 22.8-27.8 | 133.1 |
| **3** | 22.9 | 26.4 | 22.9-27.8 | 133.2 |
| **4** | 22.9 | 26.5 | 22.9-27.8 | 133.1 |
| **Average** | **22.7** | **26.4** | **22.7-27.7** | **133.1** |

*Peak melt temperature is the temperature that coincides with the peak heat flow rate (Refer Figure 2-14)

**Table 4-2 Results of the DSC analysis of the CA:MA fatty acid eutectic- Cooling cycle**

| **Heating Cycle No.** | Onset solidification temperature, $^{o}$C | *Peak solidification temperature, $^{o}$C | Solidification temperature range, $^{o}$C | Latent heat capacity, J/g |
|---|---|---|---|---|
| **1** | 21.6 | 20.5 | 21.6-18.7 | 130.0 |
| **2** | 21.6 | 20.5 | 21.6-18.6 | 129.8 |
| **3** | 21.5 | 20.5 | 21.5-18.4 | 129.6 |
| **4** | 21.7 | 20.5 | 21.7-18.5 | 129.5 |
| **Average** | **21.6** | **20.5** | **21.6-18.6** | **129.7** |

*Peak melt temperature is the temperature that coincides with the peak heat flow rate (Refer Figure 2-14)

### 4.1.2 Results of DSC test on microencapsulated paraffin

Figure 4-3 and Figure 4-4 show the output of one heating and cooling cycle respectively from the DSC test on the microencapsulated paraffin. The plots of all the heating and cooling cycles from the DSC tests on the microencapsulated paraffin are provided in Appendix C. The results from each of the four cycles of the DSC testing are tabulated in Tables 4-3 and 4-4. The results of the DSC test showed that the microencapsulated paraffin had a melt temperature range of 20.2 $^{o}$C to 25.4 $^{o}$C and a latent heat capacity of 91.1J/g.

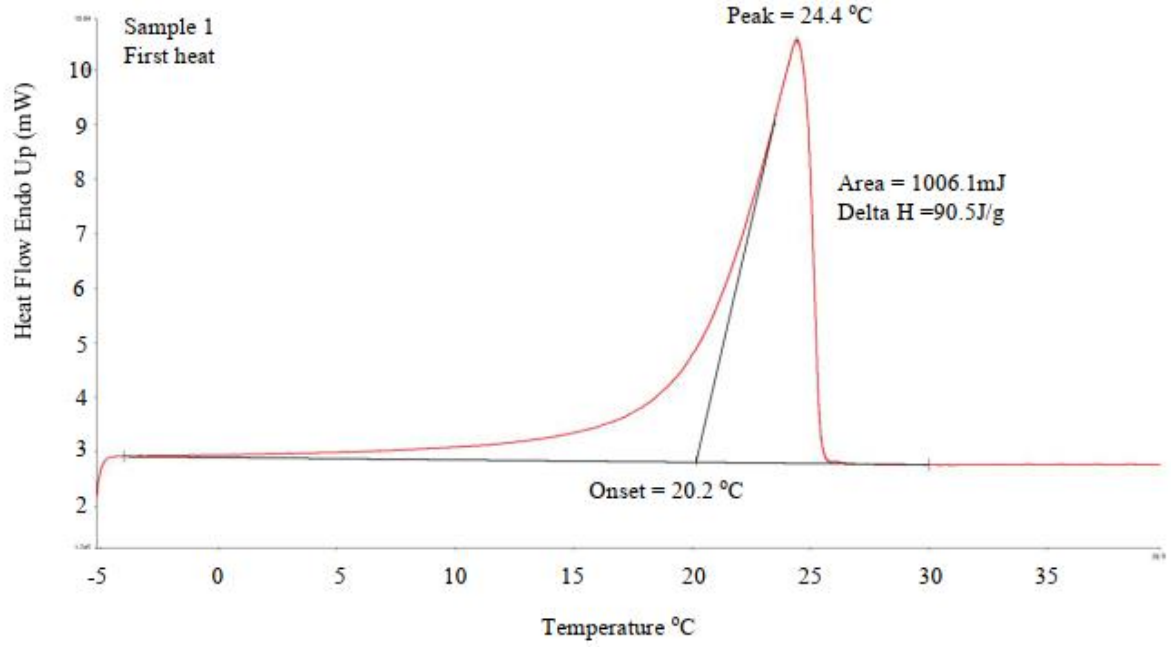


**Figure 4-3 Heating cycle enthalpy curve for microencapsulated paraffin measured by DSC**

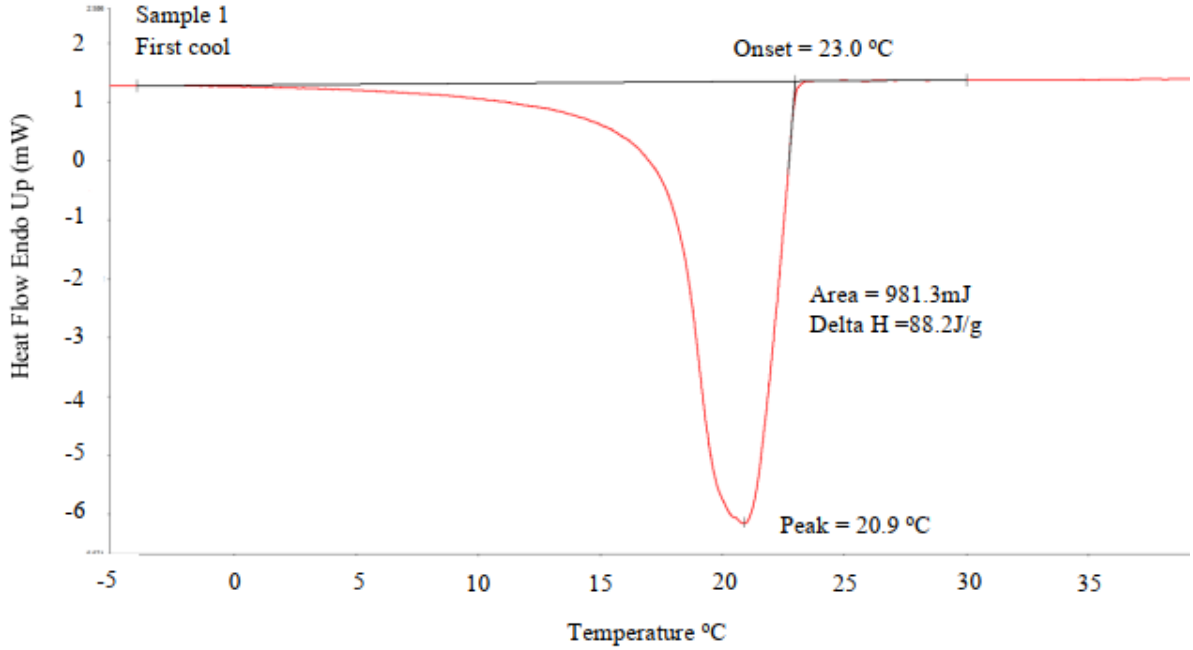


**Figure 4-4 Cooling cycle enthalpy curve for microencapsulated paraffin measured by DSC**

**Table 4-3 Results of the DSC analysis of the microencapsulated paraffin - Heating cycle**

| **Heating Cycle No.** | Onset melt temperature, °C | *Peak melt temperature, °C | Melt temperature range, °C | Latent heat capacity, J/g |
|---|---|---|---|---|
| **1** | 20.2 | 24.4 | 20.2–25.6 | 90.5 |
| **2** | 20.1 | 24.4 | 20.1-25.4 | 91.1 |
| **3** | 20.3 | 24.4 | 20.3-25.3 | 91.4 |
| **4** | 20.2 | 24.4 | 20.2-25.3 | 91.4 |
| **Average** | **20.2** | **24.4** | **20.2-25.4** | **91.1** |

*Peak melt temperature is the temperature that coincides with the peak heat flow rate (Refer Figure 2-14)

**Table 4-4 Results of the DSC analysis of the microencapsulated paraffin - Cooling cycle**

| **Heating Cycle No.** | Onset solidification temperature, °C | *Peak solidification temperature, °C | Solidification temperature range, °C | Latent heat capacity, J/g |
|---|---|---|---|---|
| **1** | 23.0 | 20.9 | 23.0-18.6 | 88.3 |
| **2** | 23.0 | 20.8 | 23.0-18.2 | 88.3 |
| **3** | 22.9 | 20.8 | 22.9-18.1 | 88.3 |
| **4** | 22.9 | 20.8 | 22.9-18.0 | 88.3 |
| **Average** | **23.0** | **20.8** | **23.0-18.2** | **88.3** |

*Peak melt temperature is the temperature that coincides with the peak heat flow rate (Refer Figure 2-14)

As reported in Section 2.3 there are many desired characteristics of a PCM, however, no one material satisfies all of them. The essential characteristics that selection should be based on are the melting temperature range and latent heat capacity. The suitable melt temperature range for a PCM that is to be used in a space cooling application in a building located in a temperate

climate is 19 $^{o}$C – 24 $^{o}$C (Waqas and Din, 2013). Although the latent heat capacity for the microencapsulated paraffin is lower than that of the CA:MA eutectic the melt temperature range for the microencapsulated paraffin is closer to the optimal range. Thermal hysteresis behaviour can be noted from the DSC heating and cooling curves of the Micronal PCM as the onset solidification temperature (23.0 $^{o}$C) is lower than the highest temperature of the melt temperature range (25.4 $^{o}$C) however the hysteresis is 3.7 $^{o}$C lower than the hysteresis in the CA:MA fatty acid eutectic. This behaviour is taken into consideration when defining the thermal behaviour of the PCM in the development of the finite element model as described in Chapter 8 of this thesis.

## 4.2 Sealing of PCMs into LWA

### 4.2.1 Results of sealing tests using Sikagard 700S and Sikabond SBR

As described in Section 3.3.3, a laboratory investigation was carried out with the aim of finding a method to prevent PCM from leaking out of the LWA-PCM composite and seeping to the surface of the concrete. Initially three methods were investigated in which samples of LWA-PCM were treated with either Sikagard 700S or Sikabond SBR. The treated LWA-PCM was either cooled in a refrigerator or stored at room temperature prior to making the concrete samples. The concrete samples were cured either at the normal temperature of 20 $^{o}$C or below 5 $^{o}$C, as discussed in Section 3.3.3.

It was observed that during the curing process a white mould-like substance appeared on the surface of all of the concrete samples regardless of treatment (Figure 4-5). A sample of the substance was analysed by the Centre for Microscopy and Analysis (CMA) department in Trinity College Dublin and it correlated very strongly with calcium stearate which is a fatty acid salt. The compound of both fatty acids contained in the eutectic is an ester. Concrete contains calcium hydroxide which could react with the ester to produce calcium stearate. It was concluded that neither of the sealants used could be relied on to seal the PCM into the LWA.

**Figure 4-5 Mould-like substance on the surface of the concrete samples**

### 4.2.2 Results of sealing tests using Conplast WP402 and Auramix 200

The second investigation into finding a method to seal the PCM into the LWA-PCM composite was also described in Section 3.3.3. In this investigation a water resisting additive, Conplast WP402 was added to the mix together with a superplasticiser called Auramix 200, with the aim of reducing the porosity and hence the permeability of the concrete.

At the end of the curing process there did not appear to be any mould on the surface (Figure 4-6. However before this method could be fully endorsed further testing was required using larger scale samples, in which the samples are repeatedly heated and cooled over a longer time period to ensure that the PCM is sealed in permanently. Given the programme for the IMPRESS project there was insufficient time to carry out further long term testing on the sealing of the LWA-PCM composite prior to construction of the full-scale huts so the risk of using a LWA-PCM composite was considered too great for the project. This led to the decision to exclude the LWA-PCM composite from further consideration in the project and to progress the option of forming the PCM-concrete composite by incorporating micro-encapsulated paraffin PCM into concrete despite its lower latent heat and greater cost.

**Figure 4-6 Concrete samples including Conplast WP402 and Auramix 200 displaying no mould growth**

## 4.3 Investigation of enhancement of conductivity- Results

As discussed in Section 3.4, an experimental study was undertaken to explore methods of improving the thermal conductivity of the PCM-concrete composite. Seven panels, 250 x 250 x 100 mm deep were manufactured as follows; Control, GGBS, Steel Fibres, LWA control, PCM, Techrete Control, Techrete Micronal (see Section 3.4 for details).

Each panel was placed in an adjusted hotplate apparatus and its thermal conductivity was determined as described in Section 3.4.3. A thermocouple in the LWA-PCM sample was damaged during the second test hence the data from this test was considered unreliable and was excluded.

The summary of the results is given in Table 4-5.

**Table 4-5 Thermal conductivity of panels**

| Type of Panel | Result 1st test W/mK | Result of 2nd test W/mK | Average Result W/mK |
|---|---|---|---|
| Control (CEM II) | 1.84 | 1.99 | 1.91 |
| Control + 50% GGBS | 1.64 | 1.86 | 1.75 |
| LWA Control | 1.00 | 1.04 | 1.02 |
| PCM + LWA | 0.74 | - | 0.74 |
| Steel Fibres | 1.79 | 2.17 | 1.98 |
| Control CEM I (hut) | 1.81 | 1.91 | 1.86 |
| Micronal (hut) | 1.31 | 1.64 | 1.48 |

As expected the presence of both the microencapsulated PCM and the LWA-PCM reduces the conductivity of the concrete by circa 20 % and 27 % respectively when compared to their equivalent samples without PCM. The reduction in thermal conductivity of 20 % in the micro-encapsulated PCM sample is lower than the 30 % reported by Hunger et al. (2009) for inclusion of 5% PCM by weight of concrete. However, the control concrete in Hunger's study had a density and thermal conductivity that would be considered high for a normal concrete at 2620 kg/m$^3$ and 3.4 W/mK respectively.

The panel containing 50% GGBS displayed an 8 % reduction in thermal conductivity. This result is surprising however it may be explained by the fact that when GGBS is included in concrete the rate of early strength gain and density is slower. (Singh et al., 2023, Xie et al., 2019, Hu et al., 2019). Although it is expected that the GGBS-concrete will achieve equivalent or greater strength after 56 days the associated cube test results showed that the strength of the GGBS concrete was still 4 % lower than the control mix at the time of testing. The lower strength of the GGBS concrete indicates that its density may also be lower which would result in a lower thermal conductivity.

As the proposed panels will be precast on special tables in Techrete's manufacturing plant, it is necessary that they gain sufficient strength within 16 – 18 hours to allow the panels to be lifted off the tables and stored elsewhere. There were concerns that using 50% GGBS would result in the panels having insufficient early age strength to allow them to be lifted safely hence GGBS was excluded from the proposed concrete mix used in the huts.

Although the addition of steel fibres led to a minor (4 %) increase in thermal conductivity the increase was surprisingly small given the high fibre dosage rate and was not considered to be significant. For this reason the inclusion of steel fibres was excluded from further consideration

in this project as their inclusion adds cost and complexity to the manufacturing process and the benefit gained from their inclusion is minimal.

The LWA sample displayed significantly lower (47 %) conductivity than the Control sample as expected due to its lower density. The addition of the PCM to the LWA reduced the conductivity further with the LWA-PCM sample having a conductivity 27 % lower than the LWA sample with no PCM. Although previous studies by the author (Niall et al., 2016) had indicated that the LWA-PCM composite performed slightly better in terms of heat storage than the microencapsulated paraffin-concrete composite at depths less than 100mm, the issues identified in Sections 4.1 and 4.2, that is, the greater thermal hysteresis behaviour of the fatty acid eutectic PCM and the need for further investigation to be certain that leakage of the PCM is mitigated, precluded the use of a LWA-PCM composite in the concrete cladding panels under investigation in this research project.

### 4.4 Selection of PCM-concrete composite

The results of the DSC tests show that both the encapsulated paraffin and the fatty acid eutectic have a melt temperature range that is suitable for a space cooling application. However the fatty acid eutectic's melt temperature range is at the higher end of the optimum range. This means that the eutectic PCM will require a higher internal temperature to be reached before it begins to melt and become effective at reducing the temperature of the environment. This makes the eutectic a less suitable PCM for use in Ireland as the higher temperatures required to charge the eutectic PCM fully do not occur often. It can also be noted that there is significant thermal hysteresis in the eutectic of 6.1 $^{o}$C. This can be attributed to minor impurities in the capric and myristic acids (Hua et al., 2023), reported to be up to 2% by the manufacturers.

As neither the Sikagard 700S nor the Sikabond SBR sealed the PCM into the LWA these products were not considered further. The use of Conplast WP402 and Auramix 200 showed potential as a method for sealing the PCM into the LWA however considerable further testing would be required to confirm if the sealing effect is maintained and withstands many phase changes over time. There were also concerns regarding the time required to manufacture sufficient quantities of LWA-PCM for the full-scale huts while also meeting the programme requirements for the Horizon 2020 IMPRESS project. Hence the use of a LWA-PCM was precluded from further consideration for this project.

With regard to improving the thermal conductivity of the PCM-concrete composite, the addition of steel fibres to the concrete mix indicated a small increase in thermal conductivity. However working with steel fibres adds difficulty and cost to the manufacturing process as they reduce the workability of the concrete mix. Also, to avoid clumping together of the steel fibres during the mixing process, in the laboratory the fibres were sprinkled into the mix by hand as the drum was rotating. It was not possible to carry out this process in the full-scale mixing process in Techrete Ltd. Another issue with the use of steel fibres is that some fibres may protrude from the surface of the finished panel which causes a safety risk. For these reasons, it was decided not to use steel fibres in the PCM-concrete mix to enhance its thermal conductivity.

For these reasons it was decided to proceed with using the microencapsulated paraffin PCM which had been successfully combined with concrete by Niall et al. (2016 and 2017) in previous research. BASF manufacture a ready-made microencapsulated paraffin product called Micronal DS 5040 X. The DSC tests that were carried out on Micronal DS 5040 X determined the melt temperature range to be 20 $^{o}$C – 25 $^{o}$C with a peak melt temperature of 24.4 $^{o}$C. The latent heat capacity was 91J/g. This melting temperature makes Micronal DS 5040 X a suitable option in the context of this research project. The paraffin is encapsulated in a high strength acrylic polymer shell. The product is in powder form with a particle size of 5μm (Figure 2-29). The high surface to volume ratio of the PCM powder provides a large area for heat exchange. Although previous research studies (Eddhahak-Ouni et al., 2014, Fenollera et al., 2013, Hunger et al., 2009) found that the inclusion of Micronal into a concrete mix reduces the strength of the concrete, as discussed in Section 2.5.2. Hunger et al. (2009) reported a 13 % decrease for every 1 % (by weight of concrete) increase in the micro-encapsulated PCM content. The use of up to 5 % Micronal by weight of concrete allows sufficient concrete strength to be achieved (20-25 MPa) for low stress elements such as non-loading bearing walls (Niall et al., 2017).

### 4.5 Design of PCM-concrete composite mix

To form the PCM-concrete composite the micro-encapsulated PCM product, Micronal, was added to a self-compacting CEM I concrete mix at a dosage rate of 5 % by weight of concrete, during the mixing process. The thermal behaviour of this composite was investigated in previous research by the author (Niall et al., 2016 and 2017). 5 % Micronal by weight of concrete has been shown to be the optimum quantity of Micronal to be used in a concrete mix application (Hunger et al., 2009, Fenollera et al., 2013). Higher quantities of Micronal yield

impractically low concrete strengths and also causes significant reduction in the thermal conductivity (20% - 45 %, refer to Figure 2-25) and density (circa 10 % (Niall et al., 2017)) which tends to counteract the increased benefit of thermal storage capacity.

In order to finalise the concrete mix designs for the internal walls of the demonstration huts, a trial mix was carried out in the concrete laboratory in TCD. To replicate the manufacturing conditions in Techrete, all the constituents for the trial concrete mix (except water) were sourced from Techrete. The design of Techrete's self-compacting concrete mix is provided in Appendix D, and the proportion of constituents is provided in Table 4-6. The mix design uses a specified characteristic strength of 30 MPa at 3 days as early strength is the main design criteria to facilitate lifting of concrete panels after 18-24 hours. The trial control concrete mix has a water cement ratio of 0.43. A 250 x 250 x 100 mm panel plus 4 no. 100 mm cubes were formed for both the trial mixes. The mix quantities for the control trial mix are also tabulated in Table 4-6.

**Table 4-6 Trial control concrete mix as per Techrete's self compacting concrete**

| Quantities | Rapid Hardening Cem I Cement (kg)*** | Water (kg) | Fine aggregate (kg) | Coarse 6-14mm (kg) | Limestone Filler (kg) | SP Premier 196 Plasterciser (l) |
|---|---|---|---|---|---|---|
| 1 $m^3$ | 360 | 155 | 790 | 1025 | 120 | 2.9 |
| 0.015$m^3$ | 5.4 | 2.325 | 11.85 | 15.4 | 1.8 | 0.0435* |

* Super plasterciser dosage 0.8% by weight of cement
** Water cement ratio 0.43
*** In accordance with I.S.EN197-1-2011

For the trial PCM-concrete mix the same base concrete mix was used and then Micronal was added to the fresh concrete during mixing. The Micronal powder was added as late as possible in the mixing process to mitigate damage to the microcapsules. Again the mix volume was sized to provide a 250mm x 250mm x100mm panel plus 4 no. 100mm cubes, so the mix volume was 0.015 $m^3$. Assuming density of concrete as 2450 kg/$m^3$, then the mass of the mix is (0.015 x 2450) which equates to 36.7 kg. Hence the required mass of Micronal for the mix volume of 0.015 $m^3$ is (36.7 x 0.05), which equates to 1.8 kg.

The density of the PCM-concrete mix is different to that of the control mix due to the addition of Micronal which has a particle density of 915 kg/$m^3$. 5% of the weight of 1 $m^3$ of concrete equates to 120 kg. 120 kg of Micronal adds 0.13 $m^3$ volume to the mix. When the additional mass and volume of the Micronal are added to the original control concrete mix this results in an estimated mix density of 2570kg/1.13 $m^3$ which equates to 2275 kg/$m^3$. As there was 120

kg of Micronal in a 1.13 $m^3$ volume, for a 1 $m^3$ volume 120/1.13 = 106 kg is required. The mass of the remaining components is (2275-106) = 2169 kg. The mass of each component of the control concrete must be adjusted by multiplying its mass by 2169/2450 = 0.88 to allow for the inclusion of the Micronal. An increased plasterciser dose was required to counteract the decrease in workability caused by the addition of Micronal as reported in Section 2.5.1.1. The mix quantities for the PCM-concrete trial mix are tabulated in Table 4-7.

**Table 4-7 Trial PCM-concrete composite mix**

| Quantities | Rapid Hardening Cem 1 Cement*** (kg) | Water (kg) | Fine aggregate (kg) | Coarse 6-14mm (kg) | Limestone Filler (kg) | Micronal 5% by mass of concrete (kg) | SP Premier 196 (l) |
|---|---|---|---|---|---|---|---|
| 1 $m^3$ | 320 | 135 | 700 | 905 | 106 | 106 | 5.0 |
| 0.015$m^3$ | 4.8 | 2.025 | 10.5 | 13.6 | 1.6 | 1.6 | 0.086* |

* Super plasterciser dosage increased for Micronal mix to 1.6% by weight of cement
** Water cement ratio 0.43
*** In accordance with I.S. EN 197-1:2011

### 4.5.1 Observations of the trial control mix

The control mix was observed to be fluid, the fresh concrete was cohesive and no segregation occured. A slump flow test was carried out in accordance with I.S. EN 12350-8, as were all slump flow tests carried out as part of this research project. The slump flow, SF, was 450mm and the time taken to reach 500mm, $T_{500}$ was 9 seconds (Figure 4-7). As SF is less than 650mm the concrete cannot be classified as self-compacting however as the concrete mix displayed sufficient workability for the purpose of manufacturing the concrete sandwich panels further flow table tests were not deemed necessary.

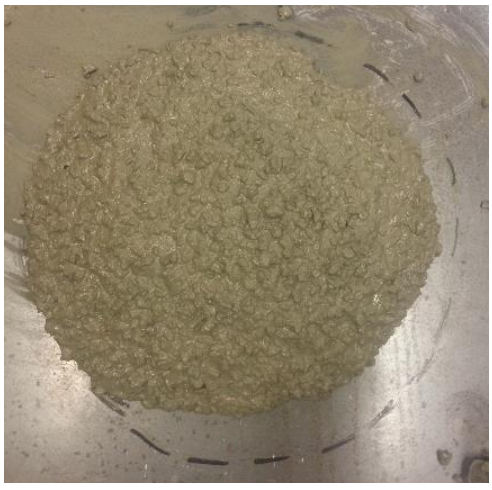

**Figure 4-7 Photograph of trial control mix**

The wet density was measured in accordance with I.S. EN 12350-6:2019, using 150 mm diameter x 300 mm high plastic cylinder, as were all wet density measurements carried out as part of this research project. The wet density was determined to be 2375 kg/m$^3$. The original mix design quantities were adjusted by multiplying by 2375/2450 = 0.969 and rounding to the nearest multiple of 5, hence the revised control mix design is as shown in Table 4-8.

**Table 4-8 Final control mix quantities**

| *Quantities | Rapid Hardening CEM 1 Cement (kg) | Water (kg) | Fine aggregate (kg) | Coarse 6-14 mm (kg) | Limestone Filler (kg) | SP Premier 196 (l) |
|---|---|---|---|---|---|---|
| Per m$^3$ | 350 | 150 | 765 | 995 | 115 | 2.8 |

w/c = 0.43

*Note figures are rounded up to nearest multiple of 5 (excluding the superplasticiser)

The concrete was placed in the 250 x 250 x 100 mm formwork and the 4 no. cubes were made (Figure 4-8). Two thermocouples were placed in the panel at equal depth intervals of 33 mm. The finished concrete samples were covered with damp hessian and left for 24 hours after which the panel and two cubes were placed in a curing tank and maintained at 20 ºC, +/-1 ºC for a further 27 days. The remaining two cubes were strength tested after 1 day to establish early strength values which are of particular importance for informing the future safe lifting of panels off the casting beds.

**Figure 4-8 Photograph of trial control mix placed in the formwork**

### 4.5.2 Observations of the PCM-concrete mix

The PCM-concrete mix was noticeably dry after the Micronal was added (Figure 4-9). The dosage of superplasticiser (SP) was increased in two stages up to the maximum of 3% of cement content. Additional water was also added at the second stage as the plasticiser is mixed with water prior to adding to the concrete mix. The mix constituents were adjusted accordingly.

**Figure 4-9 Photograph of trial dry PCM-concrete mix**

- First, an additional 0.022l of SP was added to bring the dosage up to 2% by weight of cement. The SP was added to 400 ml of the original water content that was held back from the mix, so no additional water was used at this stage.
- The mix was still very stiff so an additional 0.028 l of SP was added to bring the dosage up to 2.5%. The SP was added to 175 ml water and added to the mix.
- A further 0.028 l of SP was added to bring the dosage up to 3.0%. The SP was added to a further175 ml water and added to the mix.

In total an additional 350ml of water was used. Hence the total water content = 2.025 + 0.35 = 2.375 l. The revised water/cement ratio = 2.375/4.8 = 0.49. A higher water/cement ratio is expected to result in a concrete with higher porosity and hence lower strength. The requirement for additional water in the PCM-concrete composite is a contributory factor to the lower strengths achieved by micro-encapsulated PCM-concrete composites, as reported in Section 2.5.2.1.

The mix appeared quite stiff so a low slump was expected. For this reason a slump test was carried out on this mix, rather than a slump flow (SF) test, in accordance with I.S. EN 12350-2:2019. However the slump test failed as the concrete slowly and very cohesively collapsed (Figure 4-10). When the fresh concrete stabilised the two perpendicular diameters were measured and the slump flow was determined as 470 mm in accordance with I.S. EN 12350-8. There was no segregation of the mix components. Although with a SF of 470 mm the mix cannot be categorised as self-compacting, it displayed good workability that is suitable for the manufacture of the cladding panels hence further flow table tests were deemed unnecessary.

**Figure 4-10 Photograph of trial PCM-concrete mix**

The wet density of the PCM-concrete composite was also measured for comparison with the control mix and was 2360 kg/m$^3$. This lower wet density is expected as the microencapsulated paraffin has a lower density than the control concrete mix. The original PCM-concrete composite mix design quantities were adjusted by multiplying by 2360/2275 = 1.04. Taking account of the adjusted mix and the required increase in water/cement ratio and plasticiser content, the revised PCM –concrete mix is given in Table 4.9.

**Table 4-9 Final PCM-concrete mix**

| Quantities | Rapid Hardening Cem 1 Cement (kg) | Water (kg) | Fine aggregate (kg) | Coarse 6-14mm (kg) | Limestone Filler (kg) | SP Premier 196 (l) | Micronal (kg) |
|---|---|---|---|---|---|---|---|
| Per m$^3$ | 330 | 160 | 725 | 935 | 110 | 9.9 | 110 |

w/c = 0.49

* Based on wet density of control mix = 2360 kg/m$^3$

*Note figures (except SP) are rounded to nearest multiple of 5

The PCM- concrete was placed in the forms and covered with wet hessian. After 24 hours the samples were demoulded. Strength tests were carried out on two cubes from each mix at 24 hours and the remaining samples were placed in the curing tank at 20 $^o$C for 27 days whereupon strength tests were carried out on the remaining cubes. All strength tests were carried out in accordance with IS EN 12390-3:2019. The 1 day strengths of the concrete mixes were of particular interest because in the manufacturing of the full-scale panels the panels require sufficient strength to enable them to be lifted off the casting tables after 18 hours. The concrete strength test results are given in Table 4-10. It can be noted that the 1 day strengths of the PCM-concrete composite were relatively low at 9.6 MPa. The incorporation of a PCM into concrete will reduce the heat of hydration by circa 28 % (Hunger et al., 2009) and hence slow down the

early strength gain of the concrete panels as discussed in Section 2.5.1.2. The low 1 day strengths were discussed with Techrete Ltd and it was agreed that longer curing times would be facilitated to ensure that the panels reach a strength of 20 MPa before they were lifted from the casting tables. It was also agreed that 12 to 15 test cubes would be made when pouring the panels. The cubes would be tested at different stages starting from 18 hours after the pour and the panels would not be lifted until testing of the cubes confirmed that sufficient strength was reached.

**Table 4-10 Strength test result for trial mixes**

| **Mix type** | **1 day strength (MPa)** | | | **28 day strength (MPa)** | | | |
|---|---|---|---|---|---|---|---|
| | Cube 1 | Cube 2 | **Average** | Cube 1 | Cube 2 | **Average** | **w/c ratio** |
| Control mix | 18.3 | 17.6 | **18.0** | 34.1 | 38.8 | **36.5** | 0.43 |
| PCM-concrete | 9.6 | 9.5 | **9.6** | 29.5 | 29.4 | **29.5** | 0.49 |

### 4.5.3 Trial mix for two-layered panel carried out in Techrete Ltd

As discussed in Section 3.6, to enable the effective depth of the PCM to be assessed, one of the full-scale huts will be constructed with cladding panels in which the inner leaf comprises of layers of 60 mm of normal concrete and 65 mm of PCM-concrete composite. To investigate the process of pouring a single leaf of wall in two layers, a trial mix was carried out at Techrete's manufacturing plant. A 1.0 x 1.0 x 0.125 m deep slab comprising of a 60 mm layer of control concrete and 65 mm layer of PCM-concrete was formed. 4 no. cubes were made with the control concrete and 10 no. cubes were made with the PCM-concrete specifically to explore early age strength development. The mix components for the control concrete and the PCM-concrete are as provided in Tables 4-8 and 4-9 respectively.

The SF for the control concrete was 550 mm hence the concrete could not be categorised as self-compacting however it displayed very good workability. The control mix was poured into the mould first up to a level of 60 mm (Figure 4-11). Then the PCM-concrete was mixed. The Micronal was added to the mixer towards the end of the mixing process in order to minimise damage to the microcapsules during mixing. The SF for the PCM-concrete was 435 mm. The PCM-concrete was very stiff, cohesive and 'sticky' as can be observed in Figure 4-12. The concrete slab was vibrated using the vibration table and with the vibration the PCM concrete filled the form with minimum hand trowelling (Figure 4-13).

**Figure 4-11 60 mm layer of control mix being poured**

**Figure 4-12 PCM-concrete being poured**

**Figure 4-13 Completed trial slab**

The PCM-concrete cubes were tested at 20 hours and 24 hours and achieved strengths of 11.5 MPa and 12.5 MPa respectively. Another two cubes were tested 48 hours after casting and strengths of 22.0 MPa and 24.0 MPa were achieved. These 48 hour strengths are greater than the minimum required by Techrete to allow lifting, that is, 20 MPa, suggesting that the panels should be left to cure for 48 hours prior to lifting. The 24 hour strength of the control mix was 22.0 MPa. The fabrication of this trial panel confirmed that the formation of the inner leaf of the panel in two layers was feasible without any issues and also that the early age strength of the PCM-concrete composite was sufficient to facilitate lifting of the panels within 48 hours of casting.

## 4.6 Conclusions

This chapter described the results of laboratory investigation work that was carried out to inform the design of the PCM-concrete composite.

The results of the DSC testing showed that both types of PCM displayed suitable melt temperature ranges for a space cooling application in a building and had high latent heat capacities. However the melt temperature range of the CA:MA eutectic at 22.7 – 27.7 $^{o}$C is slightly higher than the ideal melt temperature range for a space cooling application (19 – 24 $^{o}$C), according to Waqas and Din (2013). The eutectic also displayed thermal hysteresis behaviour which hinders the solidification of the PCM overnight. These characteristics may decrease the periods during the year when the PCM is effective. For these reasons the microencapsulated PCM product, that is Micronal, was selected as the PCM to be incorporated into concrete and used in the cladding panels.

An investigation was also carried out to explore methods of sealing the fatty acid PCM into a LWA in order to mitigate the issue of leakage as previously reported by Niall et al. (2016). A number of methods were tested, as described in Section 4.2.1 and 4.2.2. The method that involved the use of a water-resisting additive called Conplast WP402 together with a superplasticiser showed good potential for preventing leakage. Although the results of these initial investigations fulfilled the first objective of this thesis, that is to create a suitable fatty acid eutectic and effectively seal it into a LWA, further long term testing is required to ensure that the PCM will remain sealed in permanently and during repeated temperature fluctuations. The programme for the IMPRESS project could not accommodate the time required for this further testing. For these reasons the Micronal, was selected as the PCM to be incorporated into concrete and used in the cladding panels.

To achieve the second objective of this research an investigation was carried out to explore the influence of including GGBS and steel fibres on the thermal conductivity of the proposed panels as described in Section 4.3. The results showed that the inclusion of 50% GGBS reduced the thermal conductivity of the concrete matrix by 8 %. This result was attributed to a slightly lower cement matrix density, indicated by the lower strength of the GGBS concrete at time of testing. The panel with steel fibres showed a small increase in thermal conductivity (4 %) which was considered to be insignificant given the variability of concrete as a material. In addition the steel fibres add complexity to the manufacturing process. For these reasons it was decided to exclude steel fibres and GGBS from the concrete mix design for the panels.

An initial trial mix was designed for both the Control concrete and the PCM-concrete composite which included 5% Micronal by weight of concrete. Trial pours were carried out for both mixes in order to refine the mix design as described in Section 4.5. The addition of the Micronal powder to the concrete mix reduced the workability considerably and additional water and plasticiser had to be added to the PCM-concrete mix in order to achieve good workability. The wet densities of both mixes were determined and adjustments were made to the quantity of each mix component accordingly. Neither of the mixes were self-compacting however both mixes were sufficiently workable for the manufacture of the panels and both mixes displayed very good cohesiveness.

Early age strength is a critical parameter for pre-cast concrete elements as they must have sufficient strength to support their self-weight before they are lifted off casting beds. The 1 day strength of the PCM-concrete was low at 9 MPa compared to 18 MPa for the Control mix. The low 1 day strength results were discussed with Techrete Ltd and it was agreed that warm curing would be provided for the cladding panels to increase the rate of early strength gain and the panels would remain on the casting table until the strength of the Control and PCM-concrete mix has reached a minimum of 20 MPa. This will be established through compression testing of cubes made from each of the mixes.

A further trial pour was carried out in Techrete Ltd to identify any issues with the process of pouring a single leaf panel in two layers using the Control concrete mix for one layer and the PCM-concrete composite for the second layer. The formation of the two layer panel proceeded without any problems arising confirming that the formation of the inner leaf of the panel in two layers was feasible. The PCM–concrete had low 20 hour and 24 hour strengths as expected. However the 48 hour strengths, 22 MPa and 24 MPa, were greater than the minimum required which provided reassurance that the panels can be lifted within two days of casting.

# Chapter 5. Thermal Laboratory Tests on Proposed Cladding Panel

## 5.1 Introduction

The overall aim of this PhD research project is to design a precast concrete sandwich panel with enhanced thermal mass properties that is suitable for the recladding of existing buildings, and which will enable passive heating and cooling behaviour to improve the energy performance of the building. The core innovative technology is the incorporation of PCMs within the concrete to form a PCM-concrete composite material which has an increased thermal storage capacity. Chapters 3 and 4 described the exploratory laboratory work that led to the selection of a suitable PCM and design of the PCM-concrete composite material to be used in the inner leaf of the precast concrete sandwich cladding panel. It is expected that the presence of the PCM will reduce overheating effects in any environment in which it is placed. The panels were subsequently used in the construction of three full-scale demonstration huts, one control hut and two huts containing the PCM-concrete composite as described in Section 3.6.

Prior to manufacturing full-scale cladding panels for use in the test huts it was important to carry out a laboratory investigation to observe the thermal conductivity behaviour of the PCM-concrete composite in the inner leaf of a cladding panel when it is bounded on its outer face by a layer of insulation. It was also of interest to determine any cold bridging effect caused by the connectors used in the panel to hold the inner and outer leaves together and to aid composite structural behaviour in the panel. Structural tests were also required to investigate the composite structural behaviour of the cladding panel and determine which type of connector should be used. The same panels were used for both the thermal tests and the structural tests.

Two types of connectors are considered in this laboratory investigation – C-Grid carbon fibre epoxy connectors and Thermomass connectors, as described in Section 2.9.2. C-Grid is an epoxy-coated composite grid made with cross-laid (non-woven), superimposed carbon fiber. Carbon fibre is four times stronger than steel by weight and has very low thermal conductivity. For this reason it is suitable for use in concrete sandwich panels as it mitigates thermal bridging between the two layers of concrete.

Thermomass connectors combine high strength with low conductivity. They are non-corrosive and chemically resistant so they are safe to use with concrete and in the potentially damp environment of the insulation layer between the two layers of concrete. Thermomass connectors are made from a fiber composite material consisting of continuous glass fibers and

a vinyl ester polymer. Thermomass connectors are particularly suitable for concrete sandwich cladding panels as they have a low thermal conductivity – 1.0 W/mK (data sheet in Appendix E) compared to 40.7 W/mK for stainless steel and hence they minimise the thermal bridging effect at connector locations.

This laboratory investigation involved thermal and structural testing of concrete sandwich panels formed using both types of connectors. There are three stages to the investigation:

- Stage A: Manufacture of 5 no. PCM-concrete sandwich panels
- Stage B: Thermal testing of the panels
- Stage C: Structural testing of panels.

This chapter describes stages A and B. The structural tests are described in Chapter 6.

### 5.2 Design of test panels

For the panels to be suitable for the re-cladding of a building it is important that the weight of the new panel is less than or equal to the weight of the panel that it is replacing so as not to overload the existing structure and foundations. In parallel with this study, another panel suitable for over-cladding was being developed as part of the IMPRESS project. This panel incorporated two very thin layers – 25 mm and 40 mm thick - of high performance fibre reinforced concrete (HPFRC). As noted in Section 3.5.1 the outer layer of the re-cladding panel does not impact the thermal behaviour of the inner layer of the panel due to the layer of thermal insulation between the wythes. A thin outer leaf presents challenges of achieving sufficient connection between the two layers to enable composite structural behaviour. Hence using a thin outer leaf for these tests panels enables any difference in composite structural behaviour due to the type of connector to be highlighted without influencing the thermal behaviour of the inner leaf of the panel due to the separating layer of insulation.

Five 900 x 600 x 200 mm deep concrete sandwich test panels were manufactured (Figure 5-1). Each panel comprised of a 20/50 mm HPFRC concrete outer leaf, 60 mm XPS insulation and a 120 mm CEM I Rapid Hardening concrete inner leaf. At the location of the connectors, the outer leaf of HPFRC is thickened locally from 20 to 50 mm to allow the connectors to be anchored to the outer leaf. To facilitate the construction of this 50 mm deep rib, two 30 mm layers of insulation were used to make up the 60 mm insulation layer. The insulation layer is reduced to 30 mm at the location of the connectors. This allows for a sufficient depth of

concrete to facilitate anchorage of the connectors. The insulation used is Fibran XPS with a thermal conductivity of 0.033 W/mK.

The panels differed as follows:

1. **Control panel**: No connectors are provided.
2. **PCM and no connectors panel:** No connectors are provided and the inner leaf includes 5% Micronal PCM. The behaviour of this panel can be compared to the behaviour of the Control panel to observe the influence of the PCM-concrete inner leaf on the overall thermal conductivity of the panel.
3. **PCM and C-Grid panel:** C-Grid connector is provided and the inner leaf includes 5% Micronal PCM. The behaviour of this panel can be compared to the behaviour of the PCM and no connector panel to observe any thermal bridging effect at the location of the C-Grid connector.
4. **PCM and Thermomass panel:** Thermomass connectors are provided and the inner leaf includes 5% Micronal PCM. The behaviour of this panel can be compared to the behaviour of the PCM with no connectors panel to observe any thermal bridging effect at the location of the Thermomass connector.
5. **Control debonded panel**: No connectors are provided and the outer leaf is debonded from the insulation layer using a sheet of plastic. Note this panel was not included in the thermal tests and was manufactured solely for the structural testing regime.

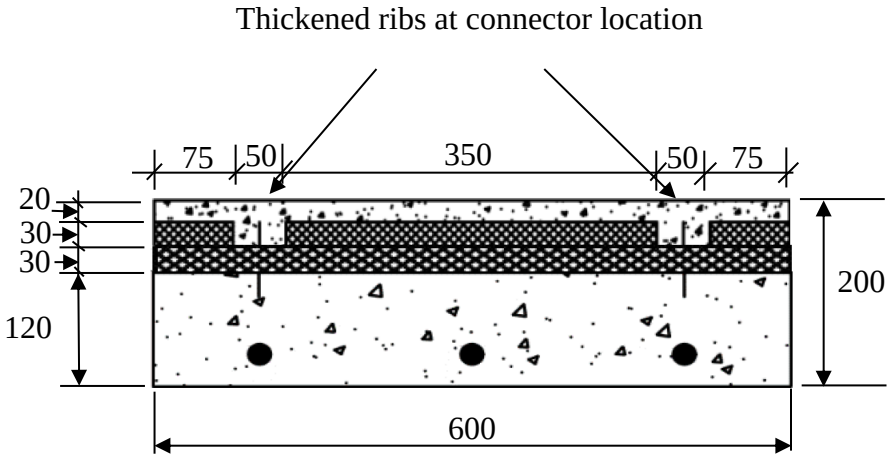


**Figure 5-1 Section through panel [All dimensions in mm]**

## 5.3 Manufacture of the test panels

The concrete mix design for the inner leaf control and the PCM-concrete composite were as per Tables 4-8 and 4-9. The mix constituents for the HPFRC outer layer were specified by the IMPRESS project partners and are provided in Table 5-1. The compressive strength of this concrete mix was found to be 96 MPa by O'Hegarty et al. (2019).

**Table 5-1 Mix constituents for HPFRC**

| Constituent | Mix 3 ($kg/m^3$) |
|---|---|
| Rapid Hardening PC | 250 |
| GGBS | 250 |
| Microsilica | 250 |
| Water | 227 |
| 10mm Limestone aggt. | 760 |
| Kilwaughter Grade 1 sand | 710 |
| Betocarb filler | 250 |
| Superplasticiser | 20 |
| CEM-fil minibar 43mm fibres | 20 |
| AntiCrak glass fiber | 1.2 |
| w/c ratio | 0.30 |

Formwork for five 900 x 600 x 200 mm deep panels was constructed. Three high yield 12 mm diameter reinforcing bars were placed in the formwork at 200 mm c/c, to reinforce the 120mm thick wythe as shown in Figure 5-2.

**Figure 5-2 Formwork and reinforcement for panels**

The control mix concrete was mixed first to form the 120 mm deep inner leaves of the two control panels. The mix displayed high workability with a slump flow (SF) of 485 mm, however as the SF is less than 650 mm the concrete cannot be categorised as self–compacting. The workability of the mix was considered to be satisfactory for the purposes of constructing the cladding panels so further flow table tests were deemed unnecessary. The mix was cohesive and no segregation occurred (Figure 5-3).

**Figure 5-3 Slump flow test of the control mix concrete**

The control concrete was placed in two of the forms and minimal vibration was required. A thermocouple was placed centrally on the concrete surface before the XPS insulation was placed. Then another thermocouple was placed centrally on the top surface of the insulation, (Figure 5-4).

**Figure 5-4 Control panel prior to HPFRC layer being poured with thermocouple in place**

The PCM-concrete composite material for the inner leaf of the remaining three panels was mixed next. The concrete was relatively stiff so a slump test was carried out rather than a slump flow test. The slump test failed as the PCM-concrete slowly collapsed however the concrete displayed good cohesiveness and no segregation occurred. The poker vibrator was used to place and compact the concrete into the formwork (Figure 5-5). Again, thermocouples were placed centrally on the concrete surface before the insulation was placed. Then another thermocouple was placed centrally on the surface of the insulation as previously.

(a) (b)

**Figure 5-5 (a) Placement of the PCM-concrete composite in the formwork and (b) Compaction of PCM-concrete with a poker vibrator**

Connectors were placed in two of the PCM-concrete composite panels. The C-Grid connectors were pushed into the fresh concrete of the inner leaf to an embedment depth of 65 mm prior to placing the central layer of insulation (Figure 5-6). The C-Grid connector protrudes above the insulation layer by 30 mm to facilitate a 30 mm embedment into the HPFRC outer leaf.

(a) (b)

**Figure 5-6 (a) Positioning of C-Grid connectors and (b) Insulation in place showing protrusion of C-Grid above the insulation**

The thermomass connectors were pushed through the first layer of insulation at 200 mm c/c, while the concrete was still fresh and before the second layer of insulation was put in position. Again the thermomass connectors were embedded into the inner leaf by 65 mm leaving a 30 mm embedment length into the outer HPFRC outer layer (Figure 5-7).

**Figure 5-7 PCM-concrete panel with Thermomass connectors**

The HPFRC was mixed in two batches. For each mix all the constituents, except the fibres, were added to the mixer and mixed for 20 minutes before the mix became workable due to the slow action of the superplasticiser. The fibres were then added in two stages and mixed for 2 minutes. A slump test was carried out and a slump of 80 mm was measured. A poker vibrator was used to assist placement of the HPFRC, and significant hand trowelling was required to achieve a smooth and level finish (Figure 5-8).

(a) (b) (c)

**Figure 5-8 (a) Placement of the HPFRC outer leaf of the panels, (b) Compaction of the HPFRC using a poker vibrator (c) Finished surface of HPFRC**

The panels were left in their moulds to facilitate stacking of the panels so that they could be stored in the laboratory without disrupting the space. The panels were covered with damp hessian and left to cure for 28 days. The panels were then demoulded and stored in the dry atmosphere of the laboratory in which the air temperature remained between 18 $^{o}$C and 20 $^{o}$C – as determined in previous thermal tests carried out in the laboratory - for a further 28 days to allow them dry out prior to testing thermally. Test cubes were made from each concrete mix and the average strength results of the cube tests are provided in Table 5-2. The compressive strength of the HPFRC is in line with previous strength test results carried out on this concrete mix by O'Hegarty et al. (2019). The 28 day results achieved for the control concrete mix are

higher than expected. As noted in Appendix D, in order to achieve higher 1 day strengths to facilitate early lifting and demoulding of panels in Techrete, the mix design uses a specified characteristic strength of 30 MPa at 3 days. The constituents of the concrete mix were as per the final control concrete mix design as detailed in Table 4-8 and the materials were sourced from the TCD laboratory. There is no obvious explanation for the higher strengths achieved however the aggregates used in the concrete mix were dry as they had been stored within the laboratory over a long period. As a result the aggregates may have absorbed water during the mixing process which would result in a lower water cement ratio and hence a higher strength concrete.

The strengths achieved for the PCM-concrete composite mix are aligned with findings in previous research (Niall et al., 2017, Fenollera et al., 2013, Hunger et al., 2009). The lower strengths achieved are to be expected as there is a significant difference between the intrinsic strength of the microcapsules and the other constituents of the concrete such as aggregates and cement. Also the inclusion of the microcapsules reduces the density of the concrete and interferes with the bond between the cement paste and aggregates. It is noted that the 57/58 day results are similar to the corresponding 28 day results indicating that the PCM-concrete composite does not continue to gain strength after 28 days as does a normal concrete mix. As discussed in Section 2.5.2.1, Cao et al. (2017) and Pilehvar et al. (2017) used SEM images which revealed weak connections and air voids between the PCM capsules and the matrix material, so even if the matrix material is gaining strength over time the reduced bond between the cement matrix and aggregates caused by the increased air voids will dictate the strength of the concrete. This finding aligns with results from previous research by the author (Niall et al. (2017)) and indicates that the presence of the PCM microcapsules is the determining factor in the strength of the PCM–concrete composite.

**Table 5-2 Strength of concrete mixes used in panels**

| Sample Type | 28 day strength (MPa) | Strength on day of structural test (MPa) (age) |
|---|---|---|
| Control mix 1[used in Control debonded] | 67.2 | 73.0 (60 days) |
| Control mix 2 [used in Control] | 80.4 | 82.0 (58 days) |
| PCM mix 1 [used in PCM - No Ties] | 29.4 | 30.9 (57 days) |
| PCM mix 2 [used in PCM C-Grid] | 35.0 | 35.9 (58 days) |
| PCM mix 3 [used in PCM + TM] | 31.9 | 31.0 (58 days) |
| HPFRC mix 1 | 94.8 | - |
| HPFRC mix 2 | 103.1 | - |

### 5.4 Thermal testing of panels

U-values, as described in Section 2.7, are often used to measure and compare the thermal energy performance of external cladding elements of a building. However U-values for typical cladding elements are often based on standardised material thermal conductivity values taken from literature and steady-state thermal conditions through the thickness of the wall. In reality though, steady-state conditions for heat transfer through a wall in a building will not occur due to fluctuating boundary conditions, that is, variations in internal and external temperatures. In addition, the thermal mass characteristics of a wall construction, in particular the presence of an insulation layer creates a time lag between a change in temperature on one side of the wall and a thermal response on the other side of the wall. In the context of this research project, the presence of PCMs within the inner leaf of the panel means that the temperature differential across the thickness of the PCM-concrete composite wall will not be linear during the phase change period and hence steady-state conditions cannot be achieved. For example the rate of heat transfer out of the wall would be lower than the rate of heat transfer into the wall as the PCM absorbs some of the heat to change phase from solid to liquid. Hence a U-value does not provide a means to undertaking an accurate calculation of real thermal performance. An accurate simulation model is required to take into account environmental conditions and the actual thermal response of a wall.

Notwithstanding the limited application of U-values in assessing thermal behaviour of walls under real conditions, given the variability of the surface resistance of a cladding panel and given the innovative nature of the cladding panel under research in this thesis, it was of interest to determine an accurate R-value and hence U-value for the panel excluding surface resistances. These values facilitate a comparison of the thermal behaviour of the panel with outer wall construction types outside the period of phase change. Desogus et al. (2011) carried out a review and comparison of different methods of measuring the thermal resistance of building components and concluded that determining the R-value of cladding elements directly using a heat flux sensor and surface temperature sensors is more accurate than using standardised R-values of the various layers of the composite system.

The test methodology adopted for the panels allowed an R-value for the cladding panels to be determined. By locating thermocouples on the external and internal surfaces of a plane panel and measuring the heat flux exiting the panel under steady-state conditions, the total thermal resistance, excluding surface resistance of each panel, was determined using equation (2-22), re-written here as equation (5-1) for clarity.

$$\dot{Q} = \frac{T_1 - T_2}{R} \cdot A \ (W) \qquad \textbf{(5-1)}$$

The U-value for the three layered wall panel can then be determined by calculating the inverse of the R-value. This method is widely accepted as the most reliable for determining U-values (Lee and Pessiki, 2004 and 2006, Nussbaumer et al., 2006, Abdou et al., 1996, Chen et al., 1994)

### 5.4.1 Experimental set up

Thermocouples were cast into the concrete sandwich panel at each interface and thermocouples were also placed on the inner and outer surfaces (Figure 5-9). Heat flux sensors were positioned on the face of the panel, one was positioned centrally and the other was located at the position of the connectors to enable any cold bridging effect caused by the connectors to be determined (Figure 3-11).

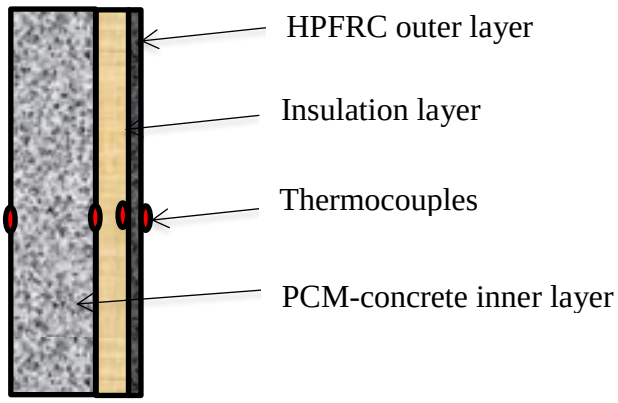


**Figure 5-9 Schematic section through a panel showing location of thermocouples**

Each panel was positioned on the hotplate apparatus, with the inner face of the inner leaf against the hot plate and secured in place with an insulation surround to minimise heat loss through the edges of the panel. The thermocouples and heat flux pads were connected to a data logger including a thermocouple to record the surrounding air temperature. The panel was heated up until a steady-state temperature differential across the concrete panel samples, $(T_h - T_c)$ was reached, that is, $\Delta T < 0.5$ °C for 4 consecutive hours (Aviram et al., 2001), where $T_h$ is the temperature of the inner hot surface and $T_c$ is the temperature of the cooler outer surface of the panel. In accordance with I.S. EN ISO 8990-1997, the temperature differential through the panel was maintained at greater than 20 °C. The panels were left in place recording data every minute for a minimum of 48 hours.

### 5.4.2 Analysis of thermal tests of panels

During the thermal testing of the panels in the adjusted hotplate apparatus, insulation was placed on all surfaces except the front and rear surfaces to ensure that heat transfer was one-dimensional through the thickness of the panel. In steady-state conditions the rate of heat transfer into the panel from the hot plate must equal the rate of heat energy emitted from the front face of the panel, that is, the rate of heat transfer through the wall must be constant.

Overall thermal conductivity of the panel was determined from:

$$k = \frac{q}{At} \cdot \frac{d}{(T_h - T_c)} = \dot{Q} \cdot \frac{d}{(T_h - T_c)} \text{ (W/mK)} \quad \textbf{(5-2)}$$

where:

k = thermal conductivity (W/mK)

A = surface area ($m^2$)

d = depth of material (m)

t = time (s)

$T_h$ = higher temperature (K)

$T_c$ = lower temperature (K)

$\dot{Q}$ = rate of heat transfer (W)

The heat flux (rate of heat transfer) exiting the cooler surface was measured and the measurement was given in $W/m^2$, which is equivalent to Joules/(sec $m^2$), that is, q/At. The depth of each panel 'd' is known as 120 mm. As thermocouples were located at the interface of each layer, the temperature differential across each individual layer could be determined from the experimental data. In theory this data could be used to determine the thermal conductivity of each layer because, due to steady-state conditions, the heat flux through each layer was the same. However the temperature differential across the HPFRC layer and the PCM-concrete composite layer was less than 20 $^oC$ hence any thermal conductivity values determined would not be in accordance with I.S. EN ISO 8990-1997. Using the temperature differential across the full depth of the panel, together with the measured heat flux values at the centre of the panel and at the location of the connectors, average thermal conductivity values for the overall panel at both locations were determined, together with R-values and U-values.

To determine the required parameters the data collected for the final four hours of steady-state conditions was used and the data collected for temperature differential and heat flux over the

four hours was averaged and used in equations (5-2), (5-1) and (2-19). Calculations to determine the overall thermal conductivity, k, the R-value and the U-value for each panel are provided in Appendix F. A sample calculation for a panel with connectors is provided as follows:

**Panel with PCM and C-Grid connector**

(i) At centre of panel:

$\dot{Q}$ = 15.06 W/m$^2$

ΔT = 27.8 K

d = 0.2 m

Hence:

- Overall thermal conductivity, k = $\dot{Q}.\frac{\mathrm{d}}{(\mathrm{T_h}-\mathrm{T_c})}$ = $\frac{15.06\ x\ 0.2}{27.8}$ = 0.108 (W/mK)
- R–value $= \frac{T_1 - T_2}{Q}$ = $\frac{27.8}{15.06}$ = 1.85 (m$^2$K/W)
- U–value = $\frac{1}{R} = \frac{1}{1.85}$ = 0.54 (W/m$^2$K)

(ii) At C- Grid connector location:

$\dot{Q}$ = 30.76 W/m$^2$

ΔT = 26.2 K

d = 0.2 m

Hence:

- Overall thermal conductivity, k = $\dot{Q}.\frac{\mathrm{d}}{(\mathrm{T_h}-\mathrm{T_c})}$ = $\frac{30.76\ \mathrm{x}\ 0.2}{26.2}$ = 0.235 (W/mK)
- R–value $= \frac{T_1 - T_2}{Q}$ = $\frac{26.2}{30.76}$ = 0.852 (m$^2$K/W)
- U–value = $\frac{1}{R} = \frac{1}{0.852}$ = 1.17 (W/m$^2$K)

A summary of the overall thermal conductivity values, the R-values and the U-values of the panels is provided in Table 5-3. It should be noted that the measured R-values do not include surface resistivity. However for comparison purposes an R-value that includes external and internal surface resistances of 0.04 m$^2$K/W and 0.13 m$^2$K/W respectively, as guided in I.S. EN ISO 6946:2017, are also provided in Table 5-3. It can be noted that the inclusion of the surface resistances result in a small increase in the R-value and hence decrease in the U-value of 8 %

to 11 % at the centre of the panel. It should also be noted that as the 50m mm wide thickened ribs of the panel only account for 1.6 % of the overall area of the panel they have a negligible effect on the overall R-value for the panel. However, as can be noted from Table 5-3, the ribs do result in a reduced R-value locally.

It is important to note that by the time steady-state conditions were reached across the panels the hot side of the panel was at circa 46 $^{o}$C. This means that any PCM within the panel was fully melted. So the thermal parameters provided in Table 5-3 are for panels containing fully melted PCM. The difference between the thermal conductivity of liquid paraffin and solid paraffin is negligible (Soares et al., 2023) so the thermal parameters are similar when the PCM is in a solid state. During the phase change process the thermal behaviour of the panel is dynamic due to the latent heat capacity of the PCM so steady-state conditions are not present and the values provided in Table 5-3 do not apply. The thermal resistance that is provided by the change of phase of the PCM is not accounted for in these figures. The figures provided in Table 5-3 can only be used when assessing and/or comparing the thermal behaviour of the panel under steady state conditions and in the absence of phase change.

**Table 5-3 Summary of thermal parameters of cladding panels**

| | Control Panel | Panel with PCM and no connector | Panel with PCM and C-Grid | Panel with PCM and Thermomass |
|---|---|---|---|---|
| Overall thermal conductivity @ centre (W/mK) | 0.130 | 0.114 | 0.108 | 0.096 |
| Overall thermal conductivity @ tie location (W/mK) | N/A | N/A | 0.235 | 0.196 |
| R-value @ centre ($m^2K/W$) | 1.54 | 1.75 | 1.85 | 2.07 |
| Air-to-Air R-value @ centre ($m^2K/W$) | 1.71 | 1.92 | 2.02 | 2.24 |
| R-value @ connector location ($m^2K/W$) | N/A | N/A | 0.85 | 1.02 |
| U-value @ centre ($W/m^2K$) | 0.65 | 0.57 | 0.54 | 0.48 |
| U-value @ connector location ($W/m^2K$) | N/A | N/A | 1.17 | 0.98 |

Overall it can be observed that the panels containing the PCM concrete composite have a lower thermal conductivity and hence a lower U-value. This is expected as the encapsulated paraffin has a lower thermal conductivity than concrete. It can also be noted that the conductivity of the panels with the connectors approximately doubles at the connector location indicating the level of thermal bridging effect caused by the connectors due to the higher thermal conductivity of the connectors relative to the insulation. Contributing to the thermal bridging effect is the thickening of the concrete and reduction of thickness of the insulation at the location of the connectors. The C-Grid connectors provide slightly less resistance to heat flow than the Thermomass connectors hence the panels with the C-Grid have a slightly higher thermal conductivity. This can be clearly seen in Figure 5-10 which shows a comparison of the heat flux at the centre of the panel and at the location of the connectors for both panels containing connectors.

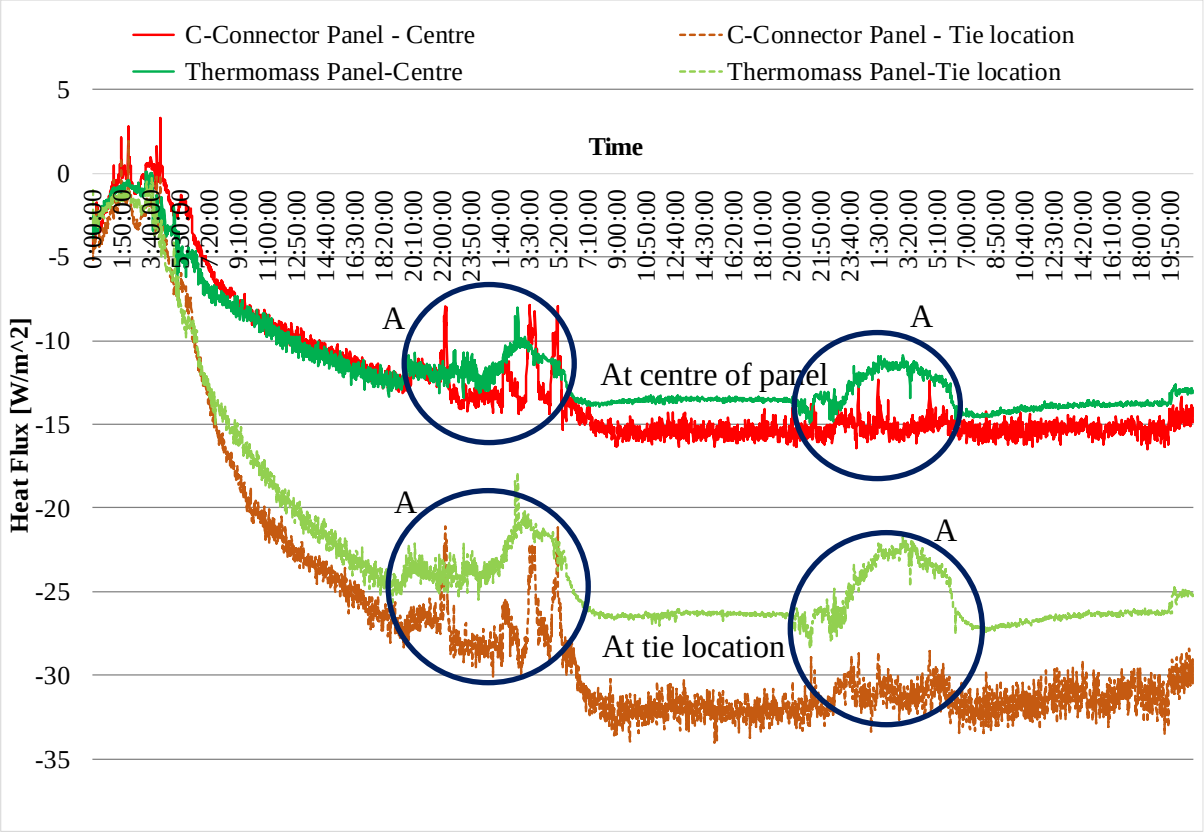


**Figure 5-10. Comparison of heat flux at the centre and at location of connectors**

It can be clearly observed from Figure 5-10 that the heat flux is greater at the location of the connectors demonstrating the reduction of thermal resistance due to the presence of the connectors. It is also clear that the heat flux at the location of the Thermomass connectors is lower than the heat flux at the location of the C-Grid. Hence the thermal bridging effect of the Thermomass connectors is less than that of the C-Grid connector. It took approximately 24

hours for the heat flux to reach a steady-state. It can be noted at the times denoted ‘A’ that the heat flux at the surface of the panel tends to reduce during the night, that is, the amount of heat energy emitted from the front of the panel and transferred to the surrounding air during the night is lower. This effect may be due to the reduced air movement in the laboratory when it is unoccupied overnight. During the day there is a higher level of air movement around the laboratory due to doors opening and closing regularly and people moving around the space. At night there is no activity in the laboratory so the movement of air adjacent to the surface of the test panel is very low. This results in lower convective heat transfer between the panel surface and the air and hence the resistance to heat transfer at this surface is higher when the surrounding air is still.

Figure 5-11 shows the temperature profile through the depth of the Control panel and the PCM panel with no connectors, taken every two hours over 24 hours starting when the panel was first placed in the hot plate apparatus. These plots provide a visual display of the enhanced thermal mass provided by the presence of PCM in the inner leaf. The inner leaf of the Control panel took 5.7 hours to reach steady-state, however the inner leaf of the PCM panel without connectors took 21.3 hours to reach steady-state. As the temperature of the PCM-concrete inner leaf increases from circa 18 $^{o}$C to 41 $^{o}$C this means that the PCM present in the wall went through a phase change during this heating period and hence the PCM absorbed and stored some of the heat energy, enhancing the wall’s thermal mass properties. When the increases in temperature of the inner surface of the inner leaf, at 120mm depth are compared it can be noted that the Control panel increases from 18 $^{o}$C to 44 $^{o}$C in 6 hours whereas the PCM panel increases from 18 $^{o}$C to 26 $^{o}$C in 6 hours demonstrating the higher thermal resistance provided by the PCM panel when phase change occurs.

The effectiveness of the insulation is also clear with nearly no increase in temperature of the outer HPFRC layer. However the panels containing the connectors show a slightly greater increase in temperature of the outer HPFRC layer indicating the thermal bridge effect of the connectors (Figure 5-12).

Figure 5-12 also highlights the higher thermal conductivity demonstrated by the PCM C-Grid panel. At 120 mm depth, the increase in temperature of the PCM C-Grid panel within each 2 hour interval is greater than that in the PCM Thermomass panel, as the heat is transferring through the 120 mm depth of the inner leaf at a faster rate. The overall temperature increase after 24 hours, at a depth of 120 mm, in the PCM C-Grid panel is 26 $^{o}$C compared to 21.5 $^{o}$C

in the PCM Thermomass panel, again indicating the higher thermal conductivity of the PCM C-Grid panel.

When comparing Figure 5-11(b) and Figure 5-12(a) it can be noted that there is no discernible difference between the rate of heat transfer through the inner leafs of the PCM Thermomass panel and the PCM panel with no connectors which is to be expected as the plots in Figures 5-11 and 5-12 are based on the temperatures at the centre of each panel and not at the connector location. However the reason that the PCM C-Grid panel is displaying a slightly higher rate of heat transfer may be due to the fact that the C-Grid connector is a continuous strip through the panel whereas the Thermomass connectors only occur at point locations and hence the thermal bridging effect caused by the Thermomass connector is localised at discrete points in the panel rather than along a continuous strip as in the panel with C-Grid.

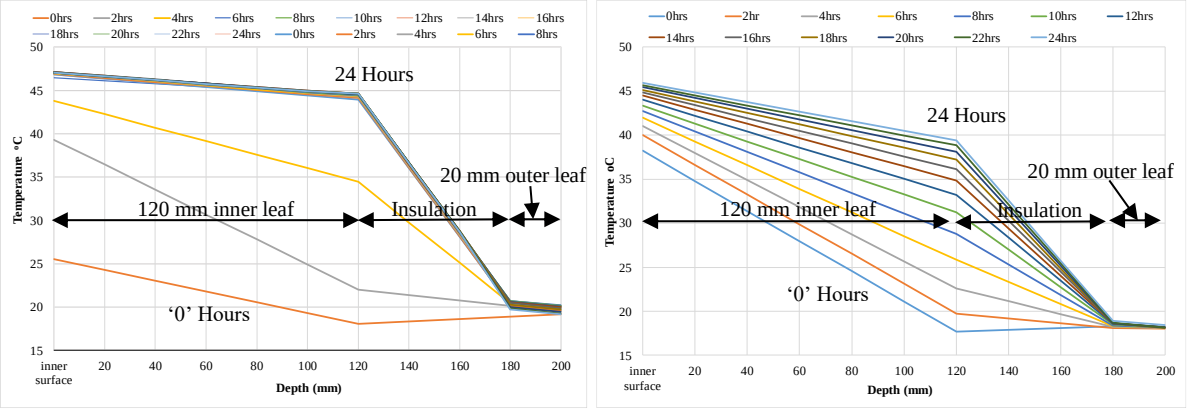


**(a)** **(b)**

**Figure 5-11 Temperature profile through (a) Control panel and (b) PCM panel with no connectors, every 2 hours for 24 hours of heating**

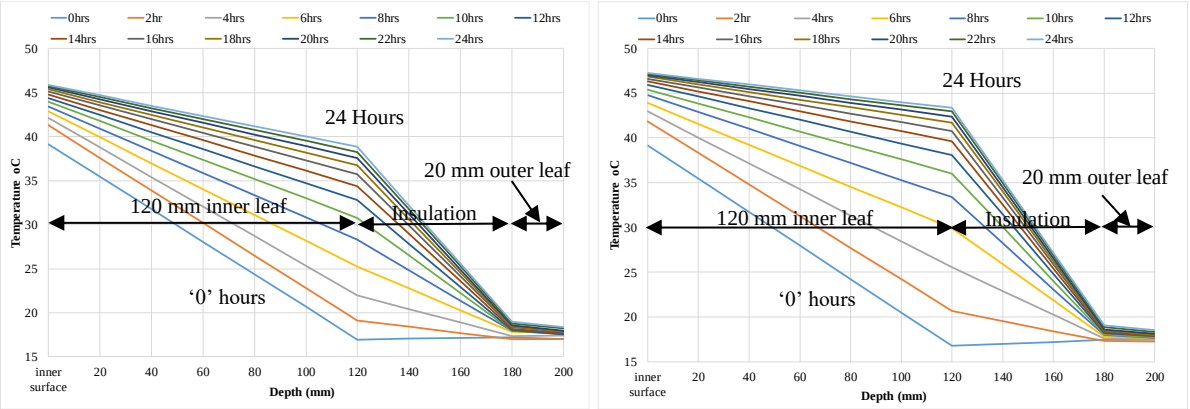


**(a)** **(b)**

**Figure 5-12 Temperature profile through panels (a) PCM with Thermomass and (b) PCM with C-Grid, every 2 hours for 24 hours of heating**

Overall the thermal tests carried out on the panels demonstrated that the panels that contain PCM in the inner leaf provide greater thermal resistivity than the Control panel due to the thermal mass provided when the PCM changes phase. Also the results of the tests show that the thermal bridging effect caused by the presence of the connectors is lower when Thermomass connectors are used compared to C-Grid connectors.

**5.5 Conclusions**

In order to observe the thermal conductivity behaviour of the PCM-concrete composite material when placed in the inner leaf of a concrete sandwich panel and bounded on one surface by a layer of insulation, 5 no. 900 x 600 x 200 mm deep concrete sandwich panels, as described in Section 5.2, were manufactured in the laboratory.

The PCM-concrete composite displayed good cohesiveness and good compaction was achieved with the use of a poker vibrator. The PCM-concrete composite achieved 28 day strengths ranging from 29.4 to 35.0 MPa which are sufficient for a non-loadbearing application such as the proposed cladding panels. There was no increase in strength for the PCM-concrete composite between 28 days and 56 days indicating that the presence of the PCM microcapsules is the determining factor in the strength of the PCM–concrete composite as discussed in Section 5.3.

The panels were placed in an adjusted hot plate apparatus. Temperature and heat flux data was recorded under steady-state conditions which was used to determine the overall thermal conductivity and the thermal resistance of each panel. Under steady-state conditions the temperature through the depth of the inner leaf of each panel varied from circa 46 $^{o}$C to 35 $^{o}$C hence any PCM present would have completely changed phase and be fully melted. So the thermal parameters determined from the data and presented in Table 5-3 are for panels containing fully melted PCM and can only be used when assessing and/or comparing the thermal behaviour of the panel under steady state conditions and in the absence of phase change.

As noted in Table 5-3, the panels containing PCM in the inner leaf have a slightly lower overall thermal conductivity than the Control panel. Given that the thermal conductivity of the insulation layer is very low at 0.033 W/mK, relative to the thermal conductivity of the concrete layers at 1.48 to1.86 W/mK, as noted in Table 4-5, the insulation layer will dominate the thermal conductivity behaviour of the overall panel. As a result the difference between the overall thermal conductivity of the panels is small.

It was also noted from Table 5-3 that there is a thermal bridging effect at the location of both types of connectors indicated by the lower thermal resistivity measured at this location. This result is expected as the connectors have a higher thermal conductivity than the insulation layer. However, the results of the thermal tests show that the Thermomass connectors provide a greater thermal resistance and hence the themal bridge effect is lower in the panel connected with Thermomass connectors.

Plots in which the temperature profile through the depth of the panels is displayed every two hours over a 24 hour period were provided in Figures 5-11 and 5-12. These plots highlighted the difference between the thermal resistance of the Control panel inner leaf and the inner leaves of the panels containing PCM. The enhanced thermal mass provided by the PCM can also be clearly observed from these plots. The Control panel took 5.7 hours to reach steady-state whereas the PCM panel without connectors took 21.3 hours to reach steady-steady. This difference is due to heat being absorbed and stored as the PCM changes phase and hence the transfer of heat energy through the inner leaf is significantly slower.

The higher overall thermal conductivity of the PCM panel with C Grid connector relative to the PCM panel with Thermomass connectors can also be observed from Figure 5-12, indicated by the higher increase in temperature over each two hour interval displayed in the inner leaf of the PCM panel with C-Grid. This result demonstrates that the rate of heat transfer across the inner leaf of the PCM panel with the C Grid connector is greater than that across the inner leaf of the PCM panel with Thermomass connectors. The plots provided in Figures 5-11 and 5-12 were compiled used temperature data collected at the centre of the panel rather than at the location of the connectors. There was no discernible difference between the temperature profiles in the PCM panel with Thermomass and the PCM panel with no connectors, indicating that the thermal bridge effect caused by the Thermomass connectors is very localised around the connector. As noted, the PCM C-Grid panel is displaying a slightly higher rate of heat transfer which may be due to the thermal bridge effect of the C-Grid connector spreading over a wider area due to the fact that the connector is a continuous strip through the panel rather than a discrete point.

This thermal testing regime allowed the overall thermal conductivity and thermal resistivity of the proposed panels to be quantified under steady-state conditions. These parameters will assist in comparing the thermal behaviour of the proposed panels to more traditional cladding options outside of phase change conditions which is important when assessing the thermal performance

of a cladding design across all seasons. The results of the thermal testing described in this chapter also leads to the selection of the Thermomass connector for the hut construction rather than the C Grid connector, due to its lower thermal bridging effect. However this decision is also subject to the results of the structural behaviour investigation detailed in Chapter 6.

# Chapter 6. Structural Laboratory Tests on Proposed Cladding Panels

## 6.1 Introduction

As the concrete sandwich cladding panels that are being developed in this research project are for the purpose of recladding existing buildings it is intended that they are only used in non-loadbearing applications. However the panels are still required to resist lateral wind loads whereby a panel is required to span vertically between floor levels and to transfer the lateral loads to the floor plate, primarily through bending. The panel must have sufficient flexural strength to transfer the loads to the floor plates without failing in flexure or shear and also have sufficient stiffness to avoid excessive deformations.

In a re-cladding situation the concrete sandwich panel is being applied to an existing structural frame so it is important to consider the self-weight of the new panel relative to the panel that it is replacing and the effect that it may have on the existing structure and foundations. Reducing the overall thickness of the sandwich panel has the benefit of reducing its weight however it reduces the thermal resistance and the stiffness of the panel which impacts the panel's ability to resist lateral loads through bending without excessive lateral deformation. However the structural capacity of a two wythe panel can be enhanced by connecting the wythes together to achieve composite action as discussed in Section 2.9.

The level of composite behaviour achieved in a concrete sandwich panel depends on the type of connectors used and the stiffness of the insulation layer. The ability of the shear connectors to transfer the shear forces through the insulated core, from one concrete wythe to the other, determines the amount of composite action that can be achieved. It has been shown that with the use of concrete connectors or robust steel truss connectors between the wythes of a sandwich panel a high degree of composite behaviour (over 90%) can be achieved (Pessiki and Mlynarczyk (2003), Bush and Stine (1994)). However as noted in Section 2.9.2 these types of connectors compromise the thermal performance of the panel. The degree of composite action that can be achieved with the more thermally efficient C-Grid and Thermomass is typically partial to non-composite.

The primary function of the insulation layer is to provide a thermal barrier between the interior and exterior environment of the building. However previous research (Frankl et al. 2011, Hegarty et al. 2019) has shown that the stiffness of the insulation layer influences the composite behaviour of a concrete sandwich panel, particularly when used with the C-Grid shear

connector. As a wind load is applied to the outer wythe of the panel, the insulation and connector must be capable of transferring the load to the inner wythe, prior to cracking of the outer wythe, in order to achieve any composite action between the layers. For this reason rigid insulation must be used. The outer wythe behaves as a plate on an elastic foundation and the insulation layer spreads the load to the stiffer inner wythe. A stiffer insulation layer will result in reduced bending in the outer wythe and increased load sharing between the two concrete wythes.

The bond between the insulation and the concrete also influences the extent of composite action achieved in a panel. Frankl et al. (2011) carried out an experimental study to determine the behaviour of precast, prestressed concrete sandwich wall panels reinforced with this CFRP shear grid using both EPS and XPS as the rigid insulation. Frankl concluded that composite action could be achieved using either EPS or XPS, however, panels constructed using EPS insulation provided a better shear transfer mechanism and achieved a higher percentage of composite action than XPS insulation due to the superior bond between the EPS and the concrete wythes. Other research studies (Choi et al. (2015), Kim and You (2015)), which also used a CFRP grid shear connector, found that the panels with XPS insulation provided a higher level of composite action. Hence it is not conclusive which type of insulation leads to a greater level of composite action. Considering all the factors, XPS insulation was selected for this study primarily due to its higher stiffness as the stiffness of the insulation has a greater impact on the load sharing behaviour than the composite behaviour due to the bond between the concrete and insulation.

The aims of the structural testing regime carried out in this research are as follows:

- Quantify the flexural capacity of the proposed panel to ensure that it is capable of resisting any potential wind loads
- Observe and quantify the load-deflection behaviour of the panels and quantify if composite behaviour occurs in the panels which include connectors
- Compare the influence of the two different types of connectors on the flexural behaviour of the panel
- Investigate the influence of the bond between the XPS insulation and the concrete wythes on the flexural behaviour of the panel

This chapter describes the methodology adopted to achieve the aims of this investigation into the structural behaviour of the proposed panel. The results of the tests are used to determine the capacity of the panel to resist typical wind loads and to understand the influence of each component of the panel on the elastic and post-cracking structural behaviour of the overall panel.

## 6.2 Methodology

### 6.2.1 Design of test panels

To achieve the aims of this investigation as denoted in Section 6.1, five 900 mm long x 600 mm wide test panels were designed and manufactured as described in Sections 5.2 and 5.3. Each panel consists of a 20 mm HPFRC outer wythe (with a 30 mm thickening at connector location, in the span direction) and 60 mm XPS insulation wythe. The inner wythe is 120 mm of either normal concrete for control panels or PCM-concrete composite for the PCM panels (Figure 5-1). The purpose of each of the test panels in this structural behaviour investigation is as follows:

- **Control no ties panel:** This panel has normal concrete in the inner wythe and does not include any connectors. The results from the tests on this panel will be compared to the results from the PCM panel with no shear connectors to observe the impact of the PCM-concrete inner leaf on flexural behaviour.

- **Control debonded panel:** This panel has no shear connectors and the outer wythe is debonded from the insulation layer using a sheet of plastic. The purpose of this panel is to enable the influence of the bond between the XPS insulation and the outer HPFRC concrete wythe to be observed (Figure 6-1).

- **PCM no ties:** The results from the tests on this panel are compared to the results from the Control panel tests to ascertain the impact, if any, of the PCM-concrete composite material in the inner wythe on the flexural behaviour of the panel.

- **PCM C-Grid connector:** This panel has a PCM-concrete inner leaf and includes two rows of C-Grid connector to connect the inner and outer wythes The flexural behaviour of this panel is compared to the behaviour of PCM no ties panel to observe the influence of the C-Grid connector on the flexural behaviour of the panel and ascertain if any composite behaviour is achieved (Figure 5-6 (a) and (b)).

- **PCM Thermomass (TM) connector:** This panel has a PCM-concrete inner leaf and includes two rows of Thermomass connectors located at 200mm centres to connect the inner and outer wythes (Figure 5-7). The flexural behaviour of this panel is compared to the behaviour of PCM no ties panel to observe the influence of the Thermomass connectors on the flexural behaviour of the panel and to ascertain if any composite behaviour is achieved.

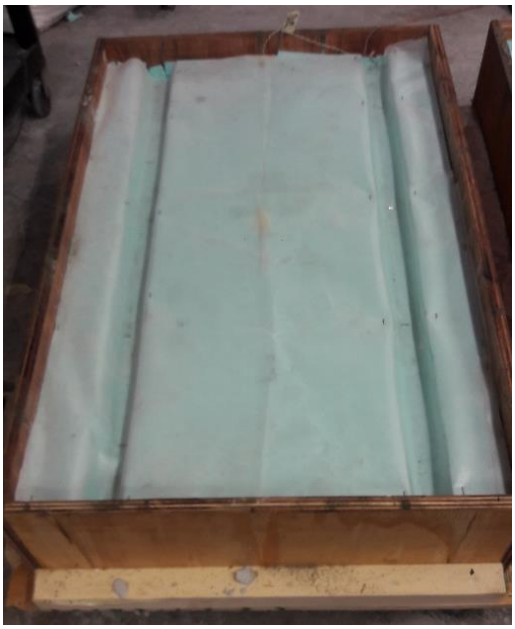

**Figure 6-1 Control debonded panel with debonding sheet prior to pouring the outer HPFRC wythe**

### 6.2.2 Experimental set up

The 900 mm long x 600 mm wide panels were set up in a structural testing rig with the HPFRC layer as the upper surface and the 120mm concrete layer as the lower surface. The lower wythe is supported by the rig at either end and the load is applied to a centrally placed spreader beam. A schematic of the test set up is shown in Figure 6-2.

Three displacement transducers were positioned across the top surface of the panel to record displacement at 100 mm in from the ends of the panel and at the mid-span of the panel. Another transducer was set up to record the mid-span deflection of the bottom surface of the panel. Strain gauges were applied to the top HPFRC surface to record strain parallel to the span. Strain gauges were applied close to the centre, either side of the loading beam and 200 mm in from either end. Strain gauges were also positioned perpendicular to the span at 200 mm in from each end. These strain gauges would indicate any two-way bending behaviour occurring in the top HPFRC layer. A strain gauge was also attached to the bottom surface of the panel at mid-span (Figure 6-2 and 6-3).

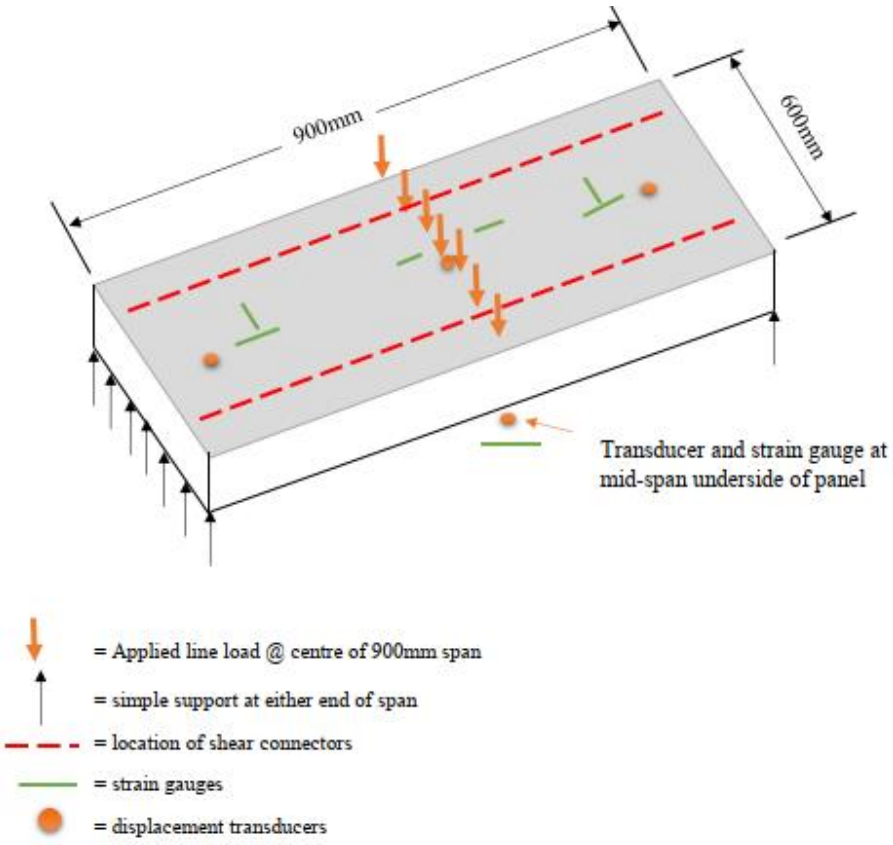


**Figure 6-2 Schematic of 3-point flexure test on panels [NTS]**

**Figure 6-3 Test panel placed in rig**

In the displacement controlled 3-point bending test the downward movement of the jack is automatically adjusted to maintain a displacement rate of the jack head of 1 mm per minute while the load resistance capacity is recorded in a load cell in series. That is, the load resistance offered by the panel to displace the panel by 1 mm is recorded at each interval. All data was recorded every 0.2 seconds. A displacement controlled test allows post-cracking toughness behaviour of the panels to be better observed as progression towards failure is usually gradual.

## 6.3 Results and analysis

### 6.3.1 Assessment of required moment capacity of panels

In a real in-situ application a horizontal wind load may be applied to a cladding panel as a uniformly distributed load. The panel typically spans vertically between the floor slabs and in modern commercial buildings this span can be typically up to 3.5 m. As applied wind load increases with height; for this analysis a design wind load for the sixth storey of a building in Dublin city was calculated as it is considered a reasonably onerous load condition. Calculations were carried out in accordance with Eurocode 1: Part 1 -4; and the Irish annex I.S. EN 1991-1-4. The calculations are presented in Appendix G. The applied wind load for an assumed location of a 6$^{th}$ storey level of a building in the Dublin Docklands was calculated to be 1 kN/m$^2$. For design the wind load must be multiplied by the load factor for variable loads which is 1.5, hence the design wind load applied to the cladding panel, $W_{Ed}$ is 1.5 kN/m$^2$. If this wind load is applied uniformly to a panel spanning 3.5 m the resulting maximum applied moment at the mid-height of the panel can be determined using the well-known equation (Davison and Owens, 2003) :

$$M_{max} = \frac{w(l)^2}{8}$$

where:

$M_{max}$ = maximum bending moment arising in the structural element

$w$ = uniformly distributed load (kN/m)

$l$ = span of the structural element (m)

Using the relevant values for the cladding panel, the maximum moment is determined as:

$$M_{max} = \frac{1.5\ (3.5)^2}{8} = 2.3 \text{ kNm}$$

So the panel would require a moment capacity of 2.3 kNm to withstand this wind load. In a 3 point bending test the moment arising at mid-span is PL/4 where P is the applied point load in kN and L is the span of the panel in m. In this case the span of the panels is 0.9 m. For the test panels to have an elastic moment capacity of 2.3 kNm:

$$\frac{PL}{4} \geq 2.3 \text{ kNm}$$

$$P \geq (2.3 \text{ x } 4)/0.9$$

$$P \geq 10.2 \text{ kN}$$

Hence the test panel must withstand an applied point load of at least 10.2 kN prior to the first crack occurring to achieve sufficient elastic bending moment capacity.

### 6.3.2 Assessment of second moment of area and flexural stiffness of fully composite and non-composite panels

The second moment of area and the flexural stiffness of the panels are determined for both non-composite and composite behaviour using a similar approach to that described in Section 2.9. The formulae provided in Table 2-9 for determining the second moment of area for the composite and non-composite behaviour of a two wythe panel assume that each wythe is made with the same material and hence each wythe has the same Young's modulus, E. These E values then cancel out above and below the line in equation (2-40) so they do not feature in the final calculation. However in this investigation, each of the panels use a different type of concrete for the inner and outer wythes and hence the Young's moduli for the wythes vary. This must be taken into account when calculating the second moment of area for each of the panels by using a modular ratio (ratio of one Young's modulus to another) to create a transformed section for one of the wythes which is then used in the calculation of the second moment of area. In addition, when applying equation (2-40) to determine the percentage of composite action, the differing E values will not cancel out hence the expression used in this analysis for determining the composite action of the panel incorporates the expression for flexural stiffness of the panel as follows:

$$k\ (\%) = \frac{E_{exp}I_{exp} - E_{nc,panel}\, I_{nc}}{E_{c,panel}I_c - E_{nc,panel}I_{nc}} \qquad \textbf{(6-1)}$$

where

- $E_{nc,panel}\ I_{nc}$ is the theoretical flexural stiffness of an elastic non-composite panel
- $E_{c,panel}\ I_c$ is the theoretical flexural stiffness of an elastic composite panel
- $E_{exp}I_{exp}$ is the actual elastic flexural stiffness of the panel during the test

The experimental flexural stiffness of each panel, $E_{exp}I_{exp}$, is determined from the mid-span deflection data, $\delta_{exp}$, (in mm) by rearranging the well-known engineer's formula for the deflection of an element subjected to a mid-span point load, as follows (Davison and Owens (2003)):

$$E_{exp}I_{exp} = PL^3/(48\delta_{exp}) \quad \textbf{(6-2)}$$

where

- P = applied load in Newtons
- L = span of the panel in mm

These values of both theoretical and experimental flexural stiffness only apply to linear elastic behaviour so only the data measured prior to the first crack occurring will be used to consider composite behaviour.

Also, as can be observed from Figure 5-1, the outer wythe has two strips of a thickened area to facilitate enhanced anchorage of the connectors. These thickened areas are included in the calculation of the second moment of area of the outer wythe. The calculations for determining the theoretical second moment of area and flexural stiffness of each type of panel for both fully composite and non-composite behaviour are provided in Appendix H. A summary of the relevant values are provided in Table 6-1. It can be noted that the Control panel has a greater flexural stiffness than the PCM-concrete panel, in both the non-composite and composite scenarios. This is due to the higher Young's modulus of the control concrete (35.2 GPa) compared to the PCM-concrete (31.4 GPa).

**Table 6-1 Second moment of area and flexural stiffness of panels for fully composite and non-composite behaviour**

| Type of panel | $I_{outer,\ wythe}$ ($mm^4$) | $I_{inner,wythe}$ ($mm^4$) | Non-composite $I_{nc}$ ($mm^4$) | [1]Flexural stiffness non-composite panel $E_{panel}$ $I_{nc}$ ($Nmm^2$) (x $10^9$) | [2]Fully composite $I_c$ ($mm^4$) | [1]Flexural stiffness fully composite panel $E_{panel}$ $I_c$ ($Nmm^2$) (x $10^9$) |
|---|---|---|---|---|---|---|
| Control concrete | 2,125,000 | 86,400,000 | 88,525,000 | 3132.8 | 254,679,190 | 10159.4 |
| PCM-concrete | 2,125,000 | 86,400,000 | 88,525,000 | 2804.5 | 246,824,800 | 9426.4 |

[1]Flexural stiffness takes into account the different E values for the inner and outer wythes
[2]$I_c$ determined taking into account the different E values for the inner and outer wythes

### 6.3.3 Results and analysis of each panel test

For each panel test the resistive load, deflection and strain data were processed and plots were compiled. On each of the plots critical events were noted and coordinated across all the plots for a particular panel. This section provides a qualitative and quantitative analysis of the structural behaviour of each panel during the tests and concludes with a summary comparison of the panels.

Initially, in each panel test, the top HPFRC wythe moved downwards as the load was applied, compressing the insulation. As further displacement was imposed, the insulation directly under the loading beam compressed more and the upper wythe was effectively acting similar to a slab on an elastic foundation as it tended to bend. The XPS insulation distributed this load to the stiffer 120 mm deep lower wythe which provided a relatively stiff support as it was supported at either end by rigid supports. The upward reaction provided by the insulation caused a moment in the upper layer which in turn, in the absence of a connector, caused the ends of the slab to tend to rotate upwards, hence a sagging moment occured under the loading beam at point A (Figure 6-4). However if the wythes were connected together, the ends of the upper wythe would be prevented from moving upwards by the connector and a hogging moment would develop at point B (Figure 6-4 (a) and (b)).

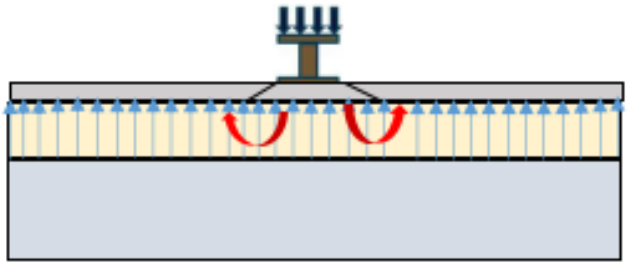

(a) Section along length of slab

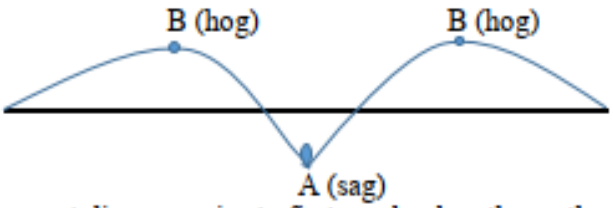


(b) Bending moment diagram prior to first crack when the wythes are connected

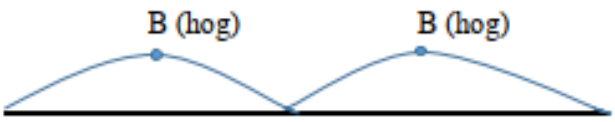


(c) Bending moment after first crack in upper layer when the wythes are connected

**Figure 6-4 Schematic showing moments acting on the upper layer**

When the first crack appeared at point A, a hinge was formed and the edges of the upper layer were free to rotate upwards about point A. In the panel with the connectors, the ends of the upper layer were held down hence a hogging moment occured at approximately the third points along the span at point B (Figure 6-4(c)). In the panels without connectors the upper layer was free to rotate upwards about point A and hence the outer ends of the panel displaced upwards. Once the HFRPC wythe failed ultimately, that is it could not provide any further contribution to moment resistance, the rate of upward displacement of the ends of the upper wythe increased and the insulation layer compressed considerably underneath the load. Once the insulation was fully compressed the full load was transferred directly to the lower wythe of concrete through the compressed insulation hence the lower wythe alone was providing the resistive load to maintain the rate of actuator head displacement at 1 mm per minute.

*6.3.3.1 Control – debonded panel with no connectors*

In the Control debonded panel a plastic layer was provided between the upper wythe and the insulation to omit any bond between the two layers. The aim of testing this panel was to enable the contribution of the bond between the upper wythe and the insulation to composite behaviour to be evaluated by comparing the structural response of this panel with the other test panels which were not debonded. Figure 6-5 shows the force-displacement plots for the upper and lower surfaces of the Control debonded panel with the key events highlighted.

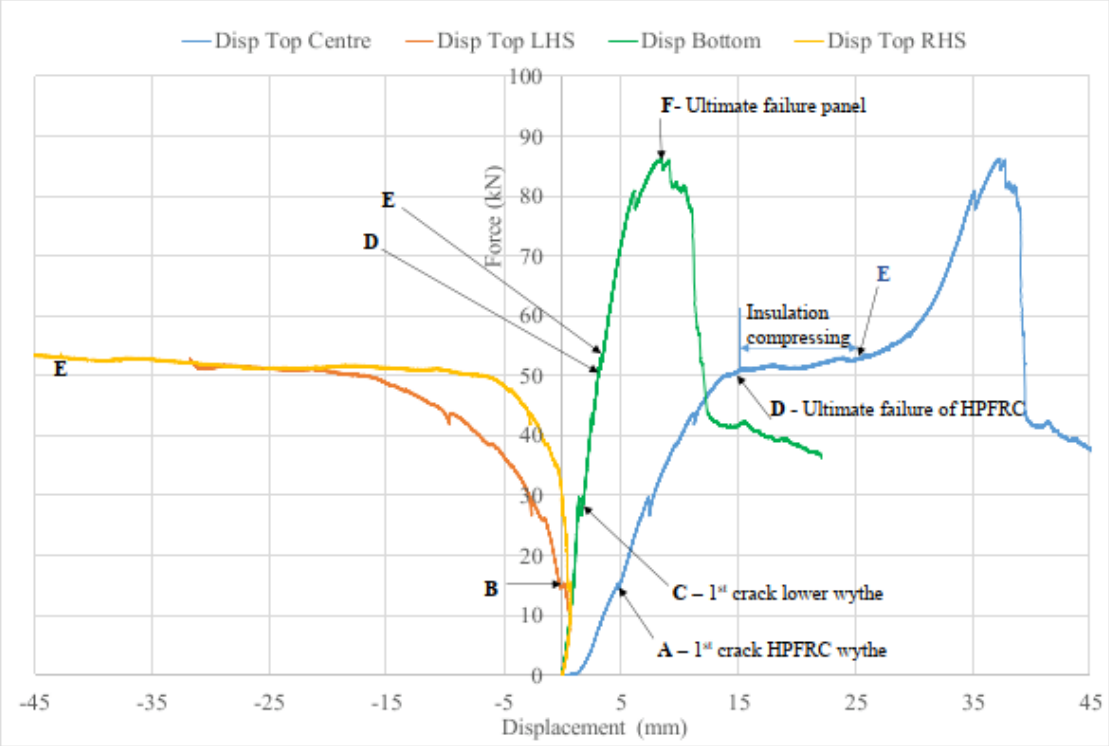


**Figure 6-5 Force-displacement plots for Control-debonded panel with key events highlighted.**

It can be noted from Figure 6-5 that the first crack occured in the upper HPFRC wythe (blue curve) when the resistive load reached 15.3 kN (Point A). The displacement of the centre of the HPFRC wythe at point A was 4.8 mm. This resistive load was greater than the minimum load that the panel must withstand prior to cracking to achieve sufficient elastic moment capacity, that is, 10.2 kN, as determined in Section 6.4.1. At this point the ends of the panel separated from the insulation layer and started to move upwards as can be observed at point B which shows that the direction of displacement of the ends of the HPFRC wythe (orange and yellow curves) changes towards negative displacement. The compression of the insulation is indicated by the divergence between the displacement of the top wythe (blue curve) and the displacement of the bottom wythe (green curve), the latter being a much stiffer response. As the insulation continued to compress and the stiffness of the upper wythe was reduced due to the crack, the lower wythe provided an increased proportion of the resistive load due to its greater stiffness. The first crack occured in the lower wythe at a resistive load of 29.5 kN (point C) with a corresponding deflection in the lower wythe of 1.69 mm.

The post cracking toughness behaviour of the upper wythe was demonstrated by its continued resistance to load up to an ultimate failure load of 50.9 kN with a corresponding deflection at point D of 15.2 mm. This post cracking toughness behaviour was in agreement with previous research carried out on a single panel made with the same concrete mix for HPFRC (O'Hegarty et al., 2020) and was attributed to the presence of fibre reinforcement in the concrete mix.

After ultimate failure of the upper HPFRC wythe (point D), the resistive force remained reasonably steady under increasing displacement, only increasing by circa 2 kN as the insulation continued to compress. The deflection of the bottom wythe remained at 3.11 mm during this period. This behaviour can be observed from Figure 6-6 which shows the displacement of the top and bottom wythe with time. At a force of 52.5 kN (point E) the insulation reached its compressibility limit and the resistive force was now wholly provided by the bottom wythe. The bottom wythe continued to provide increasing load resistance until ultimate failure occured at an applied load of 86 kN and a deflection of 8.47 mm (point F).

Up to and beyond point D, the ends of the upper wythe continued to deflect upwards indicating the presence of a moment at the mid-span of the upper wythe caused by the reaction force provided by the insulation. Due to the presence of the debonding layer and the omission of ties there was nothing to provide a resistance to the upward deflection of the ends of the upper wythe except its own self-weight. The upward deflection continued as the insulation

compressed until the insulation reached its compressibility limit (point E). At this point, the ends of the upper wythe had an upwards displacement of 55 mm so the LVDTs were removed to avoid any damage.

Figure 6-7 plots the displacement profile of the upper wythe every 2 mins during the test until the insulation reached its compressibility limit. The annotated points A, B, D, and E correspond to the same points annotated in Figure 6-5. The dashed lines indicate the displacement profile of the upper wythe after it has failed. Figure 6-8 shows a photograph of the circa 20 mm displacement of the upper wythe of the Control debonded panel at ultimate failure. The structural response of the upper wythe will be compared with the structural response of the upper wythe of the Control No Ties panel to assess the influence, if any, of the presence of a bond between the upper wythe and insulation.

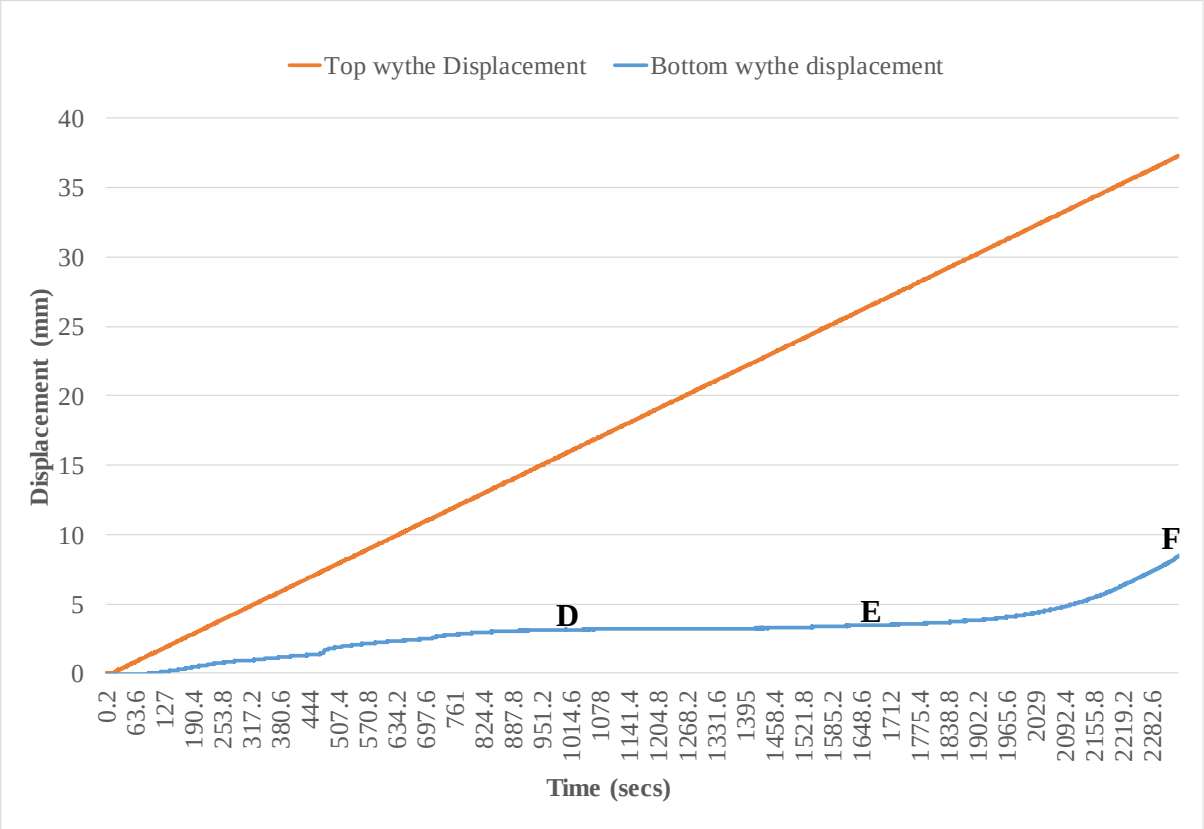


**Figure 6-6 Control de-bonded panel – displacement of top and bottom wythe versus time.**

Figure 6-9 shows a photograph of the displacement of the Control debonded panel at ultimate failure displaying cracks at mid-span of the lower wythe and extreme compression of the insulation. Figure 6-10 plots the displacement profile of the lower wythe every 2 mins during the test up until its ultimate failure. The annotated points C, D, E, and F correspond to the same points annotated in Figure 6-5.

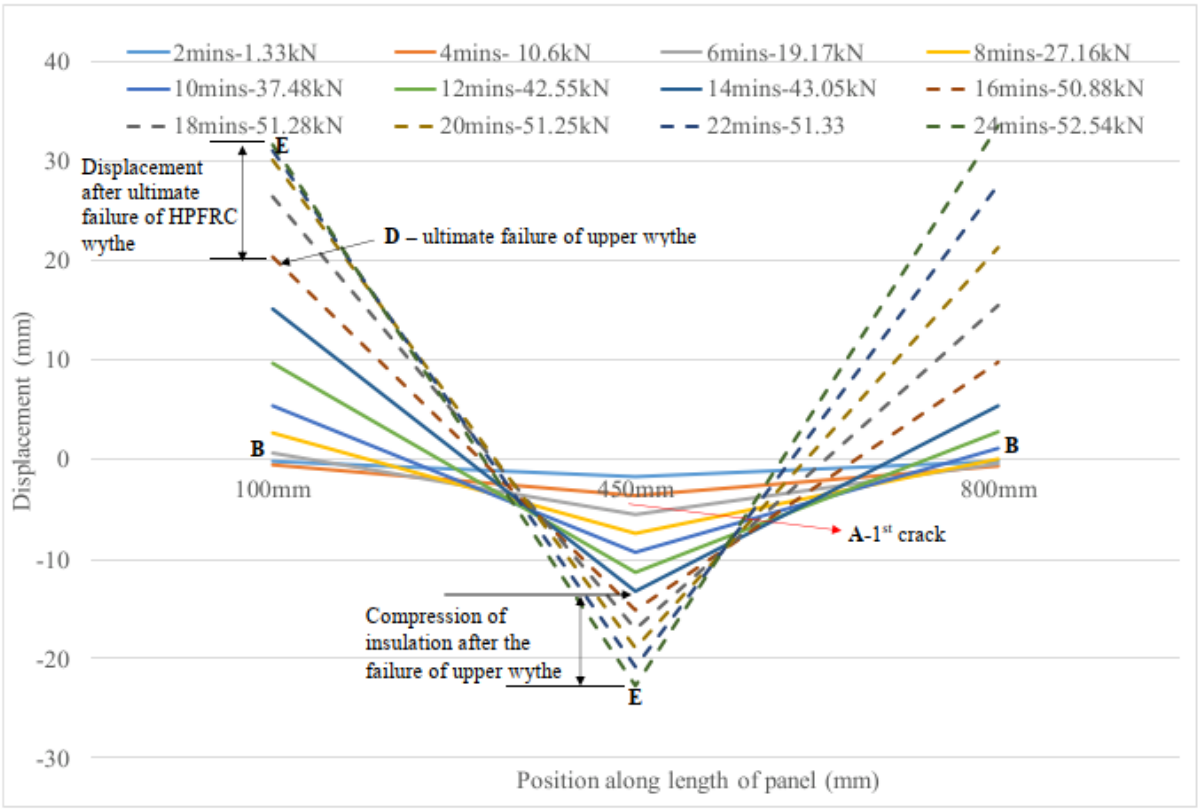


**Figure 6-7 Control-debonded panel - displacement of upper HPFRC wythe over time in the absence of ties between the wythes**

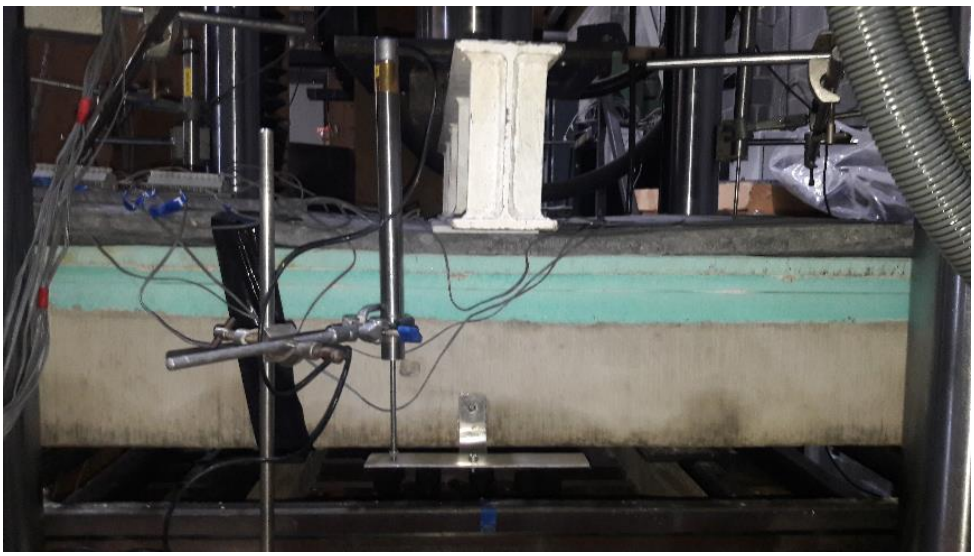

**Figure 6-8 Control-debonded panel at ultimate failure of upper wythe**

It is clear that the capacity of the thicker lower wythe determines the overall capacity of the panel. Ultimate failure of the panel occurred at a load of 86 kN, 5.6 times the load at which the first crack occurred in the outer wythe. This means that there was considerable structural capacity remaining in the panel after the first signs of distress were visible in the outer wythe

which is an important feature for the serviceability performance of structural elements. As the lower wythe was rigidly supported at either end the load must be transferred by the lower wythe to the supports which provide the reactions to maintain equilibrium hence the strength of the lower wythe controls the ultimate failure load of the panel.

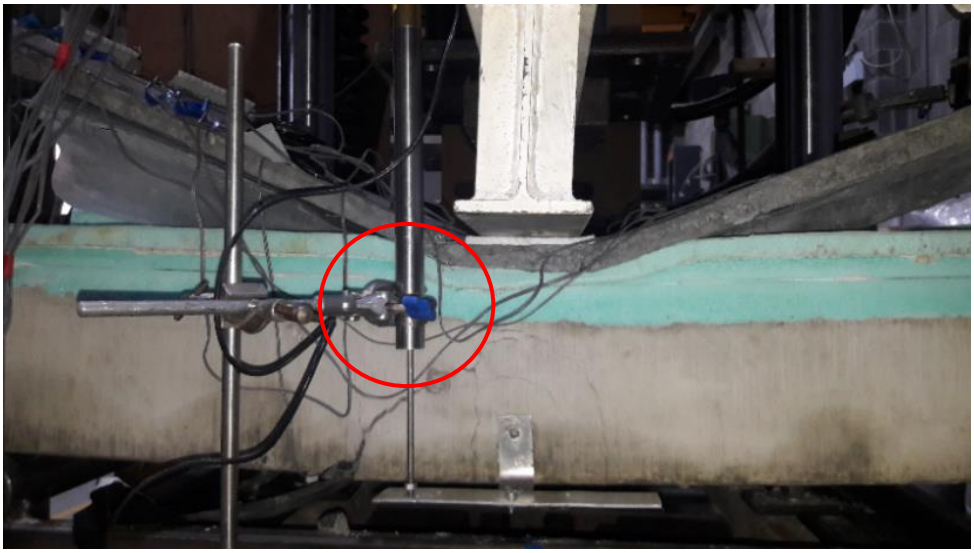

**Figure 6-9 Control-debonded panel at ultimate failure of lower wythe in the absence of ties**

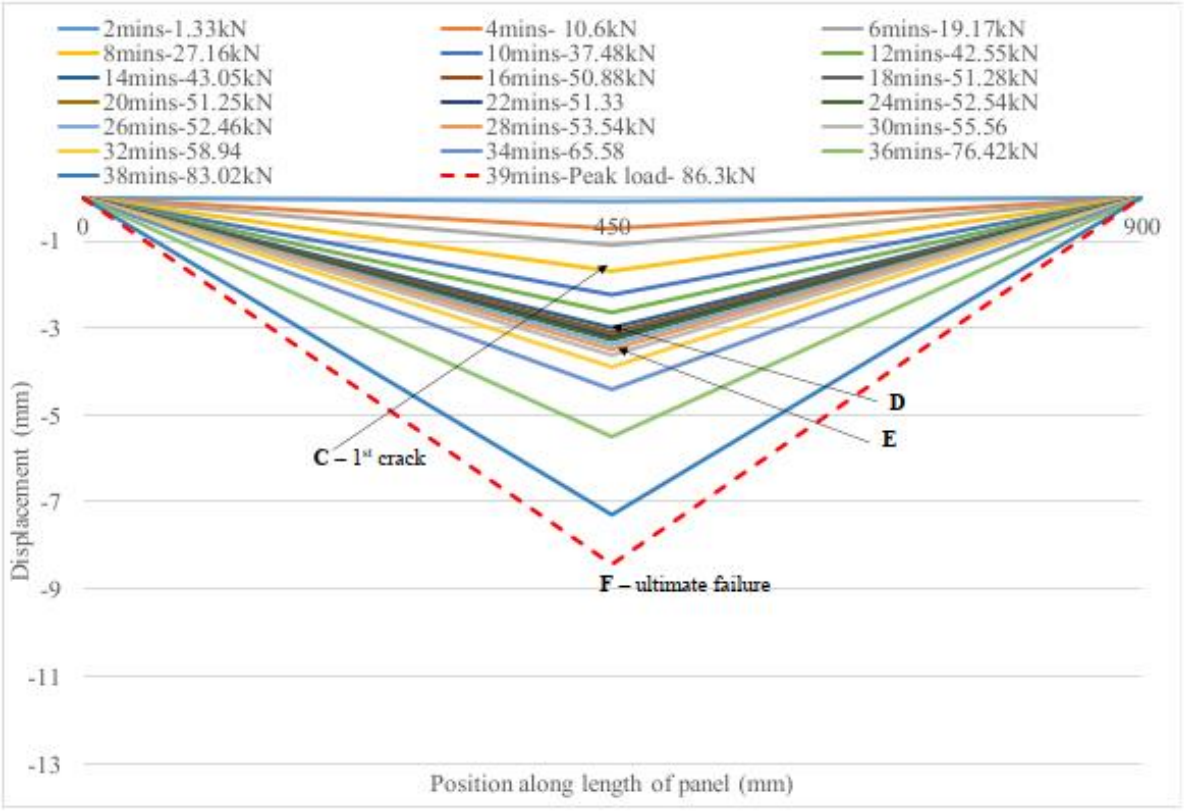


**Figure 6-10 Control-debonded panel - displacement of lower concrete wythe over time**

*6.3.3.2 Control No Ties panel*

The Control No Ties panel was identical to the Control debonded panel except that there was no debonding layer between the upper wythe and the insulation; during and after pouring the concrete the wythe was free to bond to the insulation. Figure 6-11 shows the force-displacement plots for the upper and lower surfaces of the Control No Ties panel with the key events highlighted. The overall behaviour of this panel was similar to the behaviour of the Control debonded panel however it is notable that the first crack in this panel occured in the upper wythe at a load of 28 kN, nearly double the load at first crack in the debonded panel. The deflection of the upper wythe at the first crack was similar at 5.4 mm (point A). As the only difference between the two panels is the bonding of the insulation from the upper wythe, this result indicates that a bond did form between the HPFRC and the XPS insulation which provided some lateral shear resistance between the HPFRC and the insulation which reduced the bending of the upper wythe initially and hence delayed the occurrence of the first crack. The ability of this panel to resist up to 28 kN prior to cracking confirms that the panel has nearly twice the elastic moment capacity required to resist typical wind loads as determined in Section 6.3.1**.**

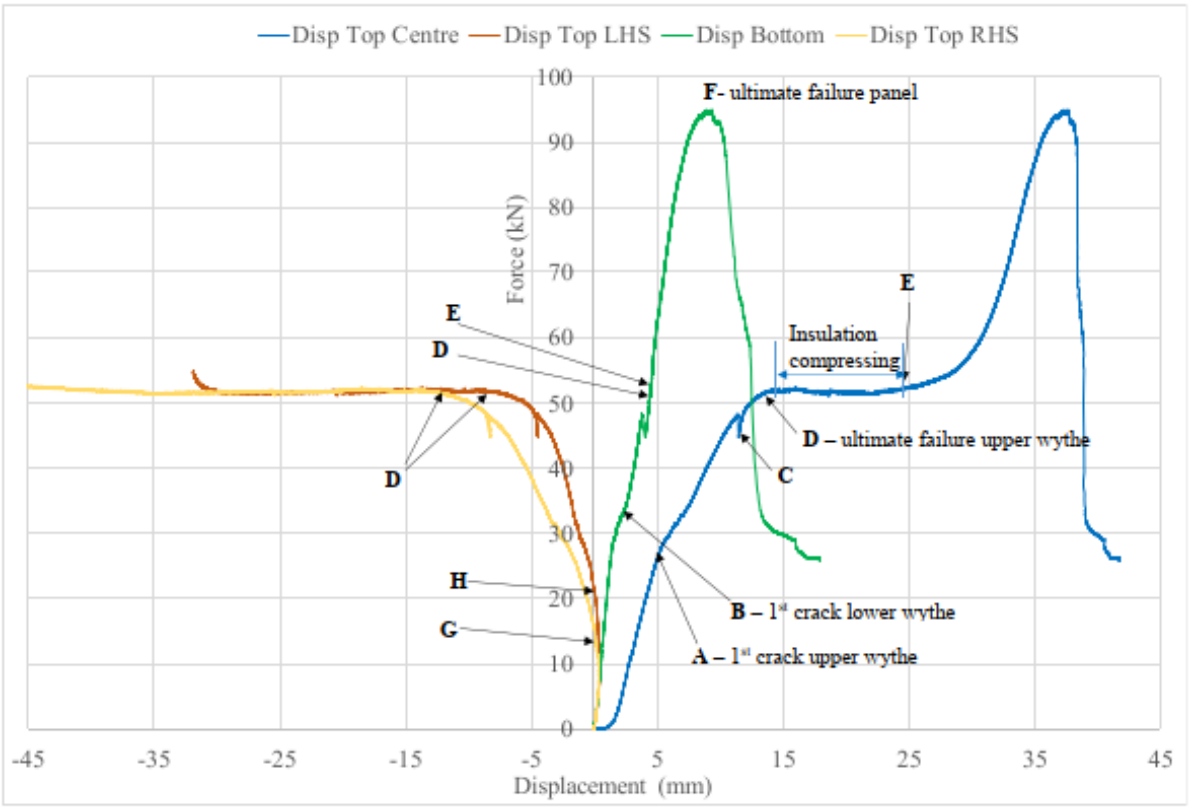


**Figure 6-11 Force-displacement plots for Control No Ties panel with key events highlighted**

With regard to the upward deflection at the ends of the upper wythe, the right and left hand side ends started to deflect upwards at resistive loads of 15.6 kN and 21.5 kN respectively (points G and H). The load at which the ends of the upper wythe of the Control debonded panel started to deflect upwards is similar at 15.3 kN however in the case of the Control No Ties panel the HPFRC upper wythe remained bonded to the top layer of insulation and in fact the two layers of insulation, which were bonded together using silicone, separated at the ends of the panel as the ends deflected upwards. The bond between the HPFRC and XPS insulation can be seen clearly in the photograph provided in Figure 6-12

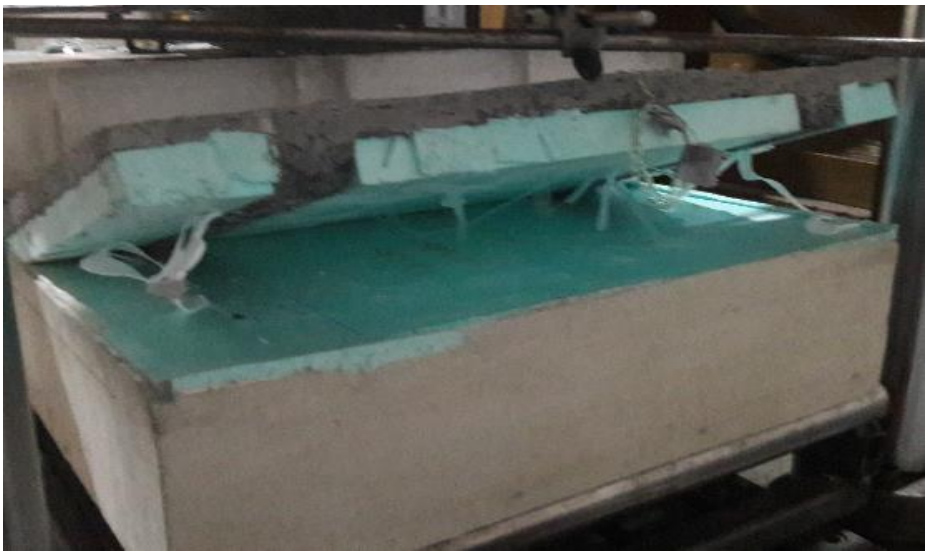

**Figure 6-12 Control No Ties panel at ultimate failure showing upward deflection at end of panel and bond loss between two layers of XPS**

After the first crack occured in the upper wythe its stiffness was reduced and the lower wythe provided a greater proportion of the resistive load. However the compression of the insulation and the post cracking toughness of the upper wythe, due to the presence of the fibres, was also providing some resistance. The rate of upward displacement at either end of the panel increaseed after the first crack and the final displacement profile of the upper wythe at the end of the displacement application can be seen in Figure 6-13 and Figure 6-14. In Figure 6-13 the dashed profiles indicate the displacement profile of the upper wythe after its ultimate failure. These dashed lines display the displacement behaviour of the upper wythe between points D and E as noted in Figure 6-11. As the upper wythe has failed it can no longer provide any additional resistive load to the applied displacement. The insulation layer has relatively low stiffness and hence compressed considerably as the displacement was applied without providing any further resistance.

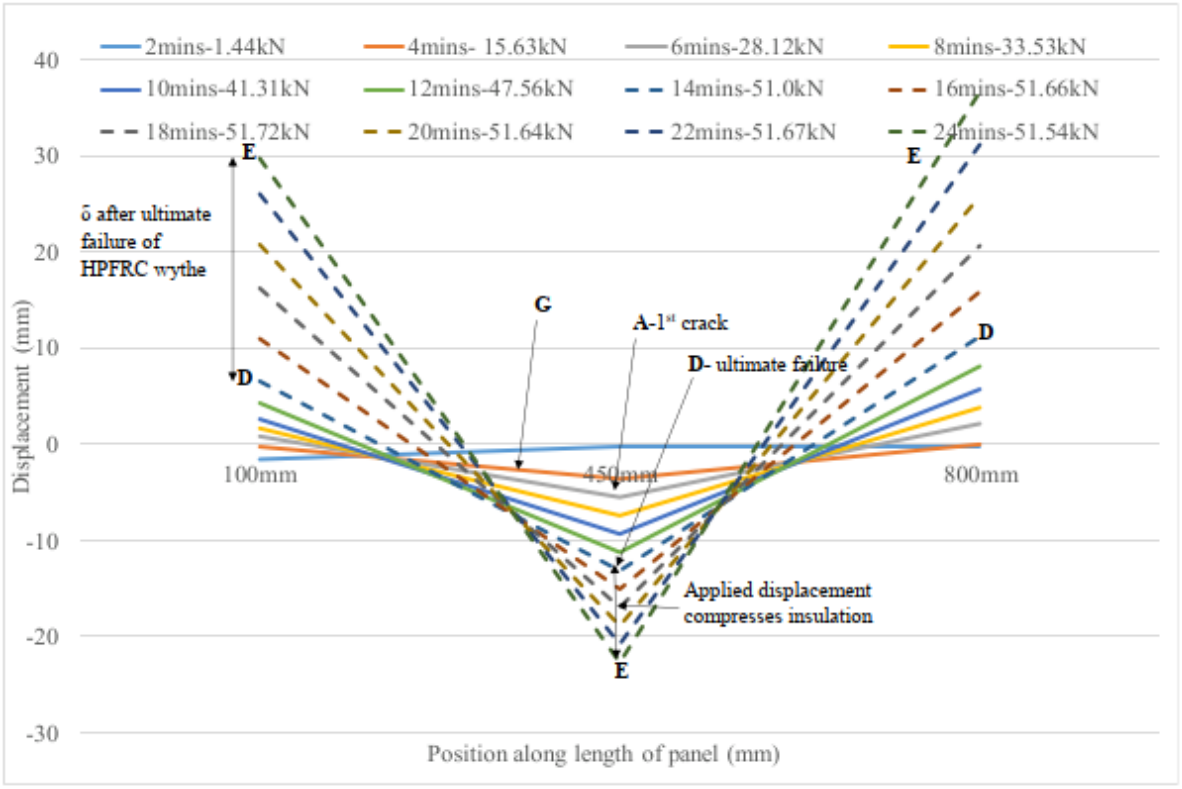


**Figure 6-13 Control No Ties panel - displacement of upper HPFRC wythe over time**

The force-displacement plot for the bottom wythe in Figure 6-11 (the green curve) shows a slight change of slope at circa 33 kN indicating an initial crack (point B). This is followed by the further cracking of the upper wythe (point C) with ultimate failure of the upper wythe occurring at a load of 51 kN and a coinciding mid-span deflection in the upper wythe of 14.1 mm (point D). After failure of the upper wythe at point D, the resistive load provided by the lower wythe remained steady between 51 kN-52 kN while the insulation compresseed (between points D and E). This can be seen clearly in Figure 6-15 which shows the plot of displacement of the top and bottom wythes against time. It can be noted that the displacement of the bottom wythe remained steady between points D and E as the insulation compresses. Figure 6-16 provides a visual of the displacement profile of the lower wythe every 2 mins during the test up to ultimate failure. The key events for the lower wythe denoted as B, D, E and F on Figure 6-11 are also denoted in Figure 6-16.

When the mid-span of the upper wythe had deflected 24.6 mm (point E), the insulation had nearly reached its compressibility limit from which point the resistive load was wholly provided by the lower wythe which continued to provide resistance until its ultimate failure at 94.9 kN and a deflection of 9.4 mm (point F).

**Figure 6-14 Control No Ties panel at ultimate failure showing deflection at end of panel and failure of the lower panel**

In summary the Control No Ties panel ultimately failed when the lower wythe provided a resistive load of 3.3 times the load which caused the first crack in the upper wythe, again displaying good serviceability performance. The bond between the upper HPFRC wythe and the insulation resulted in an increase of 12.7 kN in the load at which the first crack occurs in the upper wythe, when compared with the Control debonded panel. Hence the bond between the upper wythe and the XPS insulation results in a measurable and substantial increase in the elastic moment capacity of the panel.

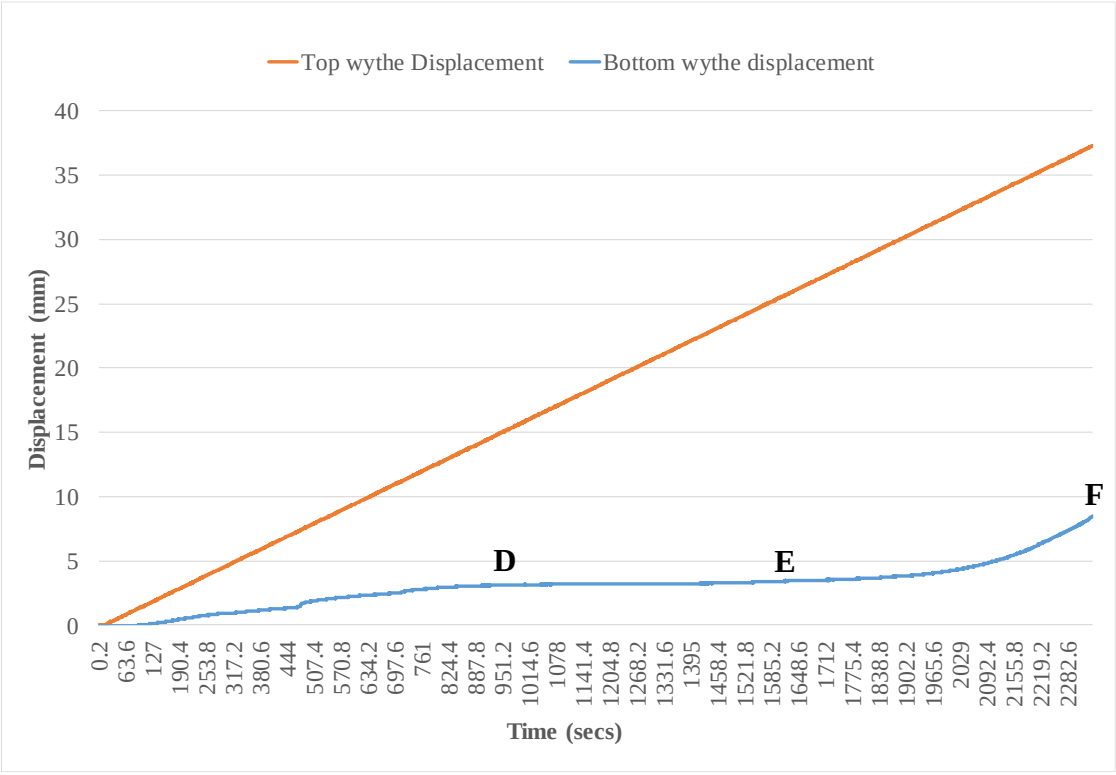


**Figure 6-15 Displacement of top and bottom wythe versus time**

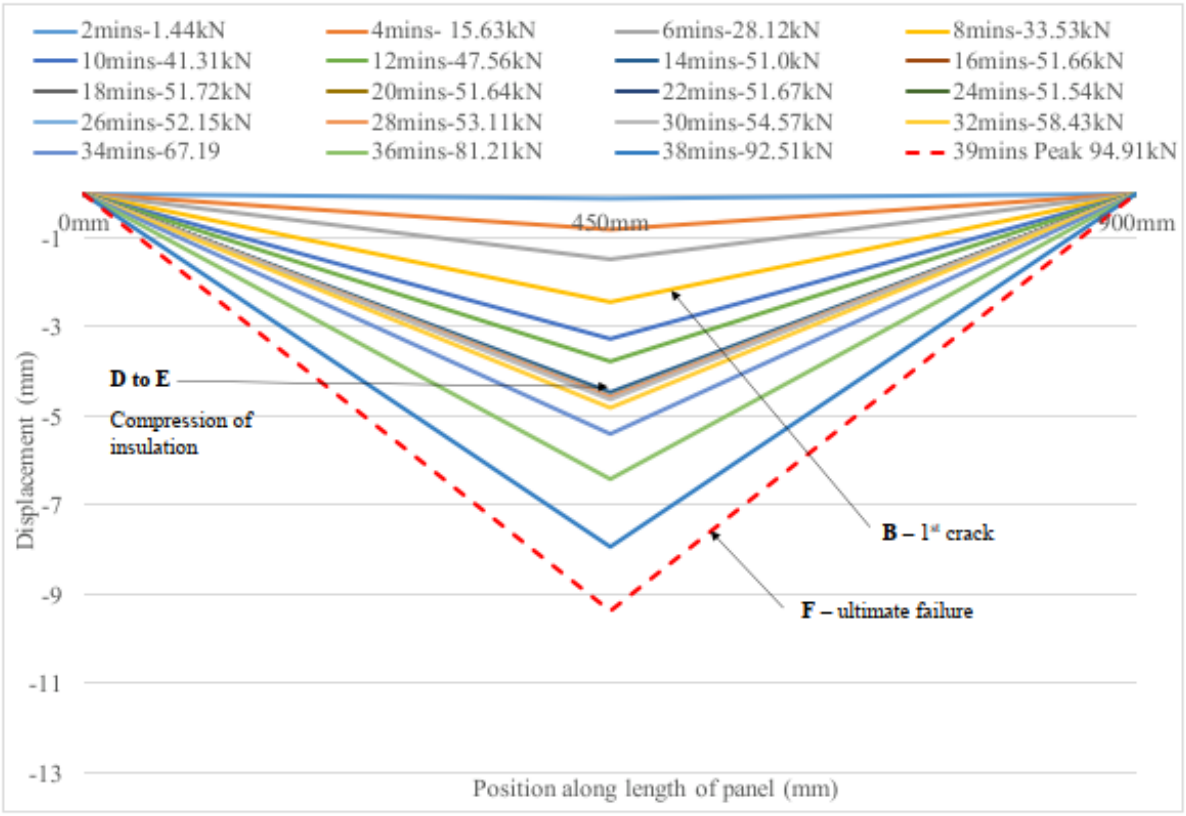


**Figure 6-16 Control No Ties panel - displacement of lower concrete wythe over time**

*6.3.3.3 PCM No Ties panel*

The PCM No Ties panel was identical to the Control No Ties panel except that the lower wythe was constructed using the PCM-concrete composite. As noted in Table 5-2, the compressive strength of the lower wythe concrete in the Control No Ties panel was exceptionally high at 81.4 MPa on the day of testing, whereas the compressive strength of the PCM-concrete composite was 29.4 MPa on the day of testing. As it is the structural capacity of the lower wythe of the panel that controls the ultimate failure of the panel, this difference in material strength is expected to impact the ultimate failure load. The data from this test is limited due to a technical failure in the data recording equipment which occurred shortly after the failure of the HPFRC wythe. However sufficient data was collected to ascertain the elastic behaviour of the panel.

Figure 6-17 shows the force-displacement plots for the upper and lower surfaces of the PCM-No ties panel with the key events highlighted.

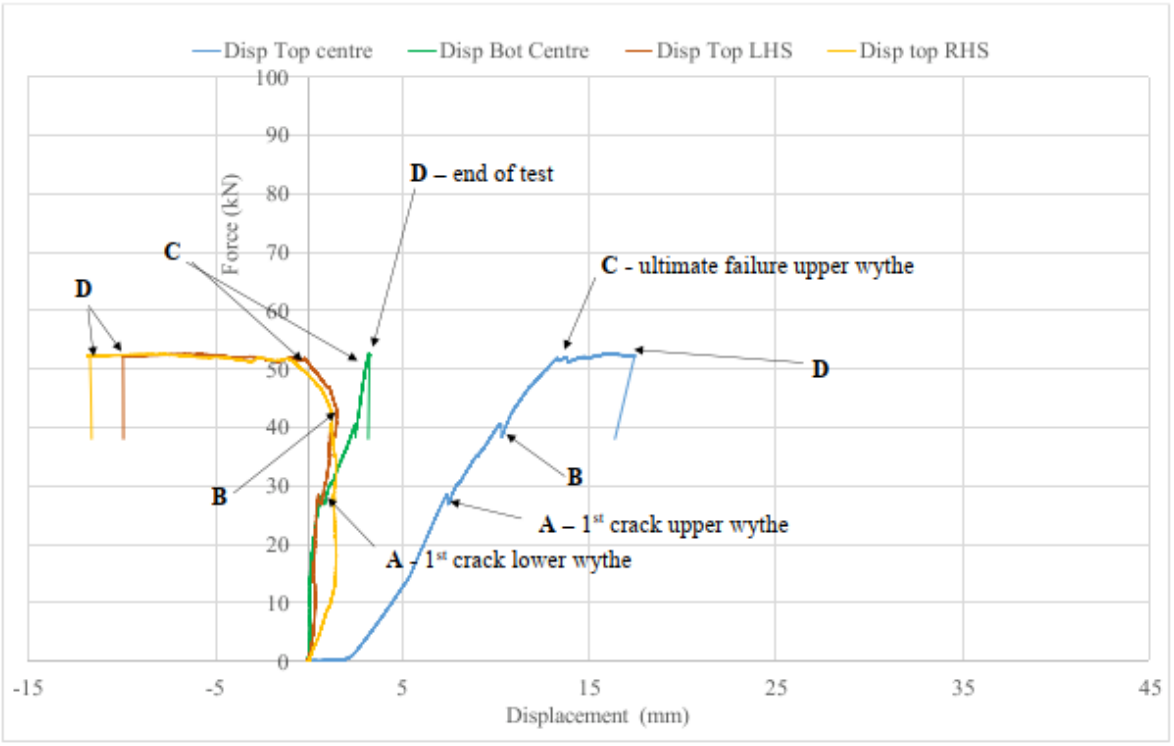


**Figure 6-17 Force displacement plots for PCM-No ties panel with key events highlighted.**

The first crack occured in the upper HPFRC wythe at a resistive load of 28.4 kN (point A) and a downward displacement of 7.4 mm which was very similar to the first crack load of the HPFRC wythe of the Control No Ties panel. This was expected as the conditions of the top two wythes of each panel were the same and the bottom two panels were comparatively stiff, though not equally so. The lower wythe also displayed a crack at this resistive load and a mid-span deflection of 0.74 mm. Comparing the force-displacement plots for the bottom wythes of the Control No Ties panel (Figure 6-11) and the PCM-No ties panel (Figure 6-17) it can be observed that the lower wythe of the Control No Ties panel appeared to provide more of the resistive load prior to the first crack than the PCM-concrete lower wythe indicated by the steeper plot for the central displacement of the bottom wythe of the PCM No Ties panel. Also the upper wythe of the PCM No Ties panel deflected more relative to the lower wythe indicating that it was resisting a greater proportion of the load. This can be explained by the fact that the PCM-concrete is a less stiff material than the Control concrete and hence will attract less load in a load sharing scenario. As noted in Appendix H the Young's moduli for the Control concrete and PCM-concrete composite are 35.2 GPa and 31.4 GPa respectively.

The ends of the upper wythe did not start deflecting upwards until a second crack occured in the upper wythe at a resistive load of 40.6 kN (point B) and the ends continued to deflect upwards as the insulation compresseed at the mid-span of the panel (Figure 6-18). The upper

wythe continued to provide some load resistance until it reached its ultimate capacity at an applied load of 51.9 kN (point C) at which point it had deflected 13.3 mm which was very similar to the failure loads and deflections of the upper wythes in the two Control panels showing consistency in behaviour of the HPFRC.

The test continued for a further 4 minutes during which the insulation wythe compressed and the resistive load only increased from 51.9 kN to 52.2 kN (point C to D). The deflection of the lower wythe increased from 3.16 mm to 3.28 mm demonstrating that the increase in the resistive load provided by the lower wythe was minimal despite the increment at the head of the actuator and the applied displacement was taken up by the compression of the insulation layer (Figure 6-19). A fault occurred in the data collection system at this point hence there is no data to confirm the ultimate load of the lower wythe and hence the panel. However the ultimate capacity of the PCM-concrete wythe can be estimated from the tests on the PCM-C Grid connector panel and the PCM-Thermomass panel as discussed presently.

The elastic behaviour of the panel indicates that the PCM No ties panel has sufficient elastic bending moment capacity to resist typical wind loads as it resisted up to 28.4 kN before the first crack occurred which is greater than the equivalent point load of a typical applied wind load which was determined in Section 6.4.1 as 10.2 kN.

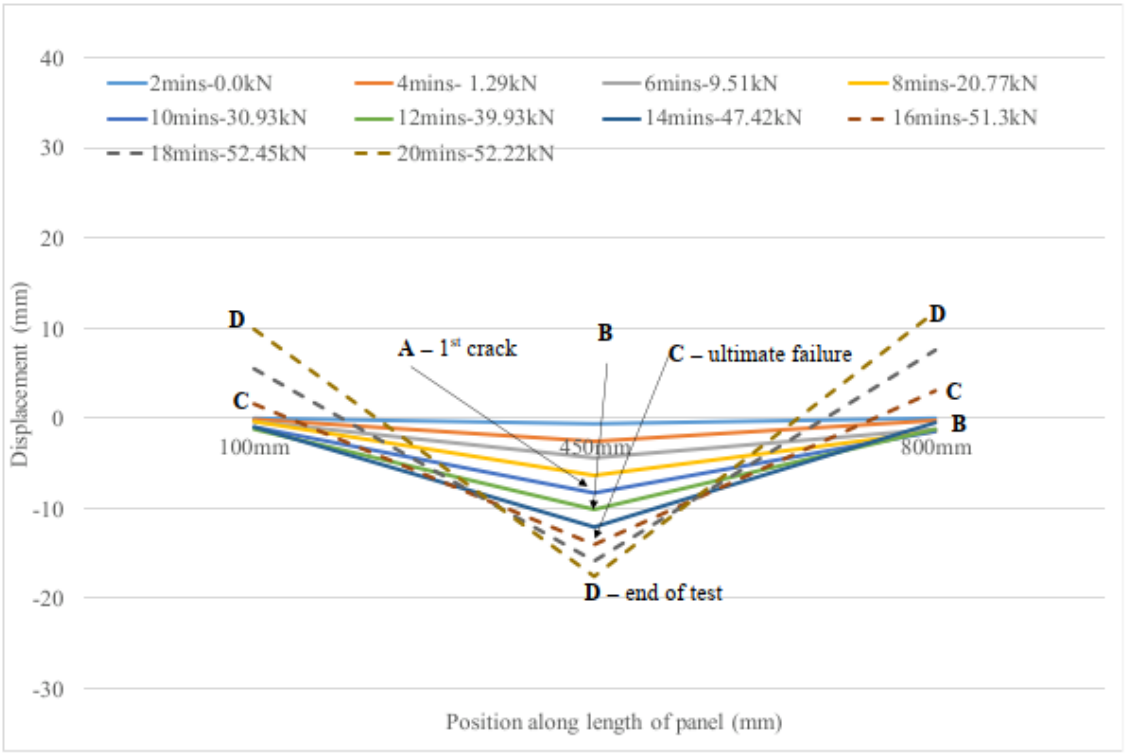


**Figure 6-18 PCM No ties panel - displacement of upper HPFRC wythe over time**

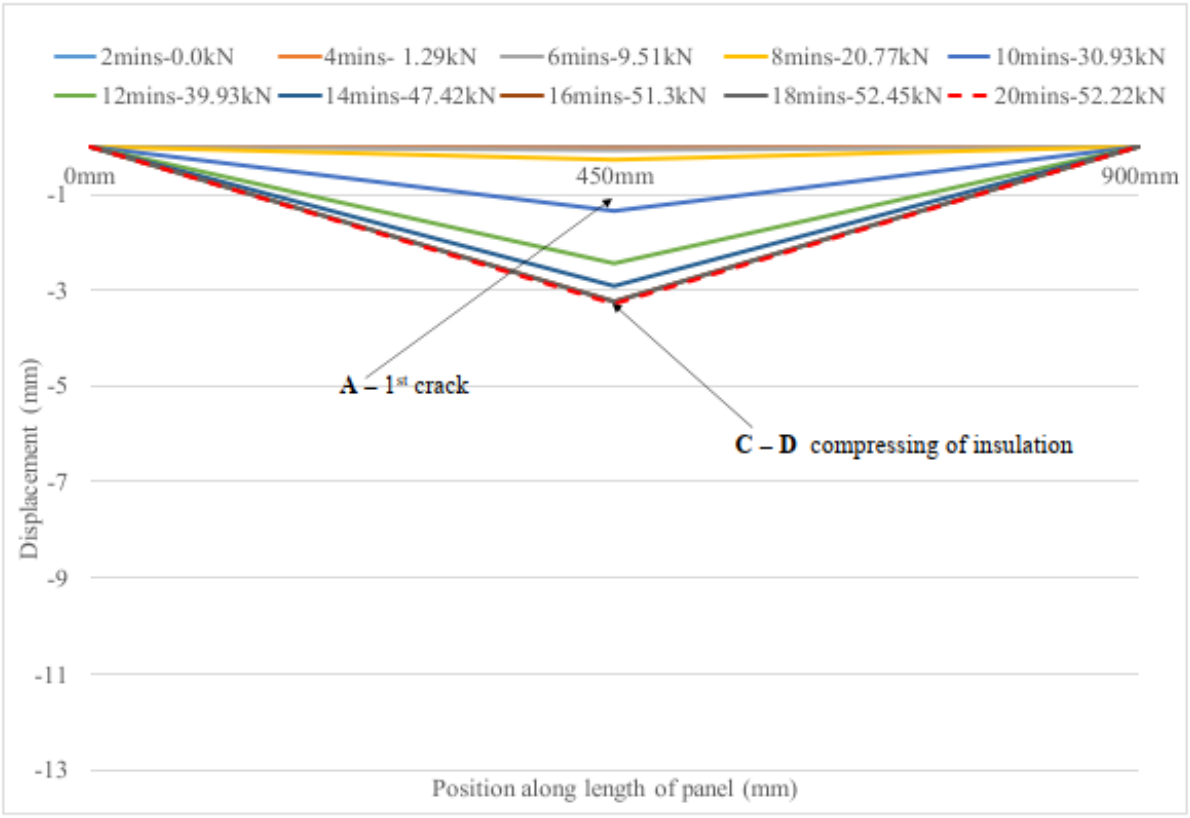


**Figure 6-19 PCM-No ties panel - displacement of lower concrete wythe over time**

*6.3.3.4 PCM C-Grid connector panel*

The PCM C-Grid panel was identical to the PCM No Ties panel except that the two wythes were connected together using two linear strips of C-Grid as a shear tie, as described in Section 5.3.

Figure 6-20 shows the force-displacement plots for the upper and lower wythes of the PCM C-Grid connector panel with the key events highlighted. A clear difference that can be noted from the horizontal displacement axis of Figure 6-20 is that the ends of the upper wythe did not deflect upwards at all during the testing which demonstrates that the 30 mm embedment of the C-Grid into the HPFRC wythe was sufficient to prevent a pull-out failure which would arise because the upper wythe tends to deflect upwards as a result of the uplift force caused by the reaction force arising in the insulation when the load is applied to the panel, as discussed in Section 6.4.3. It can also be observed from Figure 6-21, point B, that prior to the first crack occurring, the ends of the upper wythe deflected downwards by 3.5 mm indicating that the insulation is stiff enough to facilitate distribution of the applied displacement to the ends of the upper wythe. Once the ends of the upper wythe displaced downwards by 3 - 3.5 mm, there was no further downward displacement. The insulation in the vicinity of the loading beam compressed more than the insulation at the ends of the panel indicating that the insulation under

the loading beam was providing a higher proportion of the resistive load than the insulation at the ends.

It can be observed from Figure 6-20 that initially the displacement behaviour of the upper wythe (blue curve) was similar to the displacement behaviour of the upper wythes in the unconnected panels indicating that the C-Grid was not contributing any additional stiffness in resisting the compression applied by the loading beam as it displaces downwards. This was expected as the C-Grid is very thin and does not provide any out of plane stiffness under compression as discussed in Section 2.9.2. The mid-span deflection of the upper wythe progressed at a similar rate as in the panels without ties. However, unlike the previous three cases, in this panel the first crack occured in the lower wythe at an applied load of 21.4 kN and a mid-span deflection of 0.77 mm (point A). After this first crack occured in the lower wythe, its stiffness was reduced and hence its rate of deflection increased (point B, Figure 6-20). The contribution of the upper wythe to the resistive force remained similar, indicated by no change in the slope of the blue curve.

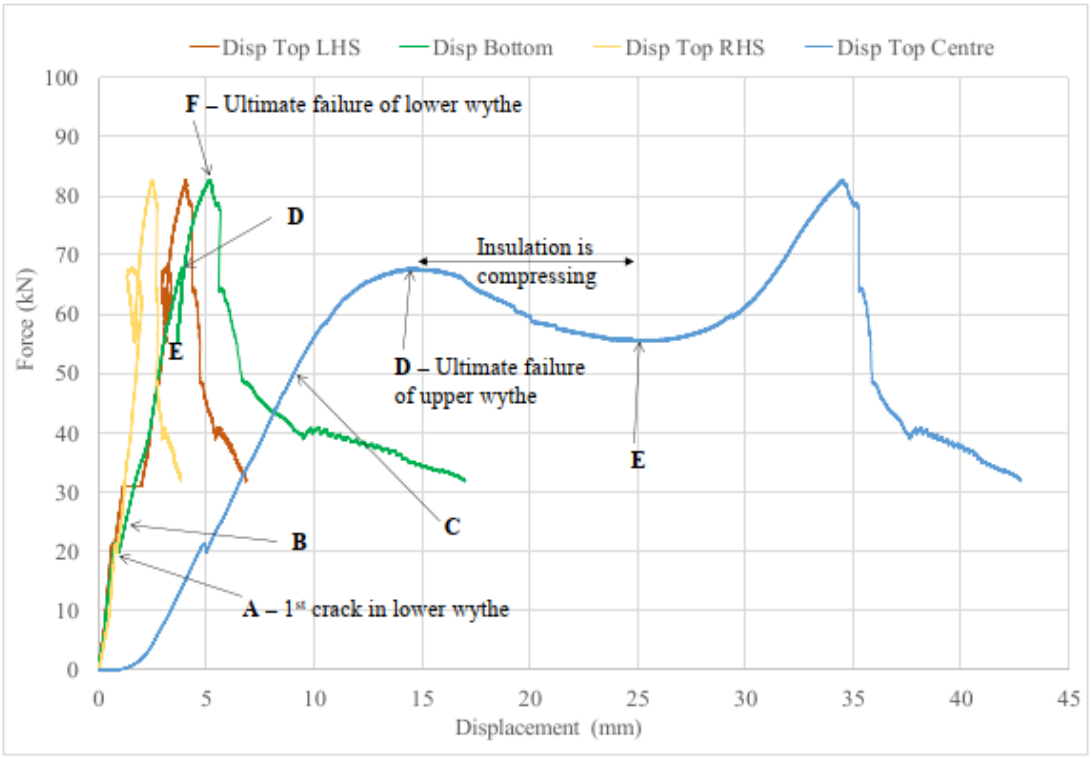


**Figure 6-20 Force displacement plots for PCM C-Grid connector panel with key events highlighted.**

As the displacement of the panel continued to increase it was interesting to note that the upper wythe did not fail at circa 50 kN as occurred in the unconnected panels. In the PCM-C-Grid panel the upper wythe only deflected circa 8.5 mm at a load of 50kN (point C) however in the

unconnected panels the upper wythes deflected 13-15 mm under a 50 kN load. This indicates that in fact the presence of the C-Grid is enhancing the stiffness of the upper wythe by preventing the uplift of the edges, minimising the curvature of the upper wythe. Given that the C-Grid has very little out of plane buckling stiffness it is suggested that the C-Grid is also contributing to the flexural stiffness of the upper layer by resisting the lateral shear effects between the HPFRC wythe and the insulation and hence limiting the ability of the upper layer to deflect downwards at mid-span and facilitating some degree of composite action.

The HPFRC wythe reached ultimate failure at a resistive load of 68 kN and a deflection of 14.6 mm (point D). This failure load is about 32% higher than those recorded during testing of the unconnected panels. This result suggests that the C-Grid provides some degree of composite action which is explored in more detail in Section 6.3.4. As happened in the unconnected panels, once the upper HPFRC wythe failed the applied displacement compressed the insulation while the resistive load, which was now provided by the lower wythe, reduced to 55.3 kN and then started to increase again over a period of 18 minutes (points D to E to F). The deflection of the bottom wythe remained stable during this period at 3.9 mm (points D to E, Figures 6-21, 6-22 and 6-23). When the insulation was fully compressed the resistive load started to increase again, provided by the PCM-concrete lower wythe which reached ultimate failure at a load of 82.7 kN and a deflection of 5.13 mm (point F).

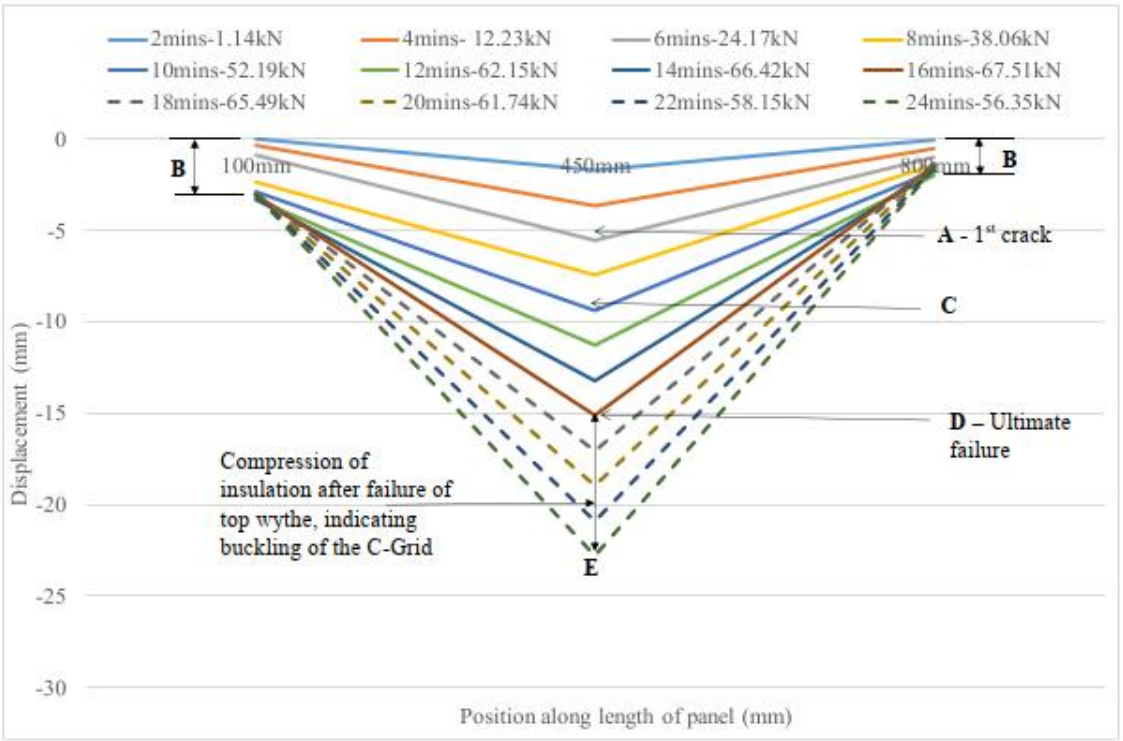


**Figure 6-21 PCM-C-Grid panel - displacement of upper HPFRC wythe over time**

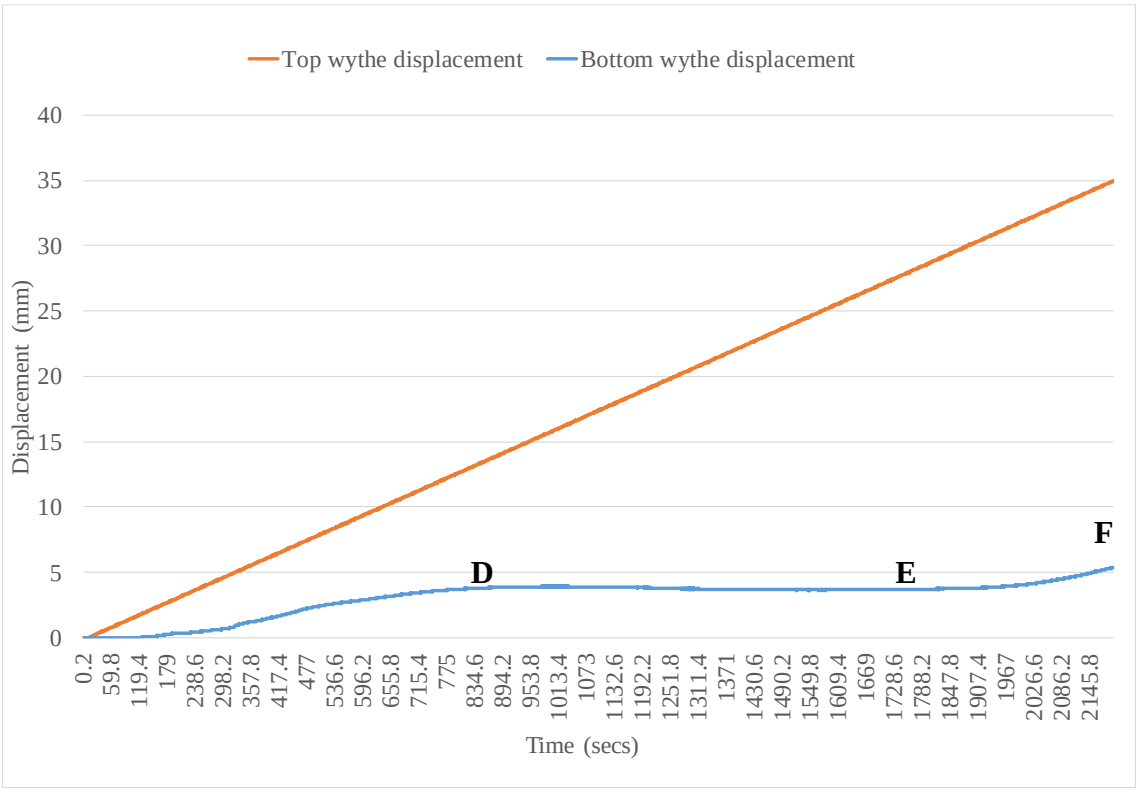


**Figure 6-22 Displacement of top and bottom wythe versus time**

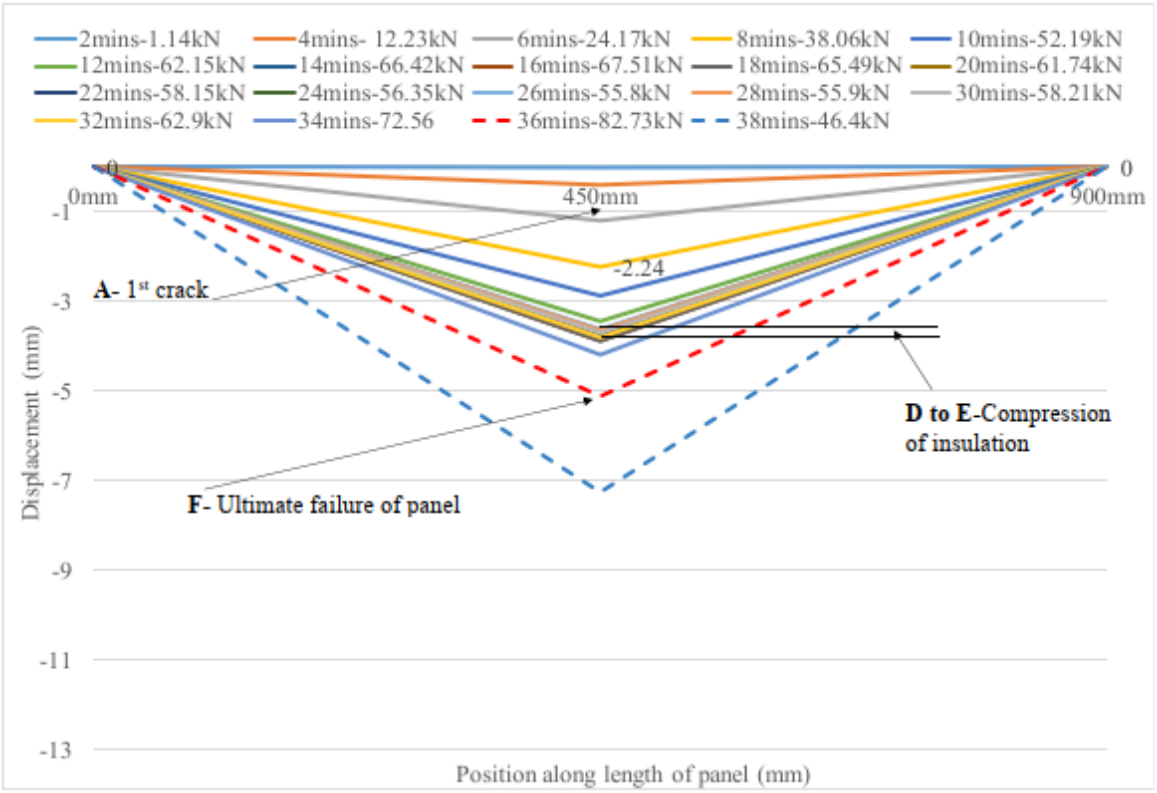


**Figure 6-23 PCM-C-Grid panel - displacement of lower PCM-concrete wythe over time**

The compression of the insulation indicated that the C-Grid had buckled in the vicinity of the loading beam which can be observed in Figure 6-24. The first crack in the upper wythe appeared at point X in Figure 6-24. As the C-Grid was preventing the ends of the upper wythe from lifting a hogging moment occurred at point Y caused by the upper wythe tending to rotate anti-clockwise about point X due to the upward reaction from the insulation. Ultimate failure of the upper wythe occured when a crack formed at point Y creating a mechanism in the upper wythe.

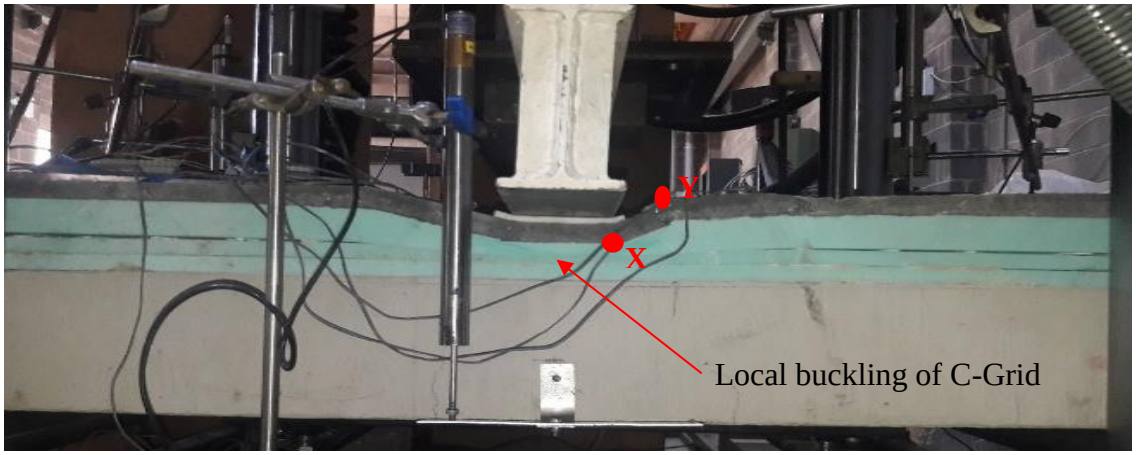


**Figure 6-24 Photograph of PCM + C-Grid connector panel – Displacement of HPFRC layer and crushing of insulation**

In summary, the load at which the PCM C-Grid panel displayed a first crack was 21 kN which is twice the minimum of 10.2 kN to provide sufficient elastic capacity to resist typical wind loads. The presence of the C-Grid tying the two wythes together prevented the uplift at the ends of the upper wythe as the displacement was applied. This resistance to displacement resulted in a hogging moment arising in the top of the upper wythe adjacent to the loading beam after the occurrence of the 1$^{st}$ crack and increased the load resistance capacity of the upper wythe which displayed an ultimate failure load 32% greater than the upper wythes of the untied panels. The ultimate failure of the panel occurred when the lower PCM-concrete wythe failed at a resistive load of 82.7 kN. This failure load is over four times the 1$^{st}$ crack load, highlighting the safe serviceability performance of the panel.

*6.3.3.5 PCM Thermomass connector panel*

The PCM Thermomass panel was identical to the PCM No Ties panel except that the two wythes were connected together using two line strips of Thermomass pin connectors located at 200 mm centres as described in Section 5.3. Figure 6-25 shows the force displacement plots for the PCM Thermomass connector panel (PCM-TM).

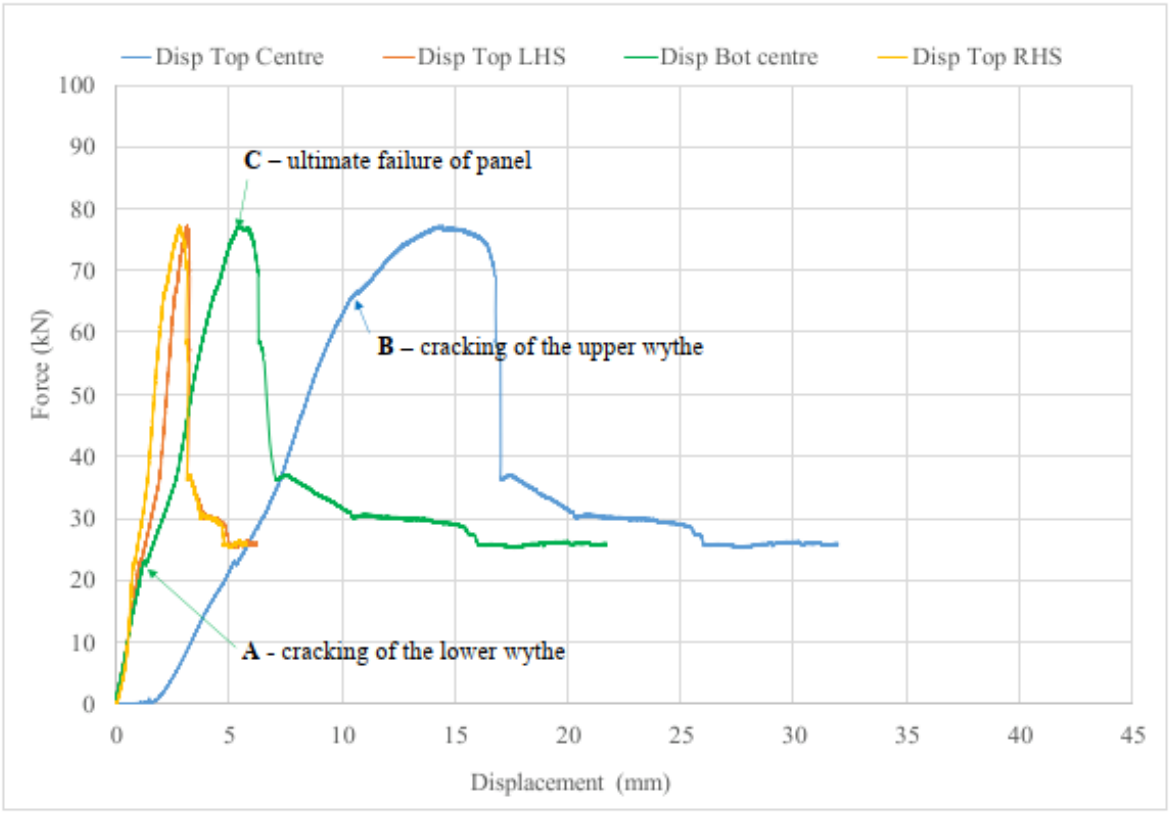


**Figure 6-25 Force displacement plots for PCM-Thermomass panel with key events highlighted.**

In contrast to the other test panels, in this panel test there was no period during which the applied displacement was absorbed solely by compression of the insulation and the resistive load provided by the lower wythe remained steady. This is due to the fact that the Thermomass connectors (TMs) have an axial stiffness that is much greater than that of the insulation (and the C-Grid) hence the TMs shared most of the applied displacement directly with the stiffer lower wythe from the start of the test, that is, the load was shared between the wythes in accordance with their relative stiffness. In this panel the first crack occurred in the lower wythe at a load of 22.4 kN (point A) which is denoted by the change of slope of the green curve in Figure 6-25. Although the upper wythe started to show signs of loss of stiffness at a load of 66.4 kN (point B) ultimate failure of the panel occurred when the lower PCM-concrete wythe failed at a load of 77 kN and a mid-span deflection of 5.85 mm (point C). At this point the upper wythe had deflected 14.9 mm (Figure 6-26) which is less than half the deflection of the upper wythes in the other panels at ultimate failure of the bottom wythe. The reason for this is that because of the axial stiffness of the TMs, the applied displacement was mostly transferred to the stiffer lower wythe and hence the less stiff upper wythe provided a lower proportion of the resistive load and thus its displacement was lower. It can also be observed from Figure 6-26 that again the ends of the upper wythe did not deflect upwards at all during the tests

confirming that the Thermomass connectors are capable of resisting the uplift forces and the embedment of 30 mm into the HPFRC provides sufficient bond strength to prevent this. The deflection of the lower wythe can be observed in Figure 6-27.

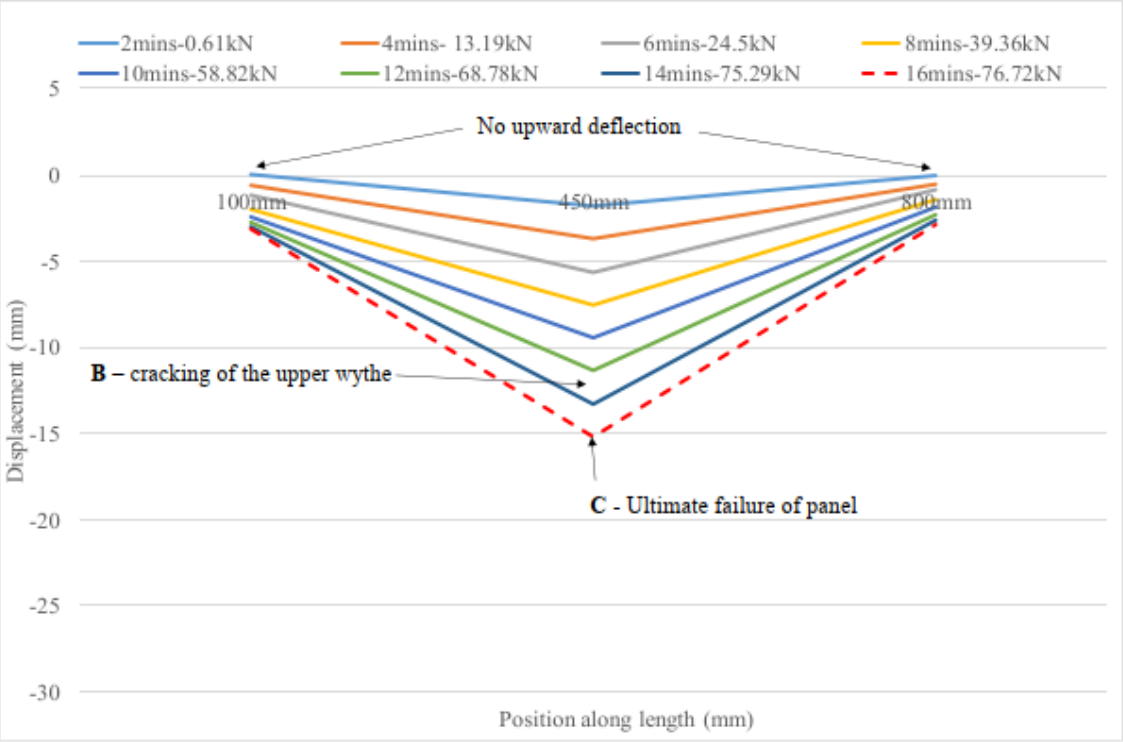


**Figure 6-26 PCM Thermomass panel - displacement of upper HPFRC wythe over time**

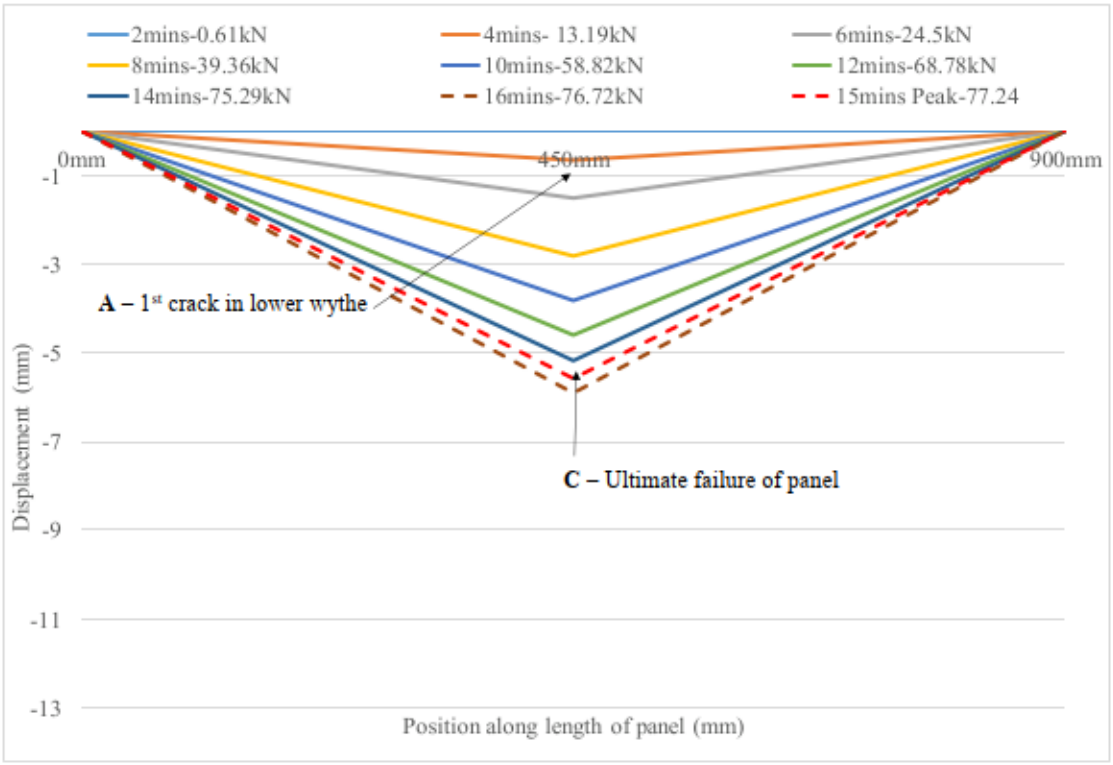


**Figure 6-27 PCM-Thermomass panel - displacement of lower concrete wythe over time**

The difference in mid-span displacement between the two wythes indicates that the insulation wythe only compressed by 9 mm compared to a difference at ultimate load of circa 28 mm-30 mm for the other panels. The small compression of the insulation can be seen in Figure 6-28 which shows the panel at ultimate failure with substantial cracking in the lower wythe. As the insulation did not compress as much under the applied displacement, more displacement was applied to the wythes and hence the two wythes must provide a higher resistive load.

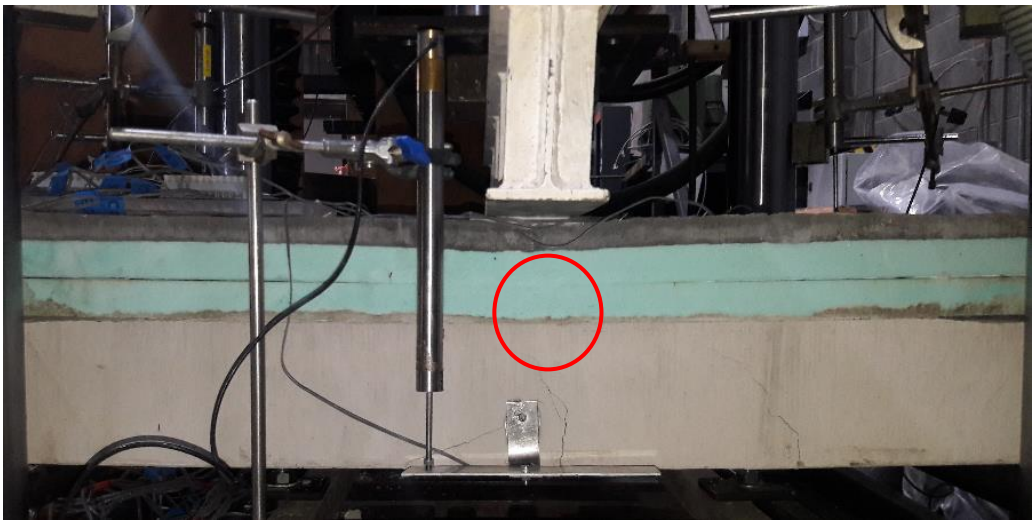

**Figure 6-28 Photograph of PCM Thermomass panel at ultimate failure**

As with the other panels, the PCM TM panel displayed sufficient elastic capacity to resist typical wind loads with a 1st crack load twice the minimum required. The ultimate resistive load of the panel, although slightly lower than the other test panels at 77 kN, was 3.5 times the 1st crack load showing that the panel provides sufficient serviceability performance. As noted in Table 5-2, the compressive strength of the PCM-concrete mix used to make the PCM TM panel was 31.0 MPa on the day of the test, lower than the compressive strength of the PCM C-Grid panel which was 35.9 MPa. As the strength of the lower wythe controls the strength of the panel this difference between the compressive strengths of the two panels may partly explain the lower ultimate resistive load of the PCM TM panel.

*6.3.3.6 Summary of structural capacity results of panel tests*

Table 6-2 provides a summary of the loads at 1st crack, the ultimate loads and the corresponding deflections for all the test panels. It can be noted that the resistive load at which the first crack occured is lowest in the debonded panel. As discussed in Section 6.3.3.1 this lower resistive force can be attributed to the lack of bond between the upper HPFRC wythe and the XPS insulation. In the presence of a bond, some lateral shear resistance between the two layers was provided which assists in resisting deflection of the upper wythe.

It is also notable from Table 6-2 that in both panels in which the wythes were connected together the first crack occured at a lower load than in the panels with no ties. As discussed in Sections 6.3.3.4 and 6.3.3.5 the first crack in the tied panels occured in the PCM-concrete lower wythe. The reason for this can be attributed to both the lower strength of the PCM-concrete mix and also to the higher proportion of load resisting capacity provided by the lower wythe earlier in the test due to the presence of the ties. The ultimate failure load of the PCM TM panel, of 77 kN, was slightly lower than that of the PCM C-Grid panel, of 82.7 kN, which as noted in Section 6.3.3.5, can be attributed to the lower strength of the PCM-concrete mix used in the lower wythe of the PCM TM.

**Table 6-2 Summary of load capacities and associated deflections of the panels.**

| Type of panel | Load at 1st crack (kN) | Deflection at 1st crack (mm) | | Ultimate load (kN) | Deflection at ultimate failure (mm) | |
|---|---|---|---|---|---|---|
| | | Upper wythe | Lower wythe | | Upper wythe | Lower wythe |
| Control debonded | 15.3 | 4.79 | 0.96 | 86.0 | 37.30 | 8.47 |
| Control panel No Ties | 28.0 | 5.42 | 1.47 | 94.9 | 37.73 | 9.37 |
| PCM-Concrete No Ties | 28.4 | 7.42 | 0.74 | - | - | - |
| PCM + C-Grid | 21.4 | 4.89 | 0.77 | 82.7 | 34.51 | 5.13 |
| PCM + TM | 22.4 | 5.28 | 1.29 | 77.0 | 14.88 | 5.85 |

Figures 6-29 and Figure 6-30 show force-displacement plots for the top wythe of each panel and the bottom wythe of each panel respectively, for comparison purposes. In Figure 6.29 it can be noted that the deflection behaviour of the upper wythe was similar in all the panels that do not have any connectors between the two wythes. The shaded area indicates the period after failure of the top HPFRC wythe during which the low stiffness insulation layer was compressing while the resistance force of the panel remained reasonably steady. When the insulation is fully compressed, the stiffer bottom wythe provided most of the resistance to the applied load with some further limited compression of the insulation occurring indicated by the difference in the relative deflection between the top and bottom wythe. It can also be observed in Figure 6-29 that in both panels that have connectors the upper wythe failed at a higher load.

There is also a noticeable difference in the behaviour of the PCM+TM panel and PCM C-Grid panel. Up to circa 40kN both panels displayed similar levels of stiffness in resisting the applied force. After 40 kN the PCM+C-Grid panel displayed lower stiffness that is, less force was required to displace the panel by 1 mm. There was more deflection in the upper wythe of the C-Grid panel relative to the lower wythe which indicates that the insulation is compressing.

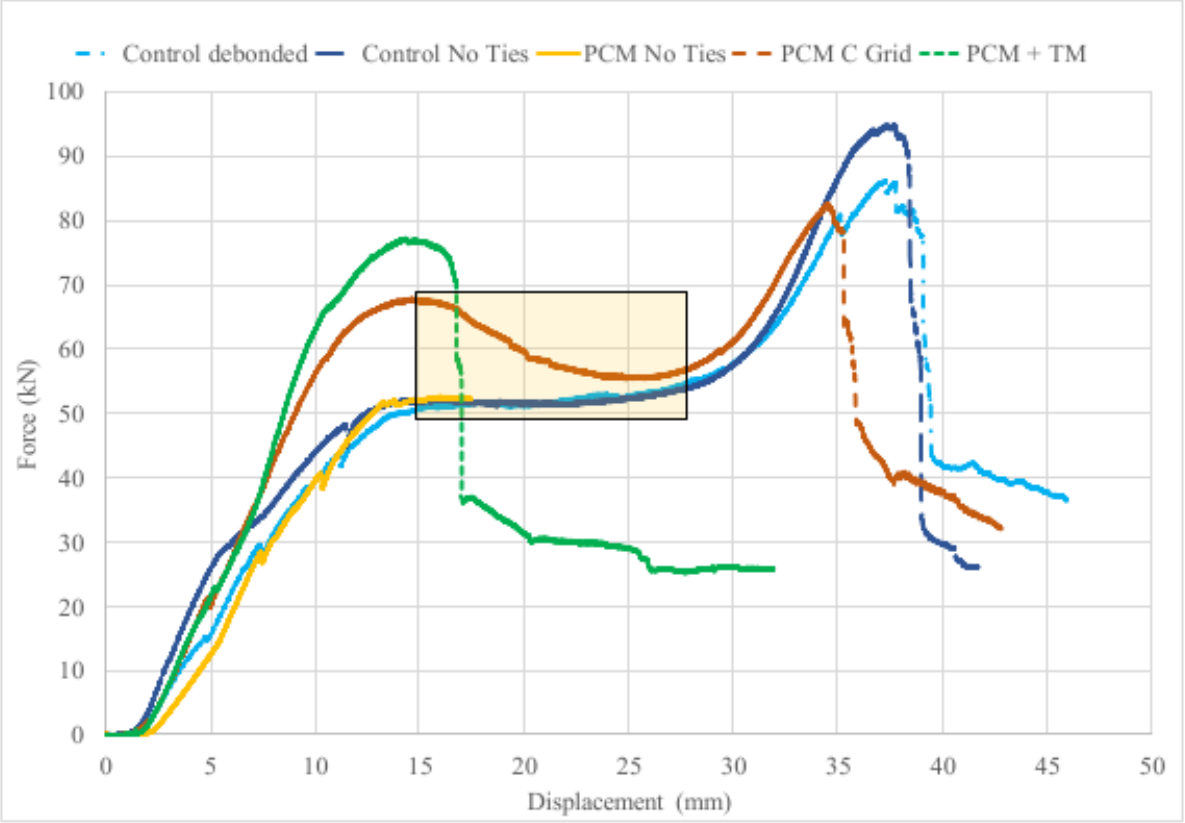


**Figure 6-29 Force-displacement plots for the upper wythes of all panels**

For this to occur the C-Grid connector must have buckled. This occured for a period of time until the insulation was fully compressed after which the resistive load was mainly provided by the bottom wythe. This stage is indicated by the curve rising again. However in the PCM+TM panel the applied displacement was largely shared with the bottom wythe through the axially stiff TM connectors rather than the insulation hence compression of the insulation was minimal. In terms of load share in the PCM+TM panel, a higher share of the load was being taken by the bottom wythe due to the stiff load path provided by the Thermomass stiffeners hence the upper wythe resisted a lower share of the applied load and did not deflect as much as the upper wythe of the other panels. The upper wythe of the PCM+TM panel did not fail until the bottom wythe had failed. A comparison of the composite behaviour of both of the connected panels is presented and discussed in Section 6.3.4.

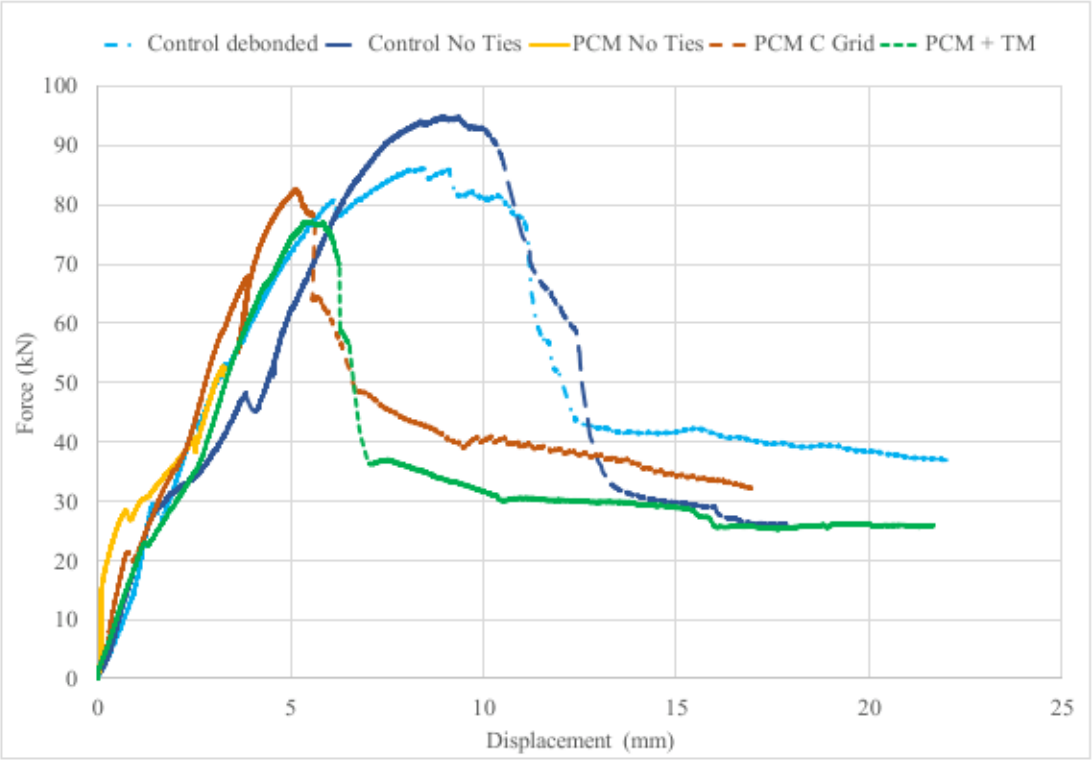


**Figure 6-30 Force-displacement plots for the lower wythes of all panels**

In Table 6-2 and Figure 6-30 it can be observed that the two panels containing normal concrete in the lower wythe reached higher ultimate strengths (87 kN and 94 kN), most likely due to the higher strength of the control concrete compared to the PCM-composite concrete. The two Control panels also deflected more however this was because they endured higher loads.

In Section 6.3.1 it was determined that to resist a reasonably onerous wind load, taken as the wind load applied to a sixth storey elevation in Dublin city less than 10 km from the coast, the panel would be required to have an elastic moment capacity of 2.3 kNm. This equates to the tests panel having a 1$^{st}$ crack load of greater than 10.2 kN. As can be noted from Table 6-2 all of the panels had a 1$^{st}$ crack load greater than 10.2 kN. In addition, the ultimate load capacity of the panels are substantially greater than the 1$^{st}$ crack load demonstrating a safe serviceability performance.

### 6.3.4 Analysis of composite behaviour

The theoretical flexural stiffness (EI) of each panel for composite and non-composite behaviour was determined as described in Section 6.3.2 and the calculations are provided in Appendix H. The experimental flexural stiffness of each panel, $E_{exp}I_{panel}$, was determined using the measured mid-span deflections, $\delta_{exp}$ and equation (6-2). Using these values the degree of composite action was assessed using equation (6-1). The output of these calculations are summarised in

Table 6-3. Figures 6-31 to 6-35 show force-displacement plots for each panel during the period of elastic behaviour. On each plot theoretical force-displacement plots for both fully composite and non-composite behaviour are added for comparison. These plots are derived by rearranging equation (6-2) for deflection and using either the theoretical composite or non-composite flexural stiffness to calculate the corresponding deflections.

**Table 6.3 Experimental flexural stiffness, $E_{exp}I_{exp}$ of each panel**

| **Panel** | **Flexural stiffness, $E_{exp}I_{exp}$ (kNm$^2$)** | [1]Flexural stiffness non-composite panel $E_{panel}$ $I_{nc}$ (kNm$^2$) | [1]Flexural stiffness fully composite panel $E_{panel}$ $I_c$ (kNm$^2$) | Degree of composite action k(%) |
|---|---|---|---|---|
| **Control debonded** | **2213.5** | 3132.8 | 10159.4 | - |
| **Control No Ties** | **2899.1** | 3132.8 | 10159.4 | - |
| **PCM No Ties** | ***13204 .0** | 2804.5 | 9426.4 | - |
| **PCM C-Grid** | **4403.4** | 2804.5 | 9426.4 | 24.1 |
| **PCM TM** | **3230.7** | 2804.5 | 9426.4 | 6.4 |

* Anomalous result

The value of flexural stiffness for the PCM No Ties panel is an anomaly arising from the fact that for a period during the test the proportion of load resistance provided by the lower wythe did not increase as demonstrated by the lack of deflection of the lower wythe between 4kN and 15kN that can be noted from Figure 6-31. As there are no ties present in this panel the insulation must be capable of transferring load from the upper wythe to the lower wythe. In this case, once the resistive load of the panel reached 4 kN, the panel responded to the additional applied displacement by deflection of the upper wythe and associated compression of the insulation with minimal additional resistive load being required from the lower wythe to maintain the rate of displacement. As a result the lower wythe did not deflect further during this period. As the stiffness of the overall panel is being determined by the deflection of the lower wythe the lack of deflection results in a very high flexural stiffness output which is anomalous.

As can be noted from Figures 6-32 and 6-33 both the Control debonded and the Control No Ties panels displayed a flexural stiffness less than that of a non-composite panel, hence there was clearly no composite action achieved. In the case of the debonded panel there was no resistance to longitudinal shear. This means that the upper wythe and insulation were free to move relative to each other and to the lower wythe. The theoretical non-composite scenario assumes that the applied displacement will be resisted by both wythes in accordance with their

relative flexural stiffnesses which is determined using the geometry of the wythes and their relative material stiffnesses, that is, Young's moduli.

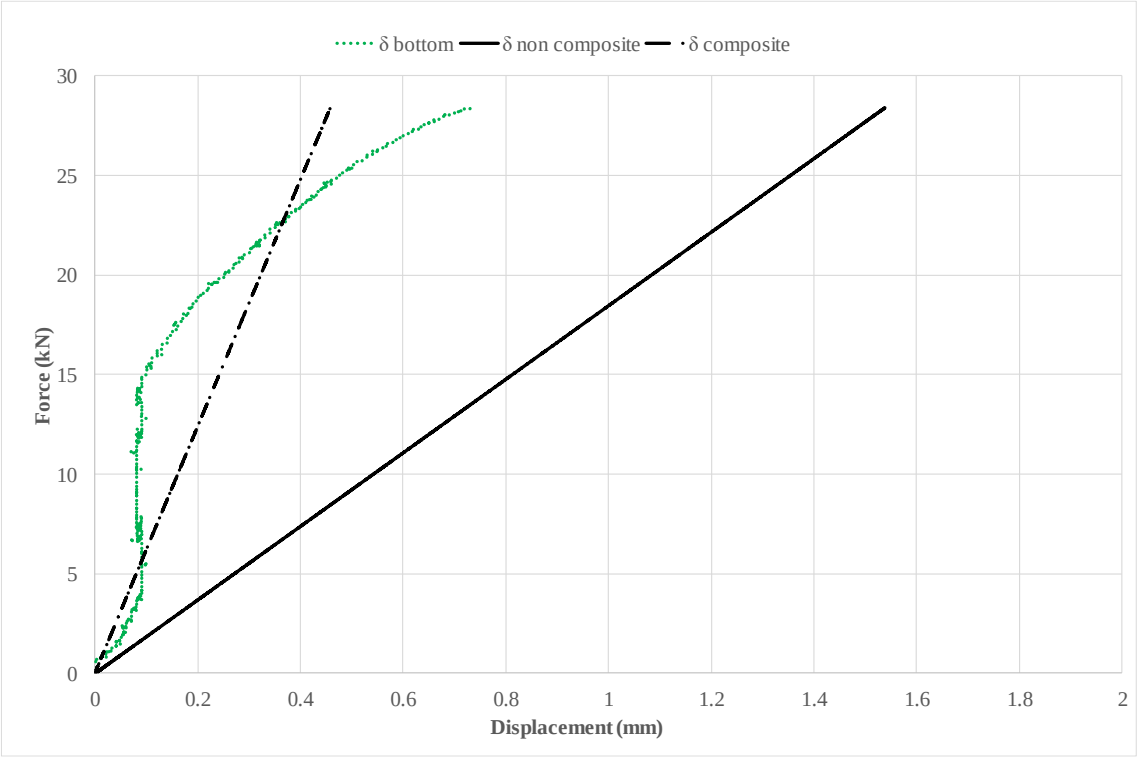


**Figure 6-31 PCM No Ties panel: Comparison of experimental force-displacement plot with theoretical composite and non-composite force displacement plots**

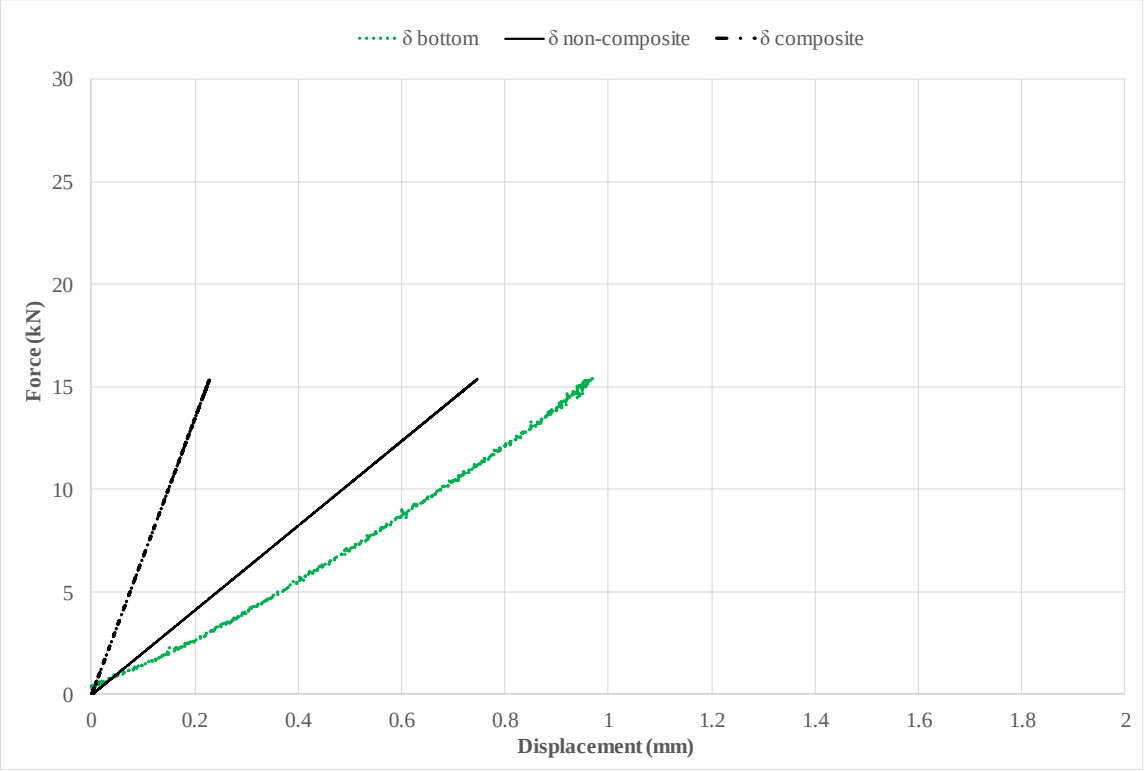


**Figure 6-32 Control debonded panel: Comparison of experimental force-displacement plot with theoretical composite and non-composite force displacement plots**

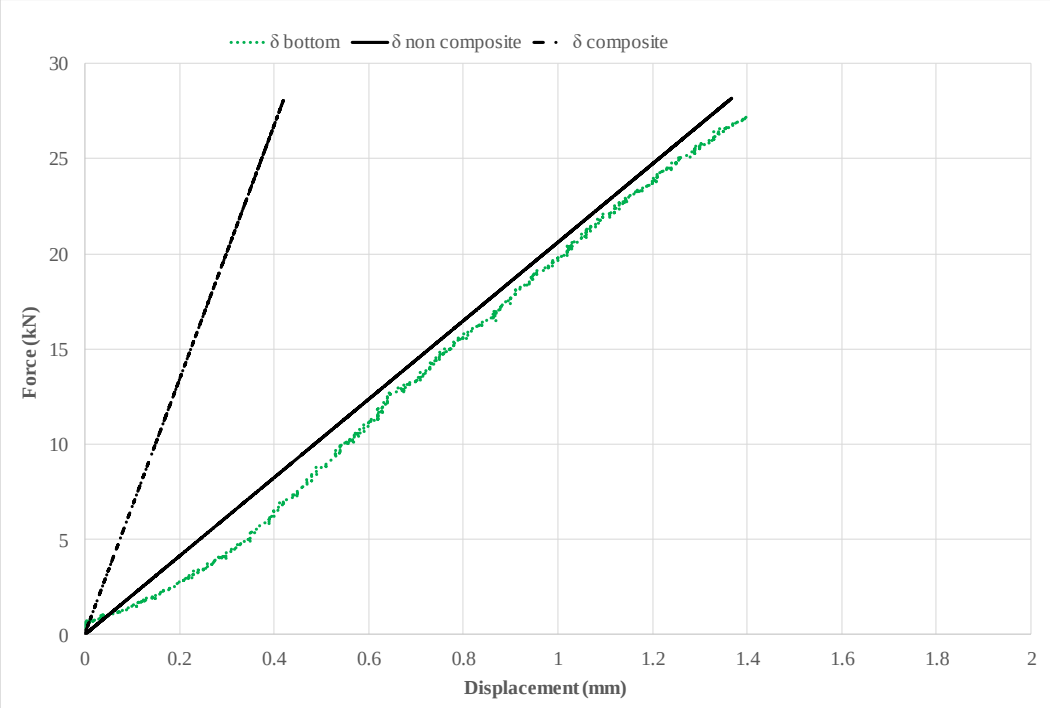


**Figure 6-33 Control No Ties panel: Comparison of experimental force-displacement plot with theoretical composite and non-composite force displacement plots**

However the actual flexural stiffness of the upper wythe is lower than its theoretical value as the upper wythe did not have a material support at either end that is rigid and there was no resistance to longitudinal movement. It was only supported vertically by the layer of insulation which is analogous to a spring support of relatively low stiffness. On the other hand, the lower wythe was supported at either end by rigid vertical supports. As the upper wythe was less stiff than theoretically predicted, more load was distributed to the lower wythe than expected and hence higher deflections occured. As a result the panel displayed a lower flexural stiffness during the test than that predicted assuming non-composite behaviour.

In the case of the Control No Ties panel, initially there was a bond between the upper wythe and the insulation which provided some resistance to longitudinal shear and allowed the two wythes to act together, hence increasing the actual stiffness of the upper wythe in terms of load distribution. As a result, slightly less load was distributed to the lower layer which, in this case, displayed lower deflections and the overall behaviour of the panel approaches that of a theoretical non-composite panel.

As can be observed from Figures 6-34 and 6-35 both the PCM C-Grid panel and PCM-TM panel displayed some degree of composite behaviour. Initially in the PCM C-Grid panel a low degree of composite action is displayed up to an applied load of 7 kN and deflection of 0.3 mm. This indicates that the C-Grid was not providing significant resistance to lateral shear at

the start of the test. As the load was increased above 7 kN there was a notable increase in the overall stiffness of the panel and a higher degree of composite action was achieved (24 %) indicating that the C-Grid was engaged. As discussed in Section 2.9.2, the C-Grid connector acts together with the insulation to resist force using truss action. The insulation provides the resistance to compression while the C-Grid provides the resistance to tension. A possible reason for the delay in engagement of the C-Grid is that some initial movement of the panel may be required to induce tension in the diagonals of the C-Grid and activate resistance.

As can be observed from Table 6-3 and Figure 6-35 the PCM TM panel displays a low degree of composite behaviour (6 %). This can be attributed to the low shear resistance of the Thermomass connectors which only provides some resistance to longitudinal shear between the wythes depending on its embedment in the concrete. Overall the flexural behaviour of the panel reflects non-composite behaviour. Due to the axial stiffness of the TM connectors, the applied displacement and corresponding resistive load were distributed directly between the wythes by the connectors and did not rely much on the insulation to transfer the load. So the wythes were connected by axially stiff supports rather than a 'spring' (insulation) support. This means that the load distribution between the wythes during the test is close to the theoretical load distribution according to the relative stiffness of unconnected wythes. The Thermomass connectors facilitate good load sharing behaviour but do not provide significant composite behaviour.

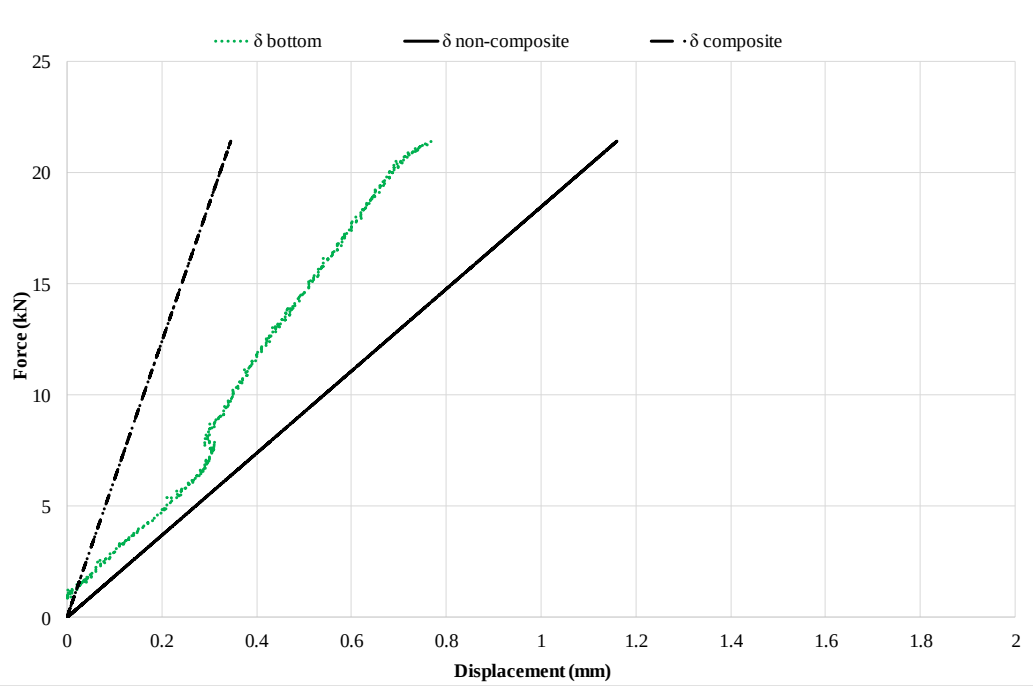


**Figure 6-34 PCM C-Grid panel: Comparison of experimental force-displacement plot with theoretical composite and non-composite force displacement plots**

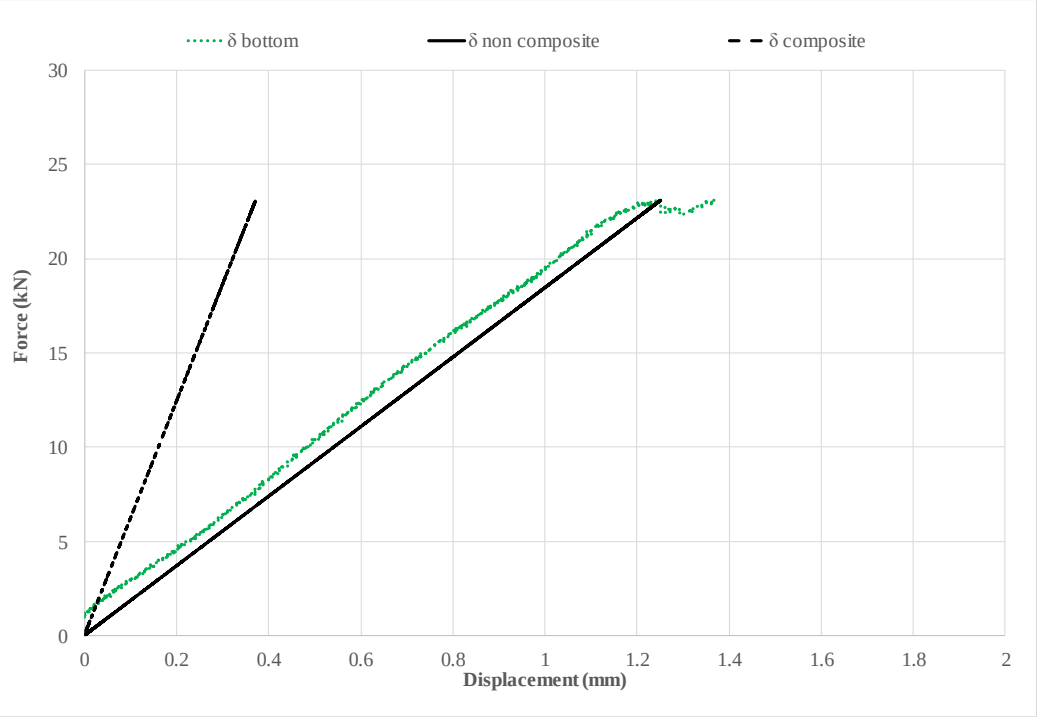


**Figure 6-35 PCM TM panel: Comparison of experimental force-displacement plot with theoretical composite and non-composite force displacement plots**

Figure 6-36 shows the experimental force-displacement plots for both the PCM TM and the PCM C-Grid panels for comparison together with the theoretical composite and non-composite force-displacement plots, including the post cracking, non-elastic behaviour. As noted previously, the PCM C-Grid panel displayed better composite action during elastic behaviour, once an initial amount of displacement occurred. The 1$^{st}$ crack occured in the bottom wythe in both panels at circa 21 kN and the stiffness of both panels reduced (point A). However both panels continued to provide resistance to increasing applied displacement with the PCM C Grid panel displaying a slightly greater stiffness than the PCM TM panel. This can be attributed to the lateral shear resistance provided by the truss action of the C-Grid, which is activated by further displacement of the panel, with the grid diagonals providing tension resistance and the insulation layer providing some resistance to compression. The Thermomass connectors provide virtually no resistance to lateral shear hence the two wythes can move laterally relative to each other. Despite this difference the overall post cracking structural response of both panels is similar.

In summary, both panels with connectors displayed partial composite action during the elastic response of the panel however the degree of composite action provided by the Thermomass connectors is insignificant in the context of the overall design capacity of the panel. Although the C-Grid displayed better capacity to facilitate partial composite action, this can only be relied

on during elastic behaviour of the panel and is subject to quality control during construction. The C-Grid has no out-of-plane stiffness. If the C-Grid gets distorted out of alignment or compressed during the manufacturing process then it may not be engaged in load resisting action prior to the 1st crack occurring in the upper wythe so its contribution to the overall stiffness of the panel is potentially variable and hence unreliable. The Thermomass connectors facilitated load sharing between the two wythes which can be reliably predicted at design stage. The overall post cracking structural responses of both panels are similar.

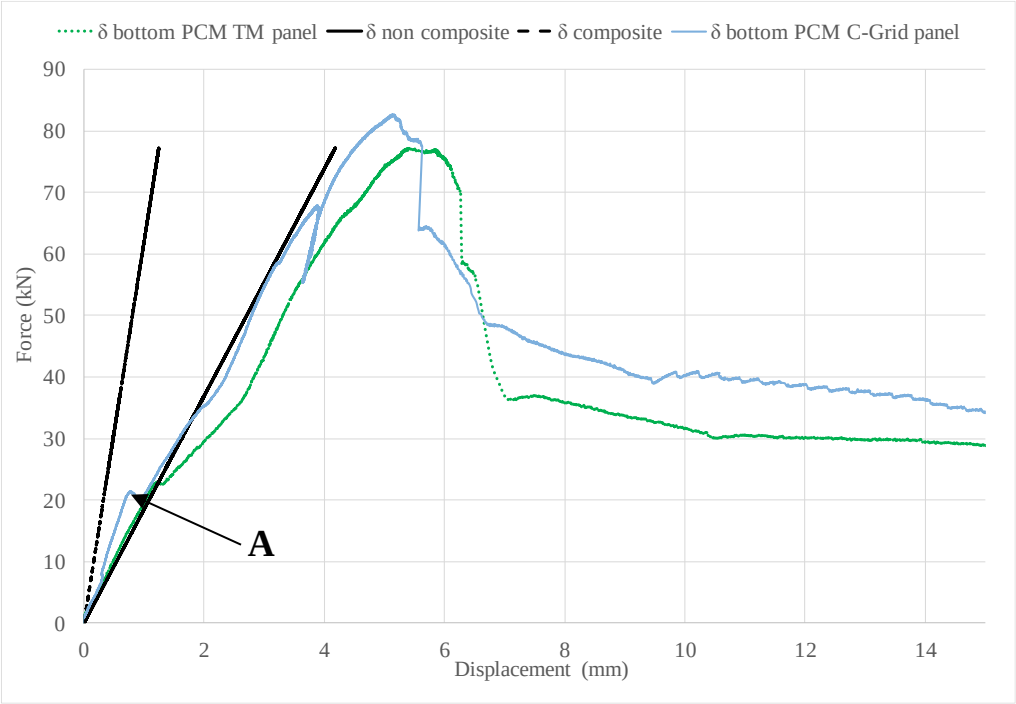


**Figure 6-36 PCM TM panel: Comparison of experimental force-displacement plot with theoretical composite and non-composite force displacement plots**

## 6.4 Conclusions

This investigation into the structural behaviour of the proposed panels enabled the elastic bending moment capacity of the panels to be quantified. As determined in Section 6.3.1 the panels must be capable of withstanding a minimum mid-span point load of typically 10.2 kN to demonstrate sufficient elastic bending moment capacity equivalent to a design wind load of 1.5 kN/m over a span of 3.5 m. The results of the tests, as summarised in Table 6.2, showed that each panel has sufficient elastic bending moment capacity to withstand this wind load. Both the PCM C-Grid and PCM TM panels constructed with PCM concrete in the lower wythe demonstrated that they have sufficient elastic bending moment capacity to withstand a mid-span point load of 21 kN which is equivalent to a design wind load of 3.0 kN/m applied to a panel spanning 3.5 m.

The ultimate capacity of each panel was controlled by the capacity of the thicker lower wythe. The ultimate capacity of the Control No Ties panel was 3.3 times the load at first crack and the PCM C-Grid panel and PCM TM panel reached ultimate loads that were 3.8 and 3.4 times the load at first crack respectively. This demonstrates that the panels have considerable structural capacity remaining after the first signs of distress appear. This post-cracking capacity is an important safety feature in structural design as any potential problems signalled by the 1$^{st}$ crack can be addressed long before there is a risk of ultimate failure.

The elastic behaviour of the PCM C-Grid and the PCM TM panels were similar however their overall responses were visibly very different. As with all the unconnected panels, the upper wythe of the PCM C-Grid panel reached ultimate failure first displaying significant displacement as the insulation compressed under the applied displacement. This was followed by a period during which the applied displacement was resisted by deformation of the insulation and little additional load resistance was provided by the lower wythe. Once the insulation had fully compressed the resistive load was nearly fully provided by the lower wythe. As the C Grid has no axial stiffness it was unable to directly transfer the applied displacement from the upper to the lower wythe. This meant that the resistive load was not distributed between the two wythes in accordance to their relative stiffnesses and hence it is difficult to quantify the load distribution between the two wythes particularly as the load distribution depends on the stiffness of the insulation used. This behaviour makes the prediction of load distribution and the resulting structural response more difficult. In contrast the Thermomass connectors are axially stiff and capable of transferring the applied displacement from the upper to the lower wythe without relying on the insulation. This means that the resistive load is shared by each wythe in accordance with their relative stiffnesses and the response of each wythe can be reliably predicted.

With regard to the contribution of the bond between the insulation and the upper wythe when comparing the response of the Control debonded panel and the Control No Ties panel, it is clear that the presence of a bond restricts the deflection of the upper wythe and hence increases the load at which the first crack occurs. This increases the elastic bending moment capacity of the panel.

With regard to the degree of composite behaviour achieved in the panels in which the upper and lower wythes were connected together, it can be concluded that despite some degree of composite behaviour displayed in both panels it should not be relied upon in the design of the

panel. The PCM TM panel displayed partial composite behaviour of 6 % which is very low. Concrete is a variable material and even a small difference between the Young's modulus assumed in design calculations and the actual Young's modulus of the concrete used in the panel could reduce the actual degree of composite action from 6 % to 0 %. Hence, for design purposes, non-composite behaviour should be assumed if Thermomass connectors are being used, to ensure that the flexural capacity of the panel is not over-estimated. However, a benefit of the Thermomass connectors is that they are stiff enough axially to transfer load between the wythes hence the load distribution between the wythes can be accurately predicted and the predicted structural response can be safely relied on.

The PCM C Grid panel initially displayed non-composite behaviour until sufficient deflection occurred after which lateral shear behaviour engaged the diagonals of the grid in load resisting behaviour through axial tension. Once the grid was engaged the panel achieved partial composite behaviour of circa 24%. It is suggested that the diagonals of the C Grid may not have been fully taut at the start of the test so the panel had to deflect to activate the lateral shear resistance in the C Grid. It is difficult to predict how much deflection and applied load is required to activate the C Grid as the condition of the C Grid prior to applying load will depend on manufacturing and construction practice. There is a risk that the panel could reach its elastic moment capacity prior to the C-Grid being activated, causing cracking of one or both wythes. Also, as the C-Grid is not axially stiff enough to transfer load from the outer wythe to the inner wythe load sharing between the two wythes is wholly dependant on the stiffness of the insulation. As insulation is not considered a structural element it cannot be relied on to transfer load in the design of a panel. For this reason the outer wythe alone would be required to have sufficient strength and stiffness to resist the expected wind loads. Hence it is concluded from this testing regime that any composite action provided by the use of the C-Grid should not be relied on in the design of the panel.

Considering all of the results of this investigation into the structural behaviour of the panels, it is concluded that Thermomass connectors are on balance the preferred connector to be used in the proposed panel. Neither of the connectors provided reliable composite action. The Thermomass connectors facilitated predictable load distribution between the two wythes and hence the structural response can be predicted more accurately. The Thermomass connectors are also widely used in industry and are an established connector solution that minimises the bowing effect that can arise in concrete sandwich panels. The PCM TM panel displayed sufficient structural capacity to resist typical wind loads with a reasonable factor of safety.

# Chapter 7. Design, Instrumentation and Manufacture of the Huts and Analysis of Data Collected

## 7.1 Introduction

From the review of the literature on the use of PCM thermal storage systems in building envelopes as discussed in Section 2.6.1, it is concluded that the majority of the investigations into the use of PCM-concrete composites involved laboratory investigations and/or numerical modelling. There is a lack of research that explores the thermal behaviour of PCM-concrete composites in real full-scale scenarios. The actual performance of the PCM-concrete composite depends on many variables which are difficult to replicate in a laboratory setting, such as varying indoor and outdoor climatic conditions. For the PCM to be engaged, the temperature of the environment in which it is located must fluctuate above and below the melt temperature of the PCM within a diurnal period. The fluctuation of the indoor temperature depends on the local climate, geometry, building use and construction details, such as area of glazing and level of insulation. For this reason it is important to monitor the thermal behaviour of the PCM-concrete composite in a 'real', full-scale setting and over the duration of twelve months to capture the thermal behaviour during all seasons. In addition, in order to validate a numerical model it is essential to have real data for both the environmental conditions and the thermal response. To address these noted gaps in the research, the fourth objective of this research project was to construct three full-scale huts using the PCM-concrete composite sandwich panels, developed and tested in the laboratory as described in Chapters 3, 4, 5 and 6. The purpose of the research into the thermal behaviour of the huts is to:

- Monitor and record the thermal behaviour of the PCM-concrete composite which is placed in a form of construction similar to that which would be used in a real building
- Monitor and record thermal data over a minimum of 12 months so that the thermal performance can be evaluated across all seasons which will enable an accurate assessment of the technical viability of the passive thermal storage system
- Provide real data which can be used to validate a model developed to simulate the thermal behaviour of PCM-concrete composite

The huts were instrumented to record both internal thermal data and local climate data. Furthermore, thermal data was recorded throughout the depth of the wall which enabled the effective depth of the PCM to be determined under the varying daily and seasonal thermal conditions.

### 7.2 Design of the huts

As described in Section 3.6, and shown in Figure 3-13, three full-scale test huts with internal dimensions of 1990 x 1990 x 1800 mm, were constructed using three different types of cladding panels, each comprising of a 70 mm thick concrete outer leaf, 120 mm insulation and a 125 mm thick inner leaf, which varied in composition as shown in Figure 7-1. This study investigates specifically the thermal behaviour of the inner leaf of the cladding panel. As there is a 120 mm layer of insulation between the inner and outer layer, the form of the outer layer has an insignificant effect on the thermal behaviour of the inner layer. The high performance fibre reinforced concrete (HPFRC) material used in the upper outer wythe of the panels examined in the structural tests was still under investigation within the IMPRESS project at the time that the panels for the huts were being manufactured. For this reason it was decided to use a 70 mm thick normal concrete outer leaf for all panels which is commonly used by Techrete Ltd. Kingspan Kooltherm K15 Cladding Board was used as the insulation layer. This product is a high performance rigid insulation with a thermal conductivity of 0.02 W/mK. The data sheet for Kooltherm insulation is provided in Appendix I.

The inner and outer layers of the concrete sandwich panel were connected together using non-conducting Thermomass connectors as described in Chapters 5 and 6.

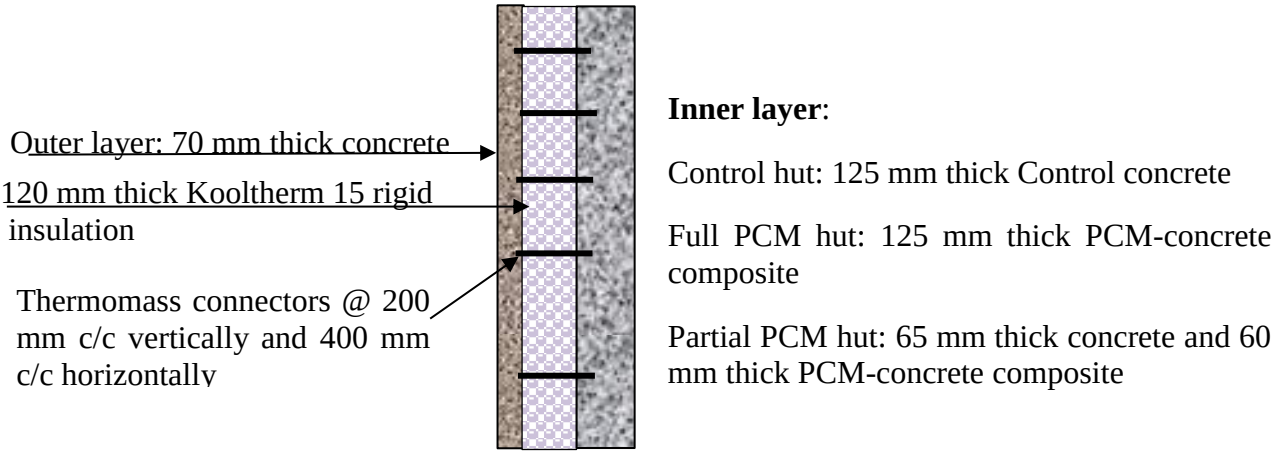


**Figure 7-1 Summary of panel design for huts**

The objective for using the PCM-concrete composite is to provide additional thermal storage to enable excess heat to be absorbed and hence reduce overheating. It is expected that when the internal air temperatures in the huts increase due to solar gain and/or the heating regime, the rate of increase of the internal air temperatures will be lower in the huts constructed with the PCM-concrete composite than in the Control hut. It is therefore also expected that the peak internal air temperature in the Control hut will be higher than in the PCM huts.

### 7.3 Instrumentation of the huts

To observe the thermal behaviour and environmental conditions, a data recording and monitoring system was designed and installed. Each hut was instrumented for collection of temperature data and internal and external environmental data (Figure 7-2). The monitoring equipment was sourced, calibrated and installed by the IMPRESS partner, Sirus International. Data sheets for the equipment and calibration certificates are provided in Appendix J.

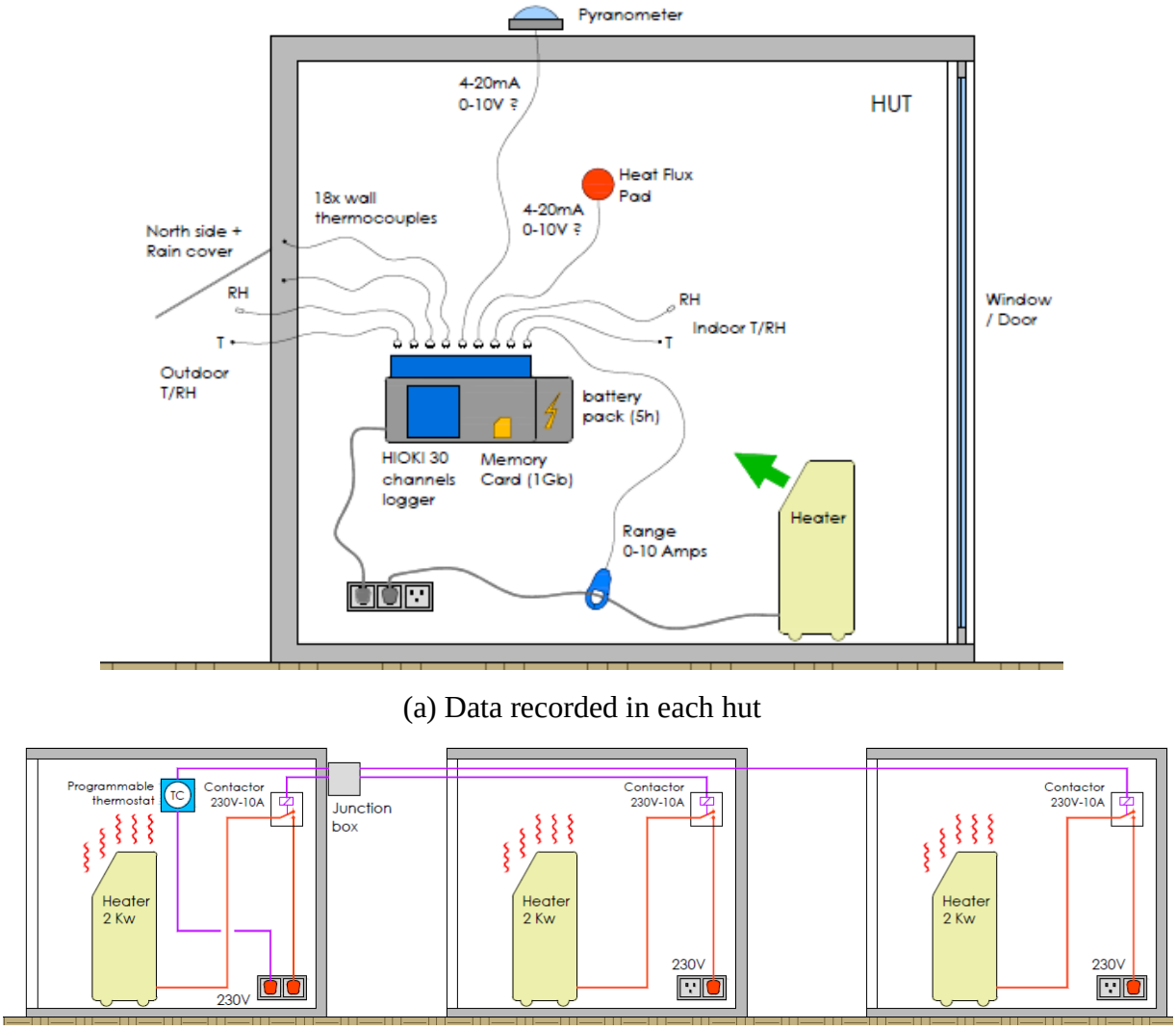


(a) Data recorded in each hut

Control Hut Full PCM Hut Partial PCM Hut

(b) Heaters in huts connected in series

**Figure 7-2 Schematic layout of instrumentation of each hut ( NTS) (Source: Sirus)**

Thermocouples were cast into the internal layer of all the panels, located at depths of 30 mm, 60 mm and 90 mm from the inside surface. Thermocouples were also located on the internal and external surfaces of the inner leaf and on the outer face of the insulation layer (Figure 7-3). Each set of 6 no. thermocouples were located at the centre of each panel, North, East and

West elevations. There were two additional sets of 6 no. thermocouples located in the North elevation panel, so in total there were 30 no. thermocouples in each hut to record the temperature throughout the depth of the wall. This number allowed for some redundancy in case any of the thermocouples were damaged during the manufacture or installation of the panels. These thermocouples enabled the varying temperature profile throughout the depth of the wall to be determined at any point in time. Furthermore, the rate of heat penetration into the wall and through the wall could be determined. All thermocouples were Class 1, Type K thermocouples and were calibrated by Sirus International prior to construction of the huts with an average accuracy of +/- 0.86 $^{o}$C.

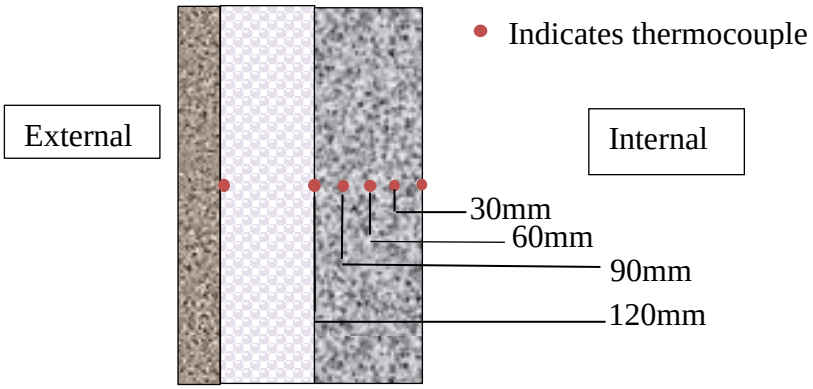


**Figure 7-3 Schematic showing thermocouples through the depth of the wall**

An EKO MF-180 heat flux sensor was located on the internal face of the North wall in each hut. The data from the heat flux pad indicated the heat flow into and out of the wall at the surface. Further, a type K thermocouple recorded the internal air temperature. A HIOKI Z2000 also recorded internal air temperature and relative humidity in each hut. The external temperature and relative humidity were also recorded using a HIOKI Z2000 and an EKO MS-602 pyranometer was used to record solar irradiance at the site (Figure 7-4).

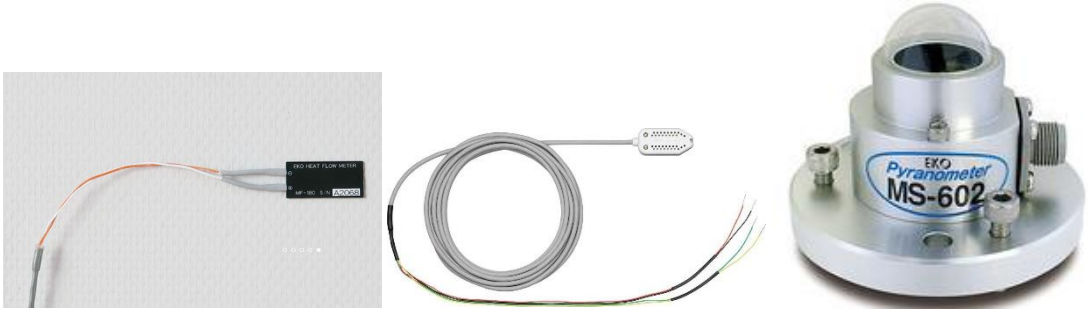


(a) (b) (c)

**Figure 7-4 (a) EKO MF-180 heat flux sensor, (b) HIOKI Z2000, (c) EKO MS-802 pyranometer**

A 2 kW element convection heater was installed in each hut (Figure 7-5(a)). The heater was placed in the centre of the hut to ensure approximately equal exposure for all walls. Air is heated in electrical coils at the base of the heater and rises as it heats. Once the heated air rises and meets the insulation layer at the ceiling level it then distributes horizontally in all directions and hence the hot air is distributed approximately evenly around the hut. The purpose of the heaters is to enable a heat load pattern to be applied to the huts that replicates a particular scenario, for example, the heat load pattern of a classroom in a school that has an overheating problem. All the heaters were linked so that they turned on and off in unison (Figure 7-2 (b)). The heater in the Control hut determines when all the heaters switch on and off. A programmable thermostat is connected to the Control hut heater and hence any pre-determined programmed heat load pattern can be applied equally to all huts. Each heater is monitored for power use using split current transformers. All the data from the thermocouples and instruments were recorded on HOIKI LR 8400 portable data loggers at 5 minute intervals, with one logger located in each hut (Figure 7-5 (b)). The data was manually downloaded from the HIOKI data loggers on a regular basis over an 18 month period. The data are analysed in Section 7.5 to assess the performance of the PCM-concrete composite.


(a) (b)

**Figure 7-5 (a) 2kW element convection heater, (b) HIOKI LR 8400 data logger**

### 7.4 Manufacturing of the panel and construction of the huts

The panels were manufactured in the Techrete Ltd manufacturing facility in Dublin. The three Control hut walls were formed in a single day and the six walls containing PCM-concrete were constructed over two days the following week in accordance with the programme provided in Appendix K. The programme was tightly scheduled and had to be strictly adhered to so as not to disrupt the normal manufacturing process and production line at the manufacturing plant. The concrete mix designs used for the Control concrete and the PCM-concrete are as provided in Tables 4-8 and 4-9. Figures 7-6 to 7-13 show photographs of the key stages of manufacture.

**Figure 7-6 Steel mesh reinforcement for the 70 mm concrete outer leaf was fixed into the formwork.**

**Figure 7-7 Concrete of the outer leaf was mixed, placed and vibrated.**

Steel mesh reinforcement for the 70 mm concrete outer leaf was fixed into the formwork (Figure 7-6). The concrete for the outer leaf was mixed, placed and vibrated (Figure 7-7). Thermocouples were taped into position on both faces of the insulation which was then placed on top of the fresh concrete. Thermomass connectors were then pushed through the insulation and into the fresh concrete of the outer leaf (Figure 7-8). The steel mesh reinforcement for the inner leaf was then fixed in place (Figure 7-9). To secure the thermocouples in the correct position within the depth of the wall, 2 mm diameter holes were drilled in the formwork at mid-length on opposing sides at the required depths of 30 mm, 60 mm and 90 mm. Fishing wire was glued to the outside face of the formwork and threaded through the holes and out the opposite side. The fishing wire was pulled very taut and glued to the outside of the formwork to maintain the tension. The thermocouples were then fed through the formwork until the tip was at the mid-point of the panel. They were then glued to the wire to fix them in place (Figure 7-10).

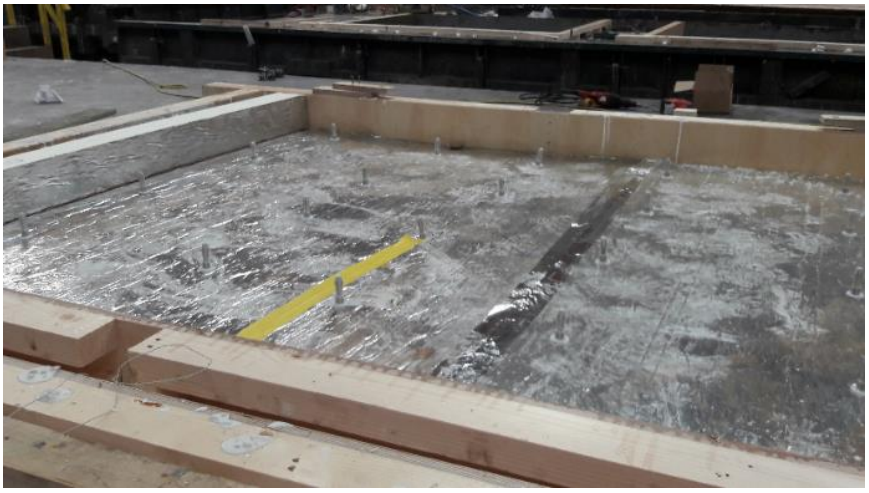

**Figure 7-8 Insulation and connectors in place**

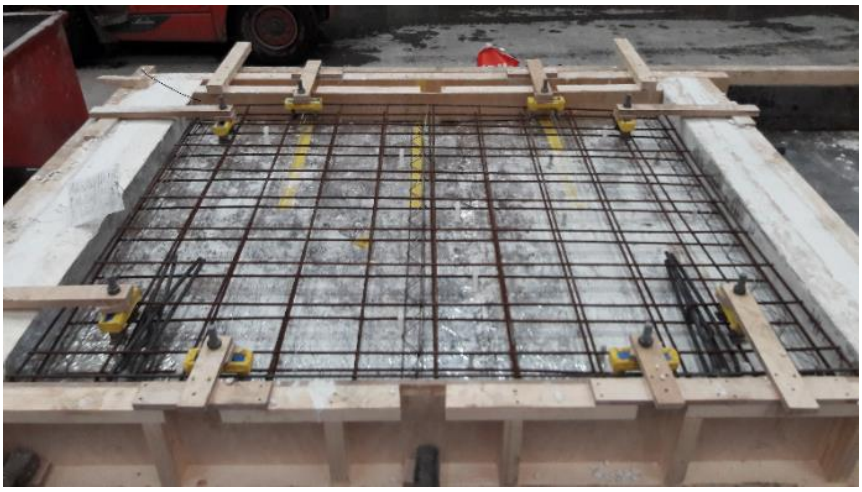

**Figure 7-9 The steel reinforcement cages for the inner leaf**

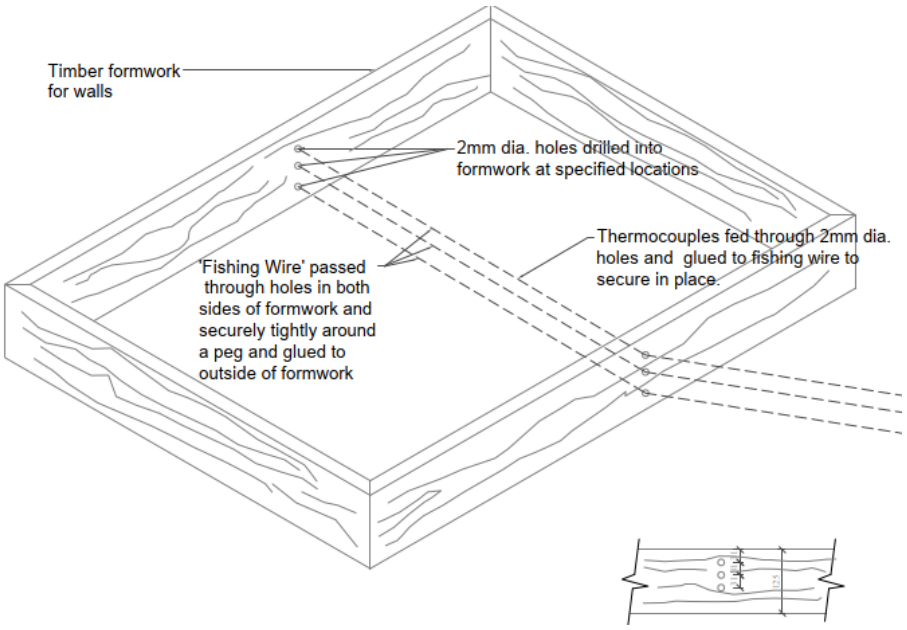


**Figure 7-10 Schematic showing method of fixing the thermocouples in place**

The fresh PCM-concrete was sufficiently workable and was compacted into place with the aid of the vibration table (Figure 7-11). The panels remained curing on the casting table for 40 hours, within a thermostatically controlled environment maintained at 19 $^{o}$C. After 40 hours, the strength of the PCM-concrete composite, determined through cube testing, was within a range of 24 MPa to 30 MPa and hence the panels had sufficient strength to facilitate striking of the formwork and lifting of the panels.

**Figure 7-11 Placement of fresh PCM-concrete composite into the panel**

The manufacture of the panels and erection of the huts proceeded without any problems which demonstrated that the PCM-concrete composite can successfully be scaled up from a laboratory environment to a real manufacturing/building scenario.

The wall panels were secured in place using internal steel brackets to connect the inner leaves to each other and the roof and floor (Figure 7-12). Potential thermal bridging at the location of the connection brackets was mitigated by using two layers of insulation at roof and floor level as shown in Figure 3-13.

The three huts were erected in an open area in Techrete's yard minimising any overshadowing during the day. All huts were South facing to maximise solar gain (Figure 7-13). The double glazed patio doors with (U-value of 1.2 W/m$^2$K) were installed and sealed at the edges. The data sheet for the doors is provided in Appendix L.

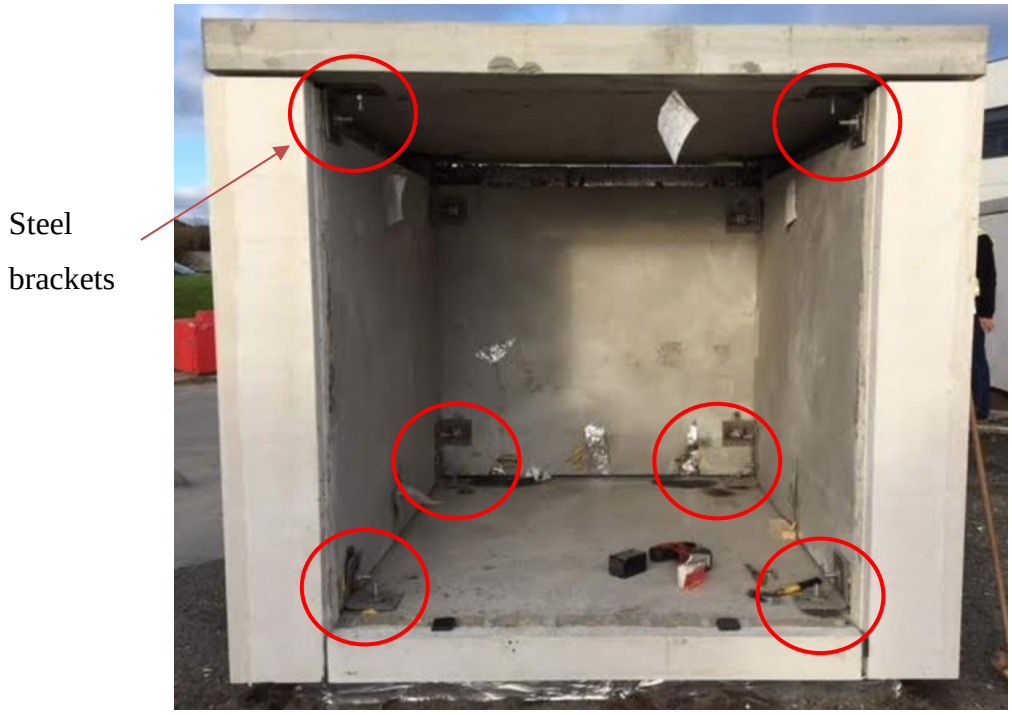


**Figure 7-12 Erection of the PCM demonstration hut prior to installation of the glazed sliding doors displaying the fixings between floors, roof and wall panels**

**Figure 7-13 Demonstration huts located in Techrete Ltd**

## 7.5 Analysis of recorded data

### 7.5.1 Overview of recorded data

As described in Section 7.3 environmental data were collected in each hut over an 18 month period. To obtain an overview of when the PCM was engaged throughout the year, Figure 7-14 displays the temperature of the surface of the wall in each hut over the 18 month period of data collection. The melt temperature range of the PCM (20 $^{o}$C – 24 $^{o}$C) is shown shaded. The plot identifies the periods during which the PCM is not active either because the temperature of the hut walls is too high during the night to allow the PCM to solidify and release its heat, or because the wall temperatures do not get high enough during the day to cause the PCM to melt.

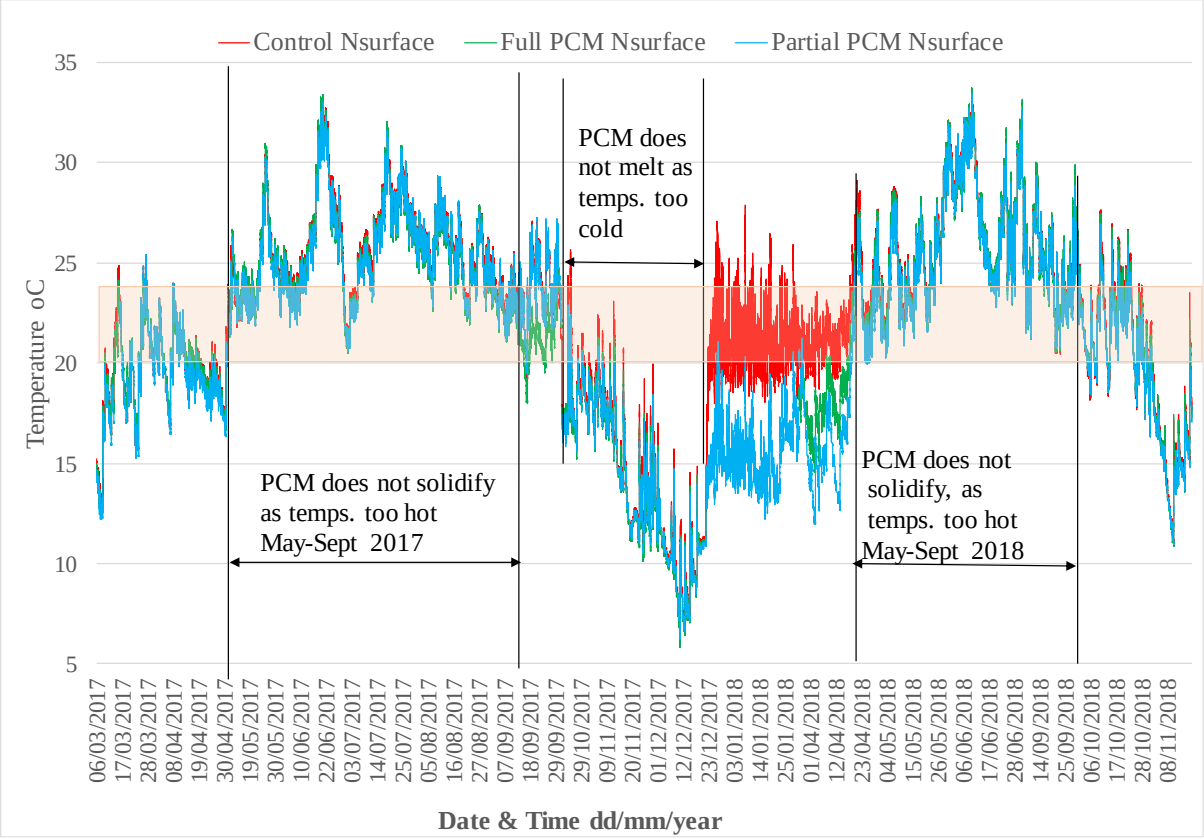


*Nsurface indicates internal surface of the North wall in each hut

**Figure 7-14 Overview of temperature on the surface of the North wall in each hut over an 18 month period.**

Overall the data indicates that in passive conditions, that is when the heaters are not switched on and no ventilation is provided at night, the PCM is only engaged circa 30% of the year, during the spring and autumn periods. A previous research study collected thermal data from huts constructed with single leaf walls of PCM-concrete without an insulation layer (Cabeza et al., 2007). This means that the walls in that study could release heat to the external air at night and solidify, enabling it to be effective the following day. In such a scenario the PCM would be more effective over a longer period during the year. However, single leaf wall construction with no insulation layer is not permissible under Irish building regulations (Part L) and would allow significant heat loss during colder weather. It is important to obtain a realistic assessment of how the PCM-concrete will react in a typical form of construction, that is, in a two wythe concrete sandwich panel which includes a layer of insulation which hinders the release of heat from the internal wall. In the two wythe wall, the release of stored heat can largely only occur in one direction, that is into the internal environment. The temperature differential between the wall and the internal environment is small compared to the temperature differential between the wall and the external air, hence the release of heat from the wall at night is relatively low compared to the study carried out by Cabeza et al. (2007). Another factor that contributes to

the low engagement of the PCM is Ireland's temperate climate is the fact that the mean daily temperature in Ireland ranges from 4 $^{o}$C in winter to 16 $^{o}$C in summer. Hence the periods during which the internal temperatures in a building may rise above 22 $^{o}$C are shorter compared with buildings within the Mediterranean as in Cabeza's study, and other hotter climates.

Although the PCM is ineffective for circa 70% of the study period during which passive conditions applied, the application of various heat load regimes and ventilation strategies allowed the behaviour of the PCM to be observed and analysed under varying non-passive environmental conditions. The collection of data in both passive and non-passive conditions also facilitated the development and validation of a software model that simulated the thermal behaviour of the PCM-concrete which can then be used to assess the performance of the PCM-concrete in different climates and under varying internal environmental conditions.

In the following sections, data for scenarios of particular interest taken over shorter periods are analysed in closer detail. The scenarios selected are as follows:

- Thermal behaviour of walls when the PCM is not engaged.
    - Thermal behaviour of PCM-concrete composite walls when PCM is solid
    - Thermal behaviour of PCM-concrete composite walls when PCM is liquid
- Thermal behaviour of walls when the PCM is engaged.
    - Thermal behaviour of wall during winter passive conditions
    - Thermal behaviour of walls during summer passive conditions
    - Thermal behaviour of walls when heaters are on and no ventilation is provided
    - Thermal behaviour of walls when heaters are on and overnight ventilation is provided to facilitate cooling of the PCM

### 7.5.2 Thermal behaviour of walls when the PCM is not engaged

As the PCM within the concrete matrix is only engaged for a certain percentage of the year it is important to observe and compare the thermal behaviour of the PCM-concrete composite and the normal concrete when the PCM is either fully solid or fully melted over a full diurnal period. The conclusions made from this comparative analysis can then be taken into consideration when examining the thermal performance of the PCM-concrete material over an annual period.

*7.5.2.1 Thermal behaviour of PCM-concrete composite walls when PCM is solid*

During the winter months, in passive conditions, that is when the heaters do not come on during the day, the internal wall temperatures in the huts often remain below the lower temperature of the PCM melt temperature range (20 $^{o}$C). Under these conditions the only difference between the huts is the thermal conductivity of the inner leaf material. The impact that this difference will have will depend on the temperature differential between the internal and external environment. On the three walled elevations of the huts the insulation layer buffers the internal environment from fluctuations in the external air temperature. The glazed elevation also buffers the internal environment from fluctuations in the external air temperature, albeit to a lesser extent due to its higher U-value. To investigate any difference in thermal behaviour between the huts in passive, 'cold' conditions, sample data for a three day period from 19$^{th}$ November 2017 to 21$^{st}$ November 2017 are plotted and displayed in Figures 7-15 to Figure 7-17.

Figure 7-15 shows a comparison between the internal air temperatures of the huts. It can be observed that there is no significant difference between the internal air temperatures of the huts when the PCM is continuously solid throughout the period, that is, any difference between the temperatures is smaller than the calibrated accuracy of the thermocouple (+/-0.86 $^{o}$C). It can also be observed that during the latter two days of the said period the internal air temperature is similar to the external air temperature so that the temperature differential between the internal and external environment is relatively small. However during the first day of the period the temperature differential is greater at circa 7-8 $^{o}$C and it can be noted that the internal air temperature in all the huts follows the same profile, indicating that the walls of the hut have a similar overall thermal conductivity.

The irradiance levels during this period are plotted in Figure 7-16. The sharp rise in temperature that can be observed between 11am and 1pm on the 19$^{th}$ and 12pm – 1pm on the 20$^{th}$, denoted as 'A' in Figure 7-15, is due to radiative heat transfer from the sun and coincides with peak irradiance levels as observed from Figure 7-16. There is close correspondence between the peaks in Figures 7-15 and 7-16 not surprisingly, showing the effect of solar gain inside the huts.

Figure 7-17 displays a plot of the temperature at the surface of the wall in each hut. Again there is no significant difference between the temperature profile of the hut walls over the same three day period and as the peak temperature is 12.7 $^{o}$C it can be assumed that the PCM is in a solid phase throughout the period. Temperature profiles through the inner leaf of the North wall

of each hut, at depths of 30 mm, 60 mm, 90 mm and 125 mm are provided in Appendix M. A comparison of these plots show that there is no significant difference between the temperatures through the depth of the wall and that there is no discernible difference between the overall thermal behaviour of the walls in each hut.

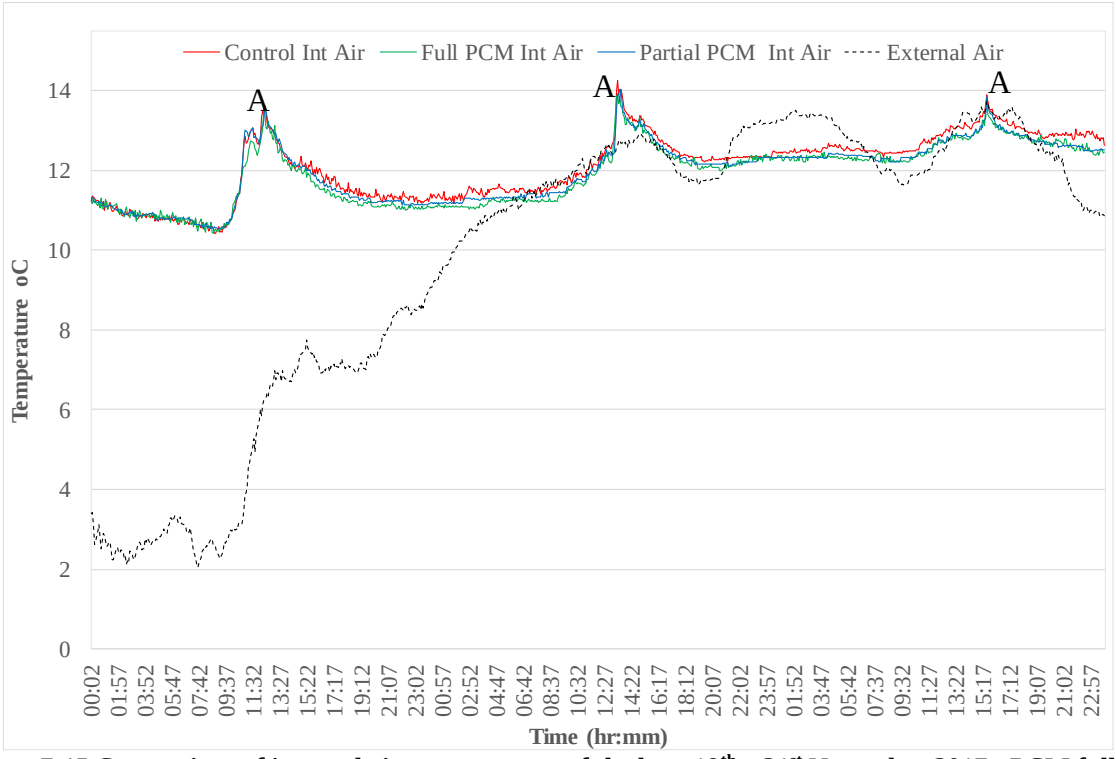


**Figure 7-15 Comparison of internal air temperatures of the huts 19th – 21st November 2017 - PCM fully solid**

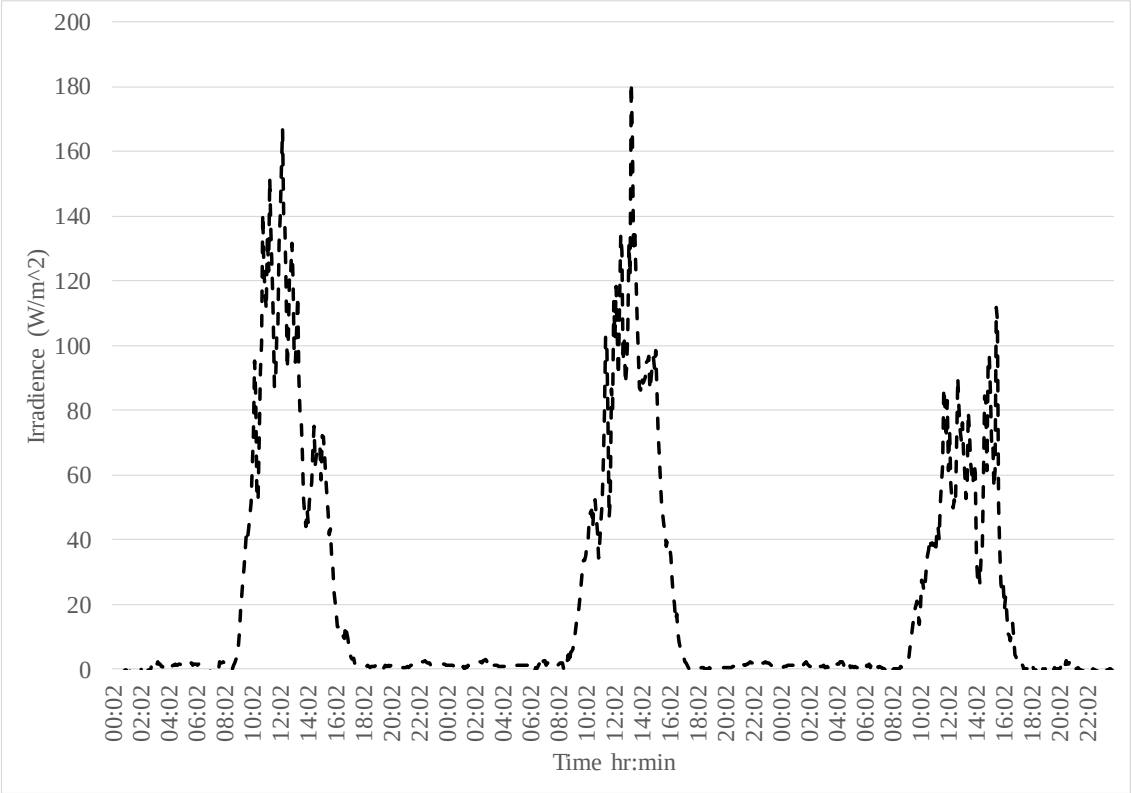


**Figure 7-16 Irradiance, 19th - 21st November, 2017**

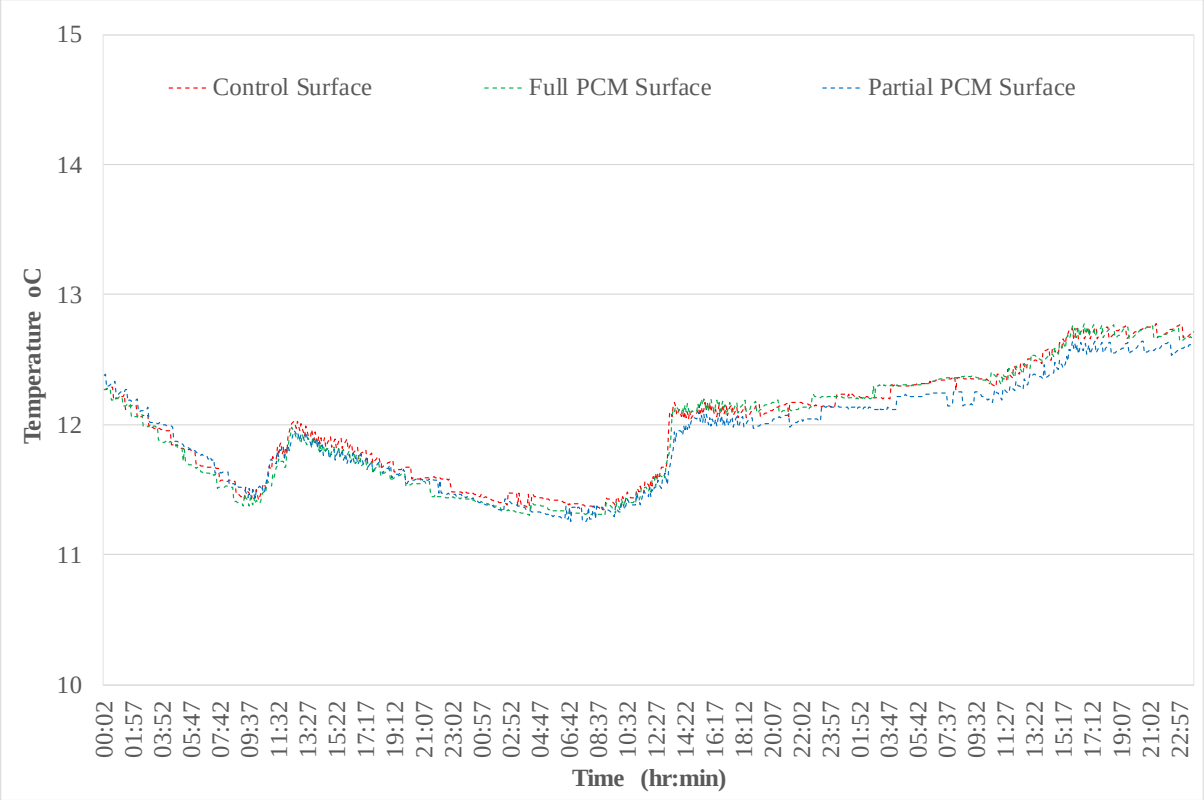


**Figure 7-17 Comparison of wall surface temperatures of the huts 19th – 21st November 2017 - PCM not engaged**

*7.5.2.2 Thermal behaviour of PCM-concrete composite walls when PCM is liquid*

During the summer months the radiators in the huts were switched off all the time so passive conditions were maintained. During certain periods over the summer season, depending on weather conditions, the huts overheated and the PCM in the walls was engaged and remained melted for long periods. Sometimes the huts did not cool down sufficiently over night to allow the PCM to solidify. This was most likely due to the fact that on nights when the external temperatures were warm the huts, being well insulated, contained the heat. To examine and compare the thermal behaviour of the hut walls when the PCM remains fully melted, data for a two day period from noon on 20th June 2017 to noon 22nd June 2017 are plotted and displayed in Figures 7-18 and 7-19.

Figure 7-18 displays the internal air temperatures of the huts and the external air temperature. The internal air temperature does not fall below 28 $^{o}$C even though the external air temperature falls to 15 $^{o}$C, hence it can be assumed that the PCM remains in a fully melted phase during this period. The profile of the internal air temperature follows the profile of the external air temperature however the amplitudes of the internal air temperature profile are lower showing the effectiveness of the insulation layer and double glazing. It can be noted from Figure 7-18

that the temperature profile of the internal air in each of the huts is very similar indicating that the heat gain/loss through the walls and glazed elevations of the huts is the same despite the presence of PCM in two of them because the temperature differential between internal air temperature and the external air is the same for each hut.

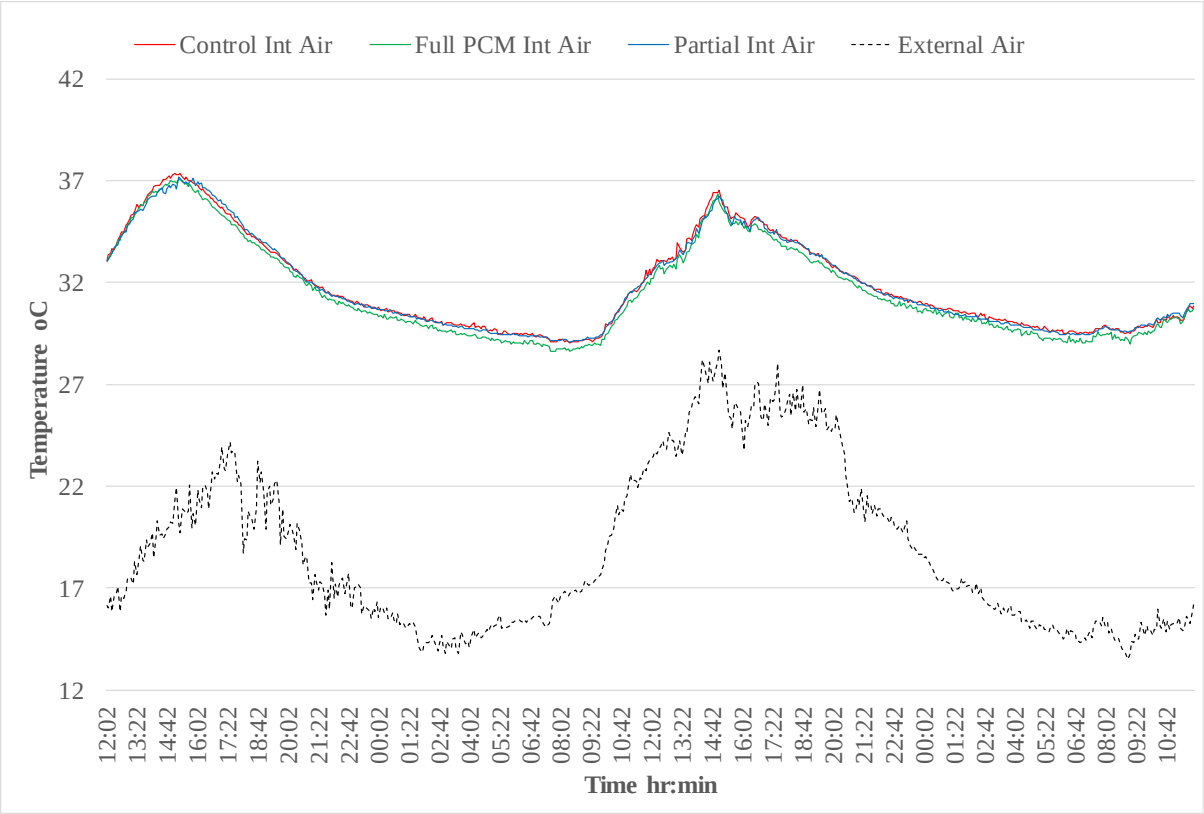


**Figure 7-18 Comparison of internal air temperatures of the huts 20th – 22nd June 2017 - PCM not engaged**

Figure 7-19 shows the temperature on the surface of the North wall in each hut. It can be noted that the temperature at the surface of the wall in each hut does not fall below 30.5 $^{o}$C which is notably high but not unexpected given the very high internal air temperatures. It can also be noted that the temperature profiles of the internal wall surfaces for each hut are indistinguishable highlighting that there is no discernable difference between the huts during this period.

Temperature profiles through the inner leaf of the Control hut, at depths of 30 mm, 60 mm, 90 mm and 125 mm are displayed in Figure 7-20. Similar plots for the Full PCM hut and the Partial PCM hut are provided in Appendix N. It can be noted from Figure 7-20 and the plots in Appendix N that the temperature profile through the inner leaf is similar for all three huts. During the period when temperatures are rising there is a temperature differential between the internal surface of the wall and the temperature at 60 mm depth of circa 1 $^{o}$C. The difference

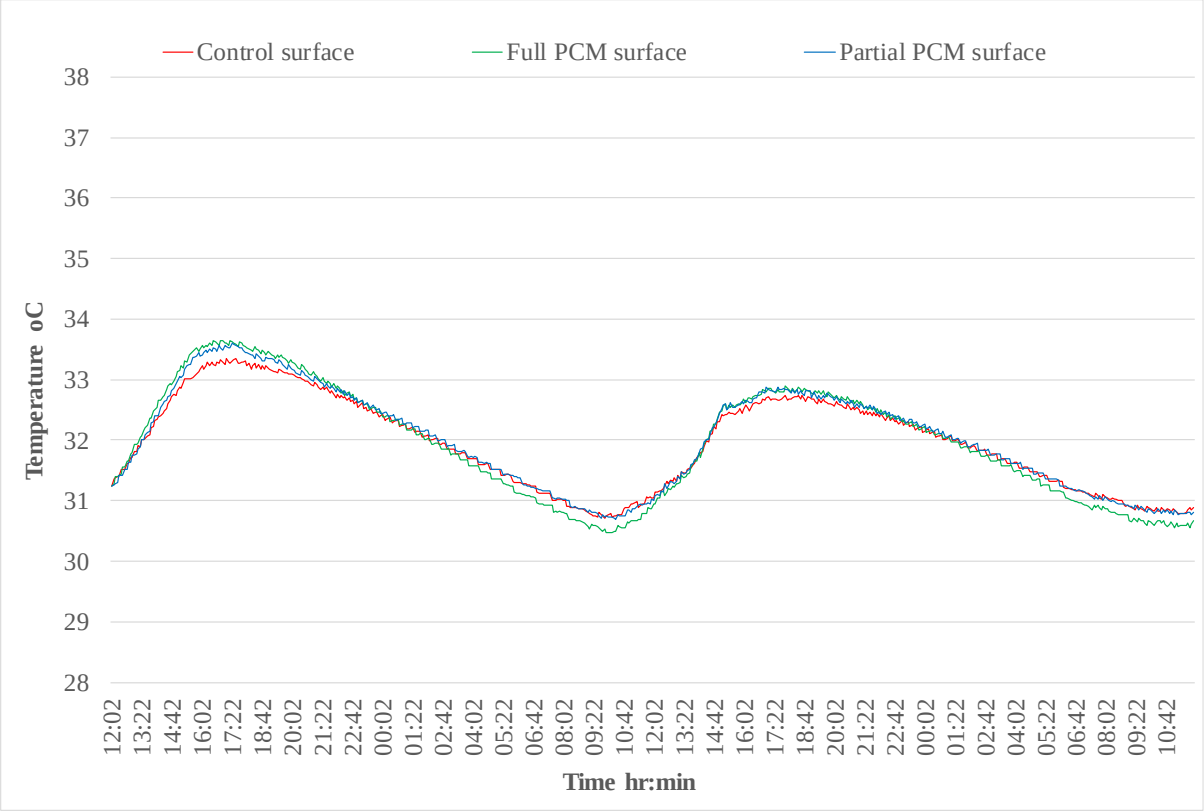


**Figure 7-19 Comparison of wall surface temperatures of the huts 20th – 22nd June 2017 - PCM fully melted**

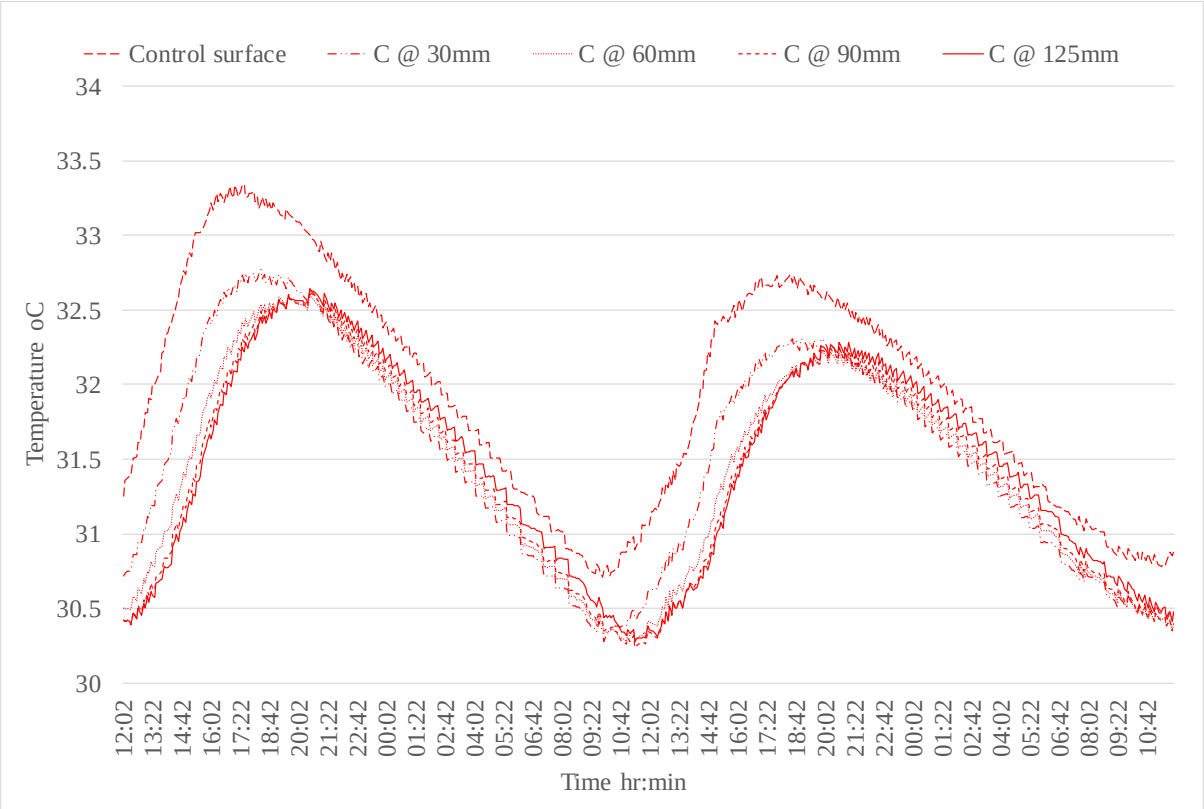


**Figure 7-20 Temperature profile at each depth through the wall of the Control hut, 20th – 21st June 2017**

in temperature between the internal air and internal wall of circa 3-4 $^{o}$C promotes heat transfer from the internal air into the cooler wall. The rate of heat transfer deeper into the wall reduces with increasing depth as, due to the specific heat capacity of the wall material, the inner wall material stores some of the heat and hence slows the rate of heat penetration deeper into the wall, creating the temperature differential between the surface and 60 mm depth. There is little difference between the temperature profiles at 60 mm, 90 mm and 125 mm in any of the huts. It can also be noted that the temperatures throughout the depth of the walls in both PCM huts remain over 30 $^{o}$C at all times so it can be assumed that the PCM is in a liquid state for the entire period. In Chapter 5 it was determined in the laboratory that, under steady-state conditions with a minimum temperature differential of 20 $^{o}$C through the depth of the test panel, the panel containing PCM had a lower overall thermal conductivity (0.10 W/mK) than the panel containing normal concrete in its inner leaf (0.13 W/mK). However, it can be concluded from this analysis of data collected from a 'real-life' scenario that while the temperature of the wall containing PCM is above the higher temperature of the PCM melt temperature range, the PCM remains in a fully melted state, and the heat transfer behaviour into and out of the wall is largely similar to that of a wall constructed with the control concrete, so each different type of wall is displaying a similar overall thermal conductivity. In this analysis steady-state conditions did not occur due to the varying internal and external temperatures and also the temperature differential across the depth of the walls was less than 20 $^{o}$C hence the heat flux at the surface of the wall would be lower. It can be concluded that under the dynamic nature of the temperatures on either side of the walls and relatively low temperature differential across the wall, the difference in overall thermal conductivity of the panels is not large enough to result in a significant difference in the rate of heat transfer through the wall.

It can also be concluded from this analysis that while the temperature of the wall remains above the upper temperature of the PCM melt temperature range, the PCM is in a liquid state and the heat transfer behaviour into and out of the wall is similar to that of the control concrete wall.

### 7.5.3 Thermal behaviour of walls when the PCM is engaged

To examine the influence of the presence of PCM in the walls of the huts under passive conditions, that is when the heaters were permanently off and there was no ventilation provided, all the data collected over the 18 months was reviewed (Figure 7-14) to identify periods during which the wall temperatures fluctuated above and below the melt temperature range of the PCM during passive conditions. Two periods were selected for closer examination, one during the winter season and one during the summer season.

*7.5.3.1 Thermal behaviour of walls under winter passive conditions*

Data from the period 9am 30th October to 8:55am on 2nd November 2018 was selected and plotted in detail to study the thermal behaviour of the walls under winter passive conditions. During this period the temperatures in the huts increased above the melt temperature range of the PCM as a result of radiative heat from the sun and despite low external air temperatures. The low external air temperatures overnight caused the wall temperatures to drop low enough for the PCM to solidify and purge its heat energy. The internal air temperatures in each hut were similar at the start of this period, ranging from 15.1 ºC to 15.5 ºC. Also the internal temperatures of the walls in each hut were very similar both across the three huts and through the depth of each wall, ranging from 17.3 ºC to 17.5 ºC. As the wall temperatures at the start of the analysis are below 20 ºC it can be assumed that the PCM is in a solid phase at the start of the analysis on the 30th October. The irradiance was relatively high on the 30th October and the 1st November as these were sunny days with minimal cloud. Figure 7-21 shows irradiance levels (up to 320 W/m$^2$) for the period together with the external air temperature (up to 10 ºC).

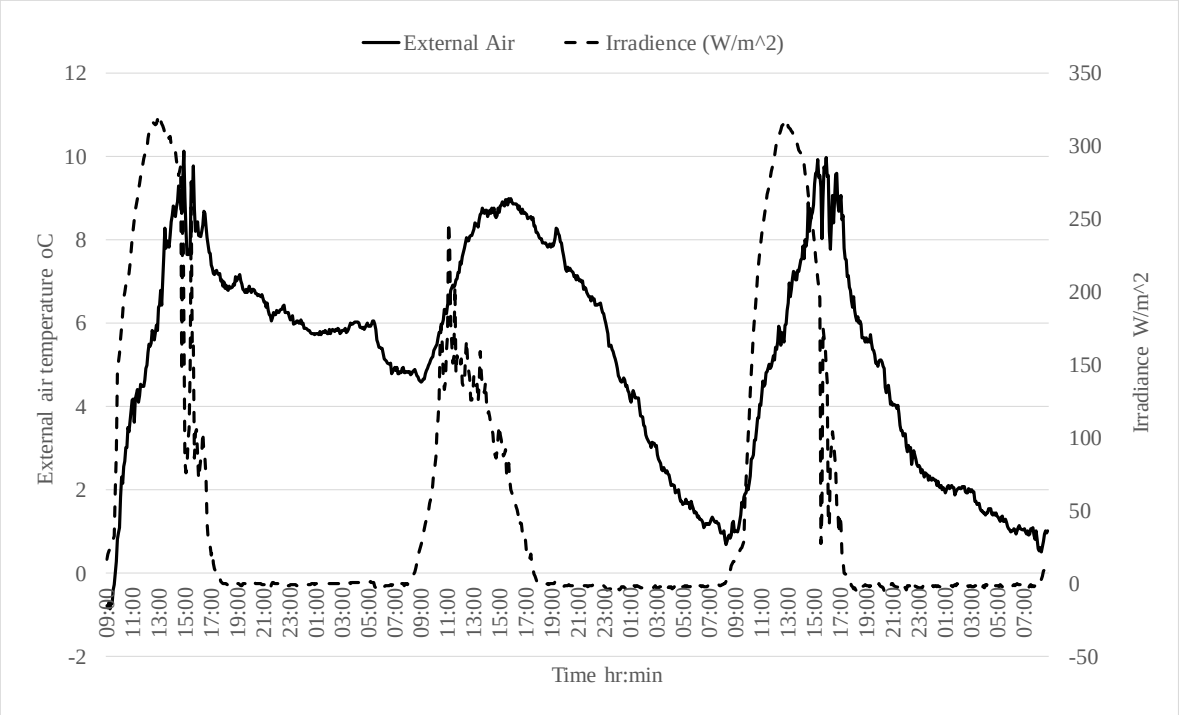


**Figure 7-21 9am, 30th Oct to 8:55am, 2nd Nov 2018- irradiance and external air temperature**

On the 30th October the irradiance remained above 200 W/m$^2$ from 10:30am to 14:40pm with peak levels of 320 W/m$^2$. On the 1st November the irradiance remained above 200 W/m$^2$ from 10:45am to 15:25pm with peak levels of 320 W/m$^2$. However on the 31st October the irradiance remained less than 200 W/m$^2$ for the whole day. The irradiance resulted in the wall temperatures increasing up to circa 23 ºC on both the 30th October and 1st November despite

external air temperature remaining below 10 ºC. As the onset melt temperature of the PCM is 20 ºC it can be assumed that the PCM within the wall partially melted on these days. However on the 31st October there was more cloud cover and less irradiance hence the wall temperatures in all the huts did not exceed 19 ºC and continued to decrease to 16 ºC so it can be assumed that the PCM within the wall solidified on the 31st October and hence the PCM was ready to absorb heat on the 1st November.

### Internal Air Temperatures

Figure 7-22 displays a comparison of the internal air temperatures of each hut over the said period. It can be observed from the figure that although the rates of heating and cooling are similar in all the huts, the peak temperatures in the Control hut on the 30th October and 1st November are greater than the peak temperatures reached in the huts containing PCM. The peak internal air temperatures for each hut on the 30th October and 1st November are provided in Table 7-1 as is the time at which the peak temperatures occur.

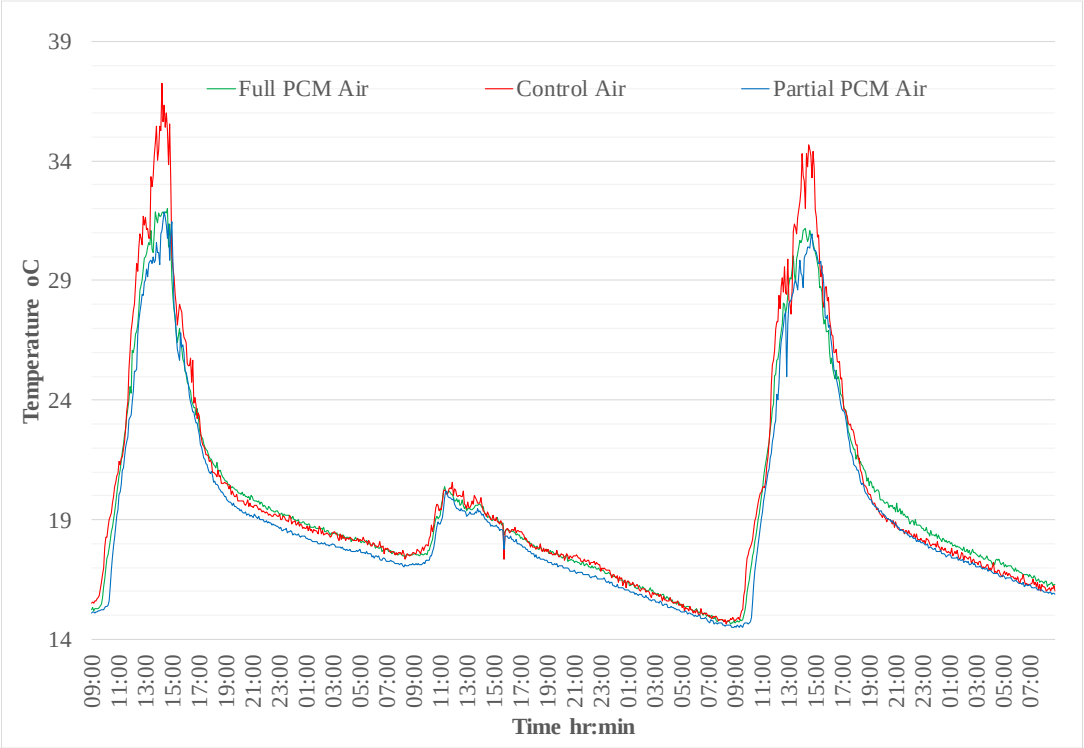


**Figure 7-22 Internal air temperatures on 30st October to 2nd November 2018**

**Table 7-1 Peak air temperatures in huts on 30st October and 1st November 2018**

| | Control hut | | Full PCM hut | | Partial PCM hut | |
|---|---|---|---|---|---|---|
| | Peak Temperature (ºC) | Time (hr:min) | Peak Temperature (ºC) | Time (hr:min) | Peak Temperature (ºC) | Time (hr:min) |
| 30th Oct | 37.3 | 14:15 | 32.0 | 14:40 | 31.9 | 14:25 |
| 1st Nov | 34.7 | 14:30 | 31.2 | 14:15 | 31.0 | 14:45 |

There is little difference between the peak temperatures of both huts containing PCM, however there is a significant difference between the peak temperatures in the PCM huts and the Control hut of circa 5 $^{o}$C on the 30$^{th}$ October and circa 3.5 $^{o}$C on the 1$^{st}$ November. It is interesting to note that peak internal air temperatures of over 30 $^{o}$C were reached despite external air temperatures of less than 10 $^{o}$C and no heaters were on in the huts, albeit in a relatively small room volume and a well-insulated space. This highlights the impact of solar gain on the internal environment particularly when ventilation is not provided. The ability of the PCM to reduce overheating effects is clearly demonstrated, however it should also be noted that the ratio of the surface area of wall to the volume of air in the test huts is relatively high compared to a typical internal space in an office or school building so in a more realistic scenario the influence of the PCM on the peak internal air temperatures may be somewhat reduced.

To determine any thermal inertia effects, the time taken for the internal air in each hut to reach a temperature of 31 $^{o}$C – selected because it is the lowest peak temperature - on the 30$^{th}$ October and 1$^{st}$ November from a start time of 9am is noted in Table 7-2.

**Table 7-2 Time taken for internal air temperatures to reach 31 $^{o}$C – from 9am**

| | Control Hut | Full PCM Hut | Partial PCM Hut |
|---|---|---|---|
| Time taken from 9am to reach 31.0 $^{o}$C, 30$^{th}$ Oct | 3hr 35mins | 4hr 25mins | 5hr 15mins |
| Time taken from 9am to reach 31.0 $^{o}$C, 1$^{st}$ Nov | 4hr 25mins | 5hr 8mins | 5hr 45mins |

The huts containing PCM also provide thermal inertia, with the Full PCM hut taking an average of 47 minutes longer than the Control hut to reach 31 $^{o}$C over the two days and the Partial PCM hut taking on average 90 minutes longer to reach 31 $^{o}$C than the Control hut. However when considering the temperature data in detail, it is noted that the Partial PCM is slower to start increasing in temperature at 9 am. Between 9 am and 10 am the air in the Partial hut only increases 0.28 $^{o}$C whereas the Control hut and Full PCM hut increase by 2.78 $^{o}$C and 1.71 $^{o}$C respectively. Subsequently, as can be observed from Figure 7-22 the rate of temperature increase in the Full PCM and Partial PCM huts are similar.

On the 31$^{st}$ October the irradiance levels are much lower and the peak temperatures in all the huts are similar at 20.6 $^{o}$C, 20.4 $^{o}$C and 20.2 $^{o}$C in the Control hut, Full PCM hut and Partial PCM hut respectively. These temperatures are too low to activate the PCM.

**Wall surface Temperatures**

Figure 7- 23 shows the temperatures on the surface of the wall in each hut during this period. It can be noted that the wall surface temperatures range from 16/17 $^{o}$C to over 24 $^{o}$C on the 30$^{th}$ October and 1$^{st}$ November which includes the melt temperature range of the PCM. Despite this there is little difference in the rate of heating between all the huts. During the cooling phase the Full PCM hut displays a slower rate of cooling which may be due to the fact that as the peak temperature in the Full PCM hut is lower than the other two huts, the temperature differential between the surface of the wall and internal air is lower during the cooling phase. Also, the temperature data collected in the Full PCM hut shows that the temperatures in the outer 60 mm of the inner leaf increase slightly above the onset melt temperature of 20 $^{o}$C hence marginally more PCM may be engaged in the Full PCM hut than the Partial PCM hut which does not contain any PCM in the outer 60 mm of the inner leaf.

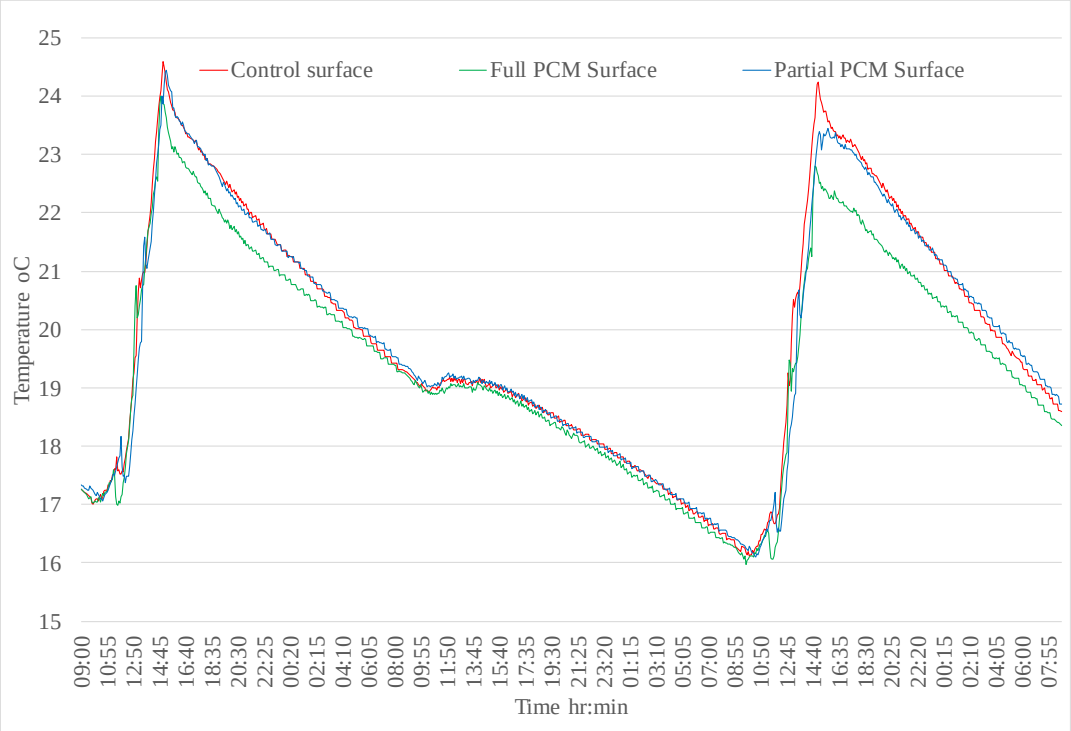


**Figure 7- 23 Temperatures on the surface of the wall in each hut**

Table 7-3 confirms the peak temperatures on the 30$^{th}$ October and 1$^{st}$ November for comparison.

**Table 7-3 Peak wall surface temperatures in huts on 30$^{st}$ October and 1$^{st}$ November 2018**

| | Control hut | | Full PCM hut | | Partial PCM hut | |
|---|---|---|---|---|---|---|
| | Peak Temperature ($^{o}$C) | Time (hr:min) | Peak Temperature ($^{o}$C) | Time (hr:min) | Peak Temperature ($^{o}$C) | Time (hr:min) |
| 30$^{th}$ Oct | 24.6 | 15:00 | 23.9 | 15:00 | 24.4 | 15:15 |
| 1$^{st}$ Nov | 24.2 | 15:05 | 22.8 | 14:50 | 23.4 | 15:45 |

The greatest difference between the peak temperatures occurs between the Full PCM hut and the Control hut on the 1st November with a difference of 1.4 ºC. The thermal inertia effects at the surface of the wall are small with the temperatures in both the Partial PCM hut and Full PCM hut lagging behind the Control hut by 20 minutes during the heating phase on the 30th October and the 1st November. This reflects the extra heat absorption of the PCM panels.

It is notable that the difference between the wall surface temperatures is small whereas the difference between the air temperature in the Control hut and both the PCM huts is perceptible at circa 5 ºC at peak values. Given that the maximum external air temperature over this period is 10 ºC and the minimum internal air temperature is higher at 15 ºC, the increase in external air temperature does not contribute significantly to the rise in the internal air temperature. The increase in temperature of the internal air and walls is largely a result of solar radiation. The faster rate of increase in the temperature of the air in the Control hut may be attributed to the fact that the Control hut walls have a lower thermal storage capacity than the walls that contain PCM. As a result the Control hut walls reflect more radiant heat back into the internal air in the hut. The walls containing PCM in both the Full PCM hut and the Partial PCM hut absorb more of the solar heat and as the PCM provides greater latent heat capacity, the increase in temperature of the PCM walls at depth is not greater than the walls of the Control hut.

**Temperature at 30 mm depth**

Figure 7-24 displays the temperatures within the North wall of each hut at a depth of 30 mm. The difference between the temperature profiles reflects the temperature profiles at the surface of the wall in each hut. The effect of the PCM in both the huts containing PCM is evident however the effect in the Full PCM hut is more significant with lower peak temperatures at a depth of 30 mm of circa 1 ºC. In the Full PCM hut there is a noticeable reduction in the rate of temperature increase at circa 20.5 ºC (Point A). This coincides with the temperature deeper within the Full PCM hut inner leaf (greater than 60mm depth) reaching the start of the melt temperature range and hence the PCM within the full 125 mm depth of the inner leaf is within the melt temperature range. As a result it is feasible that a larger volume of PCM is engaged in the Full PCM hut wall.

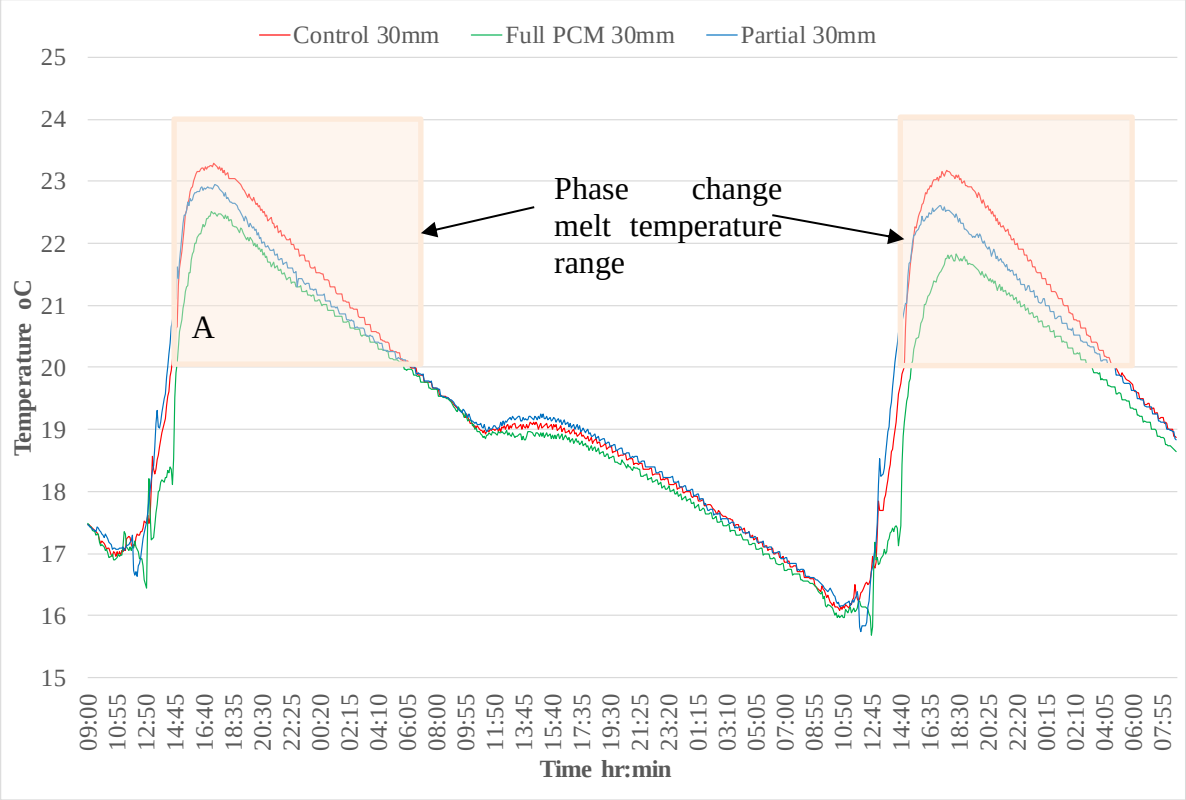


**Figure 7-24 Temperature at 30 mm depth in each hut, 30th October to 2nd November 2018**

The peak temperatures at a depth of 30 mm for each hut on the 30th October and 1st November are provided in Table 7-4. The peak temperatures are on average 2.2 ºC and 2.6 ºC higher than the onset melt temperature of the PCM in the Full PCM and Partial PCM huts respectively. Evidence that the PCM in the Full PCM hut is melting at this depth is provided by the slower rate of temperature increase in the Full PCM hut. The rate of temperature increase in the Partial PCM hut is similar to that of the Control hut up until it reaches a temperature of 22 ºC at which the rate of temperature gain reduces. The lower temperatures in the Full PCM hut compared to the Partial PCM hut is a result of the PCM in the outer 60 mm of the Full PCM hut walls partially melting and absorbing some heat as the temperatures in this zone of the wall reach the onset melt temperature of the PCM.

**Table 7- 4 Peak wall temperatures at 30 mm depth, 30th October and 1st November 2018**

| | Control hut | | Full PCM hut | | Partial PCM hut | |
|---|---|---|---|---|---|---|
| | Peak Temperature (ºC) | Time (hr:min) | Peak Temperature (ºC) | Time (hr:min) | Peak Temperature (ºC) | Time (hr:min) |
| 30th Oct | 23.3 | 17:20 | 22.5 | 17:10 | 23.0 | 17.25 |
| 1st Nov | 23.2 | 17:45 | 21.8 | 18:05 | 22.6 | 17:15 |

**Temperature at 60 mm, 90 mm and 125 mm depth**

In Figure 7-25 the temperatures at depths of 60 mm and 90 mm in all huts are plotted together to highlight any difference between the temperature profiles. The temperature plots for the Partial PCM hut and the Control hut indicate that the temperature differential between 60 mm depth and 90 depth mm is very small. There is also no significant difference between the temperature profiles of the Control hut and the Partial PCM hut which is expected as at these depths, the material of the inner leaf of the wall is the same, that is, normal concrete. In the Full PCM hut above 20 $^{o}$C, there is a small difference between the temperature at 60 mm depth and at 90 mm depth and the rate of temperature increase at 90 mm depth reduces once the temperature reaches circa 20 – 21 $^{o}$C indicating that some of the PCM at this depth is engaged and starts to melt absorbing heat and hence reducing the rate of temperature increase (Point A).

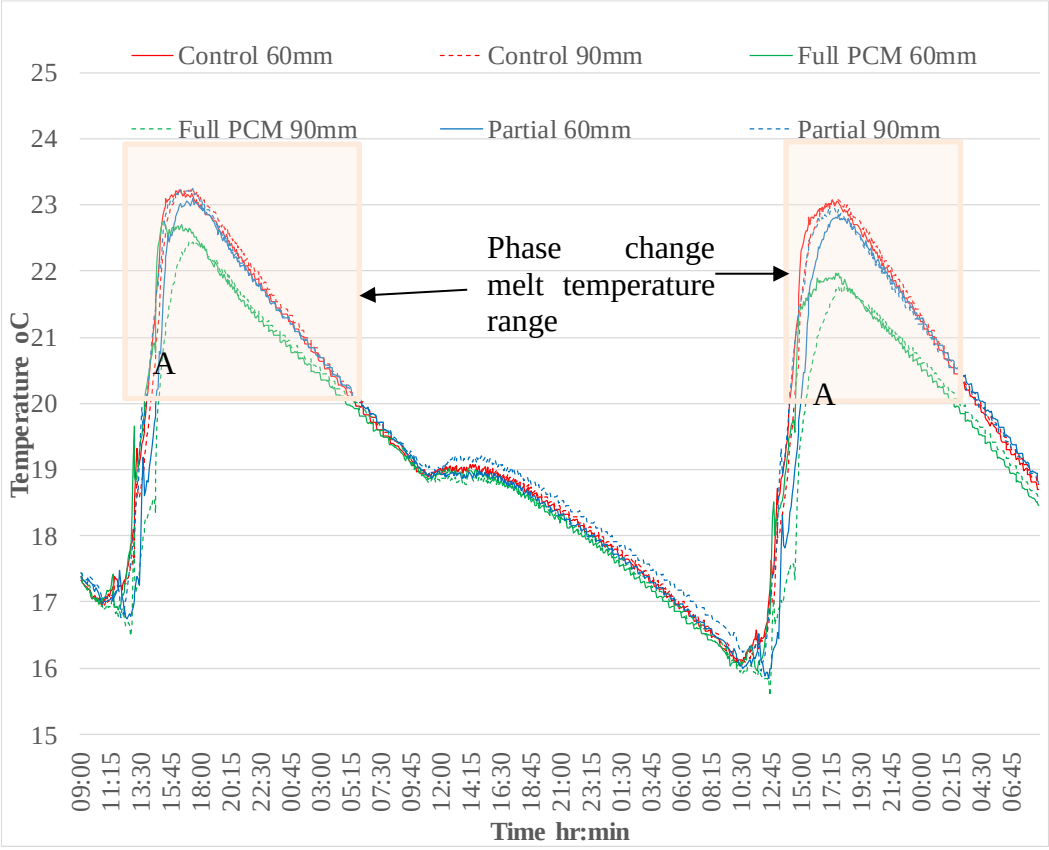


**Figure 7-25 Temperatures at 60 mm and 90 mm depth in each hut, 30th October to 2nd November 2018**

Figure 7-26 displays the temperature profile at a depth of 125 mm, the outside surface of the inner wythe of the panel. The peak temperatures at this depth are circa 1- 1.5 $^{o}$C lower than the peak temperatures recorded at 90 mm depth indicating the reduction in heat energy reaching this depth. It is notable that the temperature in both PCM huts increases above the onset melt temperature at this face by at least 1 $^{o}$C indicating potential for PCM to be engaged at this depth under these thermal conditions.

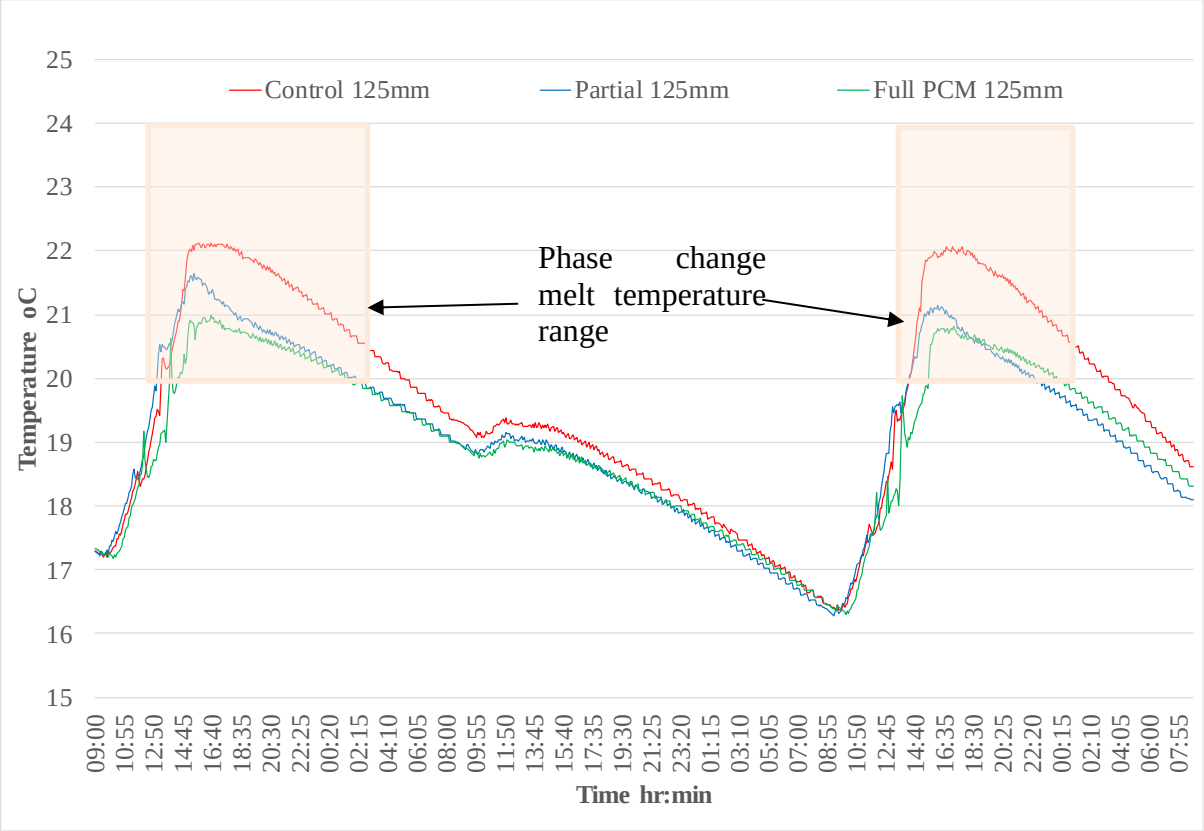


**Figure 7-26 Temperature at 125 mm depth in each hut, 30th October to 2nd November 2018**

Figure 7-27 provides the temperature profile through the depth of the North wall in each hut taken at 2 hour intervals from 9am to 21pm on the 30th October. The dashed lines are the temperature profiles post peak internal and external temperatures, during the cooling period. It can be observed that the insulation layer is buffering the internal leaf of the wall from changes in the external air temperature. Also the peak temperature at the outer surface of the inner leaf of the Control hut is 1.2 ºC higher than the same location in the Full PCM hut and 0.5 ºC higher than the Partial PCM hut. The temperatures through the depth of the wall are the same at the start of the heating period on the 30th and as the huts have the same construction and orientation, each hut is subjected to the same heating regime through solar radiation. The lower temperatures at the outer surface of the inner leaves of the PCM walls is an indication of heat being absorbed by the phase change of the PCM and hence less heat is penetrating through to the outer surface of the wall. As this effect is greater in the Full PCM hut it indicates that some of the PCM in the outer half of the inner leaf of the Full PCM hut wall is melting and absorbing slightly more heat than the wall in the Partial PCM hut which only contains PCM in the first 60 mm depth. However this additional engagement of the PCM appears to have little impact on the internal air temperatures which are similar in both PCM huts.

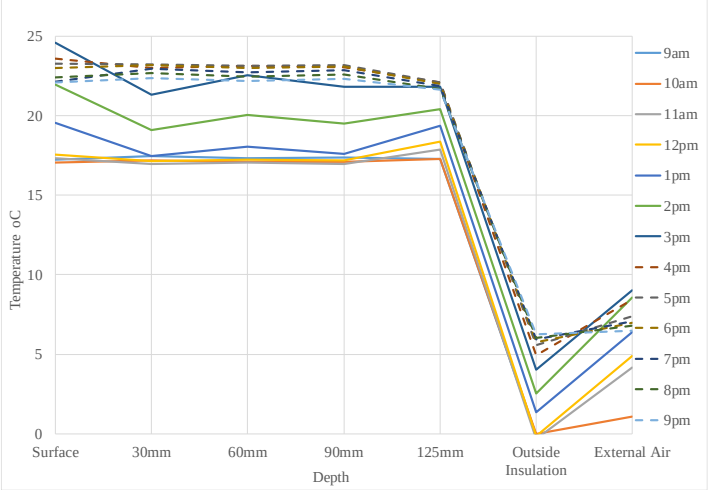


(a)

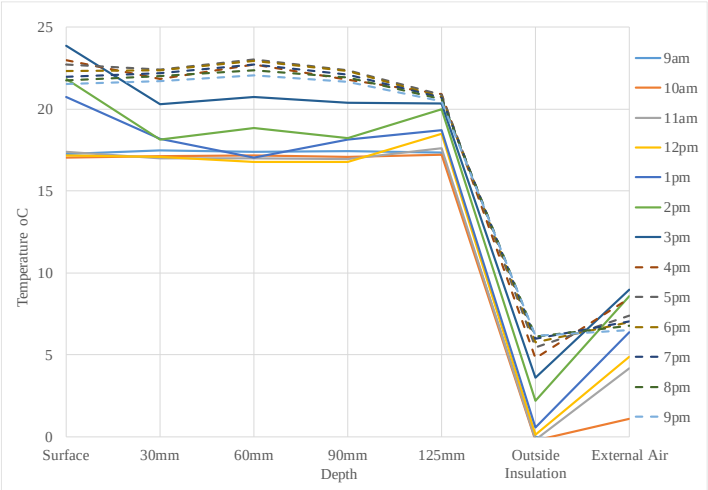


(b)

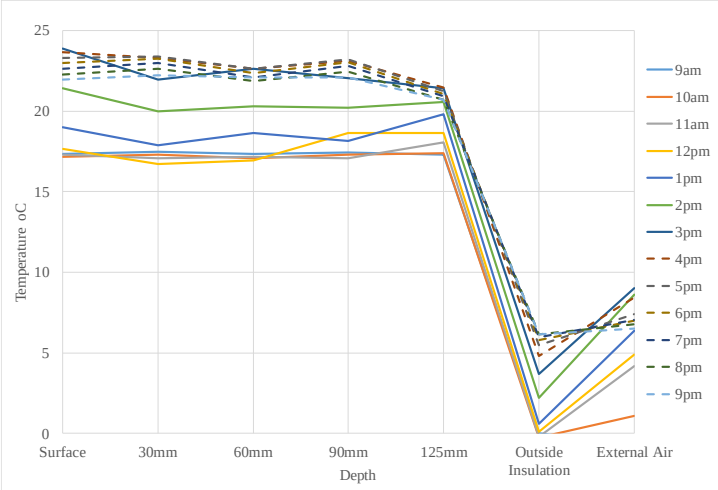


(c)

**Figure 7-27 Temperature profile through depth of wall in (a) Control hut, (b) Full PCM hut and (c) Partial PCM hut, taken at 2 hour intervals from 9am to 21pm on 30th October**

Overall this data analysis highlights the impact of solar irradiance during winter on internal temperatures in buildings. Due to the significant heat transfer to the walls of the hut through solar radiance, the temperature of the inner leaf of the hut walls increased above the onset melt temperature of the PCM and hence much of the latent heat capacity of the walls containing PCM was engaged. This resulted in lower internal air temperatures in the PCM huts with both the Full PCM hut and the Partial PCM hut providing a similar substantial reduction in internal air temperature (5 $^{o}$C).

*7.5.3.2 Thermal behaviour of walls under summer passive conditions*

Data from the period from 9am on the 9$^{th}$ June to 6am on 11$^{th}$ June 2017 were selected and plotted in detail to study the thermal behaviour of the walls under summer passive conditions. This particular data was selected as the temperatures within the walls in each of the huts were similar at the start of the period (22.3 $^{o}$C) so the baseline thermal conditions in each of the huts at the start of the period were similar. During this period the air and wall temperatures in the huts fluctuated within and above the melt temperature range but did not drop low enough at night to cause the PCM to solidify because the external air temperatures were not low enough. However it is of interest to examine the impact, if any, that the presence of PCM may have when the temperature is only fluctuating within the melt temperature range, so the PCM is only ever partially melted.

Figure 7-28 displays the external air temperatures and irradiance levels for this period. On the 9$^{th}$ June the irradiance levels increased above 200 W/m$^2$ between 7:30am and 17:30pm, peaking at levels of 1000 W/m$^2$. There were some clouds which cause the irradiance levels to fluctuate. On the 10$^{th}$ June the irradiance levels increased above 200 W/m$^2$ between 11:15am and 18:15pm, peaking at a level of 900 W/m$^2$. The external air temperature ranged from 10 $^{o}$C to 20 $^{o}$C on the 9$^{th}$ of June and 12 $^{o}$C to 22 $^{o}$C on the 10$^{th}$ June. Overall, in comparison with the winter passive external conditions, during this period the external air temperature overnight was in the order of 5 $^{o}$C to 10 $^{o}$C warmer and the irradiance levels were significantly greater over a longer period during the day, not surprisingly.

**Internal air temperatures**

Figure 7-29 displays the internal air temperatures in the huts on these days. Table 7-5 provides the peak internal air temperature reached in each hut on each day and the time at which it occurred. It can be noted that the internal air temperature profile in each hut was very similar with a peak air temperature in the Control hut of up to only 0.6 $^{o}$C greater than those reached

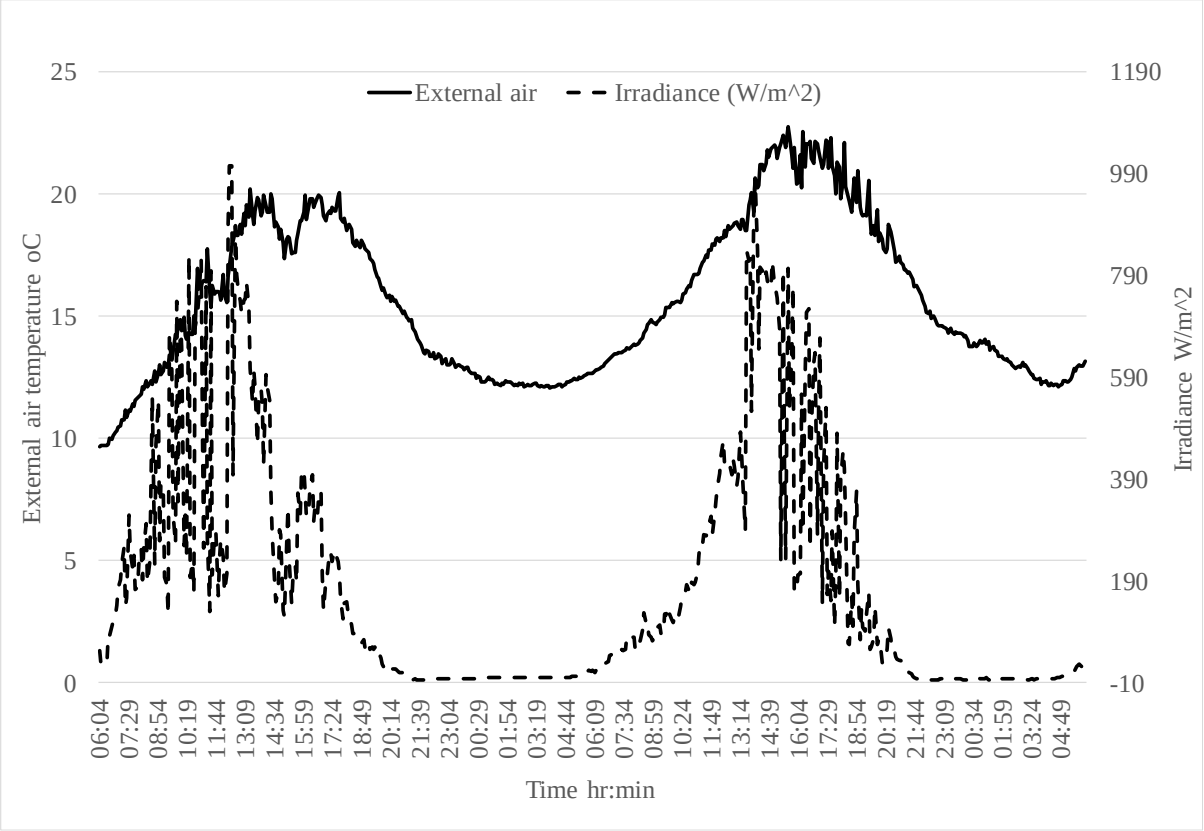


**Figure 7-28 6am, 9th June to 6am, 11th June 2017- irradiance and external air temperature**

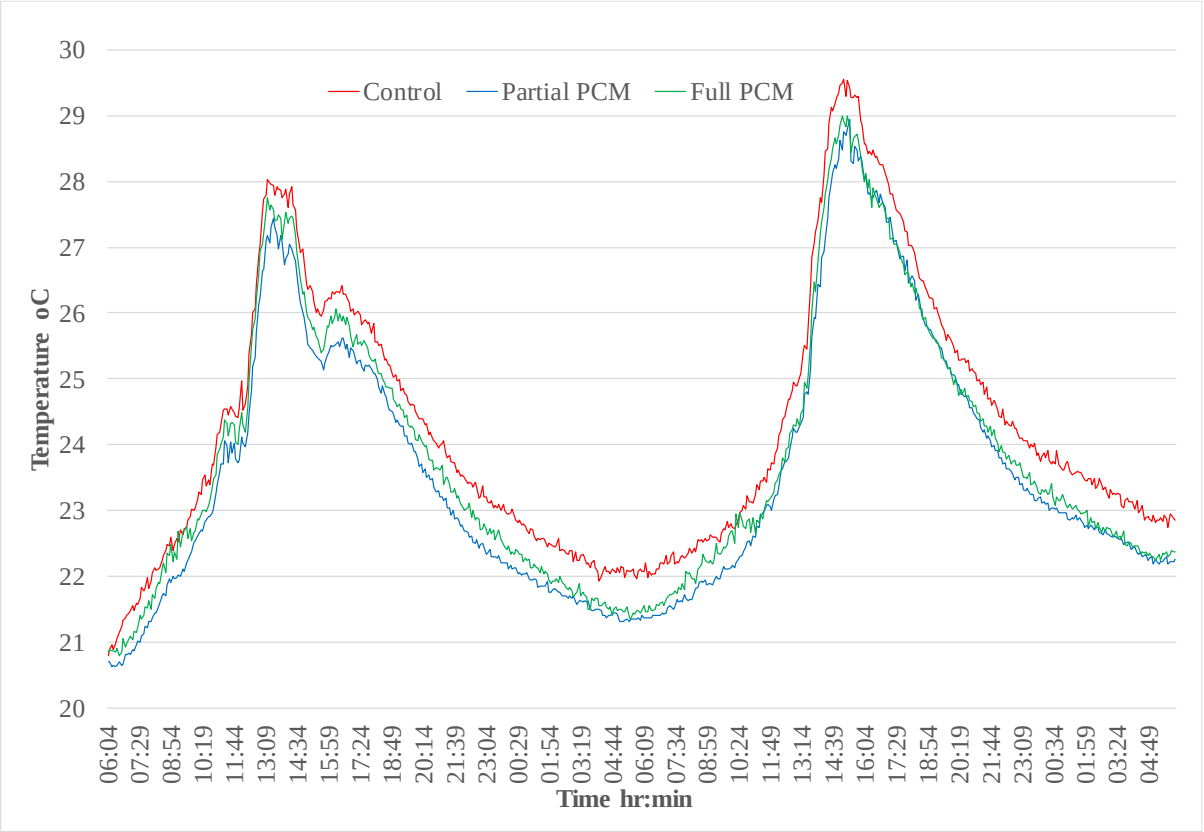


**Figure 7-29 Internal air temperatures on 9th June to 10th June 2017**

in the huts containing PCM. There was also no significant thermal inertia effect with all the peak temperatures occurring within 15 to 20 minutes of each other suggesting that the additional thermal storage capacity provided by the PCM was not being engaged. This is expected as the starting air temperatures and wall temperatures in the huts (22.3 $^{o}$C) are greater than the onset melting temperature of the PCM and also just below the onset solidification temperature of 22.9 $^{o}$C. In these thermal conditions it can be assumed that most of the PCM is in a melted state at the start of the heating period and hence cannot provide any further latent heat capacity.

**Table 7-5 Peak air temperatures in huts on 9th June to 10th June 2017**

| | Control hut | | Full PCM hut | | Partial PCM hut | |
|---|---|---|---|---|---|---|
| | Peak Temperature ($^{o}$C) | Time (hr:min) | Peak Temperature ($^{o}$C) | Time (hr:min) | Peak Temperature ($^{o}$C) | Time (hr:min) |
| 9th June | 28.0 | 13:14 | 27.4 | 13:29 | 27.8 | 13.14 |
| 10th June | 29.6 | 15:09 | 29.0 | 15:04 | 28.9 | 15:24 |

It is also interesting to note that the peak internal air temperatures achieved in the Control hut during summer passive conditions at 28 $^{o}$C, was less than that achieved during winter passive conditions at 34 $^{o}$C despite higher levels of irradiance occurring at the site during the summer dates. The heat gain in the huts is largely due to the absorption of the incident rays by the exposed concrete surfaces. The area of concrete surface that is exposed to solar irradiance is greater in winter despite the higher irradiance on the summer days. To depict the difference between the internal surface area that is exposed to solar irradiance in winter and summer, surface radiation plots were created for a hut using Comsol software, as shown in Figure 7-30. Real solar irradiance data recorded on a winter day and a summer day were imported into the software and applied to a model of the hut (as discussed presently in Chapter 8). Radiation plots for the internal surfaces were derived and extracted at particular times as noted in Figure 7-30. It can be observed from Figure 7-30 that the area of solar irradiance applied to the internal surface of the hut is greater in winter and primarily on the walls of the hut. In summer, less irradiance enters the hut and it is primarily on the floor. In this research project the floors have been thermally isolated with a layer of insulation so the floor does not absorb any significant incident solar radiation.

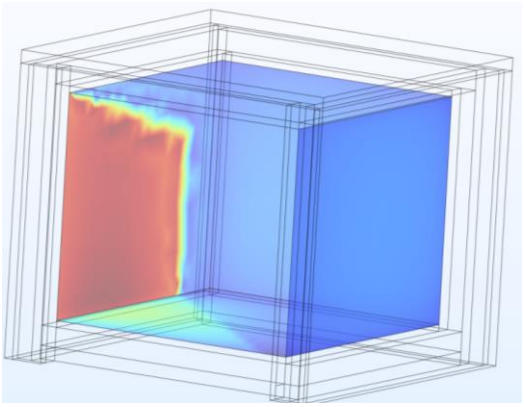

**(i) 10am -West wall**

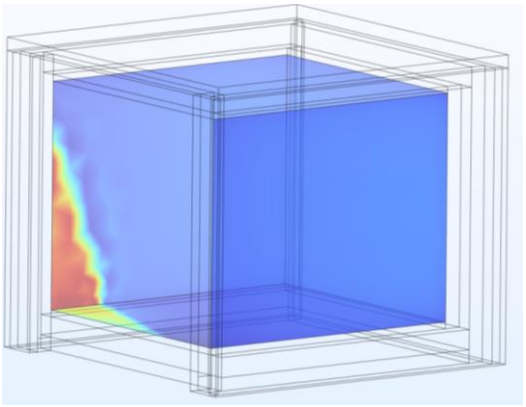

**(i) 10am – West wall**

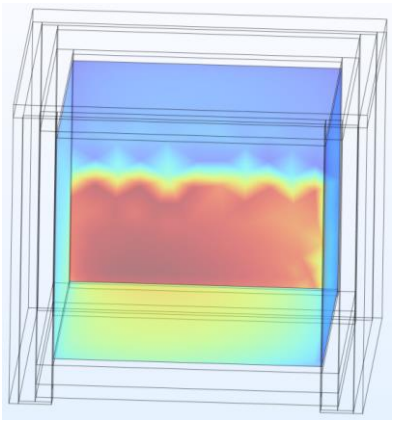

**(ii) Solar noon –*North <u>wall</u>***

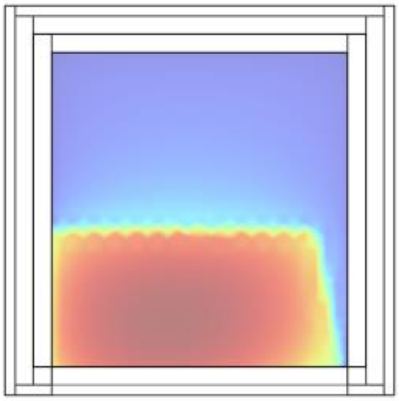

**(ii) Solar noon *<u>Floor</u> plan***

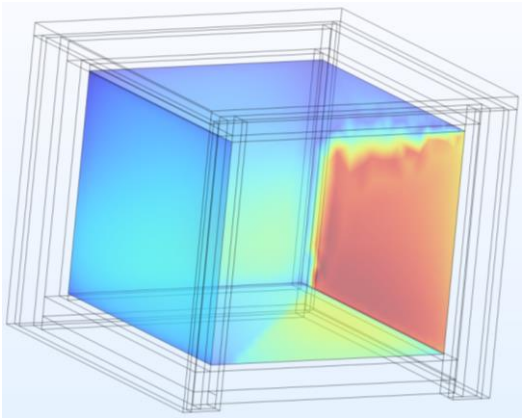

**(iii) 4pm –East wall**

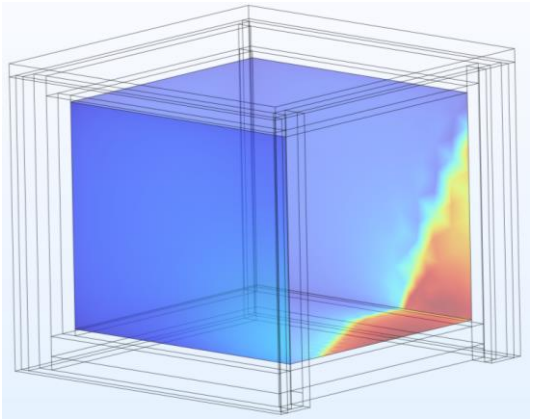

**(iii) 4pm- East wall**

**(a)** **(b)**

**Figure 7-30 Solar incidence in huts at 10am, solar noon and 4pm on (a) 30th October and (b) 10th June**

### Wall surface temperatures

Figure 7-31 displays the wall surface temperatures on the surface of the North wall in each hut between 6am on 9th June and 6am on 11th June 2017. The temperature profiles at the wall surface in each hut were similar with the Control hut displaying the highest peak temperatures of 24.5 ºC on the 9th June at 18:19pm and 25.3 ºC on 10th June at 18:39pm. The Partial PCM

hut displayed the lowest peak temperatures of 24 ºC on the 9th June at 18:24pm and 25.0 ºC on 10th June at 17:49pm, so the greatest difference between the lowest peak and highest peak temperatures was 0.5 ºC which is insignificant, that is, less than the calibrated accuracy of the thermocouples (+/- 0.86 ºC).

The range of the temperature fluctuation in each of the huts was circa 22 ºC to 25 ºC so it must be assumed that most of the PCM within the wall was melted at the beginning of this period so was unable to contribute to additional heat energy absorption behaviour. Hence the thermal profiles of the huts were similar within experimental variability.

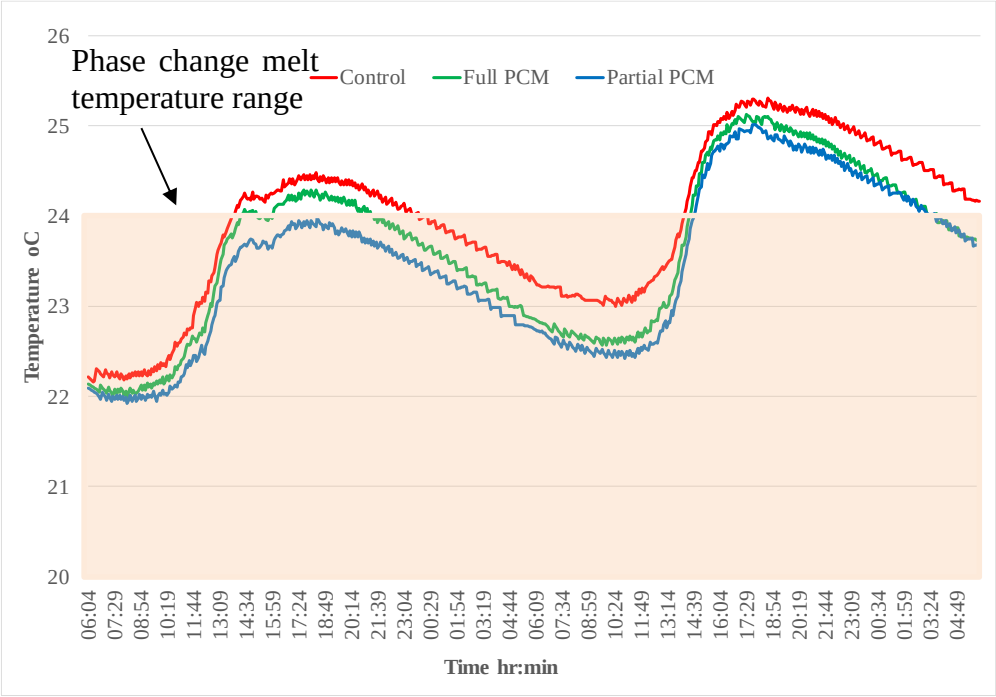


**Figure 7-31 Wall surface temperatures on 9th June to 10th June 2017**

The thermal profiles taken at 30 mm, 60 mm, 90 mm and 125 mm in June are provided in Appendix O and display similar thermal behaviour at each of the depths in all the huts. It can be noted from these plots that the PCM huts take slightly longer to start increasing in temperature at the start of the heating period. Although the impact of the PCM is minimal during this period, as the temperature of the wall is fluctuating within the melt temperature range, it can be assumed that some phase change is taking place deeper in the wall. Although the reduced rate of temperature increase caused by the melting of the PCM is insignificant at the front of the wall, the effect is cumulative with increase in depth into the wall as more heat energy is absorbed by the PCM as the heat penetrates the wall. This effect can be observed in Figures 7-32, 7-33 and 7-34 which show the temperature profiles at depths of 60 mm, 90 mm and 125 mm for each hut together on one plot. In the Control hut there is no difference in the

temperature profiles at 60 mm, 90 mm and 125 mm. However in the Full PCM hut and the Partial PCM hut the temperatures at 90 mm and 125 mm are slower to start to increase and reach lower peak temperatures than the temperatures at 60 mm. This behaviour is accentuated in the Full PCM hut which may be indicative of melting of the PCM that is present between 60 mm and 90 mm which is not present in the Partial PCM hut.

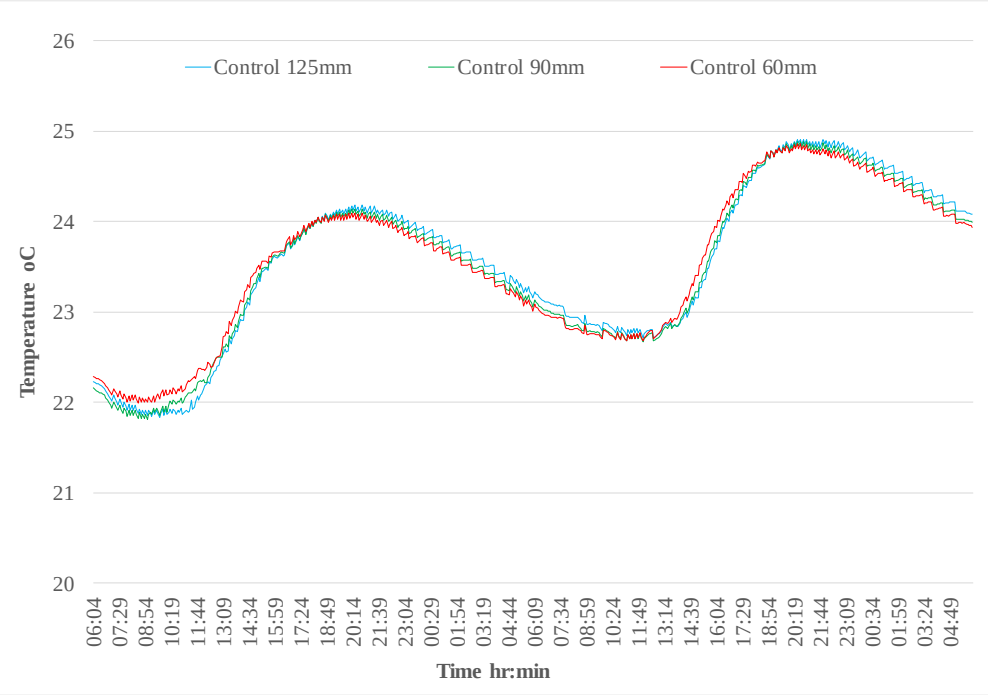


**Figure 7-32 Control hut temperature profiles at 60 mm, 90 mm and 125 mm depths, 9th June to 10th June 2017**

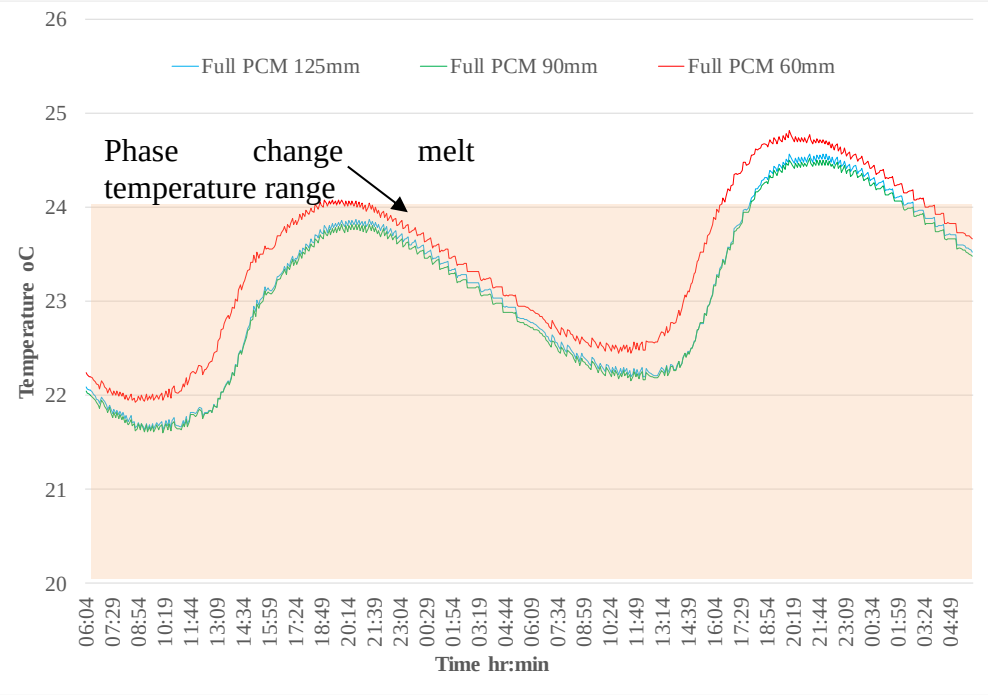


**Figure 7-33 Full PCM hut temperature profiles at 60 mm, 90 mm and 125 mm depths, 9th June to 10th June 2017**

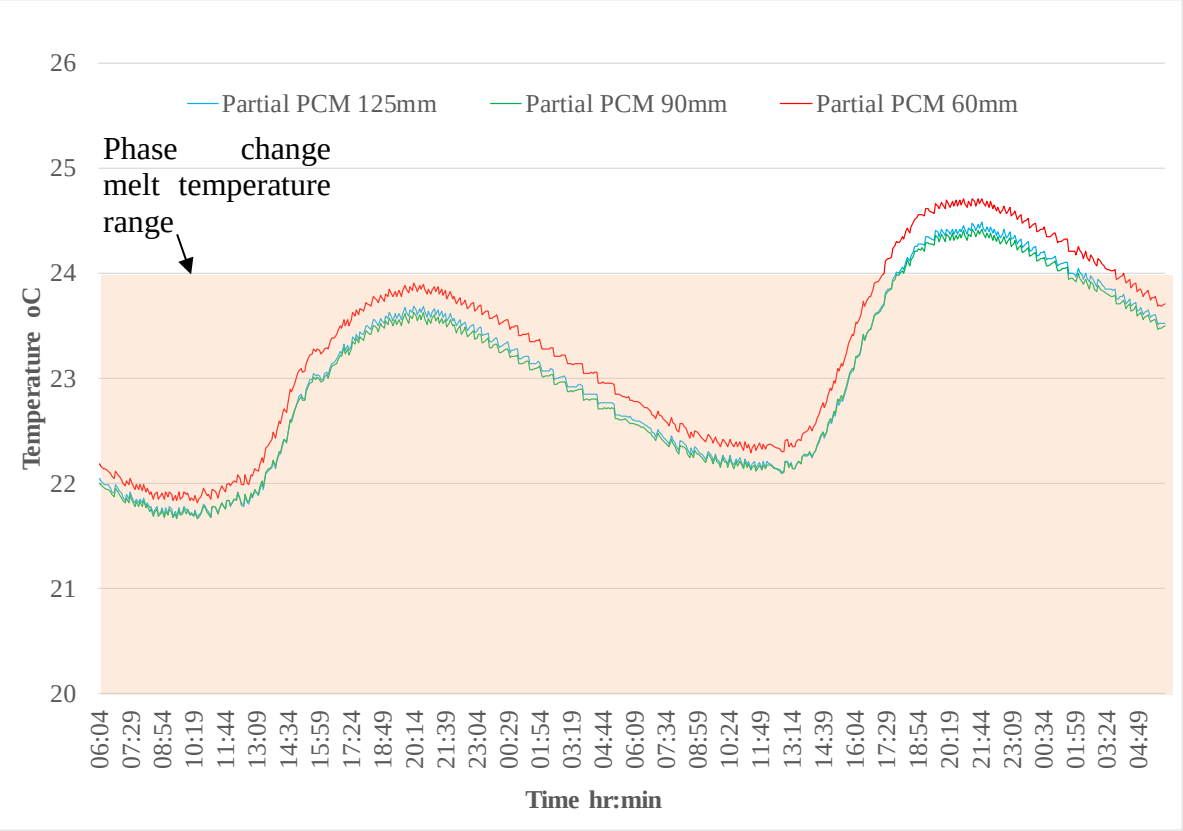


**Figure 7-34 Partial PCM hut temperature profiles at 60 mm, 90 mm and 125 mm depths, 9th June to 10th June 2017**

*7.5.3.3 Thermal behaviour of walls under applied heat load with no overnight ventilation*

To examine the influence of the presence of PCM in the walls of the huts when a heat load is applied, data from the 1st and 2nd of May 2017 is plotted in more detail. This data was selected as the air and wall temperature in each of the huts was similar at the start of the period, 00:00 on 1st May, that is, within less than 0.1 ºC of each other. Also the starting wall temperatures were circa 17 ºC so the PCM can be assumed to be solid throughout the walls. During this period the heaters were set to come on between 8:30am and 3:30pm each day, whenever the temperature fell below a set point of 20 ºC, to simulate a typical heating pattern in, say, a school environment.

**Comparison of internal air temperatures**

Figure 7-35 displays a comparison of the internal air temperatures of each hut over the two day period. It can be noted from the figure that the temperature in the Control hut increased to 27 ºC when the heaters were on and then cooled to 19 ºC overnight before increasing again on day two to 29 ºC. During the heating period on the 2nd the temperatures are slightly erratic, however this can attributed to the variance in the solar irradiance as can be observed from Figure 7-36 which displays the external air temperature and irradiance for the period.

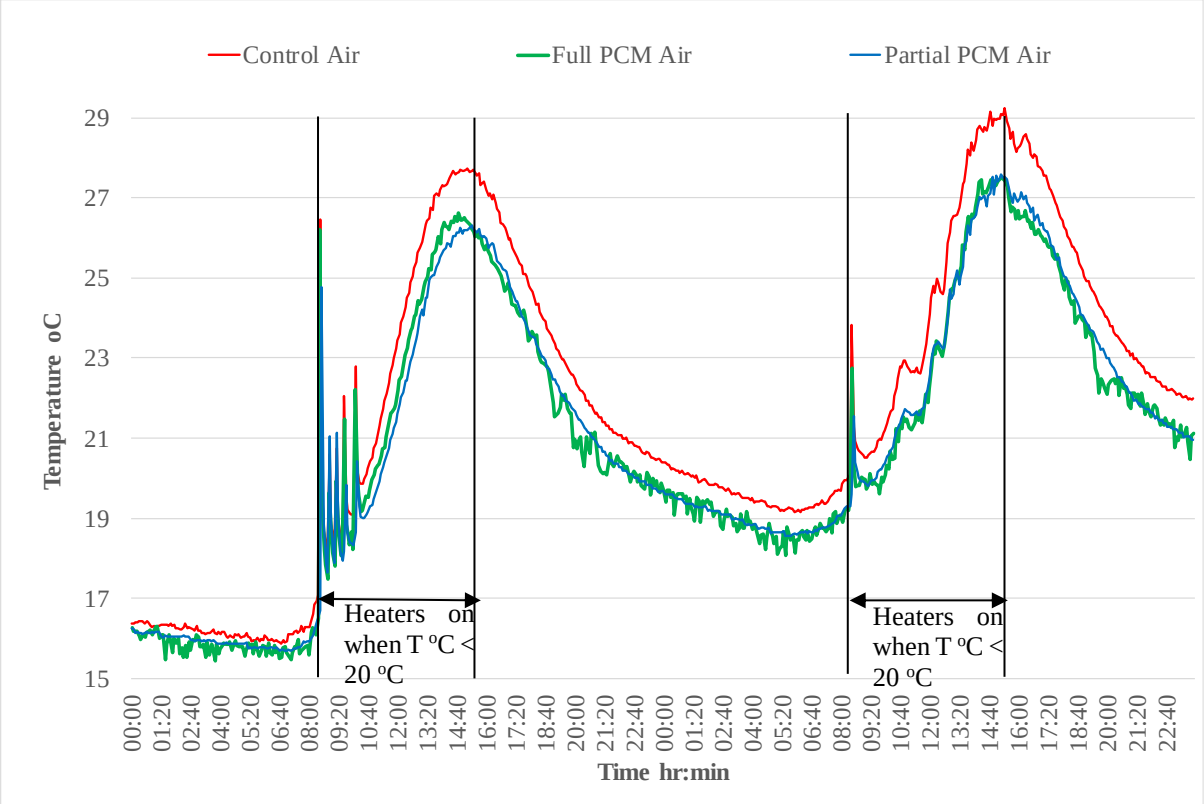


**Figure 7-35 Internal air temperatures on 1st and 2nd May 2017**

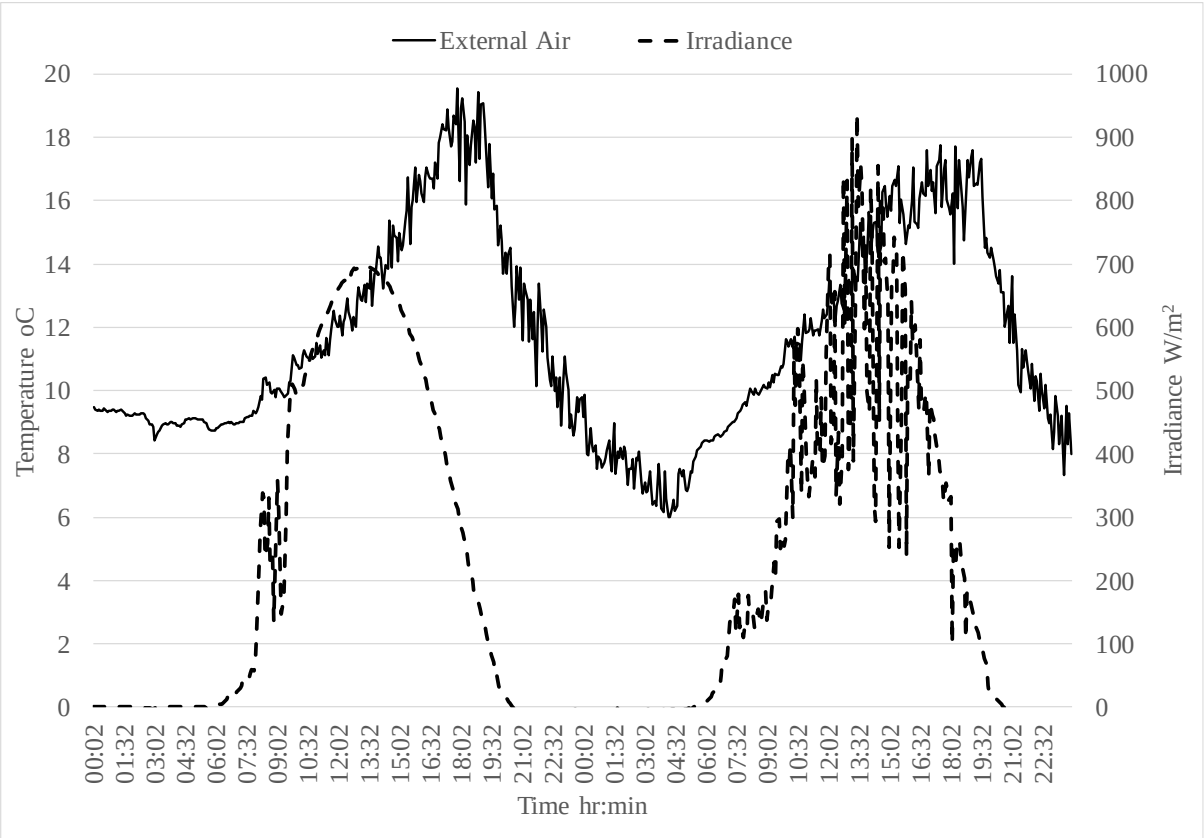


**Figure 7-36 External air temperature and Irradiance on 1st and 2nd May 2017**

The following observations can be made:

- Both PCM huts were cooler than the control hut
- During the heating period the Full PCM hut was on average 1.0 $^{o}$C cooler than the Control hut on the 1$^{st}$ May and 1.4 $^{o}$C cooler on the 2$^{nd}$ May. The greater difference on the 2$^{nd}$ day can be attributed to the fact that at the start of the heating period of day two the internal air temperatures in the PCM huts were already 0.6 $^{o}$C cooler
- During the cooling period of 3:30 pm to midnight, the Full PCM hut was on average 1.1 $^{o}$C cooler than the Control hut on 1$^{st}$ May and 1.3 $^{o}$C on 2$^{nd}$ May
- During the heating period the Partial PCM hut was on average 1.4 $^{o}$C cooler than the Control hut on the 1$^{st}$ May and 1.4 $^{o}$C cooler on the 2$^{nd}$ May.
- During the cooling period the Partial PCM hut was on average 0.9 $^{o}$C cooler than the Control hut on the 1$^{st}$ May and 1.1 $^{o}$C cooler on the 2$^{nd}$ May.

From these observations it can be concluded that when the internal air temperature increases up to circa 28 $^{o}$C, the presence of PCM results in an average reduction in the internal air temperature in the order of 1 to 1.4 $^{o}$C, a modest value. It is also interesting to note that the reduction in the internal air temperature in the PCM huts is slightly greater on the 2$^{nd}$ day when the air temperatures are also slightly higher The higher internal air temperatures lead to higher temperatures within the wall resulting in more melting of the PCM

The peak internal air temperatures for each hut are provided in Table 7-6 along with the time at which they occur.

**Table 7-6 Peak air temperatures in huts on 1$^{st}$ and 2$^{nd}$ May 2017**

| | Control hut | | Full PCM hut | | Partial PCM hut | |
|---|---|---|---|---|---|---|
| | Peak Temperature ($^{o}$C) | Time (hr:min) | Peak Temperature ($^{o}$C) | Time (hr:min) | Peak Temperature ($^{o}$C) | Time (hr:min) |
| 1$^{st}$ May | 27.7 | 15:10 | 26.6 | 14:45 | 26.3 | 14:50 |
| 2$^{nd}$ May | 29.2 | 15:25 | 27.5 | 15:15 | 27.6 | 15:15 |

It can be noted that the peak temperature of the Control hut is 1.1 $^{o}$C and 1.7 $^{o}$C higher than the peak temperature of the Full PCM hut on the 1$^{st}$ May and 2$^{nd}$ May respectively. Also the peak temperature of the Control hut is 1.4 $^{o}$C and 1.6 $^{o}$C higher than the peak temperature of the Partial PCM hut on the 1$^{st}$ May and 2$^{nd}$ May respectively. From these observations it can be

concluded that the PCM within the walls is changing phase during the heating periods, which are approximately 8 hours long, and hence somewhat reducing the peak internal air temperatures in the huts containing PCM. The rate of cooling is similar in all the huts. The difference between the internal air temperature of the Partial and Full PCM huts is insignificant and is less than the calibrated accuracy of the thermocouples hence their thermal behaviour can be considered similar.

On each day the internal air temperature in each hut started to increase from circa 7:00 am. To consider the thermal inertia effects, the time taken to reach the lowest peak temperature from 7:00 am was determined from the data. On 1st May the lowest peak temperature occurred in the Partial PCM hut at 26.3 $^{o}$C. The Control hut took 6 hours 15 mins to reach this from a starting temperature of 15.9 $^{o}$C. The Partial PCM hut took 7 hours 50 mins to reach 26.3 $^{o}$C from a starting temperature of 15.7 $^{o}$C, 95 minutes longer than the Control hut. The Full PCM hut took 7 hours 25 mins to reach 26.3 $^{o}$C from a starting temperature of 15.6 $^{o}$C, 70 mins longer than the Control hut.

On the 2nd May the lowest peak temperature occurred in the Full PCM hut at 27.5 $^{0}$C. The Control hut took 6 hours 35 mins to reach 27.5 $^{o}$C from a starting temperature of 19.3 $^{o}$C. The Full PCM hut took 8 hours 15 mins to reach 27.5 $^{o}$C from a starting temperature of 18.7 $^{o}$C, 100 minutes longer than the Control hut. The Partial PCM hut took 7 hours 50 mins to reach 27.5 $^{o}$C from a starting temperature of 18.7 $^{o}$C, 95 minutes longer than the Control hut.

This analysis of the data highlights a thermal inertia effect provided by the PCM which delays the occurrence of peak internal air temperatures by 70 to 100 minutes. In the case of a scenario in which overheating in a school is a problem, the thermal inertia effect could potentially delay the time at which the peak temperature occurs until after the occupants have left the building and hence provide further potential to reduce the demand for cooling air conditioning.

This analysis demonstrates that the presence of PCM in the walls is providing a minor beneficial effect on the thermal environment of the hut by reducing the peak temperature by just over 1 $^{o}$C and also by providing a thermal inertia effect so the rate of temperature gain of the internal air is reduced in the PCM huts. There is no discernible difference between the thermal behaviour of the two huts containing PCM which suggests that the additional PCM within the 60 mm to 125 mm depth of the Full PCM hut is not significantly engaged in phase change activity.

**Wall surface temperature**

Figure 7-37 plots the temperature on the surface of the North wall in each hut during the period 1st to 2nd May 2017 when a heat load is applied and no overnight ventilation is provided. The internal air temperatures for each hut and the external air temperature are also shown.

With regard to the wall surface temperatures it can be noted from the figure that the profile of wall surface temperatures is the same for all the huts up until the temperature reaches about 20 $^{o}$C, the start of the PCM melt temperature range. At this point the rate of temperature increase in the Full and Partial PCM hut walls slows down relative to the Control hut wall, indicating that the PCM is starting to melt and is absorbing more heat energy without increasing in temperature. There is no significant difference between the temperature profile for the wall surfaces of the Full PCM hut and Partial PCM hut which is not surprising as the first 60 mm of concrete contains PCM in both cases.

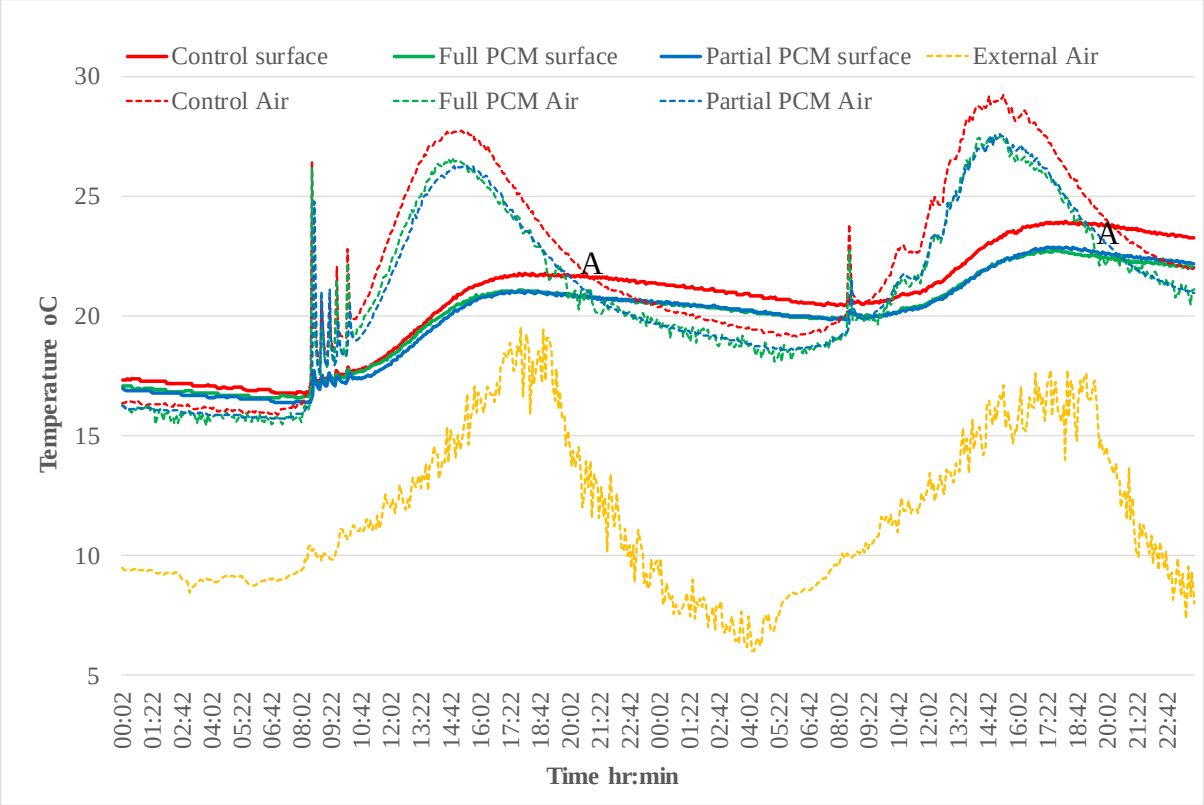


**Figure 7-37 Wall surface and internal air temperatures on 1st and 2nd May 2017**

When comparing the wall temperature profile of all the huts to the internal and external air temperatures it can be observed that the rate of cooling of the internal air in the huts follows a similar profile as the reduction in temperature of the external air until it reaches a similar temperature as the wall surface. At this point, denoted 'A' in Figure 7-37, which coincides with

a wall surface temperature of 22 – 23 $^{o}$C, the rate of cooling of the internal air slows considerably even though the external air temperature continues to drop at the same rate. This behaviour indicates that the walls are starting to release their stored heat to the internal environment. This observation aligns with the expected onset solidification temperature of the PCM (23 $^{o}$C) as reported in Section 4.1.2. The surface temperature of all the walls stays relatively steady despite a decline in external temperature. Between 17:30 pm on the 1$^{st}$ May and 8:30 am on the 2$^{nd}$ May the surface wall temperatures in each of the huts only reduced by 0.8 $^{o}$C. The temperature drop of the internal air in the Control hut and PCM huts during this period was 5.2 $^{o}$C and 4.7 $^{o}$C respectively. While the external air temperature reduced by 8.4 $^{o}$C. It is interesting to note from this analysis that the thermal mass effect provided by the PCMs is minor relative to the Control hut as the drop in internal air temperature is only dampened by 0.5 $^{o}$C in the PCM huts.

Temperature profiles were also plotted for each hut at depths of 30 mm, 60 mm, 90 mm and 125 mm. These plots are provided in Appendix P. At these depths, the walls displayed similar thermal behaviour to that displayed at the surface in that when the wall temperatures are less than 20 $^{o}$C there is no significant difference between the Control and PCM huts, however when the temperature goes over 20 $^{o}$C at these depths the rate of temperature increase in the walls with PCM is lower than the Control hut indicating that the heat absorbed is causing the PCM to change phase and hence provide latent heat capacity. There is no discernible difference between the thermal behaviour of the Partial PCM hut and the Full PCM hut at these depths. Another contributing factor to the lower rate of temperature increase at these depths within the walls of the PCM huts is that less heat is penetrating deeper into the walls containing PCM as some heat is being absorbed by the phase change of the PCM closer to the surface.

Figures 7-38 and 7-39 show the wall temperatures at 60 mm, 90 mm and 125 mm for the Full PCM hut and the Partial PCM hut separately. It can be noted that in the Partial PCM hut there is no difference between the temperature profiles at these depths. This can also be stated regarding the temperature profiles at 60 mm, 90 mm and 125 mm in the Control hut. However Figure 7-38 shows that in the Full PCM hut the temperatures at 90mm and 125 mm are slightly lower than the temperature at 60 mm depth. This shows that the rate of heat penetration between 60 mm and 90 mm is reduced indicating that some phase change may be occurring at this depth. The influence that the phase change behaviour at this depth has on the internal air temperature in the Full PCM hut is indiscernible however it does reduce the amount of heat transferred out of the inner wall surface at 125mm depth.

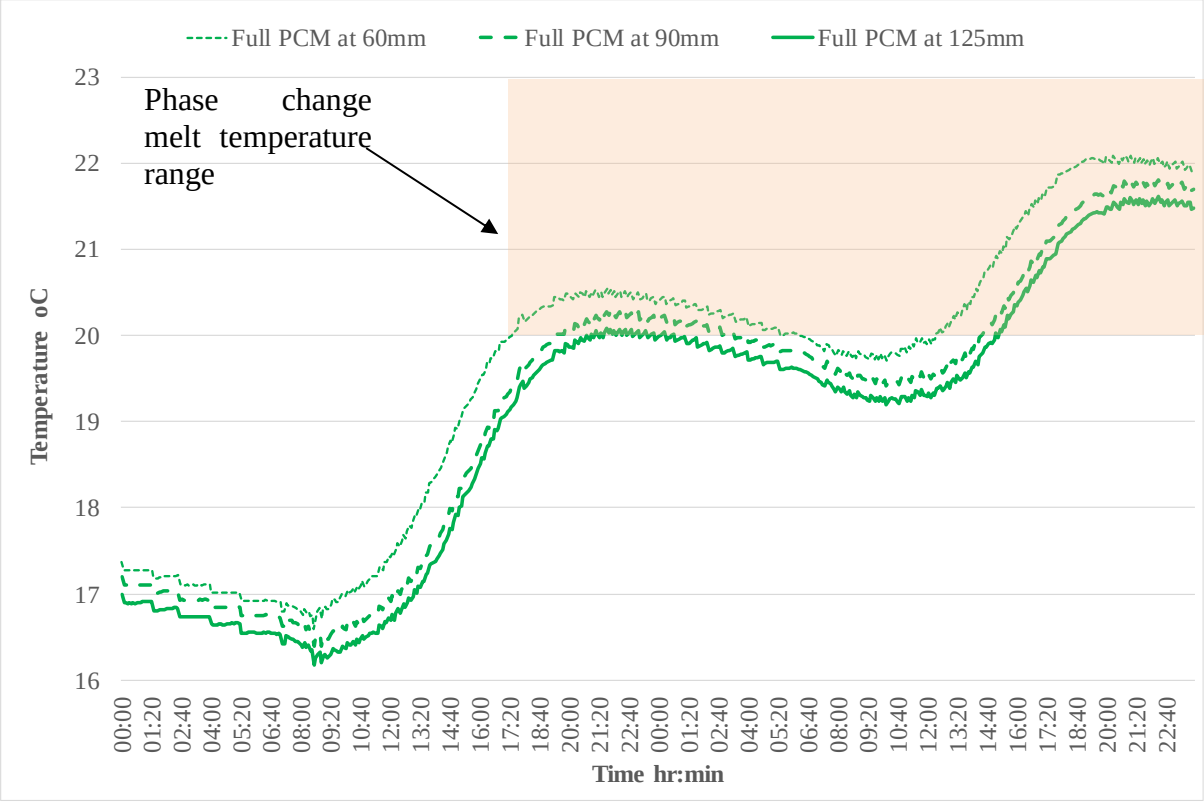


**Figure 7-38 Comparison of wall temperatures at 60 mm, 90 mm & 125 mm in Full PCM hut huts on 1st & 2nd May 2017**

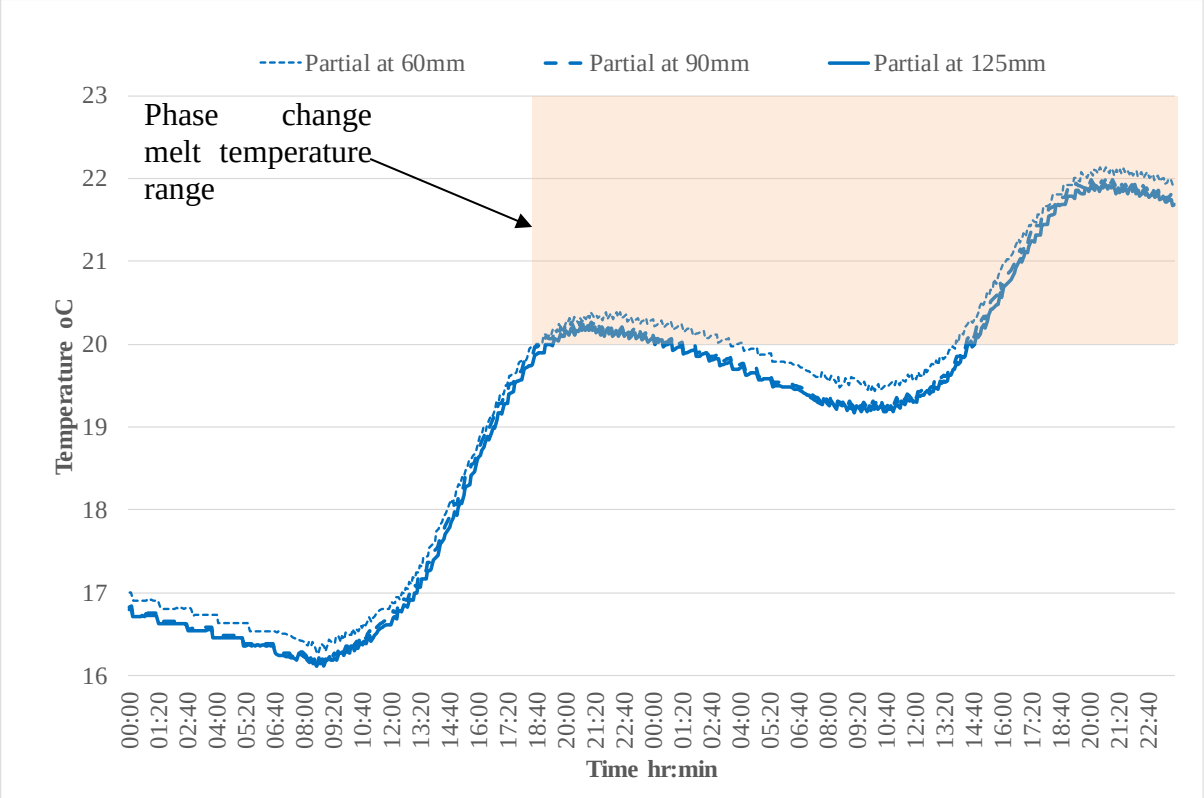


**Figure 7-39 Comparison of wall temperatures at 60 mm, 90 mm & 125 mm in Partial PCM hut huts on 1st & 2nd May 2017**

**Temperature versus depth**

Figures 7-40, 7-41 and 7-42 show Temperature versus Depth plots for the Control hut, the Full PCM hut and the Partial PCM hut respectively. The plots were produced for a 12 hour period on the 1st May during which the internal air temperatures were rising. The following observations can be made:

- The temperature throughout the depths of the walls ranges from 16.5 ºC to 21.0 ºC in the walls with the PCM hence some phase change can be expected to occur
- The temperature increase at both the front and rear surfaces of the Control hut wall during the whole period is greater than that in the PCM hut walls indicating that the PCM is absorbing and storing some of the heat energy applied to the internal surface and hence provides an insulating effect.
- The temperature difference between the front and the back of the walls of both the PCM hut is greater (circa 2.5 ºC) than that of the Control hut (circa 1.9 ºC) indicating that the PCM is hindering the rate of heat penetration through the wall.
- Again it can be noted from the plot for the Partial PCM hut that the difference in temperature of the wall between 60 mm and 125 mm is very small and similar to the Control hut highlighting the effect of the omission of the PCM in the outer 65 mm layer of the Partial PCM hut wall.

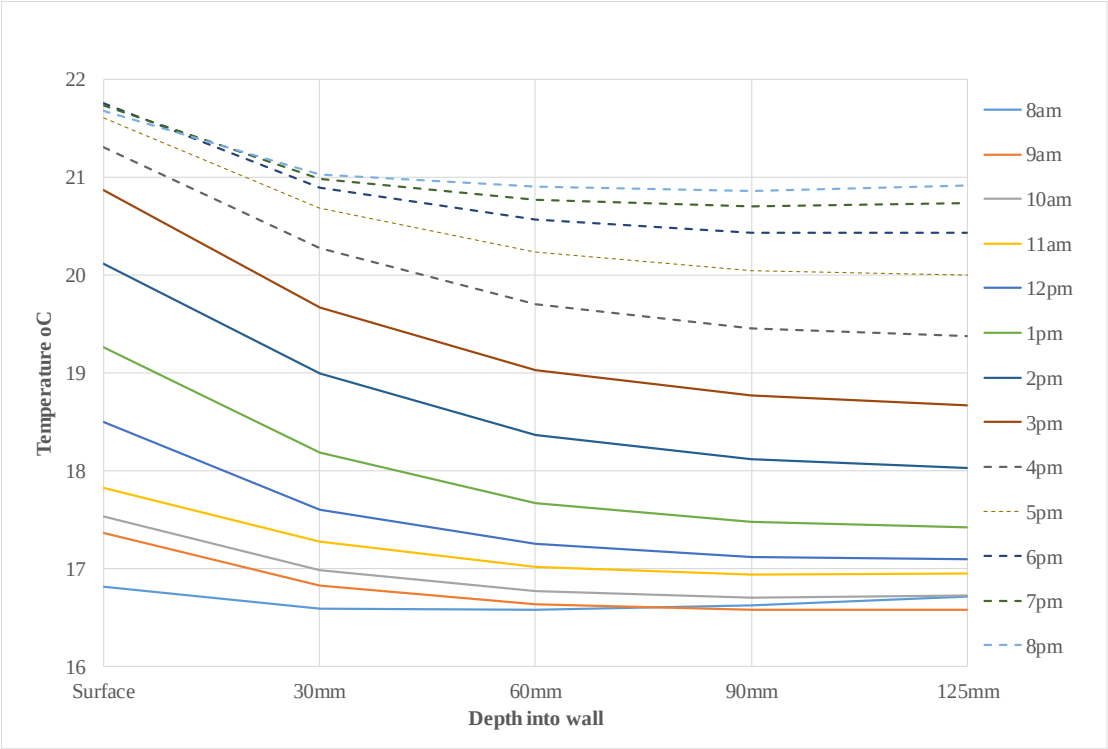


**Figure 7-40 Hourly temperature profile through the Control hut wall on 1st May 2017**

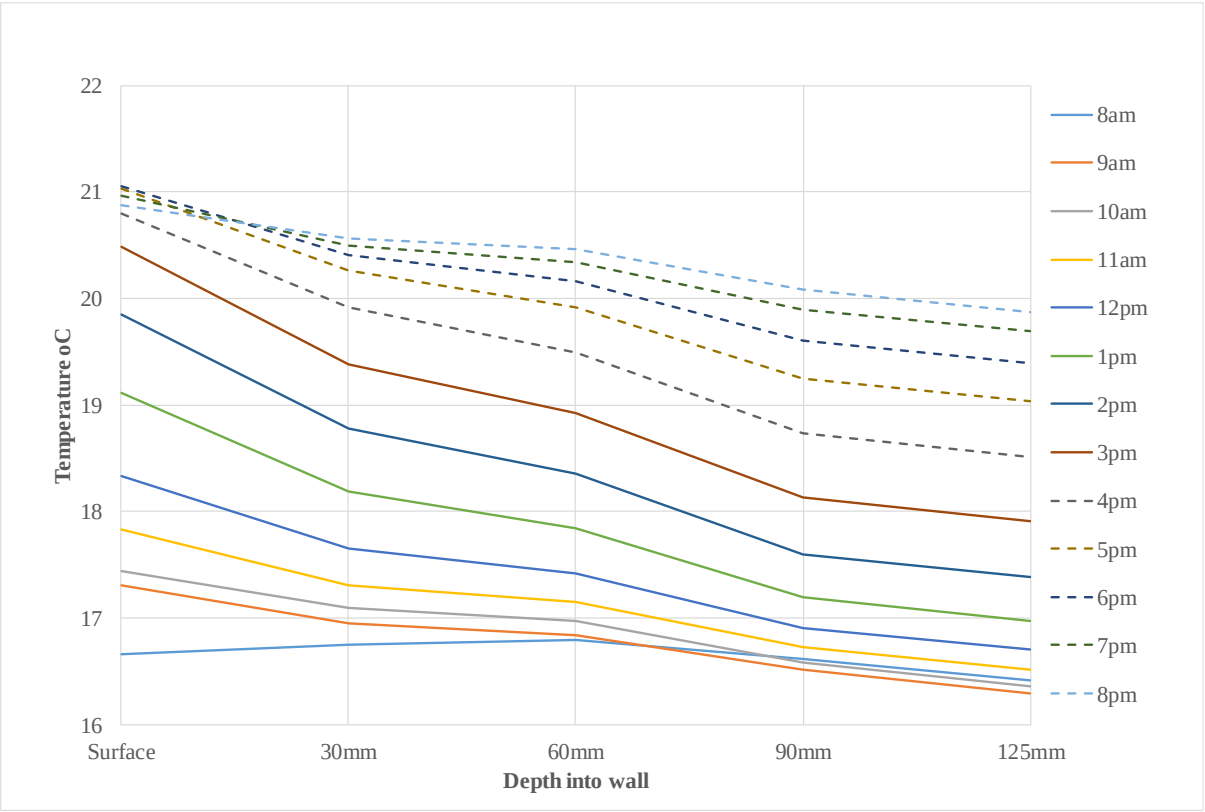


**Figure 7-41 Hourly temperature profile through the Full PCM hut wall on 1st May 2017**

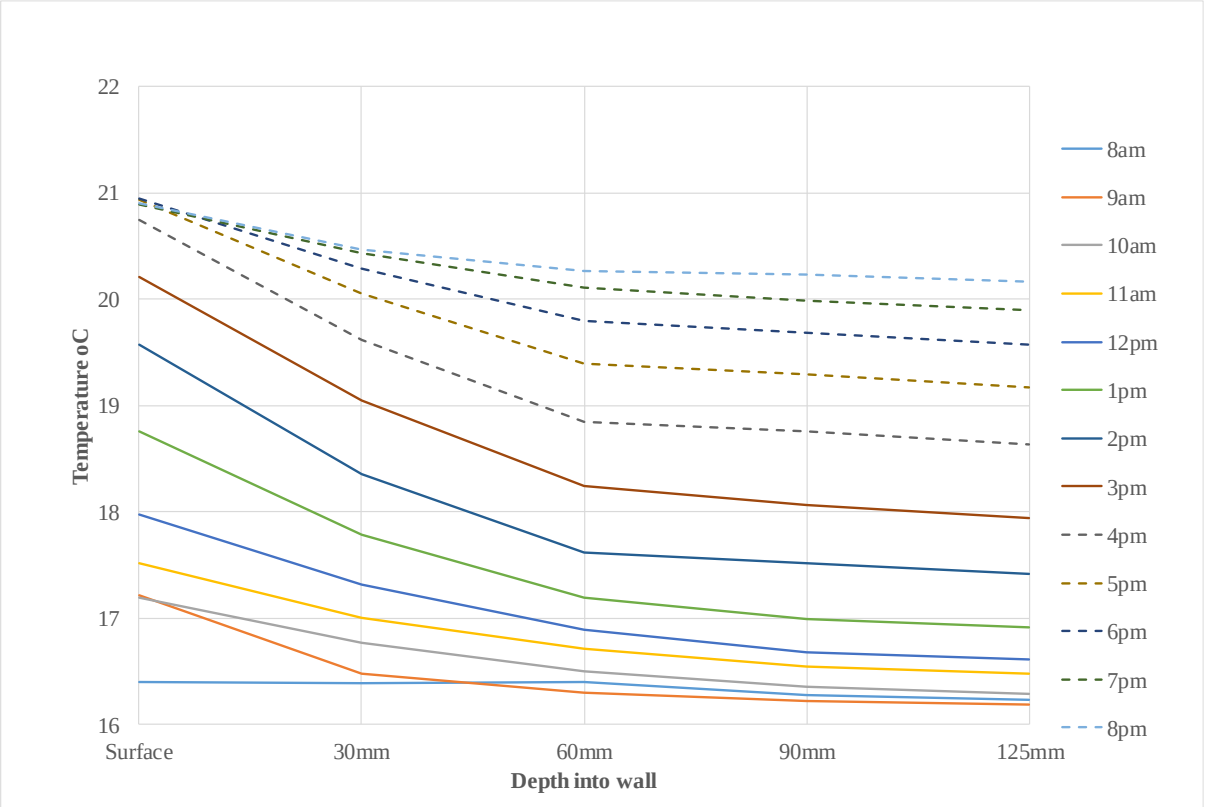


**Figure 7-42 Hourly temperature profile through the Partial PCM hut wall on 1st May 2017**

*7.5.3.4 Thermal behaviour of walls when heaters are on and natural overnight ventilation is provided*

It is clear from the data that during the periods when the internal air temperatures of the huts increase significantly during the day often the internal temperature of the hut at night does not fall low enough to cause the PCM to solidify and release its stored heat. This means that the PCM does not have any latent heat capacity available to absorb the excess heat again the following day. In order to extend the effective period of the PCM throughout the year the feasibility of 'cooling' the internal environment of the huts using natural ventilation overnight was investigated. The huts were heated during the day, 9am to 4:30pm by the radiators to simulate the summer overheating conditions ('On' set point 24 ºC, 'Off' set point 28 ºC). Natural ventilation was provided overnight by leaving the doors open 100 mm for a fixed period. The data collected during this investigation are analysed in the following sections.

**Comparison of internal air temperatures**

Figure 7-43 presents the internal air temperature in all three huts during a 24 hour period during 24th to 25th October 2017.

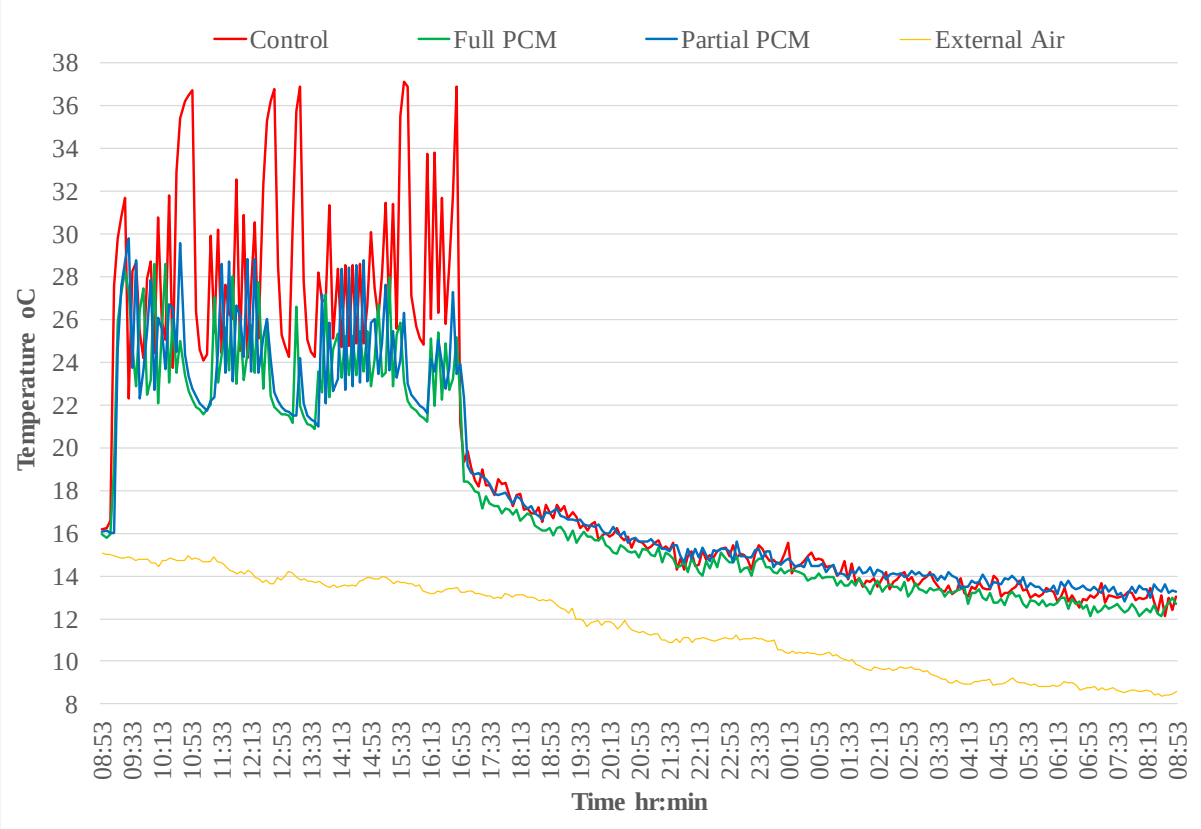


**Figure 7-43 Internal air temperatures in the huts, 24th and 25th October 2017**

When overnight ventilation was provided the internal air temperature dropped to below 14 $^{o}$C. The internal air temperatures in all the huts remained below 18 $^{o}$C from 7pm on the 23$^{rd}$ until 9am on the 24$^{th}$. The temperature of the PCM-concrete composite throughout the whole depth of the wall was below 18 $^{o}$C for circa 5 hours during the night.

Initially the air temperatures oscillated as the heaters turn on and off around the set point. It can be noted that the air temperature in the Control hut oscillated between 24 $^{o}$C and 36 $^{o}$C providing an environment in which the PCM was expected to melt. During the cooling period the air temperature reduced below the melt temperature range hence facilitating the solidification of the PCM and the associated release of heat. The following observations can be made:

- During the heating period both huts containing PCM in the walls were consistently cooler and the amplitude of the oscillations in air temperature was much smaller in the huts containing PCM
- During the heating period the average temperatures were 28.7 $^{o}$C for the Control hut, 23.9 $^{o}$C for the Full PCM hut and 24.4 $^{o}$C for the Partial PCM hut. Hence the Full PCM hut was an average of 4.7 $^{o}$C cooler than the Control hut and the Partial PCM hut was an average of 4.2 $^{o}$C cooler than the Control hut.
- The temperatures in the huts with the PCM indicated that the PCM is melting and absorbing heat.
- There is no difference in the rate of temperature decrease during the cooling period which is to be expected as the doors of the huts are open. This means that the influence of the external air temperature dominates the air cooling rather than the release of heat from the internal wall.
- The opening of the doors was successful in ensuring that the temperature of the entire wall thickness dropped below the solidification temperature range ( 22.9 $^{o}$C – 18.2 $^{o}$C)

Due to the fluctuation of the air temperature around the set point it is not possible to get an accurate measure of the thermal inertia effects.

**Wall surface temperature**

Figure 7-44 shows a comparison of the temperatures on the surface of the wall in each hut. The shaded box on the plot indicates the phase change temperature range.

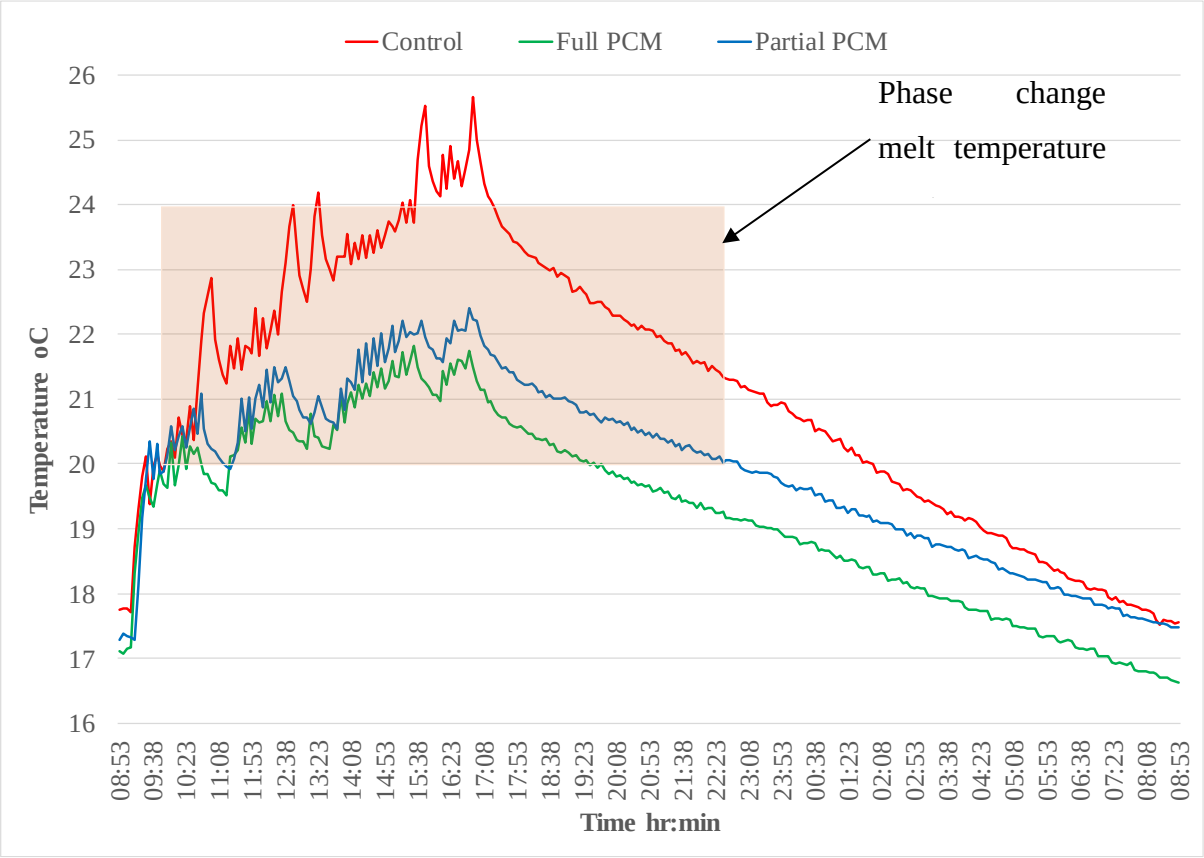


**Figure 7-44 Wall surface temperatures 24th and 25th October**

It can be observed that for the first 2 hours of heating all the walls heated up at approximately the same rate. However when the wall surface temperatures reached about 20.0 ºC the rate of temperature increase on the walls containing PCM decreased relative to the Control hut indicating that the PCM in the walls was starting to melt and hence absorbed the heat without increasing in temperature. The temperature at the surface of the PCM walls continued to rise at a slower rate due to the specific heat capacity of the concrete matrix surrounding the PCM.

The overall increase in temperature at the surface of the wall was 7.9 ºC in the Control hut, 4.6 ºC in the Full PCM and by 5.1 ºC in the Partial PCM during the heating period. The peak surface temperatures reached were 25.6 ºC in the Control hut, 21.7 ºC in the Full PCM hut and 22.4 ºC in the Partial PCM hut. The analysis of the temperatures at the surface of the wall indicates that the presence of PCM was reducing the overall increase in surface temperature in the huts.

During the cooling period, the Control hut wall surface cools down at a faster rate than the PCM huts. This was expected as the temperature differential between the wall surface in the

Control hut and the external air was greater at the start of the cooling period and also there is no PCM within the Control hut walls to create a thermal inertia for the release of heat. The temperature plots during the cooling period follow a similar profile as the external air temperature, again highlighting that due to the provision of natural ventilation the external air temperature dominates the cooling behaviour of the surface of the wall.

A summary of the peak wall surface temperatures for each hut is provided in Table 7-7 along with the time at which they occur. Table 7-7 also provides the time taken for the wall surface in each hut to reach 21.7 $^{o}$C – selected as it is the lowest peak temperature - which highlights the clear thermal inertia effect provided by the PCM in the walls. The beneficial effect of the PCMs is clear from this data. The difference between the surface temperatures of the PCM huts and the Control huts indicates the engagement of the PCM which results in lower internal air temperatures in the PCM huts of the order of 4 $^{o}$C. In addition the thermal inertia effect, enhanced by the presence of PCMs, results in the peak temperatures in the PCM huts occurring over 4 hours later than the Control hut. This effect means that the onset of uncomfortably high temperatures in a building can be delayed until later in the day hence the demand on the building cooling system may be reduced.

**Table 7-7 Peak temperature on wall surface in the huts on 24$^{th}$ – 25$^{th}$ October 2017**

| | Control Hut | Full PCM Hut | Partial PCM Hut |
|---|---|---|---|
| Peak Temperature ($^{o}$C) | 25.6 | 21.7 | 22.4 |
| Time at peak (hr:min) | 16:53 | 16:48 | 16:48 |
| Time taken to reach 21.7 $^{o}$C | 2hr 53mins | 7hrs 48mins | 6hrs 58mins |

**At 30 mm depth:**

Figure 7-45 compares the temperatures in the walls of the huts recorded at a depth of 30 mm. Similar to the temperatures at the surface of the wall, the Control hut wall heats up slightly faster as there is no PCM present to hinder the penetration of heat and it also cools down at a higher rate as the temperature differential between the wall at 30 mm depth and the surface of the wall in the Control hut is greater and there is no PCM to provide an enhanced thermal inertia.

It can be observed that initially the PCM walls heat up at approximately the same rate however the rate of temperature increase is lower than that in the Control hut. This is to be expected as the PCM within the first 30 mm of the wall will absorb heat as it melts and this process hinders the transmission of heat deeper into the wall. There is a clear decrease in the rate of temperature

increase in both PCM huts at circa 19 ºC. This is 1 ºC below the melt onset temperature however the PCM within the first 30 mm of the wall has already started to melt and absorb heat so less heat is reaching the 30 mm depth hence the rate of temperature increase reduces even if the PCM located at 30 mm has not commenced melting. The temperature profile of both PCM huts, at 30 mm deep is very similar because as the heat is entering the wall from the internal surface, the material conditions are the same for both the Full PCM and the Partial PCM and the temperature profile at 30 mm depth in the Full PCM hut, during the heating phase, is not affected by the presence of PCM deeper in the wall.

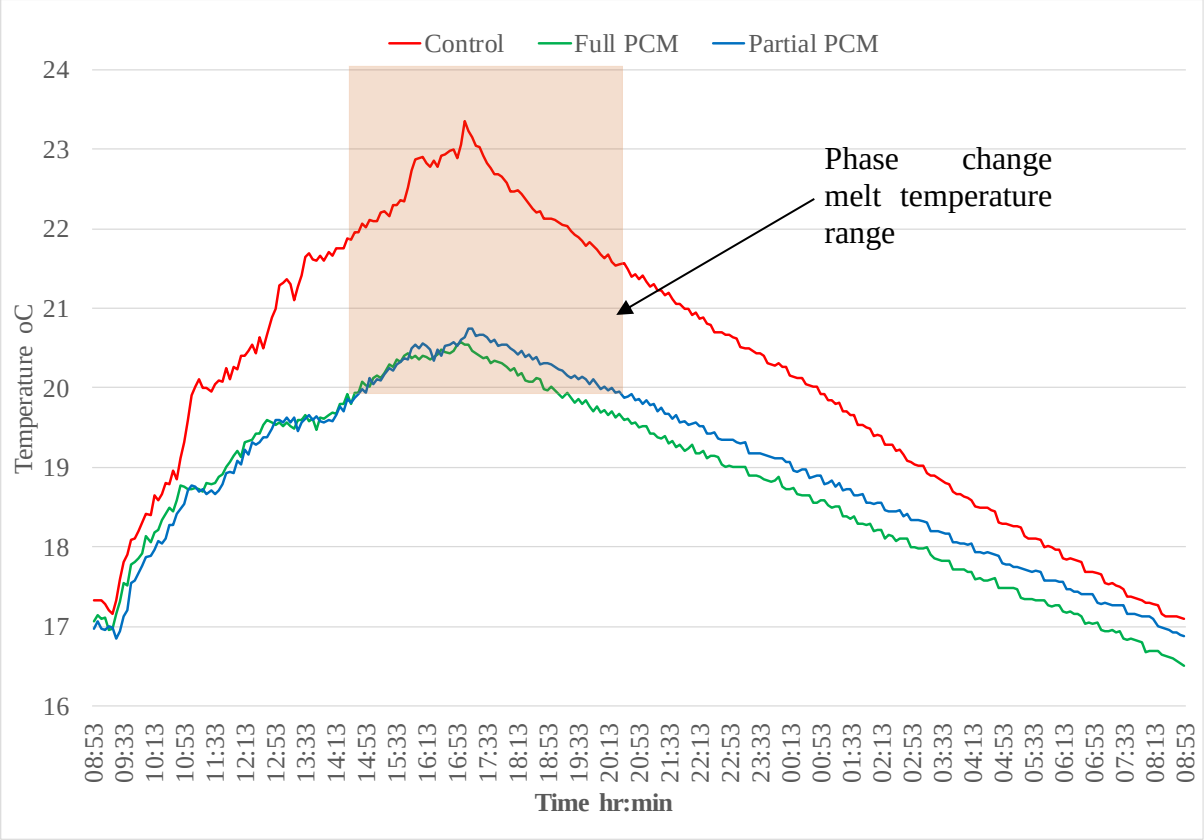


**Figure 7-45 Temperature at 30 mm depth, 24th and 25th October**

The peak temperatures reached in each hut at a depth of 30 mm and the time taken to reach it is summarised in Table 7-8. Also provided in Table 7-8 is the time taken to reach the lowest peak temperature - 20.6 ºC - in each hut. Again the thermal inertia provided by the PCM is clearly demonstrated.

**Table 7-8 Peak temperatures in huts at 30 mm depth and time taken to reach them**

| | Control Hut | Full PCM Hut | Partial PCM Hut |
|---|---|---|---|
| Peak Temperature ºC | 23.4 | 20.6 | 20.7 |
| Time at peak temperature (hr:min) | 17:03 | 16:58 | 17:08 |
| Time taken to reach 20.6 ºC | 3hr 23mins | 7hr 58mins | 8hr 8mins |

**At 60 mm depth:**

A similar comparison of temperatures was carried out at depths of 60 mm and 90 mm and at the back surface of the inner layer of wall. Figure 7-46 displays the temperature profiles at a depth of 60mm. The thermal behaviour at a depth of 60 mm is very similar to that observed at a depth of 30 mm. The overall temperature increase in the Control hut at 60 mm depth is 5.7 $^{o}$C. In the Full PCM hut and the Partial PCM hut the overall temperature increase is 3.4 $^{o}$C and 3.7 $^{o}$C respectively. The difference between the temperature increase in the Control hut and the PCM huts reflects the heat absorbed by the PCM in the first 60mm depth of wall. The difference between the overall temperature increase in the PCM huts may indicate that some of the PCM present at depths greater than 60mm in the Full PCM hut is being engaged however the effect is very minor. The temperatures in the PCM walls only exceeded the melt temperature of the PCM by less than 0.5 $^{o}$C at a depth of 60 mm so the potential for the PCM to melt at this depth is limited. Both PCM huts display a similar increase in temperature during the heating phase and cool down at a similar rate.

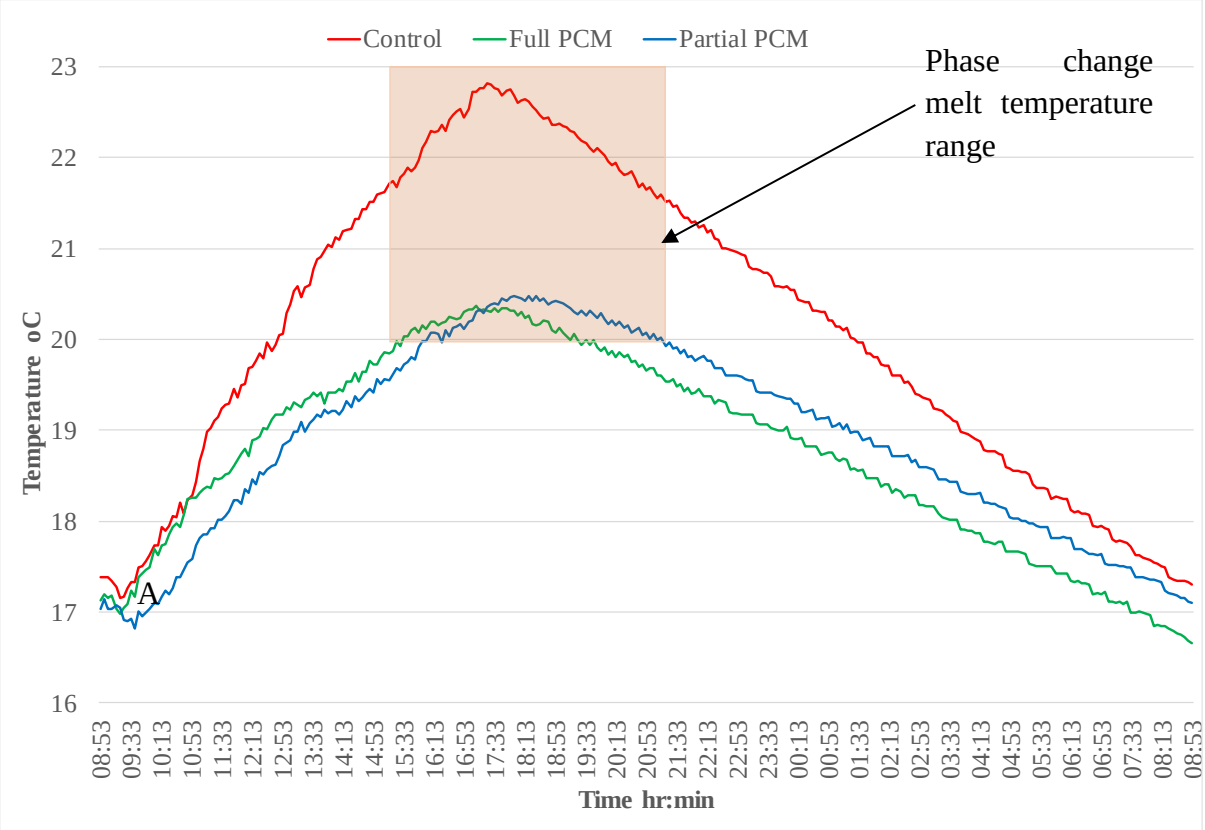


**Figure 7-46 Temperature at 60 mm depth, 24th and 25th October 2017**

The temperature profiles plotted at depths of 90 mm and 125 mm (back surface of the wall) are provided in Appendix Q. These plots show that the Full PCM hut displays a slightly lower rate of temperature increase after 18.5 $^{o}$C and a lower peak temperature than the Partial PCM

however this can be attributed to reduced heat penetration in the Full PCM hut due to the slight engagement of PCM at and around the 60 mm depth. The cooling rates of the two PCM huts are the same at 90 mm and 125 mm indicating that the Full PCM is not providing additional thermal inertia at these depths despite the presence of PCM.

In order to quantify the difference in the rates of heating and cooling between the huts, regression lines were applied to the linear sections of the temperature profiles during the heating phase and the cooling phase on 24$^{th}$ October. The slopes of the regression lines provide a numerical comparison of the difference in the rate of heating and cooling of the hut walls and are tabulated in Tables 7- 9 and 7-10. The $R^2$ value is a statistical measure of how close the data are to the fitted regression line and ranges from 0 to 1. The high $R^2$ values for the regression lines indicates that there is little variance between the recorded data and the regression line. The plots displaying the regression lines for heating and cooling at a depth of 30 mm are displayed in Figures 7-47 and 7-48 respectively. The regression line plots at depths of 60 mm, 90 mm and 125 mm are provided in Appendix R. In the equation provided for the regression lines the value of 'x' is the time elapsed in minutes divided by 5 as the data points were recorded at five minute intervals. From the slope values of the regression lines during the heating phase, it can be noted that the rate of temperature increase in the Control hut is greater than both the PCM huts and although the rate of temperature increase in the PCM huts is similar, the rate of temperature increase in the Full PCM hut is slightly lower than the Partial PCM hut at depths of 60 mm, 90 mm and 125 mm which may be an indication that a slightly higher volume of PCM melts in the Full PCM hut, absorbing more heat and slowing the rate of temperature gain in the surrounding concrete matrix however the effect is hardly perceptible.

**Table 7-9 Slopes of regression lines for heating, 24$^{th}$ October**

| | 30 mm | | 60 mm | | 90 mm | | 125 mm | |
|---|---|---|---|---|---|---|---|---|
| | Slope | $R^2$ | Slope | $R^2$ | Slope | $R^2$ | Slope | $R^2$ |
| Control hut | 0.06 | 0.96 | 0.06 | 0.98 | 0.06 | 0.98 | 0.06 | 0.98 |
| Full PCM hut | 0.03 | 0.95 | 0.03 | 0.96 | 0.03 | 0.97 | 0.03 | 0.97 |
| Partial PCM hut | 0.03 | 0.95 | 0.04 | 0.98 | 0.04 | 0.97 | 0.04 | 0.96 |

**Table 7-10 Slopes of regression lines for cooling, 24$^{th}$ October**

| | 30 mm | | 60 mm | | 90 mm | | 125 mm | |
|---|---|---|---|---|---|---|---|---|
| | Slope | $R^2$ | Slope | $R^2$ | Slope | $R^2$ | Slope | $R^2$ |
| Control hut | 0.03 | 1.00 | 0.03 | 1.0 | 0.03 | 1.0 | 0.03 | 1.0 |
| Full PCM hut | 0.02 | 1.00 | 0.02 | 1.0 | 0.02 | 1.0 | 0.02 | 1.0 |
| Partial PCM hut | 0.02 | 1.00 | 0.02 | 1.0 | 0.02 | 1.0 | 0.02 | 1.0 |

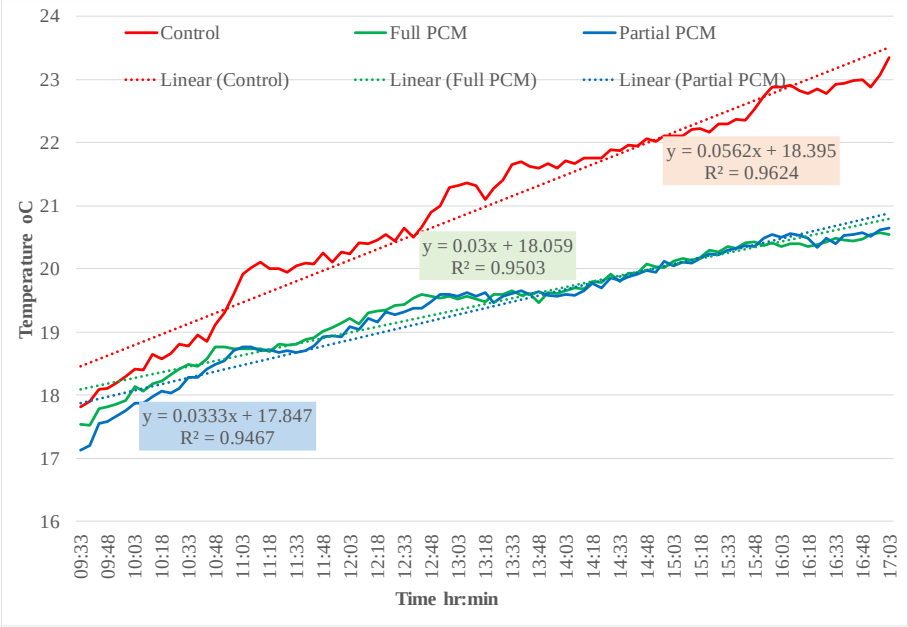


**Figure 7-47 Regression lines for heating phase of temperature profiles at 30 mm depth**

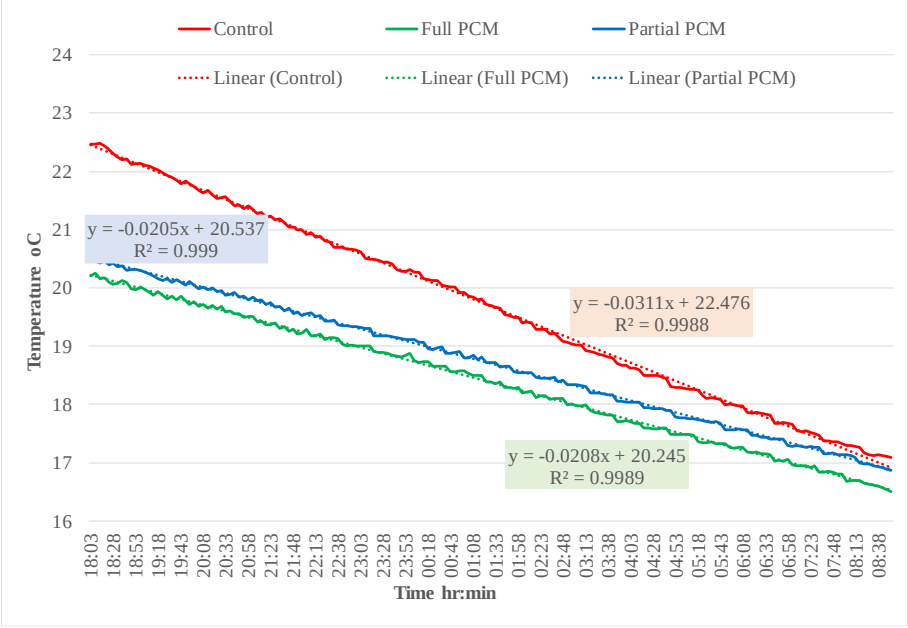


**Figure 7-48 Regression lines for cooling phase of temperature profiles at 30 mm depth**

With regard to cooling, it can be noted that the rate of temperature decrease in all the huts is highly linear, highlighting that the cooling behaviour is dominated by the ventilation provided. As can be observed from Figure 7-43, when the doors are opened in the hut, the internal air temperatures drop immediately and follow the external air temperature profile, remaining circa 4 ºC above the external temperature. This results in a relatively high temperature differential between the internal air and the wall of circa 8 ºC in the Control hut and circa 4 ºC in the PCM huts which results in heat transfer out of the wall and into the air. The slower rate of heat loss in the PCM huts can be attributed to both the lower temperature differential and the thermal inertia provided by the requirement for the melted PCM to solidify to release the absorbed heat.

**Temperature versus Depth**

To observe the rate of heat transfer through the depth of the walls in each hut Figures 7-49, 7-50 and 7-51 were produced for the Control hut, Full PCM hut and the Partial PCM hut respectively showing the internal air temperatures, the wall surface temperature and the temperatures at 30 mm, 60 mm, 90 mm and 125 mm (back surface) depth through the wall. In Figure 7-49 it can be noted that between a depth of 30 mm and the back face of the wall the thermal behaviour is very similar in both heating and cooling phases verifying that the heat transfers through the depth of the wall at a uniform rate, as expected.

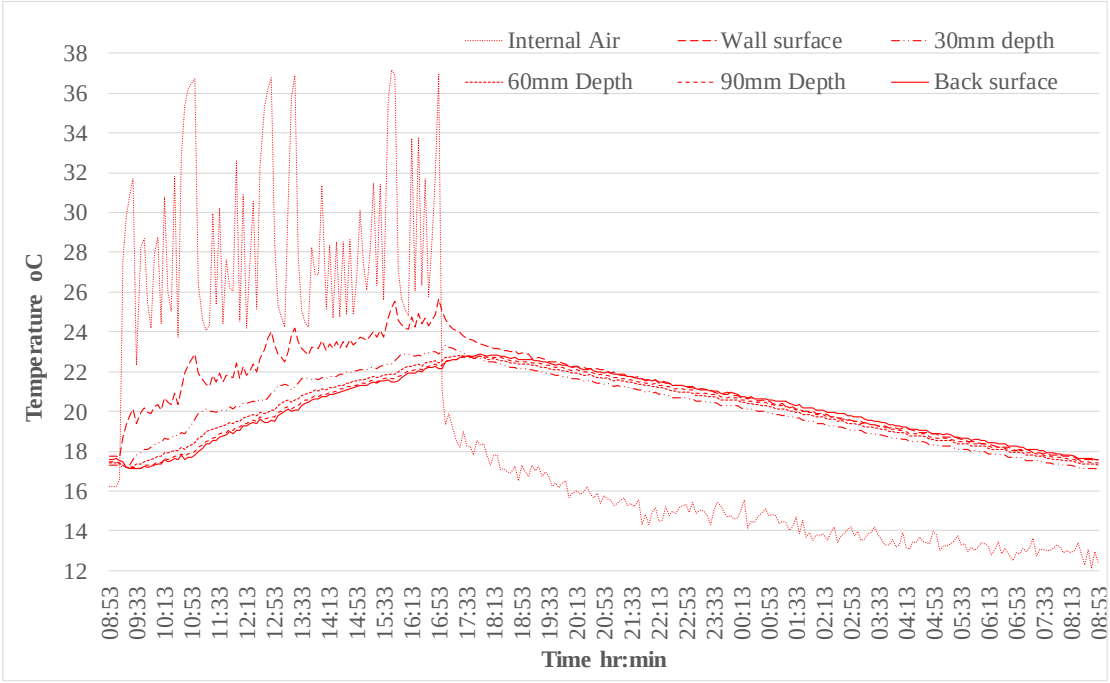


**Figure 7-49 Temperature throughout depth of Control hut 24th and 25th October**

In Figure 7-50 at each depth the temperature reaches or is above the onset melt temperature of the PCM, 20.0 ºC. It can be noted that there is no difference in temperature between the back surface and at 90 mm depth indicating that the PCM is not engaged at 90 mm or deeper and at this depth the thermal behaviour of the wall is similar to the Control wall. If Figure 7-50 is compared to Figure 7-49 for the Control hut, the difference in temperature between 60 mm and 90 mm depth is greater in the Full PCM hut indicating that some PCM is melting and preventing heat passing deeper to 90 mm.

Figure 7-51 shows that there is no difference in the thermal behaviour between 60 mm depth and the back face of wall – which consists of normal concrete- that is, it heats and cools at the same rate and there is minimal difference in temperature. However there is a difference in temperature between 30 mm and 60 mm depth in the heating phase highlighting that the melting of the PCM reduces the rate of heat transfer into the wall.

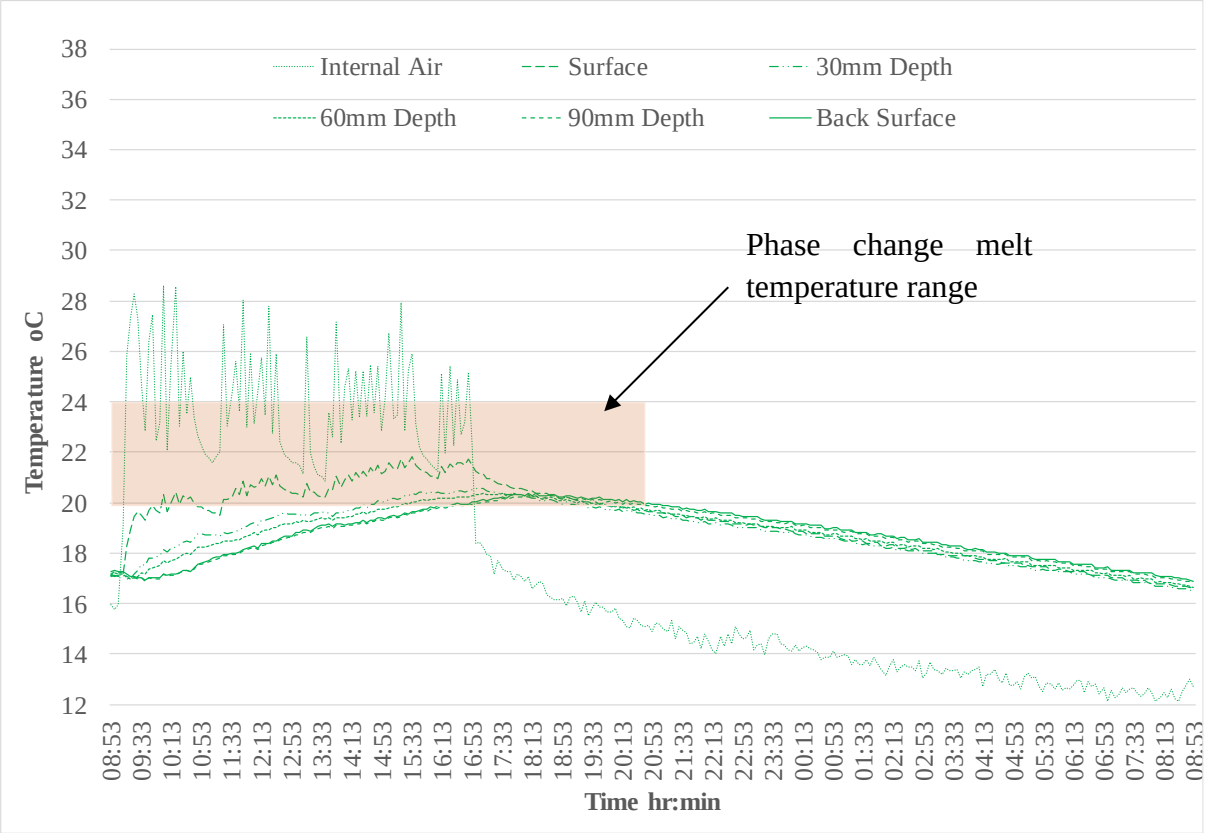


**Figure 7-50 Temperature throughout depth of Full PCM hut 24th and 25th October**

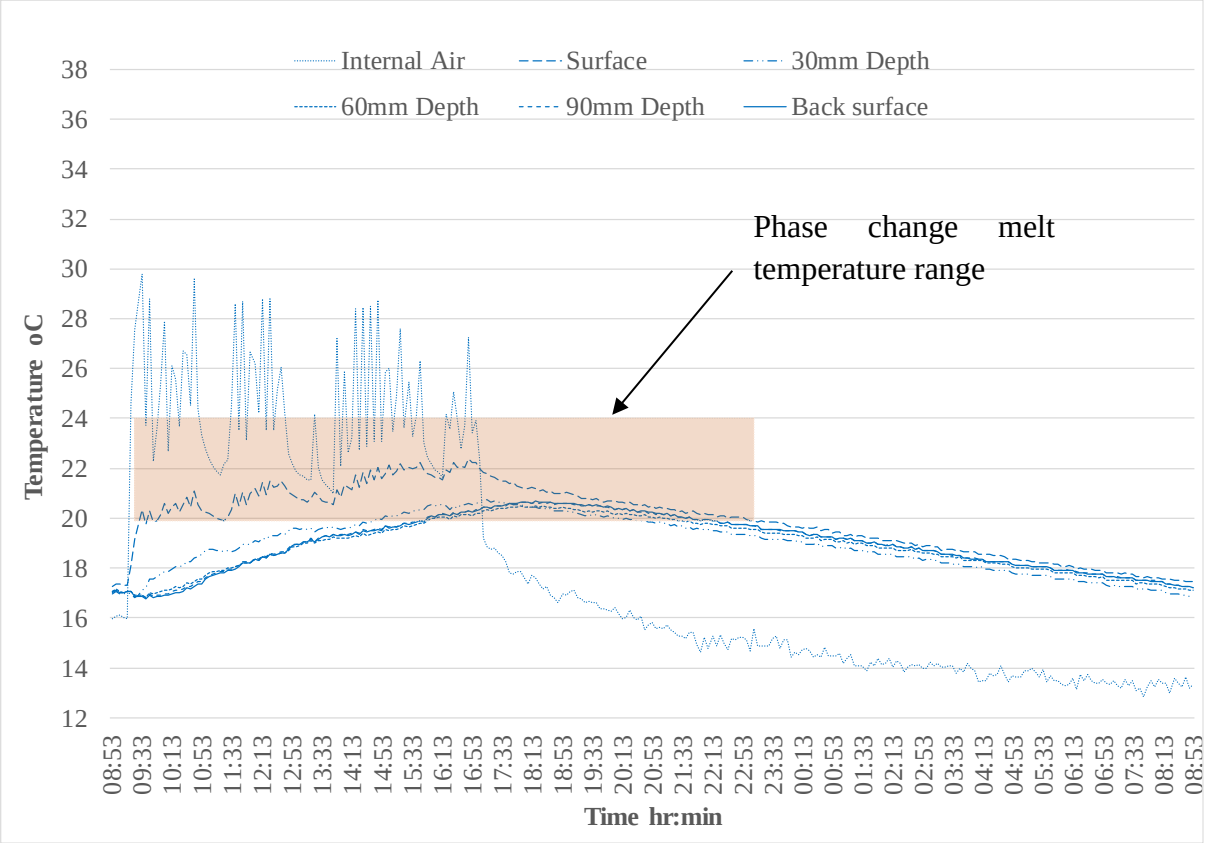


**Figure 7-51 Temperature throughout depth of Partial PCM hut 24th and 25th October**

Figures 7-52, 7-53 and 7-54 show the profile of temperature versus depth for each hut every hour for a 12 hour period from 9:00am on 24th October, during which the internal air temperatures were rising for the first 8 hours and then the heaters were switched off at 4:30pm. The dashed lines indicate the cooling period**.** It can be noted that there is a greater increase in temperature of the back face of the Control hut than the back face of both the PCM huts highlighting the heat stored through the PCM walls. It can be clearly observed from the plots that the overall temperature of the Control hut wall increases more during the 12 hours than the walls containing PCM-concrete composite highlighting the latent heat stored by the PCM.

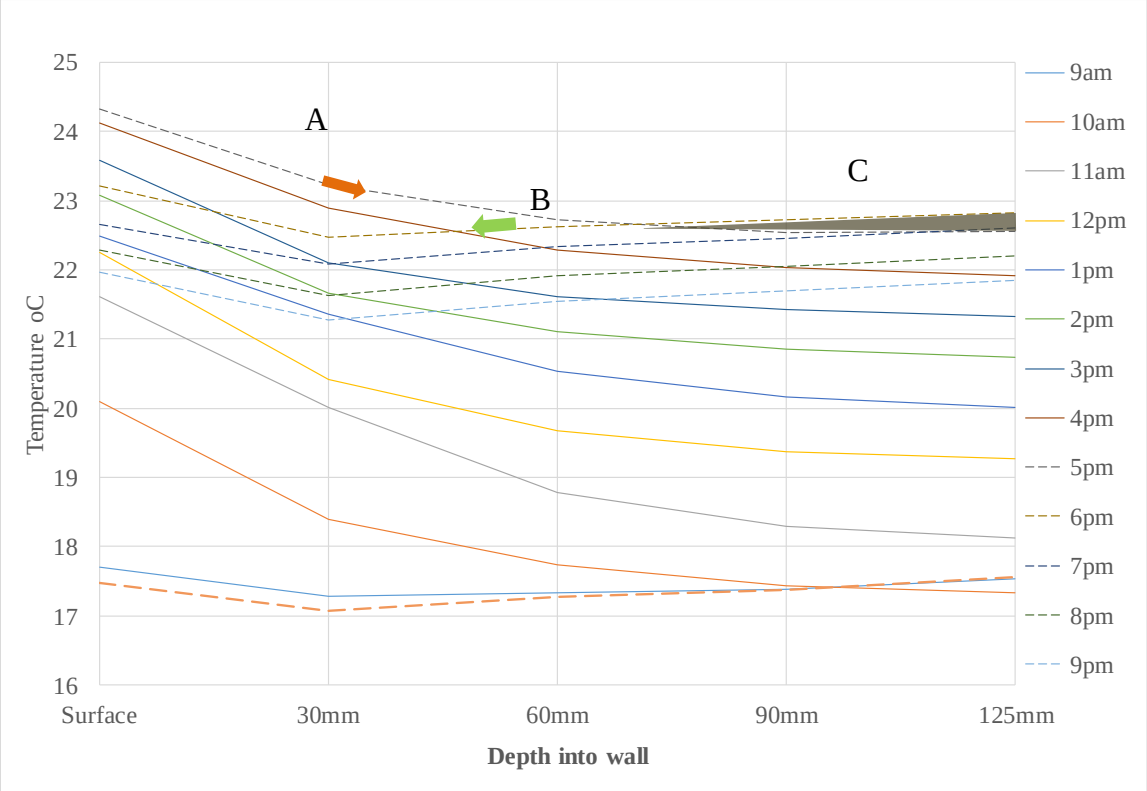


**Figure 7-52 Temperature through depth of Control hut 24th October, 9am to 9pm**

Point A in each of the Figures 7-52, 7-53 and 7-54 highlights that at the start of the cooling period, at 5 pm, heat is still travelling inwards from the surface to 125 mm depth. However between 5 pm and 6 pm the inner 60 mm of wall, nearest to the cooling internal air, reduces in temperture while the temperature of the outside 65 mm of the wall continues to rise – indicated by the shaded area C. By 6 pm the coolest part of the wall is at 30 mm depth and the heat is travelling inwards from the inner surface of the wall towards the 30 mm depth zone as well as transferring out of the wall into the cooler internal air. Heat is also travelling from the hotter material between 60 mm and 125 mm depth towards the 30 mm depth, point B. The entire depth of the wall reduces in temperature from 6 pm onwards however the outside surface of

the wall at 125 mm depth remains slightly hotter than the temperature at 30mm depth during the whole cooling period meaning that the heat will be migrating towards the internal surface of the wall rather than exiting the outside surface due to the presence of the insulation.

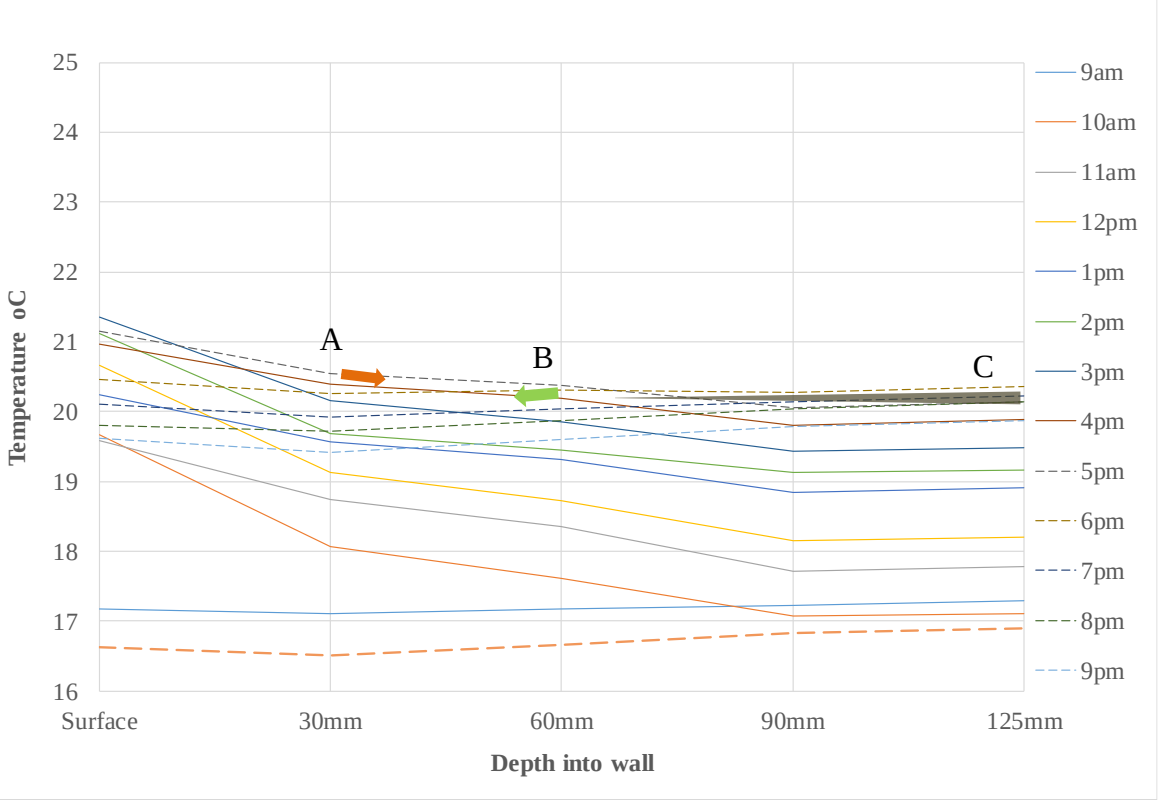


**Figure 7-53 Temperature throughout depth of Full PCM hut 24th October, 9am to 9pm**

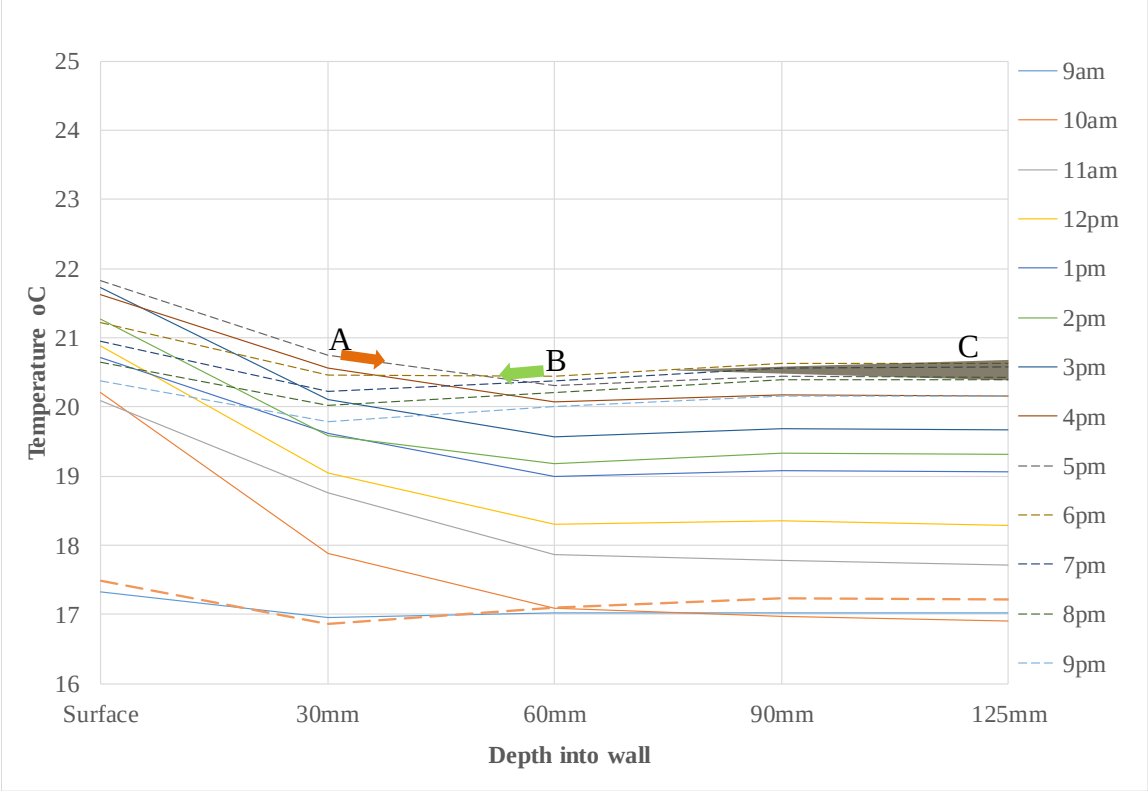


**Figure 7-54 Temperature throughout depth of Partial PCM hut 24th October, 9am to 9pm**

Although this study is focused on using PCMs to reduce overheating in a building it is interesting to note that the temperature of the outside face of the inner layer of the wall panels increased by 5.3 $^{o}$C in the Control hut, 3.1 $^{o}$C in the Full PCM and by 3.6 $^{o}$C on the Partial PCM during the heating period. This indicates that less heat passes through the PCM walls and hence the presence of PCM reduces heat loss in the huts as more heat is stored in the walls closer to the inner surface.

### 7.6 Discussion and conclusions

In order to observe the impact of the PCM-concrete composite material on the thermal mass behaviour of the concrete sandwich panel under 'real life' conditions three full-scale huts were constructed using the 2 wythe concrete sandwich panels to form the walls. Each hut was identical except for the material used in the inner wythe of the cladding panel as described in Section 7.2. The manufacture of the cladding panels demonstrated that the PCM-concrete can be successfully used in full-scale construction elements without causing any problems in production. The huts were instrumented to record thermal and environmental data as described in Section 7.3 and data was collected over an 18 month period which allowed the performance of the PCM-concrete composite to be observed over a duration that included all seasons.

An initial analysis of the temperature profile on the surface of the North wall in each hut was carried out and it highlighted that, under passive conditions (that is, with the heaters switched off and no ventilation provided), the thermal conditions within the depth of the wall that would provide potential for the PCM to change phase only occurred during 30% of the year. This is due to the temperatures in the walls not being high enough to allow the PCM to melt or not dropping low enough overnight to allow the PCM to solidify and purge its heat energy so that it is ready to absorb heat again the next day. It is important to note that this outcome is related both to the form of construction and the local climate. The cladding panels included a layer of insulation as is typical in buildings in Ireland. This layer of insulation hinders the ability of the inner leaf to release its heat overnight and the PCM to solidify as heat loss can only occur from the inner surface of the wall. This means that the rate of decrease in temperature of the internal air in the hut may be relatively low and hence the temperature differential between the wall and the internal air is also relatively low. A compounding factor is the temperate Irish climate. In summer, the external temperatures, level of irradiance and the length of the daylight period are high enough to increase the internal temperatures above the melt temperature range of the PCM, however the overnight temperatures do not drop low enough for long enough to facilitate

the solidification of the PCM thoughout the walls. It is expected that if the PCM-concrete composite was located in a form of construction that included less insulation and also in a climate which provided greater fluctuation in the diurnal temperature for longer periods during the year, it would have a greater impact on reducing overheating in internal environments of buildings. The validity of this expectation will be investigated through the development and application of a model which simulates the thermal mass behaviour of the PCM-concrete material in Chapter 8.

As there are large periods of time during which the PCM is either fully melted or fully solid, in Section 7.5.2 data that was recorded during periods when the PCM was not engaged was analysed in order to observe any difference in the thermal mass behaviour between the walls containing PCM-concrete and the walls containing normal concrete. From these analyses it can be concluded that the thermal mass behaviour of the PCM-concrete composite is similar to that of normal concrete when the PCM is either fully melted or fully solid.

Further analyses were carried out in Section 7.5.3 on data recorded during periods when the wall temperatures fluctuated above and below the melt temperature range of the PCM in summer and winter. During the winter under passive conditions the air temperatures in the huts reached over 30 $^{o}$C despite external air temperatures remaining below 10 $^{o}$C. The only source of heat was irradiance from the sun which remained above 200W/m$^2$ for circa 4.5 hours over the two sunny days discussed. However as it was winter the sun was low in the sky hence more irradiance reached the North walls of the huts to transfer heat through radiation than would occur in summer when the sun is higher in the sky. It was found that there was no significant difference between the internal air temperatures of the two PCM huts however the peak temperatures of the huts containing PCM were on average 5 $^{o}$C and 3.5 $^{o}$C lower than the peak air temperatures in the Control hut. This result demonstrates the potential of the PCM-concrete composite to reduce overheating effects caused by solar gain in buildings. However, it should be noted that the ratio of wall surface area to volume of internal air is relatively high in the huts compared to an actual building such as a school classroom or open plan office. There is evidence of limited engagement of the PCM at depths greater than 60 mm in the Full PCM hut however this does not impact the internal air temperature but there is an economic cost in providing the PCM in concrete.

Under summer passive conditions the temperatures within the walls only fluctuated within the melt temperature range. Due to the shorter night time period and higher external air

temperatures the wall temperatures within all the huts did not fall below 22 $^{o}$C, hence the PCM did not have the opportunity to fully solidify. This resulted in an insignificant difference, of the order of 0.5 $^{o}$C, between the peak air temperatures in the PCM huts and the Control hut. It is interesting to note that despite having irradiance levels greater than 200W/m$^2$ for periods of circa 12 hours on the 9$^{th}$ June and 7 hours on the 10$^{th}$ June, the peak internal air temperatures of 28 $^{o}$C and 29 $^{o}$C respectively are lower than those which occurred during the winter passive conditions. This highlights that in the absence of ventilation, overheating of well insulated buildings due to solar gain can be more onerous in winter than in summer.

Further analyses were carried out on data collected under non-passive conditions, that is, a heating regime was applied to the internal environment of the huts. Two scenarios were analysed in detail, one in which the heaters were on and no ventilation was provided to assist cooling overnight and a second scenario where a heating regime was applied to induce higher internal air temperatures and overnight ventilation was provided by opening the sliding door by a fixed dimension for a set period of time. In both scenarios the internal air temperature of the Control hut increased from circa 16.5 $^{o}$C at the start of the analysis to peaks of 27.7 $^{o}$C to 29.2 $^{o}$C.

When no overnight ventilation was provided the peak internal air temperatures of the Full PCM hut and the Partial PCM hut are lower by on average 1.4 $^{o}$C and 1.6 $^{o}$C respectively which demonstrates that the PCM can have only a slight beneficial impact under these conditions. A thermal inertia effect was also observed with the air temperatures in both PCM huts lagging 1.5 to 2 hours behind the Control hut. This thermal inertia provided by the PCM-concrete composite could be a beneficial property in the case of a school if use of the PCM-concrete composite delays the time of the occurrence of the peak temperatures until after closing hours.

When no overnight ventilation was provided the internal air temperature in the huts did not fall below 18.5 $^{o}$C despite the external air temperature dropping to 6.0 $^{o}$C. Also the wall temperatures did not fall below 19.5 $^{o}$C. As discussed in Section 4.1 the solidification temperature range of the microencapsulated PCM is 23 $^{o}$C to 18 $^{o}$C so if the temperatures within the walls do not fall below 18 $^{o}$C the PCM cannot completely solidify. However it did partially solidify and the PCM was effective the following day at reducing the internal air temperatures in the huts containing the PCM-concrete composite compared to the Control hut, even allowing for the fact that the PCM hut temperatures were lower at the start of the second day due to the impact of the PCM on day 1.

With regard to the effective depth of the PCM, there was evidence that the PCM located at depths greater than 60 mm was engaged in the Full PCM hut but the impact it had was insignificant. Overall under the conditions of the applied heat load and no ventilation the engagement of the PCM within the first 60 mm depth of wall and its effectiveness at reducing the internal air temperatures is evident in both the huts containing the PCM-concrete composite. However, there was no significant difference between the behaviour of the Full PCM and Partial PCM huts. Hence, for reasons of economy, there is a justification for specifying PCM only within the first 60 mm of the internal wall depth.

In order to try to achieve complete solidification of the PCM overnight and examine if this resulted in improved effectiveness of the PCM, natural ventilation was provided in the huts in addition to the applied heat load. The ventilation resulted in the internal air temperature profile quickly aligning with the external air temperature. The temperatures within the walls fell below 18 $^{o}$C for circa 5 hours overnight facilitating solidification of the PCM within the walls. During the heating period the following day, the average internal air temperatures of the Full PCM hut and Partial PCM hut were 4.8 to 4.3 $^{o}$C lower than the internal air temperature in the Control which is a significant effect. That data recorded within the depth of the walls clearly indicated the melting of the PCM and the subsequent resulting lower temperatures of the walls containing PCM. The PCM-concrete composite also provided a significant thermal inertia effect with the temperatures within the PCM-concrete composite walls taking 4 to 5 hours longer to reach a selected temperature than the Control hut walls. This thermal inertia effect means that any required usage of air conditioning to cool a building could be reduced by 4 to 5 hours or mitigated completely if the time that it takes for the internal air to reach the desired onset temperature of the air conditioning is delayed until the building users have left, for example after 3pm for a school or after 6pm for an office. With regard to the effective depth of the PCM within the wall there is some evidence of engagement of the PCM in the Full PCM hut at a depth between 60 mm and 90 mm however it is very minor.

It can be concluded from the analyses carried out that the impact that the presence of a PCM-concrete composite has on reducing overheating varies considerably between each of the scenarios analysed. In order to compare the performance of the PCM-concrete composite across the various environmental conditions, Table 7-11 provides a summary of key factors and outcomes under each scenario analysed. The peak temperatures reached in the Control hut in each scenario is provided along with the length of the heating period. Another factor which is of interest is the temperature difference between the internal air and the internal temperature

within the wall. The greater this temperature differential is the greater the rate of heat transfer between the air and wall. These factors are provided for in the Control hut as an indication of thermal behaviour in the absence of PCM. Table 7-11 also summarises the key metrics of the performance of the huts containing PCM-concrete composite, that is, the reduction in peak internal air temperature relative to the Control hut and any thermal inertia effect. The temperature range of the PCM-concrete material within the walls from the start of the heating period to the end of the heating period is also noted.

**Table 7-11 Summary of key measures of PCM behaviour under passive and non-passive conditions**

| | Passive conditions | | | | Heating load applied | | | |
|---|---|---|---|---|---|---|---|---|
| | Winter | | Summer | | No overnight ventilation | | With overnight ventilation | |
| | Control hut | | Control hut | | Control hut | | Control hut | |
| Average difference in temperature between internal air and wall at 30 mm depth during heating phase. (°C) | 9.3 | | 1.7 | | 5.6 | | 7.9 | |
| Length of heating period (hr:min) | 5:10 | | 7:10 | | 7:00 | | 7:30 | |
| Average peak air temperature in the Control hut (°C) | 35.9 | | 28.8 | | 28.5 | | 28.7 | |
| | Full | Partial | Full | Partial | Full | Partial | Full | Partial |
| Average temperature range of wall during heating phase (°C) | 17.4-22.5 | 17.4-23.1 | 22.0-24.0 | 21.8-23.8 | 16.7 -20.5 | 16.3 – 20.4 | 17.1 – 21.0 | 17.0-21.0 |
| Reduction in peak internal air temperature relative to Control hut (°C) | 4.4 | 4.5 | 0.6 | 0.4 | 1.4 | 1.6 | 4.7 | 4.2 |
| Additional time taken to reach a set temperature relative to Control hut (hr:min) | 0:46 | 1:32 | 0:30 | 0:10 | 0:55 | 2:05 | 4:55 | 4:05 |

It can be noted from Table 7-11 that under summer passive conditions the PCM-concrete composite has no significant impact on the internal air temperature despite the internal air temperature in the huts reaching 28 °C. Also there was no thermal inertia effect. This result can

be attributed to the higher temperature of the PCM-concrete composite at the start of the heating period which would indicate that the PCM was only partially solid at the start so its ability to absorb heat through phase change was limited. Also the average temperature differential between the internal air of the Control hut and internally within the wall was relatively low at 1.9 $^{o}$C. In contrast during winter passive conditions, the PCM can be assumed to be fully solid at the start of the heating phase and the wall temperatures increase to 2.5-3 $^{o}$C above the onset melt temperature. The average temperature differential between the wall and the internal air temperature in the Control hut is significantly greater than the differential during summer passive conditions at 9.3 $^{o}$C. These conditions result in a reduction in peak internal air temperature of approximately 4.5 $^{o}$C which is quite significant.

The only scenario that resulted in a significant thermal inertia effect is when a heat load was applied and overnight ventilation was provided. The reason for this is that the increase in internal air temperature occurs more rapidly when an artificial heat load is applied compared to under passive conditions when the air heats up more gradually. In the case of a heat load being applied without overnight ventilation the average temperature differential, as noted in Table 7-11, is lower hence less of the PCM within the wall is activated and as a result the thermal inertia effect is reduced.

It can also be noted from Table 7-11 that the PCM-concrete composite was equally effective during winter passive conditions and non-passive conditions with overnight ventilation. The fact that under winter passive conditions the PCM-concrete composite reached higher temperatures that extended further into the melt temperature range of the PCM did not lead to a greater effectiveness at reducing internal air temperatures. This could be due to the shorter heating period under winter passive conditions and also that as the main heat source under passive conditions is solar irradiance, the volume of PCM-concrete composite that reaches the peak temperatures noted is likely to be lower as the solar irradiance does not reach all the wall surfaces. However when an artificial heat load is applied the primary source of heat is the internal air which is applied evenly over the full surface area of wall and hence engages a higher volume of PCM.

With regard to the effective depth of the PCM, although the data provided some evidence of phase change of the PCM at depths greater than 60 mm under non-passive conditions it was relatively minor. This result only applies to the environmental conditions analysed as a scenario that provided a greater temperature differential between the internal air and the wall over a

longer period of time may lead to increased heat transfer into the wall and engagement of the PCM located deeper in the wall.

The conclusions of these analyses highlights the multitude of factors that influence the effectiveness of the PCM-concrete composite at reducing internal air temperatures. The data clearly shows that the inclusion of PCMs into concrete is an effective if limited strategy for reducing overheating effects in a building and hence the demand on cooling systems under certain thermal conditions. The PCM-concrete composite was effective at reducing internal air temperatures by over 4$^{o}$C during winter passive conditions and when a heating load is applied with the provision of overnight ventilation. A key factor in the effectiveness of the PCM-composite is the relatively high average temperature differential between the internal air and the PCM-composite material in the wall during the heating period, circa 8 – 9 $^{o}$C. Another critical factor is the temperature differential between the internal air and the wall material during the cooling period which must be sufficient to facilitate complete solidification of the PCM overnight. During winter passive conditions sufficient temperature differential for cooling was provided by the low external temperatures which were below 10$^{o}$C all the time while the applied heating period through irradiance was only circa 5 hours. Under the applied heat load, a sufficient temperature differential during the cooling period was provided through natural ventilation. It can be concluded from the analyses that the provision of a suitable overnight ventilation system would extend the annual period during which the PCM is effective.

The observations made of the thermal behaviour of the PCM-concrete composite are only applicable to the particular conditions of the huts, that is, the geometry, orientation, form of construction, positioning of glazing and local climate. Furthermore the data collected can be used to develop a software model that can simulate the thermal response of the PCM- concrete. This model can then be used to simulate the thermal behaviour for other buildings and varying environmental conditions, and is the subject of the next chapter.

# Chapter 8. Thermal Modelling of the Huts containing PCM-concrete Composite

## 8.1 Introduction

The analysis of heat transfer within PCM composite material is challenging due to its complex thermal behaviour which is influenced by several parameters. When selecting the PCM material for a building application, the literature on this topic states that the melting/freezing temperature of the PCM should coincide with the desired internal room temperature. However for the PCM to have a positive effect on reducing the energy use in a building it is critical that the air temperature in the location where the PCM is located fluctuates sufficiently within a 24 hour period to ensure that the PCM material changes phase. Many factors influence this requirement including the thermo-physical properties of the PCM and the material it is embedded in, along with the local climate, building geometry and use of the building. As all buildings differ, each building will require a unique optimal solution for the application of a PCM composite material as a thermal energy storage system. The development of numerical simulation tools is necessary to achieve a practical and economic application of this technology. Coinciding real data is required to validate a PCM numerical model.

For this reason one of the aims of this PhD research project is to develop a model that can accurately predict the thermal behaviour of a PCM-concrete composite material when it is placed in environments with different internal temperature profiles and different external climatic conditions. This chapter describes the development of a numerical simulation model that simulates the thermal behaviour of the PCM-concrete composite using COMSOL multi-physics software. The model is validated using the real temperature and weather data recorded in the huts over an 18 month period as described in Chapter 7. For any project in a particular location the orientation, geometry, fenestration and form of construction will always vary. However the geographical characteristics that may influence the performance of the PCM-concrete, such as solar altitude and daylight hours, while they vary daily and seasonally, they do not vary much year to year and are the same for all buildings in a given location. For this reason the validated model is used to investigate the impact of geographical location on the potential of PCM-concrete to achieve beneficial thermal mass effects and also to determine the effective depth of a PCM-concrete composite under different conditions.

### 8.2 Outline plan for development of a thermal behaviour model for the full-scale huts

To achieve the aim of developing a software model to simulate the thermal behaviour of the PCM-concrete composite under various environmental conditions, a finite element model of the huts constructed in Techrete Ltd was created using COMSOL Multiphysics modelling software. In the model, virtual temperature probes were located at the same positions as the actual thermocouples embedded in the walls of the huts, as described in Chapter 7. Actual internal and external temperature data and solar irradiance recorded at the huts were applied to the model and each simulation was preconditioned by setting the initial temperatures of all the domains as the corresponding actual temperatures recorded in the huts. The model was validated by comparing the simulated temperatures recorded at the probes in the model with the actual temperatures recorded at the corresponding thermocouples in the hut.

The outline procedure for the development of the model was as follows:

1. A 3-dimensional (3-D) model of a 1.0 m x 1.0 m section of panel, as used in the Control hut, was created. The purpose of this initial simulation study was to investigate if the model could accurately simulate the heat transfer behaviour of concrete that does not contain any PCM.
2. 3-dimensional models of 1.0 m x 1.0 m sections of panel, as used in the Full PCM hut and the Partial PCM hut, were created. The material properties of the inner leaf were adjusted to reflect the properties determined for the PCM-concrete composite.
3. The COMSOL software was programmed to simulate the thermal behaviour and characteristics of the PCM and PCM concrete composite.
4. The 3-D models of the panels were validated using the data collected from the huts.
5. When the 3-D models were simulating the thermal behaviour of the panels accurately, 3-D models of each hut were created within COMSOL. Real environmental data, that is, external air temperatures and irradiance, collected at the site of the actual huts, was applied to the models by setting the initial temperatures as the corresponding actual temperatures recorded in the huts. The simulated internal air temperatures and temperatures within the walls were compared to the real collected data for each hut to ensure that the model was simulating the thermal performance of the PCM-concrete accurately under 3-dimensional conditions.
6. The COMSOL model was then used to carry out scenario modelling to investigate the influence of geographical location on potential performance of PCM-concrete.

Sections 8.3 and 8.4 describe the development of the simulation model in further detail.

## 8.3 3-D thermal modelling of cladding panels

### 8.3.1 3-D modelling of Concrete panel with no PCM

Initially, a 1.0 m x 1.0 m 3-dimensional model was created in COMSOL comprising of a 70 mm thick concrete outer leaf, a 120 mm insulation layer (Kingspan Kooltherm K15) and a 125 mm concrete inner leaf, reflecting what was used in the Control demonstration hut. The purpose of this initial simulation study was to investigate if the model is accurately simulating the conductive heat transfer behaviour of the concrete that does not contain any PCM. Within the model, probes were located corresponding to locations of thermocouples throughout the depth of the panels in the hut. The thermal properties for each layer were allocated to the model, that is, density, thermal conductivity and specific heat capacity. The values of thermal conductivity ($k_{conc}$) and density ($\rho_{conc}$) for the concrete layers were taken from the results from the laboratory investigations ($k_{conc}$ = 1.86 W/mK; $\rho_{conc}$=2335 kg/m$^3$). The specific heat capacity for the concrete ($C_{p,conc}$) was calculated using material data for each component of the concrete mix ($C_{p,conc}$=881 J/kgK). Material properties for the insulation were taken from the Kingspan data sheet, namely 0.02 W/mK, 1450 J/kgK and 35 kg/m$^3$ for thermal conductivity, specific heat capacity and density respectively.

A selection of 24 hour time periods were chosen for use in the initial modelling based on a high fluctuation in the actual wall temperature during the 24 hour period. One period selected was from 8am on 27$^{th}$ Dec to 9am on 28$^{th}$ Dec 2017. The 24 hour dynamic temperature profile of the internal wall surface in the Control hut for this period was imported into the model and applied to the internal surface of the model panel. The initial temperature of the inner leaf was set at 18.7$^o$ C as this was the temperature throughout the actual wall at the start of this time period, thereby ensuring that the model was preconditioned. The heaters were on during this period between 9am and 2pm, with an 'on' set point of 18 $^o$C and an 'off' set point of 22 $^o$C. The applied temperature at the inside face of the wall increased to a maximum of 27 $^o$C. The corresponding dynamic external air temperature data recorded during this period was also extracted from the hut data, imported to the model and applied to the external face of the model panel. The mesh was selected as 'physics defined' which allows COMSOL to apply an appropriate mesh based on the physics that is being simulated, in this case heat transfer, and the model geometry. In this model the physics defined mesh is called 'finer' and is as displayed in Figure 8-1 which also provides a schematic of the model geometry and boundary conditions.

Figure 8-2 displays the external air and internal wall surface temperatures that were applied to the boundaries.

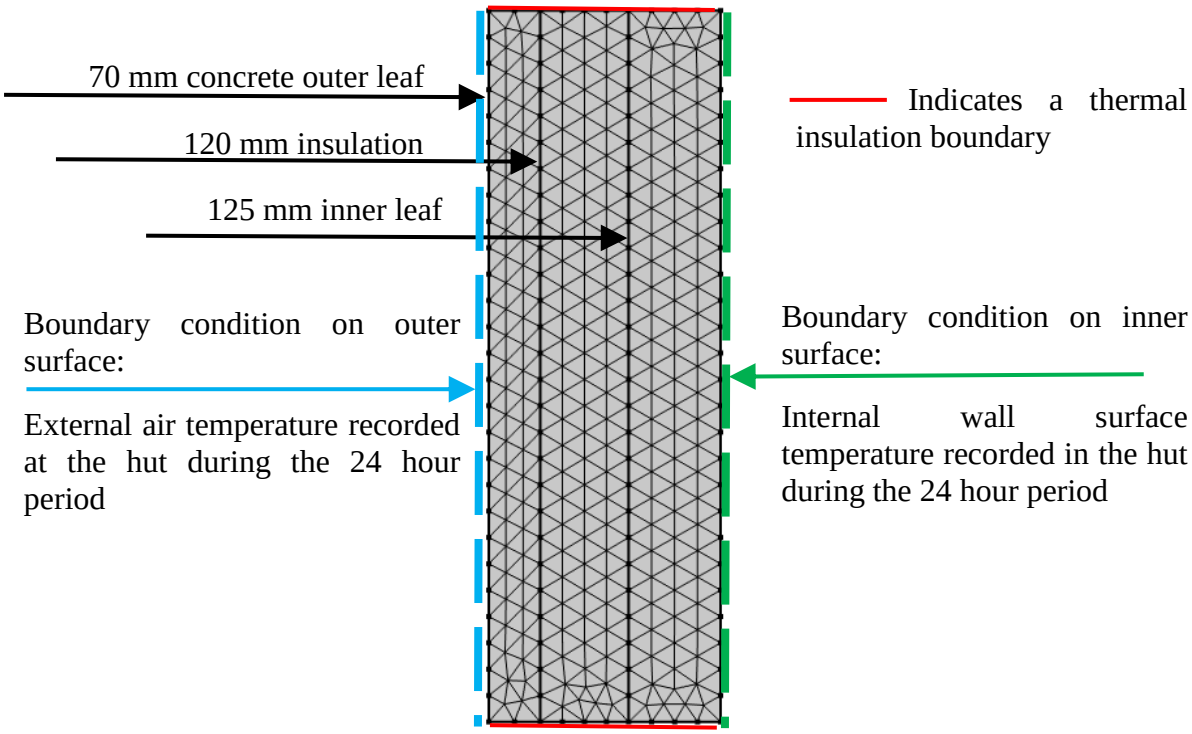


**Figure 8-1 Schematic of model geometry, mesh and boundary conditions**

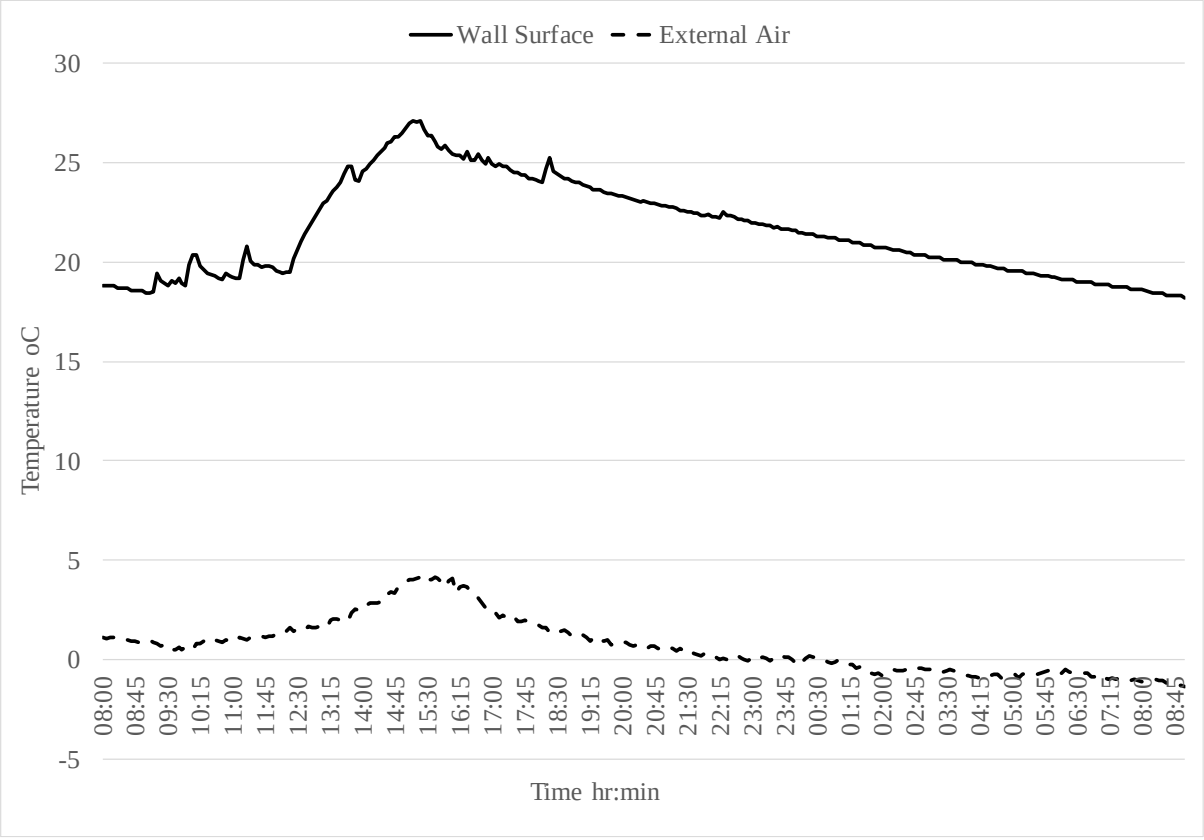


**Figure 8-2 External air and internal wall surface temperatures applied to the model**

The simulation calculated the temperature at each probe at five minute intervals throughout the time period. The results of the simulation were plotted against the real temperature data recorded at each thermocouple in the control hut. Figure 8-3 shows a comparison between the real temperature data and the results of the simulation at each thermocouple depth within the inner leaf of the wall. It can be observed that generally, the thermal behaviour of the probes in the simulation follows a similar pattern as the actual thermocouples in the hut at each thermocouple location. There is a notable difference at the start of the simulation when the heaters are switching on and off about the set point – the simulation temperature rises quicker and is on average 0.42 $^{o}$C higher than the actual temperature from the huts during this initial period. When the heaters remain off, due to the internal air temperature being greater than the 'off' set point temperature of 22 $^{o}$C, the real temperatures and simulated temperatures are very similar.

The slopes of the curves during the cooling period are also similar, albeit the simulated temperatures display slight inertial behaviour at the peak and are slower to start cooling. As a result the simulation temperatures are on average 0.39 $^{o}$C higher than the actual temperature difference during the cooling period. A similar pattern was seen in similar simulations using different time periods albeit with smaller differences between the simulated and actual temperatures. Although there was a small difference between the simulation results and the actual data, the simulation can be considered to be sufficiently accurate in modelling the heat transfer through the wall as the difference is less than the calibrated accuracy of the type K thermocouples used in the huts (+/-0.86 $^{o}$C).

To investigate if the accuracy of the model could be improved any further, a sensitivity analysis was carried out on the material properties of the model. A parametric sweep was performed in which the thermal conductivity of the concrete was varied between 1.6 W/mK and 2.0 W/mK in increments of 0.1 W/mK and the specific heat capacity was varied between 750 J/kg and 1000 J/kg in increments of 50 J/kg. Simulation results were obtained for each combination of these values. All the results were plotted together and the combinations that produced the closest correlation to the real data were determined. Figure 8-4 shows the four most accurate combinations ($C_p$ = 850 J/kg and $k_c$ =1.8 W/mK; $C_p$ = 850 J/kg and $k_c$ =1.9 W/mK; $C_p$ = 900 J/kg and $k_c$ =1.8; $C_p$ = 900 J/kg and $k_c$ =1.9 W/mK;) along with the actual data and the data from the original simulation using experimental values for the thermal conductivity and specific heat capacity, $k_c$ =1.86 W/mK and $C_p$ = 881 J/kg respectively.

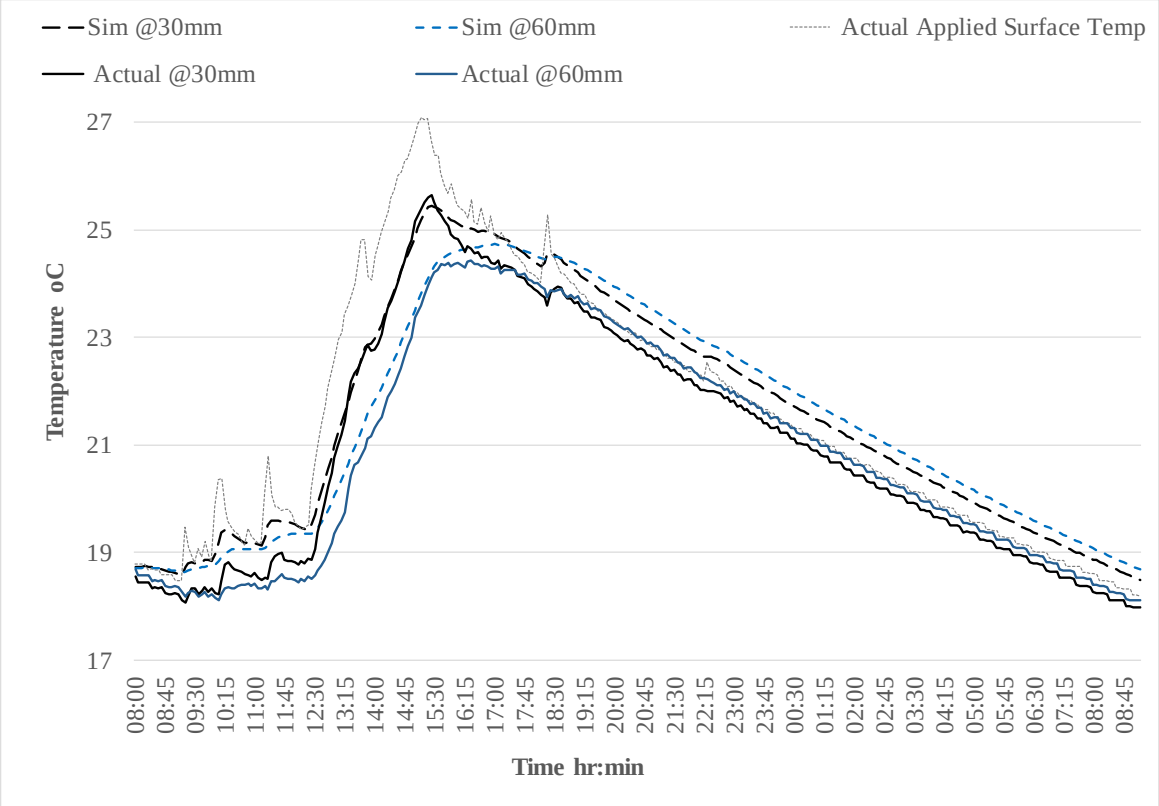


(a)

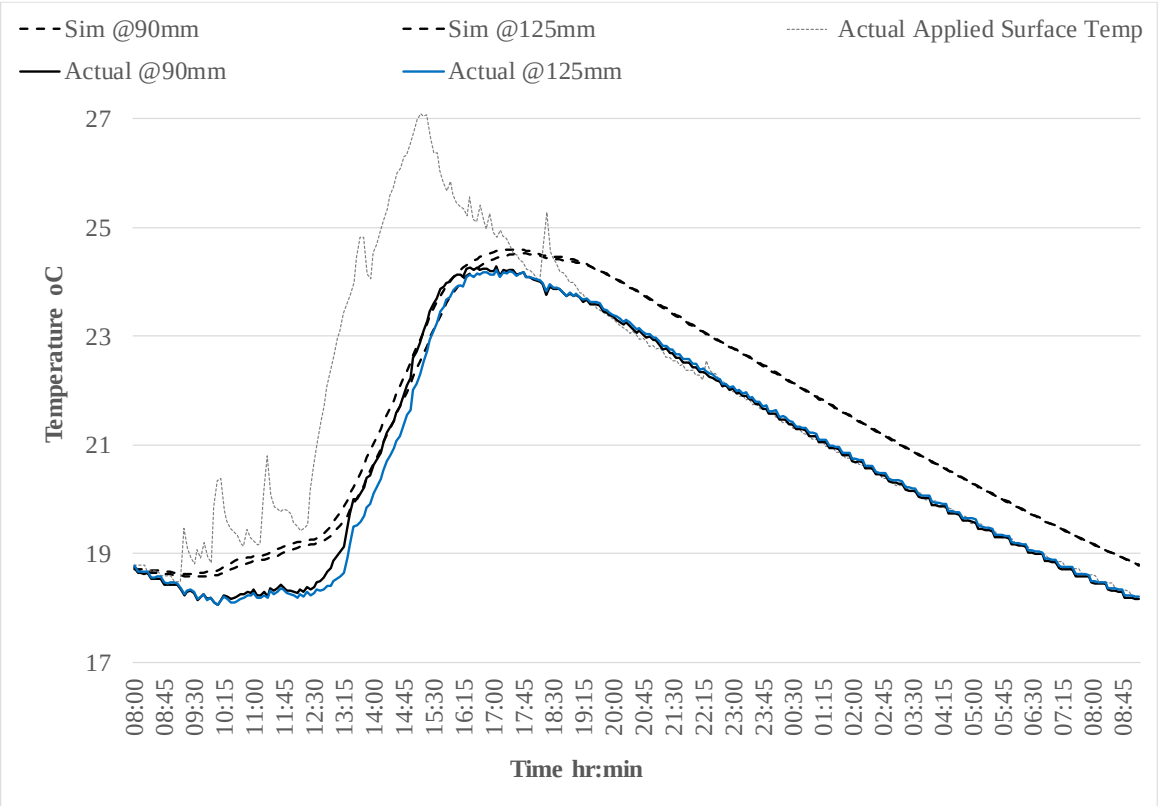


(b)

**Figure 8-3 Comparison of simulated temperatures and real temperatures in Control hut wall on 27th to 28th Dec 2017 at (a) 30 mm and 60 mm depth, (b) at 90 mm and 125 mm depth**

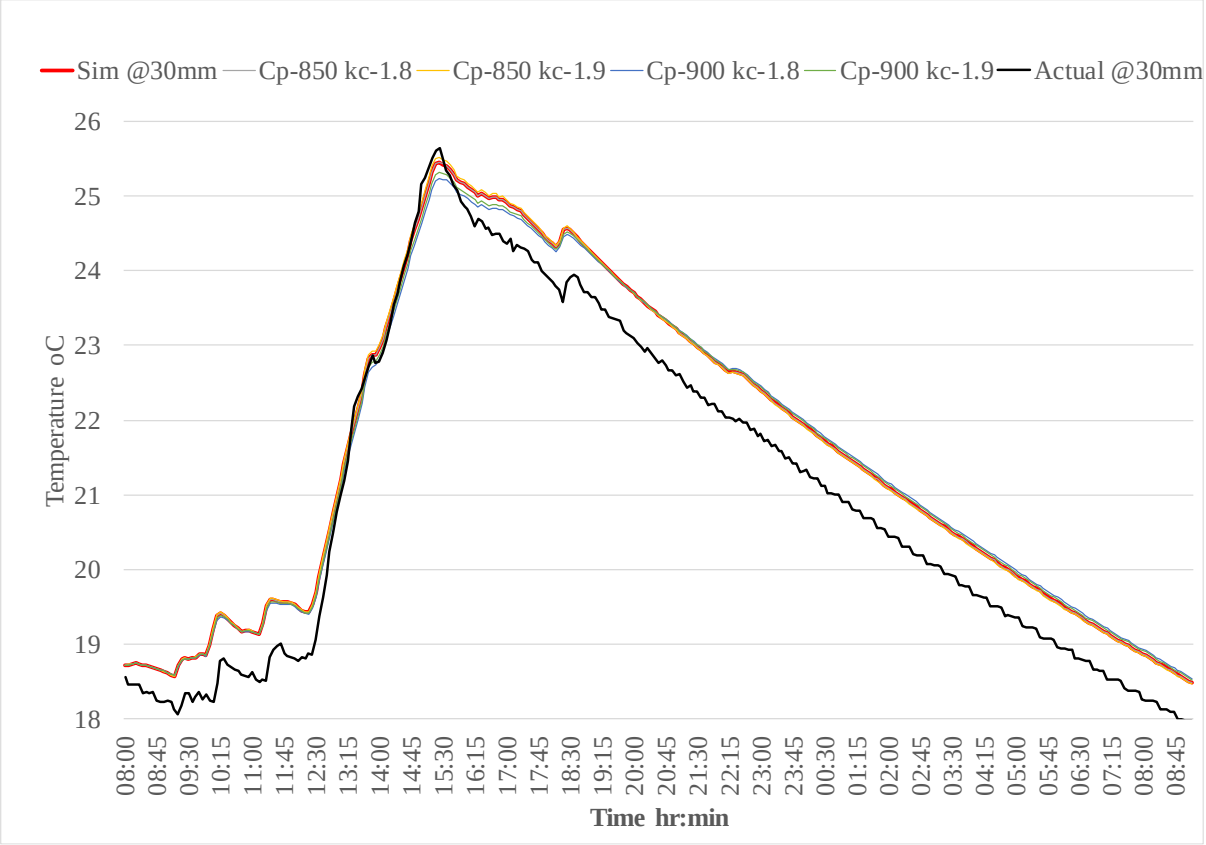


**Figure 8-4 Comparison of actual temperature data and simulation data at 30 mm depth for various combinations of kc and Cp,c.**

It can be noted from Figure 8-4 that there is no discernible difference between the simulations which used the four combinations of $k_c$ and $C_{p,c}$ and the original simulation which used $k_c$ =1.86 W/mK and $C_p$ = 881 J/kg. For this reason the values adopted for the thermal conductivity and specific heat capacity of the Control concrete were $k_c$ =1.86 W/mK and $C_p$ = 881 J/kg for all further simulations.

Another model refinement exercise was carried out to check if the mesh size used in the simulations is sufficiently fine. In COMSOL the mesh size can be either ‘user defined’ or ‘physics defined’, that is, it is automatically tailored to each type of heat transfer interface. When a ‘physics defined’ mesh is selected, the mesh and element size is adapted to the physics settings as set up by the user in the model. The default element size selected by COMSOL when the model was initially set up was defined as ‘finer’ and is shown in Figure 8-5 (a). To explore whether the use of a smaller mesh element would result in more accurate simulations, simulations were run using an ‘extra fine’ mesh and an ‘extremely fine’ mesh as shown in Figure 8-5 (b) and (c) respectively.

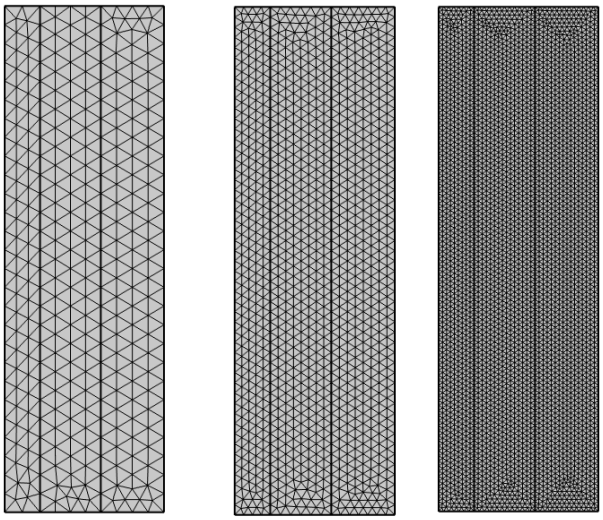

(a) Finer (b) Extra fine (c) Extremely fine

**Figure 8-5 Image of mesh sizes used in initial simulations**

Figure 8-6 shows a comparison of simulated temperatures at a depth of 30 mm in the North wall of the Control hut for each different mesh size. It can be noted from Figure 8-6 that there is practically no difference between the simulated temperatures derived using the extra fine mesh and the extremely fine mesh.

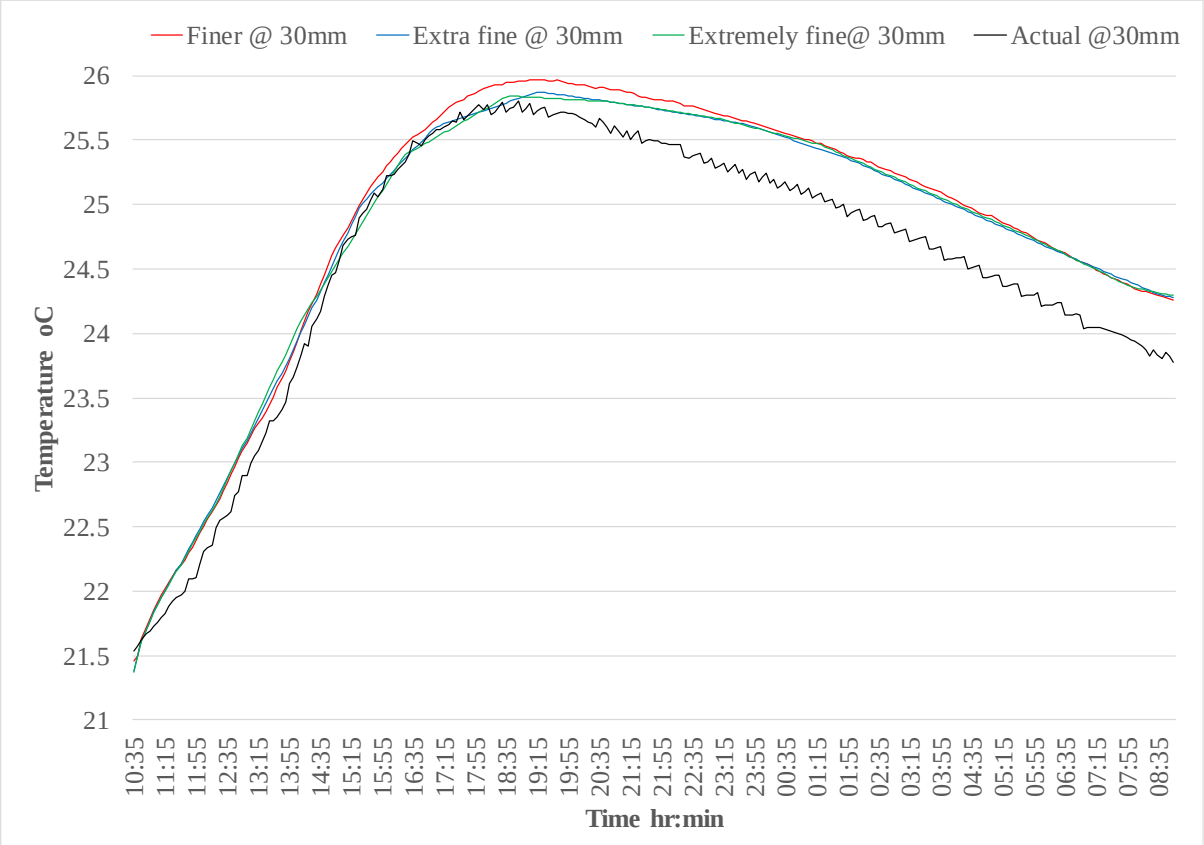


**Figure 8-6 Comparison of simulated temperatures at the depth of 30 mm derived using 'Finer', 'Extra Fine' and 'Extremely fine' meshes**

The extra fine mesh and extremely fine mesh provide marginally more accurate results than the finer mesh, however the difference is insignificant. For the 3-D, 1.0 m x 1.0 m models, the extra fine mesh was adopted however when the 3-D model of the huts was developed the finer mesh was adopted in order to reduce the significant computation cost of the simulations, with no significant loss of accuracy anticipated.

It was concluded that the COMSOL model was simulating the thermal behaviour of the Control concrete with sufficient accuracy using a fine mesh. The next step in the development of the model is to define the thermal behaviour of the microencapsulated paraffin PCM within COMSOL.

### 8.3.2 Modelling of the PCM

The Heat Transfer Module in COMSOL Multiphysics uses the Apparent Heat Capacity method to model PCMs as described in Section 2.8.2. In this method the latent heat is included as an additional term in the heat capacity when defining the material properties of the PCM. This method is the most suitable for phase transitions from liquid to solid, or solid to liquid.

As the melting and solidification of the PCM occurs across a temperature range, $\Delta T$, it is assumed that the transformation occurs in a temperature interval between $(T_{pc}-\Delta T/2)$ and $(T_{pc}+\Delta T/2)$ where $T_{pc}$ is the peak phase change temperature (24 $^{o}$C for the Micronal PCM used in this project). In this interval, the material phase is modelled by a smoothed function, $\theta$, representing the fraction of phase before transition:

- When all PCM is solid, $\theta = 1$ @ $T \leq (T_{pc} - \Delta T/2)$
- When all PCM is melted, $\theta = 0$ @ $T \geq (T_{pc} + \Delta T/2)$

The density, $\rho$, effective thermal conductivity $k_{eff}$ and the specific enthalpy, H (heat absorbed or released), of the PCM are expressed by (COMSOL Heat transfer module user's guide):

$$\rho = \theta\rho_{sol} + (1 - \theta)\rho_{liq} \quad \textbf{(8-1)}$$

$$k_{eff} = \theta k_{,sol} + (1 - \theta)k_{,liq} \quad \textbf{(8-2)}$$

$$H = 1/\rho\,(\theta\rho_{sol}.H_{sol} + (1 - \theta)\rho_{liq}H_{liq}) \quad \textbf{(8-3)}$$

where the sol and liq subscripts refer to the material properties of the PCM when it is in a solid and liquid state respectively.

The apparent specific heat capacity $C_p$ at temperature T for the PCM material is given by the equivalent heat capacity, $(\rho H)+ C_L$, where $C_L$ is the latent heat (Kylili et al. 2016):

$$C_p = 1/\rho[\theta\rho_{sol}.C_{psol} +(1- \theta)\rho_{liq}.C_{pliq}] + (H_{liq} - H_{sol})\frac{da_m}{dT} \quad \textbf{(8-4)}$$

where:

$$a_m = \text{mass fraction} = \frac{1}{2}.\frac{(1-\theta)\rho_{liq}-\theta\rho_{sol}}{\rho} \quad \textbf{(8-5)}$$

The Micronal PCM was set up as a new material in COMSOL. The material properties for the solid and liquid phases of the PCM are specified separately and are provided in Table 8-1.

**Table 8-1 Material properties of Micronal PCM used in the COMSOL model**

| Parameter | Value |
|---|---|
| Phase change temperature range, ΔT | 5.23 $^oC$ |
| Peak phase change temperature, $T_{pc}$ | 24.4 $^oC$ |
| Specific heat capacity of solid PCM, $C_{psol}$ | 1972 J/kg*K |
| Specific heat capacity of liquid PCM, $C_{pliq}$ | 1647 J/kg*K |
| Latent heat capacity of PCM during melting, $H_{sol}$ | 91000 J/kg |
| Latent heat capacity of PCM during solidification, $H_{liq}$ | 88200 J/kg |
| Density of solid PCM, $\rho_{sol}$ | 870 kg/$m^3$ |
| Density of liquid PCM, $\rho_{liq}$ | 750 kg/$m^3$ |
| Thermal conductivity of solid PCM, $k_{sol}$ | 0.22 W/mK |
| Thermal conductivity of liquid PCM, $k_{liq}$ | 0.17 W/mK |

The phase change temperatures, specific heat and latent heat capacities were derived from the DSC tests as described in Section 4.1.2. The other data was sourced from the suppliers of Micronal, BASF. These values are combined with the phase transition function θ, so that there is a smooth transition from solid to liquid (and vice versa) across the phase change temperature range and the thermal behaviour during phase change can be accurately modelled.

### 8.3.3 Incorporating thermal hysteresis behaviour of PCM into the COMSOL model

As noted in Section 4.1.2, some thermal hysteresis behaviour was observed from the DSC heating and cooling enthalpy curves for the Micronal PCM. That is, the onset solidification temperature (23.0 $^oC$) was lower than the highest temperature of the melt temperature range (25.4 $^oC$). This behaviour adds further complexity to the model of the phase change behaviour.

The thermal hysteresis behaviour can be described graphically by plotting the heating and cooling enthalpy curve against temperature using the results of the DSC tests, as shown in Figure 8-7.

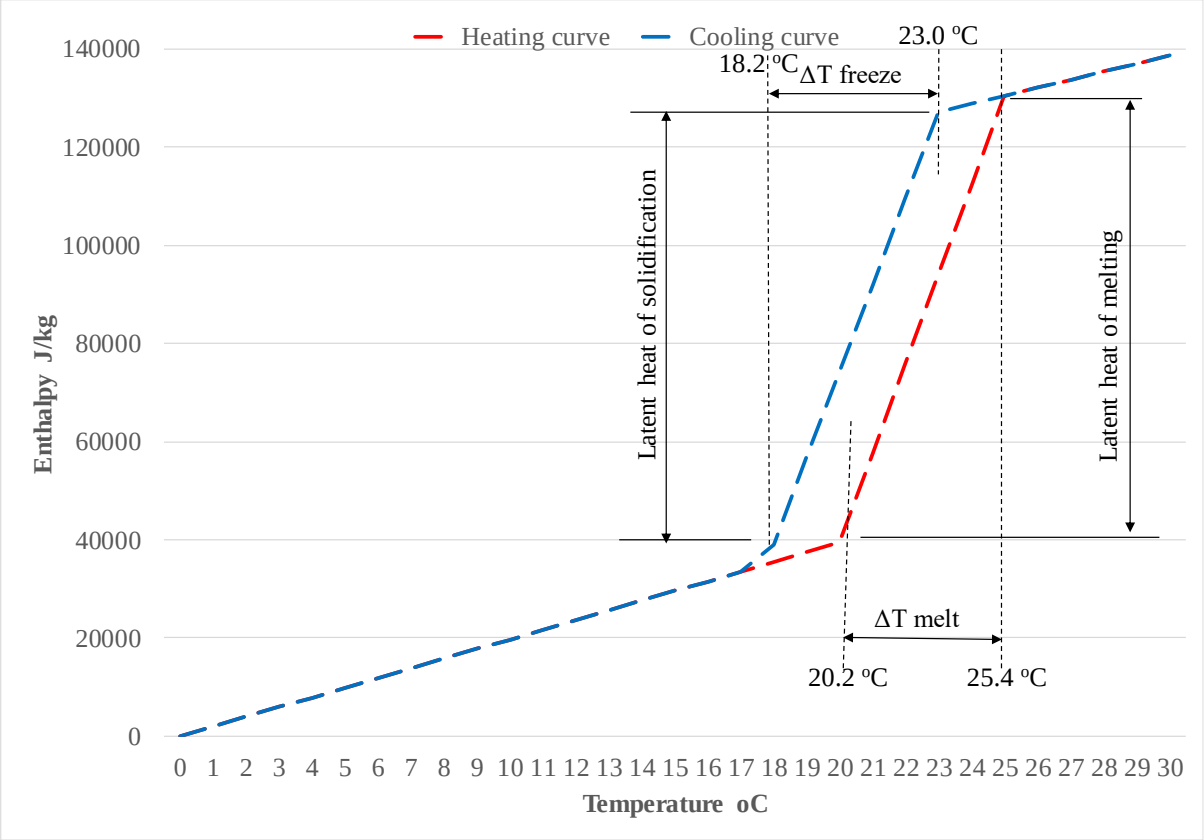


**Figure 8-7 Heating and cooling enthalpy curves for Micronal PCM showing thermal hysteresis**

When the material is in the solid state and is being heated, the enthalpy is given by the red curve. As the material passes the highest temperature of the melting phase change temperature range, that is 25.4 ºC, the PCM is completely liquid. When the PCM is subsequently cooled, it will follow the upper blue curve, thus the PCM remains in a completely liquid state until its temperature falls below the highest temperature of the solidification phase change temperature range, that is 23.0 ºC. During the solidification phase change, the PCM does not become completely solid until the lowest temperature of the solidification temperature range is reached, that is at 18.2 ºC. In the completely melted or completely solid state, the two enthalpy curves overlap.

The overall heat capacity of the PCM is the derivative of the enthalpy curves with respect to temperature and it is different depending on whether the material is being heated or cooled. To incorporate this thermal hysteresis into the COMSOL model, two separate enthalpy functions were created, one for the melting phase and one for the solidification phase. These functions were then used in the equation to define the temperature dependant heat capacity of the PCM during phase change. The enthalpy functions were defined in COMSOL as follows:

- Enthalpy function, Solid to liquid [H_StoL]:

$$Cpsol*T+LHmelt*step1((T-Tmelt)/dTmelt) \quad \textbf{(8-6)}$$

- Enthalpy Function, Liquid to Solid [H_LtoS]:

$$Cpliq*T+LHfrz*step1((T-Tfreeze)/dTfreeze) \quad \textbf{(8-7)}$$

where:

- T is the temperature in the element of PCM as determined by COMSOL
- Tmelt is the peak melt temperature of the PCM – 24.4 $^{o}$C
- Tfreeze is the peak solidification temperature of the PCM – 20.8 $^{o}$C
- dTmelt is the melt phase change temperature range – 5.2 $^{o}$C
- dTfreeze is the solidification phase change temperature range – 4.8 $^{o}$C
- LHmelt is the latent heat of PCM during the melt phase change – 91000 J/kg
- LHfrz is the latent heat of PCM during the solidification phase change – 88200 J/kg
- Cpsol is the specific heat capacity of solid PCM – 1972 J/(kg.K)
- Cpliq is the specific heat capacity of liquid PCM - 1647 J/(kg.K)
- Step1 is a smoothed step function that defines how much latent heat has been absorbed or released (Figure 8-8)

The plot for step1 is shown in Figure 8-8. If the value of the argument of step1, that is for example (T-Tmelt)/dTmelt), is less than -0.5 then the value of step1 is 0. If the value of the argument is greater than +0.5 then the value of step1 is 1. When the value of the argument lies between -0.5 and +0.5 then the corresponding value of step1 lies between 0 and 1. This step function is applied to the phase change element of the enthalpy functions (8-6) and (8-7) to account for the phase change occurring over a temperature range.

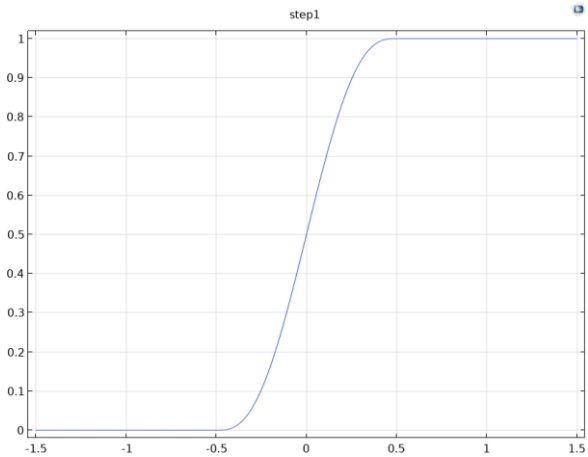


**Figure 8-8 Plot of step function step1**

The heat capacity for the PCM is then defined as follows:

$$\text{Heat capacity} = \text{SorL}*d(H\_StoL(T),T)+(1-\text{SorL})*d(H\_LtoS(T),T) \quad \textbf{(8-8)}$$

where the differentiation operator takes the derivatives of the two different enthalpy functions with respect to temperature and the SorL variable defines the local PCM behaviour as either *Solid* or *Liquid*. The SorL variable is either zero or one and can be different in each element of the mesh. It was defined as follows:

$$\text{SorL} - (\text{if}(T>T\_top,0,\text{if}(T<T\_bot,1,\text{SorL}))) \quad \textbf{(8-9)}$$

where:

- T_top is the temperature at which all the PCM is melted - 25.4 $^{o}$C
- T_bot is the temperature at which all the PCM has solidified- 18.2 $^{o}$C

If the current temperature of the mesh element is greater than T_top then the PCM has passed its solid-to-liquid phase-change temperature, so SorL is taken as '0'. Referring back to the heat capacity equation (8-8), this results in the liquid-to-solid enthalpy curve (H_LtoS) being followed. If the current temperature is less than T_bot, then the PCM has passed its liquid-to-solid phase-change temperature, so SorL is taken as '1'. This results in the solid-to-liquid enthalpy curve (H_StoL) being followed. When neither of the previous two conditions are satisfied, the SorL variable is taken as its previous value, meaning that there is no change of curve while in the intermediate zone. A previous solution operator was set up to allow COMSOL access the value of the SorL variable at the previous time step for use in its current computation. The initial value of SorL is set at '0' if the PCM is expected to be fully melted at the start of the simulation and set at '1' if the PCM is expected to be fully solid at the start of the simulation.

### 8.3.4 3-D modelling of the panel incorporating PCM-concrete composite

The material properties of the PCM-concrete composite material are dynamic in that they will vary with temperature and also with depth. Defining these dynamic properties within the COMSOL software was a particular challenge of this project. The PCM-concrete composite material was modelled using the Heat Transfer in Porous Media module in COMSOL. A porous media was chosen to reflect the fact that the PCM-concrete concrete is not a fully homogenous material. The PCM exists in discrete capsules suspended within and dispersed evenly through the concrete matrix material. In between the location of the PCM capsules, heat transfer will occur in accordance with the thermal properties of the concrete matrix material alone.

In COMSOL a porous media is defined as a solid matrix material with a specified percentage of pores which are filled with a fluid. To set up the PCM-concrete material, the Control concrete mix was used as the main matrix material in the porous media. The density, thermal conductivity and specific heat capacity of this concrete had been previously determined in the laboratory and these values were used to define the material properties of the solid matrix material of the porous media. The fluid material within the pores was assigned as the PCM material with material properties and thermal behaviour as defined in 8.3.2 and 8.3.3. The volume fraction of Micronal that was added to the concrete was determined as 30% (Appendix T) and set as the volume fraction of the porosity, that is, the volume fraction of pores filled with PCM, set as $(1 - \theta_c)$, where $\theta_c$ is the volume fraction of concrete, that is, 70%. Therefore, the effective thermal conductivity of the porous media was defined as:

$$k_{eff} = k_c\theta_c + k_{PCM}\,(1 - \theta_c) \qquad \textbf{(8-10)}$$

The subscript c refers to concrete.

Similarly the effective specific heat capacity of the porous media was defined as:

$$(\rho Cp)_{eff} = \rho_c\, C_{p,c}\, \theta_c + \rho_{PCM} C_{p,PCM}(1 - \theta_c) \qquad \textbf{(8-11)}$$

The model as described in Section 8.2.1 was adjusted to replace the material of the 125 mm thick inner leaf of the panel with the PCM-concrete composite material, as defined by the porous media set up in COMSOL. This model was validated using the data collected in the Full PCM hut.

A number of different 24 hour periods of actual data collected at the Full PCM hut was selected for the simulation studies. The periods selected were ones during which the internal air temperature increased sufficiently to ensure that some of the PCM within the depth of the wall would change phase. One particular period of interest was 23rd – 25th October 2017 during which the heaters were from 9am to 4:30pm to simulate the summer overheating conditions ('On' set point 24 $^{o}$C, 'Off' set point 28 $^{o}$C) and natural ventilation was provided at night by leaving the doors open 100 mm to assist the discharge of heat from the internal walls. The actual data from this period was analysed in Section 7.5.3.4. Figure 8-6 shows a plot of the actual temperatures recorded within the inner leaf of the North wall of the Full PCM hut during this period. The shaded areas indicate when the temperature of the PCM-concrete inner leaf increased above 20 $^{o}$C which is the onset melt temperature of the PCM.

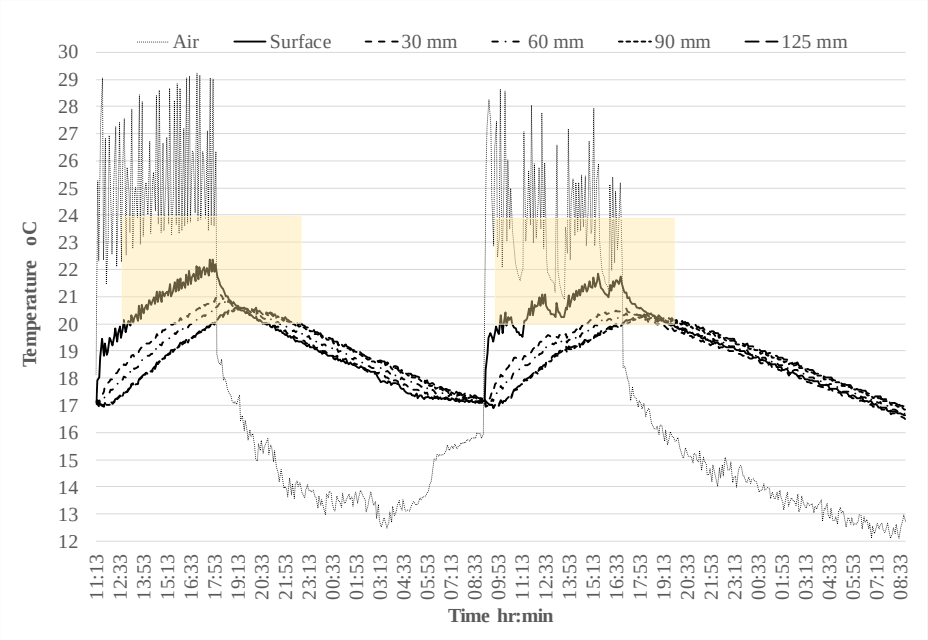


**Figure 8-9 Actual temperature data for the inner leaf of the North wall of the Full PCM hut, 23rd – 25th October 2017**

The actual temperature profile recorded at the internal surface of the wall during this period was imported into the model and applied as heat input to the internal surface of the 3-D model. The external temperature recorded was also imported and applied to the external surface of the model panel. Figures 8-10 and 8-11 show comparisons between the simulated temperatures and actual temperatures recorded at depths of 30 mm and 60 mm, and 90 mm and 125 mm respectively within the PCM-concrete composite wall.

The simulated and actual temperatures follow a similar pattern with an average difference of 0.42 ºC at 30 mm depth, 0.41 ºC at 60 mm depth, 0.44 ºC at 90 mm depth and 0.35 ºC at 125 mm depth during the 46 hour period. It can be noted that the simulation temperatures increase at a slightly faster rate during the heating period, while the rate of cooling is similar for both. These observations may indicate that the thermal conductivity of the PCM-concrete composite in the model is too high. However, a parametric sweep was carried out in which the thermal conductivity and specific heat capacity of the matrix concrete were varied, as described in Section 8.3.1. The results of this investigation showed that changing these parameters did not improve the accuracy of the simulated results. This type of modelling process was carried out for a number of data sets taken from different weather seasons and applied heat load patterns, leading to differences between the simulated results and real data of no more than 0.32 ºC – 0.46 ºC. As this difference between the simulated temperatures and the actual temperatures is less than the calibrated accuracy of the thermocouples used, the model was deemed to be sufficiently accurate in modelling the thermal behaviour of the PCM-concrete composite.

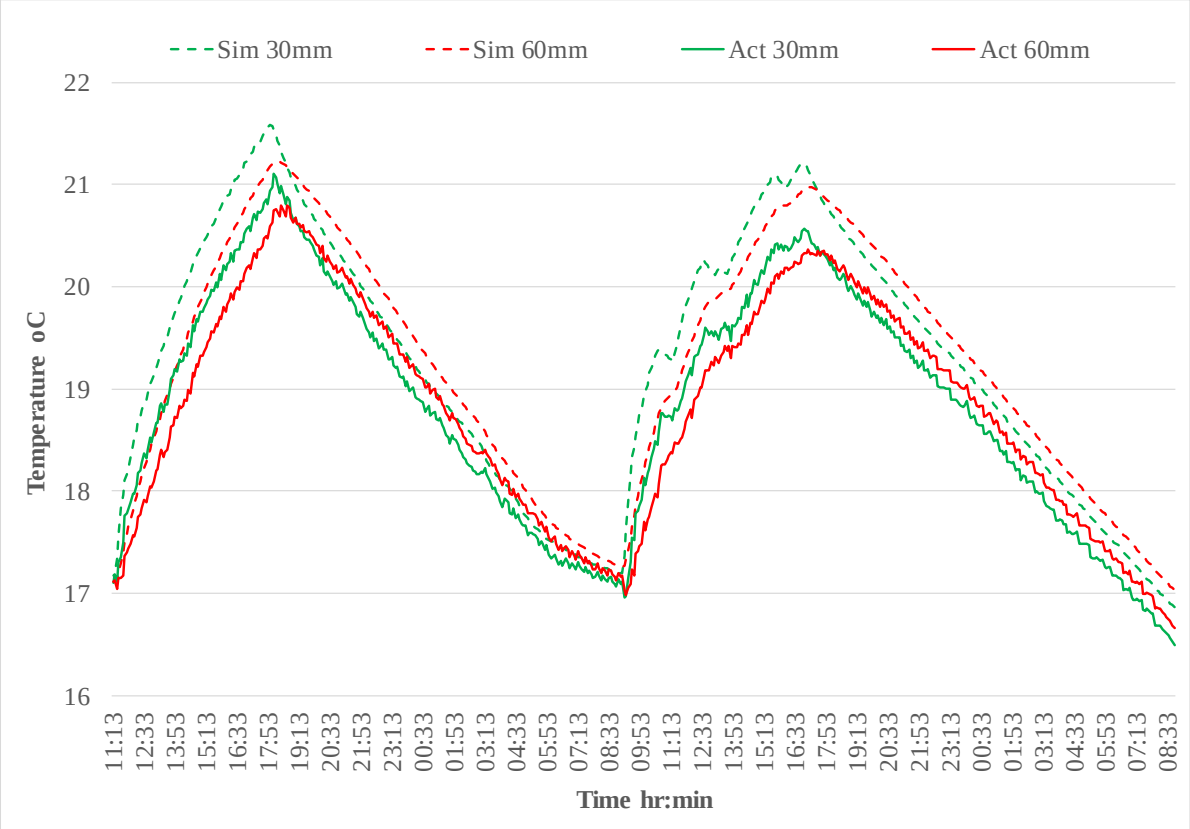


**Figure 8-10 Comparison of simulated and actual temperatures recorded at depths of 30 mm and 60 mm, Full PCM hut, 23rd to 25th October 2017**


**Figure 8-11 Comparison of simulated and actual temperatures recorded at depths of 90 mm and 125 mm, Full PCM hut, 23rd to 25th October 2017**

## 8.4 3-D Thermal modelling of the full-scale huts

### 8.4.1 Setting up the geometry and initial conditions of the model

As described in Sections 8.2 and 8.3 the 3-D panel models created in COMSOL simulate the thermal behaviour of both the Control concrete and the PCM-composite concrete with sufficient accuracy. The next step in the process for developing a simulation model for the full-scale huts was to create a 3-D geometric model in COMSOL that reflected the geometry of the full-scale huts as constructed in Techrete.

A geometric model was built in COMSOL in accordance with the as-constructed drawings of the hut, as shown in Figure 3-13 (a) and (b) and described in Sections 3.6 and 7.1. The hut geometry was orientated so that the glazed façade was facing South. The internal space of the hut was defined as a fluid domain of air. The glazed elevation was assigned from COMSOL's inbuilt library of materials as double glazing with a U-value of 1.2 $W/m^2K$.

Virtual probes were located in the model to coincide with the location of the thermocouples in the actual huts. The model is set up to output the temperature at each probe every five minutes during a simulation. These simulated temperatures can then be compared to the actual temperatures recorded in the huts to validate the model. A probe was also located at the centre of the air domain of the hut to coincide with the thermocouples located in the actual huts to record internal air temperature. The block of air was also set up as a domain probe which outputs the average temperature of the entire internal block of air in the model of the hut.

Once a model of the hut had been 'built', specific data was entered or imported to set up a simulation for a particular time period. Given the number of probes and the complexity of the thermal behaviour being modelled, the computational cost of a simulation is relatively high. For this reason the maximum time period for a simulation was restricted to 24 hours which resulted in a typical simulation running time of 5 to 6 hours. Four different 24 hour time periods were selected for the simulation. These time periods coincide with the time periods analysed in Chapter 7 and the aim of modelling these periods is to investigate if the 3-D model of the huts is accurately simulating the thermal behaviour of the following:

1. 19th November 2017 – the walls during winter environmental conditions when any PCM present remains solid

2. 21st June 2017 – the walls during summer environmental conditions when any PCM present remains liquid

3. 1st November 2018 – the walls during winter environmental conditions when any PCM present goes through a phase change

4. 10th June 2017 - the walls during summer environmental conditions when any PCM present goes through a phase change

To set up the model for a particular time period, data recorded at the huts during that time period were imported into the model. Each simulation is preconditioned as the initial temperature of each element of the model is set as the actual temperature recorded for that element at the start of the time period. All time periods commence at midnight and the difference between the actual temperature of the internal walls in each type of hut was negligible. The initial temperature of the internal walls was taken as the average of the temperatures recorded at 30 mm, 60 mm 90 mm and 125 mm depth. The deviation of these temperatures from the average was less than 0.15 $^{o}$C. The surface temperature was omitted from this calculation as it is influenced by the adjacent air temperature. The varying external air temperature as recorded at the hut locations during the relevant time period was imported as an interpolation function and applied to all the external surfaces of the model over time.

### 8.4.2 Modelling heat transfer

The purpose of the model is to accurately simulate heat transfer behaviour between the walls and the internal air of the hut. The COMSOL model consists of a heat transfer model coupled with a surface-to-surface radiation model with a solar position as an external radiation source. The model combines conductive heat transfer through the walls, convective heat transfer through the indoor air, and radiant heat transfer between the radiative heat source, the sun, and the walls.

#### *8.4.2.1 Modelling conductive heat transfer*

Conductive heat transfer through the depth of the walls depends on the thermal properties of the wall material, that is, the thermal conductivity, heat capacity and density. Each type of material used in the hut was created under the materials tab and assigned to the associated geometric element. The thermal properties of the Control concrete and insulation, as used in the 3-D panel models, were entered (refer to Section 8.3.1). In the model for the Full PCM hut,

the PCM and porous media materials were set up as described in 8.3.2, 8.3.3 and 8.3.4 and assigned to the inner leaf walls of the model.

*8.4.2.2 Modelling convective heat transfer*

Convective heat transfer will occur between the internal air and wall. The most accurate method to model convective heat transfer involves computational fluid dynamics (CFD) and requires the velocity of the air to be known. However the velocity of the air within the huts is not known and the use of CFD adds considerable complexity and computation cost to a model. COMSOL provides two simplified methods for modelling convection effects. One method involves applying a convective heat flux boundary condition on the wall-air boundary with an assumed convective heat transfer coefficient. The boundary condition is defined as follows;

$$\text{Heat flux at the boundary, } q = h(T_{ext} - T)\ W/m^2 \qquad \textbf{(8-12)}$$

where:

- h is the heat transfer coefficient ($W/m^2K$)
- $T_{ext}$ is the air temperature
- T is the wall temperature

This approach to modelling the convective heat transfer is useful if heat transfer is only being modelled through the solid walls, as was the case in the 3-D panel COMSOL models. $T_{ext}$ can be defined as the internal air temperature recorded at the hut. For free convection situations COMSOL provides a convective correlation that will compute the heat transfer coefficient for given air temperatures and surface geometries. However this method assumes the presence of an infinite external reservoir of air and the heat carried away from the wall surface goes into the ambient airspace without changing its temperature, so the air temperature itself cannot be modelled. For this reason this method for modelling convective heat transfer was dismissed for the 3-D models of the huts.

COMSOL provides a second method for including convective heat transfer in an enclosed space where the convective currents are 'free', that is there is no forced convection. In this method, referred to as the *equivalent conductivity for convection* feature, the effective thermal conductivity of the air is adjusted based upon correlations for the horizontal and vertical dimensions of a rectangular cavity. The air domain is meshed and COMSOL computes the temperature of each element of air at each time step. The thermal conductivity of the air is adjusted by an empirical correlation factor that depends on the cavity dimensions and the

temperature variation across the cavity. The dimensions of the cavity are entered, and in this case these are the internal dimensions of the hut. COMSOL automatically determines and updates the temperature difference across the cavity. A continuous temperature field is produced at the boundary and the heat flux at the boundary is computed subject to the temperature gradient at the wall surface. This method for including convective heat transfer effects was adopted for the 3-D models of the huts.

*8.4.2.3 Modelling radiative heat transfer*

During the time periods being modelled the heaters in the huts were switched off, that is passive conditions existed. The only heat source was the sun. The 'Heat Transfer in Solids' module in COMSOL models heat transfer in solids and fluids by conduction and convection. To model heat transfer by radiation, COMSOL's 'Surface-to-Surface Radiation' module was coupled with the 'Heat Transfer in Solids' module. This physical coupling facilitated the incorporation of an external radiation source of heat into the model. The external radiation source was defined as solar and the GPS co-ordinates of the huts were entered to define the location. The relevant date and start time were entered for each time period to define the correct position of the sun path in the model.

The solid surfaces which would be subjected to solar irradiance, that is the external and internal wall surfaces and the floor and ceiling surfaces, were set up as 'Diffuse' surfaces in the model. A diffuse surface is one that reflects radiation uniformly in all directions. To model the effects of irradiance on the exposed surfaces of the huts the emissivities of the surfaces must be defined. Emissivity is a measure of the ability of a surface to emit energy by radiation, and it can depend on the wavelength of the radiation. This is particularly relevant for thermal problems where the temperature variation is large or when there is exposure to a high-temperature source of radiation such as the sun.

If a surface of temperature T is exposed to ambient conditions which are at a lower temperature, $T_{amb}$ then the surface will radiate at many wavelengths, and the total radiative heat flux, q is:

$$q = \int_0^\infty \varepsilon_\lambda \sigma (T^4 - T_{amb}^4) d\lambda \qquad \textbf{(8-13)}$$

where

- $\varepsilon_\lambda$ is the wavelength-dependent emissivity
- $\sigma$ is the Stephan-Boltzmann constant, 5.667 x $10^{-8}$ ($W/m^2K^4$)

The above equation is reciprocal, that is it applies whether the surface is hotter or colder than the ambient environment. If the ambient environment is at a higher temperature, incident radiation will be absorbed by the surface. The amount of radiation absorbed by a surface is referred to as its absorptivity and according to Kirchoff's identity it is equal to the emissivity of the surface for a given wavelength.

In the model of the huts the solid surfaces can be assumed to be opaque, that is all incident radiation is either absorbed or reflected, and there is no transmission of radiation through the walls. It is also assumed that reflected radiation is reflected evenly in all directions, that is, it is diffusively reflected. This is a valid assumption for all surfaces other than highly polished surfaces.

Figure 8-12 provides a summary schematic of incoming irradiation G and outgoing radiosity, J, on the hut walls. The outgoing radiosity J is the sum of the diffusely reflected and the emitted radiation, that is,

$$J = \rho G + \varepsilon_\lambda \sigma T^4 \qquad \textbf{(8-14)}$$

where:

- ρ is the diffuse reflectivity factor (also referred to as albedo)
- T is the temperature of the wall surface

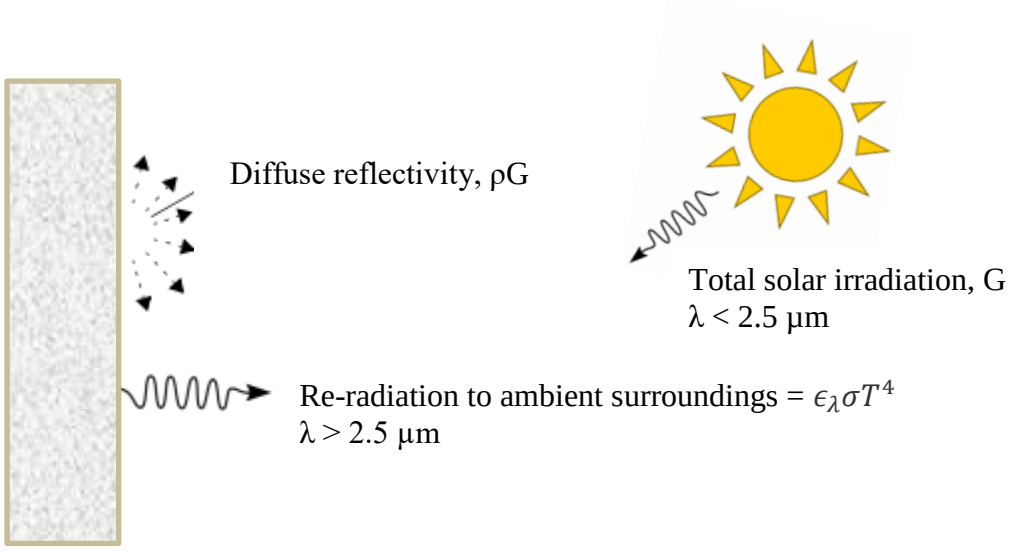


**Figure 8-12 Schematic of incoming solar radiation and outgoing radiosity acting on the hut walls**

The net inward radiative heat flux, q, that is the heat going into the wall, is given by the difference between the irradiance and the radiosity:

$$q = G - J \quad \textbf{(8-15)}$$

Substituting in equation (8-14) for J:

$$q = G - \rho G - \varepsilon_\lambda \sigma T^4 \quad \textbf{(8-16)}$$

Rearranging:

$$q = (1- \rho)G - \varepsilon_\lambda \sigma T^4 \quad \textbf{(8-17)}$$

where:

- $(1-\rho)$ is the absorptivity of the wall

As most opaque bodies behave as ideal grey bodies, that is the absorptivity and emissivity are equal, the heat flux at the wall surface, equation (8-17) can be written as:

$$q = \varepsilon_\lambda (G - \sigma T^4) \quad \textbf{(8-18)}$$

This expression was used to define the boundary condition of the wall surfaces in the COMSOL model. The solar irradiance G was user defined and the global irradiance data recorded by the pyranometer at the site of the huts for the relevant period was imported as an interpolated function. The temperature of the wall is computed at each step by COMSOL.

COMSOL allowed two different emissivity values to be entered for each opaque surface, one for short wavelength radiation, < 2.5 μm, which is suitable for solar radiation and one for longer wavelengths, > 2.5 μm, which is suitable for ambient conditions (defined in COMSOL as objects at a temperature below ~700 K). By splitting the bands at the default of 2.5 μm, the fraction of absorbed solar radiation on each surface is defined primarily by the user defined solar emissivity/absorptivity. The re-radiation at longer wavelengths and the reabsorption of this radiation is defined by the user defined ambient emissivity of the surface. The solar and ambient emissivities for the concrete surfaces were taken from literature as follows:

- Solar emissivity/absorptivity = 0.65 (Patil et al., 2018, Bretz et al., 1998)
- Ambient emissivity/absorptivity = 0.9 (Anderson 2006, Gupta, 2003, Myers, 2006)

Note that the air domain and the glazing domain were defined as transparent domains that allow radiation to pass through without having any effect on the domains themselves.

### 8.5 Validating the 3-D models using the actual data collected at the huts

In order to validate the COMSOL 3-D models, twelve models were set up in COMSOL as described in Section 8.4, one for each hut in each of the time periods as noted in Section 8.4.1. Initially simulations were carried out on the Control hut for each time period to ensure that the thermal behaviour of the Control concrete is being modelled with sufficient accuracy under the extended 3-D model conditions which include radiative and convective heat transfer conditions in addition to conduction. The simulated results of each hut were plotted against the actual results for each wall of the hut. The simulated internal air temperature was also plotted with the actual internal air temperature for each hut during each time period.

To ascertain the accuracy of the simulation results the absolute value of the simulated temperature ($T_{sim}$) minus the actual temperature ($T_{act}$) as recorded by the thermocouples, was calculated for each output at each thermocouple location. The average difference was calculated and denoted as 'Average $|T_{sim} - T_{act}|$'. To determine the precision of the Average $|T_{sim} - T_{act}|$ data, the standard deviation of each set of temperatures simulated at each thermocouple location was determined by calculating the square root of the variance of each data set. The variance of each data set was found by subtracting the Average $|T_{sim} - T_{act}|$ from each data point in the set, $|T_{sim} - T_{act}|$ and squaring the result. The variance is the average value of these squared values, that is:

$$\text{Variance} = \frac{\Sigma\,[|\text{Tsim,i} - \text{Tact,i}| - (\text{Average } |\text{Tsim} - \text{Tact}|)]^2}{\text{Number of data points}} \qquad \textbf{(8-19)}$$

All of the 48 no. plots comparing the simulated results and actual temperatures for each wall and the internal air, in each hut, during the four different time periods are provided in Appendix S along with the tabulated values for Average $|T_{sim} - T_{act}|$ and associated standard deviations. Figures 8-13 to 8-16 are examples of the plots provided in Appendix S and show simulated temperatures versus actual temperatures for the Control hut on 1st November 2018 and the Full PCM hut on the 10th June 2017.

The statistical data provided in Appendix S is summarised in Table 8-2. The values for Average $|T_{sim} - T_{act}|$ for each wall in a particular hut were averaged. The overall change in temperature in the walls and internal air, that is, the difference between the lowest temperature and the highest temperature, that occurred during the relevant time period is also noted as it is expected that a larger temperature difference will result in a higher value for the Average $|T_{sim} - T_{act}|$ as the difference between the simulation and actual results may accumulate.

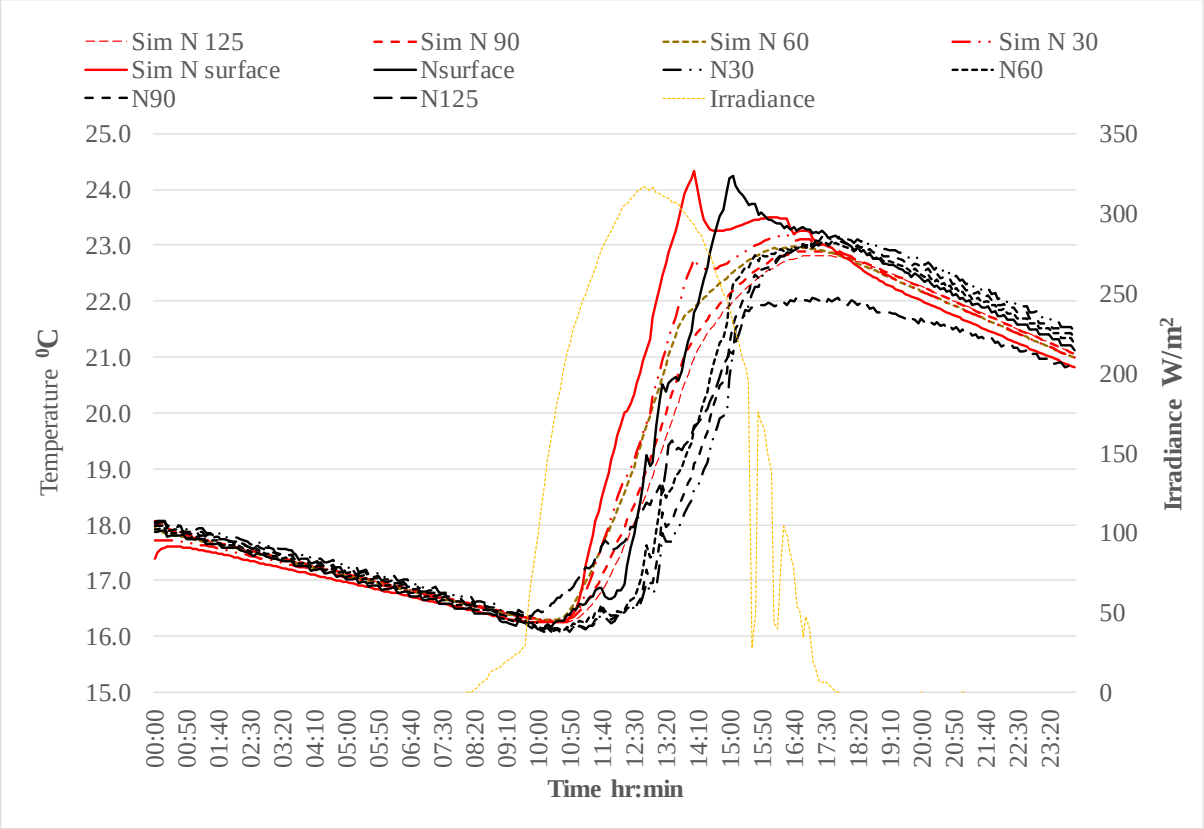


**Figure 8-13 1st November 2018, Control hut, North wall inner leaf simulated versus actual temperatures**

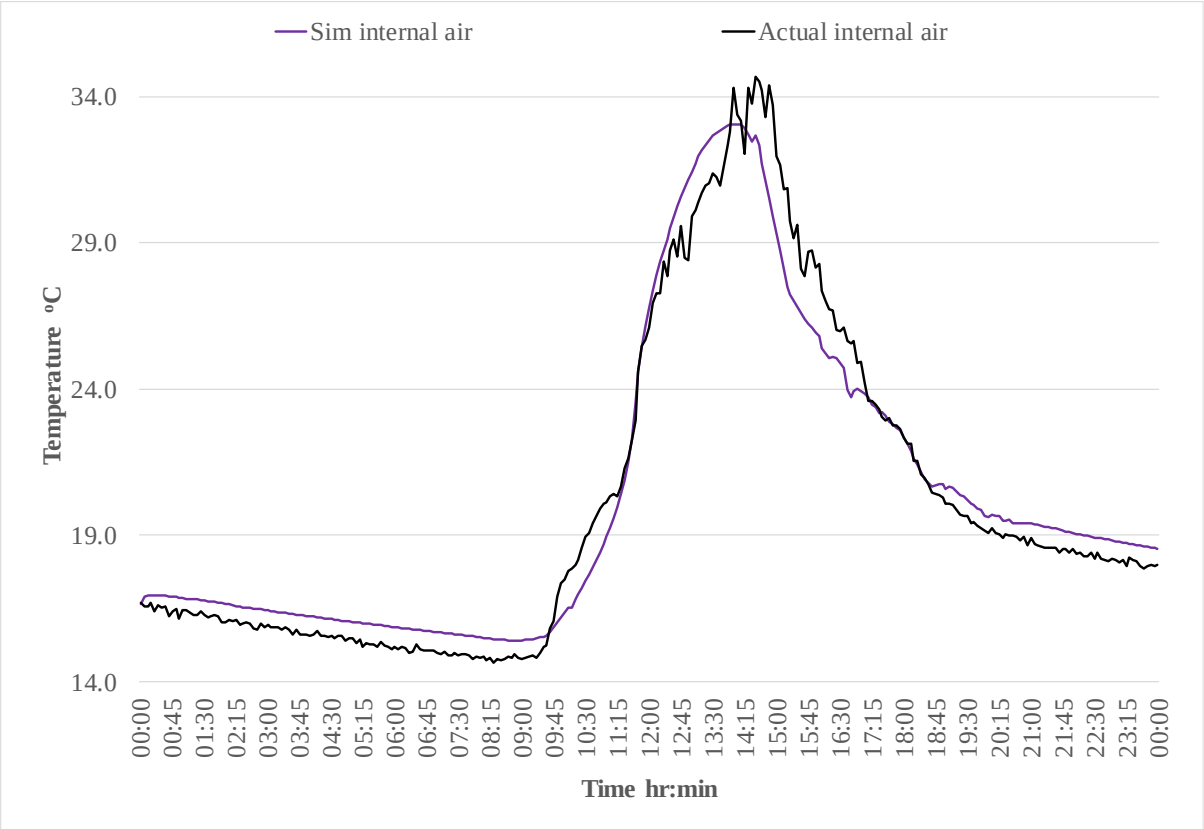


**Figure 8-14 1st November 2018, Control hut, simulated versus actual internal air temperatures**

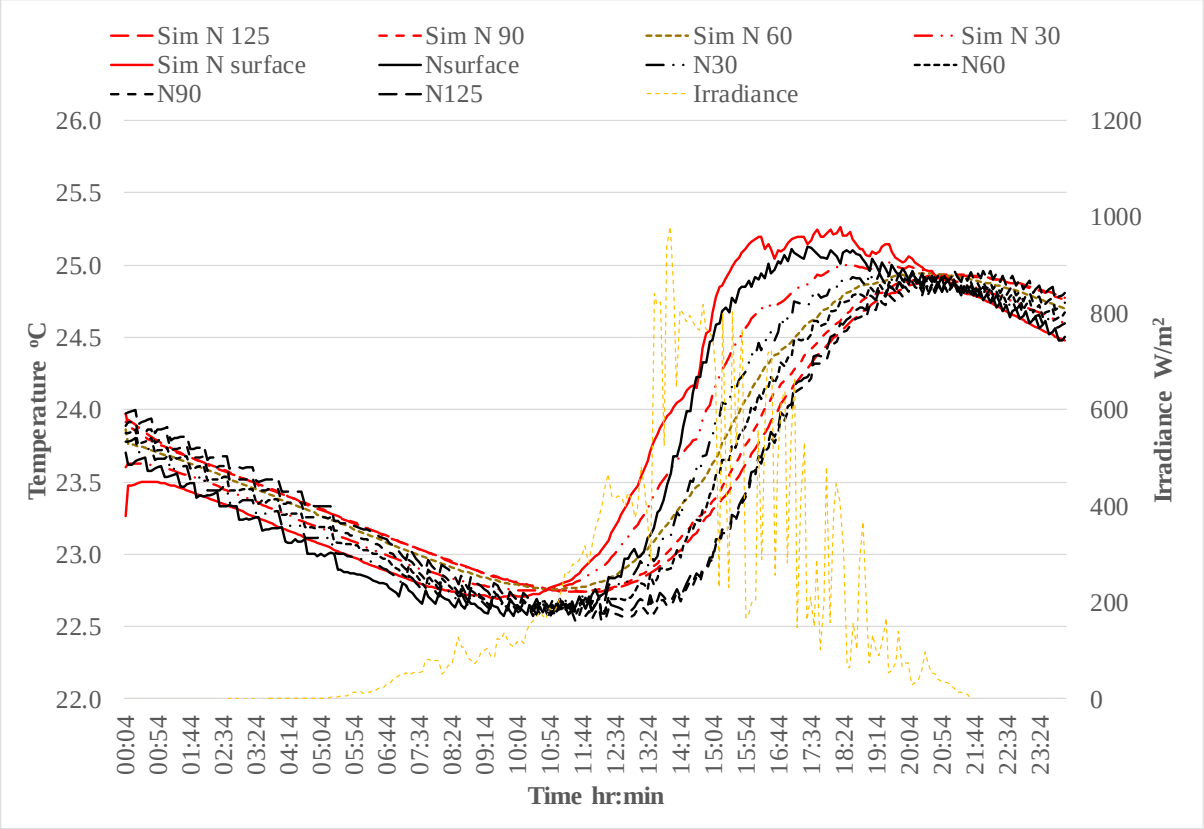


**Figure 8-15 10th June 2017 Full PCM hut, North wall inner leaf simulated versus actual temperatures**

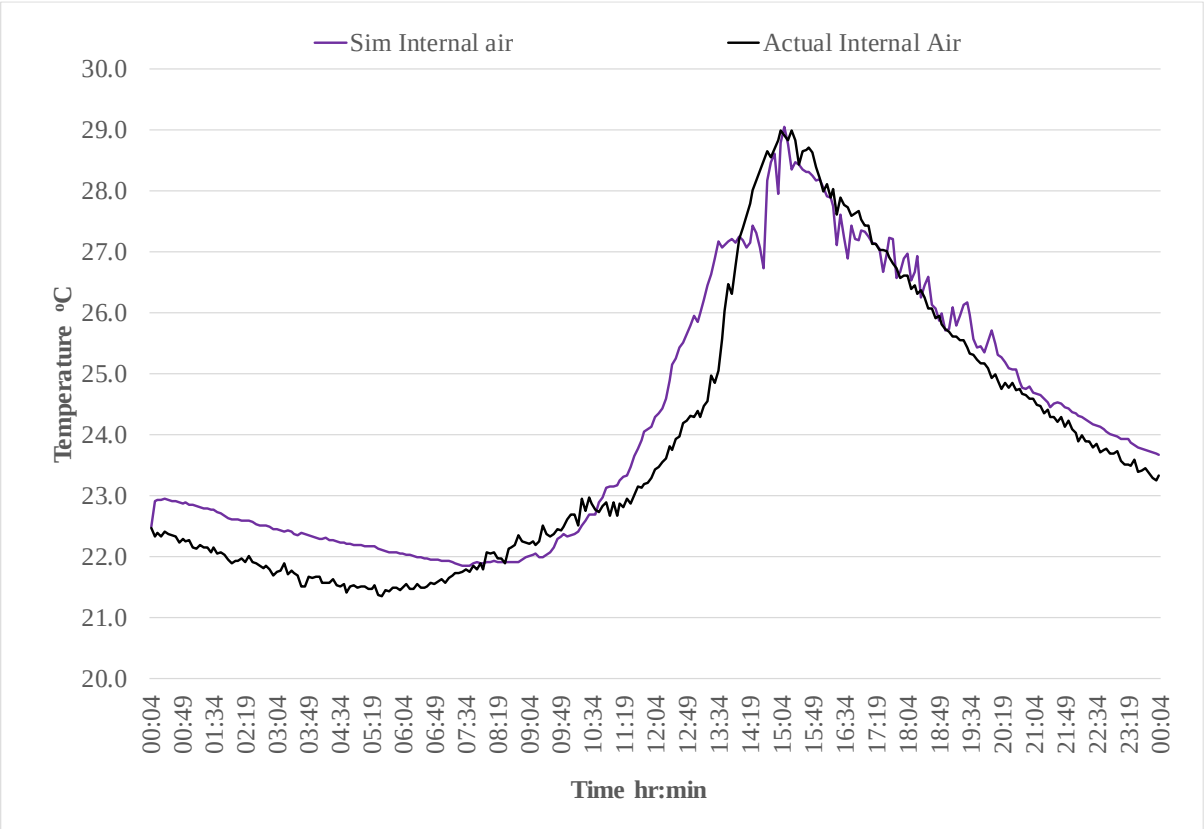


**Figure 8-16 10th June 2017 Full PCM hut, simulated versus actual internal air temperatures**

It can be noted from Table 8-2 that the accuracy of the simulations when the PCM is both engaged (10th June 2017) and not engaged (21st June 2017) are similar for both types of hut when the magnitude of the difference between the lowest and highest temperature in a particular hut, ΔT, is similar, that is 7.0 ºC to 7.5 ºC for the air and 2.2 ºC to 2.4 ºC for the walls, indicating that the thermal behaviour of the PCM-concrete is being modelled with similar accuracy whether phase change occurs or not. It can also be noted that the accuracy of the simulations carried out on the same day are similar for the Control concrete hut and the Full PCM hut indicating that the thermal behaviour of the PCM-concrete is being modelled with similar accuracy as the normal concrete.

**Table 8-2 Summary of statistical analysis of COMSOL simulation results**

| | | Control Hut | | Full PCM Hut | |
|---|---|---|---|---|---|
| Condition | Element | ΔT (ºC) | Average $\|T_{sim} - T_{act}\|$ (ºC) | ΔT (ºC) | Average $\|T_{sim} - T_{act}\|$ (ºC) |
| PCM not engaged (solid) | Wall | 0.7 | 0.13 | 0.6 | 0.1 |
| 19th Nov 2017 | Air | 3.0 | 0.5 | 3.0 | 0.3 |
| PCM not engaged (liquid) | Wall | 2.4 | 0.2 | 2.2 | 0.2 |
| 21st June 2017 | Air | 7.4 | 0.6 | 7.0 | 0.7 |
| PCM engaged winter | Wall | 7.0 | 0.4 | 5.8 | 0.6 |
| 1st Nov 2018 | Air | 19.6 | 0.8 | 16.0 | 1.3 |
| PCM engaged summer | Wall | 2.4 | 0.2 | 2.4 | 0.1 |
| 10th June 2017 | Air | 7.4 | 0.5 | 7.5 | 0.5 |

It can also be noted from Table 8-2 that the Average $|T_{sim} - T_{act}|$ values for the internal air temperatures are generally higher than for the wall temperatures. The use of a simplified method within COMSOL (*Equivalent conductivity for convection),* as described in Section 8.4.2.2, to account for the convective heat transfer effects may contribute to this slightly lower accuracy. A more rigorous approach using computational fluid dynamics may improve the accuracy of the simulation of the air temperatures. Another contributing factor to the higher Average $|T_{sim} - T_{act}|$ for the air is that the simulated temperature provided is the average temperature of the entire domain of internal air whereas the actual air temperature within the hut was recorded by a thermocouple located at the centre of the hut. Although the internal dimensions of the hut are relatively small it is still likely that small variations in temperature may occur across the air domain. It can also be noted from the statistical data provided in Appendix S that the accuracy of the simulated temperature at the surface of the walls is also

generally slightly lower which can be attributed to a simplified approach to modelling the convective effects of the internal air.

All values for the Average $|T_{sim} - T_{act}|$ at each thermocouple location in each wall are less than 0.86 $^{o}$C, the calibrated accuracy of the thermocouples with one exception, for the internal air of the Full PCM hut on the 1$^{st}$ November 2018 which is notably higher at 1.3 $^{o}$C. However, the difference between the lowest and peak air temperatures, $\Delta T$, during this period was also notably higher at 16.0 $^{o}$C. As can be noted from Figure 8-17 this can be attributed to the slightly earlier cooling of the air in the simulation. This results in larger differences in temperature between the simulated results and actual results at a given time during the cooling period following the peak temperature. However it can also be noted that the profile for the internal air temperature for both the simulated temperatures and recorded temperatures are similar and the peak temperature is the same for both indicating that the overall simulated thermal behaviour of the internal air is very close to the actual recorded thermal behaviour of the internal air in the hut.

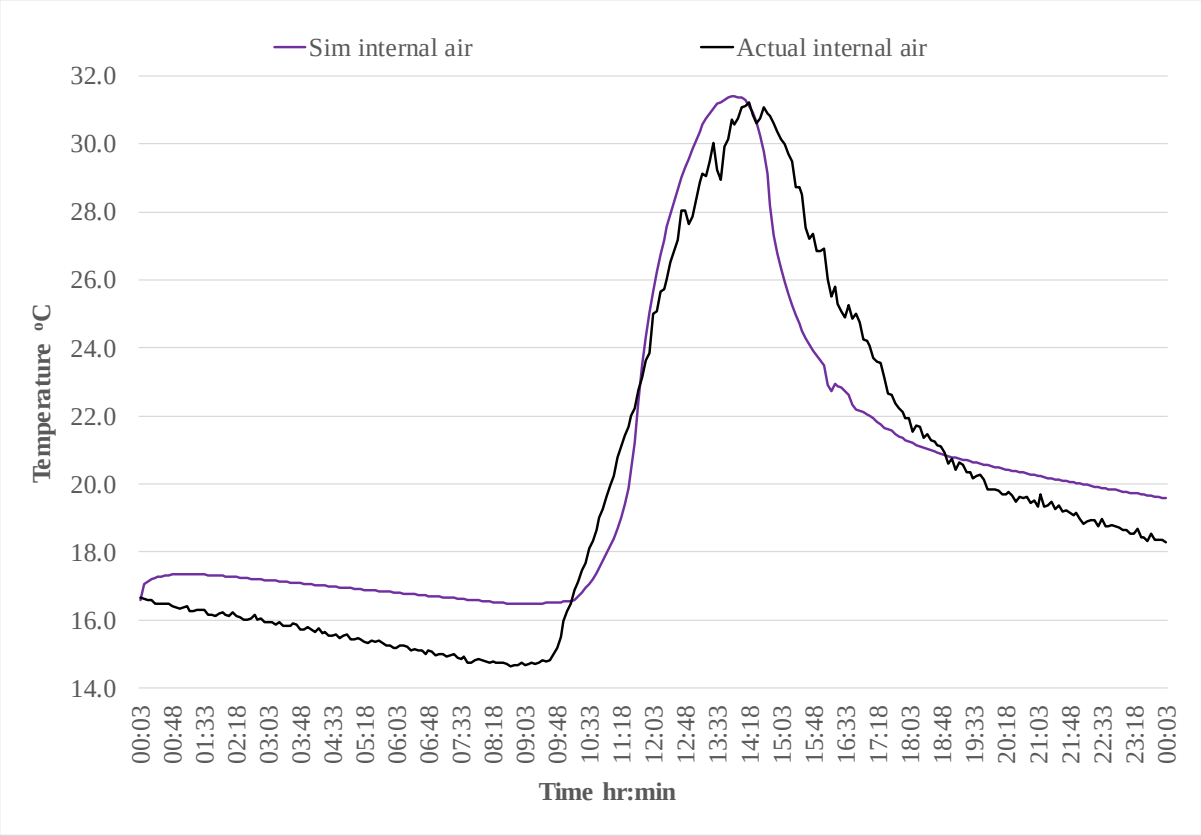


**Figure 8-17 1$^{st}$ November 2018 Full PCM hut, simulated versus actual internal air temperatures**

As noted in Section 8.3.4, in the 3-D models of the wall panels, the simulations generally displayed a marginally higher rate of heating. This general trend can also be observed in the plots of the 3-D simulations of the huts provided in Appendix S. This trend explains the higher value for Average $|T_{sim} - T_{act}|$ with an increase in temperature difference across the heating period, $\Delta T$, as the difference between $T_{sim}$ and $T_{act}$ accumulates.

The thermocouples used to measure temperature in the huts had a calibrated accuracy of +/- 0.86 $^{o}$C. With the exception of the data set measuring internal air on the 1$^{st}$ November 2018, all values for Average $|T_{sim} - T_{act}|$ were below 0.86 indicating that the COMSOL model simulates temperatures with similar accuracy as the thermocouples used in the huts. All simulations displayed good accuracy in the initial phase of the simulation prior to the start of the heating phase when the applied irradiance starts to enter the hut. The difference between the simulation and actual temperatures increases during the heating phase and subsequent evening cooling phase albeit while remaining acceptably low. This is expected as the complexity of the model increases with the introduction of irradiance and convection effects as the air heats up.

The graphical and statistical comparative analysis carried out on the results of the COMSOL model simulations of various environmental conditions demonstrates the validity of the developed COMSOL model. The results obtained from the simulations were aligned with the real temperatures recorded in the huts and hence the model can be used to reliably predict the thermal behaviour and impact of the PCM-concrete in a 'real world' full-scale scenario. The model can be used to observe and quantify any effects of using the PCM-concrete in various global locations and environmental conditions and for different geometries.

## 8.6 Scenario modelling

### 8.6.1 Introduction

There are many factors that influence the thermal mass performance of PCM-concrete in a building, including the geographical location, local climate, season, use, geometry and orientation of the building along with form of construction and extent and positioning of glazing. For this reason a simulation tool is essential to estimate the potential benefit of using PCM-concrete as the impact of the presence of PCM-concrete is unique to each project. For different projects in a given location the geometry, orientation and fenestration will always vary however the geographical characteristics of the location, such as distance from the sun,

solar altitude and daylight hours, which vary daily and seasonally, do not vary from year to year. For this reason, in this section the model developed in COMSOL to simulate the thermal behaviour of PCM-concrete is used to demonstrate the influence of geographical location and season on the potential thermal mass benefit of using PCM-concrete for a fixed geometry, orientation and fenestration. Geographical location has a significant influence on the intensity and duration of solar irradiance received by a building as well as prevailing ambient conditions. Several factors contribute to the variance in irradiance across different geographical locations including the tilt of the Earth's axis, the solar altitude angle and atmospheric conditions.

As displayed in Figure 8-18, the Earth's axis is tilted at 23.5 degrees relative to its orbit around the sun. During a summer season the hemisphere that is tilted towards the sun receives more intense irradiance as the solar radiation has a shorter distance to travel. The hemisphere that is tilted away from the sun experiences winter conditions with lower irradiance due to the longer distance that the solar radiation must travel.

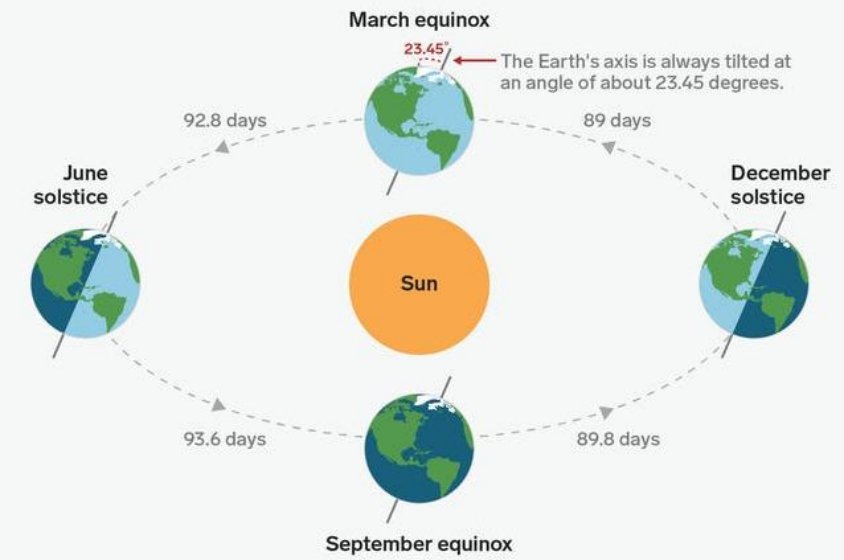


**Figure 8-18 Seasonal effects caused by Earth's axial tilt (Source: https://www.timeanddate.com/astronomy/seasons-causes.html)**

Atmospheric conditions including cloud cover, air pollution and atmospheric moisture content also affect the intensity of solar irradiance. Approximately 20% of solar radiation is absorbed by gaseous molecules in the atmosphere (Solanski, 2008) which reduces the solar radiation reaching the Earth's surface. Also, as the solar radiation passes through the atmosphere some of the solar rays interact with the gaseous molecules and particles and is scattered, causing some sun rays to change direction. Scattered radiation is referred to as diffuse radiation and on a clear day it accounts for approximately 15 - 20 % of the direct

radiation, which is the radiation which is neither absorbed nor scattered. The total radiation reaching the Earth's surface, referred to as global radiation, is the sum of the direct and diffuse radiation. As the distance between the sun and a location on Earth's surface increases the proportion of radiation that is absorbed increases and more scattering occurs resulting in reduced direct solar radiation reaching the surface and an increased proportion of diffuse radiation.

Locations within the same hemisphere also experience different intensities of solar irradiance at a given time due to differences in the solar altitude angle, which is the angle of the sun relative to the earth's horizon. The solar altitude angle describes how high the sun is and is $0^{o}$ at sun rise and $90^{o}$ at noon over the equator. As distance from the equator, that is latitude, increases the solar altitude angle decreases and hence the solar radiation must travel a longer distance leading to reduced intensity of solar irradiance. Due to the tilt of Earth's axis, the solar altitude angle is higher during the summer and lower during the winter. The solar altitude angle also varies with time of day and it is greatest at solar noon which is the time at which the sun is due South at a given location. Solar noon does not typically coincide with 12:00pm local time. The time at which solar noon occurs depends on latitude and time of the year.

To explore the scale of the impact of geographical location on the potential thermal mass performance of PCM concrete, three Northern hemisphere cities were selected, Oslo, Dublin and Madrid. The cities selected are spread apart in latitude to highlight the influence of the solar altitude angle. The latitude and longitude co-ordinates of each location are provided in Table 8-3.

**Table 8-3 Latitude and longitude for Oslo, Madrid and Dublin**

| | **Oslo** | **Dublin** | **Madrid** |
|---|---|---|---|
| **Latitude** | 59.913869 | 53.349805 | 40.416775 |
| **Longitude** | 10.752245 | -6.260310 | -3.703790 |

### 8.6.2 Selection of dates and data for modelling

Initially two dates were selected, 21st December 2022 and 21st June 2022, which are the shortest and longest days of the year respectively in the Northern hemisphere. Historical weather data was sourced by setting up a researcher's account with Solcast (www.solcast.com), an online weather database. For each location and date, external air temperature, global irradiance, diffuse irradiance and cloud opacity were downloaded. Cloud opacity describes the percentage of sky that contains cloud. A visual indication of cloud opacity is provided in Figure 8-19.


**Figure 8-19 Visual representation of cloud opacity measurements**
(https://www.globe.gov/web/s-cool/home/observation-and-reporting/observing-cloud-cover)

Figure 8-20 (a) and (b) compare the solar irradiance at each location on each date. It can be observed that the solar irradiance is erratic in Dublin and Madrid on the 21st June 2022, caused by cloud cover in these locations. A similar effect occurs in Madrid on 21st December 2022. Cloud cover is an additional variable that impacts the solar irradiance applied to a building. It is a random variable, that is, it cannot be predicted or controlled however in order to mitigate the effect of cloud cover from this study further analysis of historical weather data across the three sites was carried out in order to find dates, either the same or relatively close to each other, in which there is no or very low cloud cover during the time period that the solar irradiance would enter the huts.

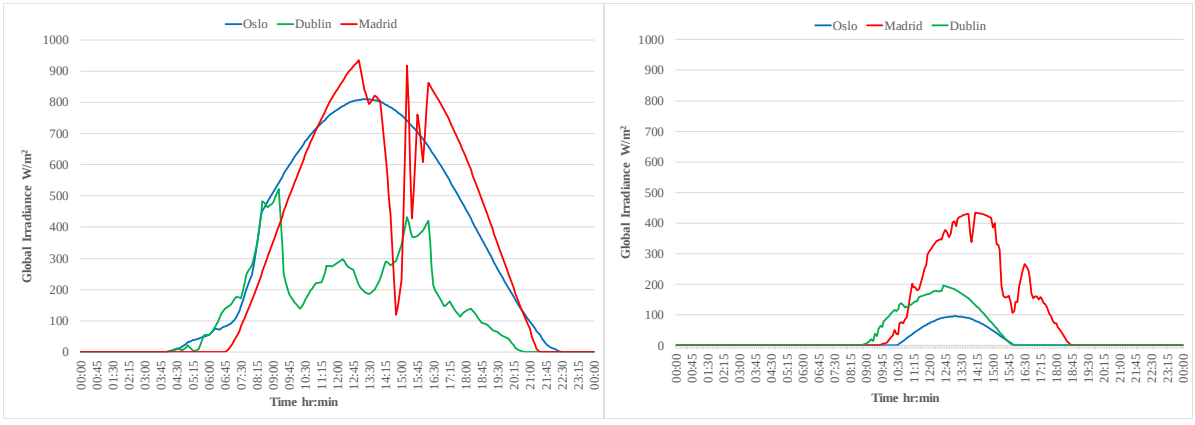


(a) (b)

**Figure 8-20 Global solar irradiance in Oslo, Dublin and Madrid on (a) 21st June 2022 and (b) 21st December 2022.**

As Ireland typically experiences a lot of cloudy weather, this analysis commenced using the Irish national weather service, Met Eireann. Using the Met Eireann website www.met.ie (https://www.met.ie/climate/available-data/historical-data), initially the average daily solar irradiance during December and June in 2022, 2021 and 2020 at Dublin airport was downloaded and reviewed. The three days with the highest irradiance in each month and year were noted. For each of these days, hourly data for cloud height and cloud amount was downloaded and reviewed. The dates selected for 2022 in both June and December had the

least cloud cover when comparing the best dates in all three years. Using the Solcast historical database (https://toolkit.solcast.com.au/historical/timeseries-async/request), solar irradiance data and cloud opacity data was downloaded for Oslo, Dublin and Madrid during June and December 2022. This data was plotted and reviewed in order to identify for each location the days with the highest solar irradiance and lowest cloud opacity during the daylight hours. The aim of the analysis was not just to select the days with the highest irradiance and lowest cloud cover but also to keep the days selected for each city no longer than seven days apart within the relevant month. Table 8-4 provides the final dates selected for each city and month.

**Table 8-4 Dates selected for winter and summer modelling in Oslo, Dublin and Madrid**

| Location | June 2022 | December 2022 |
|---|---|---|
| **Oslo** | 20th June | 5th December |
| **Dublin** | 20th June | 7th December |
| **Madrid** | 22nd June | 10th December |

Figures 8-21 and Figure 8-22 display the global irradiance (GI), diffuse irradiance (DI) and cloud opacity (CO) data for the relevant dates for each city for June and December respectively. It is clear from Figure 8-21 that the intensity of irradiance is greater in Madrid and lowest in Oslo as expected. This is due to the higher solar altitude angle in Madrid which is closer to the equator. It can also be observed from Figure 8-21 that in Oslo and Dublin the sky is clear during the period in which the inside of the hut is expected to be exposed to solar irradiance given that it is only the South elevation that is glazed. In Madrid, the cloud opacity increases up to 20% between 2:30 and 3:30 which indicates the presence of some isolated clouds, referring to Figure 8-19. The direct irradiance reduces during this period. However, as described later in this section, the surface area within the hut that is subjected to direct irradiance at this time is minimal as it is very close to the local solar noon time (14:15pm) and the sun is high in the sky. As expected the diffuse irradiance increases during this period as the solar radiation is subjected to more scattering due to the increase in cloud cover.

For the dates selected in December 2022, Figure 8-22 shows that the sky is clear in Oslo and Dublin during the time period in which the internal surfaces of the hut are exposed to direct irradiance. In Madrid the cloud opacity increases up to 20% between 14:00 pm and 14:30 pm indicating some isolated clouds but otherwise the sky is clear during the day. As expected, the intensity of the irradiance is lowest in Oslo due to the low solar altitude angle.

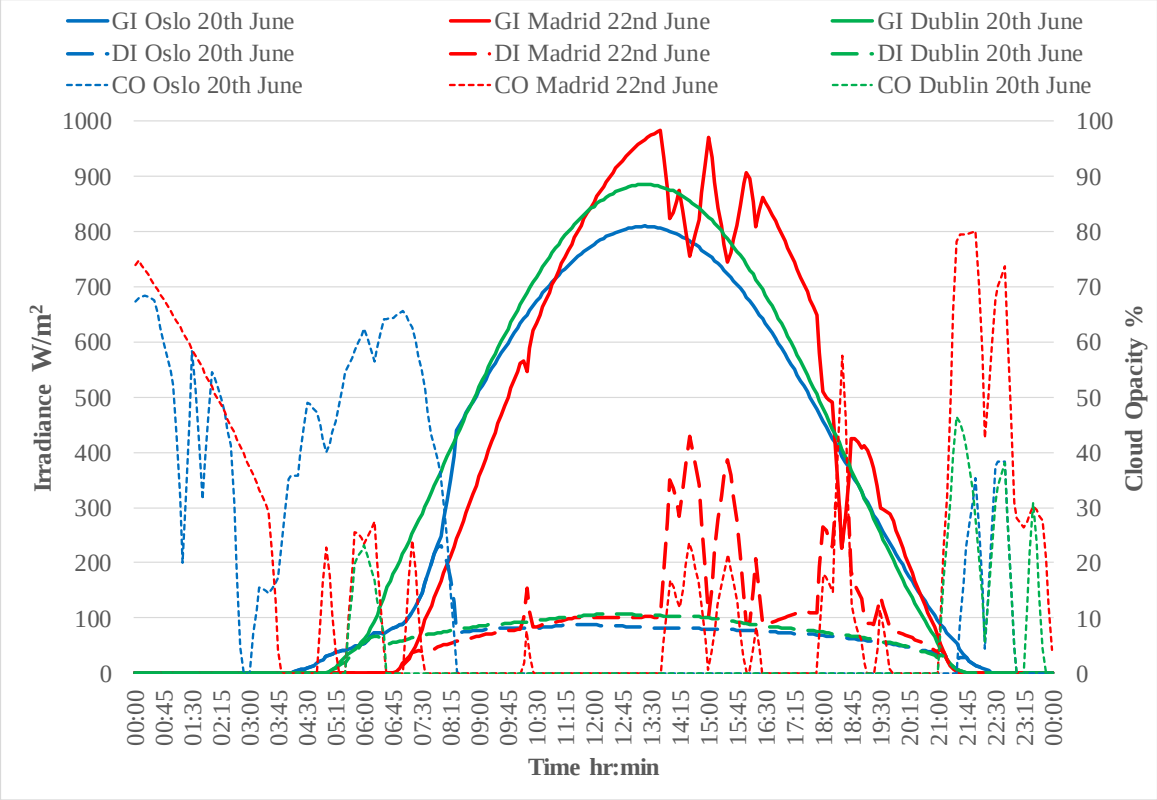


**Figure 8-21 Comparison of the global irradiance (GI), diffuse irradiance (DI) and cloud opacity (CO) for Oslo, Dublin and Madrid on selected dates in June**

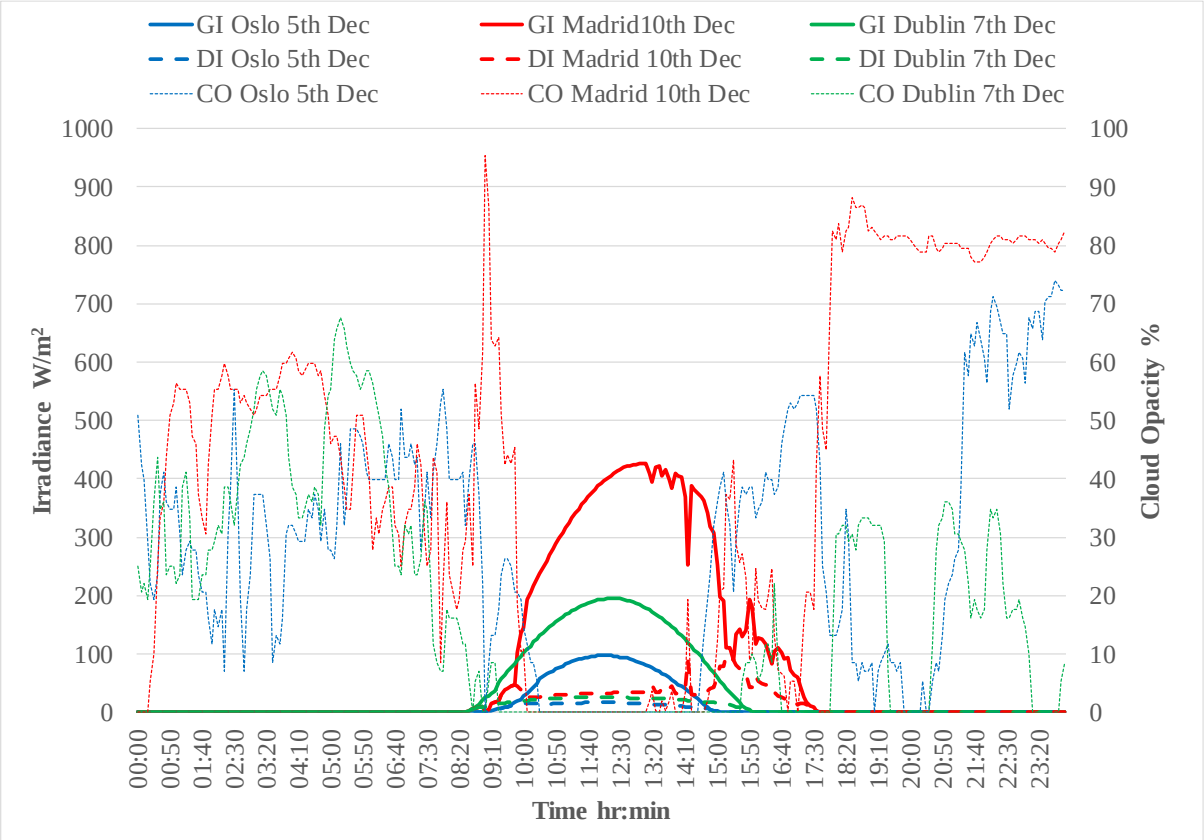


**Figure 8-22 Comparison of the global irradiance (GI), diffuse irradiance (DI) and cloud opacity (CO) for Oslo, Dublin and Madrid on selected dates in December**

Table 8-5 provides solar data for each season and each location. It can be noted from Table 8-5 that during June the total daylight hours reduce as the latitude decreases, that is as the distance from the equator decreases, hence Oslo has the longest period of daylight and Madrid has the shortest. As the hut that is being modelled only has glazing in the South elevation, the time period during which direct irradiance enters the hut is shorter than the total daylight hours during June. However the huts are also exposed to diffuse irradiation during the whole daylight period so the hut located in Oslo potentially has a longer exposure to diffuse irradiation than the hut located in Madrid. On a clear day diffuse irradiance is approximately 10 – 15 % of the global irradiance however it is applied to a greater surface area in the hut compared to direct irradiance, especially in summer when the sun is higher in the sky so less direct irradiance enters the hut. As a result diffuse irradiance can have a significant influence on the internal air temperatures of the huts, especially given the relatively high ratio of internal surface area to volume of air in the huts. It can also be noted from Table 8-5 that the solar altitude angle increases as latitude decreases, indicating that at any given time the sun is higher in the sky over Madrid than it is over Oslo. The higher the solar altitude angle the less direct irradiance enters the hut however the irradiance has a greater intensity.

**Table 8-5 Solar data for selected dates in June and December 2022 (Source: www.timeanddate.com)**

| | **June 2022** | | | **December 2022** | | |
|---|---|---|---|---|---|---|
| | **Oslo 20th** | **Dublin 20th** | **Madrid 22nd** | **Oslo 5th** | **Dublin 7th** | **Madrid 10th** |
| **Sun rise (hr:min)** | 03:53 | 04:56 | 06:44 | 08:58 | 08:25 | 08:26 |
| **Sun set (hr:min)** | 22:43 | 21:56 | 21:48 | 15:16 | 16:08 | 17:48 |
| **Solar noon(hr:min)** | 13:18 | 13:26 | 14:16 | 12:07 | 12:16 | 13:07 |
| **Total daylight hours** | 18hrs 49mins | 17hrs 00mins | 15hrs 04mins | 6hrs 17mins | 7hrs 42mins | 9hrs 21mins |
| **Solar altitude angle @ solar noon** | 54$^{o}$ | 60$^{o}$ | 73$^{o}$ | 8$^{o}$ | 14$^{o}$ | 27$^{o}$ |

Referring to the solar data during December as provided in Table 8-5 it can be noted that the daylight hours are shortest in Oslo and longest in Madrid. Considering the solar altitude angles the sun is lowest in the sky in Oslo. Although this means that a higher surface area within the hut is exposed to direct irradiance, the intensity of the irradiance is low due to the very low angle of the radiation rays. Also, the hut in Oslo has the shortest exposure to diffuse radiation

during the winter due to the short period of daylight. Figures 8-23 and 8-24 provide diagrammatic representations of the sun paths for each location on the selected dates which highlights the differences in daylight hours and solar altitude angle.

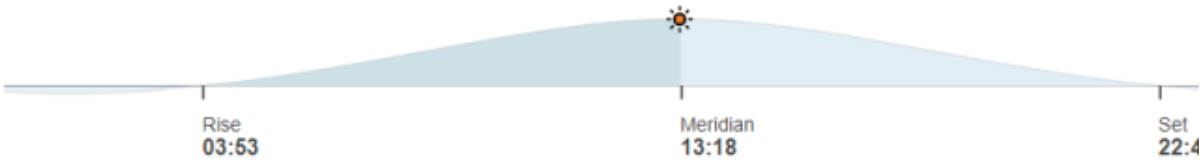


(a) Oslo 20th June

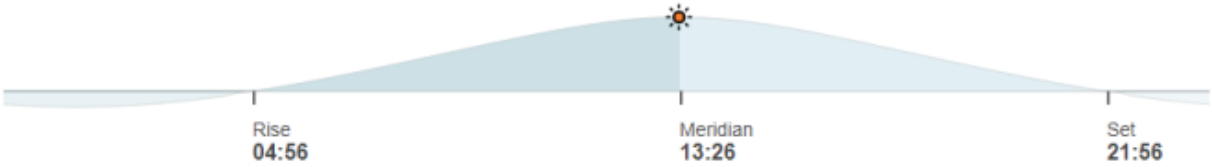


(b) Dublin 20th June


(c) Madrid 22nd June

**Figure 8-23 Sun paths for Oslo, Dublin and Madrid on the 20th, 20th and 22nd of June 2022 respectively (Source: www.timeanddate.com)**


(a) Oslo 5th December


(b) Dublin 7th December

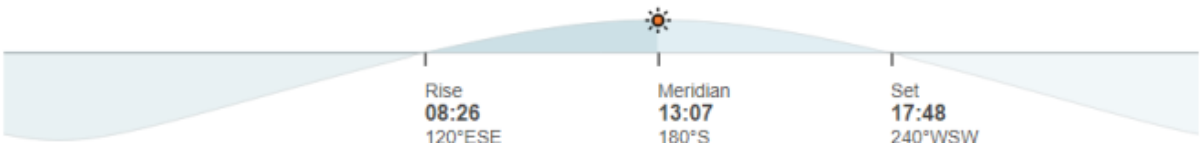


(c) Madrid 22nd December

**Figure 8-24 Sun paths for Oslo, Dublin and Madrid on the 5th, 7th and 10th of December 2022 respectively (Source: www.timeanddate.com)**

### 8.6.3 Setting up the COMSOL models

Using the COMSOL model developed as described in Sections 8.3 and 8.4, three models were created which replicated the geometry of the as-built huts. To set up the model for a particular location and date, the associated global irradiance, diffuse irradiance and external air temperature data, as sourced from SolCast, were imported into the model as interpolation functions and applied to all the relevant surfaces of the model. The initial temperature of the external leaves of the wall was set as the external air temperature at the time of the start of the simulation. The initial internal air temperature and internal wall temperature were both set at 18 $^{o}$C in all cases. All simulations commenced at midnight and simulated a time period of 24 hours. The relevant latitude and longitude co-ordinates were entered for the location being simulated along with the date and any time difference between local time and coordinated universal time (UTC) to ensure COMSOL incorporates the correct sun path for the specified time and location.

Eighteen different simulations were carried out, one for each type of hut in each of the three locations, during both June (summer) and December (winter). Plots displaying the temperature for each thermocouple location in each wall (North, East and West) for each of the eighteen simulations are provided in Appendix U.

### 8.6.4 Results and analysis of the summer simulations

Figure 8-25 displays the simulated internal air temperatures and average wall temperature at a depth of 60 mm for each type of hut in Oslo on 20$^{th}$ June 2022. A depth of 60 mm was chosen as it is the centre point of the inner leaf wall thickness. The average wall temperature at 60 mm is determined by averaging the temperature at 60 mm depth in the East, West and North walls of the hut. Although the temperatures in the East, West and North walls will differ due to variation in exposure to irradiance, the variation is the same for each type of hut due to identical geometry and orientation. Using an average wall temperature for each hut allows the thermal behaviour in the different types of huts to be compared with clarity on a single plot.

Detailed plots provided in Appendix U (Figures U-1 to Figures U-18) show temperatures at each thermocouple location in the East, West and North walls on a single plot which allows the different thermal behaviour between the walls of a particular hut to be observed. It can be observed from Figures U-1 to U-3 in Appendix U that in Oslo on 20$^{th}$ June 2022, the North wall temperatures are lower than the East and West wall temperatures in each hut reflecting the higher surface area exposed to direct irradiance on the East and West walls due to the high

solar altitude angle (54$^{o}$ at solar noon). This effect can also be observed from Figure 8-26 which provides images of surface radiosity extracted from the simulation results at 10 am, solar noon (13:18 pm) and 5 pm.

The air temperature in the No PCM hut reaches a peak of 32.8 $^{o}$C. The peak air temperatures in the Partial PCM and Full PCM huts are noticeably lower at 30.4 $^{o}$C and 29.8 $^{o}$C respectively indicating that the PCM-concrete is successful at reducing the air temperature. A thickness of 60 mm of PCM-concrete reduces the air temperature by 2.4 $^{o}$C which is significant, however there is little difference between the air temperature in the Partial PCM hut and the Full PCM hut (0.6 $^{o}$C) indicating that under the environmental conditions applied in the simulation, there is no added benefit of providing PCM-concrete at a depth greater than 60 mm. This confirms the similar result found in Chapter 7.

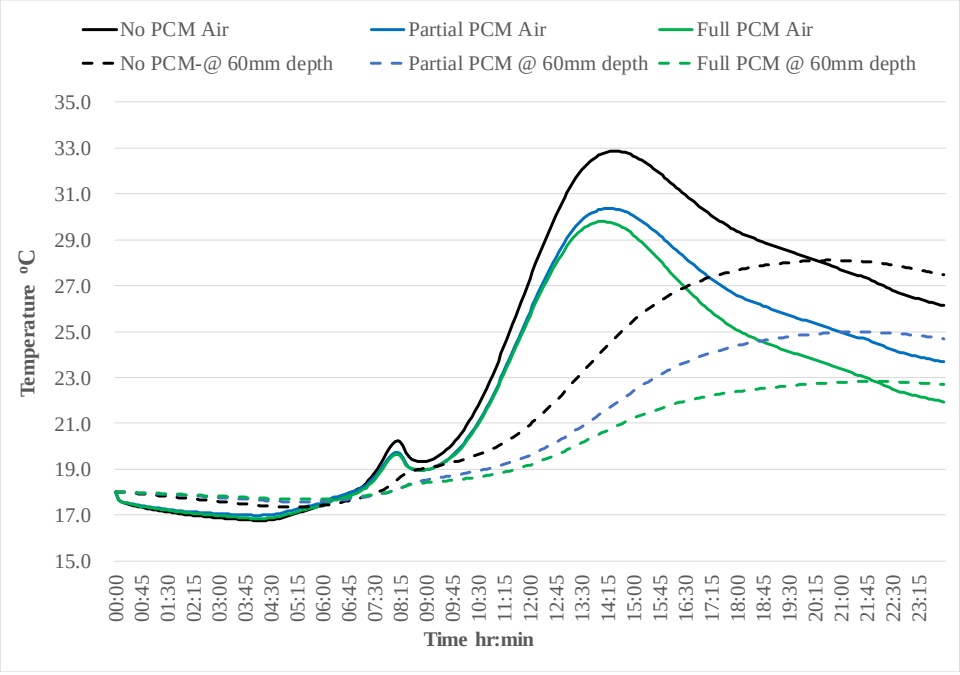


**Figure 8-25 Simulated internal air temperatures and wall temperature at a depth of 60 mm for each type of hut in OSLO on 20$^{th}$ June 2022.**

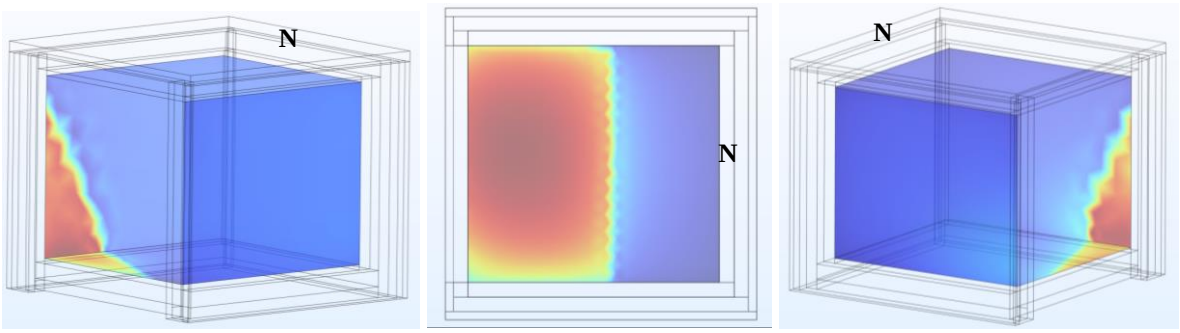


(a) West wall @ 10 am (b) Floor at solar noon (c) East wall @ 5 pm

**Figure 8-26 Surface area exposed to direct irradiance at 10 am, solar noon and 5 pm, in Oslo, 20$^{th}$ June 2022**
Note: N denotes position of North wall

It is also clear from Figure 8-25 that the wall temperature at a depth of 60 mm is lower in the Full PCM hut than in the Partial PCM hut although this lower wall temperature is not translating into significantly lower air temperatures. The lower temperatures in the walls of the Full PCM huts can be explained by the fact that the heat penetrates to the full depth of the wall, that is 125 mm, increasing the temperatures at this depth above the onset melt temperature of the PCM (20.2 $^{o}$C). This can be observed from the detailed plots of the wall temperatures at all depths provided in Appendix U. Also, as can be observed from the DSC results as displayed in Figure 4-3, some melting will commence at temperatures lower that the onset melt temperature. The melting of the PCM at depths greater than 60 mm reduces the rate of temperature increase across the full depth of the wall and this results in a lower averaged wall temperature in the Full PCM hut. However the lower wall temperatures at depths greater than 60 mm do not have a significant influence on the internal air temperature.

Figure 8-27 shows the equivalent simulated internal air temperatures and average wall temperature at a depth of 60 mm for each type of hut in Dublin on 20$^{th}$ June 2022. The peak air and wall temperatures in Dublin are lower than those in Oslo due to the smaller internal surface area exposed to direct irradiance as a result of the higher solar altitude angle (60$^{o}$ at solar noon). This can be observed from Figure 8-28 which shows the surface radiosity at 10 am, solar noon (13:26 pm ) and 5 pm. However the general trends in Figure 8-27 are similar to Figure 8-25.

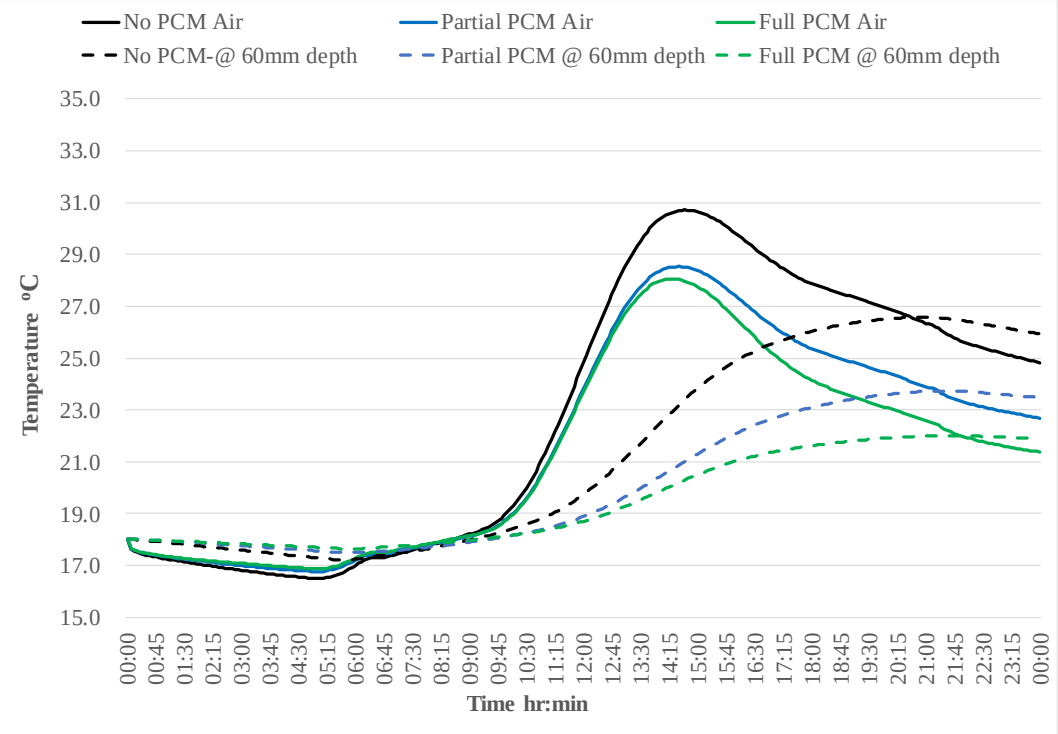


**Figure 8-27 Simulated internal air temperatures and wall temperature at a depth of 60 mm for each type of hut in Dublin on 20$^{th}$ June 2022.**

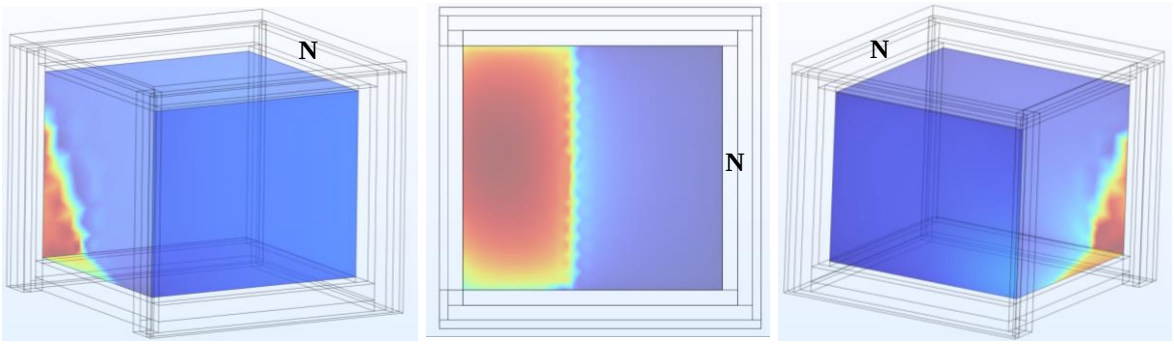


(a) West wall @ 10 am (b) Floor at solar noon (c) East wall @ 5 pm

**Figure 8-28 Surface area exposed to direct irradiance at 10 am, solar noon and 5 pm, in Dublin on 20th June 2022**

Note: N denotes position of North wall

The air temperature in the No PCM hut reaches a peak of 30.7 ºC. The peak air temperatures in the Partial PCM and Full PCM huts are noticeably lower at 28.5 ºC and 28.0 ºC respectively. Again the PCM-concrete is successful at reducing the air temperature with a thickness of 60 mm of PCM-concrete reducing the air temperature by 2.2 ºC. Providing a full depth of 125 mm of PCM-concrete composite only increased the reduction in internal air temperature by 0.5 ºC again indicating that the beneficial effect of providing PCM-concrete diminishes at a depths greater than 60 mm.

Figure 8-29 displays the simulated internal air temperatures and average wall temperature at a depth of 60 mm for each type of hut in Madrid on 22nd June 2022. Although Madrid would be considered to have a hotter summer climate than Dublin or Oslo, the peak internal air and wall temperatures are lower than those in Dublin and Oslo despite a higher intensity of irradiance (and higher external air temperature), highlighting the influence of the solar altitude angle on internal temperatures in buildings. In addition, internal air temperatures start to increase at an earlier time in Dublin and Oslo as the sunrise time is earlier and hence the huts are exposed to diffuse irradiance earlier.

Figure 8-30 shows that at 10 am, in Madrid, direct irradiance is not entering the hut, and the distribution of radiosity is diffuse. It is important to note that the colours in the plots of Figure 8-30 depict relative radiosity at a particular time, not absolute values. In Figure 8-30(a), most of the internal surface of the hut is depicted in a red/orange indicating similar levels of radiosity which is a result of diffuse irradiance rather than direct irradiance. Analysis of the simulation output confirmed that direct irradiance would not enter the hut in Madrid until 11:15am.

A contributing factor to the lower temperatures is the considerably smaller floor and/or wall area that is exposed to direct irradiance, leading to lower wall temperatures and hence lower internal air temperatures. It can be noted from the full plots of the simulation results that are provided in Appendix U, (Figures U-1 to U-9) that the temperatures in each of the walls, North, East and West in the Madrid huts are the same throughout the period whereas in Oslo and Dublin the East and West walls are warmer than the North wall reflecting the fact that the irradiance only strikes the East and West wall in the summer. In Madrid, due to the higher solar altitude angle (73º at solar noon), there is less irradiance reaching the East and West walls so the temperatures are similar to the North wall. The air temperature in the No PCM hut reaches a peak of 28.2 ºC. The peak air temperatures in the Partial PCM and Full PCM huts are lower at 25.8 ºC and 25.5 ºC respectively, again demonstrating that the provision of 60 mm PCM-concrete can result in a reduction in peak internal air temperature of 2.4 ºC. Providing an additional 65 mm PCM-concrete in the Full PCM hut only resulted in a further reduction of 0.3 ºC in the internal air temperature which is negligible.

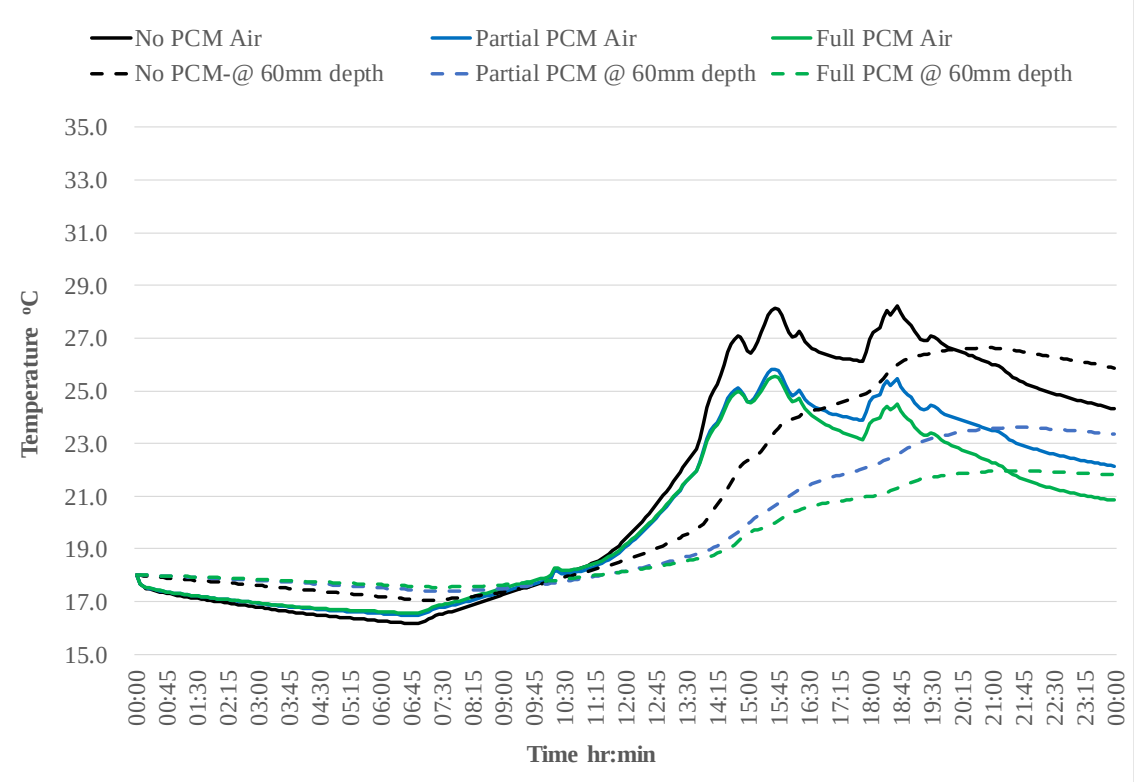


**Figure 8-29 Simulated internal air temperatures and wall temperature at a depth of 60 mm for each type of hut in Madrid on 20th June 2022.**

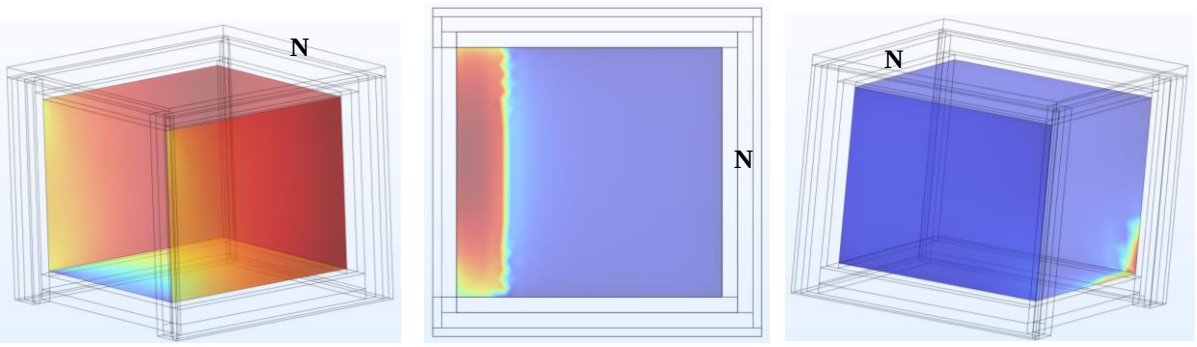


(a) West wall @ 10 am (b) Floor at solar noon (c) East wall @ 5 pm

**Figure 8-30 Surface area exposed to direct irradiance at 10 am, solar noon and 5 pm, in Madrid on 20th June 2022**

Note: N denotes position of North wall

Table 8-6 summarises the key results of the simulations of the huts in summer. In all locations the inclusion of a 60 mm thick layer of PCM-concrete composite reduced the internal air temperature by 2.2 ºC to 2.4 ºC. The inclusion of an additional 65 mm depth of PCM-concrete in the Full PCM huts did not provide a significant increase in reduction of peak air temperatures. The reduction ranged from 0.3 ºC in Madrid to 0.6 ºC in Oslo. In Madrid and Dublin the wall temperatures in the Full PCM huts reached circa 22-23 ºC. This highlights again the influence of latitude and solar altitude angle on the thermal mass performance of PCM-concrete composite – as latitude reduces and the solar altitude angle increases, the potential of PCM-concrete to melt and hence reduce internal air temperatures reduces. As the huts are well insulated, the external ambient temperature has a lesser effect on internal air temperature than the solar gain.

**Table 8-6 Summary of the key results from the summer simulations**

| | Peak internal air temperature (ºC) | | | Reduction in internal air temperature (ºC) | |
|---|---|---|---|---|---|
| | No PCM | Partial PCM | Full PCM | Partial PCM | Full PCM |
| **Oslo** | 32.8 | 30.4 | 29.8 | 2.4 | 3.0 |
| **Dublin** | 30.7 | 28.5 | 28.0 | 2.2 | 2.7 |
| **Madrid** | 28.2 | 25.8 | 25.5 | 2.4 | 2.7 |
| | Time direct irradiance enters hut (hr:min) | | Time direct irradiance leaves hut (hr:min) | | Duration of exposure to direct irradiance |
| **Oslo** | 08:50 | | 17:50 | | 9hrs 00mins |
| **Dublin** | 09:20 | | 17:40 | | 8hrs 20mins |
| **Madrid** | 11:15 | | 17:25 | | 6hrs 10mins |

### 8.6.5 Results and analysis of the winter simulations

Figure 8-31 displays the simulated internal air temperatures and average wall temperature at a depth of 60 mm for each type of hut in Oslo on 5th December 2022. The air temperature in the No PCM hut reaches a peak of 17.3 ºC. The peak air temperatures in the Partial PCM and Full PCM huts are slightly higher at 17.5 ºC and 17.7 ºC respectively. It can be noted from Figure 8-31 that the rate of initial decrease in temperature is lower in both huts containing PCM-concrete composite. The PCM-concrete walls are slower to release heat as the PCM-concrete composite has a lower thermal conductivity and higher specific heat capacity. This lower rate of temperature decrease means that the walls of the Partial and Full PCM huts are at a slightly higher temperature at the start of the heating phase, which in turn leads to the slightly higher peak temperatures.

It can be observed from Figures U-10 to U-12 in Appendix U that the North wall temperatures are higher than the East and West wall temperatures in each hut reflecting the higher surface area exposed to direct irradiance on the North walls due to the low solar altitude angle (8º) . This effect can also be observed from Figure 8-32 which provides images of surface radiosity extracted from the simulation results at 10 am, solar noon (12:07 pm) and 5 pm.

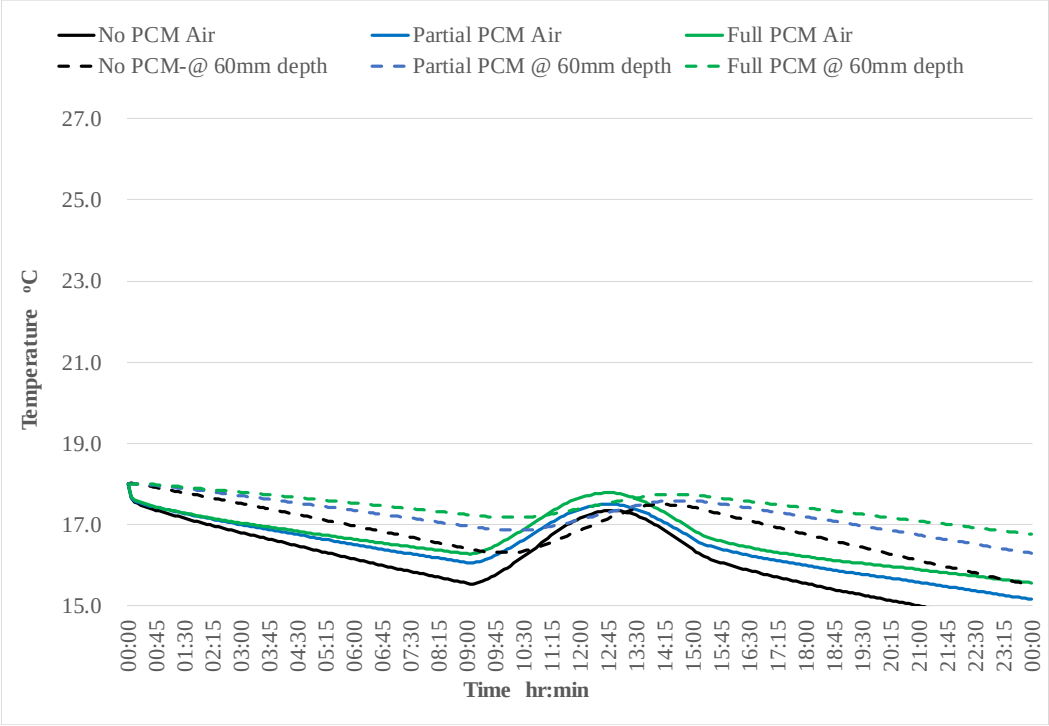


**Figure 8-31 Simulated internal air temperatures and wall temperature at a depth of 60 mm for each type of hut in Oslo on 5th December 2022.**

N

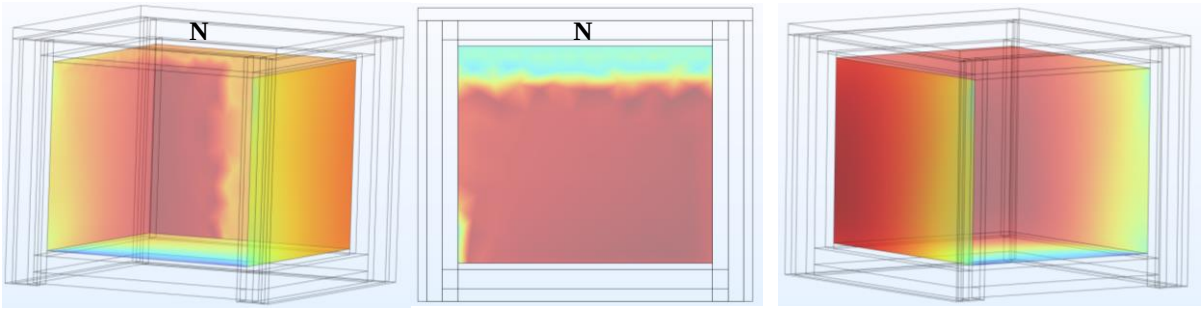


(a) West wall @ 10 am (b) North wall at solar noon (c) East wall @ 5 pm

**Figure 8-32 Surface area exposed to direct irradiance at 10 am, solar noon and 5 pm, in Oslo on 5th December 2022**

Note: N denotes position of North wall

At solar noon all the direct irradiance is on the North wall, there is no direct irradiance on the floor of the hut. This is the opposite effect to the temperature distribution in the walls of the huts during the summer season when the North wall was not exposed to any direct irradiance and hence displayed lower temperatures than the East and West walls throughout the simulation. Although a greater surface area of internal wall in the Oslo huts is exposed to direct irradiance during the 5th December compared to the summer date of the 20th June, the temperatures are much lower as the intensity and duration of the irradiance – both direct and diffuse – are considerably lower.

The low wall temperatures that occurred in all the huts do not facilitate any melting of the PCM. There may be some initial melting of PCM in the North wall as the surface and 30 mm deep temperatures increase above 18 $^{o}$C (refer to Figure 4-3) however it is not sufficient to influence the internal air temperature.

Figure 8-33 shows the simulated internal air temperatures and average wall temperature at a depth of 60 mm for each type of hut in Dublin on 7th December 2022. The internal air temperature in the No PCM hut reaches a peak of 20.3 $^{o}$C. The peak internal air temperatures in the Partial PCM and Full PCM huts are insignificantly lower at 19.8 $^{o}$C and 20.0 $^{o}$C respectively.

On examining the wall temperatures for each hut provided in Figures U-13 to U-15 in Appendix U it can be noted that temperatures within the East and West walls in the huts containing PCM-composite do not exceed 19 $^{o}$C so it is expected that no PCM melted in these walls. The temperature of the North wall in both PCM huts reaches 22 $^{o}$C which is greater than the onset

melt temperature of 20.4 ºC so partial melting of the PCM occurs. However it is clear that this level of engagement of the PCM is insufficient to result in a significantly lower air temperature.

The peak air and wall temperatures in Dublin are higher than those in Oslo despite the lower surface area exposed to direct irradiance as can be observed from Figure 8-34. The higher temperatures in the Dublin huts are due to the relatively higher intensity of the irradiance as a result of the greater solar altitude angle (14º). In addition the hut in Dublin is exposed to both diffuse and direct irradiation for 1 hour, 15 minutes longer than the hut in Oslo.

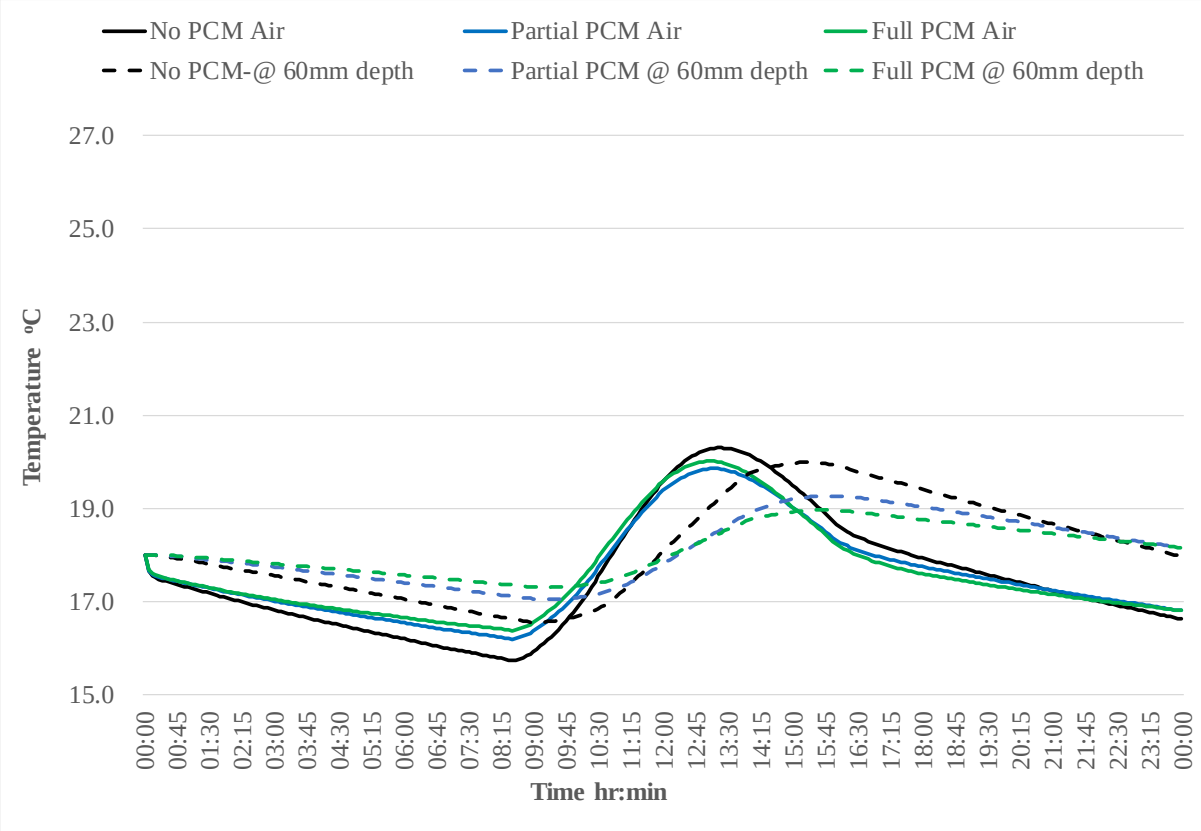


**Figure 8-33 Simulated internal air temperatures and wall temperature at a depth of 60 mm for each type of hut in Dublin on 7th December 2022.**

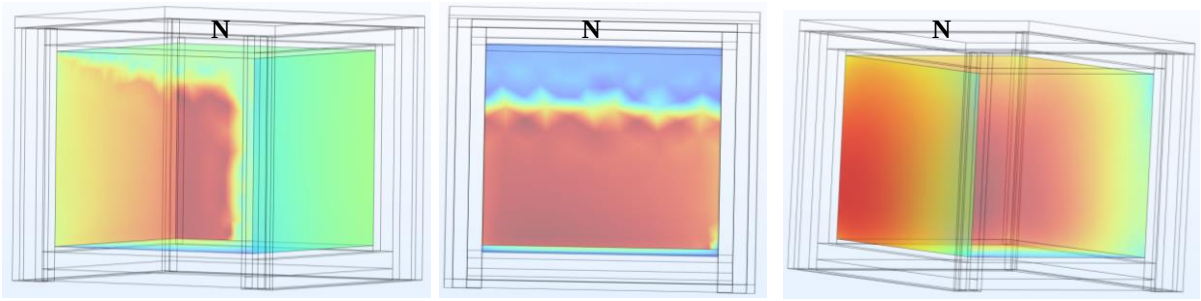


(a) West wall @ 10 am (b) North wall at solar noon (c) East wall @ 5 pm

**Figure 8-34 Surface area exposed to direct irradiance at 10 am, solar noon and 5 pm, in Dublin on 7th December 2022**

Note: N denotes position of North wall

Figure 8-35 displays the simulated internal air temperatures and average wall temperature at a depth of 60 mm for each type of hut in Madrid on 10th December 2022. The peak internal air temperatures are 5 – 6 ºC higher than in Dublin, reflecting the fact that the intensity of irradiance is approximately double that which occurred in Dublin – refer to Figure 8-22. The air temperature in the No PCM hut reaches a peak of 26.4 ºC. The peak air temperatures in the Partial PCM and Full PCM huts are lower at 24.8 ºC and 24.7 ºC respectively showing that the provision of 60 mm depth of PCM-concrete composite can reduce the air temperature by 1.6 ºC. The provision of an additional 65 mm of PCM-concrete in the Full PCM hut provides no additional beneficial reduction in internal air temperature. On examination of the temperatures within the walls of the huts containing PCM, referring to Figures U-16 to U-18 in Appendix U it can be noted that all the walls, East, West and North reach peak temperatures of 22 – 23 ºC, so melting of the PCM occurs in all the walls. This is in contrast to the PCM huts in Dublin in which only the North wall became warm enough to facilitate partial melting of the PCM. It can also be noted that in the Full PCM hut, at depths greater than 60 mm, the temperature peaks at 20 to 21 ºC indicating that there is only limited engagement of PCM at this depth.

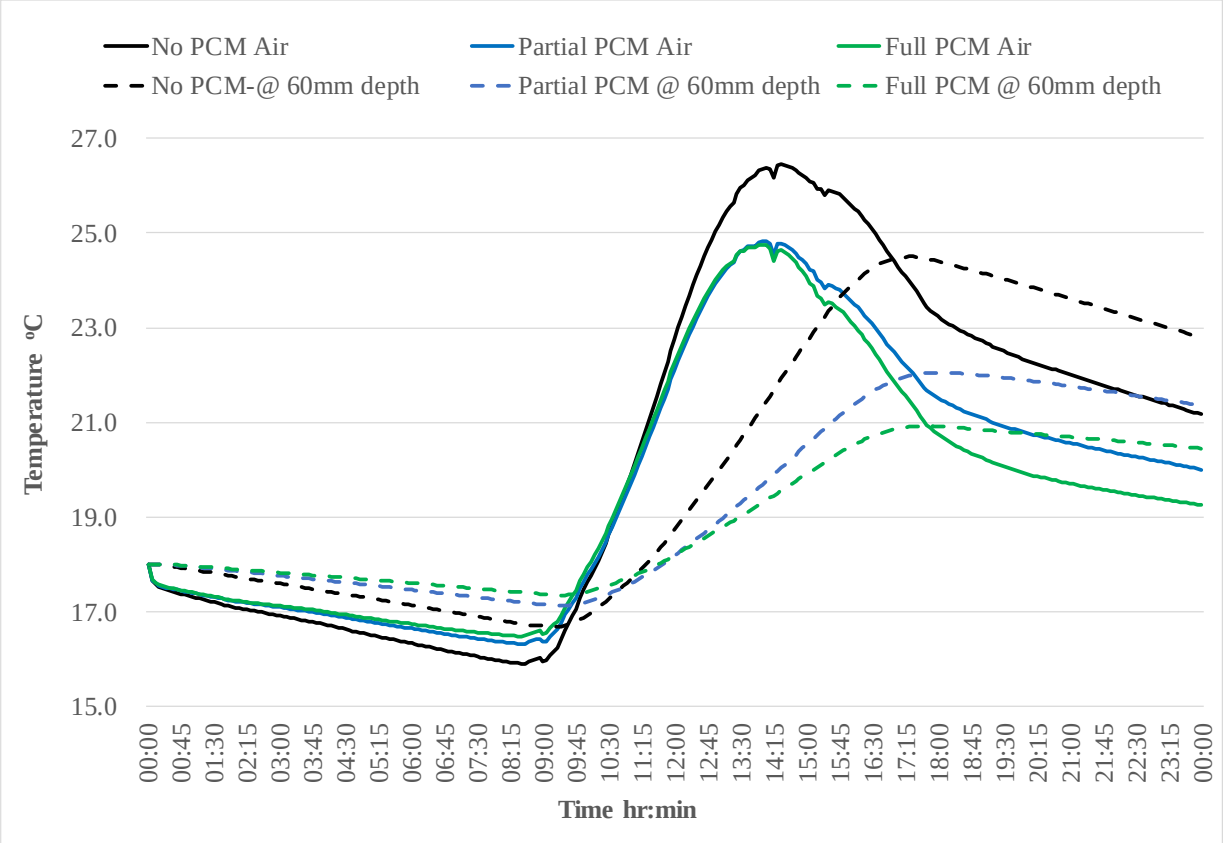


**Figure 8-35 Simulated internal air temperatures and wall temperature at a depth of 60 mm for each type of hut in Madrid on 10th December 2022**

In addition to being exposed to a higher intensity of irradiance the irradiance enters the hut in Madrid for a longer period, 8 hours and 5 minutes as a result of the longer daylight hours in Madrid during December. It can be observed from Figure 8-36(c) that the East wall of the hut is still exposed to direct irradiance at 5 pm in contrast to the huts in Oslo and Dublin. As the peak temperatures of the walls in the PCM huts do not reach the top temperature of the melt temperature range, that is 25.4 $^{o}$C, only partial melting of the PCM occurs. However reaching a peak temperature of circa 23 $^{o}$C in all three walls is sufficient to achieve a 1.6 $^{o}$C reduction in peak internal air temperature.

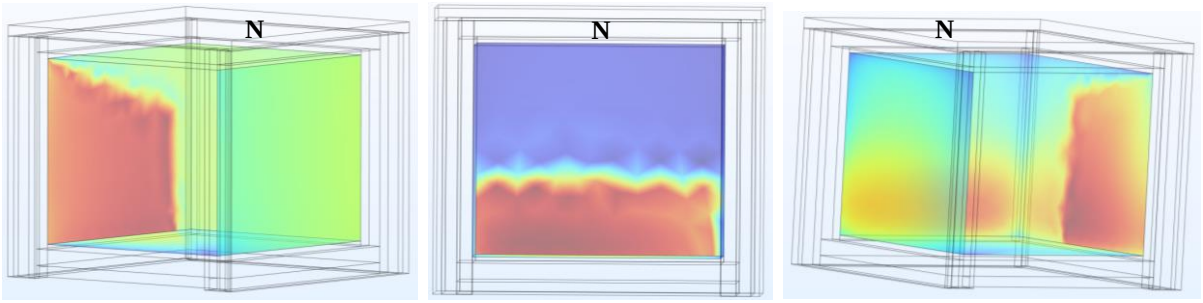


(a) West wall @ 10 am (b) North wall at solar noon (c) East wall @ 5 pm

**Figure 8-36 Surface area exposed to direct irradiance at 10 am, solar noon and 5 pm, in Madrid on 10th December 2022**

Note: N denotes position of North wall

Table 8-7 summarises the key results of the simulations of the huts in winter. In Oslo and Dublin the temperatures of the walls did not increase sufficiently to induce any melting of the PCM due to the short daylight hours and low solar altitude angle that reduced the intensity of irradiance. In Madrid the wall temperatures increased above the onset melt temperature and induced melting of the PCM resulting in a 1.6 $^{o}$C reduction in the peak internal air temperature. The inclusion of an additional 65 mm depth of PCM-concrete in the Full PCM huts did not provide a significant increase in reduction of peak air temperatures.

**Table 8-7 Summary of the key results from the winter simulations**

| | Peak internal air temperature ($^{o}$C) | | | Reduction in internal air temperature ($^{o}$C) | |
|---|---|---|---|---|---|
| | No PCM | Partial PCM | Full PCM | Partial PCM | Full PCM |
| **Oslo** | 17.3 | 17.5 | 17.7 | - | - |
| **Dublin** | 20.3 | 19.8 | 20.0 | 0.5 | 0.3 |
| **Madrid** | 26.4 | 24.8 | 24.7 | 1.6 | 1.7 |
| | Time direct irradiance enters hut (hr:min) | | Time direct irradiance leaves hut (hr:min) | | Duration of exposure to direct irradiance |
| **Oslo** | 09:25 | | 14:45 | | 5hrs 20mins |
| **Dublin** | 09:00 | | 15:35 | | 6hrs 35mins |
| **Madrid** | 09:15 | | 17:20 | | 8hrs 05 mins |

### 8.6.6 Conclusions of scenario modelling

The results of the simulations carried out during winter and summer climate conditions, as detailed in Sections 8.6.4 and 8.6.5 demonstrate the influence of geographical location on the thermal mass performance of PCM-concrete composite material, made possible by the development of a validated COMSOL model.

Overall, during the summer season, the peak internal air temperatures decreased as latitude decreased. As latitude decreases the solar altitude angle increases resulting in less direct solar irradiance entering the hut and this has a larger influence on the internal air temperature than the external air temperature. In addition, as latitude decreases the daylight hours also decrease leading to less diffuse irradiance. During the summer, the temperatures of the walls within the huts containing PCM increased up to 22 $^{o}$C – 24 $^{o}$C, facilitating sufficient melting of the PCM to achieve a reduction in internal air temperatures of 2.2 $^{o}$C to 2.4 $^{o}$C at all locations. When examining the area of internal wall that is exposed to direct irradiance it is worth noting that the area reduces as latitude reduces, due to the increase in the solar altitude angle. In each location, the North wall was not subjected to direct irradiance in summer. This observation can inform the placement of PCM-concrete in a building within a particular geographical location. To benefit from the PCM-concrete composite, in the scenarios that were modelled, the PCM-concrete would be better placed in the floor rather than the North wall, particularly in higher latitudes as a greater area of floor is exposed to irradiance due to the lower solar altitude angle.

To investigate the extent of benefit gained in summer conditions by placing PCM in the floor of the hut rather than the North wall of the hut, a further simulation was carried out on the Full PCM hut in Oslo on the 20$^{th}$ June in which the internal floor insulation was removed virtually and the PCM-concrete composite material was assigned to the floor slab. Removing the layer of floor insulation enables the floor slab to provide additional thermal mass regardless of the presence of PCM in the floor. For this reason two simulations were run, one with a Control concrete floor and one with a PCM-concrete floor. The material of the North wall was changed to Control concrete with no PCM. Figure 8-37 shows the original internal air temperature of the Full PCM hut with PCM-composite walls together with the air temperature results of the two simulations. The internal air temperature of the No PCM hut is also shown for comparison. The full set of simulated wall temperatures for both simulations are provided in Appendix U (Figures U-19 and U-20). It can be noted that by just removing the insulation layer from the floor, the additional thermal mass provided by a normal concrete floor (No PCM)) reduces the peak internal air temperature in the Full PCM hut by 3.2 $^{o}$C (29.5 $^{o}$C to 26.3 $^{o}$C). The overall

difference between the internal air temperature of the No PCM hut and the Full PCM hut with the floor exposed, and PCM removed from the North wall is 6.7 ºC. When the material of the floor is changed from normal concrete to PCM-concrete composite the peak air temperature reduces by a further 1.5 ºC. This analysis demonstrates the impact of optimising the position of the PCM-concrete composite for each geographical location and building geometry.

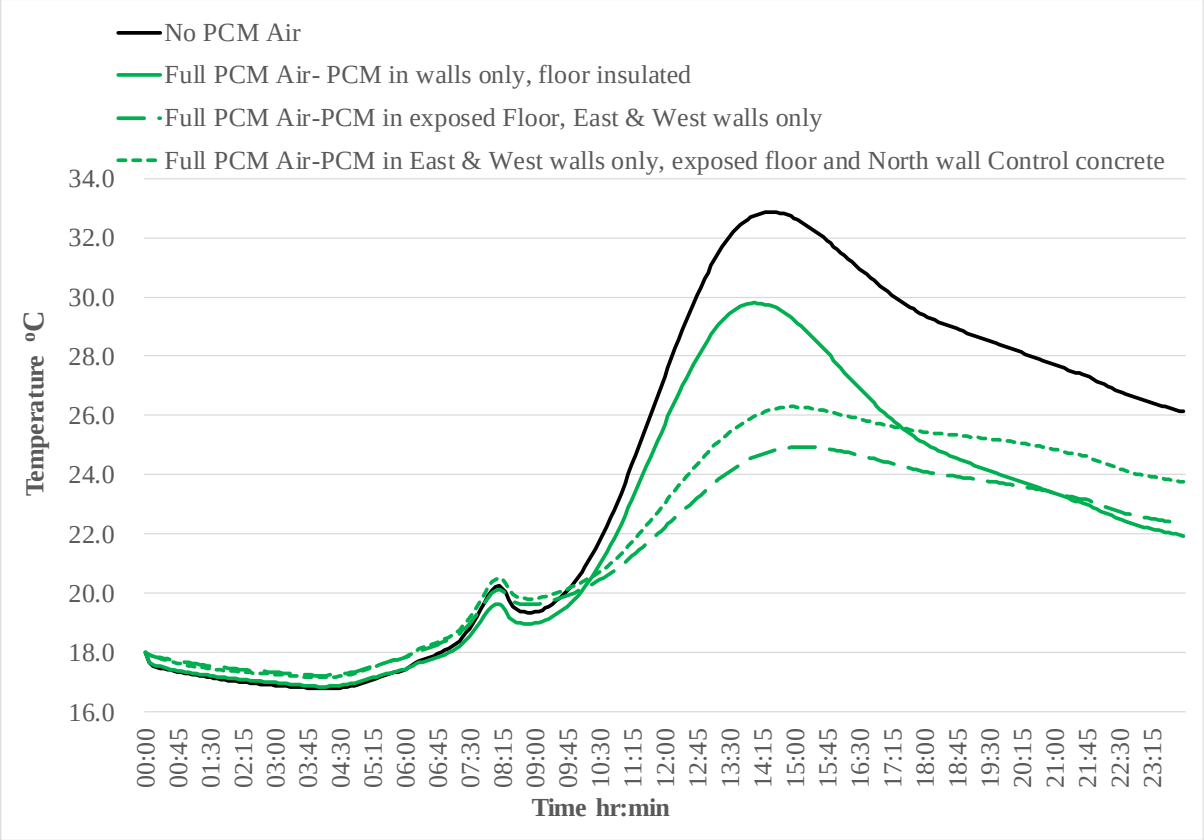


**Figure 8-37 Oslo 20th June 2022, simulated air temperatures in Full PCM hut when floor is insulated and exposed, with and without PCM**

During the winter season the peak internal air temperatures increased as latitude decreased. Although at higher latitudes a greater surface area within the hut is exposed to direct irradiance the intensity and duration of the irradiance is lower. In Oslo and Dublin the temperatures did not increase sufficiently to engage the PCM. However in Madrid, as a result of higher intensity of irradiance and longer daylight hours, the internal air temperature reached 26.4 ºC in the No PCM hut. All walls, East, North and West within the PCM huts reached temperatures of 22 – 23 ºC which resulted in sufficient PCM melting to achieve a 1.6 ºC reduction in peak internal air temperature.

During the winter season, in contrast to the summer season, due to the lower solar altitude angles, most of the direct irradiance is applied to the North wall. The floors are only exposed to very low level of direct irradiance. Hence to benefit from the enhanced thermal mass

properties of PCM-concrete during the winter season the PCM should be placed in the walls, especially the North wall.

The analysis confirmed that there is no significant benefit in providing an additional 65 mm of PCM-concrete in the walls of the huts.

### 8.7 Conclusions for thermal modelling of PCM-concrete composite

This chapter presented the development of a numerical simulation model using COMSOL multi-physics software, to simulate the thermal mass behaviour of PCM-concrete composite material. The model was validated using the thermal and environmental data collected from the full-scale huts constructed in Dublin as discussed in Chapter 7. Subsequently the validated model was use to carry out scenario modelling to demonstrate the influence of geographical location on potential thermal mass performance of the PCM-concrete.

Initially to develop the model, two dimensional models of a wall panel, 1.0 m x 1.0 m were created. The actual external air temperature and internal wall surface temperature recorded over a selected 24 hour period were applied as boundary conditions to the respective surfaces in the model. This modelling exercise concluded that the COMSOL model was simulating the thermal behaviour of the Control concrete with sufficient accuracy using a 'finer' mesh and the experimentally determined material properties for the Control concrete.

As described in Section 8.3.2 the Apparent Heat Capacity method was used to describe the thermal behaviour behaviour of the PCM, before, during and after phase change. The material thermal properties of the microencapsulated paraffin as determined by DSC testing were combined with a smoothing function to define the phase change conditions. Thermal hysteresis behaviour was also incorporated into the model as described in Section 8.3.3.

Once the PCM thermal behaviour was defined the PCM-concrete material was created in COMSOL. The PCM-concrete was modelled as a porous material to reflect the fact that the PCM-concrete is not a fully homogenous material, as discussed in Section 8.3.4. Another 3-D wall panel model was created with the PCM-concrete assigned to the inner leaf. Actual temperature data collected at the huts during selected periods were applied to the model and the simulated internal wall temperatures were compared to the actual temperatures. Although it was noted that the simulation temperatures consistently increased at a slightly faster rate during the heating period, the differences between the simulated results and real data, were in the range of 0.32 $^{o}$C – 0.46 $^{o}$C. This is less than the calibrated accuracy of the thermocouples

used and the model was deemed to be sufficiently accurate in modelling the thermal behaviour of the PCM-concrete composite.

Following the validation of the 3-D panel models, 3-dimensional models that replicated the geometry of the full-scale huts as constructed in Techrete were created in COMSOL as described in Section 8.4.1. Actual internal and external temperature data and solar irradiance recorded at the huts were applied to the model and the model was validated by comparing the simulated temperatures recorded at the probes in the model with the actual temperatures recorded at the corresponding thermocouples in the hut. Four 24 hour time periods were selected for the simulations. These time periods coincide with the time periods analysed in Chapter 7 and included summer and winter time periods and periods during which the PCM was engaged and not engaged.

A statistical analysis of the simulated data was carried out as described in Section 8.5. It was concluded from this analysis that that COMSOL model is simulating temperatures within the hut at the same or improved accuracy as the thermocouples used in the huts. The thermal behaviour of the PCM-concrete is being modelled with similar accuracy whether phase change occurs or not. It was also concluded that the accuracy of the simulations carried out on the same day are similar for the Control concrete hut and the Full PCM hut indicating that the thermal behaviour of the PCM-concrete is being modelled with similar accuracy as the normal concrete.

The simulated temperatures for the internal air displayed slightly lower accuracy which is attributed to the adoption of a simplified approach to modelling the convective heat transfer at the wall/air boundary. Another contributing factor is that the simulated air temperature is for the entire air domain whereas the actual internal air temperature was recorded by a thermocouple at a point location in the centre of the hut. Generally the accuracy of the simulations was lower during the heating phase which can be expected due to the increased complexity of the computation when irradiance and convective effects increase. Overall the results of the simulations aligned closely with the real temperatures recorded at the huts demonstrating that the developed COMSOL model can be used to reliably predict the thermal behaviour and impact of the PCM-concrete composite.

The validated COMSOL model was used to investigate the influence of geographical location on PCM-concrete performance selecting three Northern hemisphere cities with different latitudes, namely Oslo, Dublin and Madrid. Dates were selected in December and June to

represent summer and winter conditions. Historical weather data including global irradiance, diffuse irradiance and external air temperature, for each location on the selected dates were imported into the relevant models. A total of eighteen simulations were carried out on each type of hut in each location, that is No PCM, Partial PCM and Full PCM during both June (summer) and December (winter).

The scenario modelling clarified the influence of geographical location on the potential of PCM-concrete to reduce internal air temperatures and hence have a beneficial impact on overheating issues in buildings. The analysis demonstrated that under summer conditions, PCM-concrete provided more beneficial thermal mass effect at higher latitudes, that is, further from the equator. As latitude increases the solar angle decreases hence a higher surface area inside the hut is exposed to irradiance, which provides a greater potential for engagement of the PCM. It can also be concluded that in summer conditions the PCM-concrete composite would be better placed in the floor rather than the North wall as no direct irradiance reaches the North wall.

In contrast the scenario modelling during winter conditions demonstrated that the potential for PCM-concrete to be a viable solution for reducing overheating in building improves as latitude decreases. The reason for this conclusion is that the solar altitude angle is so low at higher latitudes in winter, that temperatures did not increase enough to engage the PCM, that is overheating did not occur in Oslo and Dublin in winter conditions. The PCM-concrete did display potential for reducing high internal air temperature in Madrid which occurred due to the higher intensity of irradiance and longer daylight hours. It can also be noted that under winter conditions, placing the PCM-concrete in the walls rather than the floor provides increased potential for engagement of the PCM.

# Chapter 9. Conclusions and Recommendations

## 9.1 Summary of work done

To inform the key objectives of this research project a literature review was completed in all relevant topics concerning the use of PCMs in buildings to provide additional thermal storage capacity and hence improve the overall energy performance of a building. The literature review provided evidence that the inclusion of PCMs in building envelopes can lead to a reduction in the energy demand of a building by reducing internal air temperatures and hence lowering the demand on air conditioning systems. Previous research studies identified different methods for incorporating PCMs into building materials however the two presiding methods for combining PCMs and concrete are to add microencapsulated paraffin to fresh concrete during the mixing process or to vacuum a liquid PCM into a lightweight aggregate which is then used in the concrete mix. While previous research has concluded that both methods of forming a PCM-concrete composite led to enhanced thermal mass behaviour, the lightweight aggregate-PCM composite (LWA-PCM) was more effective. However, the PCM leaked from the LWA resulting in staining on the panel surface. To investigate if the LWA-PCM could be used in the cladding panels to be developed in this research study, a laboratory study was carried out in which a fatty acid eutectic PCM was manufactured and vacuumed into lightweight aggregate. A number of different techniques to mitigate leakage were explored including cooling the LWA-PCMs prior to mixing, cold curing, sealing the LWA-PCM with sealants prior to mixing and using additives in the concrete to limit the migration of water.

It is also clear from the literature that the addition of PCMs to concrete has an impact on the fresh and hardened properties of concrete, in particular the workability, strength and thermal conductivity. The reduction in thermal conductivity is attributed to the typically low thermal conductivity of PCMs which reduces the efficiency of the thermal mass behaviour of PCM concrete as the heat transfer rate into the material is reduced, hence some PCM at greater depths may not be activated. In order to explore if the thermal conductivity of a PCM-concrete can be improved without adding complexity to the manufacturing process, two relatively simple methods of improving the thermal conductivity were investigated in the laboratory, namely the addition of steel fibres and the addition of GGBS to the concrete mix.

The initial laboratory investigations informed the final design of the PCM-concrete composite which was then used in the inner leaf of the precast concrete cladding panels. This research was an integral part of a European Horizon2020 project involving precast concrete sandwich

panels for retrofitting or overcladding of building facades. For this thesis, prior to manufacture of full-scale cladding panels, five number two wythe test sandwich panels were made in the laboratory, including panels with and without PCM in the inner leaf.. Two of the panels included two different types of non-conductive shear connectors, C-Grid and Thermomass, connecting the inner and outer wythes of the panel together. Thermal testing was carried out on the panels to observe and compare any thermal bridging effect at the location of the connectors. The thermal data recorded during the tests was used to determine the overall thermal conductivity, R-values and U-values for each panel under steady-state conditions.

Structural testing was also carried out on the same five panels to determine the composite structural behaviour of the two layers of the sandwich panel under different connectivity scenarios, as provided by the shear connectors. It was necessary to ensure that the panels had sufficient strength and stiffness to withstand expected lateral wind loads in service. Each panel was subjected to a displacement controlled 3-point bending test and the structural response was recorded and analysed.

As concluded from the literature review, there is a scarcity of research into the thermal performance of PCM-concrete composites in a full-scale scenario, in a real form of construction and over a time period incorporating all seasons. In order to address this gap, three full-scale huts were constructed using the designed and tested concrete sandwich cladding panels with a PCM-concrete inner leaf. The huts were instrumented to record internal and external environmental data over an 18 month period. The recorded data was analysed and the thermal mass behaviour of the PCM-concrete composite was quantified.

As reported widely in the literature, there is a significant number of variables that influence the potential of a PCM-composite material to provide a beneficial thermal mass effect in a building. An individual building requires a bespoke solution, hence numerical simulation models are essential to achieve efficient application of this technology. For this reason a finite element model was developed using COMSOL Multiphysics software and used to simulate the thermal behaviour of the PCM-concrete composite. The model was validated using the data recorded in the huts and then used to investigate the influence of geographical location on the potential thermal performance of the PCM-concrete composite.

## 9.2 Principal conclusions and achievement of objectives

In order to discuss the achievement of the objectives of this research, which were set out in Section 1.3, they are reiterated here and addressed individually as follows

**1. To create a eutectic fatty acid PCM to be vacuum impregnated into lightweight aggregate and to evaluate the effectiveness of different methods of sealing the PCM into lightweight aggregate to prevent leakage.**

The first objective of this project was approached by initially creating a Capric acid:Myristic acid eutectic with a mass ratio of 75:25 in the laboratory. This eutectic PCM was characterised using DSC testing which confirmed the melt temperature range to be 22.7 $^{o}$C to 27.7 $^{o}$C and the latent heat capacity to be 133 J/g. This melt temperature range is suitable for a space cooling application. The eutectic displayed a higher latent heat capacity than the microencapsulated paraffin PCM, however the eutectic also displayed greater thermal hysteresis which reduces the temperature at which the PCM starts to release heat. One of the issues that reduces the effectiveness of a PCM in a space cooling application is that the temperature of the PCM does not drop sufficiently overnight to enable it to completely solidify and be ready to absorb heat the following day. Thermal hysteresis behaviour compounds this issue. It can be concluded that the eutectic created shows good potential as a PCM, however further experimental work is required to reduce the thermal hysteresis.

The CA:MA eutectic was vacuum impregnated into a lightweight aggregate and various methods were used to prevent the leakage of the PCM out of the lightweight aggregate. The investigation showed that leakage of the PCM could be prevented through the use of a water resisting additive called Conplast WP402 together with a superplasticiser to facilitate a lower water content. Although this outcome fulfils the first objective of the thesis, further long term testing is required to ensure that the PCM will remain permanently sealed into the lightweight aggregate during repeated phase changes.

**2. To assess different simple methods of improving the thermal conductivity of a PCM-concrete composite through laboratory testing.**

The second objective of this thesis involved evaluating the influence of the addition of GGBS and steel fibres on the thermal conductivity of the concrete. The investigation concluded that the addition of GGBS reduced the thermal conductivity of the concrete by approximately 8%. This result was surprising, however it may be due to the fact that GGBS concrete has a slower rate of strength gain and hence density gain. Although GGBS concrete is expected to achieve a

denser cement matrix than a concrete made with 100 % ordinary Portland cement after 56 days, strength tests indicated that the sample may not have reached its full density at the time of testing, which resulted in slightly lower thermal conductivity values. The addition of steel fibres resulted in a 4 % increase in thermal conductivity which was considered to be insignificant. It was concluded that steel fibres would be excluded from the concrete mix as their inclusion adds cost and complexity to the manufacturing process and the benefit gained from their inclusion is minimal. The thermal conductivity tests also confirmed that the thermal conductivity of the LWA-PCM concrete composite (0.74 W/mK) was half that of the micro-encapsulated PCM-concrete composite (1.48 W/mK). This difference can be attributed to the difference in density of the aggregates used in each mix, as the LWA have significantly lower density than the limestone aggregates. This result means that while the micro-encapsulated PCM has a lower latent heat capacity than the fatty acid eutectic used in the LWA-PCM, the micro-encapsulated PCM-concrete can potentially provide a greater latent heat capacity than the LWA-PCM-concrete because if the heating period is sufficiently long, the heat energy will transfer deeper into the wall or floor due to its higher conductivity, causing more PCM to melt.

The conclusions of the laboratory investigations carried out to fulfil the first and second objectives led to the selection of the micro-encapsulated PCM to be used in the final mix design for the PCM-concrete composite sandwich panels. Trial mixes were carried out to refine the mix design. As expected, the addition of the micro-encapsulated PCM reduced the workability of the fresh concrete considerably however with a small increase in water content and plasticiser, sufficient workability was achieved to enable the manufacture of the full-scale panels to proceed without any issues. In addition, the PCM-concrete showed sufficient strength after 48 hours to enable the cladding panels to be removed from the casting tables in the precast factory which is an important factor in the manufacturing process of full scale panels.

**3. To thermally characterise the proposed concrete sandwich cladding panels and carry out a laboratory investigation to evaluate the composite structural behaviour of the two layers of the sandwich panel under different connectivity scenarios and ensure that the panels have sufficient strength and stiffness to withstand expected lateral wind loads.**

The fulfilment of the third objective of this project included thermal characterisation and structural testing of the proposed concrete sandwich cladding panels. The thermal characterisation investigation determined the overall thermal conductivity and thermal resistivity of the panels under steady-state conditions at the centre and at the location of the

connectors. As the thermal conductivity of the insulation layer is very low relative to the concrete layers, the insulation is the dominant contributor to the overall thermal conductivity behaviour. The panel with the PCM-concrete inner leaf displayed an overall thermal conductivity 12 % lower than the control panel which can be attributed to the low thermal conductivity of the PCM. At the locations of the C-Grid and Thermomass connectors, the thermal conductivity increased by 117 % and 104 % respectively which is expected as the connectors have a higher thermal conductivity then the insulation. Although both types of connectors caused a thermal bridge effect, the R-value results confirmed that the Thermomass connector provided 20 % more thermal resistance than the C-Grid connector, hence the thermal bridging effect is lower in the panel connected with Thermomass connectors.

The results of the structural testing regime confirmed that the PCM-concrete panels have sufficient elastic bending moment capacity to resist a design wind load equivalent to 3 $kN/m^2$ over a span of 3.5m, which is double that of a typical design wind load of 1.5 $kN/m^2$. The panels also displayed considerable post-cracking structural capacity, which is an important safety feature in structural design. The post-cracking capacity can be attributed to the inclusion of fibres in the HPFRC outer wythe and steel reinforcement in the inner wythe of the cladding panel. With regard to the degree of composite behaviour in the connected panels, it was concluded from the analysis of the test results that while both panels displayed some degree of composite behaviour it should not be relied on in the structural design of the panels. In the case of the C-Grid connector, a certain amount of deflection of the panel took place prior to composite action occurring. This was attributed to lack of tautness in the diagonals of the C-Grid at the start of testing which may be the result of manufacturing and construction controls hence is outside the control of design. In addition, as the C-Grid does not provide any axial stiffness it is not capable of transferring the applied load from the outer leaf to the inner leaf, hence load sharing behaviour between the two concrete wythes is initially minimal and dependant on the stiffness of the insulation layer. This means that to avoid cracking of the panel the outer wythe alone must have sufficient elastic bending moment capacity to resist a large proportion of the applied loads because, due to the low relative stiffness of insulation, the proportion of applied load transferred to the inner wythe will be relatively small. In contrast, the Thermomass connector provides sufficient axial compression stiffness to transfer loads between the wythes without relying on the insulation. This means that the resistive load is immediately shared by each wythe in accordance to their relative stiffness and hence can be reliably predicted by design calculations. The panel connected with Thermomass connectors

displayed partial composite behaviour of 6.4 %, however it was concluded that as this result is sensitive to the assumed Young's modulus value for concrete, which is a variable material, non-composite (but load sharing) behaviour should be assumed in the design of the panels to ensure that the flexural capacity is not over-estimated. The thermal and structural testing regime provided an understanding of the behaviour of the panels, achieving the third objective of this thesis and led to the selection of the Thermomass connector for use in the full-scale panels for the huts.

**4. To analyse the thermal behaviour and thermal mass impact of the PCM-concrete composite in a full scale scenario, during all seasons, through the construction of three full-scale huts using the PCM-concrete cladding panels and the instrumentation of the huts to record thermal and environmental data, over an 18 month period.**

The fourth and primary objective of this project involved the construction and instrumentation of three full-scale huts, two of which contained the PCM-concrete composite in the inner leaf of the precast concrete sandwich cladding panels. The manufacture of the panels and erection of the huts proceeded without any issues, demonstrating that the PCM-concrete can be successfully used in full-scale construction elements. Thermal and environmental data in the huts were collected over an 18 month period and analysed and the following key conclusions were drawn:

- The thermal mass behaviour of the PCM-concrete composite is similar to that of normal concrete when no phase change occurs, that is, when the PCM remains fully solid or fully liquid within a diurnal period.
- Under winter passive conditions, that is, in the absence of an artificial heat load, solar gain can lead to greater internal air temperatures than in summer due to greater solar irradiance entering the hut as a result of a lower solar altitude angle. However, as the low solar altitude angle also results in a higher area of wall being subjected to irradiance there is more potential for a larger volume of PCM to melt and contribute to the thermal mass effect of lowering the internal air temperature. In the case of the huts, in winter passive conditions, the presence of PCM led to a reduction of the peak internal air temperature in the order of 4.5 $^{o}$C which is 13 % lower than the peak internal air temperature reached in the control (non-PCM) hut. It must be noted though that the ratio of wall surface area to volume of internal air is relatively high in the huts compared to a space in an actual building.

- Under summer passive conditions the PCM-concrete composite had no significant impact on the internal air temperature despite the internal air temperature in the huts reaching 28 $^{o}$C. This result can be attributed to the higher temperature of the PCM-concrete composite at the start of the heating period, which was 22 $^{o}$C, which would indicate that the PCM was only partially solidified, so its ability to absorb heat through phase change the following day was limited. This result highlights that it is critical that the PCM is completely solid at the start of each heating phase in order to achieve significant reduction in internal air temperature. The ability of the PCM to completely solidify overnight in summer conditions is hindered by the shorter night time period and higher external temperatures.
- A comparison of the performance of the PCM-concrete under winter and summer passive conditions highlighted the influence of the temperature differential between the wall and air during the heating phase. Under winter conditions, this temperature differential was much greater at 9.3 $^{o}$C as opposed to 1.7 $^{o}$C under summer conditions, resulting in a higher heat flux at the wall surface, hence more heat was transferred into the wall in winter, facilitating more melting of the PCM.
- Further analyses was carried out in which an artificial heat load was introduced to the hut in the form of a convective heater. Two scenarios were considered in detail, that is, with and without overnight ventilation. When overnight ventilation was provided a 17 % reduction in the peak air temperature was achieved in both PCM huts. When no ventilation was provided the reduction was only 5%. It was concluded that the overnight ventilation allowed the temperature of the wall to decrease at a faster rate and hence the PCM had a longer time to achieve complete solidification and also the heat released by the solidification was not confined in the hut by the well-insulated walls and glazing.
- Another observation from this analysis is that during the day selected for the case of no ventilation, there was significant solar irradiance. Hence the applied heat load was a combination of the convection heater and solar irradiance. In the scenario in which overnight ventilation was provided, the day was cloudy hence the heat load was mainly from the convection heater with some diffuse solar irradiance. The total applied load in both cases was similar, confirmed by the same initial and peak internal air temperatures in the control hut. However as solar irradiance is only applied to a portion of the wall area it cannot be assumed that the internal wall temperatures are evenly distributed through all the walls. There may be a volume of PCM material within, for example, the

North wall, that does not melt leading to a lower thermal mass effect. In the case where the heat load is provided primarily by the convection heater, the heat is roughly evenly distributed throughout the space hence all the PCM-composite has equal potential to melt and provide beneficial thermal mass effect. It can be concluded from this observation that the source and type of heat load influences the potential of the PCM-concrete within a building to provide a beneficial space cooling effect

- With regard to the effective depth of the PCM, although the data provided some evidence of phase change of the PCM at depths greater than 60 mm, under some conditions it was relatively minor. Hence, for reasons of economy, there is a justification for specifying PCM only within the first 60 mm of the internal wall depth. However this conclusion only applies to the environmental conditions analysed. A scenario that induces a greater temperature differential between the internal air and the wall over a longer period of time may lead to increased heat transfer into the wall and engagement of the PCM located deeper in the wall.

Overall the data shows that the inclusion of PCMs into concrete can be an effective strategy for reducing overheating effects in a building and hence the demand on cooling systems under certain thermal conditions. However it can be concluded from an overview of all the data across the 18 month monitoring period that under passive conditions, the thermal conditions within the depth of the wall that would provide potential for the PCM to change phase only occurred during about one third of the year. It is important to note that this outcome is related both to the form of construction, well insulated in this case and the local climate, which is temperate in Ireland. It is expected that if the PCM-concrete composite were to be located in a form of construction that included less insulation and also in a climate which provided greater fluctuation in the diurnal temperature for longer periods during the year, it would have a greater impact on reducing overheating in internal environments of buildings. It can be concluded from the analyses that the provision of a suitable overnight ventilation system would extend the annual period during which the PCM is effective.

**5. To develop a software model that can accurately simulate the thermal behaviour of the PCM-composite panels in various full-scale environmental conditions and which is validated using the environmental data collected at the huts.**

The fifth and final objective of this project was to develop a finite element model that can simulate the thermal behaviour of the PCM-concrete which is validated using data from full-scale samples recorded under ‘real’ building conditions. The development of the model was

described in detail in Chapter 8. The PCM-concrete composite material was modelled as a porous material with PCM within the pores. The thermal properties and phase change behaviour were defined in the model including thermal hysteresis behaviour. The model was used to carry out sensitivity studies on the thermal properties of the concrete matrix material, the latent heat of the PCM and the volume of PCM filled pores. The model included the three modes of heat transfer, conduction, convection and radiation to simulate heat transfer through the walls, between the air and the walls and from solar irradiance to the walls respectively.

Models of the full-scale huts were created and actual internal and external temperature data and solar irradiance recorded at the huts were applied to the model. The model was validated by comparing the simulated temperatures with the actual temperatures recorded at the hut. The following conclusions were drawn from this analysis:

- The COMSOL model simulated temperatures within the hut at the same or improved accuracy as the thermocouples used in the huts.
- The thermal behaviour of the PCM-concrete was modelled with similar accuracy whether phase change occurs or not.
- The thermal behaviour of the PCM-concrete was modelled with similar accuracy as the normal concrete model.
- There was slightly less accuracy in the simulated air temperatures which was attributed to the use of a simplified approach to modelling convective heat transfer. Also the simulated air temperature was for the entire air domain whereas the actual internal air temperature was recorded by a thermocouple at a point location in the centre of the hut

Overall the results of the simulations aligned closely with the real temperatures recorded in the huts demonstrating that the developed COMSOL model can be used to reliably predict the thermal behaviour and impact of the PCM-concrete composite, achieving the fifth objective of this project.

The validated COMSOL model was then used to investigate the influence of geographical location (in which external temperature and the intensity, timing and altitude of solar irradiance varied daily depending on the season) on PCM-concrete performance. This scenario modelling demonstrated that under summer conditions, PCM-concrete provided more beneficial thermal mass effect at higher latitudes, due to the lower solar altitude angle whereby the walls are more exposed to solar irradiance, providing greater potential for the PCM to melt. It can also be

concluded that in summer conditions the PCM-concrete composite is more effective at reducing internal air temperatures when placed in the floor rather than the North wall as no direct irradiance reaches the North wall. In contrast, during winter conditions the simulation demonstrated that the potential for PCM-concrete to provide enhanced thermal mass improves as latitude decreases. The reason for this conclusion is that the solar altitude angle is so low at higher latitudes in winter, that temperatures did not increase enough to engage the PCM. However, at lower latitudes angles the PCM-concrete was effective at reducing internal air temperatures and it was also noted that, under winter conditions, placing the PCM-concrete in the walls rather than the floor provides increased potential for engagement of the PCM.

### 9.3 Impact of research

Overall this research study has demonstrated that the PCM-concrete composite can successfully provide enhanced thermal mass benefits. The fulfillment of the five objectives has furthered the knowledge in this field of research in a number of areas. Firstly, the design, manufacture and structural testing of the full-scale PCM-concrete panels provides evidence that PCM-concrete can be successfully up-scaled for use in real construction projects using standard manufacturing methods.

Secondly, the construction and thermal monitoring of the huts provides a thermal data set collected within a 'real', full-scale form of construction, throughout all seasons which enables the impact of this form of technology to be realistically assessed across a full annual period. Prior to this study there was only one previous research study (Cabeza et al., 2007) which assessed PCM-concrete in a full-scale scenario. In this study huts were constructed using a single leaf wall hence heat could be absorbed/released from both internal and external surfaces. This arrangement is not reflective of a real form of construction as external cladding panels typically have an inner leaf and outer leaf which are separated by a layer of insulation which limits heat transfer at the outer surface of the inner leaf. Cabeza et al.'s study recorded three weeks of data so the findings are limited to the environmental conditions that existing during the three test periods.

The collection of a thermal data set over a full year highlighted one of the main limitations of this technology which is that the PCM only provides beneficial effects during a portion of the year. The extent of potential beneficial thermal mass is influenced by many factors however it is clear that its potential is greater in a scenario in which the diurnal temperature fluctuation is relatively large. The economic benefit of the technology is not only subject to the bespoke

application of the technology for a particular building but also to the type and cost of the local energy provided to the building and hence can only be assessed on a case–by-case basis.

The number of variables that impact the thermal performance of PCM-concrete hinders the investigation of this technology in a laboratory or on site. The third and primary impact of this research study is the development of a simulation model which facilitates bespoke solutions to be developed for any geographical location and building geometry, with optimisation of parameters including phase change temperature, latent heat capacity, effective depth and location of PCM-concrete composite. The annual thermal data set allowed the model to be validated using data collected in a real form of construction. This has furthered the knowledge in the field of research as any models developed in previous research studies were only validated using limited data collected in a laboratory setting. The ability to simulate the thermal behaviour of a PCM-concrete composite will enhance research into this form of technology and make its use more accessible.

A fourth impact of this research is that the experimental design of the partial PCM hut provided an inner leaf in which the temperature data gathered allowed the effective depth of the PCM to be assessed confirming that PCMs located at depths greater than 60mm were ineffective. Although this finding is specific to the local climate conditions and geometry of the huts it highlights the order of magnitude of the effective depth of PCM concrete and the factors that influence it.

Finally a limitation that must be considered in the application of this technology is that to gain the thermal mass benefit of the PCM-concrete the material must be left exposed within the building. This requirement may not align with architectural intent and may cause challenges in the installation of mechanical and electrical services to the building.

### 9.4 Recommendations for future research

This study has made a contribution to the understanding of the potential thermal mass benefit provided by a PCM-concrete composite located in the walls of a building. The achievement of beneficial thermal mass effects is influenced by many variables including geographic and building specific characteristics, hence it is important that the performance of a PCM-concrete is assessed under full-scale and realistic building conditions. However full-scale experimental studies are significantly constrained by the cost of the necessary resources and time and the

results cannot be assumed to apply universally. A limitation of this study is that the thermal behaviour of the PCM-concrete as recorded in the huts can only be assumed for similar climate conditions, geometry and form of construction. To expand the understanding of this technology modelling tools are essential. The development of a simulation model in this study, validated using real data from a full-scale experiment, contributes to the progression of the investigation into the potential of PCM-concrete composites and facilitates efficient progression of further research in this topic.

This research study has highlighted some areas of particular interest for further study as follows:

- In Ireland's temperate climate, it was noted from the hut data that the thermal conditions that would potentially engage the PCM-concrete composite in enhancing the thermal mass only arose during approximately 30 % of the year. A limitation of this finding is that it can only be assumed under similar environmental and geometric conditions. The simulation model could be used to investigate the performance of PCM-concrete placed in a typical room with concrete floors, walls and ceilings, in various different climatic regions, across a whole year period, to determine an overview of which geographical locations and seasons would potentially benefit most from this technology.
- The performance of the PCM-concrete composite is also subject to the ratio of the exposed surface area of the PCM-concrete elements and the enclosed volume of air within the space. Further research could be conducted to investigate if there is a limit to this ratio at which the PCM-concrete ceases to be effective.
- Another aspect highlighted by this study is that the performance of the PCM-concrete placed in a room is influenced by the mode of heat transfer to the PCM-concrete elements. Heat transfer from solar irradiance may only engage certain areas of the PCM as the irradiance is not evenly distributed over the wall and floor surfaces. However an artificial convective heat source and heat derived from building use may be distributed reasonably evenly to all exposed surface areas enabling greater access to the latent heat of the PCM. The performance of PCM-concrete when exposed to different modes of heat source could be explored using the simulation model.
- Further research to confirm the long term performance of the preferred sealing method would be of interest in order to establish if LWA-PCM composite is a viable method

for incorporating PCM into concrete, particularly as it has displayed good thermal mass performance in previous research.

- Previous research has demonstrated that fatty acid eutectics are particularly effective at enhancing thermal mass as they provide a relatively high latent heat capacity combined with a narrow melt temperature range. Bio-based fatty acid eutectics are less flammable than paraffins and are derived from vegetables and animals rather than fossil fuels. For these reasons further research to develop suitable fatty acid eutectics and refine them to mitigate thermal hysteresis would be beneficial to the overall promotion of PCM use in TES systems.
- There are some limitations to the simulation model developed in this study in that it does not simulate the effects of occupancy behaviour and it also assumes complete air tightness. The model could be developed further to allow other factors that influence the internal thermal environment in a building to be incorporated.
- As noted in Chapter 1 of this thesis, it was the intention of the IMPRESS project to use the developed PCM-concrete cladding panels to clad a section of a school building in Coventry, England. After the Grenfeld Tower fire the school board pulled out of the IMPRESS project due to fire safety restrictions. The Grenfeld fire resulted in an increase in regulatory oversight and public concern regarding the fire performance of cladding materials. As stated by Nair et al. (2022), organic PCMs are flammable hence fire resistant containment solutions need to be developed to facilitate the safe use of PCMs in a building application. Also full-scale fire testing of proposed panels will be required prior to use in a real building project.
- The presence of PCMs can contribute proportionately higher additional thermal mass in a lightweight form of building envelope. It would be interesting to explore the potential for incorporating a PCM into a foamed geopolymer concrete to achieve a lighter, thinner and more sustainable cladding panel with effective thermal mass properties.

## References


Abdou, O. A., Murali, K., Morsi, A., 1996. Thermal performance evaluation of a prefabricated fiber-reinforced plastic building envelope system. Energy and Buildings, vol. 24, pp. 77-83

Aguayo, M., Das, S., Castro, C., Kabay, N., Sant, G., Neithalath, N., 2017. Porous inclusions as hosts for phase change materials in cementitious composites: Characterization, thermal performance, and analytical models. Constr. Build. Mater. 134, 574–584. https://doi.org/10.1016/j.conbuildmat.2016.12.185

Aguayo, M., Das, S., Maroli, A., Kabay, N., Mertens, J.C.E., Rajan, S.D., Sant, G., Chawla, N., Neithalath, N., 2016. The influence of microencapsulated phase change material (PCM) characteristics on the microstructure and strength of cementitious composites: Experiments and finite element simulations. Cem. Concr. Compos. 73, 29–41. https://doi.org/10.1016/j.cemconcomp.2016.06.018

Akeiber, H., Nejat, P., Majid, M.Z.Abd., Wahid, M.A., Jomehzadeh, F., Zeynali Famileh, I., Calautit, J.K., Hughes, B.R., Zaki, S.A., 2016. A review on phase change material (PCM) for sustainable passive cooling in building envelopes. Renew. Sustain. Energy Rev. 60, 1470–1497. https://doi.org/10.1016/j.rser.2016.03.036

Alkan, C., 2023. 1 - Thermal energy storage methods, in: Pielichowska, K., Pielichowski, K. (Eds.), Multifunctional Phase Change Materials. Woodhead Publishing, pp. 1–93. https://doi.org/10.1016/B978-0-323-85719-2.00010-9

Alkan, C., Sarı, A., Karaipekli, A., Uzun, O., 2009. Preparation, characterization, and thermal properties of microencapsulated phase change material for thermal energy storage. Sol. Energy Mater. Sol. Cells 93, 143–147. https://doi.org/10.1016/j.solmat.2008.09.009

AL-Saadi, S.N., Zhai, Z. (John), 2013. Modeling phase change materials embedded in building enclosure: A review. Renew. Sustain. Energy Rev. 21, 659–673. https://doi.org/10.1016/j.rser.2013.01.024

Anderson, B. 2006. Chapter 3: Thermal properties of Building Structures. CIBSE Guide A: Environmental Design. Norwich: Chartered Institute of Building Services Engineers (CIBSE).

Ascione, F., Bianco, N., De Masi, R.F., De' Rossi, F., Vanoli, G.P., 2014. Energy refurbishment of existing buildings through the use of phase change materials: Energy savings and indoor comfort in the cooling season. Appl. Energy 113, 990–1007. https://doi.org/10.1016/j.apenergy.2013.08.045

Atinafu, D.G., Dong, W., Huang, X., Gao, H., Wang, G., 2018. Introduction of organic-organic eutectic PCM in mesoporous N-doped carbons for enhanced thermal conductivity and energy storage capacity. Appl. Energy 211, 1203–1215. https://doi.org/10.1016/j.apenergy.2017.12.025

Aviram, D. P., Fried, A. N., Roberts, J. J., 2001. Thermal properties of a variable cavity wall. *Building and Environment*, 36, 1057-1072

Baetens, R., Jelle, B.P., Gustavsen, A., 2010. Phase change materials for building applications: A state-of-the-art review. Energy Build. 42, 1361–1368. https://doi.org/10.1016/j.enbuild.2010.03.026

Baghban, M.H., Hovde P.J., Gustavsen A., 2010. Numerical simulation of a building envelope with high performance materials, In: *COMSOL conference. Paris; 2010*

Barreneche, C., Solé, A., Miró, L., Martorell, I., Fernández, A.I., Cabeza, L.F., 2013. Study on differential scanning calorimetry analysis with two operation modes and organic and inorganic phase change material (PCM). Thermochim. Acta 553, 23–26. https://doi.org/10.1016/j.tca.2012.11.027

Ben Romdhane, S., Amamou, A., Ben Khalifa, R., Saïd, N.M., Younsi, Z., Jemni, A., 2020. A review on thermal energy storage using phase change materials in passive building applications. J. Build. Eng. 32, 101563. https://doi.org/10.1016/j.jobe.2020.101563

Bentz, D.P., Turpin, R., 2007. Potential applications of phase change materials in concrete technology. Cem. Concr. Compos. 29, 527–532. https://doi.org/10.1016/j.cemconcomp.2007.04.007

Bentz, D. P., Peltz, M. A., Duran-Herrera, A., Valdez, P. and Juarez, C. A., 2011. Thermal properties of high-volume fly ash mortars and concretes. *Journal of Building Physics* 34(3) 263-275

Berardi, U., Gallardo, A.A., 2019. Properties of concretes enhanced with phase change materials for building applications. Energy Build. 199, 402–414. https://doi.org/10.1016/j.enbuild.2019.07.014

Bretz, S., Akbari, H., Rosenfeld, A., 1998. Practical issues for using solar-reflective materials to mitigate urban heat islands. Atmos. Environ. 32, 95–101. https://doi.org/10.1016/S1352-2310(97)00182-9

Bunn, W. G., 2011. CFRP Grid/Rigid Foam Shear Transfer Mechanism for Precast,Master of Science, Civil Engineering, North Carolina State University, Prestressed Concrete Sandwich Wall Panels.

Bush, TD., Stine, GL., 1994. Flexural behavior of composite precast concrete sandwich panels with continuous truss connectors. PCI J:112–21

Byrne, A., Byrne, G., & Robinson, A., 2017 Compact facility for testing steady and transient thermal performance of building walls. *Energy and Buildings*, 152, 602-614

Cabeza, L.F., Barreneche, C., Martorell, I., Miró, L., Sari-Bey, S., Fois, M., Paksoy, H.O., Sahan, N., Weber, R., Constantinescu, M., Anghel, E.M., Malikova, M., Krupa, I., Delgado, M., Dolado, P., Furmanski, P., Jaworski, M., Haussmann, T., Gschwander, S.,

Fernández, A.I., 2015. Unconventional experimental technologies available for phase change materials (PCM) characterization. Part 1. Thermophysical properties. Renew. Sustain. Energy Rev. 43, 1399–1414. https://doi.org/10.1016/j.rser.2014.07.191

Cabeza, L.F., Castell, a., Barreneche, C., de Gracia, a., Fernández, a. I., 2011. Materials used as PCM in thermal energy storage in buildings: A review. Renew. Sustain. Energy Rev. 15, 1675–1695. https://doi.org/10.1016/j.rser.2010.11.018

Cabeza, L.F., Castellón, C., Nogués, M., Medrano, M., Leppers, R., Zubillaga, O., 2007. Use of microencapsulated PCM in concrete walls for energy savings. Energy Build. 39, 113–119. https://doi.org/10.1016/j.enbuild.2006.03.030

Cabeza LF, Navarro L, Pisello AL, Olivieri L, Bartolom´e C, Sanchez J, Alvarez S, Tenorio JA., 2020. Behaviour of a concrete wall containing micro-encapsulated PCM after a decade of its construction. Sol Energy 2020;200:108–13. https://doi.org/10.1016/j.solener.2019.12.003.

Cao, V.D., Pilehvar, S., Salas-Bringas, C., Szczotok, A.M., Rodriguez, J.F., Carmona, M., Al-Manasir, N., Kjøniksen, A.-L., 2017. Microencapsulated phase change materials for enhancing the thermal performance of Portland cement concrete and geopolymer concrete for passive building applications. Energy Convers. Manag. 133, 56–66. https://doi.org/10.1016/j.enconman.2016.11.061

Castellón, C., Günther, E., Mehling, H., Hiebler, S., Cabeza, L.F., 2008. Determination of the enthalpy of PCM as a function of temperature using a heat-flux DSC-A study of different measurement procedures and their accuracy. Int. J. Energy Res. 32, 1258–1265. https://doi.org/10.1002/er.1443

Cellat, K., Beyhan, B., Güngör, C., Konuklu, Y., Karahan, O., Dündar, C., Paksoy, H., 2015. Thermal enhancement of concrete by adding bio-based fatty acids as phase change materials. Energy Build. 106, 156–163. https://doi.org/10.1016/j.enbuild.2015.05.035

Cellat, K., Tezcan, F., Beyhan, B., Kardaş, G., Paksoy, H., 2017. A comparative study on corrosion behavior of rebar in concrete with fatty acid additive as phase change material. Constr. Build. Mater. 143, 490–500. https://doi.org/10.1016/j.conbuildmat.2017.03.165

Çengel, Y.A., Ghajar, A.J., 2015. Heat and mass transfer: fundamentals & applications, Fifth edition. ed. McGraw Hill Education, New York, NY.

Chen, B., Salmon, D., Hancock, E., Detloff, H., Campus, O., 1994. Measurement of Energy Efficiency of Building Envelopes. pp. 132-132.

Chen, C., Guo, H., Liu, Y., Yue, H., Wang, C., 2008. A new kind of phase change material (PCM) for energy-storing wallboard. Energy Build. 40, 882–890. https://doi.org/10.1016/j.enbuild.2007.07.002

Choi, I., Kim, J., You, Y.-C., 2016. Effect of cyclic loading on composite behavior of insulated concrete sandwich wall panels with GFRP shear connectors. Compos. Part B Eng. 96, 7–19. https://doi.org/10.1016/j.compositesb.2016.04.030

Choi, I., Kim, J., Kim, H-R., 2015. Composite behavior of insulated concrete sandwich wall panels subjected to wind pressure and suction, Materials 8 (2015) 1264–1282, https://doi.org/10.3390/ma8031264

COMSOL Heat Transfer Module User's Guide, 2018.

Cook, D. J. and Uher, C., 1974. The thermal conductivity of fibre reinforced concrete. Cement and Concrete research (4) 497-509

Cui, H., Memon, S.A., Liu, R., 2015a. Development, mechanical properties and numerical simulation of macro encapsulated thermal energy storage concrete. Energy Build. 96, 162–174. https://doi.org/10.1016/j.enbuild.2015.03.014

Cui, Y., Xie, J., Liu, J., Pan, S., 2015b. Review of Phase Change Materials Integrated in Building Walls for Energy Saving. Procedia Eng. 121, 763–770. https://doi.org/10.1016/j.proeng.2015.09.027

Cunha, S., Aguiar, J.B., Tadeu, A., 2016. Thermal performance and cost analysis of mortars made with PCM and different binders. Constr. Build. Mater. 122, 637–648. https://doi.org/10.1016/j.conbuildmat.2016.06.114

D'Alessandro, A., Pisello, A.L., Fabiani, C., Ubertini, F., Cabeza, L.F., Cotana, F., 2018. Multifunctional smart concretes with novel phase change materials: Mechanical and thermo-energy investigation. Appl. Energy 212, 1448–1461. https://doi.org/10.1016/j.apenergy.2018.01.014

Darkwa, J., Su, O., 2012. Thermal simulation of composite high conductivity laminated microencapsulated phase change material (MEPCM) board. Appl. Energy 95, 246–252. https://doi.org/10.1016/j.apenergy.2012.02.062

Davison, B., Owens, G., 2003. Steel Designers Manual. The Steel Construction Institute, Blackwell Publishing

Desogus G., Mura, S., Ricciu, R., 2011. Comparing different approaches to in situ measurement of building components thermal resistance. Energy Build;43:2613–20

Diaconu, B.M., Cruceru, M., 2010. Novel concept of composite phase change material wall system for year-round thermal energy savings. Energy Build. 42, 1759–1772. https://doi.org/10.1016/j.enbuild.2010.05.012

Dincer, I., Rosen, M.A., 2001. Energetic, environmental and economic aspects of thermal energy storage systems for cooling capacity. Appl. Therm. Eng. 21, 1105–1117. https://doi.org/10.1016/S1359-4311(00)00102-2

Drissi, S., Ling, T.-C., Mo, K.H., Eddhahak, A., 2019. A review of microencapsulated and composite phase change materials: Alteration of strength and thermal properties of cement-based materials. Renew. Sustain. Energy Rev. 110, 467–484. https://doi.org/10.1016/j.rser.2019.04.072

Dumas, J.-P., Gibout, S., Zalewski, L., Johannes, K., Franquet, E., Lassue, S., Bédécarrats, J.-P., Tittelein, P., Kuznik, F., 2014. Interpretation of calorimetry experiments to characterise phase change materials. Int. J. Therm. Sci. 78, 48–55. https://doi.org/10.1016/j.ijthermalsci.2013.11.014

Eddhahak-Ouni, A., Drissi, S., Colin, J., Neji, J., Care, S., 2014. Experimental and multi-scale analysis of the thermal properties of Portland cement concretes embedded with microencapsulated Phase Change Materials (PCMs). Appl. Therm. Eng. 64, 32–39. https://doi.org/10.1016/j.applthermaleng.2013.11.050

Eurocode 1: Actions on Structures Part 1 -4; General Actions – Wind actions

European Parliament and Council of European Union, 2018. Energy Performance of Buildings Directive.

Eyres, N.R., Hartree, D.R., Ingham, J., Jackson, R., Sarjant, R.J., Wagstaff, J.B., 1946. The calculation of variable heat flow in solids. *Philosophical Transactions of the Royal Society of London Series A, Mathematical and Physical Sciences*, 240, 1–57

Faraj, K., Khaled, M., Faraj, J., Hachem, F., Castelain, C., 2021. A review on phase change materials for thermal energy storage in buildings: Heating and hybrid applications. J. Energy Storage 33, 101913. https://doi.org/10.1016/j.est.2020.101913

Farid, M.M., Khudhair, A.M., Razack, S.A.K., Al-Hallaj, S., 2004. A review on phase change energy storage: materials and applications. Energy Convers. Manag. 45, 1597–1615. https://doi.org/10.1016/j.enconman.2003.09.015

Farnam, Y., Esmaeeli, H.S., Zavattieri, P.D., Haddock, J., Weiss, J., 2017. Incorporating phase change materials in concrete pavement to melt snow and ice. Cem. Concr. Compos. 84, 134–145. https://doi.org/10.1016/j.cemconcomp.2017.09.002

Fenollera, M., Míguez, J., Goicoechea, I., Lorenzo, J., Ángel Álvarez, M., 2013. The Influence of Phase Change Materials on the Properties of Self-Compacting Concrete. Materials 6, 3530–3546. https://doi.org/10.3390/ma6083530

Fernandez, A.I., Martínez, M., Segarra, M., Martorell, I., Cabeza, L.F., 2010. Selection of materials with potential in sensible thermal energy storage. Sol. Energy Mater. Sol. Cells 94, 1723–1729. https://doi.org/10.1016/j.solmat.2010.05.035

Figueiredo, A., Lapa, J., Vicente, R., Cardoso, C., 2016. Mechanical and thermal characterization of concrete with incorporation of microencapsulated PCM for applications in thermally activated slabs. Constr. Build. Mater. 112, 639–647. https://doi.org/10.1016/j.conbuildmat.2016.02.225

Frankl, B.A., Lucier, G.W., Hassan, T.K., Rizkalla, S.H., 2011. Behavior of precast, prestressed concrete sandwich wall panels reinforced with CFRP shear grid. *PCI Journal*, 42–54Ghoshdastidar, P.S., 2012. Heat transfer, 2nd ed. ed. Oxford University Press, New Delhi.

Frankl, B., 2008. Structural Behavior of Insulated Precast Prestressed Concrete Sandwich Panels Reinforced with CFRP Grid, Department of Masters Thesis, Civil, Construction and Environmental Engineering, North, Carolina State University, Raleigh, NC.

Ghoshdastidar, P.S., 2012. Heat Transfer. Oxford University Press

Gowreesunker, B.L., Tassou, S.A., Kolokotroni, M., 2012. Improved simulation of phase change processes in applications where conduction is the dominant heat transfer mode. Energy Build. 47, 353–359. https://doi.org/10.1016/j.enbuild.2011.12.008

Gupta, R. P. 2003. Remote Sensing Geology, Springer

Hashemi, H.T. and Sliepcevich, C.M., 1967. A numerical method for solving two-dimensional problems of heat conduction with change of phase. *Chemical Engineering Programme Symposium series,* 63, 34–41

Hasse, C., Grenet, M., Bontemps, A., Dendievel, R., Sallée, H., 2011. Realization, test and modelling of honeycomb wallboards containing a Phase Change Material. Energy Build. 43, 232–238. https://doi.org/10.1016/j.enbuild.2010.09.017

Haurie, L., Serrano, S., Bosch, M., Fernandez, A.I., Cabeza, L.F., 2016. Single layer mortars with microencapsulated PCM: Study of physical and thermal properties, and fire behaviour. Energy Build. 111, 393–400. https://doi.org/10.1016/j.enbuild.2015.11.028

Hawes, D.W., Feldman, D., 1992. Absorption of phase change materials in concrete. Sol Energy Mater Sol Cell 1992;27(2):91-101

He, H., Yue, Q., Gao, B., Zhang, X., Li, Q., Wang, Y., 2013. The effects of compounding conditions on the properties of fatty acids eutectic mixtures as phase change materials. Energy Convers. Manag. 69, 116–121. https://doi.org/10.1016/j.enconman.2013.01.026

Hohne, G., Hemminger, W., Hammersheim, H. J., 2003. Differential Scanning Calorimetry, 2nd Edition, New York, Springer Verlag Heidelberg.

Howlader, M. K., Rashid, M. H., Mallick, D. and Haque, T., 2012. Effects of aggregate types on thermal properties of concrete. *Journal of Engineering and Applied Sciences* Vol. 7 No. 7

Hu, Y., Tang, Z., Li, W., Li, Y., Tam, V. W. Y., 2019. Physical-Mechanical Properties of Fly Ash/GGBFS Geopolymer Composites with Recycled Aggregates. Construction and Building Materials 226 (November 2019): 139–51. https://doi.org/10.1016/j.conbuildmat.2019.07.211.

Hua, W., Lv, X., Zhang, X., Ji, Z., Zhu, J., 2023. Research progress of seasonal thermal energy storage technology based on supercooled phase change materials. J. Energy Storage 67, 107378. https://doi.org/10.1016/j.est.2023.107378

Hunger, M., Entrop, a. G., Mandilaras, I., Brouwers, H.J.H., Founti, M., 2009. The behavior of self-compacting concrete containing micro-encapsulated Phase Change Materials. Cem. Concr. Compos. 31, 731–743. https://doi.org/10.1016/j.cemconcomp.2009.08.002

International Energy Agency (IEA), 2023 (https://www.iea.org/energy-system/buildings).

International Energy Agency (IEA) Technology Roadmap on Energy Efficient Building Envelopes, 2013

Irish Building Regulations Technical Guidance Document L 2022. Conservation of Fuel and Energy - Dwellings

I.S. EN ISO 6946:2017 Building components and building elements - Thermal resistance and thermal transmittance - Calculation methods

I.S. EN ISO 8990-1997. Thermal Insulation. Determination of steady-state thermal transmission properties - calibrated and guarded hot box

I.S. EN 12390-2:2019 Testing Hardened Concrete – Part 2: Making and curing specimens for strength tests

I.S EN 12390-3:2019 Testing Hardened Concrete – Part 3: Compressive strength of test specimens.

I.S. EN 12350-8 Testing fresh concrete - Part 8: Self-compacting concrete - Slump-flow test.

I.S. EN 12350-6:2019 Testing fresh concrete - Part 6: Density

I.S. EN 197-1:2011 Cement Composition, specifications and conformity criteria for common cements

I.S. EN 1991-1-4 Irish annex to Eurocode 1: Actions on Structures Part 1 -4; General Actions – Wind actions

Jayalath, A., San Nicolas, R., Sofi, M., Shanks, R., Ngo, T., Aye, L., Mendis, P., 2016. Properties of cementitious mortar and concrete containing micro-encapsulated phase change materials. Constr. Build. Mater. 120, 408–417. https://doi.org/10.1016/j.conbuildmat.2016.05.116

Jelle, B.P., Kalnæs, S.E., 2017. Chapter 3 - Phase Change Materials for Application in Energy-Efficient Buildings, in: Pacheco-Torgal, F., Granqvist, C.-G., Jelle, Bjørn Petter, Vanoli, G.P., Bianco, N., Kurnitski, J. (Eds.), Cost-Effective Energy Efficient Building Retrofitting. Woodhead Publishing, pp. 57–118. https://doi.org/10.1016/B978-0-08-101128-7.00003-4

Jeong, S.-G., Chung, O., Yu, S., Kim, Sughwan, Kim, Sumin, 2013. Improvement of the thermal properties of Bio-based PCM using exfoliated graphite nanoplatelets. Sol. Energy Mater. Sol. Cells 117, 87–92. https://doi.org/10.1016/j.solmat.2013.05.038

Kalnæs, S.E., Jelle, B.P., 2015. Phase change materials and products for building applications: A state-of-the-art review and future research opportunities. Energy Build. 94, 150–176. https://doi.org/10.1016/j.enbuild.2015.02.023

Kaviany, M. 2011. Essentials of Heat Transfer: Principles, Materials and Applications. New York, Cambridge University Press.

Kastiukas, G., Zhou, X., Castro-Gomes, J., 2016. Development and optimisation of phase change material-impregnated lightweight aggregates for geopolymer composites made from aluminosilicate rich mud and milled glass powder. Constr. Build. Mater. 110, 201–210. https://doi.org/10.1016/j.conbuildmat.2016.02.029

Kenisarin, M., Mahkamov, K., 2016. Passive thermal control in residential buildings using phase change materials. Renew. Sustain. Energy Rev. 55, 371–398. https://doi.org/10.1016/j.rser.2015.10.128

Khan, R.J., Bhuiyan, Md.Z.H., Ahmed, D.H., 2020. Investigation of heat transfer of a building wall in the presence of phase change material (PCM). Energy Built Environ. 1, 199–206. https://doi.org/10.1016/j.enbenv.2020.01.002

Kheradmand, M., Azenha, M., De Aguiar, J.L.B., Castro-Gomes, J., 2016. Experimental and numerical studies of hybrid PCM embedded in plastering mortar for enhanced thermal behaviour of buildings. Energy 94, 250–261. https://doi.org/10.1016/j.energy.2015.10.131

Kheradmand, M., Castro-Gomes, J., Azenha, M., Silva, P.D., De Aguiar, J.L.B., Zoorob, S.E., 2015. Assessing the feasibility of impregnating phase change materials in lightweight aggregate for development of thermal energy storage systems. Constr. Build. Mater. 89, 48–59. https://doi.org/10.1016/j.conbuildmat.2015.04.031

Khudhair, A.M., Farid, M.M., 2004. A review on energy conservation in building applications with thermal storage by latent heat using phase change materials. Energy Convers. Manag. 45, 263–275. https://doi.org/10.1016/S0196-8904(03)00131-6

Kim, Y.-R., Khil, B.-S., Jang, S.-J., Choi, W.-C., Yun, H.-D., 2015. Effect of barium-based phase change material (PCM) to control the heat of hydration on the mechanical properties of mass concrete. Thermochim. Acta 613, 100–107. https://doi.org/10.1016/j.tca.2015.05.025

Kim, J., You, Y-C., 2015. Composite behavior of a novel insulated concrete sandwich wall panel reinforced with GFRP shear grids: effects of insulation types, Materials 8 (2015) 899–913, https://doi.org/10.3390/ma8030899.

Klimeš, L., Charvát, P., Mastani Joybari, M., Zálešák, M., Haghighat, F., Panchabikesan, K., El Mankibi, M., Yuan, Y., 2020. Computer modelling and experimental investigation of phase change hysteresis of PCMs: The state-of-the-art review. Appl. Energy 263, 114572. https://doi.org/10.1016/j.apenergy.2020.114572

Kosny, J., and Kossecka, E., 2013. Understanding a Potential for Application of Phase-Change Materials (PCMs) in Building Envelopes. *ASHRAE Transactions* 119(1), 1-11

Kousksou, T., Bruel, P., Jamil, A., El Rhafiki, T., Zeraouli, Y., 2014. Energy storage: Applications and challenges. Sol. Energy Mater. Sol. Cells 120, 59–80. https://doi.org/10.1016/j.solmat.2013.08.015

Kuznik, F., David, D., Johannes, K., Roux, J.-J., 2011. A review on phase change materials integrated in building walls. Renew. Sustain. Energy Rev. 15, 379–391. https://doi.org/10.1016/j.rser.2010.08.019

Kuznik, F., Johannes, K., Franquet, E., Zalewski, L., Gibout, S., Tittelein, P., Dumas, J.-P., David, D., Bédécarrats, J.-P., Lassue, S., 2016. Impact of the enthalpy function on the simulation of a building with phase change material wall. Energy Build. 126, 220–229. https://doi.org/10.1016/j.enbuild.2016.05.046

Kylili, A., Theodoridou, M., Ioannou, I., Fokaides, P., 2016. Numerical heat transfer analysis of Phase Change Material (PCM) – enhanced plasters. *Proceedings of COMSOL conference Munich, Germany 2016*

Lamberg, P., Lehtiniemi, R., Henell, A.-M., 2004. Numerical and experimental investigation of melting and freezing processes in phase change material storage. Int. J. Therm. Sci. 43, 277–287. https://doi.org/10.1016/j.ijthermalsci.2003.07.001

Lamrani, B., Johannes, K., Kuznik, F., 2021. Phase change materials integrated into building walls: An updated review. Renew. Sustain. Energy Rev. 140, 110751. https://doi.org/10.1016/j.rser.2021.110751

Lecompte, T., Le Bideau, P., Glouannec, P., Nortershauser, D., Le Masson, S., 2015. Mechanical and thermo-physical behaviour of concretes and mortars containing phase change material. Energy Build. 94, 52–60. https://doi.org/10.1016/j.enbuild.2015.02.044

Lee, T., Hawes, D.W., Banu, D., Feldman, D., 2000. Control aspects of latent heat storage and recovery in concrete. Sol. Energy Mater. Sol. Cells 62, 217–237. https://doi.org/10.1016/S0927-0248(99)00128-2

Lee B. J., Pessiki, S., 2006. Thermal performance evaluation of precast concrete three-wythe sandwich wall panels. Energy and Buildings, vol. 38, pp. 1006-1014, 2006

Lee B. J., Pessiki, S., 2004. Analytical investigation of thermal performance of precast concrete three-wythe sandwich wall panels," PCI Journal, vol. 49, pp. 88-101, 2004.

Li, M., Wu, Z., Tan, J., 2013. Heat storage properties of the cement mortar incorporated with composite phase change material. Appl. Energy 103, 393–399. https://doi.org/10.1016/j.apenergy.2012.09.057

Lin, K., Zhang, Y., Xu, X., Di, H., Yang, R., Qin, P., 2004. Modeling and simulation of under-floor electric heating system with shape-stabilized PCM plates. Build. Environ. 39, 1427–1434. https://doi.org/10.1016/j.buildenv.2004.04.005

Lin, Y., Alva, G., Fang, G., 2018. Review on thermal performances and applications of thermal energy storage systems with inorganic phase change materials. Energy 165, 685–708. https://doi.org/10.1016/j.energy.2018.09.128

Ling, T.-C., Poon, C.-S., 2013. Use of phase change materials for thermal energy storage in concrete: An overview. Constr. Build. Mater. 46, 55–62. https://doi.org/10.1016/j.conbuildmat.2013.04.031

Long, C. 1999. Essential Heat Transfer Essex, Pearson Education Limited.

Losch, E. (2003). Bowing of insulated precast concrete wall panels. PCI Journal, 48(6), 126-129.

Ma, Q., Bai, M., 2018. Mechanical behavior, energy-storing properties and thermal reliability of phase-changing energy-storing concrete. Constr. Build. Mater. 176, 43–49. https://doi.org/10.1016/j.conbuildmat.2018.04.226

Mandilaras, I.D., Kontogeorgos, D.A., Founti, M.A., 2015. A hybrid methodology for the determination of the effective heat capacity of PCM enhanced building components. Renew. Energy 76, 790–804. https://doi.org/10.1016/j.renene.2014.11.078

Marani, A., Madhkhan, M., 2018. An innovative apparatus for simulating daily temperature for investigating thermal performance of wallboards incorporating PCMs. Energy Build. 167, 1–7. https://doi.org/10.1016/j.enbuild.2018.02.029

Marani, A., Nehdi, M.L., 2019. Integrating phase change materials in construction materials: Critical review. Constr. Build. Mater. 217, 36–49. https://doi.org/10.1016/j.conbuildmat.2019.05.064

Marin, J.M., Zalba, B. n, Cabeza, L.F., Mehling, H., 2003. Determination of enthalpy temperature curves of phase change materials with the temperature-history method: improvement to temperature dependent properties. Meas. Sci. Technol. 14, 184–189. https://doi.org/10.1088/0957-0233/14/2/305

Mazo, J., Delgado, M., Marin, J.M., Zalba, B., 2012. Modeling a radiant floor system with Phase Change Material (PCM) integrated into a building simulation tool: Analysis of a case study of a floor heating system coupled to a heat pump. Energy Build. 47, 458–466. https://doi.org/10.1016/j.enbuild.2011.12.022

Memon, S.A., 2014. Phase change materials integrated in building walls: A state of the art review. Renew. Sustain. Energy Rev. 31, 870–906. https://doi.org/10.1016/j.rser.2013.12.042

Memon, S.A., Cui, H.Z., Zhang, H., Xing, F., 2015. Utilization of macro encapsulated phase change materials for the development of thermal energy storage and structural lightweight aggregate concrete. Appl. Energy 139, 43–55. https://doi.org/10.1016/j.apenergy.2014.11.022

Memon, S.A., Lo, T.Y., Barbhuiya, S.A., Xu, W., 2013. Development of form-stable composite phase change material by incorporation of dodecyl alcohol into ground granulated blast furnace slag. Energy Build. 62, 360–367. https://doi.org/10.1016/j.enbuild.2013.03.026

Min, H.-W., Kim, S., Kim, H.S., 2017. Investigation on thermal and mechanical characteristics of concrete mixed with shape stabilized phase change material for mix design. Constr. Build. Mater. 149, 749–762. https://doi.org/10.1016/j.conbuildmat.2017.05.176

Mirsadeghi, M., Cóstola, D., Blocken, B., Hensen, J.L.M., 2013. Review of external convective heat transfer coefficient models in building energy simulation programs: Implementation and uncertainty. Appl. Therm. Eng. 56, 134–151. https://doi.org/10.1016/j.applthermaleng.2013.03.003

Myers, R. L. 2006 The Basics of Physics, Greenwood Publishing Group Incorporated.

Nagy, B., Nehme, S. and Szagri, D., 2015. Thermal properties and modeling of fiber reinforced concretes. *Energy Procedia* 78 (2015) 2742 – 2747

Nair,A. M., Wilson, C., Huang, M. J., Griffiths, P., Hewitt, N.,2022. Phase change materials in building integrated space heating and domestic hot water applications: A review. Journal of Energy Storage, 54. 105227

Naito, C., Hoemann, J., Beacraft, M., Bewick, B., 2012. Performance and Characterization of Shear Ties for Use in Insulated Precast Concrete Sandwich Wall Panels. J. Struct. Eng. 138, 52–61. https://doi.org/10.1061/(ASCE)ST.1943-541X.0000430

Navarro, L., De Gracia, A., Castell, A., Álvarez, S., Cabeza, L.F., 2015. PCM incorporation in a concrete core slab as a thermal storage and supply system: Proof of concept. Energy Build. 103, 70–82. https://doi.org/10.1016/j.enbuild.2015.06.028

Navarro, L., De Gracia, A., Colclough, S., Browne, M., McCormack, S.J., Griffiths, P., Cabeza, L.F., 2016a. Thermal energy storage in building integrated thermal systems: A review. Part 1. active storage systems. Renew. Energy 88, 526–547. https://doi.org/10.1016/j.renene.2015.11.040

Navarro, L., De Gracia, A., Niall, D., Castell, A., Browne, M., McCormack, S.J., Griffiths, P., Cabeza, L.F., 2016b. Thermal energy storage in building integrated thermal systems: A

review. Part 2. Integration as passive system. Renew. Energy 85, 1334–1356. https://doi.org/10.1016/j.renene.2015.06.064

Niall, D. West, R., McCormack, S., 2016. Assessment of Two Methods of Enhancing Thermal Mass Performance of Concrete Through the Incorporation of Phase-Change Materials. SDAR* Journal of Sustainable Design & Applied Research: Vol. 4: Iss. 1, Article 1.DOI: 10.5072/FK2154KV1J Available at: http://arrow.dit.ie/sdar/vol4/iss1/1

Niall, D., Kinnane, O., West, R.P., McCormack, S., 2017. Mechanical and thermal evaluation of different types of PCM–concrete composite panels. J. Struct. Integr. Maint. 2, 100–108. https://doi.org/10.1080/24705314.2017.1318039

Nolan, P. J. 2012. Physics for Science and Engineering Students. 1st edition. Lakeville, Minnesota: Physics Curriculum & Instruction

Nussbaumer, T., Wakili, K. G., Tanner, C., 2006. Experimental and numerical investigation of the thermal performance of a protected vacuum-insulation system applied to a concrete wall. Applied Energy, vol. 83, pp. 841-855, 2006.

O'Hegarty, R., Kinnane, O., 2020. Review of precast concrete sandwich panels and their innovations. Constr. Build. Mater. 233, 117145. https://doi.org/10.1016/j.conbuildmat.2019.117145

O'Hegarty, R., Kinnane, O., Grimes, M., Newell, J., Clifford, M., West, R., 2021. Development of thin precast concrete sandwich panels: Challenges and outcomes. Constr. Build. Mater. 267, 120981. https://doi.org/10.1016/j.conbuildmat.2020.120981

O'Hegarty, R., West, R., Reilly, A., Kinnane, O., 2019. Composite behaviour of fibre-reinforced concrete sandwich panels with FRP shear connectors. Eng. Struct. 198, 109475. https://doi.org/10.1016/j.engstruct.2019.109475

Ohlsson, K.E.A., Östin, R., Grundberg, S., Olofsson, T., 2016. Dynamic model for measurement of convective heat transfer coefficient at external building surfaces. J. Build. Eng. 7, 239–245. https://doi.org/10.1016/j.jobe.2016.06.005

Osterman, E., Butala, V., Stritih, U., 2015. PCM thermal storage system for 'free' heating and cooling of buildings. Energy Build. 106, 125–133. https://doi.org/10.1016/j.enbuild.2015.04.012

Pasupathy, A., Velraj, R., 2006. Effect of double layer phase change material in building roof for year round thermal management. Energy and Buildings 40, 193-203.

Pasupathy, A., Velraj, R., Seeniraj, R.V., 2008. Phase change material-based building architecture for thermal management in residential and commercial establishments. Renew. Sustain. Energy Rev. 12, 39–64. https://doi.org/10.1016/j.rser.2006.05.010

Patil, S. R., Lodha, R. and Keste, A A. 2018 Concrete Solar Collector – an Experimental Investigation in Solar Passive Energy Materials Today Proceedings Volume 23, Part 2, (2020) p.366-372

Pessik, S., Mlynarczyk, A., 2003. Experimental Evaluation of the Composite Behavior of Precast Concrete Sandwich Wall Panels. PCI J. 48, 54–71. https://doi.org/10.15554/pcij.03012003.54.71

Pilehvar, S., Cao, V.D., Szczotok, A.M., Valentini, L., Salvioni, D., Magistri, M., Pamies, R., Kjøniksen, A.-L., 2017. Mechanical properties and microscale changes of geopolymer concrete and Portland cement concrete containing micro-encapsulated phase change materials. Cem. Concr. Res. 100, 341–349. https://doi.org/10.1016/j.cemconres.2017.07.012

Pomianowski, M., Heiselberg, P., Jensen, R.L., 2013. Full-scale investigation of the dynamic heat storage of concrete decks with PCM and enhanced heat transfer surface area. Energy Build. 59, 287–300. https://doi.org/10.1016/j.enbuild.2012.12.013

Pomianowski, M., Heiselberg, P., Jensen, R.L., 2012. Dynamic heat storage and cooling capacity of a concrete deck with PCM and thermally activated building system. Energy Build. 53, 96–107. https://doi.org/10.1016/j.enbuild.2012.07.007

Pomianowski, M., Heiselberg, P., Jensen, R.L., Cheng, R., Zhang, Y., 2014. A new experimental method to determine specific heat capacity of inhomogeneous concrete material with incorporated microencapsulated-PCM. Cem. Concr. Res. 55, 22–34. https://doi.org/10.1016/j.cemconres.2013.09.012

Que, L., Zhang, X., Ji, J., Gao, L., Xie, W., Liu, L., Ding, X., 2021. Numerical simulation and experimental research progress of phase change hysteresis: A review. Energy Build. 253, 111402. https://doi.org/10.1016/j.enbuild.2021.111402

Raj, V.A.A., Velraj, R., 2010. Review on free cooling of buildings using phase change materials. Renew. Sustain. Energy Rev. 14, 2819–2829. https://doi.org/10.1016/j.rser.2010.07.004

Regin, a. F., Solanki, S.C., Saini, J.S., 2008. Heat transfer characteristics of thermal energy storage system using PCM capsules: A review. Renew. Sustain. Energy Rev. 12, 2438–2458. https://doi.org/10.1016/j.rser.2007.06.009

Royon, L., Karim, L., Bontemps, A., 2014. Optimization of PCM embedded in a floor panel developed for thermal management of the lightweight envelope of buildings. Energy Build. 82, 385–390. https://doi.org/10.1016/j.enbuild.2014.07.012

Salmon, D. C., A. Einea, M. K. Tadros, and T. D. Culp. 1997. Full Scale Testing of Precast Concrete Sandwich Panels. ACI Structural Journal, V. 94, No. 4 (July–August): pp. 354–362

Sani, A.K., Olawoore, I.O., Singh, R.M., 2021. Assessment of impregnating phase change materials into lightweight aggregates for development of thermal energy storage aggregate composites. Constr. Build. Mater. 305, 124683. https://doi.org/10.1016/j.conbuildmat.2021.124683

Sarath, K.P., Feroz Osman, M., Mukhesh, R., Manu, K.V., Deepu, M., 2023. A review of the recent advances in the heat transfer physics in latent heat storage systems. Therm. Sci. Eng. Prog. 42, 101886. https://doi.org/10.1016/j.tsep.2023.101886

Sennour, L., Lucier, G.W., Rizkalla, S. H., 2013. Structurally Composite, Thermally Efficient Precast Concrete, Concrete Plant International. 2013

Shams, A., Horstmann, M., Hegger, J., 2014. Experimental investigations on Textile-Reinforced Concrete (TRC) sandwich sections. Compos. Struct. 118, 643–653. https://doi.org/10.1016/j.compstruct.2014.07.056

Sharifi, N.P., Sakulich, A., 2015. Application of phase change materials to improve the thermal performance of cementitious material. Energy Build. 103, 83–95. https://doi.org/10.1016/j.enbuild.2015.06.040

Sharma, A., Tyagi, V.V., Chen, C.R., Buddhi, D., 2009. Review on thermal energy storage with phase change materials and applications. Renew. Sustain. Energy Rev. 13, 318–345. https://doi.org/10.1016/j.rser.2007.10.005

Sharshir, S.W., Joseph, A., Elsharkawy, M., Hamada, M.A., Kandeal, A.W., Elkadeem, M.R., Kumar Thakur, A., Ma, Y., Eid Moustapha, M., Rashad, M., Arıcı, M., 2023. Thermal energy storage using phase change materials in building applications: A review of the recent development. Energy Build. 285, 112908. https://doi.org/10.1016/j.enbuild.2023.112908

Shi, X., Memon, S.A., Tang, W., Cui, H., Xing, F., 2014. Experimental assessment of position of macro encapsulated phase change material in concrete walls on indoor temperatures and humidity levels. Energy Build. 71, 80–87. https://doi.org/10.1016/j.enbuild.2013.12.001

Shukla, R., 2019. Unconnected insulated concrete sandwich panels. MSc Dissertation, Trinity College Dublin and Birla Institute of Technology and Science, Pilani, pp.108

Singh, R. P., Vanapalli, k. R., Cheela, V. R. S., Peddireddy, S. R., Sharma, H. B., Mohanty, B., 2023. Fly Ash, GGBS, and Silica Fume Based Geopolymer Concrete with Recycled Aggregates: Properties and Environmental Impacts. Construction and Building Materials 378 (May 2023): 131168. https://doi.org/10.1016/j.conbuildmat.2023.131168.

Snoeck, D., Priem, B., Dubruel, P., De Belie, N., 2016. Encapsulated Phase-Change Materials as additives in cementitious materials to promote thermal comfort in concrete constructions. Mater. Struct. 49, 225–239. https://doi.org/10.1617/s11527-014-0490-5

Soares, N., Costa, J.J., Gaspar, a. R., Santos, P., 2013. Review of passive PCM latent heat thermal energy storage systems towards buildings' energy efficiency. Energy Build. 59, 82–103. https://doi.org/10.1016/j.enbuild.2012.12.042

Soares, N., Matias, T., Durães, L., Simões, P.N., Costa, J.J., 2023. Thermophysical characterization of paraffin-based PCMs for low temperature thermal energy storage applications for buildings. Energy 269, 126745. https://doi.org/10.1016/j.energy.2023.126745

Solanski, C. S. 2008 Renewable Energy Technologies: Practical Guide for Beginners, Prentice Hall Of India Pvt. Limited

Solomon, G.R., Karthikeyan, S., Velraj, R., 2013. Sub cooling of PCM due to various effects during solidification in a vertical concentric tube thermal storage unit. Appl. Therm. Eng. 52, 505–511. https://doi.org/10.1016/j.applthermaleng.2012.12.030

Song, G., Ma, S., Tang, G., Yin, Z., Wang, X., 2010. Preparation and characterization of flame retardant form-stable phase change materials composed by EPDM, paraffin and nano magnesium hydroxide. Energy 35, 2179–2183. https://doi.org/10.1016/j.energy.2010.02.002

Sopal, G. 2013. Use of CFRP Grid As Shear Transfer Mechanism For Precast Concrete Sandwich Wall Panels, Ph.D., Civil Engineering, North Carolina State University

Souayfane, F., Fardoun, F., Biwole, P.-H., 2016. Phase change materials (PCM) for cooling applications in buildings: A review. Energy Build. 129, 396–431. https://doi.org/10.1016/j.enbuild.2016.04.006

Stritih, U., Tyagi, V.V., Stropnik, R., Paksoy, H., Haghighat, F., Joybari, M.M., 2018. Integration of passive PCM technologies for net-zero energy buildings. Sustain. Cities Soc. 41, 286–295. https://doi.org/10.1016/j.scs.2018.04.036

Sweeney, A. 2014. PhD Thesis. Trinity College Dublin

Tang, W., Wang, Z., Mohseni, E., Wang, S., 2018. A practical ranking system for evaluation of industry viable phase change materials for use in concrete. Constr. Build. Mater. 177, 272–286. https://doi.org/10.1016/j.conbuildmat.2018.05.112

Teychenne, D. C., Franklin, R. and Erntroy, H., 1997. Design of normal concrete mixes. *BRE press*

The Concrete Centre, 2012. Thermal Mass Explained

Tyagi, V.V., Buddhi, D., 2007. PCM thermal storage in buildings: A state of art. Renew. Sustain. Energy Rev. 11, 1146–1166. https://doi.org/10.1016/j.rser.2005.10.002

Tyagi, V.V., Kaushik, S.C., Tyagi, S.K., Akiyama, T., 2011. Development of phase change materials based microencapsulated technology for buildings: A review. Renew. Sustain. Energy Rev. 15, 1373–1391. https://doi.org/10.1016/j.rser.2010.10.006

Voller, V.R., 1997. An overview of numerical methods for solving phase change problems. *In: Minkowycz WJ, Sparrow EM, editors. Advances in numerical heat transfer. Taylor & Francis*, 341–80

Voller, V., Cross, M., 1981. Accurate solutions of moving boundary problems using the enthalpy method. International Journal of Heat Mass Transfer 24(3), 545–56

Wadso, L., Karlsson, J. and Tammo, K., 2012. Thermal properties of concrete with various aggregates. Cement and Concrete Research 48.

Wang, R., Ren, M., Gao, X., Qin, L., 2018. Preparation and properties of fatty acids based thermal energy storage aggregate concrete. Constr. Build. Mater. 165, 1–10. https://doi.org/10.1016/j.conbuildmat.2018.01.034

Waqas, A., Ud Din, Z., 2013. Phase change material (PCM) storage for free cooling of buildings—A review. Renew. Sustain. Energy Rev. 18, 607–625. https://doi.org/10.1016/j.rser.2012.10.034

Wei, Z., Falzone, G., Wang, B., Thiele, A., Puerta-Falla, G., Pilon, L., Neithalath, N., Sant, G., 2017. The durability of cementitious composites containing microencapsulated phase change materials. Cem. Concr. Compos. 81, 66–76. https://doi.org/10.1016/j.cemconcomp.2017.04.010

World Business Council for Sustainable Development, 2009. Energy Efficiency in Buildings – Transforming the market

Xiao, W., Wang, X., Zhang, Y., 2009. Analytical optimization of interior PCM for energy storage in a lightweight passive solar room. Appl. Energy 86, 2013–2018. https://doi.org/10.1016/j.apenergy.2008.12.011

Xie, J., Chen, W., Wang, J., Fang, C., Zhang, B., Liu, F., 2019. Coupling Effects of Recycled Aggregate and GGBS/Metakaolin on Physicochemical Properties of Geopolymer Concrete. Construction and Building Materials 226 (November 2019): 345–59. https://doi.org/10.1016/j.conbuildmat.2019.07.311.

Yinping, Z., Yi, J., Yi, J., 1999. A simple method, the -history method, of determining the heat of fusion, specific heat and thermal conductivity of phase-change materials. Meas. Sci. Technol. 10, 201–205. https://doi.org/10.1088/0957-0233/10/3/015

Young, B.A., Falzone, G., Wei, Z., Sant, G., Pilon, L., 2018. Reduced-scale experiments to evaluate performance of composite building envelopes containing phase change materials. Constr. Build. Mater. 162, 584–595. https://doi.org/10.1016/j.conbuildmat.2017.11.160

Yuan, Y., Zhang, N., Tao, W., Cao, X., He, Y., 2014. Fatty acids as phase change materials: A review. Renew. Sustain. Energy Rev. 29, 482–498. https://doi.org/10.1016/j.rser.2013.08.107

Zeinelabdein, R., Omer, S., Gan, G., 2018. Critical review of latent heat storage systems for free cooling in buildings. Renew. Sustain. Energy Rev. 82, 2843–2868. https://doi.org/10.1016/j.rser.2017.10.046

Zeng, C., Liu, S., Shukla, A., 2017. Adaptability research on phase change materials based technologies in China. Renew. Sustain. Energy Rev. 73, 145–158. https://doi.org/10.1016/j.rser.2017.01.117

Zhang, D., Li, Z., Zhou, J., Wu, K., 2004. Development of thermal energy storage concrete. Cem. Concr. Res. 34, 927–934. https://doi.org/10.1016/j.cemconres.2003.10.022

Zhang, D., Zhou, J., Wu, K., Li, Z., 2005. Granular phase changing composites for thermal energy storage. Sol. Energy 78, 471–480. https://doi.org/10.1016/j.solener.2004.04.022

Zhang, D., Fung, A.S., Siddiqui, O., 2007. Numerical studies of integrated concrete with a solid–solid phase change material. *In: Proceedings of the 2nd canadian solar buildings conference,* Calgary, Canada, June 10–14, 2007

**Appendix A Data sheets for sealant products**

1. Sikagard 700 S:
https://irl.sika.com/content/dam/dms/ie01/c/sikagard-700-s.pdf

2. SikaBond SBR:
https://irl.sika.com/content/dam/dms/ie01/s/sikabond_sbr_.pdf

3.Conplast WP402:

https://www.preconproducts.co.uk/templates/downloads/Fosroc/Fosroc%20Data%20Sheet%20Catalogue/Technical%20Data%20Sheets/Admixtures/Conplast%20WP402%200215.pdf

4. Auramix V200:

https://www.fosroc.com/english/product/show/fosroc-auramix-v200

**Appendix B Specification for heat flux pad, Hukseflux HFP01**

https://www.hukseflux.com/uploads/product-documents/HFP01SC_v1808.pdf

## Appendix C DSC results

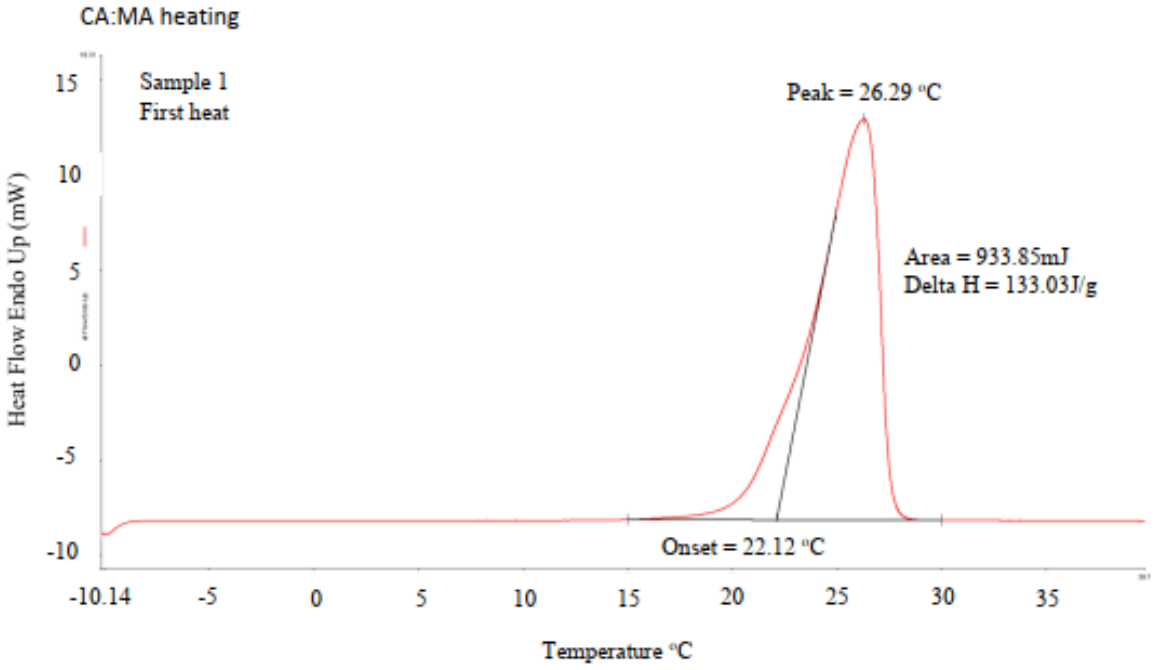


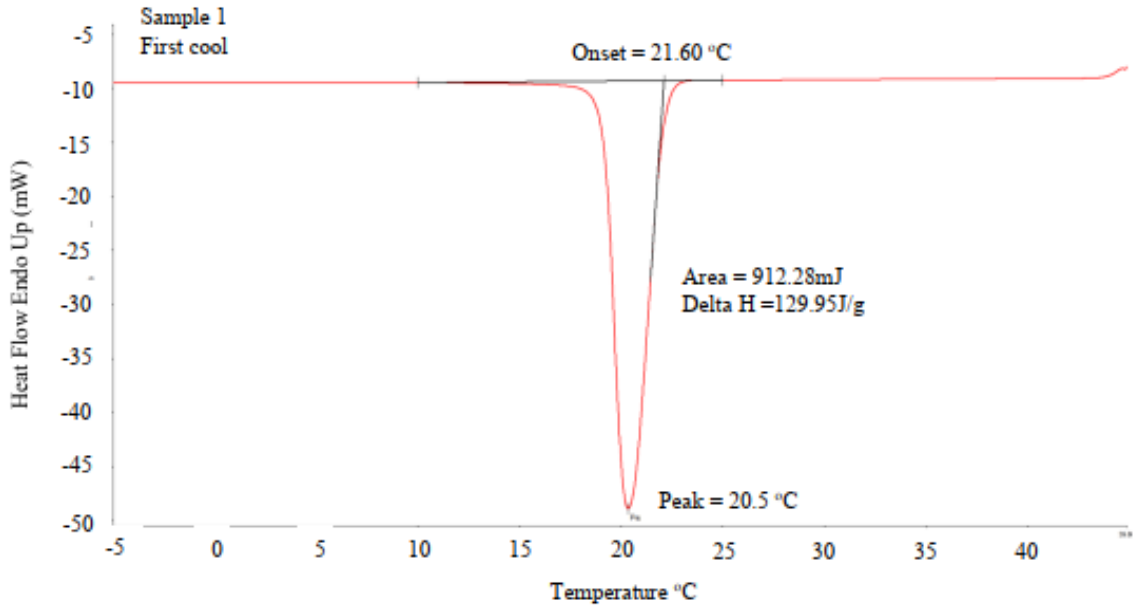

**MICRONAL**

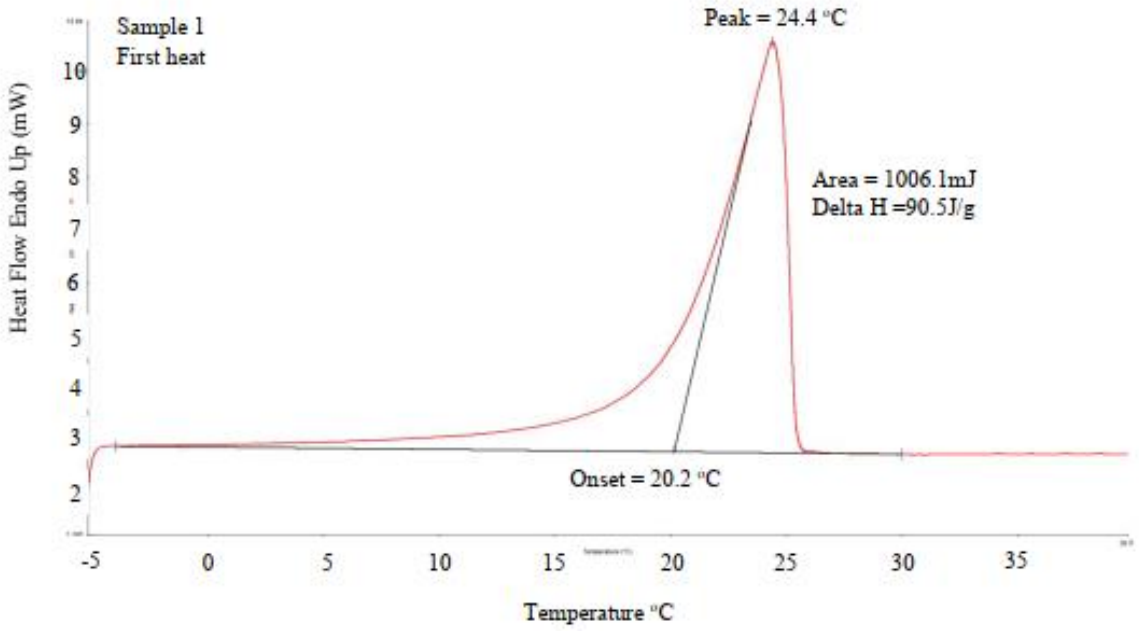
Sample 1
First heat
Peak = 24.4 °C
Area = 1006.1mJ
Delta H =90.5J/g
Onset = 20.2 °C
Heat Flow Endo Up (mW)
Temperature °C

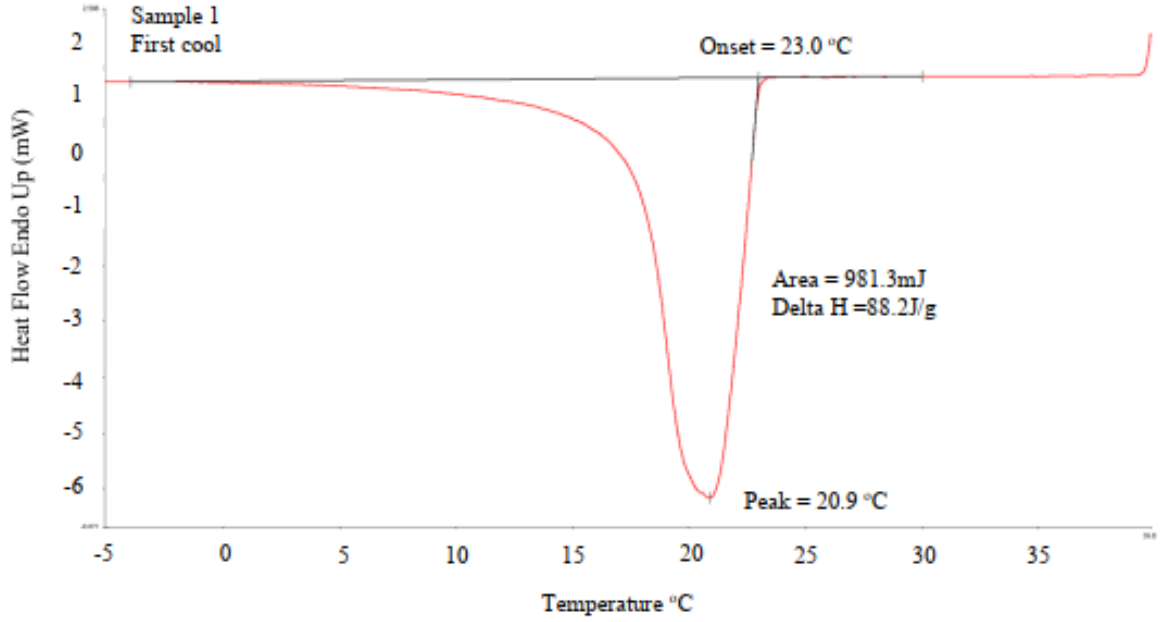
Sample 1
First cool
Onset = 23.0 °C
Area = 981.3mJ
Delta H =88.2J/g
Peak = 20.9 °C
Heat Flow Endo Up (mW)
Temperature °C

**Appendix D Mix Design for 'Techrete's self-compacting concrete (Teychenne et al, 1997)**

1. Characteristic strength 30MPa @ 3 days. Note: Early strength is the main design criteria to facilitate lifting of concrete panels after 18-24 hours.

   5% defectives hence k=1.64

   Previous data available for 20 or more results (Techrete laboratory) hence standard deviation, s = 4

   Margin = ks = 1.64 x 4 = 6.56

   **Target mean strength @ 3 days = 30 +6.56 = 36.6MPa**

**2.** Cement strength class 42.5 & Crushed Aggregate (20mm).
Compressive strength with a water/cement ratio 0.5, @ 3 days = 27MPa

From chart: **W/C ratio required = 0.43**

**3.** Slump 60 – 180, Max 20mm crushed aggregate; Fine aggregate uncrushed;
hence water content = (2/3)195 + (1/3)225 = **205kg.**

With the use of superplasticiser the water content can be reduced by 25% in accordance with advice from Techrete's technical department:

Hence water content = 205 x 0.75 = 153.75 = **155kg**

**Cement content = 155/0.43 = 360kg.**

**4.** Wet Density assuming crushed aggregates (relative density 2.65) & water content 155kg = 2450kg/$m^3$

Aggregate content = 2450 – 155 – 360 = 1935kg

5. % fines passing 600μm sieve = 52% (Techrete Technical Department) hence proportion of fine aggregate 47%

   **Fine aggregate = 0.47 x 1935 = 910kg** (including 120kg Limestone filler as per Techrete's practice)

   **Coarse Aggregate = 1935 – 910 = 1935kg**

| Quantities | Rapid Hardening Cem I Cement (kg)*** | Water (kg) | Fine aggregate (kg) | Coarse 6-14mm (kg) | Limestone Filler (kg) | SP Premier 196 Plasterciser (l) |
|---|---|---|---|---|---|---|
| 1 $m^3$ | 360 | 155 | 790 | 1025 | 120 | 2.9 |
| 0.015$m^3$ | 5.4 | 2.325 | 11.85 | 15.4 | 1.8 | 0.0435* |

* Super plasterciser dosage 0.8% by weight of cement
** Water cement ratio 0.43
*** In accordance with I.S. EN 197-1:2011

**Appendix E Data sheet for Thermomass connector**

http://www.thermomass.com/website/wp-content/uploads/2017/04/thermomass_mcms_series_datasheet.pdf

**Appendix F Calculations for the thermal conductivity, R-values and U-values for panels**

**Control Panel and no connectors**

(i) At centre of panel:

$\dot{Q}$ = 18.0 W/m$^2$

ΔT = 27.7K

d = 0.2m

Hence:

- Overall thermal conductivity, k = $\dot{Q}.\frac{\mathrm{d}}{(\mathrm{T_h}-\mathrm{T_c})}$ = $\frac{18\ x\ 0.2}{27.7}$ = 0.130 (W/mK)
- R–value $= \frac{T_1 - T_2}{Q}$ = $\frac{27.7}{18}$ = 1.54 (m$^2$K/W)
- U–value = $\frac{1}{R} = \frac{1}{1.54}$ = 0.65(W/m$^2$K)

**Panel with PCM and no connectors**

(i) At centre of panel:

$\dot{Q}$ = 16.36 W/m$^2$

ΔT = 28.7K

d = 0.2m

Hence:

- Overall thermal conductivity, k = $\dot{Q}.\frac{\mathrm{d}}{(\mathrm{T_h}-\mathrm{T_c})}$ = $\frac{16.36\ x\ 0.2}{28.7}$ = 0.114 (W/mK)
- R–value $= \frac{T_1 - T_2}{Q}$ = $\frac{28.7}{16.36}$ = 1.75 (m$^2$K/W)
- U–value = $\frac{1}{R} = \frac{1}{1.75}$ = 0.57 (W/m$^2$K)

**Panel with PCM and C- connectors**

(i) At centre of panel:

$\dot{Q}$ = 15.06 W/m$^2$

ΔT = 27.8K

d = 0.2m

Hence:

- Overall thermal conductivity, k = $\dot{Q}.\frac{\mathrm{d}}{(\mathrm{T_h}-\mathrm{T_c})}$ = $\frac{15.06\ x\ 0.2}{27.8}$ = 0.108 (W/mK)
- R–value $= \frac{T_1 - T_2}{Q}$ = $\frac{27.8}{15.06}$ = 1.85 ($m^2$K/W)
- U–value = $\frac{1}{R} = \frac{1}{1.85}$ = 0.54 (W/$m^2$K)

(ii) At C-connector location:

$\dot{Q}$ = 30.76 W/$m^2$

ΔT = 26.2K

d = 0.2m

Hence:

- Overall thermal conductivity, k = $\dot{Q}.\frac{\mathrm{d}}{(\mathrm{T_h}-\mathrm{T_c})}$ = $\frac{30{,}76\ x\ 0.2}{26.2}$ = 0.235 (W/mK)
- R–value $= \frac{T_1 - T_2}{Q}$ = $\frac{26.2}{30.76}$ = 0.852 ($m^2$K/W)
- U–value = $\frac{1}{R} = \frac{1}{0.852}$ = 1.17 (W/$m^2$K)

**Panel with PCM and Thermomass connectors**

(i) At centre of panel:

$\dot{Q}$ = 13.5 W/$m^2$

ΔT = 28.0K

d = 0.2m

Hence:

- Overall thermal conductivity, k = $\dot{Q}.\frac{\mathrm{d}}{(\mathrm{T_h}-\mathrm{T_c})}$ = $\frac{13.5\ x\ 0.2}{28}$ = 0.096 (W/mK)
- R–value $= \frac{T_1 - T_2}{Q}$ = $\frac{28}{13.5}$ = 2.07 ($m^2$K/W)

- U–value = $\frac{1}{R} = \frac{1}{2.07}$ = 0.483 (W/m$^2$K)

(ii) At Thermomas connector location:

$\dot{Q}$ = 25.9 W/m$^2$

ΔT = 26.4K

d = 0.2m

Hence:

- Overall thermal conductivity, k = $\dot{Q}.\frac{d}{(T_h - T_c)} = \frac{25.9\ x\ 0.2}{26.4}$ = 0.196 (W/mK)
- R–value $= \frac{T_1 - T_2}{Q} = \frac{26.4}{25.9}$ = 1.02 (m$^2$K/W)
- U–value = $\frac{1}{R} = \frac{1}{2.07}$ = 0.98 (W/m$^2$K)

A summary of the overall thermal conductivity values, the R-values and the U-values of the panels is provided in Table 5-3. It should be noted that the R-values do not include surface resistivity.

**Table F-1 Summary of thermal parameters of cladding panels**

| | Control Panel | Panel with PCM and no Ties | Panel with PCM and C-Connectors | Panel with PCM and Thermomass |
|---|---|---|---|---|
| Overall thermal conductivity @ centre | 0.130 | 0.114 | 0.108 | 0.096 |
| Overall thermal conductivity @ tie location | N/A | N/A | 0.235 | 0.196 |
| R-value @ centre | 1.54 | 1.75 | 1.85 | 2.07 |
| R-value @ tie location | N/A | N/A | 0.852 | 1.02 |
| U-value @ centre | 0.65 | 0.57 | 0.54 | 0.483 |
| U-value @ tie location | N/A | N/A | 1.17 | 0.98 |

**Appendix G Calculations to determine applied wind load**

**Reference: I.S. EN 1991-1-4 Irish National Annex to Eurocode 1: Actions on Structures Part 1-4 – Wind Actions**

Assume top storey of a six storey building in Dublin City. So:

- Height of building = 3.5m x 6 = 21m

1. **Basic wind velocity**, $v_b = v_{b,map} \cdot c_{alt} \cdot c_{dir}$ *(Clause 4.1)*

Where:

- $v_{b,map}$ = basic wind speed for Dublin = 25m/s
- $c_{alt}$ = altitude factor = 1+0.001A where A = altitude of site above mean sea level (m)
- $c_{dir}$ = directional factor , conservatively taken as 1 *(A.NA.2(c))*

Typical street level around the dockland area of Dublin is 3 – 3.5mOD so A is assumed to be 3.5m

$$c_{alt} = 1 + 0.001(3.5) = 1.0035$$

Hence:

$$\text{Basic wind velocity, } v_b = 25 \times 1.0035 = \mathbf{25.09m/s}$$

2. **Pressure due to wind**, $q_b = 0.613\ v_b^2$

$$q_b = 0.613\ (25.09)^2 = 386\ N/m^2 = \mathbf{0.39kN/m^2}$$

3. Site is assumed to be in town so orography is assumed to be insignificant

4. **Peak velocity pressure** $q_p = c_{e\,(z)} \cdot c_{e,T} \cdot q_b$ (*NA.2.17* )

Where:

- $c_e(z)$ is 2.9 taken from Figure NA 7, taking z = 21m & $h_{dis}$ = 3m. Assuming distance upwind to shoreline = 5km
- $c_{e,T}$ is 0.88 taken from Figure NA 8, taking z = 21m & $h_{dis}$ = 3m Assuming distance upwind to shoreline = 5km

$$q_p = 2.9 \cdot 0.88 \cdot 0.39 = 0.995 \text{ say } \mathbf{1kN/m^2}$$

**Appendix H Second moment of area and flexural stiffness calculations**

**Stiffness calculations for panels:**

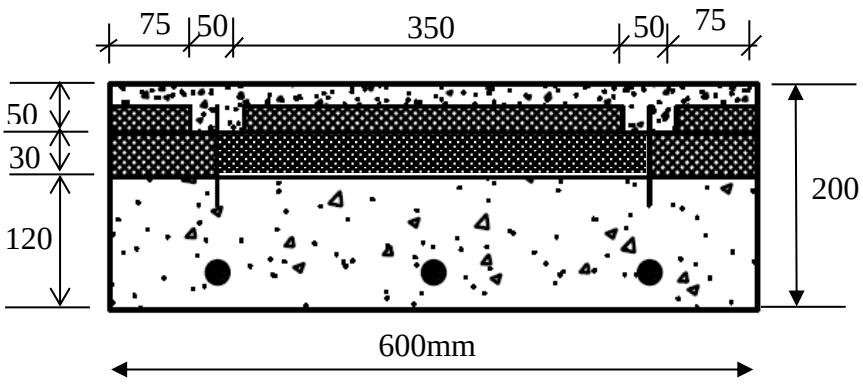


**1. Stiffness of HPFRC outer wythe:**

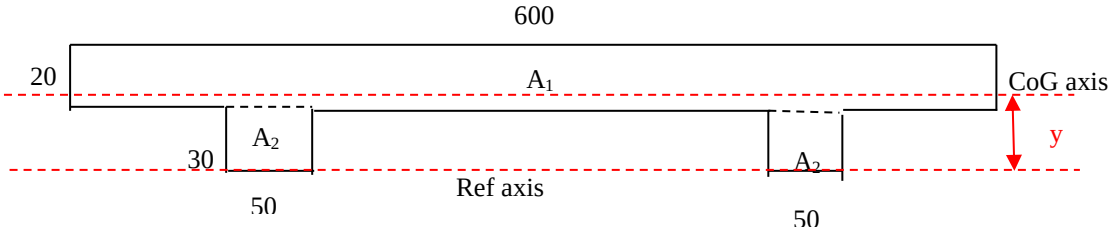


(i) Find position of centre of gravity of section, 'y'. Take moments of area around reference axis.

$A_1$ = 20 x 600mm = 12000mm$^2$

$A_2$ = 30 x 50 = 1500mm$^2$

$A_{total}$ = 12000 + 2(1500) = 15000mm$^2$

$A_{total}.y$ = (12000 x 40) +2(1500 x 15)

15000 . y = 480000 + 45000

y = 525000/15000 = 35mm

(ii) To find second moment of area of outer wythe, $I_{outer}$:

Take moments of area around CoG axis:

$I_{outer} = [I_1 + A_1.h_1^2] + 2[I_2 + A_2.h_2^2]$ where $I_1$ & $I_2 = (bd^3/12)$ of each rectangular area

$I_{outer} = (600)20^3/12 + 12000(40-35)^2 + 2[50(30)^3/12 + 1500(35-15)^2]$

**$I_{outer}$** = 400000 + 300000 + 2[712500] = **<u>212.5 x 10$^4$ mm$^4$</u>**

**2. Stiffness of Control inner wythe:**

$I_{inner} = bd^3/12 = 600(120)^3/12 =$ **$\underline{8640 \times 10^4\ mm^4}$**

Second moment of area for Non-composite panel, $I_{nc} = I_{inner} + I_{outer}$

$$I_{nc} = 86400000 + 2125000$$

$$\mathbf{I_{nc} = 8852.5 \times 10^4\ mm^4}$$

**3. Flexural stiffness of non-composite panels:**

As the outer and inner wythes of each of the panels are formed with different types of concrete, each wythe has a different Young's modulus, E. The Young's moduli of each type of concrete was determined in laboratory tests and the results are given in table below.

| Type of concrete | Young's modulus E (GPa) |
|---|---|
| HPFRC | 43.1 |
| Control Concrete | 35.2 |
| PCM-Concrete | 31.4 |

**Flexural stiffness of non-composite Control panel:**

$$E_{panel}\ I_{nc} = E_{HPFRC} I_{outer} + E_{conc}\ I_{inner}$$

$$E_{panel}\ I_{nc} = 43.1(2125000) + 35.2(86400000)$$

$$E_{panel}\ I_{nc} = 3132867500 kNmm^2$$

$$E_{panel}\ I_{nc} = 3132.8 kNm^2$$

**Flexural stiffness of non-composite PCM-Concrete panel:**

$$E_{panel}\ I_{nc} = E_{HPFRC} I_{outer} + E_{pcm,conc}\ I_{inner}$$

$$E_{panel}\ I_{nc} = 43.1(2125000) + 31.4(86400000)$$

$$E_{panel}\ I_{nc} = 2804547500 kNmm^2$$

$$E_{panel}\ I_{nc} = 2804.5 kNm^2$$

**4. Second moment of area of composite section:**

Stiffness of HPFRC outer wythe:

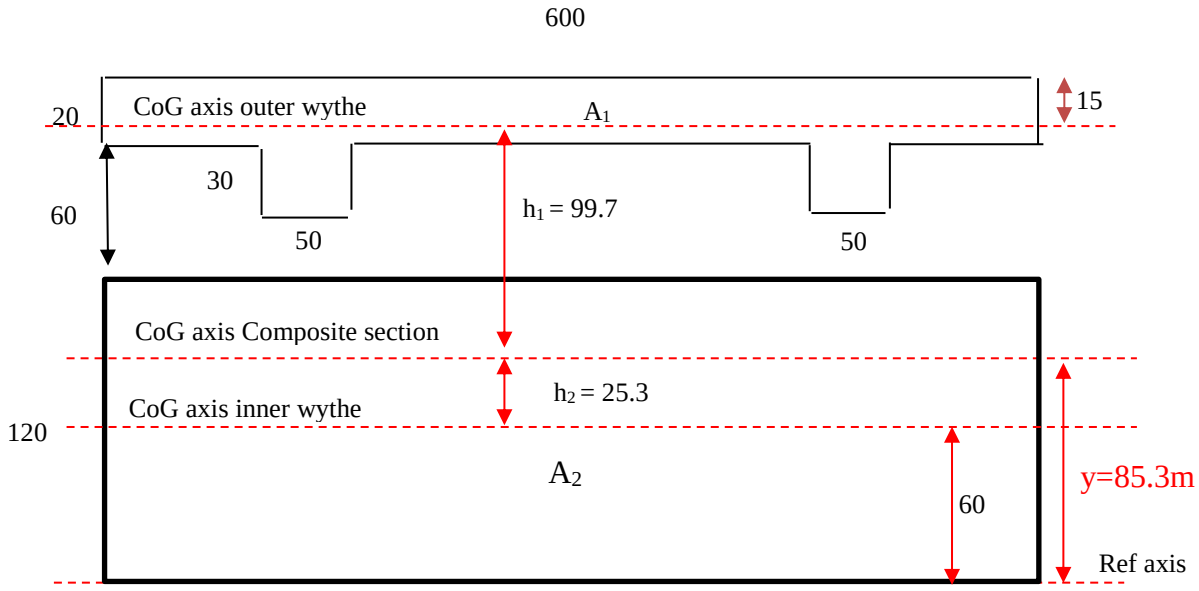


**<u>Control panels:</u>**

**(i) Find position of centre of gravity of composite section, 'y'. Take moments of area around reference axis:**

As the outer wythe is made with HPFRC it has a higher Young's modulus than the inner wythe. The young's modulus for the HPFRG, $E_{HPFRC}$ was determined in the laboratory as 43.1GPa. The young's modulus for the control concrete, $E_{conc}$ was determined in the laboratory as 35.2GPa. The HPFRC will be used as the 'base material' and the inner wythe is concerted to a transformed section by multiplying the width by the modular ratio $E_{conc}/ E_{HPFRC}$

Modular ratio = 35.2/43.1 = 0.82

Width of inner wythe = 600 x 0.82 =492mm

$A_1 = 15000mm^2$

$A_2 = 120 \times 492 = 59040mm^2$

$A_{total} = 15000 + 59040 = 74040mm^2$

$A_{total}.y = (15000 \times (200-15)) + (59040 \times 60)$

$74040.\ y = 2775000 + 3542400$

$y = 6317400/74040 =$ **85.3mm**

**(ii) Determine second moment of area of composite section for control panel $I_{cc}$:**

Use the parallel axis theorem: $I_{cc} = [I_1 + A_1.h_1^2] + [I_2 + A_2.h_2^2]$

where

$I_1 = 2125000mm^4$

$I_2 = (bd^3/12)$ of transformed inner wythe, ie 'b'=492mm = $492(120)^3/12 = 70848000mm^4$

$I_{cc} = [2125000 + 15000.(99.7)^2] + [70848000 + 59040.(23.5)^2]$

$I_c = 151226350 + 103452840 =$ **$\underline{25467.92 \times 10^4\ mm^4}$**

**Flexural stiffness of fully composite Control panel:**

$$E_{panel}\ I_c = E_{HPFRC}[I_1 + A_1.h_1^2] + E_{conc}[I_2 + A_2.h_2^2]$$

$$E_{panel}\ I_c = 43.1(151226350) + 35.2(103452840)$$

$$E_{panel}\ I_c = 10159395650kNmm^2$$

$$E_{panel}\ I_c = 10159.4kNm^2$$

**PCM panels**

**(iii) Find position of centre of gravity of composite section, 'y'. Take moments of area around reference axis:**

As before the young's modulus for the HPFRG, $E_{HPFRC}$ 43.1GPa. The young's modulus for the pcm-concrete composite, $E_{pcm,conc}$ was determined in the laboratory as 31.4GPa. The HPFRC will be used as the 'base material' and the inner wythe is concerted to a transformed section by multiplying the width by the modular ratio $E_{pcm,conc}/ E_{HPFRC}$

Modular ratio = 31.4/43.1 = 0.72

Width of inner wythe = 600 x 0.72 =435mm

$A_1 = 15000mm^2$

$A_2 = 120 \times 435 = 52200mm^2$

$A_{total} = 15000 + 52200 = 67200mm^2$

$A_{total}.y = (15000 \times (200-15)) + (52200 \times 60)$

$67200 . y = 2775000 + 3132000$

y = 5907000/67200 = **88mm**

**To find second moment of area of composite section for PCM panels $I_{c,pcm}$:**

Use the parallel axis theorem: $I_{cc} = [I_1 + A_1.h_1^2] + [I_2 + A_2.h_2^2]$

where

$h_1 = 88 – 60 = 28mm$

$h_2 = 200\text{-}88\ \text{-}15 = 97mm$

$I_1 = 2125000mm^4$

$I_2 = (bd^3/12)$ of transformed inner wythe, ie 'b'=435mm $= 435(120)^3/12 = 62640000mm^4$

$I_{c,pcm} = [2125000 + 15000(97)^2] + [62640000 + 52200(28)^2]$

$I_{c,pcm} = 143260000 + 103564800 =$ **$\underline{24682.5 \times 10^4\ mm^4}$**

**Flexural stiffness of fully composite PCM-concrete panel:**

$$E_{panel}\ I_{c,pcm} = E_{HPFRC}[I_1 + A_1.h_1^2] + E_{pcm,conc}[I_2 + A_2.h_2^2]$$

$$E_{panel}\ I_{c,pcm} = 43.1(143260000) + 31.4(103564800)$$

$$E_{panel}\ I_{c,pcm} = 9426440720kNmm^2$$

$$E_{panel}\ I_{c,pcm} = 9426.4kNm^2$$

| Type of panel | $I_{outer,\ wythe}$ ($mm^4$) x $10^4$ | $I_{inner,wythe}$ ($mm^4$) x $10^4$ | Non-composite $I_{nc}$ ($mm^4$) x $10^4$ | [1]Flexural stiffness non-composite panel $E_{panel}\ I_{nc}$ ($kNm^2$) | [2]Fully composite $I_c$ ($mm^4$) x $10^4$ | [1]Flexural stiffness fully composite panel $E_{panel}\ I_c$ ($kNm^2$) |
|---|---|---|---|---|---|---|
| Control concrete | 212.5 | 8640 | 8852.5 | 3132.8 | 25467.9 | 10159.4 |
| PCM-concrete | 212.5 | 8640 | 8852.5 | 2804.5 | 24682.5 | 9426.4 |

[1]Flexural stiffness takes into account the different E values for the inner & outer wythes

[2] $I_c$ determined taking into account the different E values for the inner & outer wythes

**Appendix I Data sheet for Kooltherm insulation**

https://www.kingspan.com/ie/en/products/insulation-boards/wall-insulation-boards/kooltherm-k15-rainscreen-board/?s=t

**Appendix J Data sheets and calibration certificates for monitoring equipment in the huts**

1. EKO Heat Flow Sensors calibration cert

EKO INSTRUMENTS CO., LTD.

To whom it may concern;

## Calibration Certificate

| | | | |
|---|---|---|---|
| Manufacturer : | EKO Instruments Co., Ltd. | Calibration date : | February 19, 2016 |
| Model : | MF-180 | Serial number : | A1846 |
| Description : | Heat Flow Sensor | EKO Ref. number : | EX16-036 |
| Cable : | 10m | | |

We hereby certify that calibration results of above instrument are as follows;

| | | |
|---|---|---|
| Sensitivity | 0.02706 | [mV / W·m$^{-2}$] |
| Internal Resistance | 498 | [Ω] |

I. Sunaga / Manager of Mfg. Dept.

T. Konuma / Inspector

WITH HIOKI DATALOGGER HZ

Page 1 of 1

EKO INSTRUMENTS CO., LTD.

To whom it may concern;

# Calibration Certificate

| | | | |
|---|---|---|---|
| Manufacturer : | EKO Instruments Co., Ltd. | Calibration date : | February 19, 2016 |
| Model : | MF-180 | Serial number : | A1847 |
| Description : | Heat Flow Sensor | EKO Ref. number : | EX16-036 |
| Cable : | 10m | | |

We hereby certify that calibration results of above instrument are as follows;

| | | |
|---|---|---|
| Sensitivity | 0.02694 | [mV / W·m$^{-2}$] |
| Internal Resistance | 503 | [Ω] |

I. Sunaga / Manager of Mfg. Dept.

T. Konuma / Inspector



WITH
HIOKI
DATALOGGER
#3

2. EKO Pyranometer calibration cert

EKO INSTRUMENTS CO., LTD.

# Calibration Certificate

Requester : EKO INSTRUMENTS Europe B.V.
Luitsfestraat 55, Unit 32, 2521 AL,
Den Haag, The Netherlands

ISO 17025 / ISO 9847

#74155

| | | | |
|---|---|---|---|
| Manufacturer : | EKO Instruments Co., Ltd. | | |
| Description : | Pyranometer | Certificate Number : | S14046415-EX14-297 |
| Model : | MS-802 | Issue date : | December 03, 2014 |
| ISO Classification : | Second Class | Calibration Date : | December 03, 2014 |
| Serial Number : | S14046415 | Calibration Procedure : | LM-10 |
| Accessories : | Cable | | |
| Product Conditions : | | | |

Calibration Conditions

| | | |
|---|---|---|
| Temperature | 25±3 | [°C] |
| Direct Radiation | 1000±50 | [W/m$^2$] |
| Sun Simulator in-stability | 0.3 | [%] |

Calibration Results

| | | | |
|---|---|---|---|
| Sensitivity | 6.98 | [μV/W·m$^2$] | |
| Uncertainty | 0.67 | [%] | *(Coverage factor k = 1.96)* |

The above product is calibrated and traceable to the reference pyranometer in compliance with ISO\IEC9847 Direct beam calibration (type IIc). Measurement uncertainties at the time of calibration are consistent with the Guide to the Expression of Uncertainty in Measurement (GUM).

| Reference Instruments | Model | S/N | Sensitivity [μV/W·m$^2$] | Calibration due |
|---|---|---|---|---|
| Pyranometer | MS-802 | PRN-REF.01 | 7.729 | 2015/3/1 |
| Digital Multimeter | 34401A | MY41014361 | | 2016/8/5 |

**EKO Instruments Co., Ltd.**
**1-21-8, Hatagaya, Shibuya-ku, Tokyo, 151-0072, Japan**
M.Tukamoto／Calibration responsible

## Calibration Results

| n | Ref. Irradiance [W/m²] | Pyranometer Output [mV] | Sensitivity [μV/W m⁻²] | n | Ref. Irradiance [W/m²] | Pyranometer Output [mV] | Sensitivity [μV/W m⁻²] |
|---|---|---|---|---|---|---|---|
| 1 | 999.67 | 6.98 | 6.98 | 6 | 999.67 | 6.98 | 6.98 |
| 2 | 999.67 | 6.98 | 6.98 | 7 | 999.67 | 6.98 | 6.98 |
| 3 | 999.67 | 6.98 | 6.98 | 8 | 999.67 | 6.98 | 6.98 |
| 4 | 999.67 | 6.98 | 6.98 | 9 | 999.67 | 6.98 | 6.98 |
| 5 | 999.67 | 6.98 | 6.98 | 10 | 999.67 | 6.98 | 6.98 |
| Σ Mean (n=10) | | 6.98 | 6.98 | | | | |
| Std. deviation | | | 0.0014 | | | | |

## Calibration Procedure

The pyranometer was calibrated against a calibrated reference pyranometer using a 1000 W/m² (AM1.5 class AAA) sun simulator as source. The pyranometer is situated on a horizontal table and aligned to the optical axis of a normal incidence light source. By alternating the position of the calibrated reference pyranometer with the test pyranometer the output signal of both pyranometers are recorded and used to solve the equation of the unknown sensitivity variable. The operating conditions are maintained constant (e.g. ambient temperature and normal incidence irradiance), hence the pyranometer uncertainty figure from 10 readings (*n*) is determined by taking into account the sensitivity uncertainty (Ur), uncertainty of temperature (Ut), normal distribution (d), and repeatability (Ur) of the reference pyranometer and the max. deviation of the incident irradiance between the measurement intervals.

## Uncertainty

The expanded calibration uncertainty associated with the pyranometer sensitivity figure is calculated as the square root of the sum of the squares of the reported uncertainties:

| | |
|---|---|
| 1) Uncertainty of reference (Ur) | 0.31% |
| 2) Uncertainty of temperature (Ut) | 0.14% |
| 3) Repeatability (Ur) | 0.04% |
| 4) Distribution (d) | 0.02% |
| Total uncertainty (Uc) | 0.34% |
| Expanded uncertainty (U) | 0.67% *(Coverage factor k = 1.96)* |

*Expanded Uncertainty* = $1.96 \times \sqrt{((Ur^2 + Ut^2 + Ur^2 + d^2))}$

## Traceability

Annually the reference pyranometer MS-802 is calibrated against the primary standard PMO-6 according to the sun-and-shade method under ISO9846. The primary standard is directly traceable to the WRR (World Radiometric Reference) and maintained in the group of standard radiometers calibrated every 5 years during the IPC. The data logger is traceable to JEMIC (Japan Electric Meters Inspection Corporation).

EKO INSTRUMENTS EUROPE B.V.

*Note: The sensitivity of the sensor will slightly deviate with time when it is exposed to radiation. Therefore it is advised to re-calibrate the sensor every two years. For calibration services contact EKO Instruments Co., Ltd. The date on the calibration certificate represents the date of calibration and is considdered relative from the date of manufacture to the moment of first time operation as long as the pyranometer was stored in its original packaging.*

The packaging was opened for 1st time

19th December 2016.

Dr. SA. GALLAGHER

3. Hioki Dataloggers calibration cert

HIOKI

No. 201609044795
Date 2016-11-29
(YYYY-MM-DD) 1 / 1

# CALIBRATION CERTIFICATE

Customer SIRIS - IMPRESS
DATALOGGER 1

HIOKI E.E. CORPORATION
Katsuhiro Tokuchi
Inspector
Quality Assurance Department

Model Name : MEMORY HiLOGGER
Model Number : LR8400-20
SerialNo : 161133222
Customer Record No. : -----
Calibration Date : 2016-11-29

The above listed product(s) is/are calibrated in accordance with the HIOKI standards. This also certifies that all reference instruments used in the calibration process can be traced back to all or some of the official standards laboratories of the nations affiliated with the International Committee for Weights and Measures (CIPM), such as the National Institute of Advanced Industrial Science and Technology, the National Institute of Information and Communications Technology, and NIST (National Institute of Standards and Technology).

***Instruments used***

| Model Name | Model Number | Serial No. | Control No. | Cal. Period |
|---|---|---|---|---|
| VOLTAGE CURRENT SOURCE | R6161 | 05540027 | 000-12-083 | 2017-04 |
| FREQUENCY COUNTER | 5318A | 3418A01148 | 506-44-020 | 2017-11 |
| COLD JUNCTION UNIT | HT-06X-DK | HT34A010 | 000-67-106 | 2017-04 |
| DIGITAL RESISTANCE BOX | ADR-1202G | 27B-0048 | 000-30-065 | 2017-02 |

HIOKI

No. 2016H044796
Date 2016-11-29
(YYYY-MM-DD) 1 / 1

# CALIBRATION CERTIFICATE

Customer SIEGS - IMPRESS
DATA LOGGER 2

HIOKI E.E. CORPORATION

Inspector
Quality Assurance Department

Model Name : MEMORY HiLOGGER
Model Number : LR8400-20
SerialNo : 161133223
Customer Record No. : -----
Calibration Date : 2016-11-29

The above listed product(s) is/are calibrated in accordance with the HIOKI standards. This also certifies that all reference instruments used in the calibration process can be traced back to all or some of the official standards laboratories of the nations affiliated with the International Committee for Weights and Measures (CIPM), such as the National Institute of Advanced Industrial Science and Technology, the National Institute of Information and Communications Technology, and NIST (National Institute of Standards and Technology).

***Instruments used***

| Model Name | Model Number | Serial No. | Control No. | Cal. Period |
|---|---|---|---|---|
| VOLTAGE CURRENT SOURCE | 86161 | 055400027 | 000-12-083 | 2017-04 |
| FREQUENCY COUNTER | 5318A | 3418A01148 | 506-44-020 | 2017-11 |
| COLD JUNCTION UNIT | HT-06X-DE | HT34A010 | 000-67-106 | 2017-04 |
| DIGITAL RESISTANCE BOX | ADR-1202G | 270-0048 | 000-30-065 | 2017-02 |

HIOKI

No. 20161044797
Date 2016-11-30
(YYYY-MM-DD) 1/1

# CALIBRATION CERTIFICATE

Customer SIRIS - IMPRESS
DATALOGGER 3

HIOKI E.E. CORPORATION

Katsuhiro Tokuchi

Inspector
Quality Assurance Department

Model Name : MEMORY HiLOGGER
Model Number : LR8400-20
SerialNo : 161133226
Customer Record No. : -----
Calibration Date : 2016-11-30

The above listed product(s) is/are calibrated in accordance with the HIOKI standards. This also certifies that all reference instruments used in the calibration process can be traced back to all or some of the official standards laboratories of the nations affiliated with the International Committee for Weights and Measures (CIPM), such as the National Institute of Advanced Industrial Science and Technology, the National Institute of Information and Communications Technology, and NIST (National Institute of Standards and Technology).

***Instruments used***

| Model Name | Model Number | Serial No. | Control No. | Cal. Period |
|---|---|---|---|---|
| VOLTAGE CURRENT SOURCE | 8818 | 85548027 | 000-12-083 | 2017-04 |
| FREQUENCY COUNTER | 53181A | 3418A01148 | 506-44-020 | 2017-11 |
| COLD JUNCTION UNIT | HT-06X-DK | HT34A010 | 000-67-106 | 2017-04 |
| DIGITAL RESISTANCE BOX | ADR-12020 | 270-0008 | 000-30-065 | 2017-02 |

4. EKO MF-180 Heat flux sensor

https://www.eko-instruments.com/media/ik0jz0nr/ps_heat_flux_sensors-eng-09-2022.pdf

## Appendix K Programme for manufacture of hut walls

Pour 3 walls for one hut in one day

Note: This programme is based on the assumption that the following will be in place prior to 7am on Monday morning:

- Formwork for all walls is assembled and on table.
- Insulation boards are cut to size, dry and resting up against associated formwork, together with a roll of insulation tape

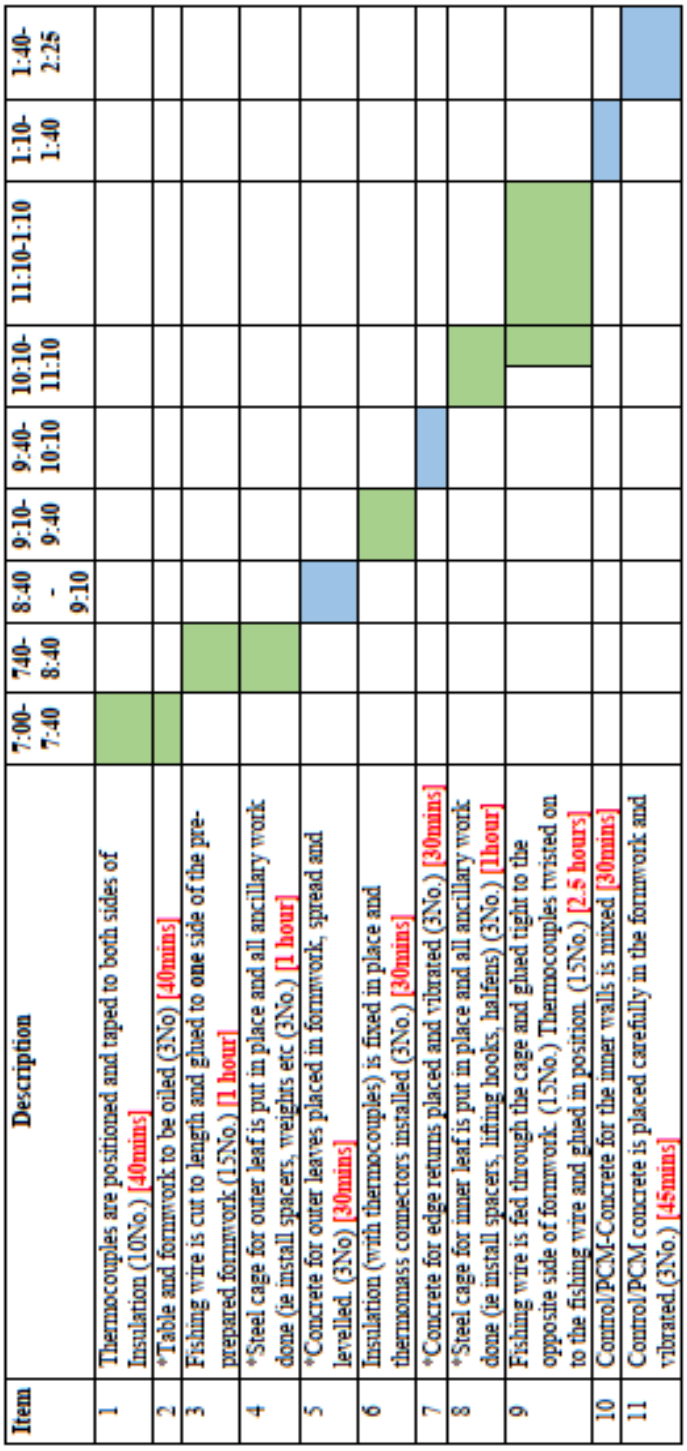

| Item | Description | 7:00-7:40 | 7:40-8:40 | 8:40 - 9:10 | 9:10-9:40 | 9:40-10:10 | 10:10-11:10 | 11:10-1:10 | 1:10-1:40 | 1:40-2:25 |
|---|---|---|---|---|---|---|---|---|---|---|
| 1 | Thermocouples are positioned and taped to both sides of Insulation (10No.) [40mins] | | | | | | | | | |
| 2 | *Table and formwork to be oiled (3No) [40mins] | | | | | | | | | |
| 3 | Fishing wire is cut to length and glued to **one** side of the pre-prepared formwork (15No.) [1 hour] | | | | | | | | | |
| 4 | *Steel cage for outer leaf is put in place and all ancillary work done (ie install spacers, weights etc (3No.) [1 hour] | | | | | | | | | |
| 5 | *Concrete for outer leaves placed in formwork, spread and levelled. (3No) [30mins] | | | | | | | | | |
| 6 | Insulation (with thermocouples) is fixed in place and thermomass connectors installed (3No.) [30mins] | | | | | | | | | |
| 7 | *Concrete for edge returns placed and vibrated (3No.) [30mins] | | | | | | | | | |
| 8 | *Steel cage for inner leaf is put in place and all ancillary work done (ie install spacers, lifting hooks, halfens) (3No.) [1hour] | | | | | | | | | |
| 9 | Fishing wire is fed through the cage and glued tight to the opposite side of formwork. (15No.) Thermocouples twisted on to the fishing wire and glued in position. (15No.) [2.5 hours] | | | | | | | | | |
| 10 | Control/PCM-Concrete for the inner walls is mixed [30mins] | | | | | | | | | |
| 11 | Control/PCM concrete is placed carefully in the formwork and vibrated.(3No.) [45mins] | | | | | | | | | |

**Appendix L Data sheet for double-glazed patio door to hut**

https://www.munsterjoinery.ie/media/wysiwyg/product_grid/uPVC_Doors_IRE_18.pdf

## Appendix M Plots of North wall temperatures in each hut, 19th – 21st November, 2017

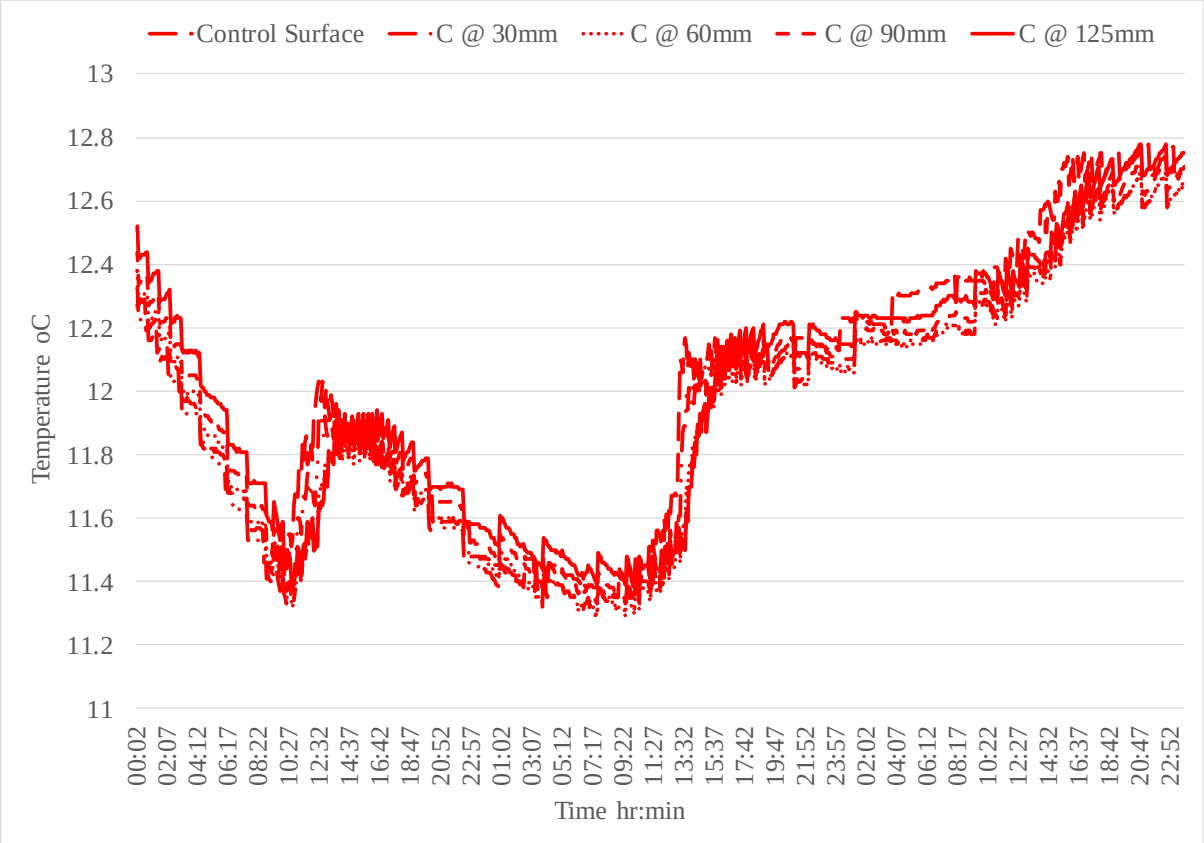


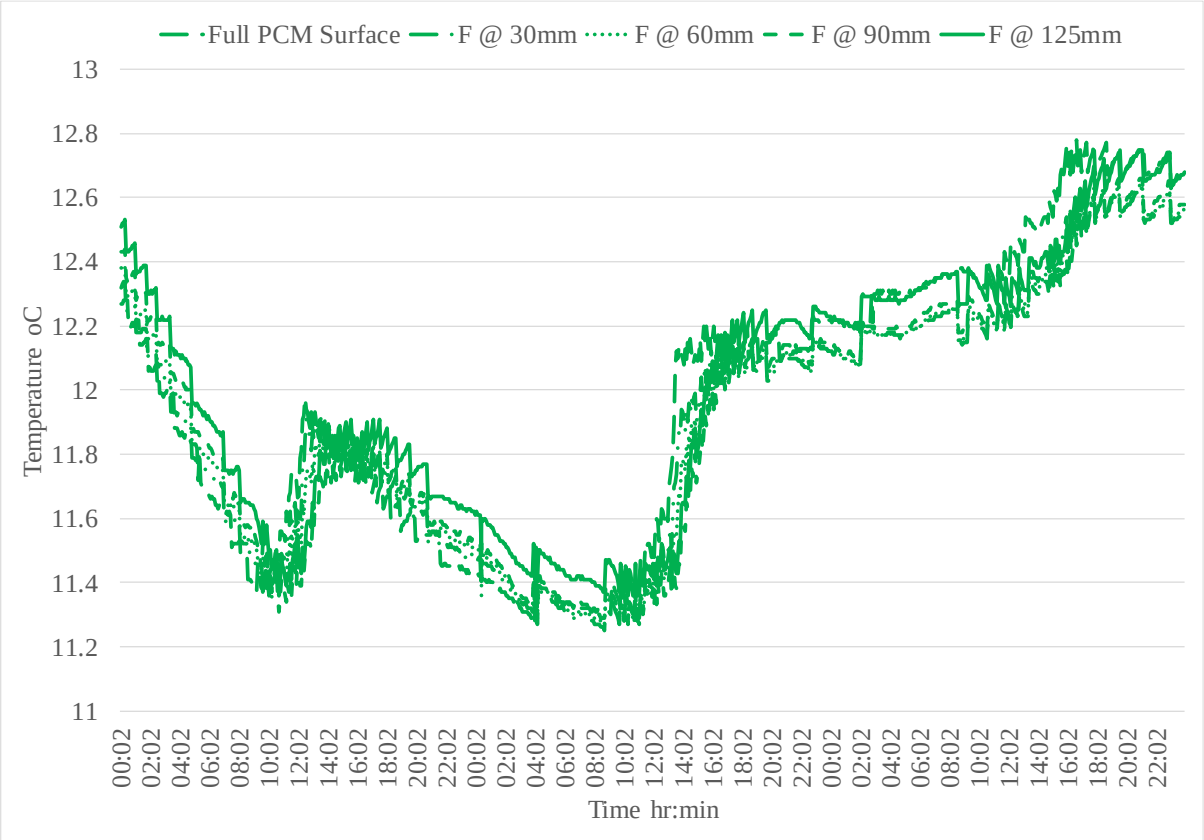

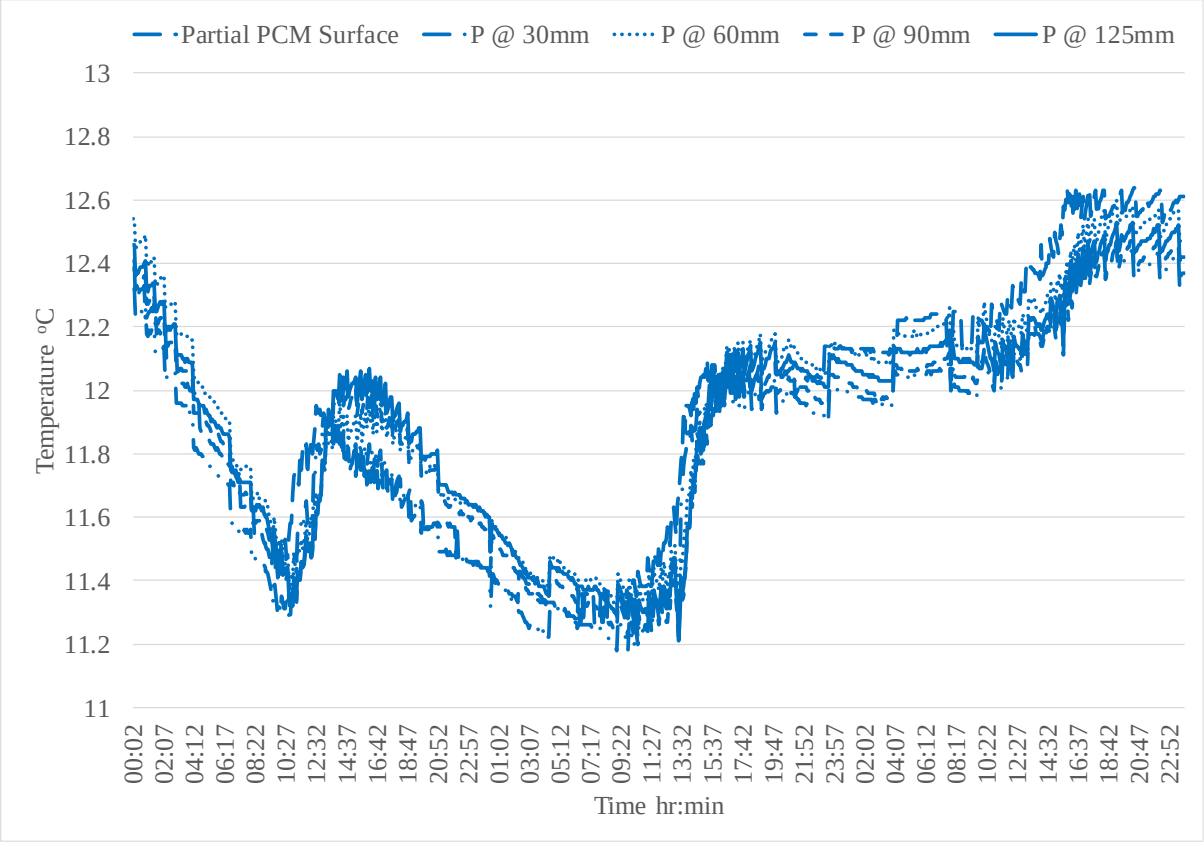
Partial PCM Surface
P @ 30mm
P @ 60mm
P @ 90mm
P @ 125mm
Temperature °C
13
12.8
12.6
12.4
12.2
12
11.8
11.6
11.4
11.2
11
00:02
02:07
04:12
06:17
08:22
10:27
12:32
14:37
16:42
18:47
20:52
22:57
01:02
03:07
05:12
07:17
09:22
11:27
13:32
15:37
17:42
19:47
21:52
23:57
02:02
04:07
06:12
08:17
10:22
12:27
14:32
16:37
18:42
20:47
22:52
Time hr:min

## Appendix N Plots of North wall temperatures in each hut, 20th – 22nd June, 2017

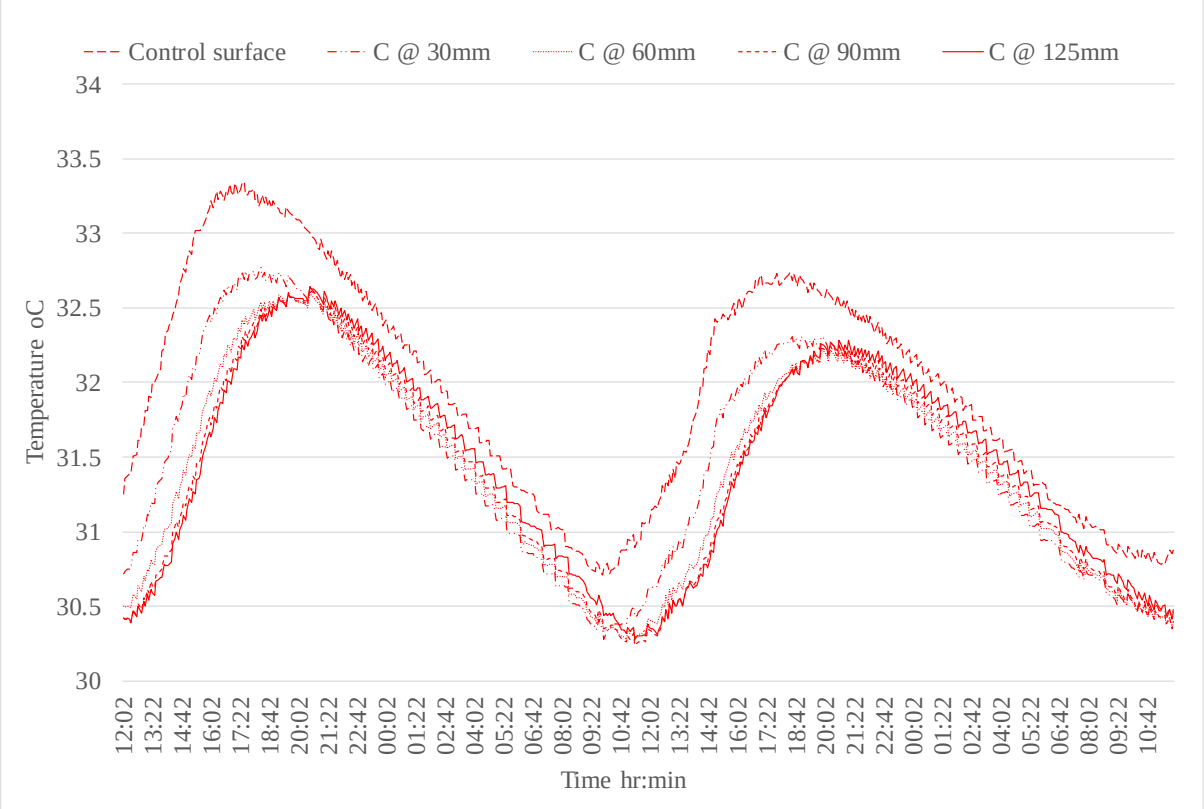


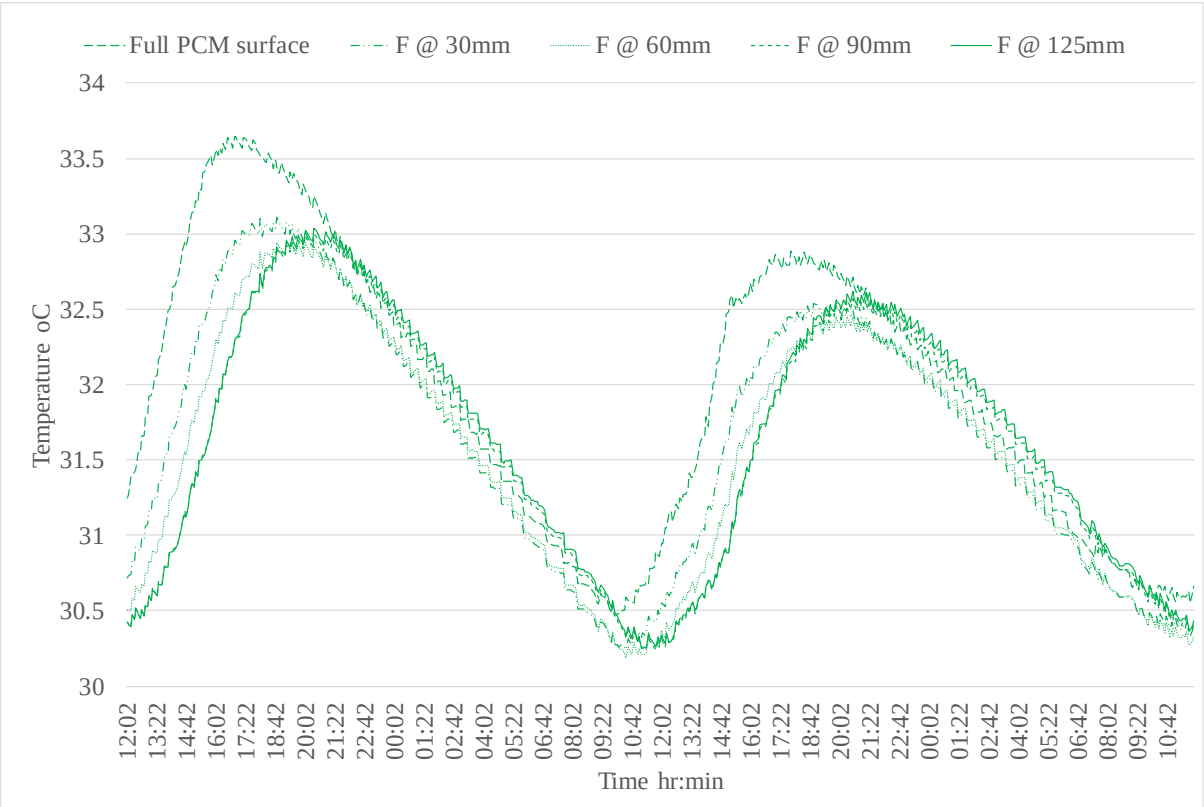

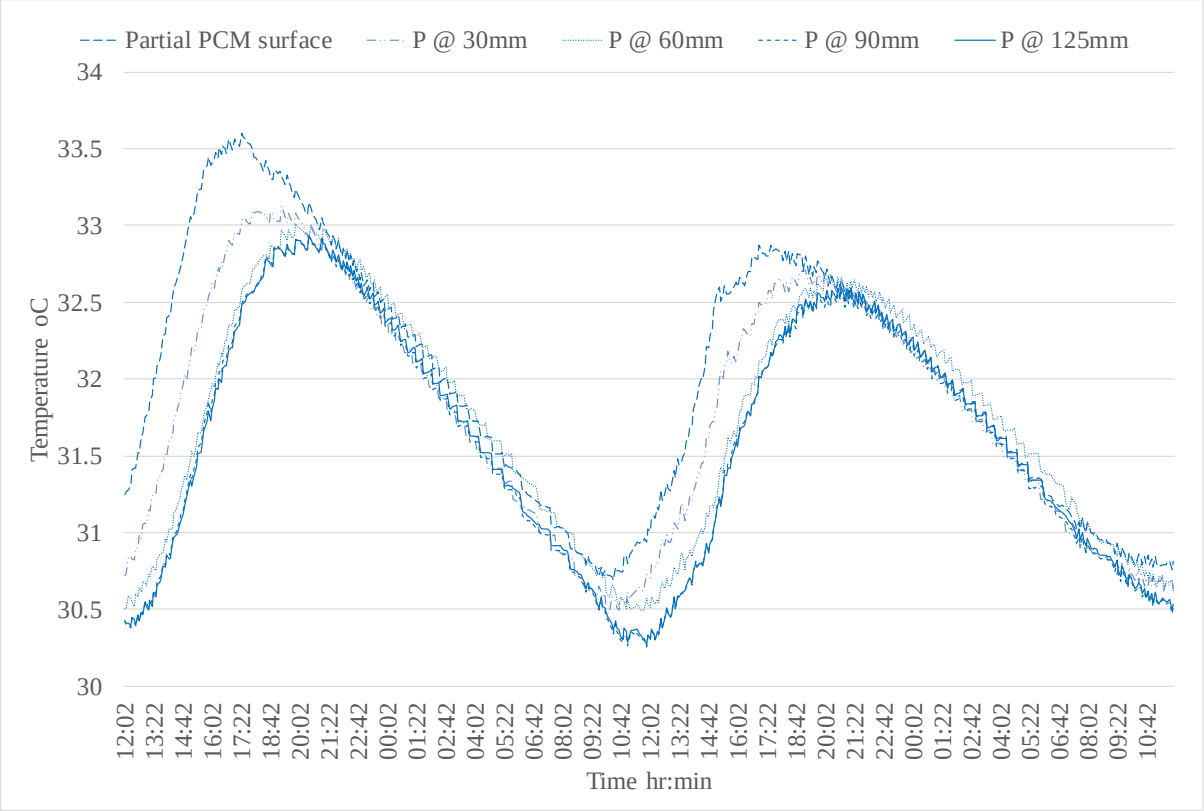
Partial PCM surface
P @ 30mm
P @ 60mm
P @ 90mm
P @ 125mm
Temperature oC
34
33.5
33
32.5
32
31.5
31
30.5
30
12:02
13:22
14:42
16:02
17:22
18:42
20:02
21:22
22:42
00:02
01:22
02:42
04:02
05:22
06:42
08:02
09:22
10:42
12:02
13:22
14:42
16:02
17:22
18:42
20:02
21:22
22:42
00:02
01:22
02:42
04:02
05:22
06:42
08:02
09:22
10:42
Time hr:min

## Appendix O Plots of North wall temperatures in each hut, 9th – 10th June, 2017

### Temperature at 30 mm depth

Figure O-1 presents the temperature profile at a depth of 30 mm into the North wall of each hut.

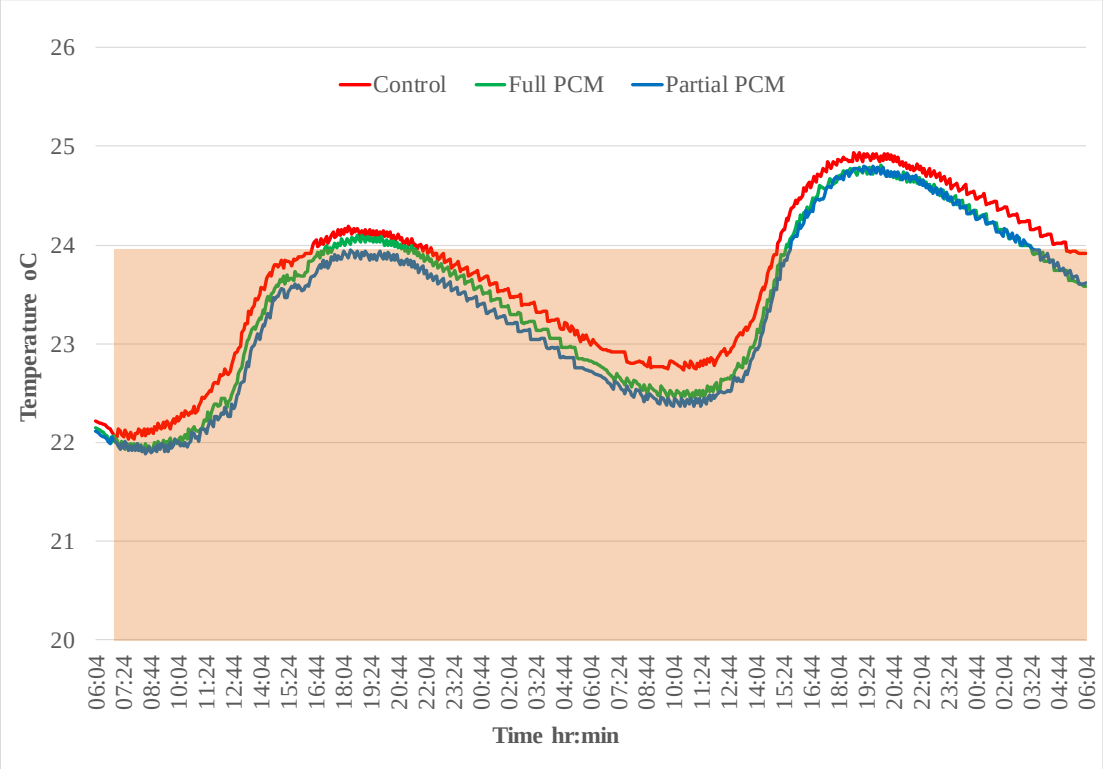


**Figure O-1 Temperatures at 30 mm depth, 9th June to 10th June 2017**

There is no significant difference in the thermal behaviour of the hut walls at this depth. The temperatures fluctuate between 22 ºC and 25 ºC. The temperatures in the Full PCM hut and Partial PCM hut are on average 0.04 ºC and 0.27 ºC lower than the temperature in the Control wall over the whole period so although the PCM huts are consistently at a lower temperature the difference is insignificant.

### Temperature at 60 mm, 90 mm and 125 mm depth

Figure O-2 displays the temperature profile plots for each hut at a depth of 60 mm. Again there is minimal difference in the temperature profile between the Control hut and the huts containing PCM.

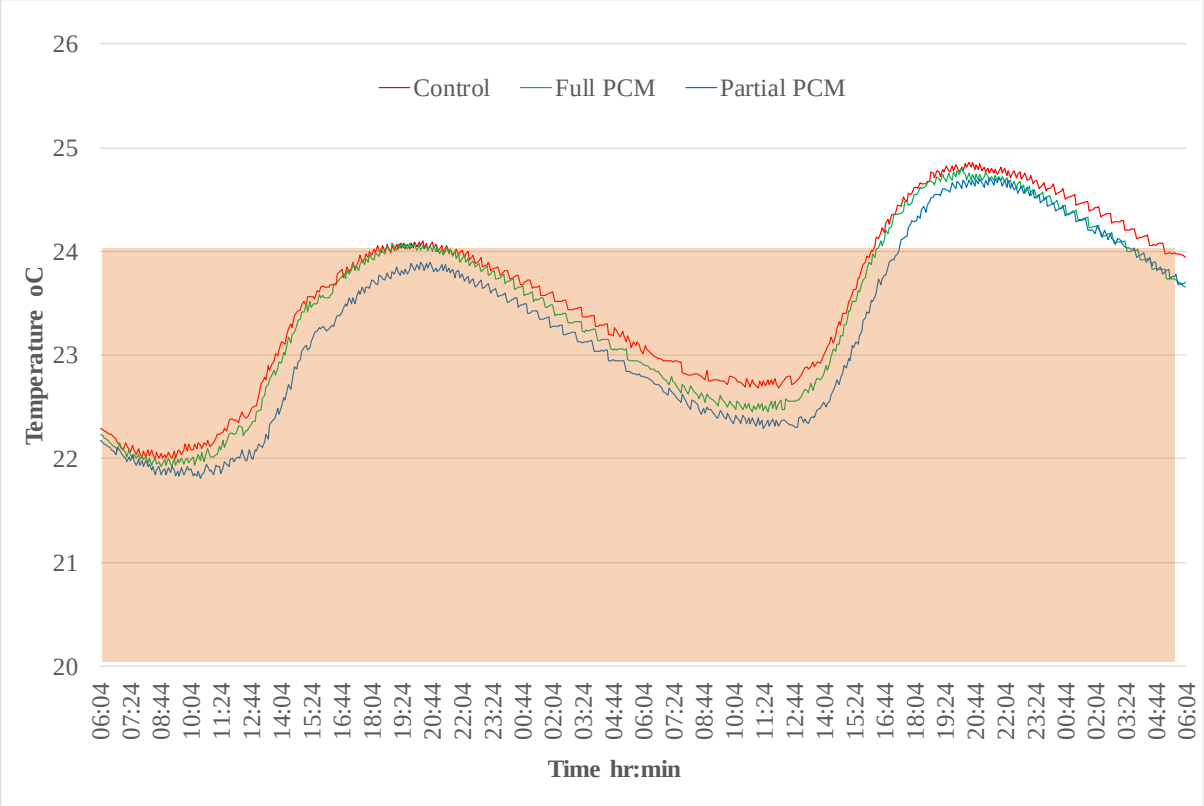


**Figure O-2 Temperature at 60 mm depth, 9th June to 10th June 2017**

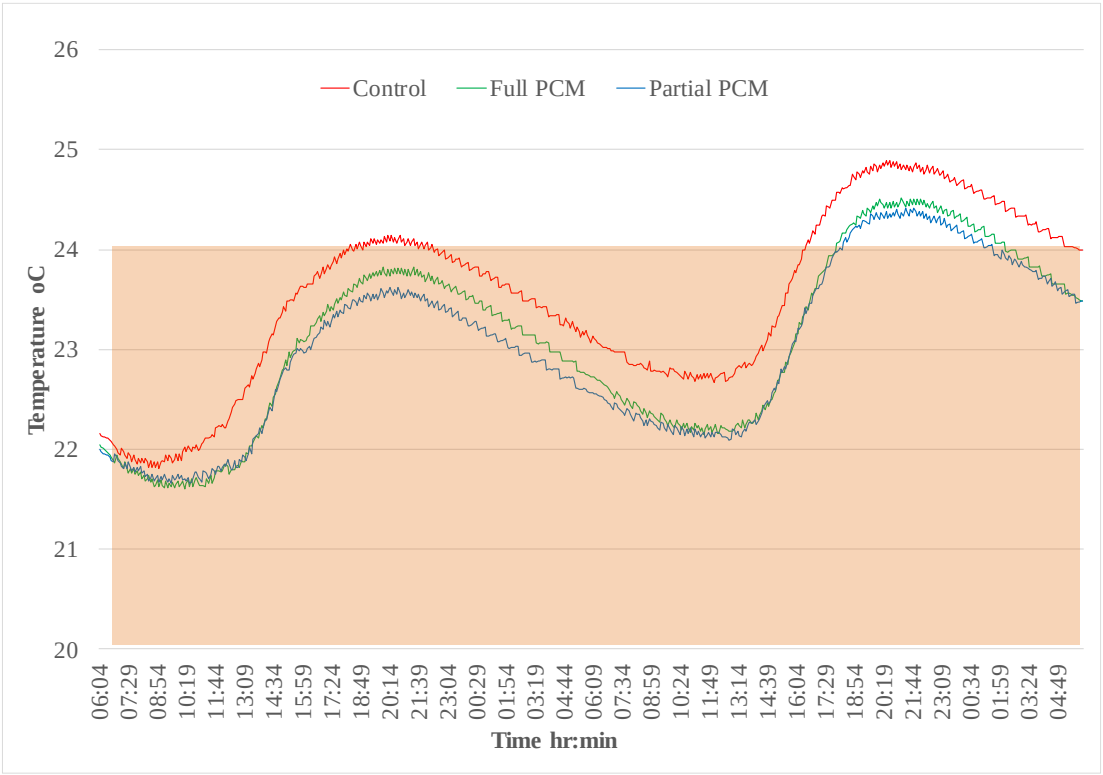


**Figure O-3 Temperature at 90 mm depth, 9th June to 10th June 2017**

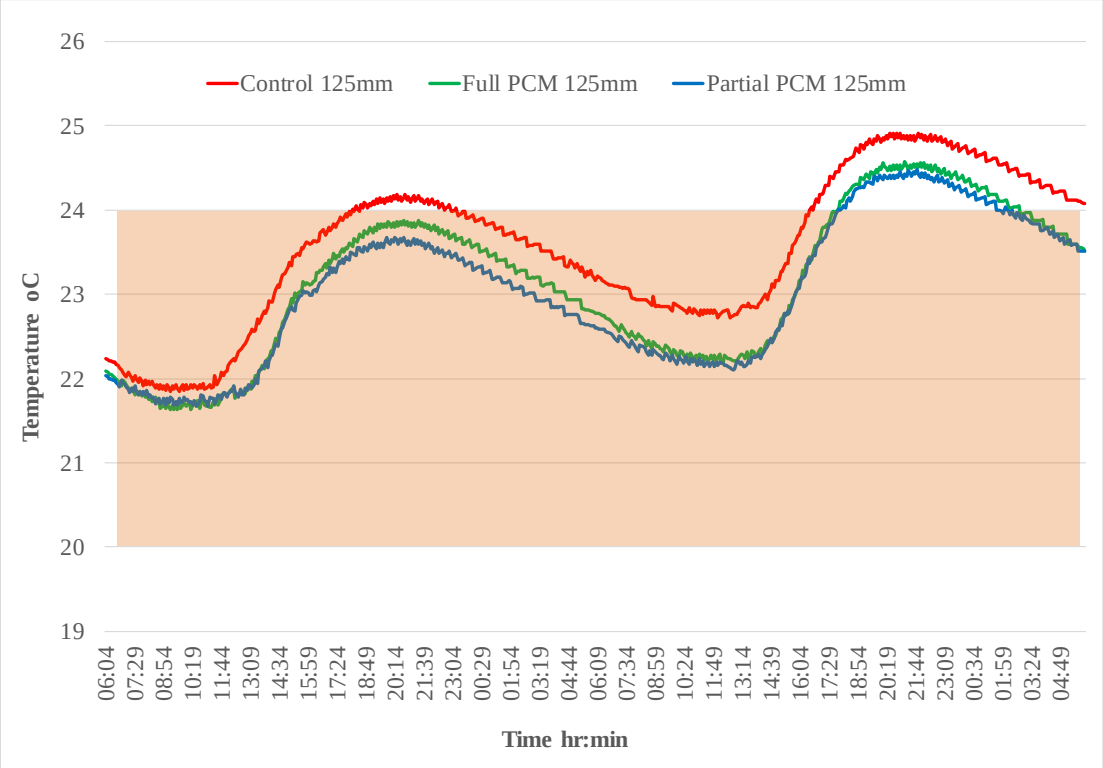


**Figure O-4 Temperature at 125 mm depth, 9th June to 10th June 2017**

## Appendix P Plots of North wall temperatures in each hut, 1st – 2nd May, 2017

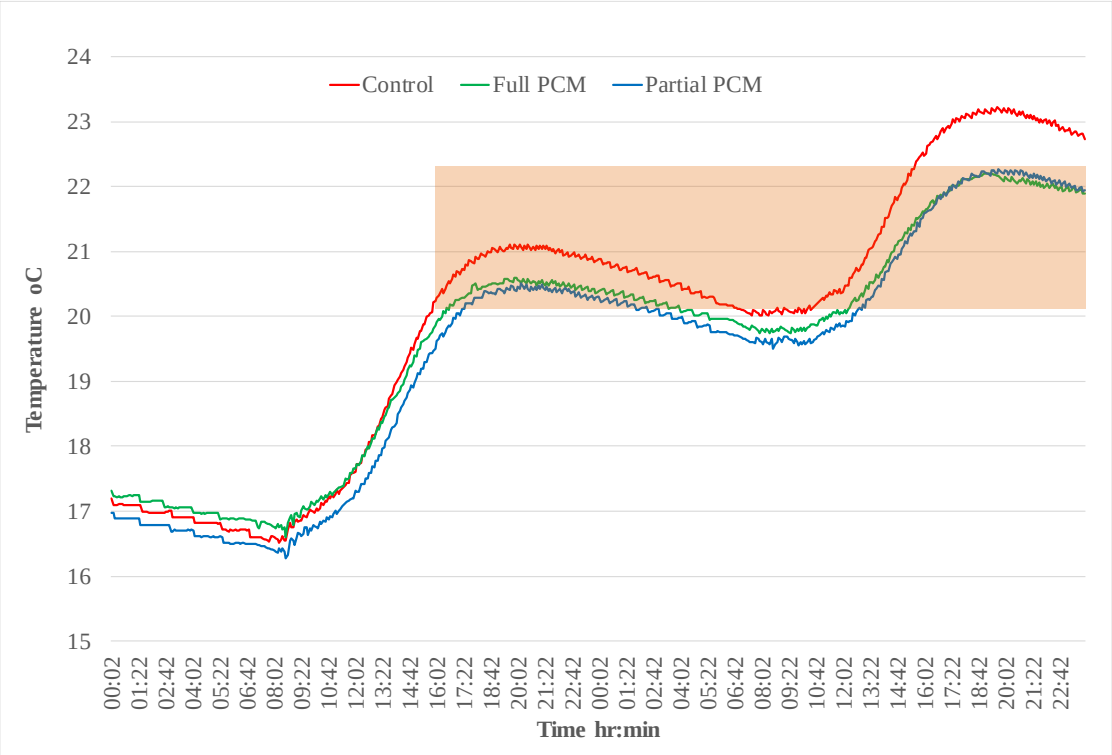


**Figure P-1 Temperature of the wall in each hut at a depth of 30 mm on 1st and 2nd May 2017**

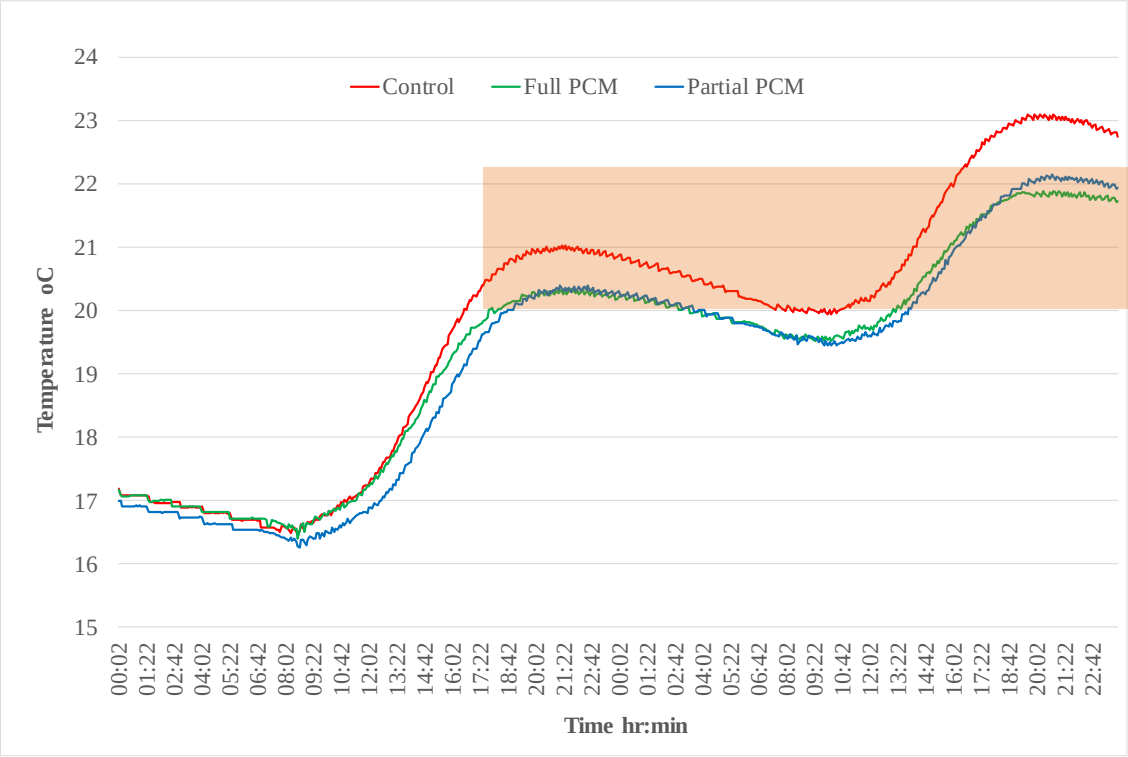


**Figure P-2 Temperature of the wall in each hut at a depth of 60 mm on 1st and 2nd May 2017**

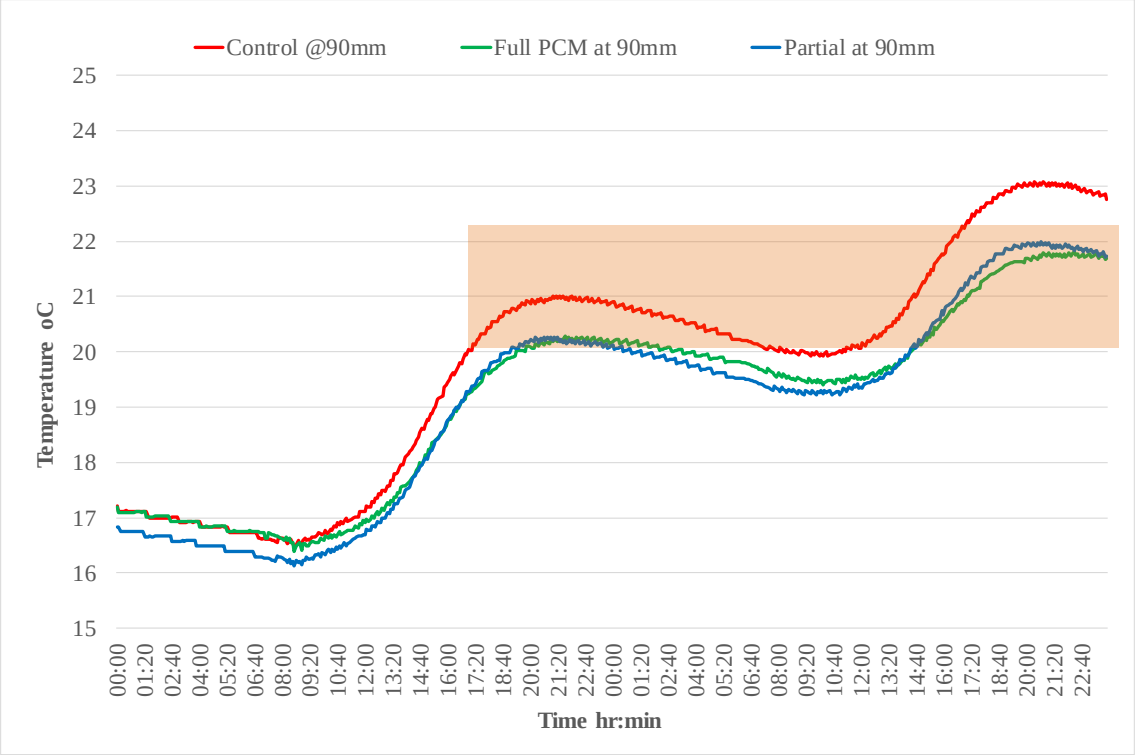


**Figure P-3 Comparison of wall temperatures at 90 mm in all huts on 1st and 2nd May 2017**

**Appendix Q Plots of North wall temperatures at 90 mm and 125 mm depths in each hut, 24th – 25th October, 2017**

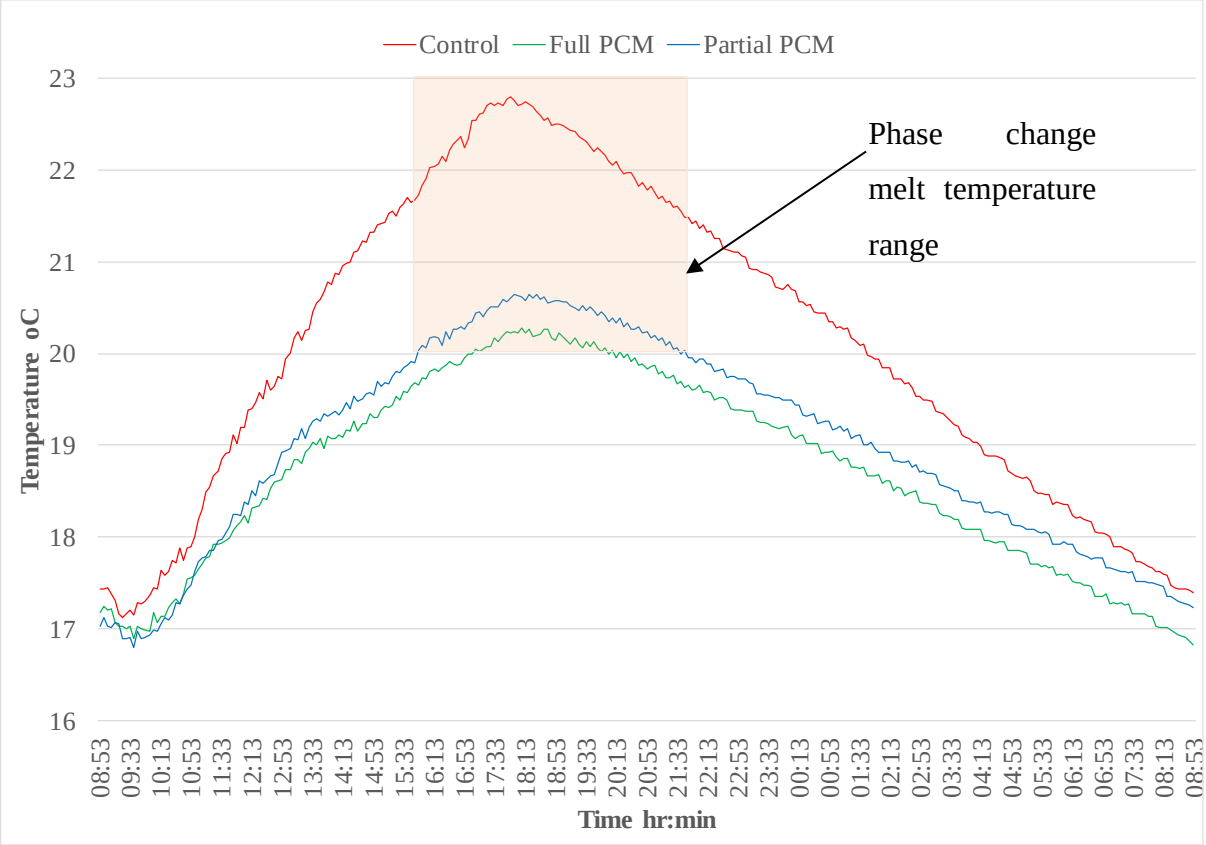


**Figure Q-1 Temperature at 90 mm depth, 24th and 25th October 2017**

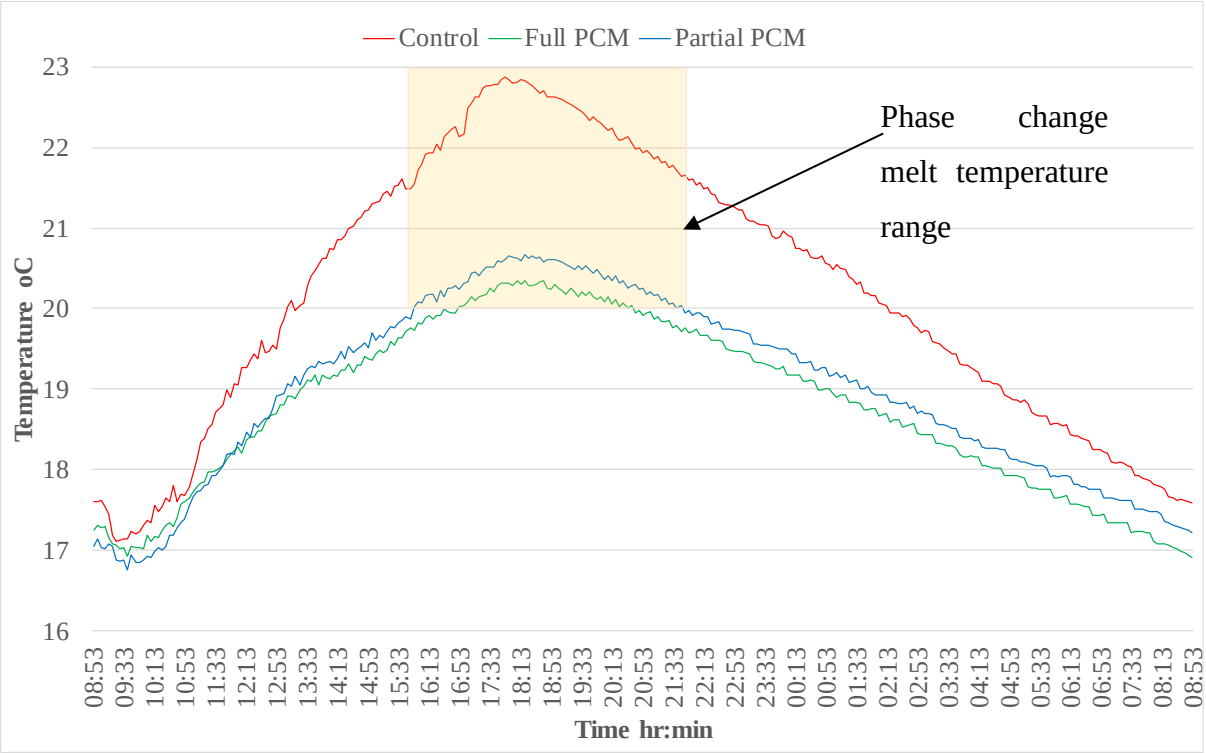


**Figure Q-2 Temperature at back surface of wall, 24th and 25th October 2017**

**Appendix R 'Regression line' plots for North wall temperatures at depths of 60 mm, 90 mm and 125 mm, 24th October 2017**

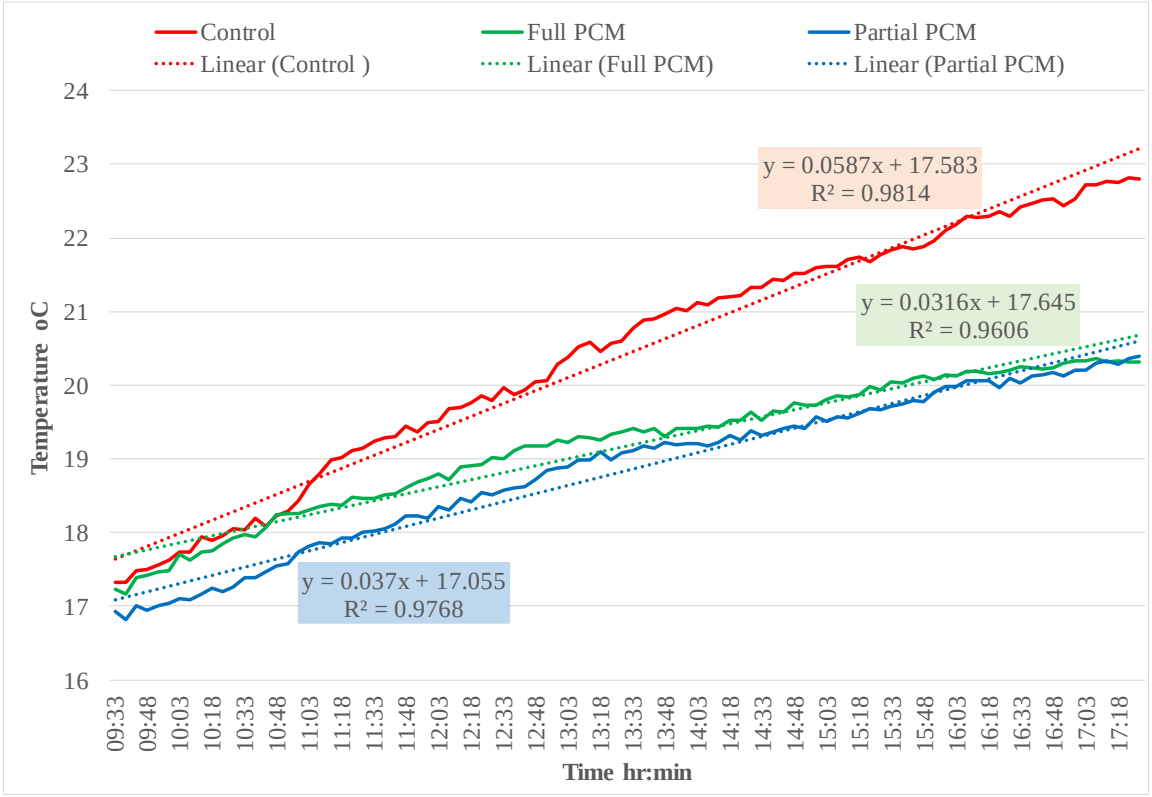


**Figure R-1 Regression line for heating phase of temperature profiles at 60 mm depth**

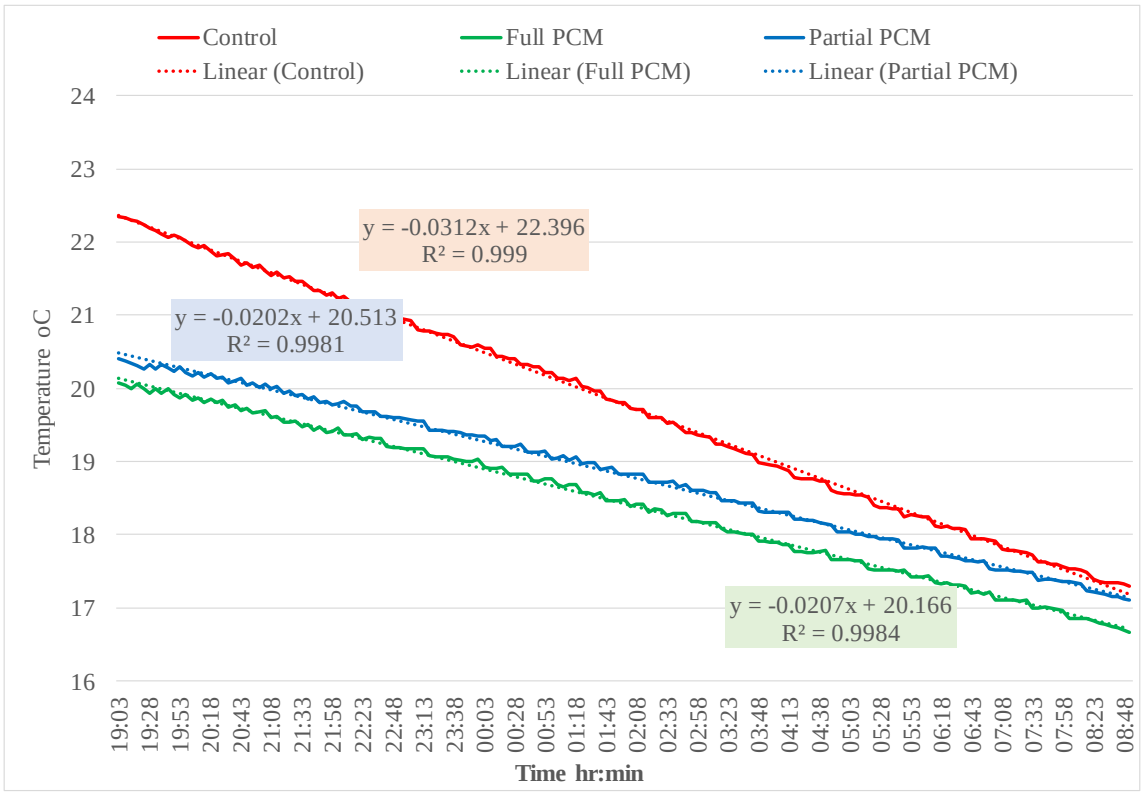


**Figure R-2 Regression line for cooling phase of temperature profiles at 60 mm depth**

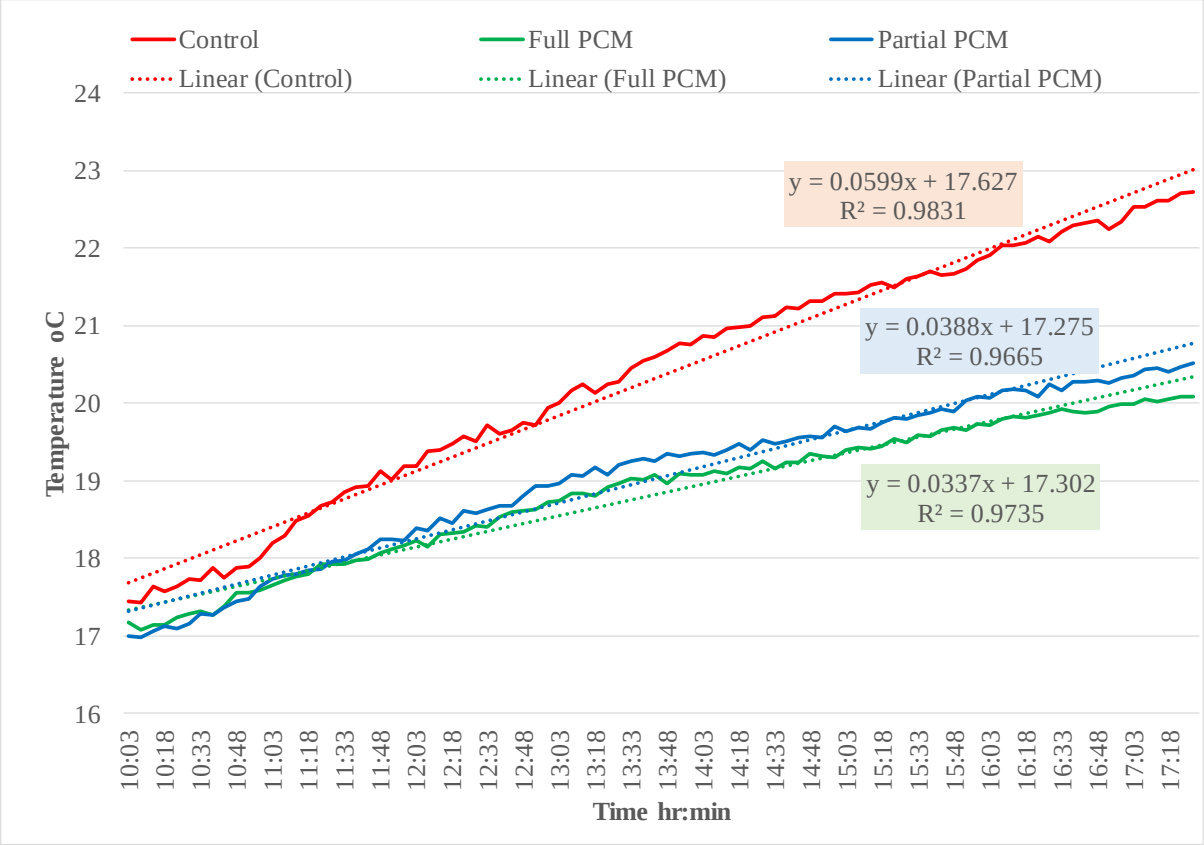


**Figure R-3 Regression line for heating phase of temperature profiles at 90 mm depth**

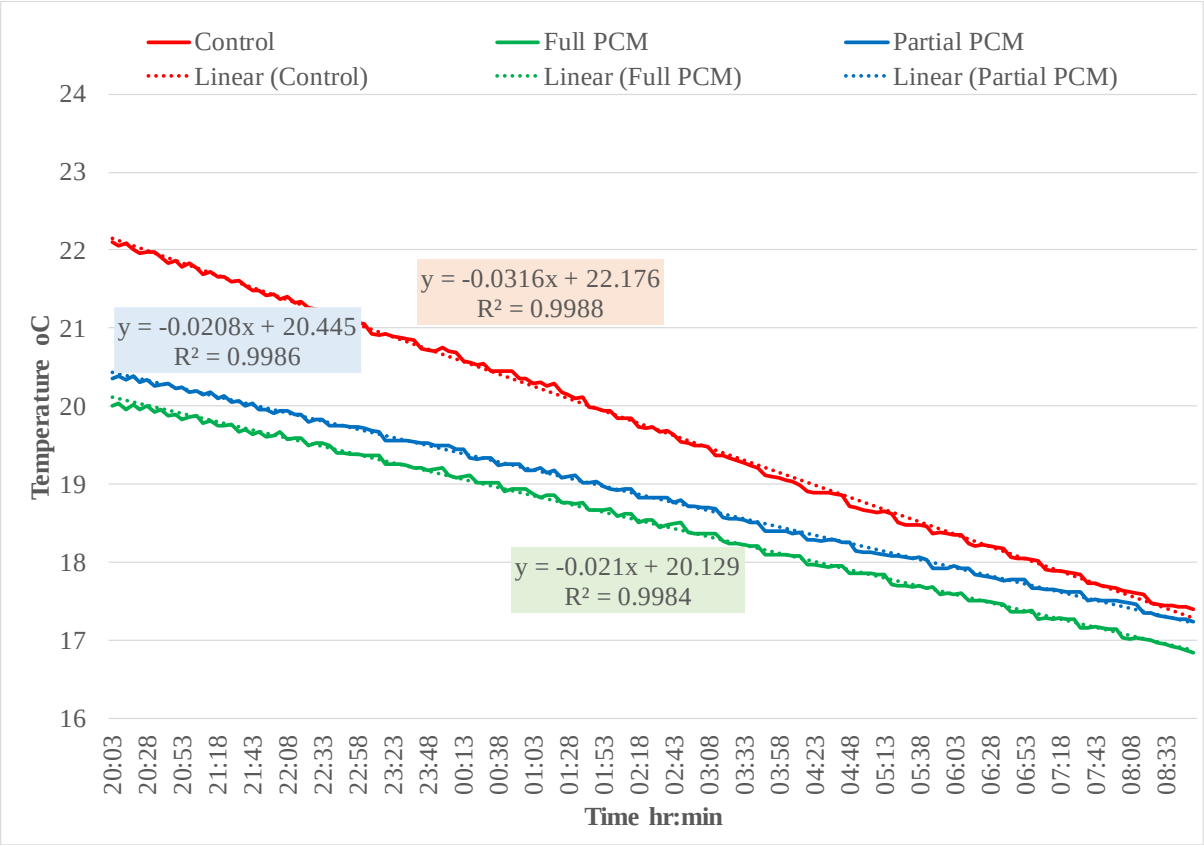


**Figure R-4 Regression line for cooling phase of temperature profiles at 90 mm depth**

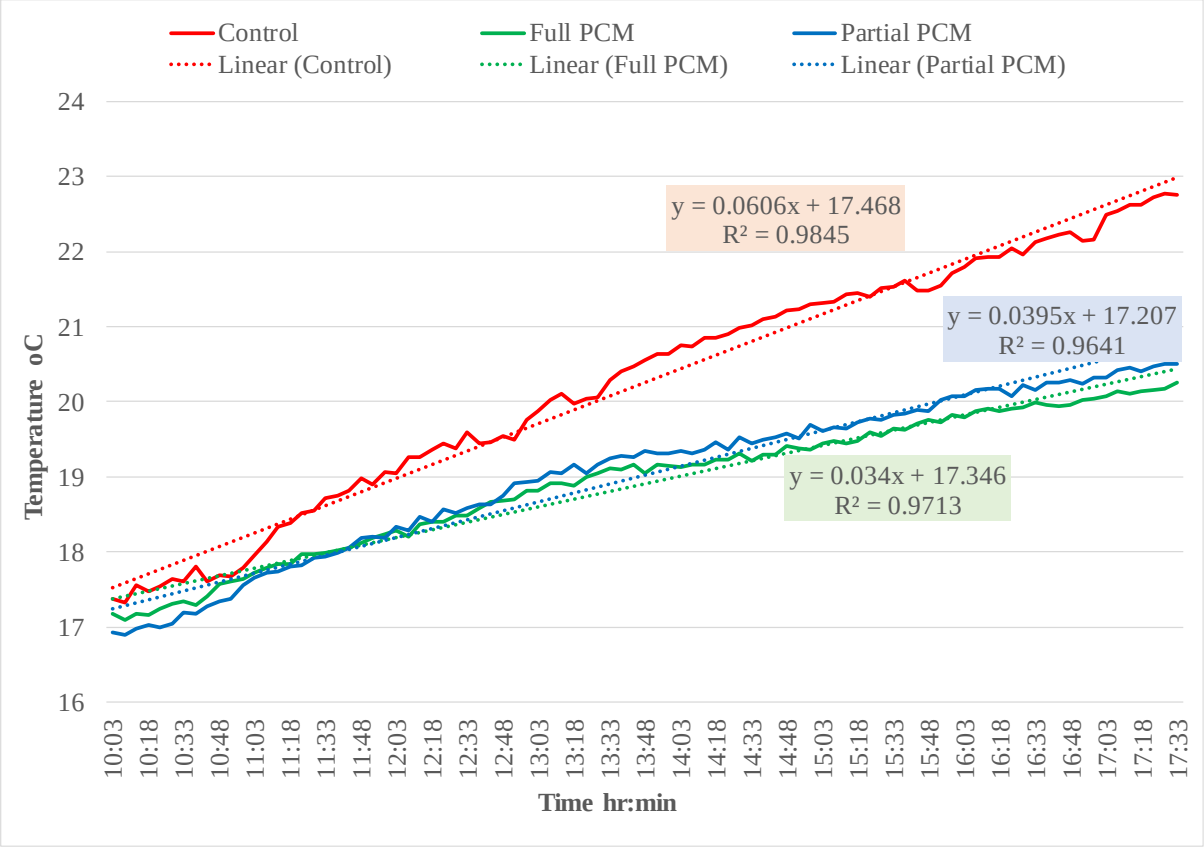


**Figure R-5 Regression line for heating phase of temperature profiles at 125 mm depth**

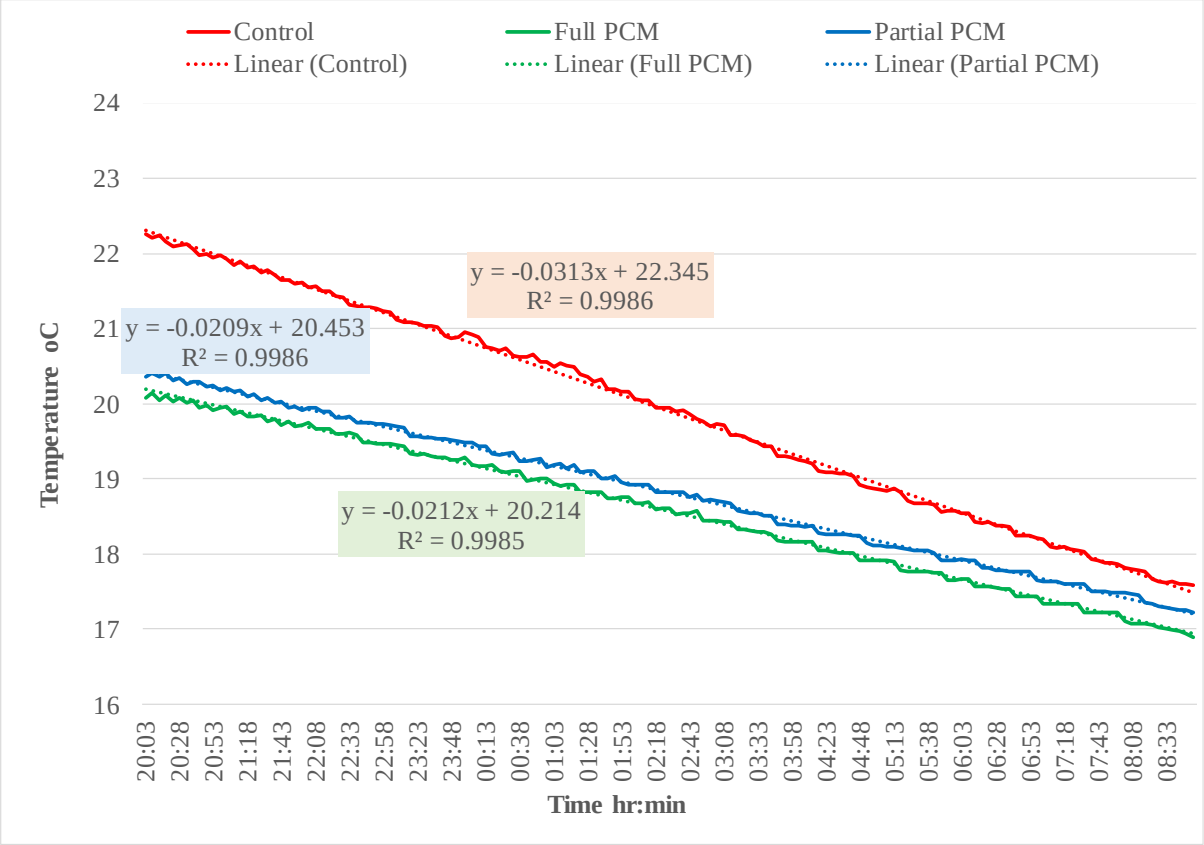


**Figure R-6 Regression line for cooling phase of temperature profiles at 125 mm depth**

**Appendix S Plots showing simulated versus actual temperatures in Control and Full PCM huts**

**A. Validation of the COMSOL model for the Control hut**

**1. 19th November 2017 Control hut -winter passive conditions:**

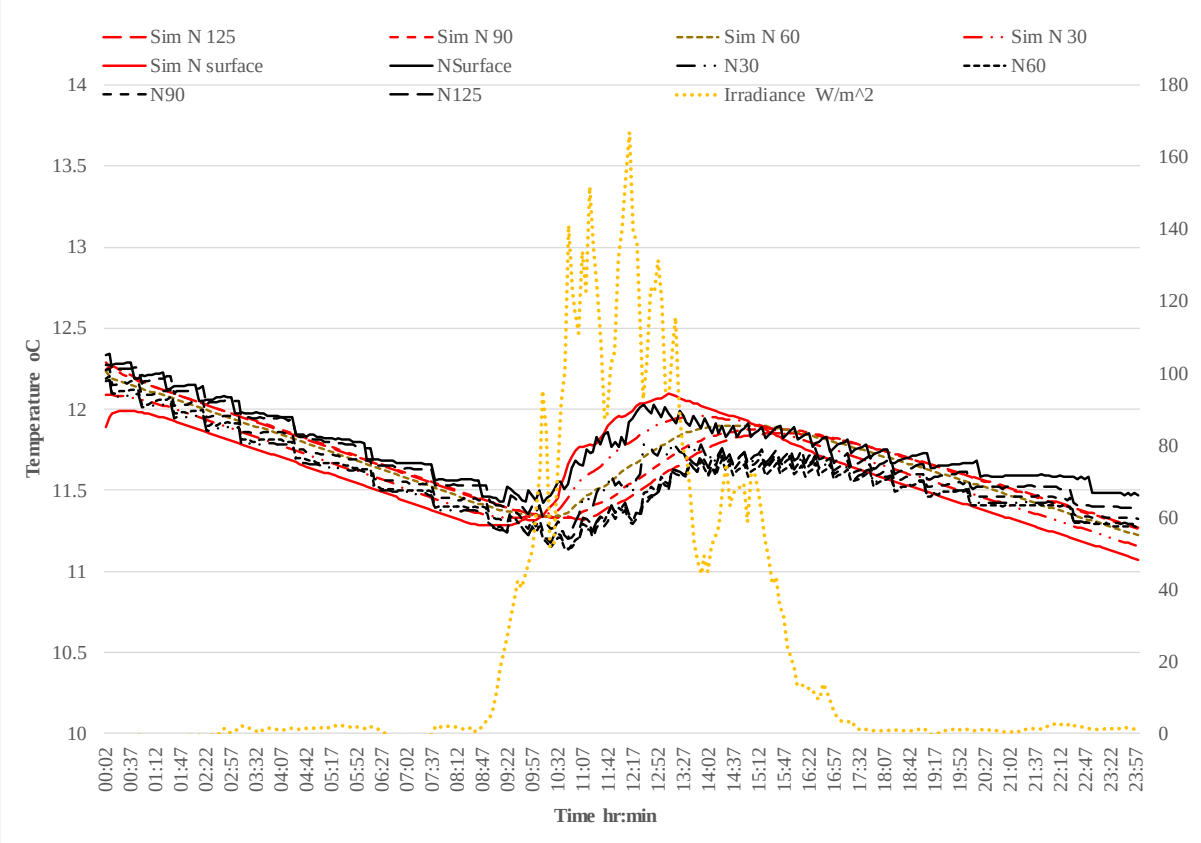


**19th November 2017, Control hut, North wall inner leaf simulated versus actual temperatures**

| Depth | Average $\lvert T_{sim} - T_{act} \rvert$ (°C) | Standard deviation (°C) | Accuracy of simulated temperatures (°C) |
|---|---|---|---|
| Surface | 0.19 | 0.09 | 1.06 |
| 30 mm | 0.09 | 0.07 | 0.96 |
| 60 mm | 0.12 | 0.09 | 0.99 |
| 90 mm | 0.09 | 0.07 | 0.96 |
| 125 mm | 0.06 | 0.04 | 0.93 |

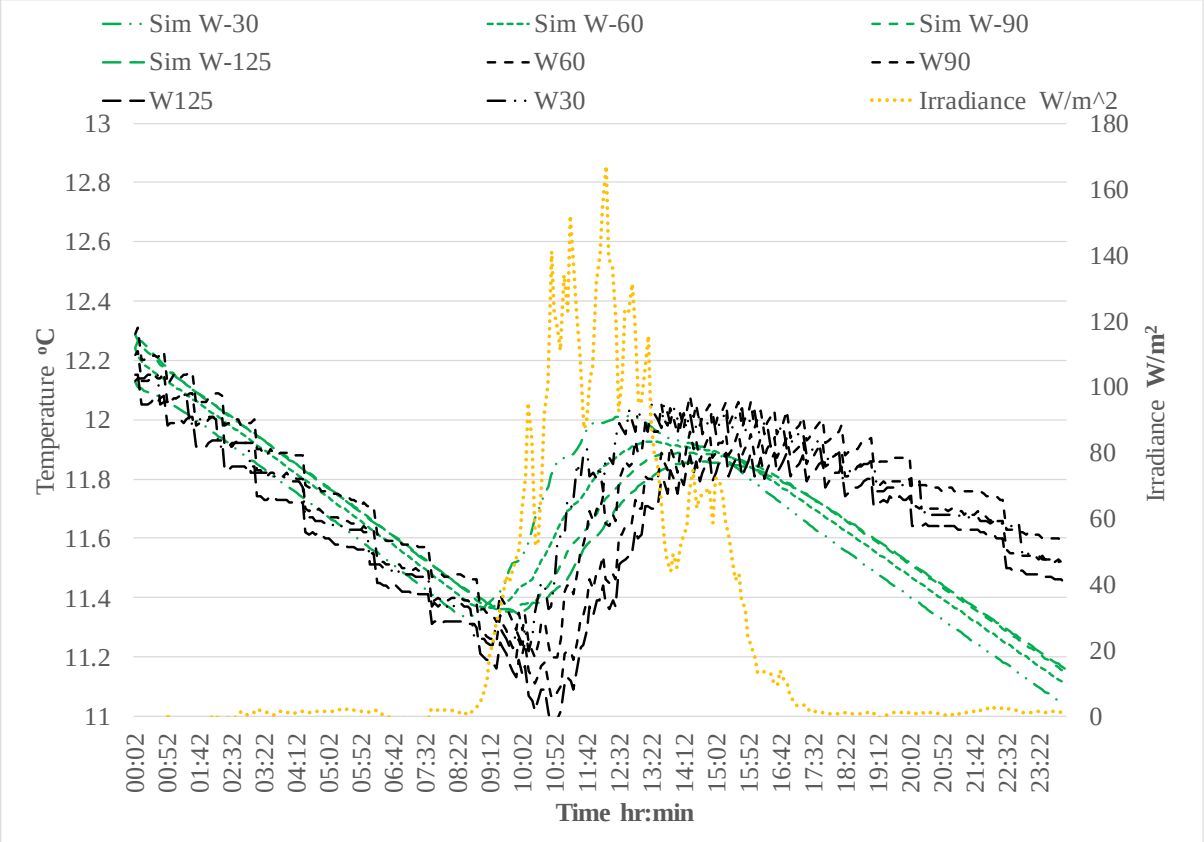


**19th November 2017, Control hut, West wall inner leaf simulated versus actual temperatures**

| Depth | Average $\lvert T_{sim} - T_{act} \rvert$ (°C) | Standard deviation (°C) | Accuracy of simulated temperatures (°C) |
|---|---|---|---|
| 30 mm | 0.17 | 0.15 | 1.04 |
| 60 mm | 0.17 | 0.15 | 1.04 |
| 90 mm | 0.15 | 0.11 | 1.02 |
| 125 mm | 0.16 | 0.09 | 1.03 |

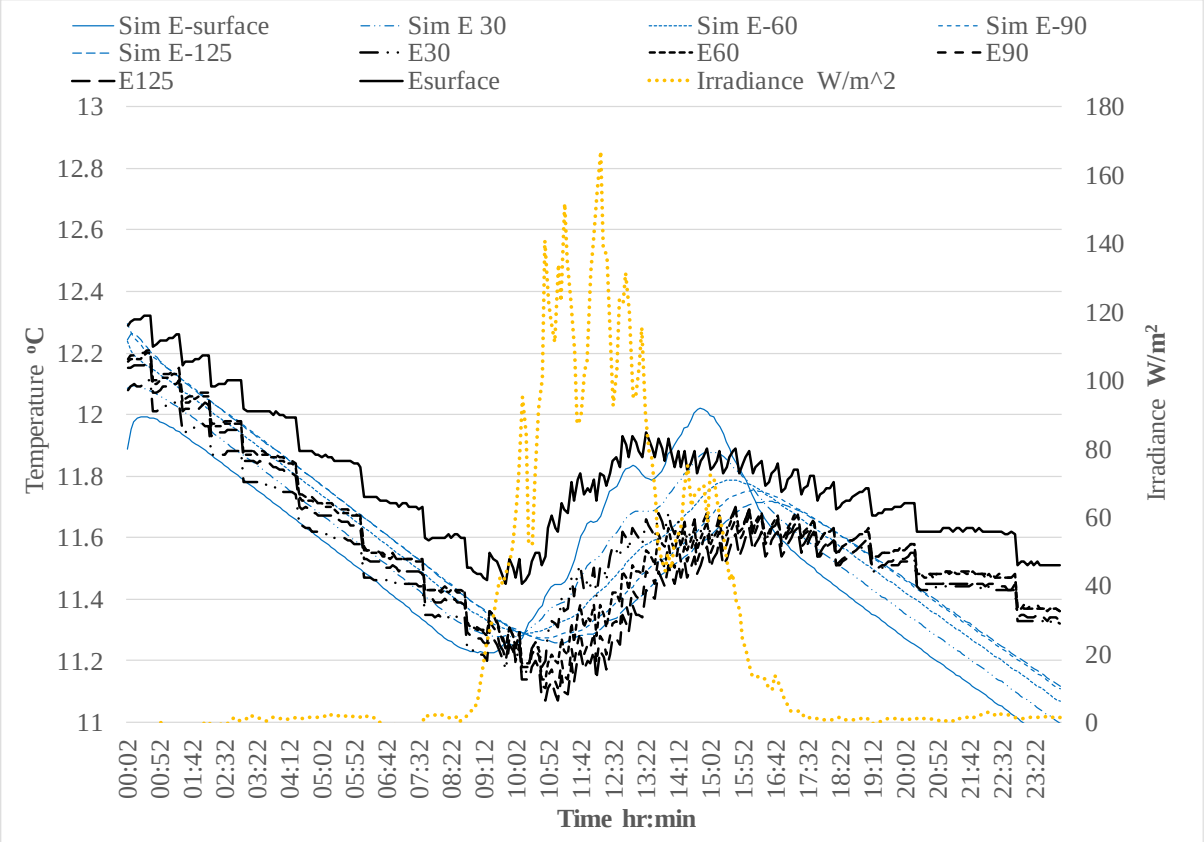


**19th November 2017, Control hut, East wall inner leaf simulated versus actual temperatures**

| Depth | Average $\lvert T_{sim} - T_{act} \rvert$ (°C) | Standard deviation (°C) | Accuracy of simulated temperatures (°C) |
|---|---|---|---|
| Surface | 0.28 | 0.14 | 1.15 |
| 30 mm | 0.09 | 0.09 | 0.96 |
| 60 mm | 0.08 | 0.08 | 0.95 |
| 90 mm | 0.08 | 0.06 | 0.95 |
| 125 mm | 0.09 | 0.05 | 0.96 |

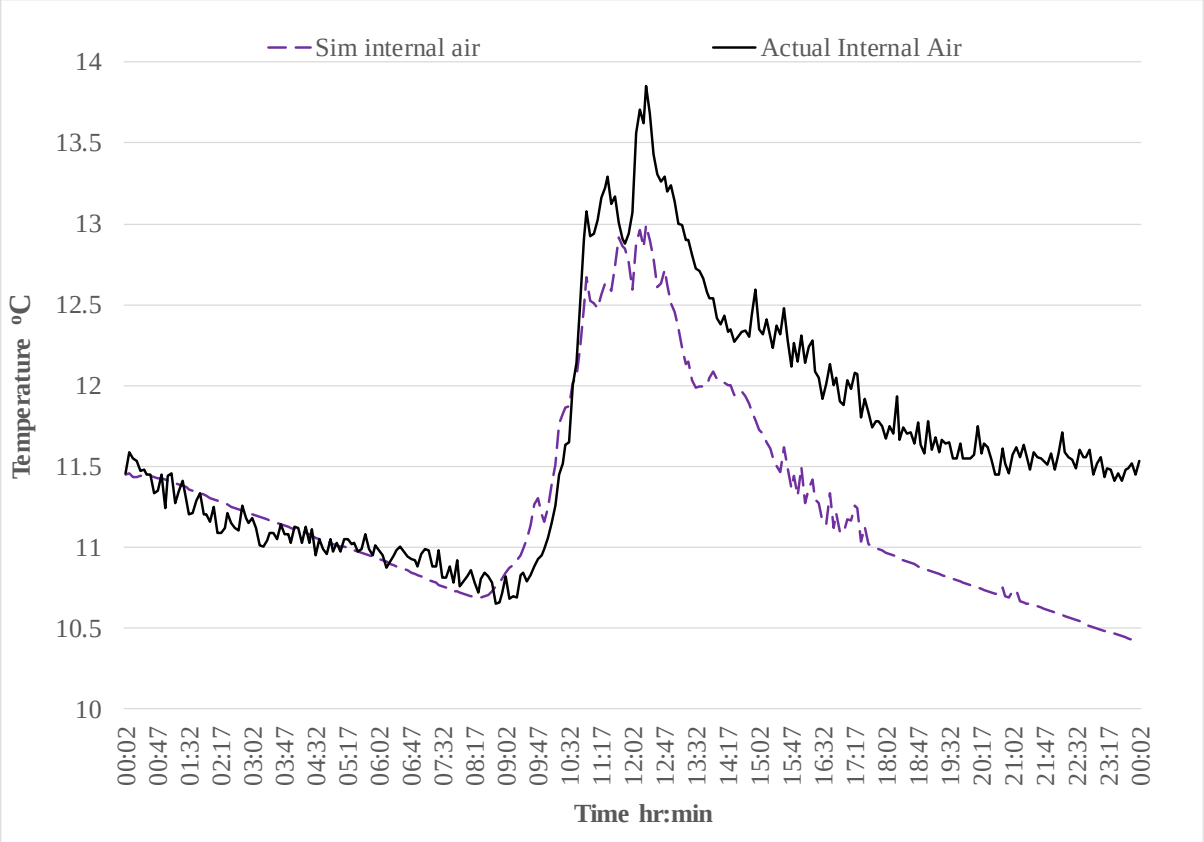


**19th November 2017, Control hut, simulated versus actual internal air temperatures**

| Average $\|T_{sim} - T_{act}\|$ (°C) of internal air | Standard deviation (°C) | Accuracy of simulated temperatures (°C) |
|---|---|---|
| 0.46 | 0.37 | 1.33 |

## 2. 21st June 2017 Control hut –summer passive conditions:

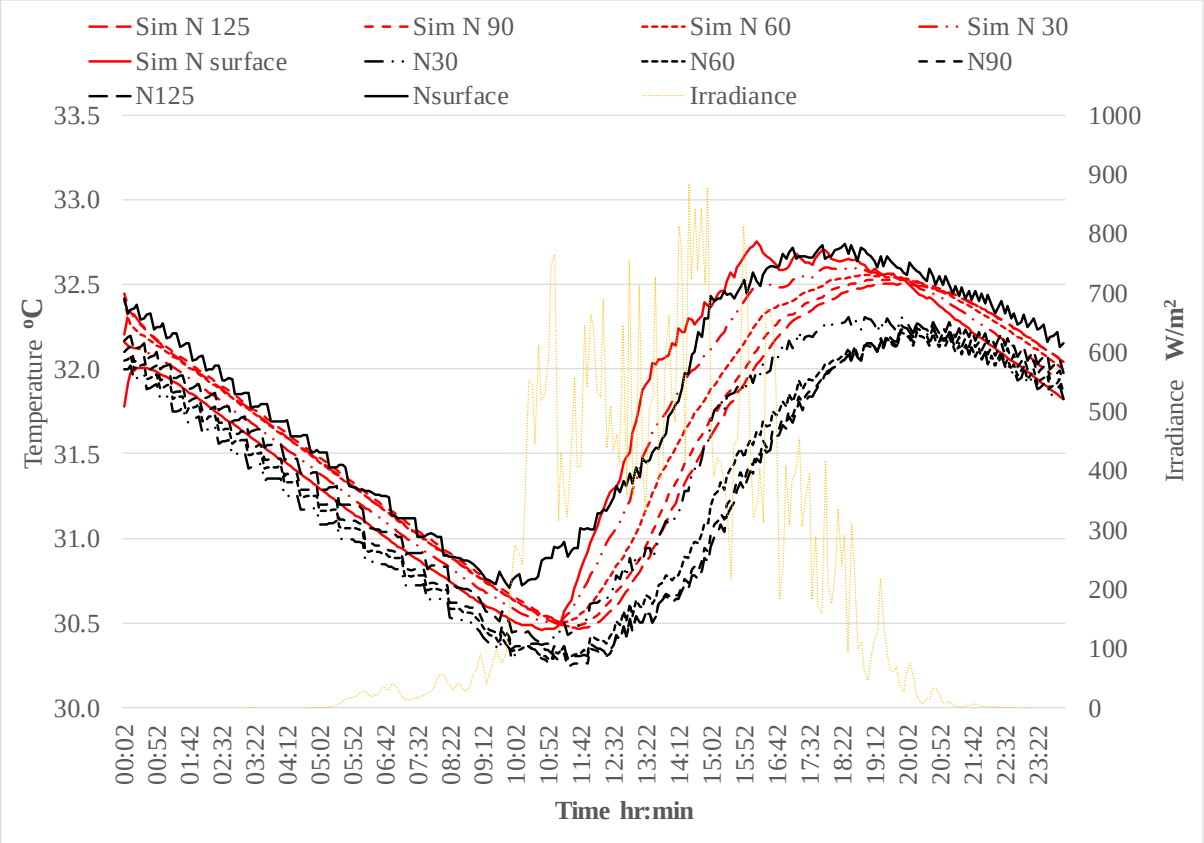


**21st June 2017, Control hut, North wall inner leaf simulated versus actual temperatures**

| Depth | Average $\lvert T_{sim} - T_{act} \rvert$ (°C) | Standard deviation (°C) | Accuracy of simulated temperatures (°C) |
|---|---|---|---|
| Surface | 0.20 | 0.11 | 1.07 |
| 30 mm | 0.28 | 0.14 | 1.15 |
| 60 mm | 0.34 | 0.17 | 1.21 |
| 90 mm | 0.32 | 0.16 | 1.19 |
| 125 mm | 0.24 | 0.18 | 1.11 |

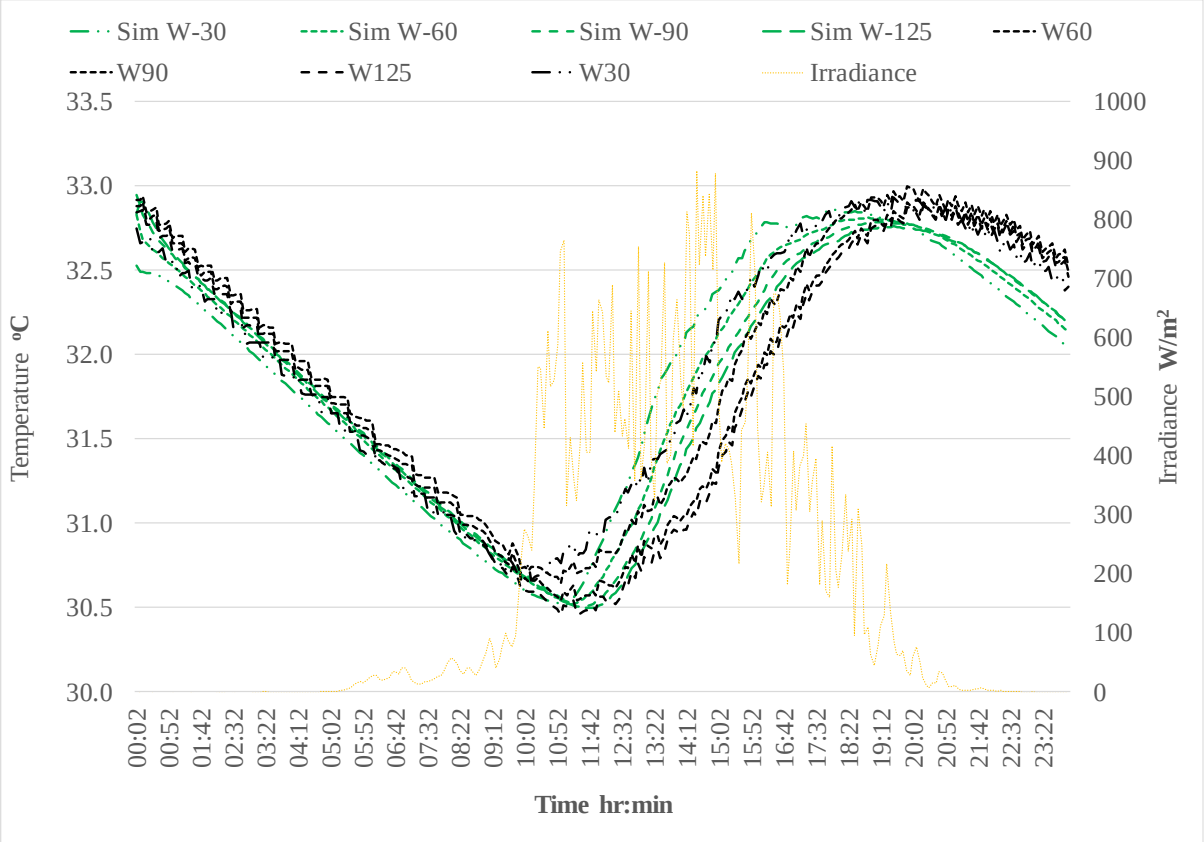


**21st June 2017, Control hut, West wall inner leaf simulated versus actual temperatures**

| Depth | Average $\lvert T_{sim} - T_{act} \rvert$ (°C) | Standard deviation (°C) | Accuracy of simulated temperatures (°C) |
|---|---|---|---|
| 30 mm | 0.15 | 0.12 | 1.02 |
| 60 mm | 0.19 | 0.12 | 1.06 |
| 90 mm | 0.14 | 0.15 | 1.01 |
| 125 mm | 0.13 | 0.14 | 1.00 |

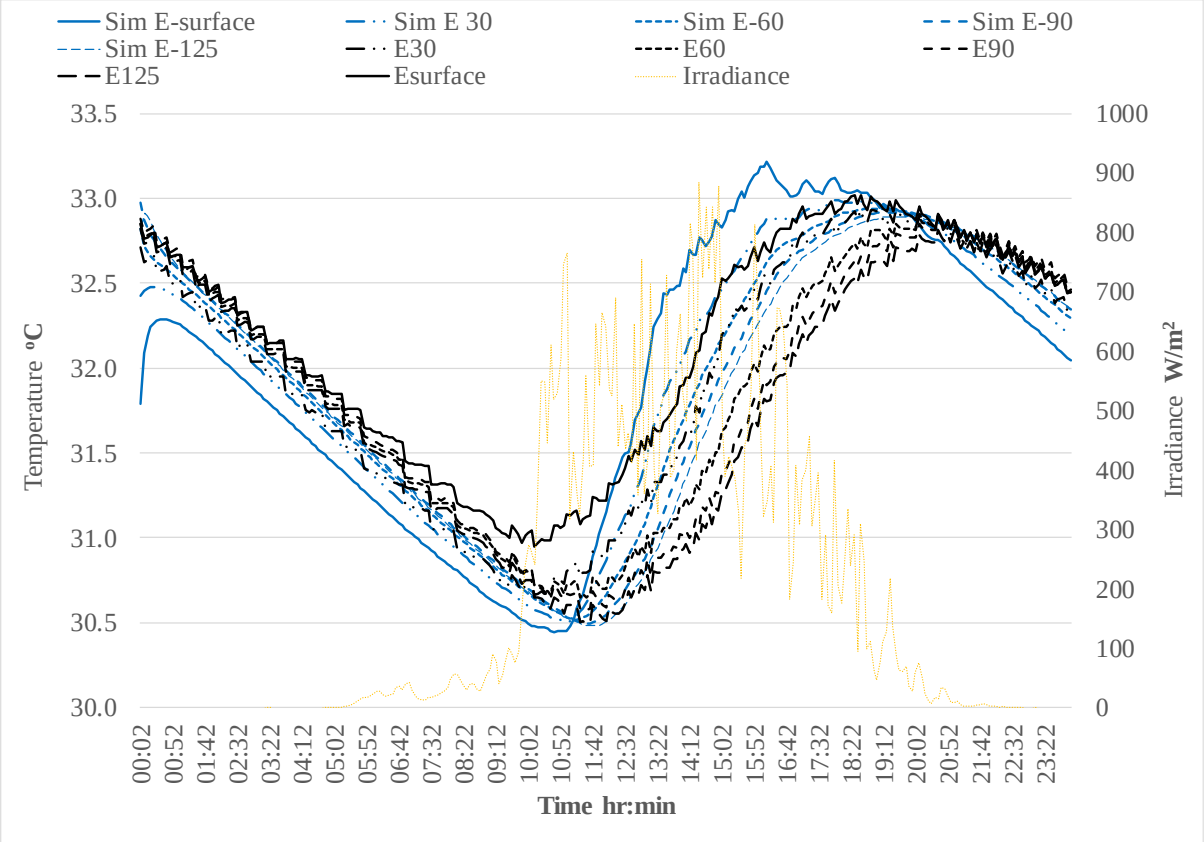


**21st June 2017, Control hut, East wall inner leaf simulated versus actual temperatures**

| Depth | Average $\lvert T_{sim} - T_{act} \rvert$ (ºC) | Standard deviation (ºC) | Accuracy of simulated temperatures (ºC) |
|---|---|---|---|
| Surface | 0.36 | 0.18 | 1.23 |
| 30 mm | 0.13 | 0.13 | 1.00 |
| 60 mm | 0.18 | 0.15 | 1.05 |
| 90 mm | 0.18 | 0.17 | 1.05 |
| 125 mm | 0.16 | 0.18 | 1.03 |

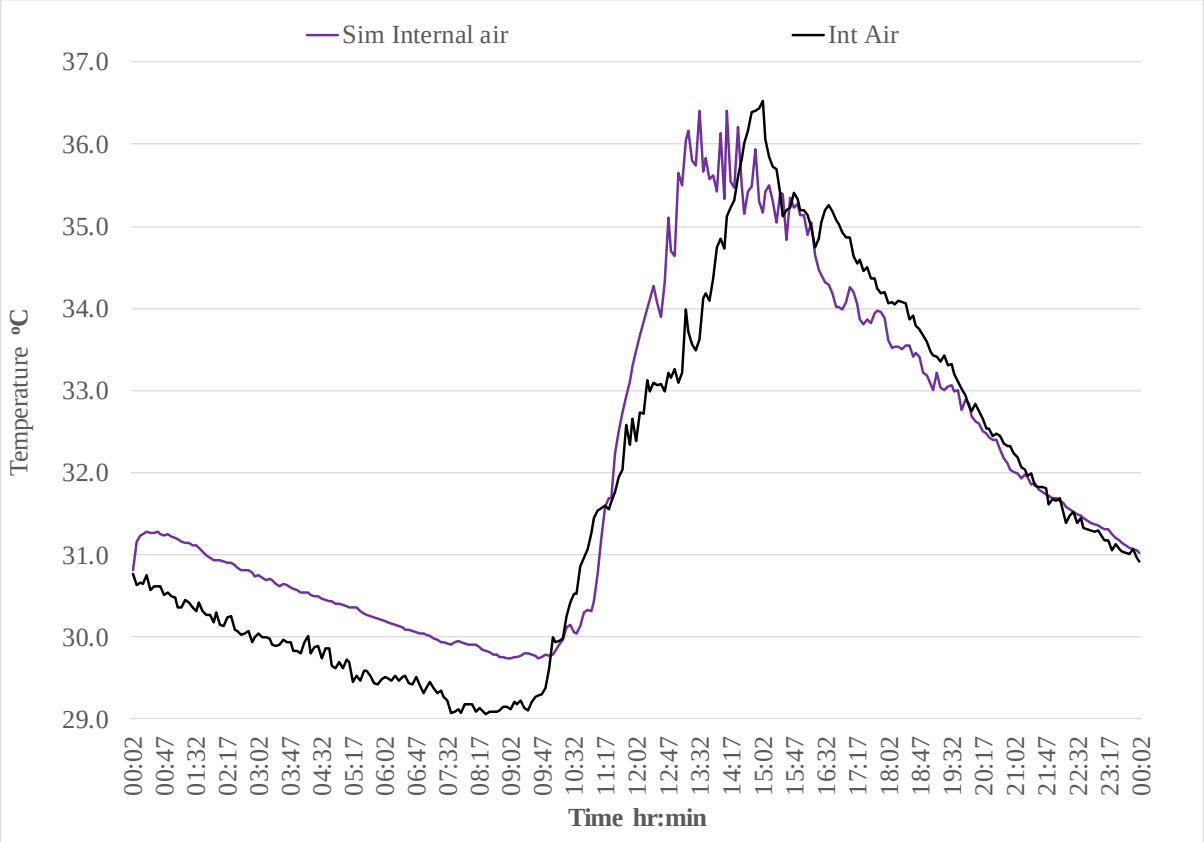


**21st June 2017, Control hut, simulated versus actual internal air temperatures**

| Average $\|T_{sim} - T_{act}\|$ (ºC) of internal air | Standard deviation (ºC) | Accuracy of simulated temperatures (ºC) |
|---|---|---|
| 0.59 | 0.44 | 1.46 |

### 3. 1st November 2018 Control hut -winter passive conditions,

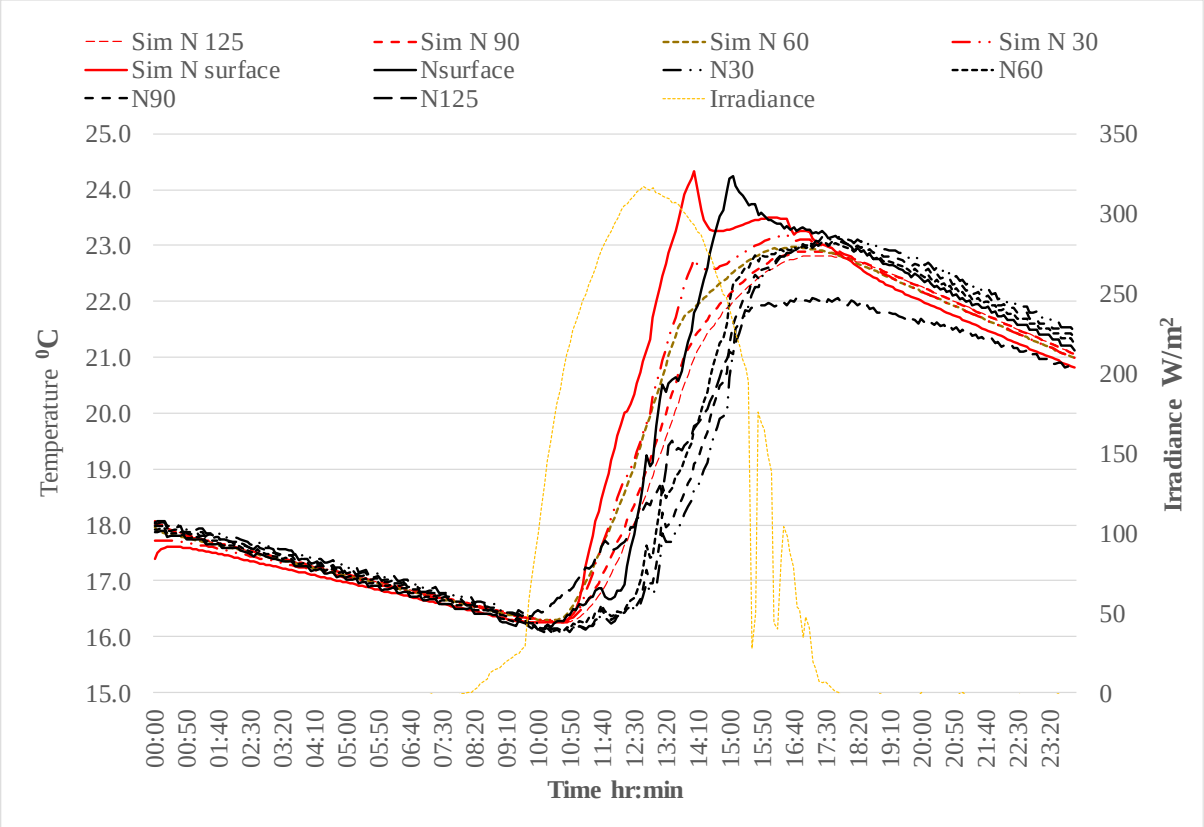


**1st November 2018, Control hut, North wall inner leaf simulated versus actual temperatures**

| Depth | Average $\|T_{sim} - T_{act}\|$ (°C) | Standard deviation (°C) | Accuracy of simulated temperatures (°C) |
|---|---|---|---|
| Surface | 0.47 | 0.76 | 1.34 |
| 30 mm | 0.71 | 1.04 | 1.58 |
| 60 mm | 0.41 | 0.68 | 1.28 |
| 90 mm | 0.39 | 0.61 | 1.26 |
| 125 mm | 0.37 | 0.34 | 1.24 |

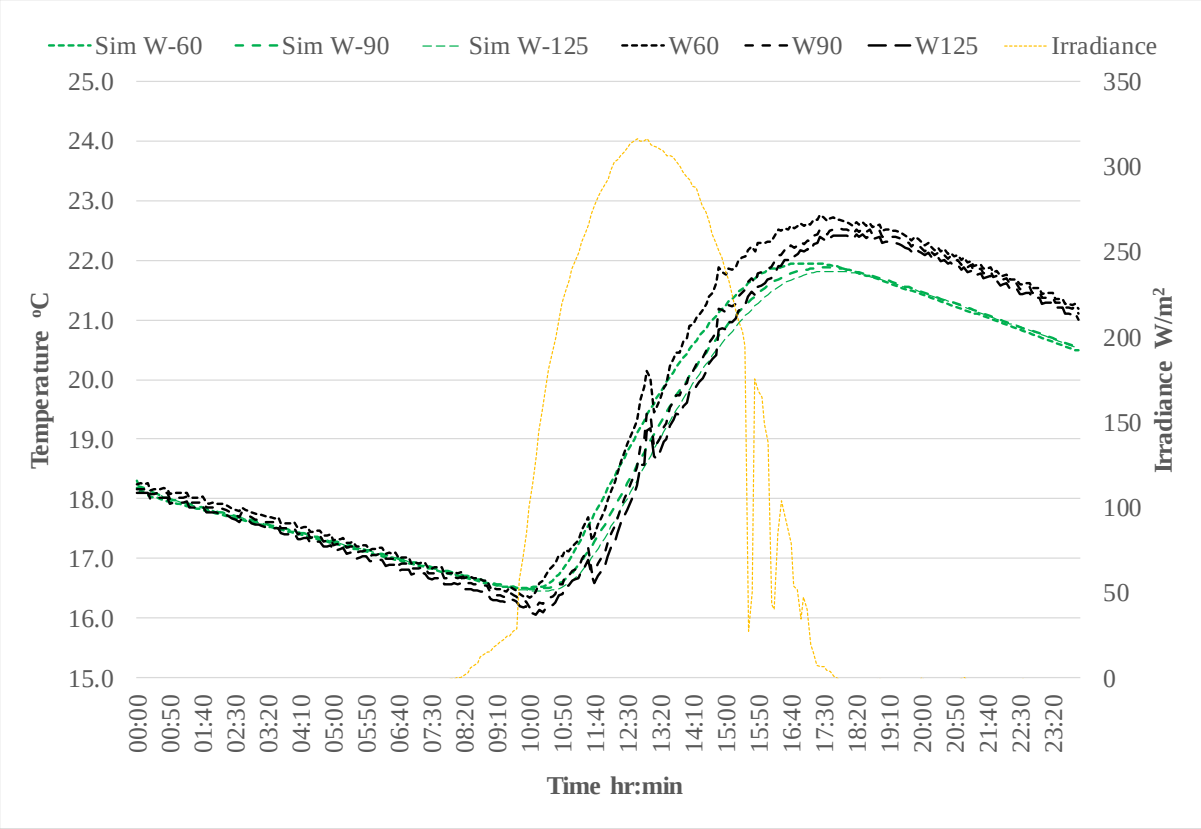


**1st November 2018, Control hut, West wall inner leaf simulated versus actual temperatures**

| Depth | Average $\lvert T_{sim} - T_{act} \rvert$ (°C) | Standard deviation (°C) | Accuracy of simulated temperatures (°C) |
|---|---|---|---|
| 60 mm | 0.38 | 0.32 | 1.25 |
| 90 mm | 0.29 | 0.28 | 1.16 |
| 125 mm | 0.29 | 0.23 | 1.16 |

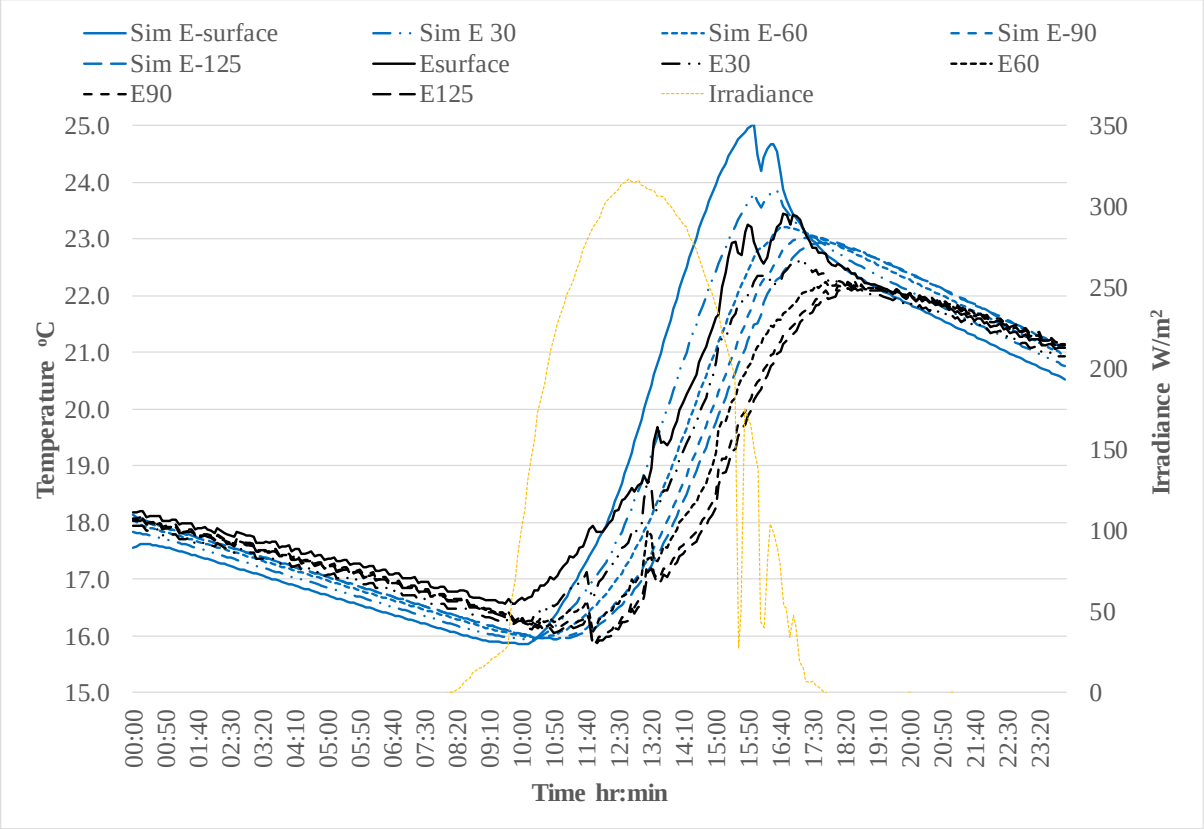


**1st November 2018, Control hut, East wall inner leaf simulated versus actual temperatures**

| Depth | Average $\lvert T_{sim} - T_{act} \rvert$ (°C) | Standard deviation (°C) | Accuracy of simulated temperatures (°C) |
|---|---|---|---|
| Surface | 0.69 | 0.58 | 1.56 |
| 30 mm | 0.44 | 0.47 | 1.31 |
| 60 mm | 0.47 | 0.50 | 1.34 |
| 90 mm | 0.44 | 0.47 | 1.31 |
| 125 mm | 0.40 | 0.42 | 1.27 |

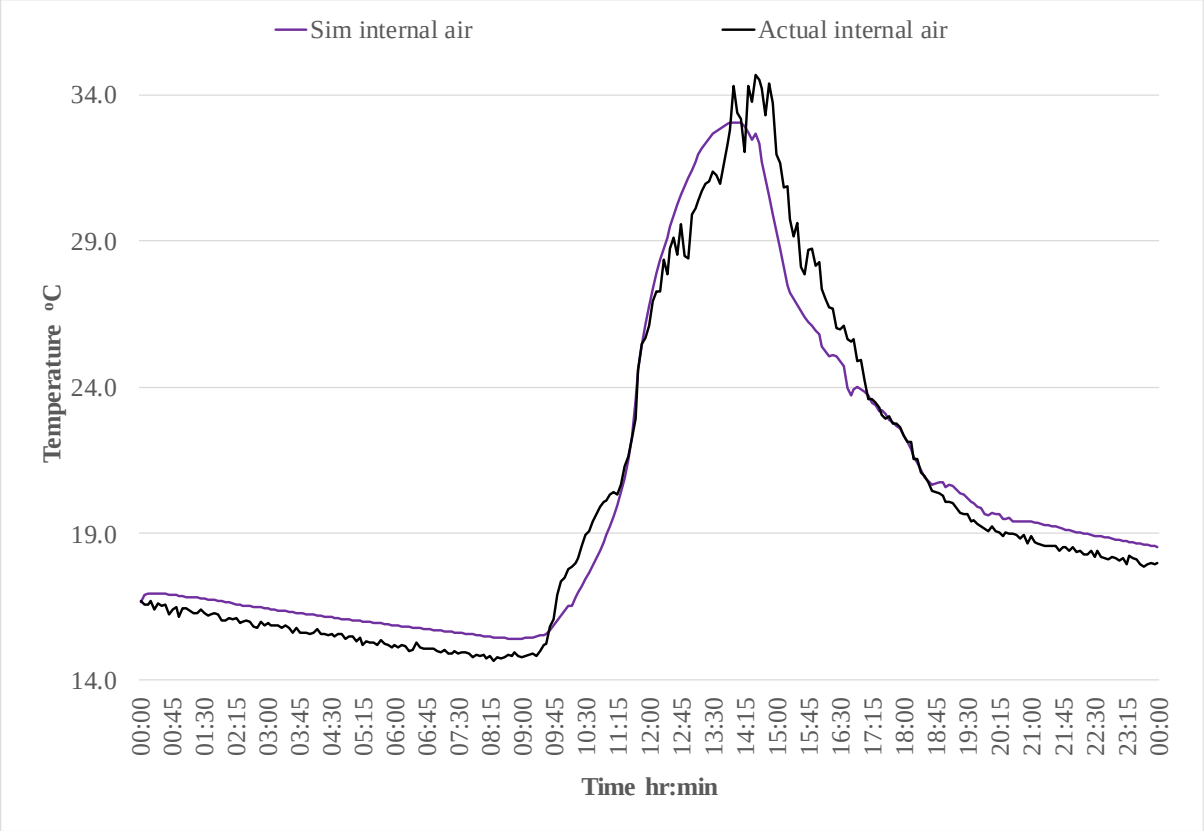


**1st November 2018, Control hut, simulated versus actual internal air temperatures**

| Average $\lvert T_{sim} - T_{act} \rvert$ (ºC) of internal air | Standard deviation (ºC) | Accuracy of simulated temperatures (ºC) |
|---|---|---|
| 0.81 | 0.65 | 1.68 |

## 4. 10th June 2017 Control hut –summer passive conditions

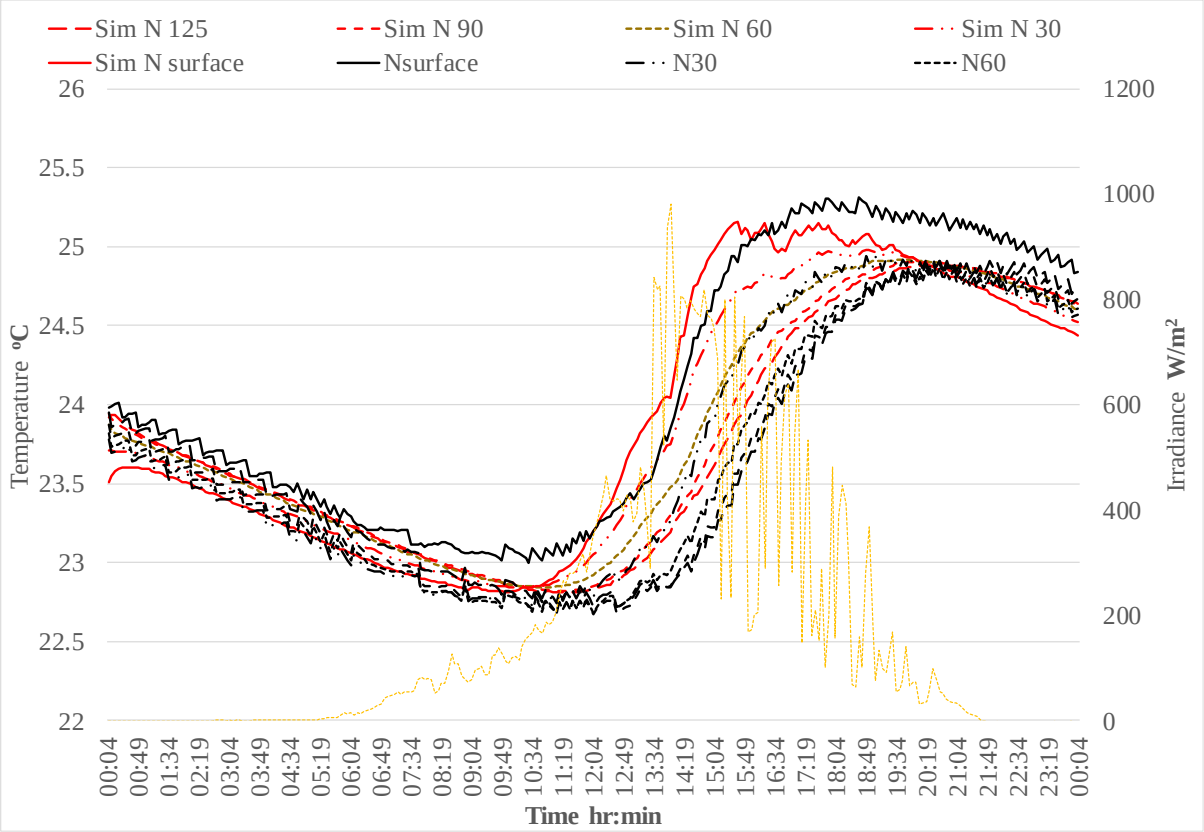


**10th June 2017 Control hut, North wall inner leaf simulated versus actual temperatures**

| Depth | Average $\lvert T_{sim} - T_{act} \rvert$ (°C) | Standard deviation (°C) | Accuracy of simulated temperatures (°C) |
|---|---|---|---|
| Surface | 0.25 | 0.10 | 1.12 |
| 30 mm | 0.14 | 0.15 | 1.01 |
| 60 mm | 0.18 | 0.16 | 1.05 |
| 90 mm | 0.15 | 0.13 | 1.02 |
| 125 mm | 0.11 | 0.12 | 0.97 |

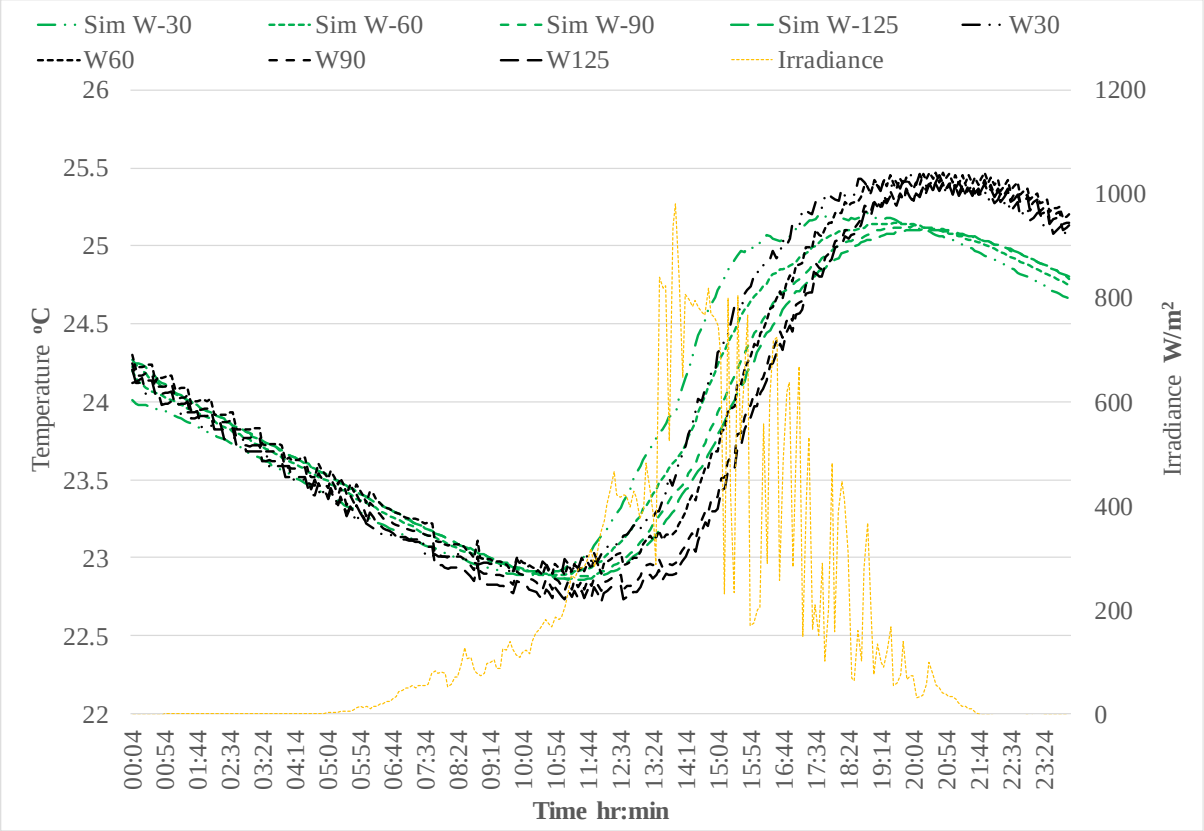


**10th June 2017 Control hut, West wall inner leaf simulated versus actual temperatures**

| Depth | Average $\lvert T_{sim} - T_{act} \rvert$ (°C) | Standard deviation (°C) | Accuracy of simulated temperatures (°C) |
|---|---|---|---|
| 30 mm | 0.17 | 0.16 | 1.04 |
| 60 mm | 0.18 | 0.16 | 1.05 |
| 90 mm | 0.17 | 0.15 | 1.04 |
| 125 mm | 0.19 | 0.11 | 1.06 |

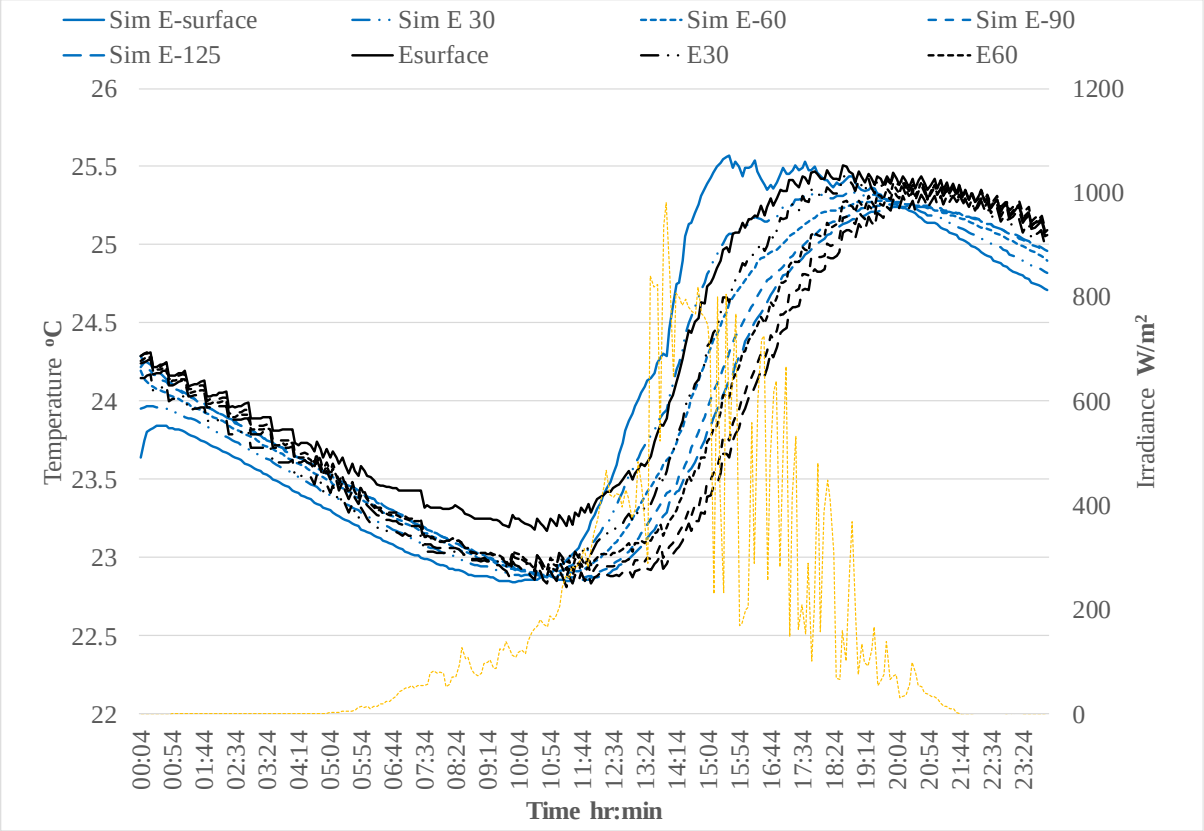


**10th June 2017 Control hut, East wall inner leaf simulated versus actual temperatures**

| Depth | Average $\lvert T_{sim} - T_{act} \rvert$ (°C) | Standard deviation (°C) | Accuracy of simulated temperatures (°C) |
|---|---|---|---|
| Surface | 0.32 | 0.15 | 1.19 |
| 30 mm | 0.13 | 0.13 | 1.00 |
| 60 mm | 0.14 | 0.14 | 1.01 |
| 90 mm | 0.13 | 0.14 | 1.00 |
| 125 mm | 0.11 | 0.13 | 0.99 |

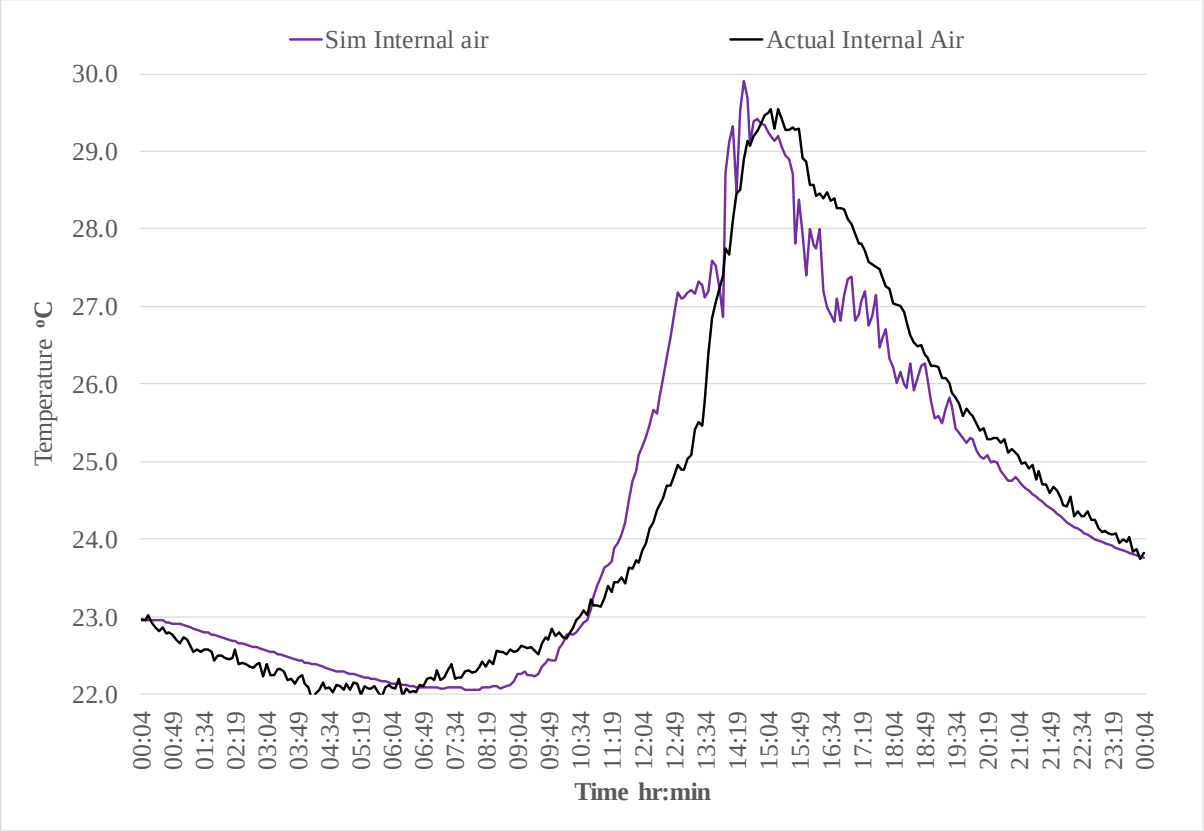


**21st June 2017, Control hut, simulated versus actual internal air temperatures**

| Average $\lvert T_{sim} - T_{act} \rvert$ (°C) of internal air | Standard deviation (°C) | Accuracy of simulated temperatures (°C) |
|---|---|---|
| 0.45 | 0.47 | 1.32 |

## B. Validation of COMSOL model for Full PCM hut

### 5. 19th November 2017 Full PCM hut -winter passive conditions,

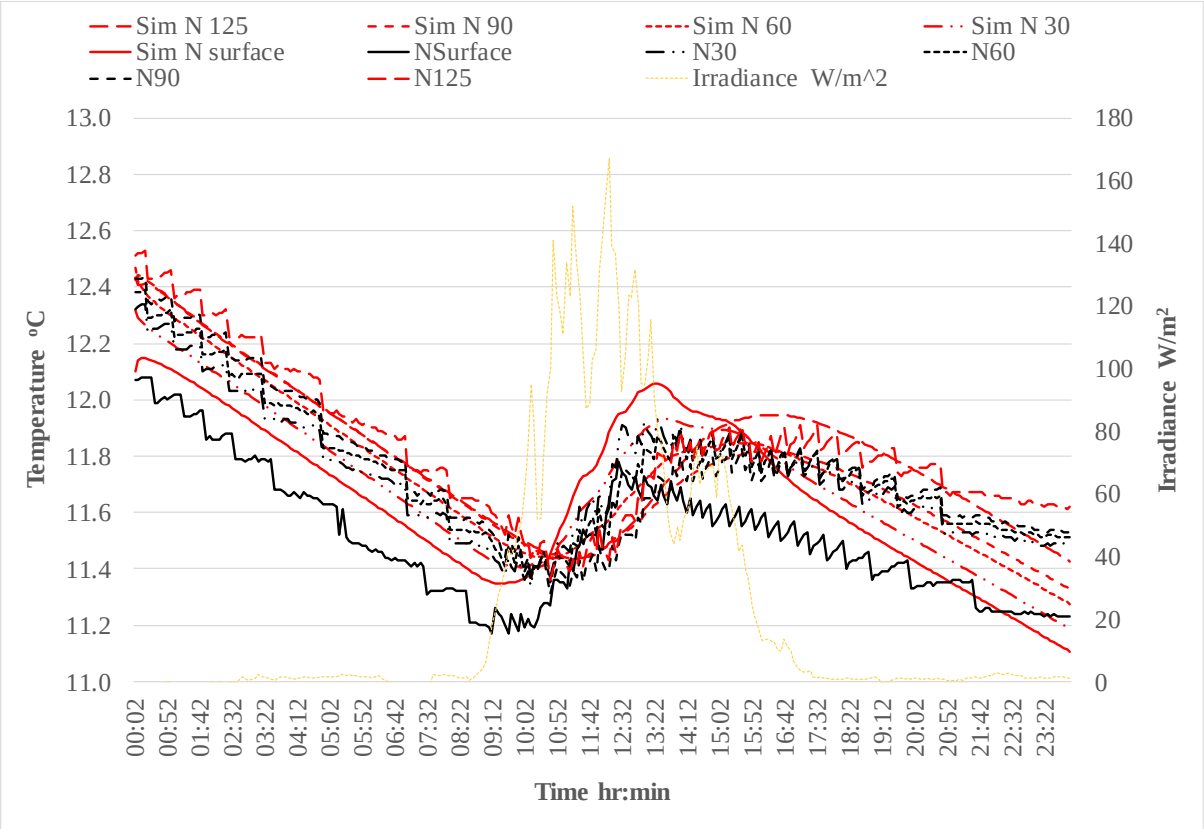


**19th November 2017, Full PCM hut, North wall inner leaf simulated versus actual temperatures**

| Depth | Average $\lvert T_{sim} - T_{act} \rvert$ (ºC) | Standard deviation (ºC) | Accuracy of simulated temperatures (ºC) |
|---|---|---|---|
| Surface | 0.16 | 0.09 | 1.03 |
| 30 mm | 0.06 | 0.07 | 0.93 |
| 60 mm | 0.05 | 0.05 | 0.92 |
| 90 mm | 0.05 | 0.04 | 0.92 |
| 125 mm | 0.06 | 0.04 | 0.93 |

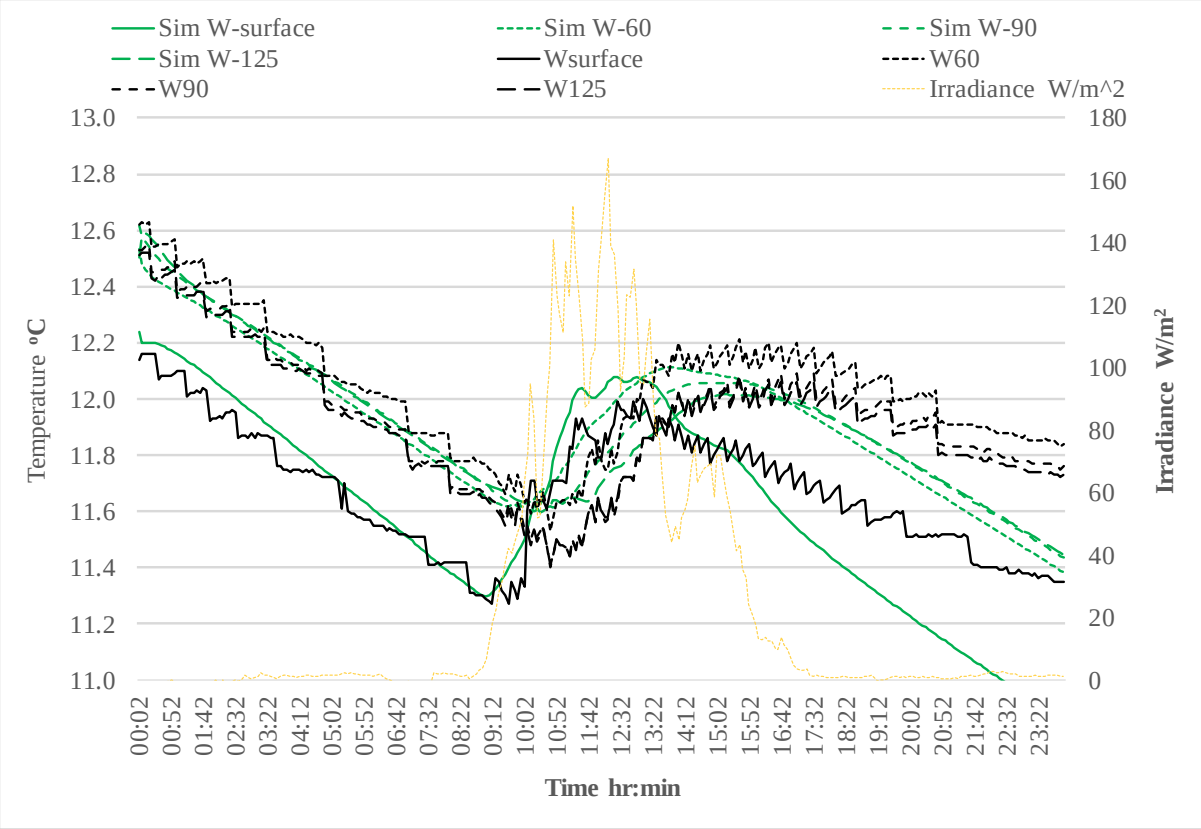


**19th November 2017, Full PCM hut, West wall inner leaf simulated versus actual temperatures**

| Depth | Average $\lvert T_{sim} - T_{act} \rvert$ (ºC) | Standard deviation (ºC) | Accuracy of simulated temperatures (ºC) |
|---|---|---|---|
| Surface | 0.15 | 0.14 | 1.01 |
| 60 mm | 0.16 | 0.11 | 1.03 |
| 90 mm | 0.10 | 0.08 | 0.97 |
| 125 mm | 0.08 | 0.06 | 0.95 |

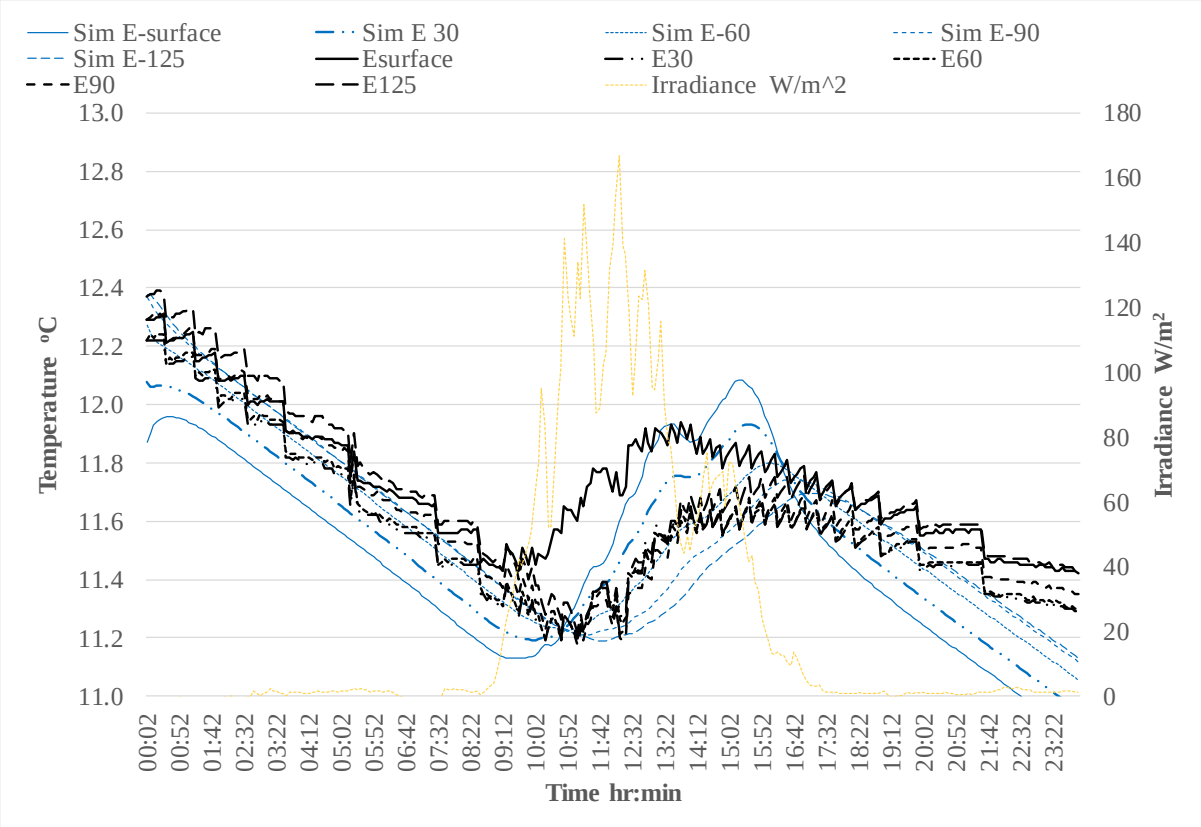


**19th November 2017, Full PCM hut, East wall inner leaf simulated versus actual temperatures**

| Depth | Average $\lvert T_{sim} - T_{act} \rvert$ (ºC) | Standard deviation (ºC) | Accuracy of simulated temperatures (ºC) |
|---|---|---|---|
| Surface | 0.28 | 0.12 | 1.15 |
| 30 mm | 0.13 | 0.08 | 1.00 |
| 60 mm | 0.06 | 0.06 | 0.93 |
| 90 mm | 0.06 | 0.05 | 0.93 |
| 125 mm | 0.11 | 0.08 | 0.98 |

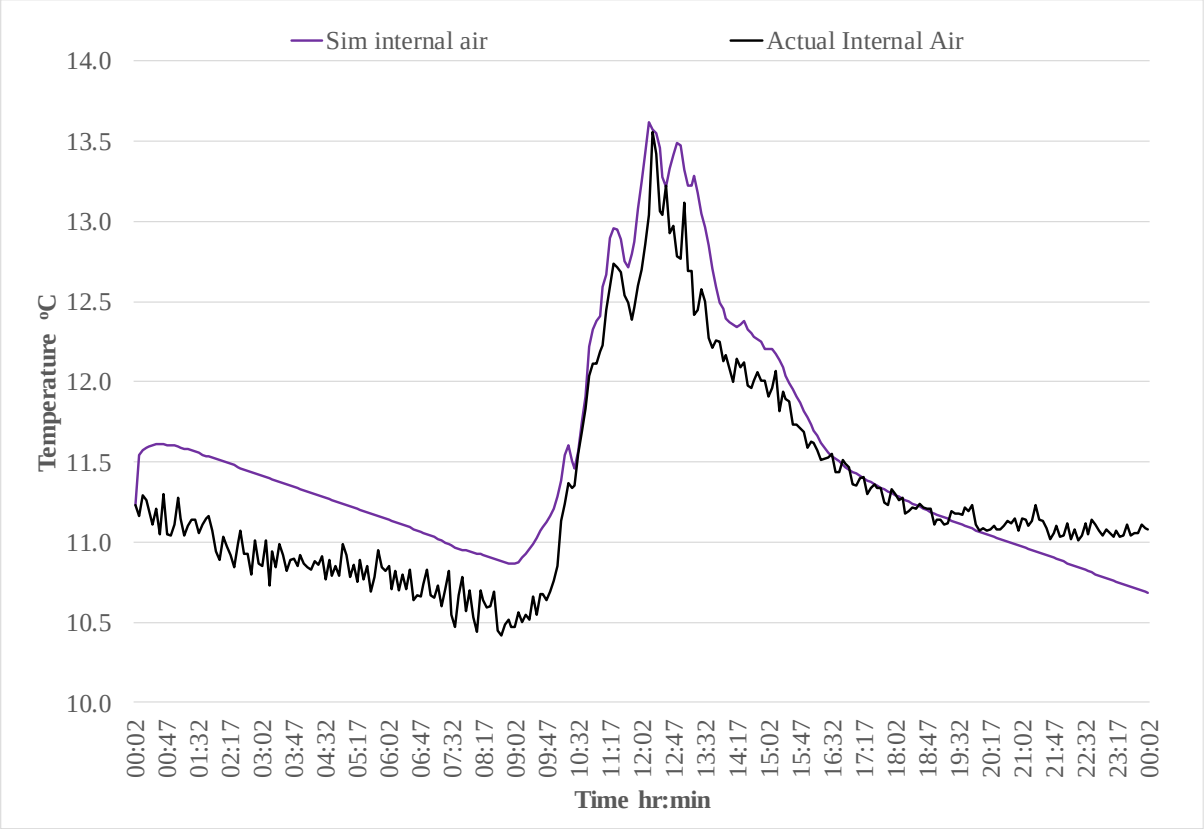


**19th November 2017, Full PCM hut, simulated versus actual internal air temperatures**

| Average $\lvert T_{sim} - T_{act} \rvert$ (ºC) of internal air | Standard deviation (ºC) | Accuracy of simulated temperatures (ºC) |
|---|---|---|
| 0.3 | 0.18 | 1.17 |

## 6. 21st June 2017 Full PCM hut –summer passive conditions

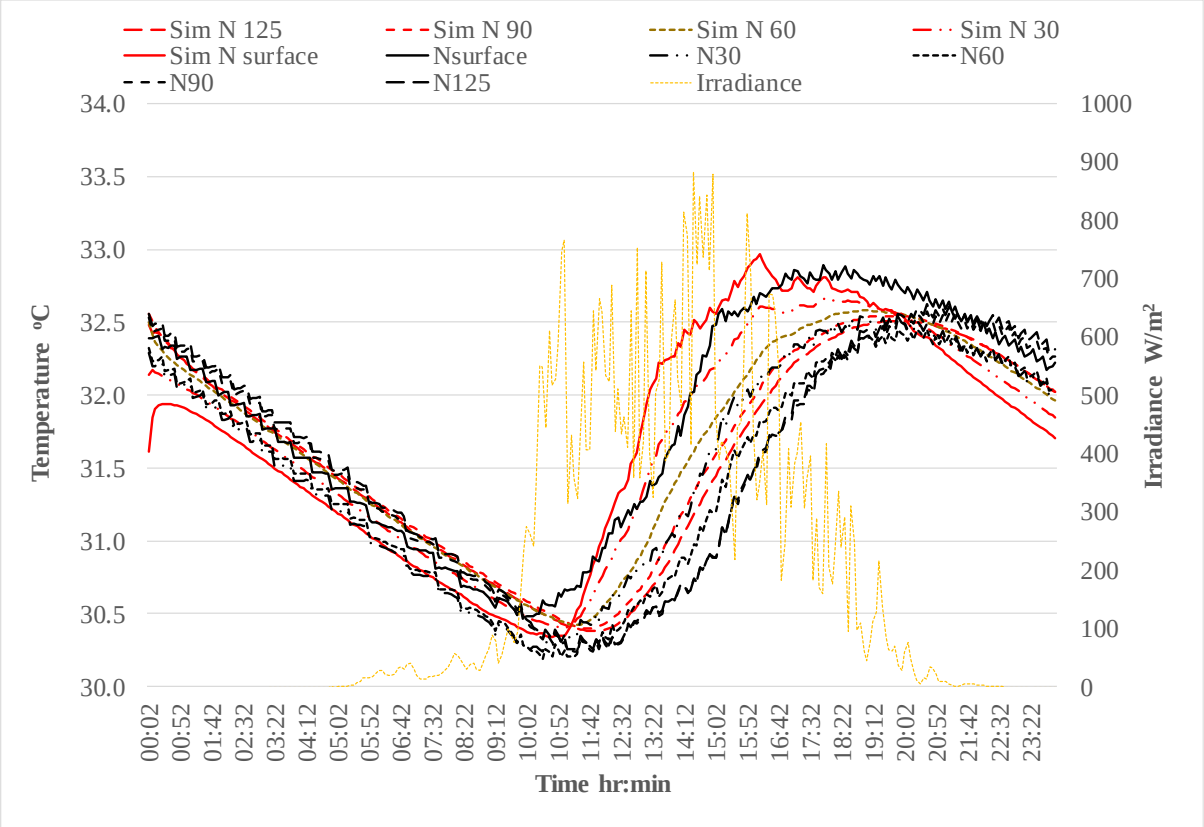


**21st June 2017 , Full PCM hut, North wall inner leaf simulated versus actual temperatures**

| Depth | Average $\lvert T_{sim} - T_{act} \rvert$ (°C) | Standard deviation (°C) | Accuracy of simulated temperatures (°C) |
|---|---|---|---|
| Surface | 0.24 | 0.15 | 1.11 |
| 30 mm | 0.20 | 0.19 | 1.07 |
| 60 mm | 0.23 | 0.16 | 1.10 |
| 90 mm | 0.17 | 0.17 | 1.04 |
| 125 mm | 0.15 | 0.12 | 1.02 |

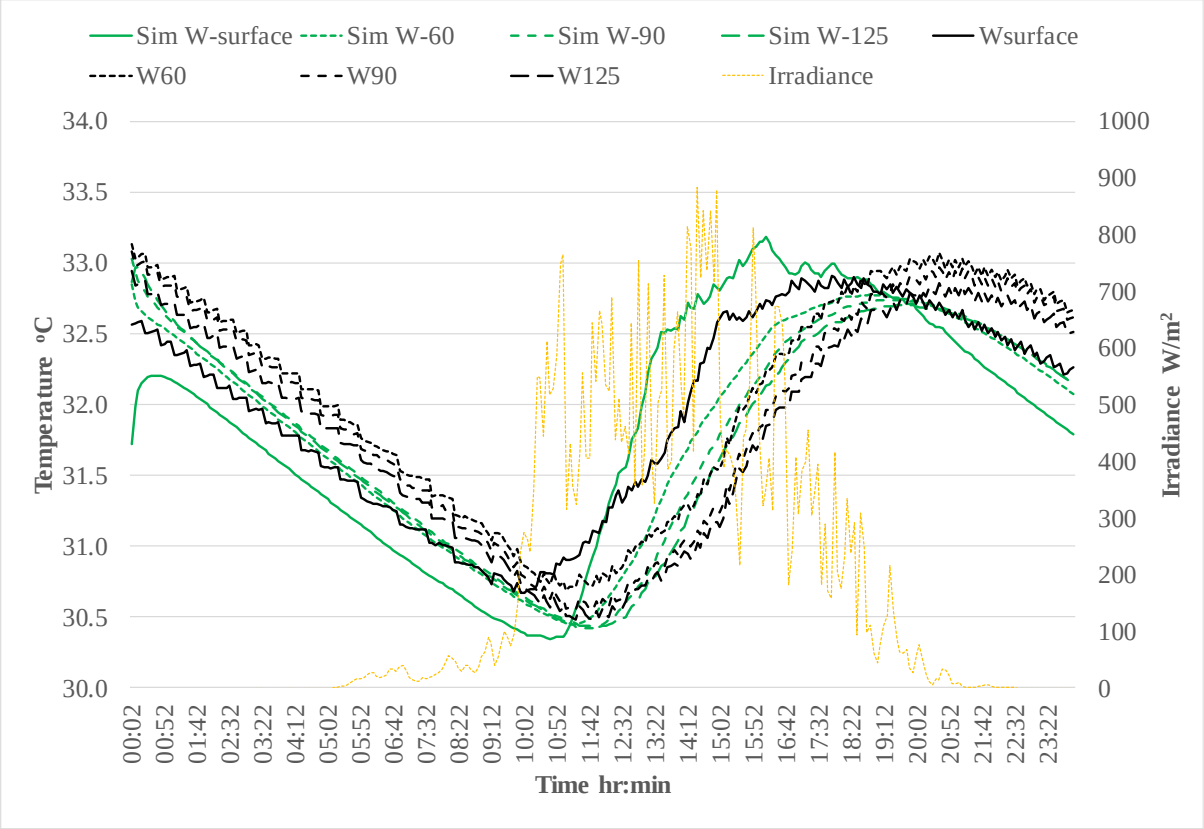


**21st June 2017 , Full PCM hut, West wall inner leaf simulated versus actual temperatures**

| Depth | Average $\lvert T_{sim} - T_{act} \rvert$ (ºC) | Standard deviation (ºC) | Accuracy of simulated temperatures (ºC) |
|---|---|---|---|
| Surface | 0.28 | 0.16 | 1.15 |
| 60 mm | 0.32 | 0.13 | 1.19 |
| 90 mm | 0.24 | 0.11 | 1.11 |
| 125 mm | 0.17 | 0.10 | 1.04 |

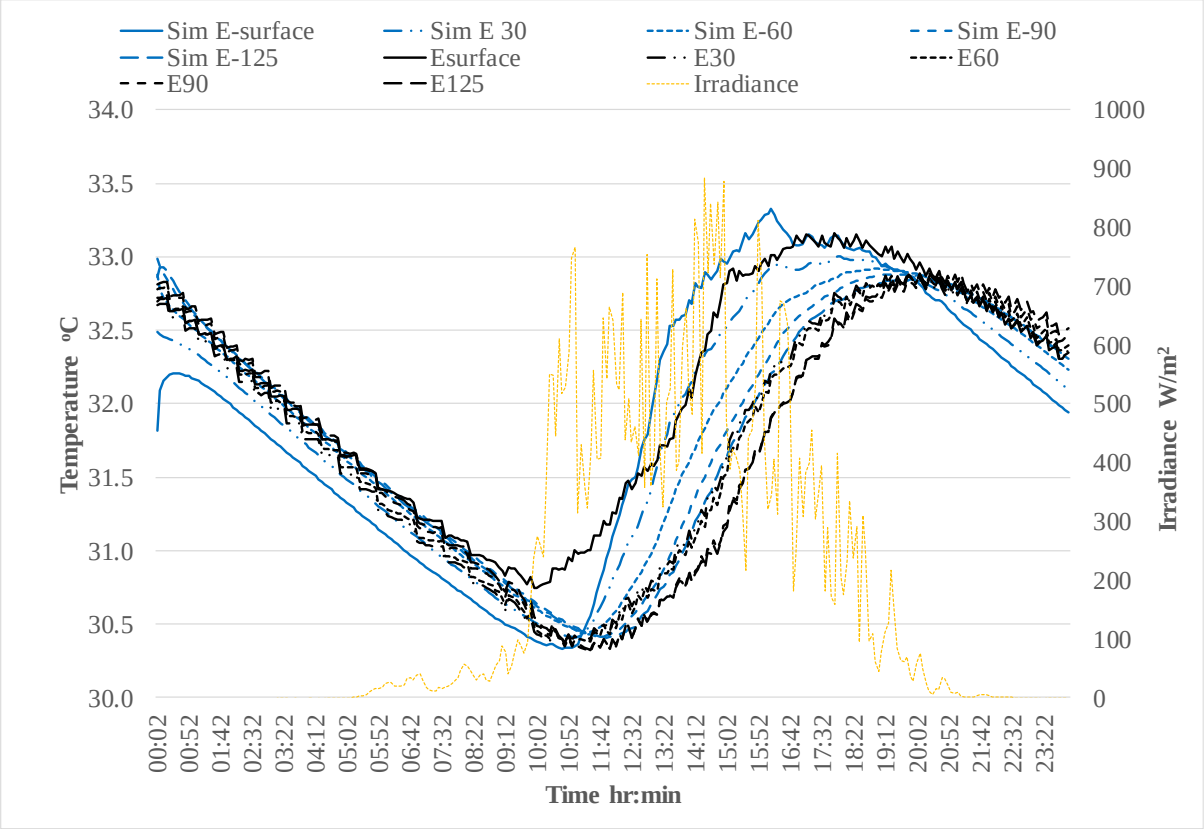


**21st June 2017 , Full PCM hut, East wall inner leaf simulated versus actual temperatures**

| Depth | Average $\lvert T_{sim} - T_{act} \rvert$ (°C) | Standard deviation (°C) | Accuracy of simulated temperatures (°C) |
|---|---|---|---|
| Surface | 0.30 | 0.16 | 1.17 |
| 30 mm | 0.24 | 0.29 | 1.11 |
| 60 mm | 0.14 | 0.12 | 1.01 |
| 90 mm | 0.14 | 0.17 | 1.01 |
| 125 mm | 0.11 | 0.12 | 0.98 |

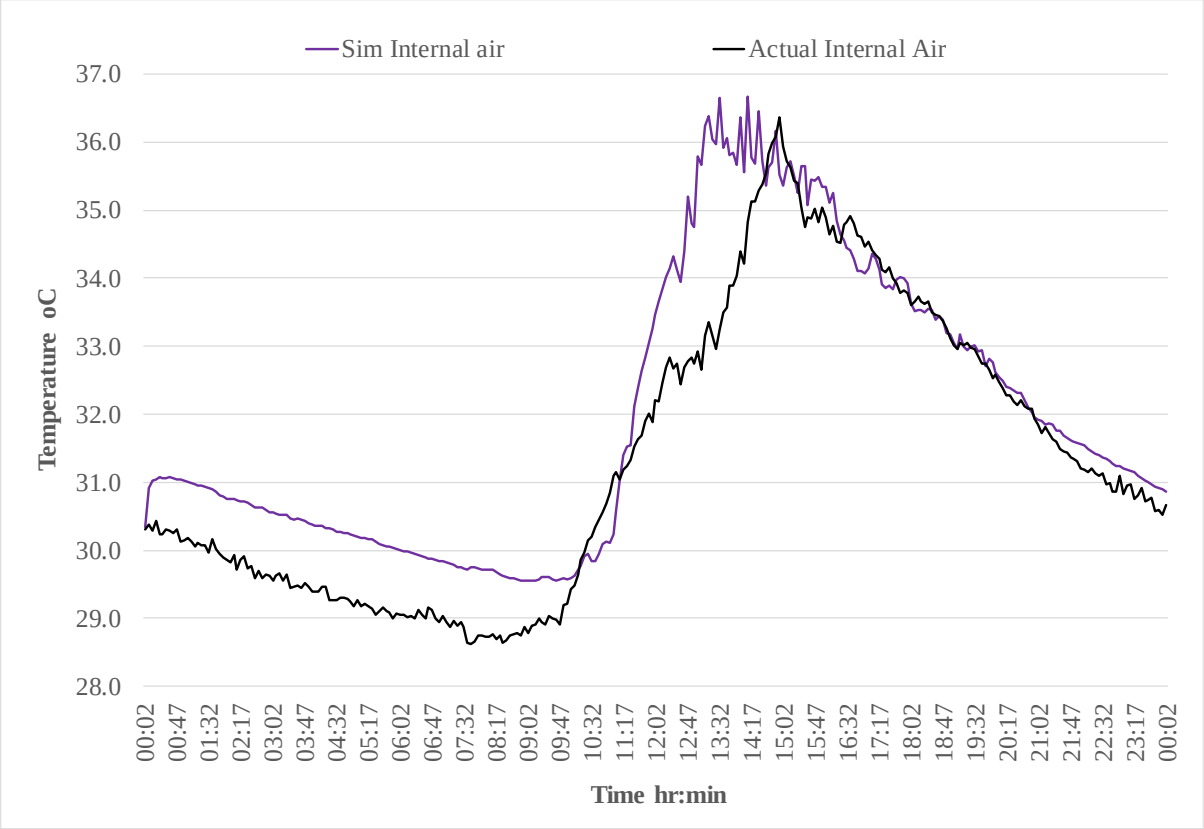


**21st June 2017 Full PCM hut, simulated versus actual internal air temperatures**

| Average $\|T_{sim} - T_{act}\|$ (ºC) of internal air | Standard deviation (ºC) | Accuracy of simulated temperatures (ºC) |
|---|---|---|
| 0.7 | 0.60 | 1.57 |

## 7. 1st November 2018 Full PCM hut -winter passive conditions

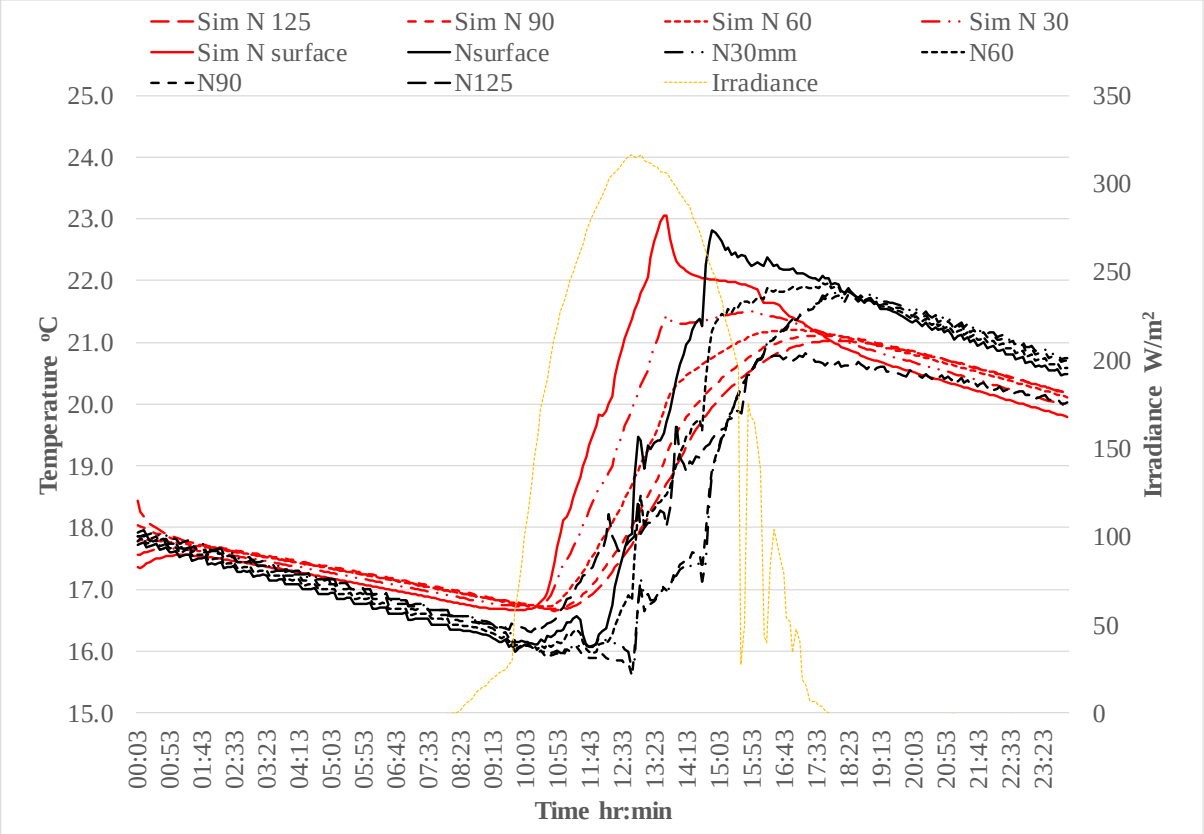


**1st November 2018, Full PCM hut, North wall inner leaf simulated versus actual temperatures**

| Depth | Average $\lvert T_{sim} - T_{act} \rvert$ (ºC) | Standard deviation (ºC) | Accuracy of simulated temperatures (ºC) |
|---|---|---|---|
| Surface | 0.84 | 0.75 | 1.70 |
| 30 mm | 0.94 | 1.29 | 1.80 |
| 60 mm | 0.59 | 0.13 | 1.45 |
| 90 mm | 0.64 | 0.31 | 1.50 |
| 125 mm | 0.27 | 0.02 | 1.13 |

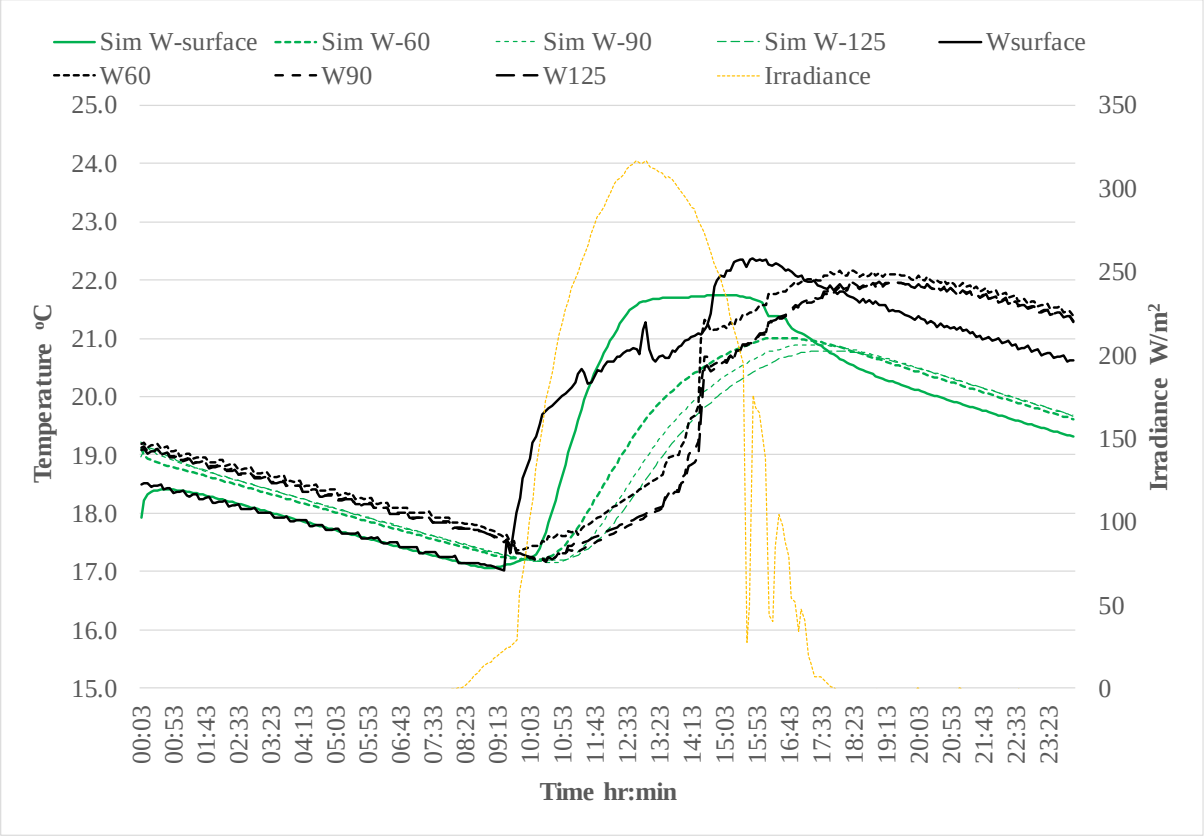


**1st November 2018, Full PCM hut, West wall inner leaf simulated versus actual temperatures**

| Depth | Average $\lvert T_{sim} - T_{act} \rvert$ (ºC) | Standard deviation (ºC) | Accuracy of simulated temperatures (ºC) |
|---|---|---|---|
| Surface | 0.64 | 0.57 | 1.50 |
| 60 mm | 0.79 | 0.57 | 1.65 |
| 90 mm | 0.62 | 0.56 | 1.48 |
| 125 mm | 0.61 | 0.56 | 1.47 |

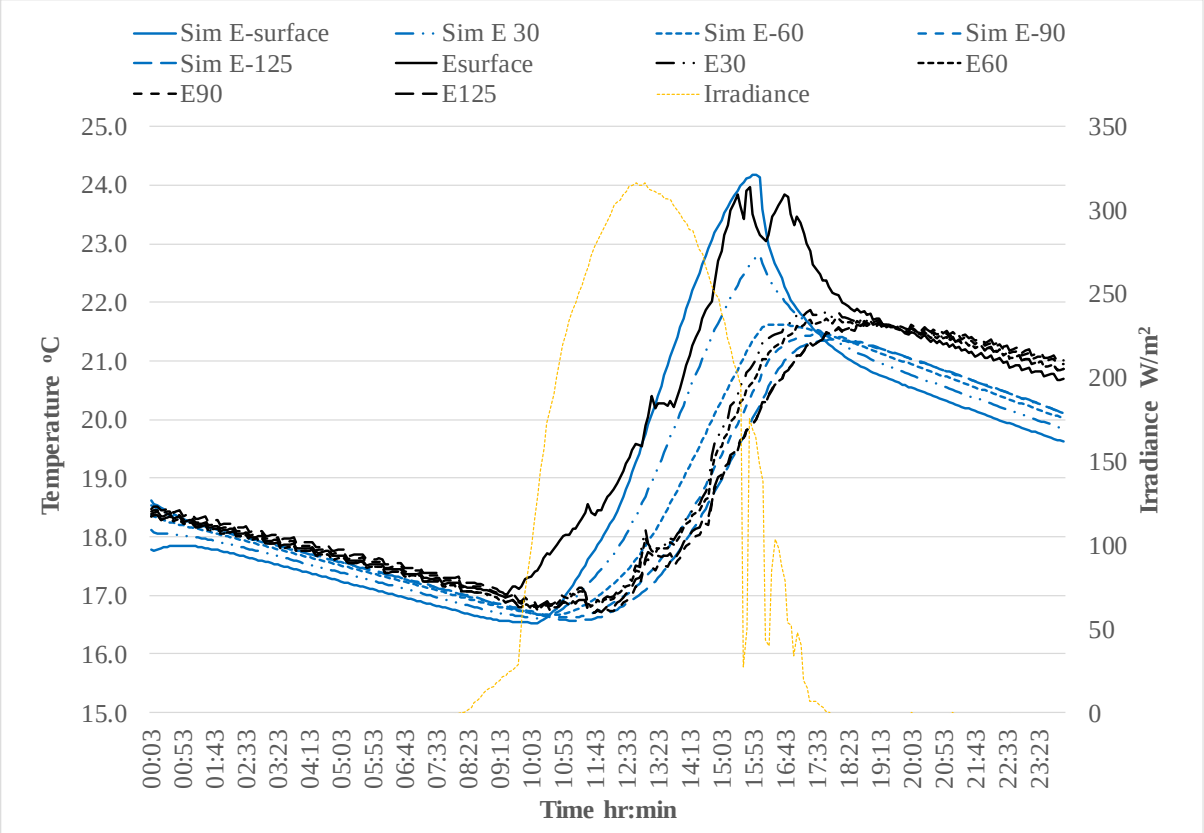


**1st November 2018, Full PCM hut, East wall inner leaf simulated versus actual temperatures**

| Depth | Average $\lvert T_{sim} - T_{act} \rvert$ (°C) | Standard deviation (°C) | Accuracy of simulated temperatures (°C) |
|---|---|---|---|
| Surface | 0.68 | 0.32 | 1.54 |
| 30 mm | 0.62 | 0.56 | 1.48 |
| 60 mm | 0.33 | 0.29 | 1.19 |
| 90 mm | 0.29 | 0.24 | 1.15 |
| 125 mm | 0.28 | 0.23 | 1.14 |

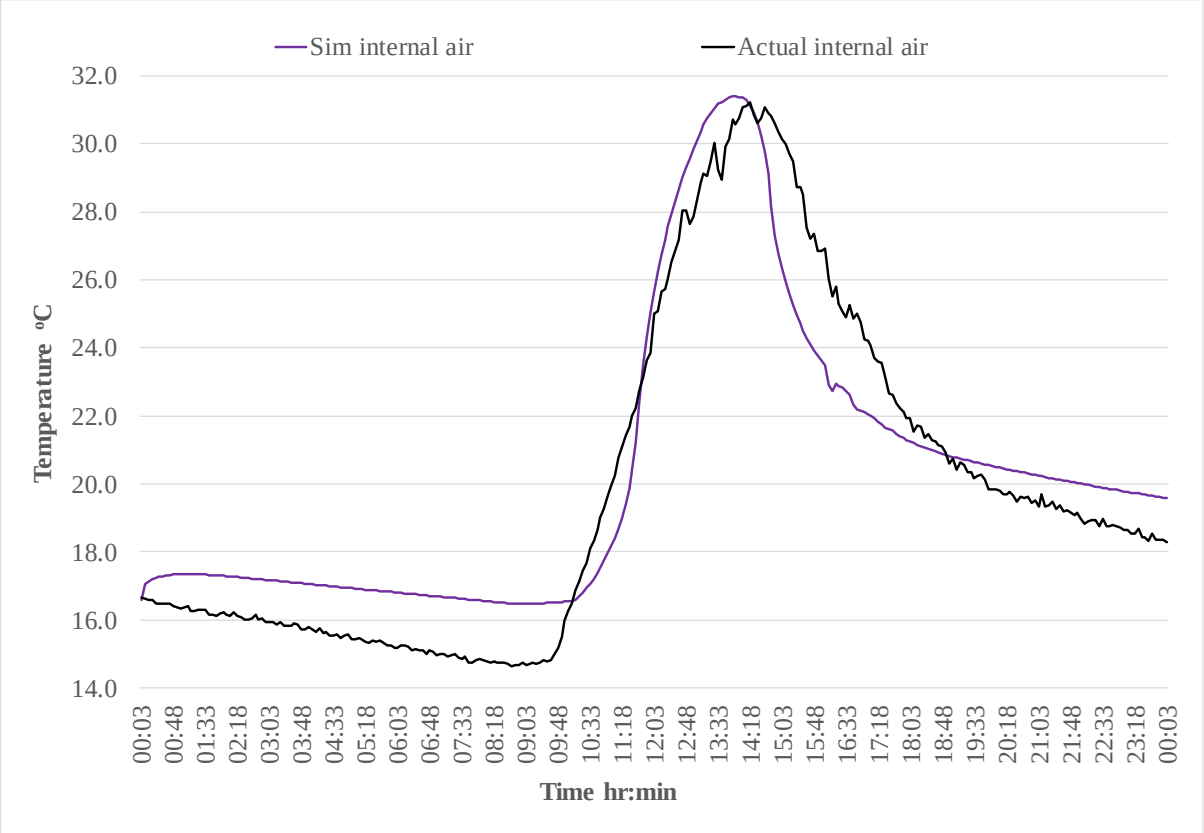


**1st November 2018 Full PCM hut, simulated versus actual internal air temperatures**

| Average $\lvert T_{sim} - T_{act} \rvert$ (°C) of internal air | Standard deviation (°C) | Accuracy of simulated temperatures (°C) |
|---|---|---|
| 1.34 | 0.77 | 2.2 |

## 8. 10th June 2017 Full PCM hut –summer passive conditions

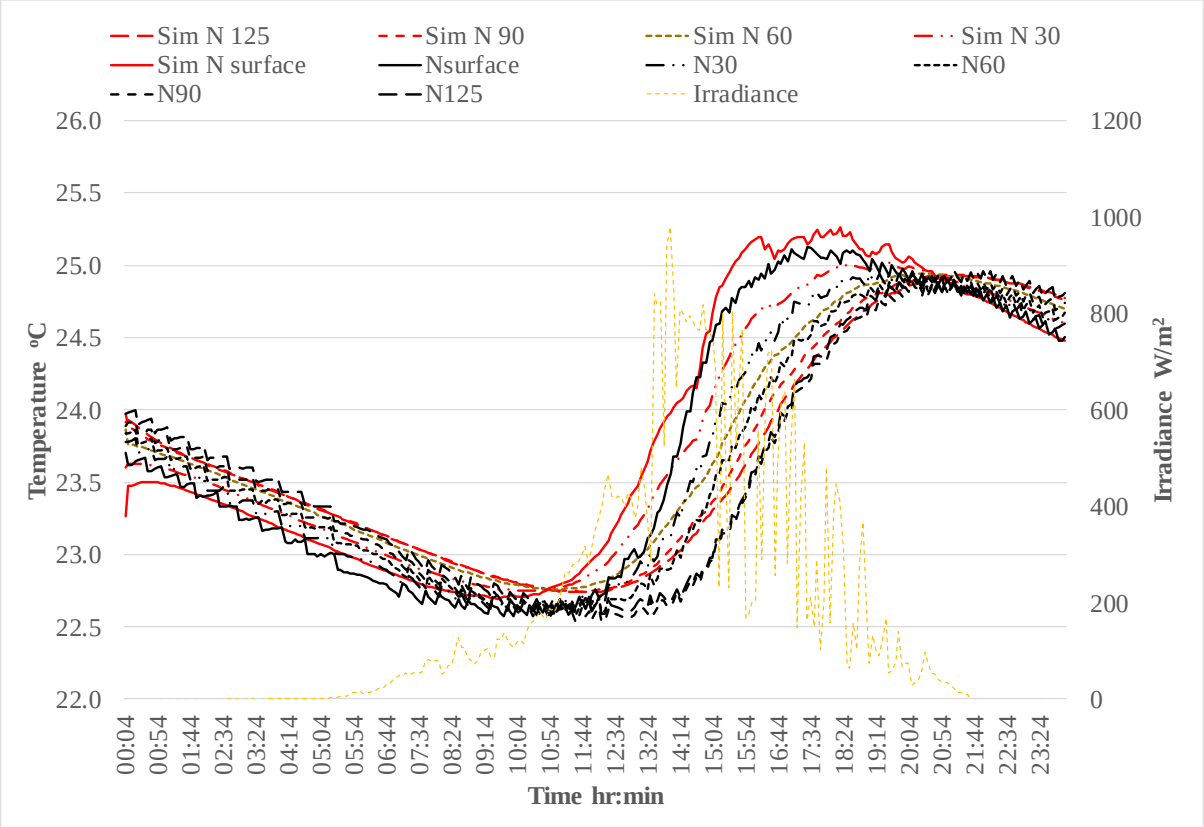


**10th June 2017 , Full PCM hut, North wall inner leaf simulated versus actual temperatures**

| Depth | Average $\lvert T_{sim} - T_{act} \rvert$ (ºC) | Standard deviation (ºC) | Accuracy of simulated temperatures (ºC) |
|---|---|---|---|
| Surface | 0.12 | 0.12 | 0.99 |
| 30 mm | 0.13 | 0.10 | 1.00 |
| 60 mm | 0.11 | 0.07 | 0.98 |
| 90 mm | 0.14 | 0.11 | 1.01 |
| 125 mm | 0.09 | 0.08 | 0.96 |

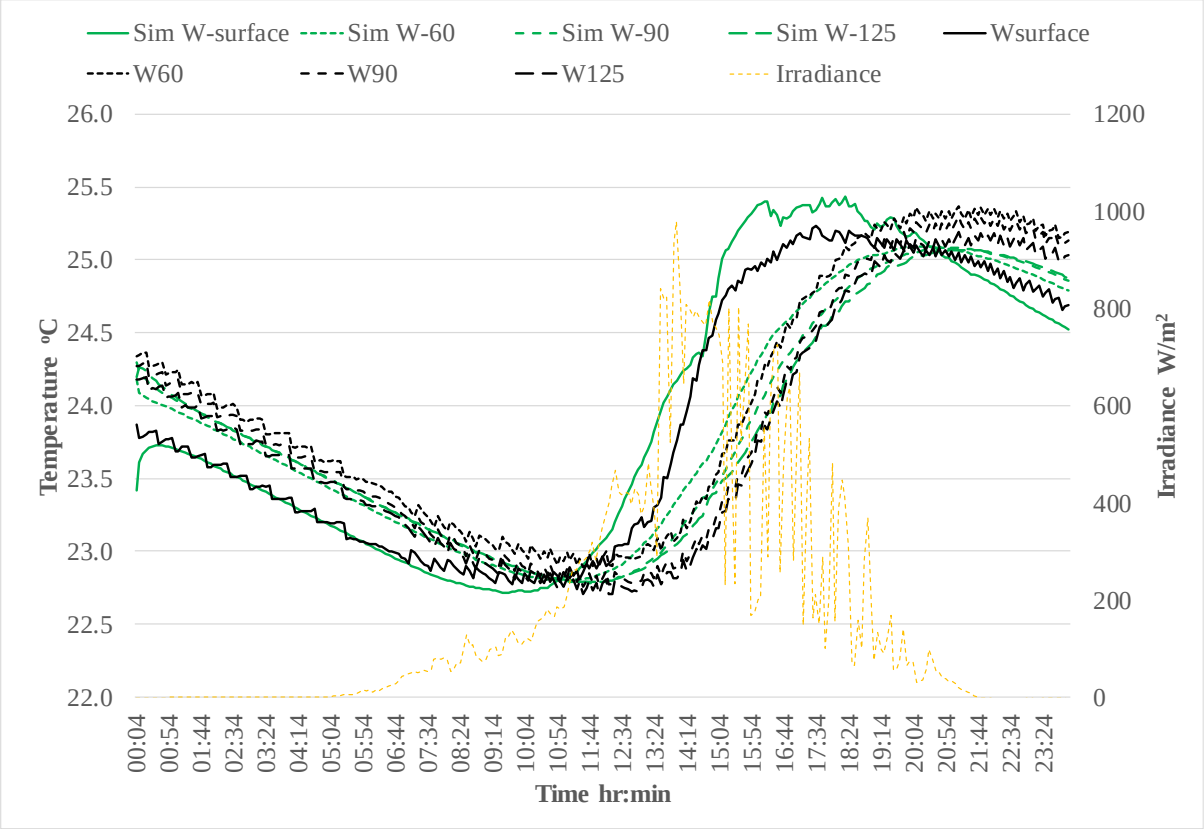


**10th June 2017 , Full PCM hut, West wall inner leaf simulated versus actual temperatures**

| Depth | Average $\lvert T_{sim} - T_{act} \rvert$ (°C) | Standard deviation (°C) | Accuracy of simulated temperatures (°C) |
|---|---|---|---|
| Surface | 0.13 | 0.13 | 1.00 |
| 60 mm | 0.18 | 0.08 | 1.05 |
| 90 mm | 0.10 | 0.08 | 0.97 |
| 125 mm | 0.07 | 0.06 | 0.94 |

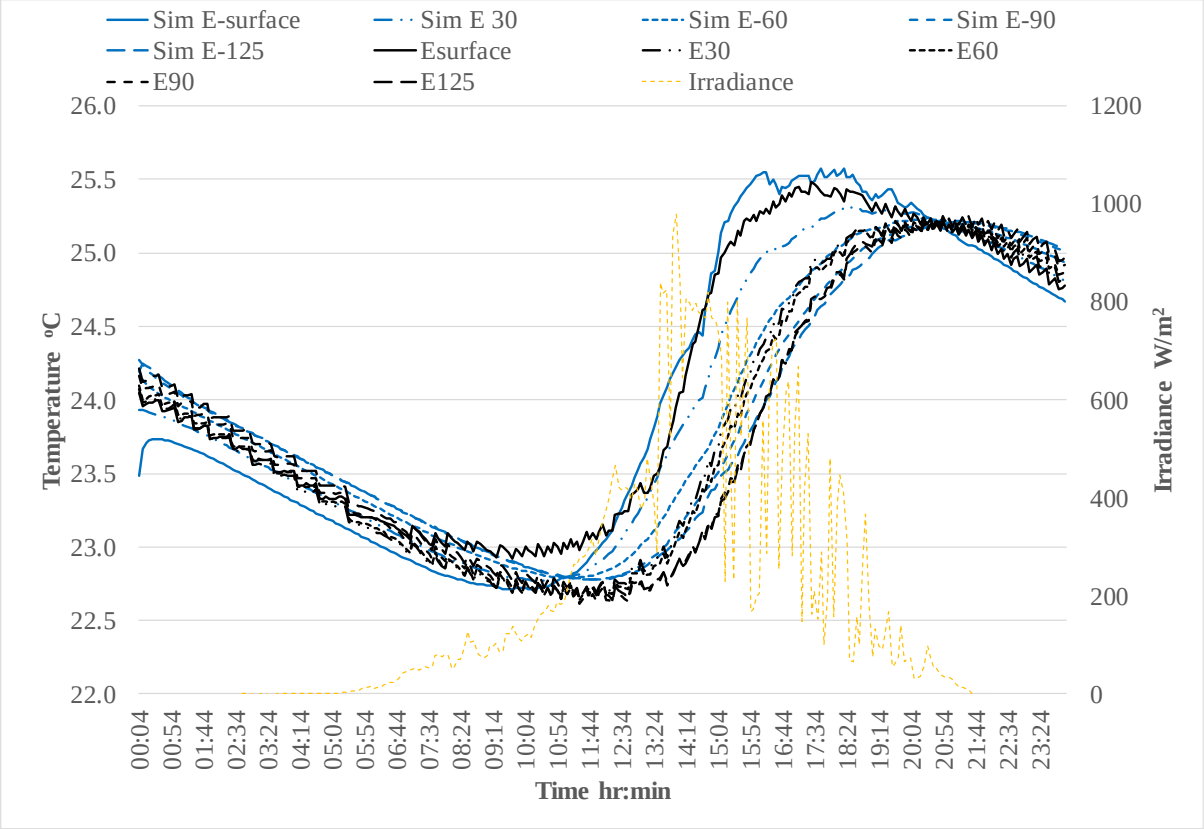


**10th June 2017 , Full PCM hut, East wall inner leaf simulated versus actual temperatures**

| Depth | Average $\lvert T_{sim} - T_{act} \rvert$ (ºC) | Standard deviation (ºC) | Accuracy of simulated temperatures (ºC) |
|---|---|---|---|
| Surface | 0.16 | 0.09 | 1.03 |
| 30 mm | 0.17 | 0.21 | 1.04 |
| 60 mm | 0.11 | 0.08 | 0.98 |
| 90 mm | 0.11 | 0.07 | 0.98 |
| 125 mm | 0.08 | 0.05 | 0.95 |

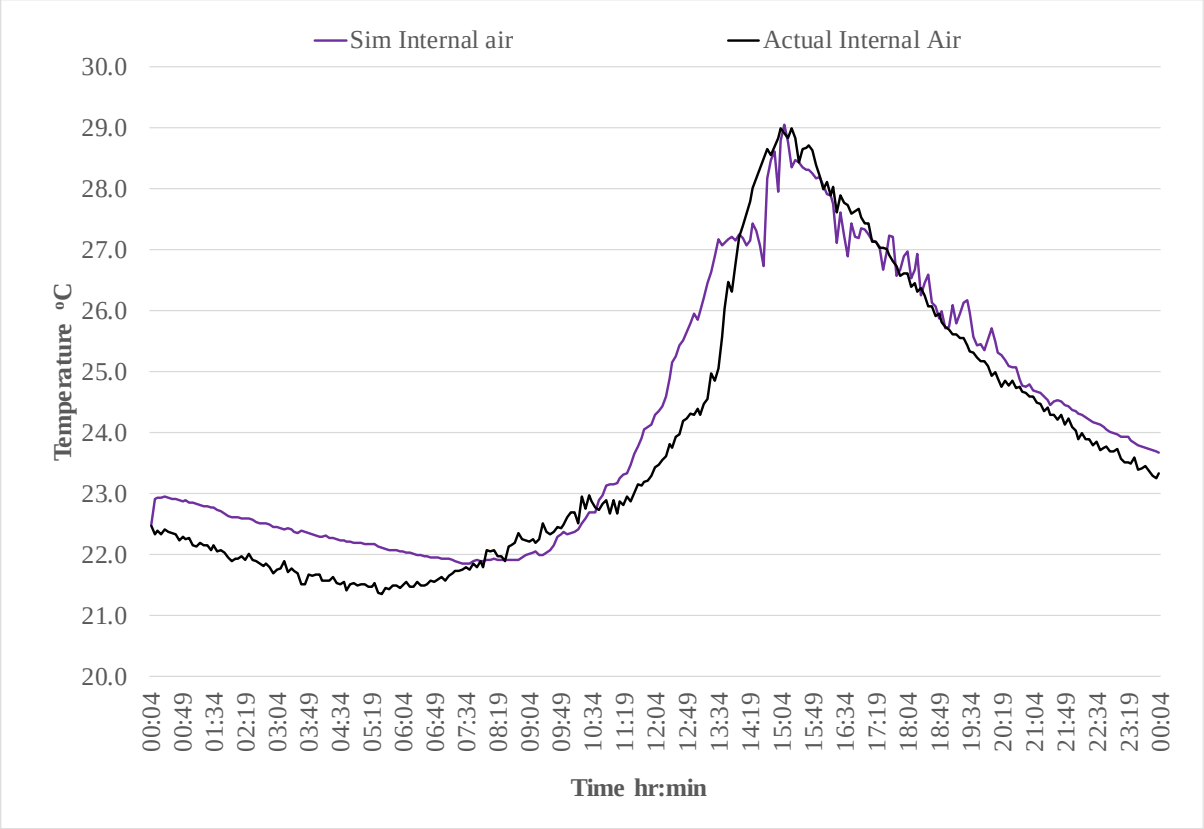


**10th June 2017 Full PCM hut, simulated versus actual internal air temperatures**

| Average $\lvert T_{sim} - T_{act} \rvert$ (ºC) of internal air | Standard deviation (ºC) | Accuracy of simulated temperatures (ºC) |
|---|---|---|
| 0.49 | 0.37 | 1.36 |

**10th June 2017 Partial PCM hut –summer passive conditions**

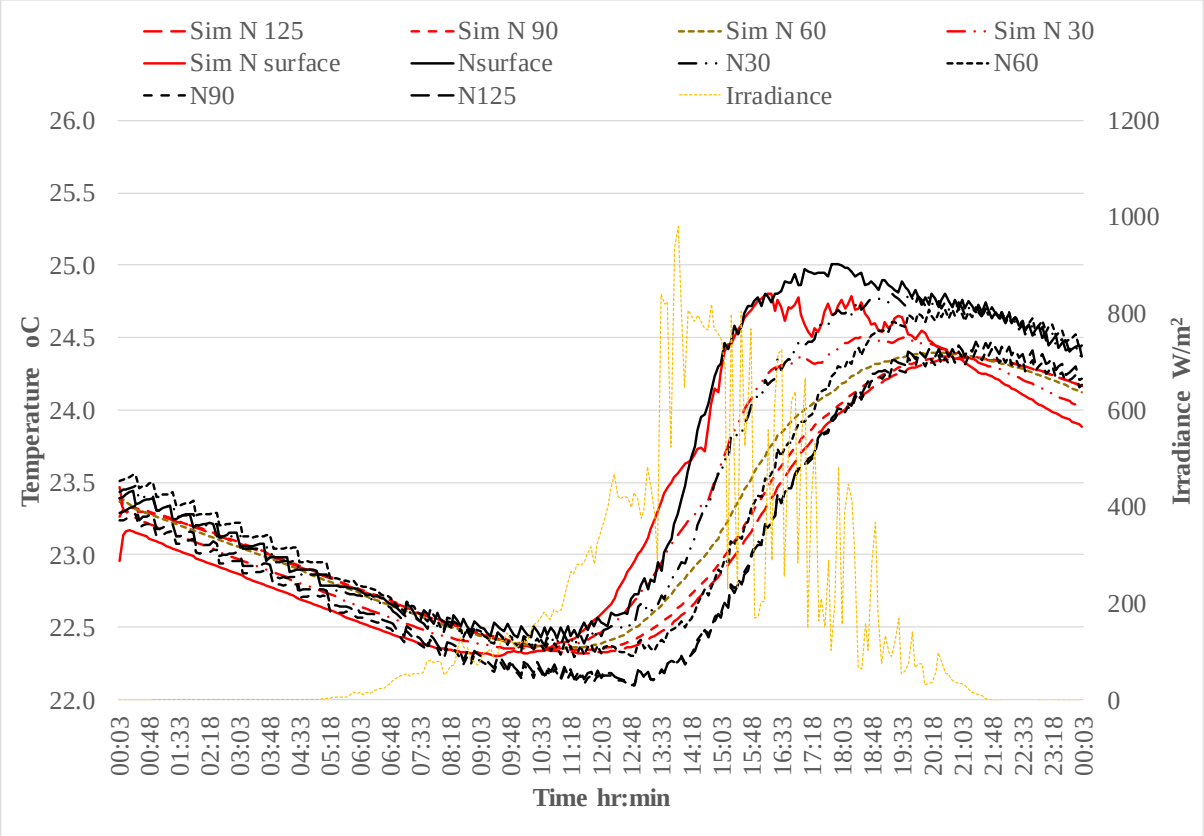


**10th June 2017, Partial PCM hut, North wall inner leaf simulated versus actual temperatures**

| Depth | Average $\|T_{sim} - T_{act}\|$ (ºC) | Standard deviation (ºC) | Accuracy of simulated temperatures (ºC) |
|---|---|---|---|
| Surface | 0.24 | 0.13 | 1.10 |
| 30 mm | 0.16 | 0.12 | 1.02 |
| 60 mm | 0.15 | 0.11 | 1.01 |
| 90 mm | 0.16 | 0.10 | 1.02 |
| 125 mm | 0.13 | 0.07 | 0.99 |

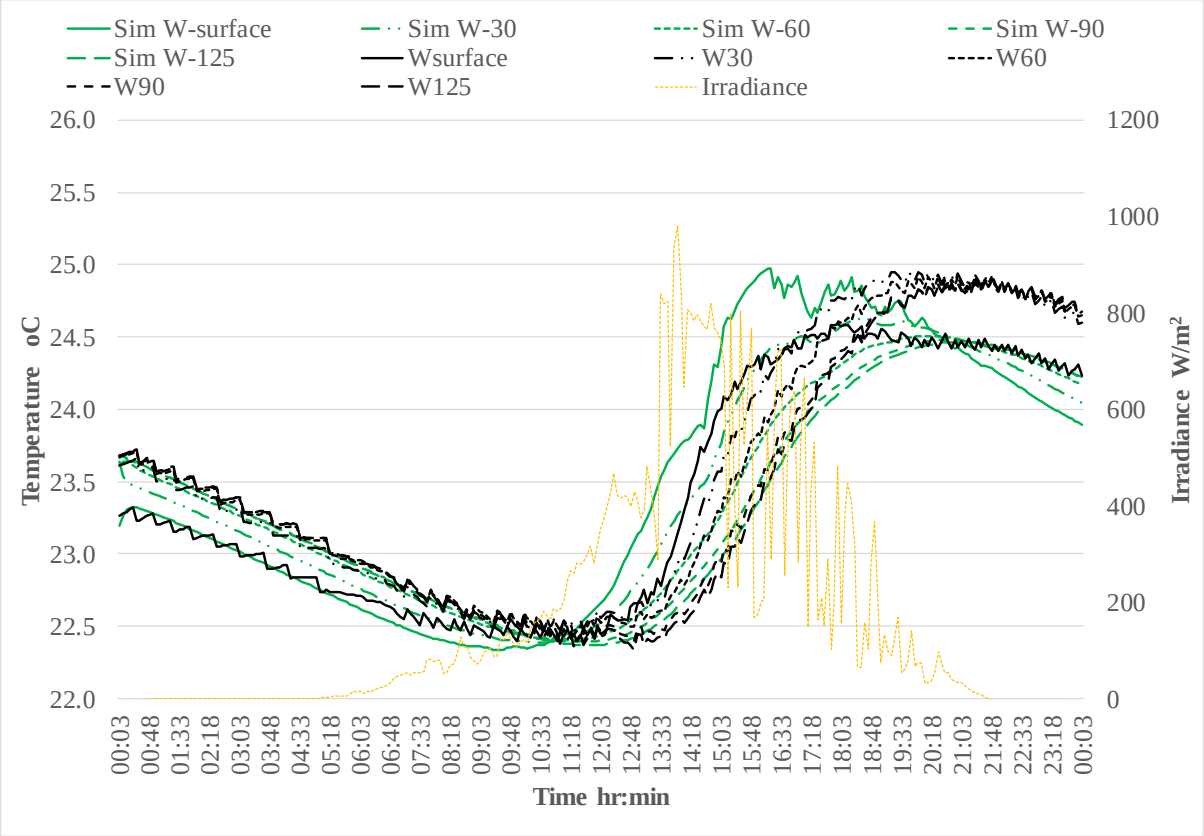


**10th June 2017, Partial PCM hut, West wall inner leaf simulated versus actual temperatures**

| Depth | Average $\lvert T_{sim} - T_{act} \rvert$ (°C) | Standard deviation (°C) | Accuracy of simulated temperatures (°C) |
|---|---|---|---|
| Surface | 0.19 | 0.18 | 1.05 |
| 30 mm | 0.21 | 0.15 | 1.07 |
| 60 mm | 0.16 | 0.15 | 1.02 |
| 90 mm | 0.13 | 0.14 | 0.99 |
| 125 mm | 0.14 | 0.15 | 1.00 |

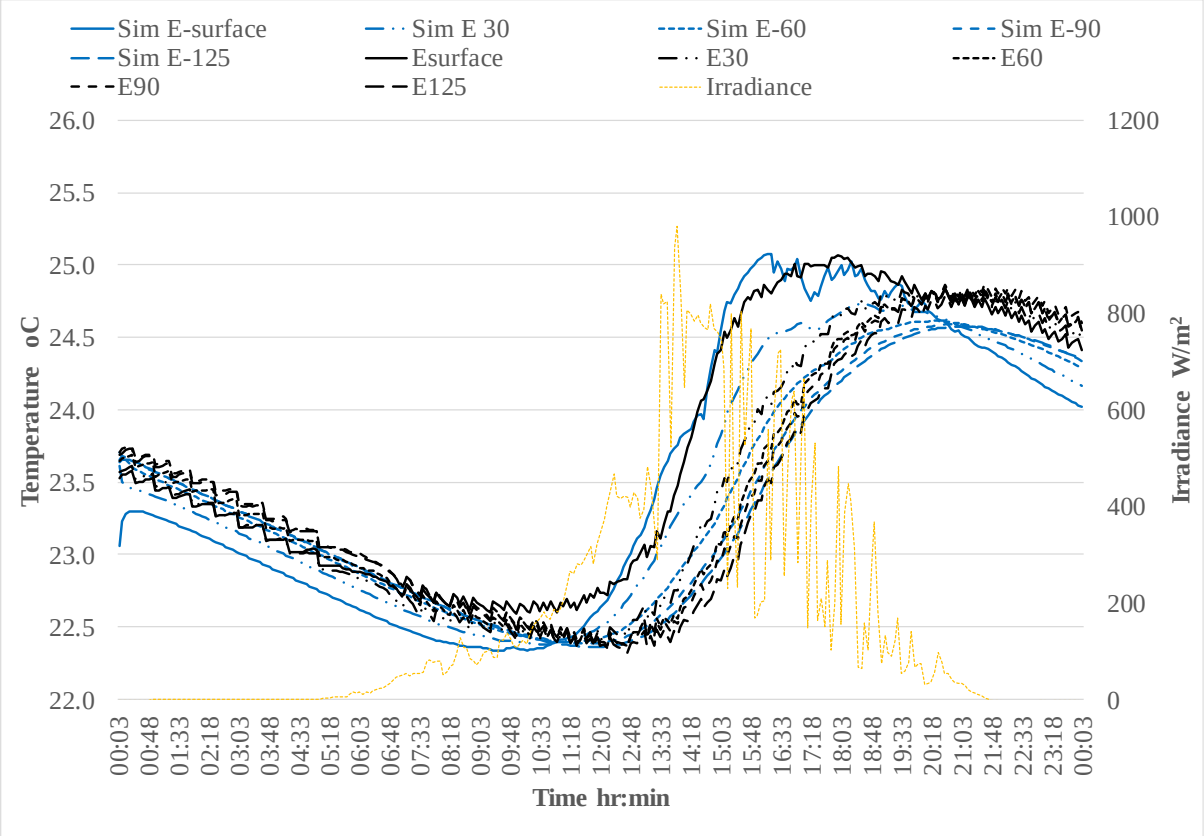


**10th June 2017, Partial PCM hut, East wall inner leaf simulated versus actual temperatures**

| Depth | Average $\lvert T_{sim} - T_{act} \rvert$ (ºC) | Standard deviation (ºC) | Accuracy of simulated temperatures (ºC) |
|---|---|---|---|
| Surface | 0.22 | 0.10 | 1.08 |
| 30 mm | 0.16 | 0.14 | 1.02 |
| 60 mm | 0.11 | 0.09 | 0.97 |
| 90 mm | 0.11 | 0.08 | 0.97 |
| 125 mm | 0.10 | 0.07 | 0.96 |

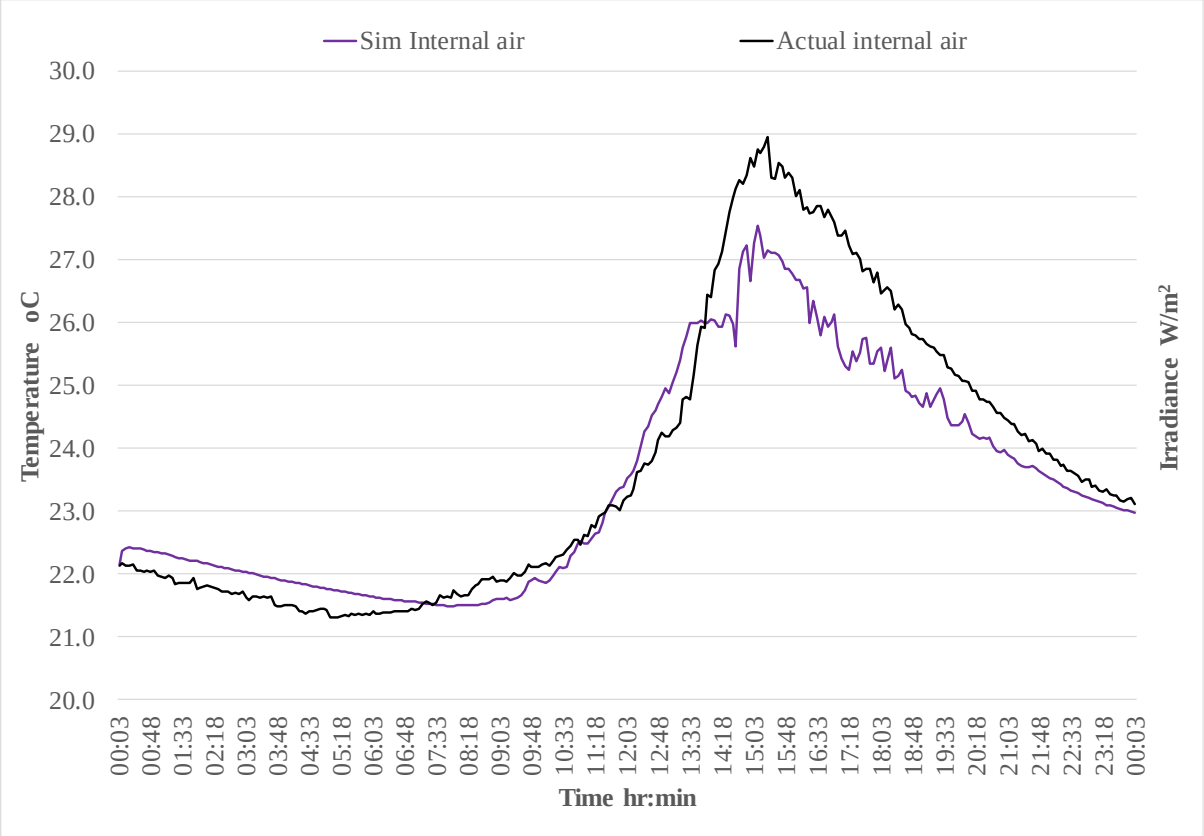


**10th June 2017 Partial PCM hut, simulated versus actual internal air temperatures**

| Average $\lvert T_{sim} - T_{act} \rvert$ (ºC) of internal air | Standard deviation (ºC) | Accuracy of simulated temperatures (ºC) |
|---|---|---|
| 0.58 | 0.49 | 1.44 |

## Appendix T Volume fraction of Micronal added to the concrete

**Table U-1 Final PCM-concrete mix**

| Quantities | Rapid Hardening Cem 1 Cement (kg) | Water (kg) | Fine aggregate (kg) | Coarse 6-14mm (kg) | Limestone Filler (kg) | SP Premier 196 (l) | Micronal (kg) |
|---|---|---|---|---|---|---|---|
| Per $m^3$ | 330 | 160 | 725 | 935 | 110 | 9.9 | 110 |

w/c = 0.48

* Based on wet density of control mix = 2360 $kg/m^3$

Density of Micronal is 350 $kg/m^3$.

Volume of 110 kg = 110/350 = 0.314 $m^3$

## Appendix U Plots of scenario simulation results in Oslo, Dublin and Madrid during June and December

### A. June

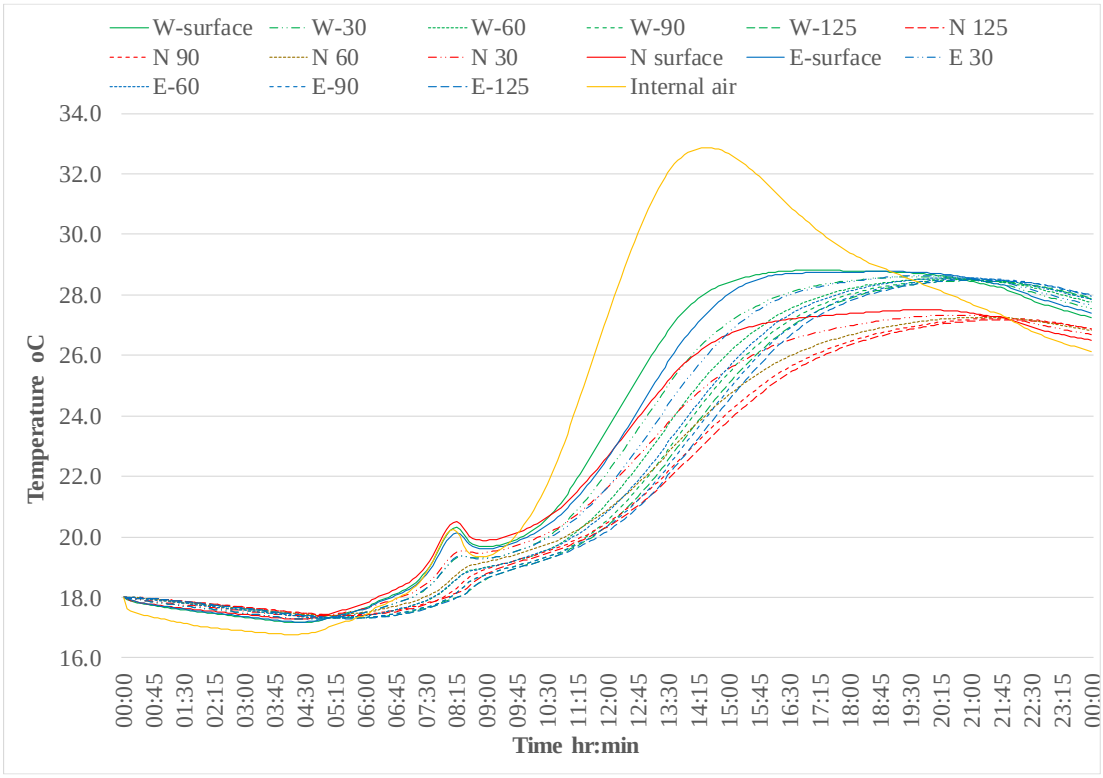


**Figure U-1 Oslo 20th June No PCM**

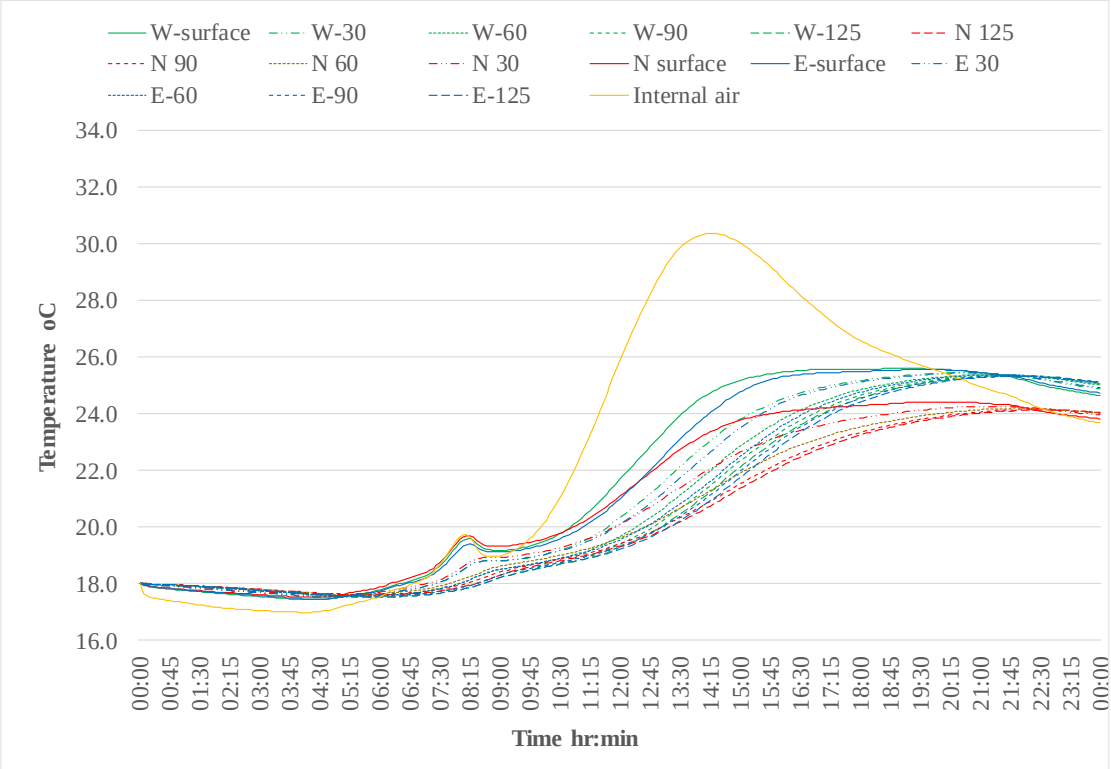


**Figure U-2 Oslo 20th June 60 mm PCM-concrete**

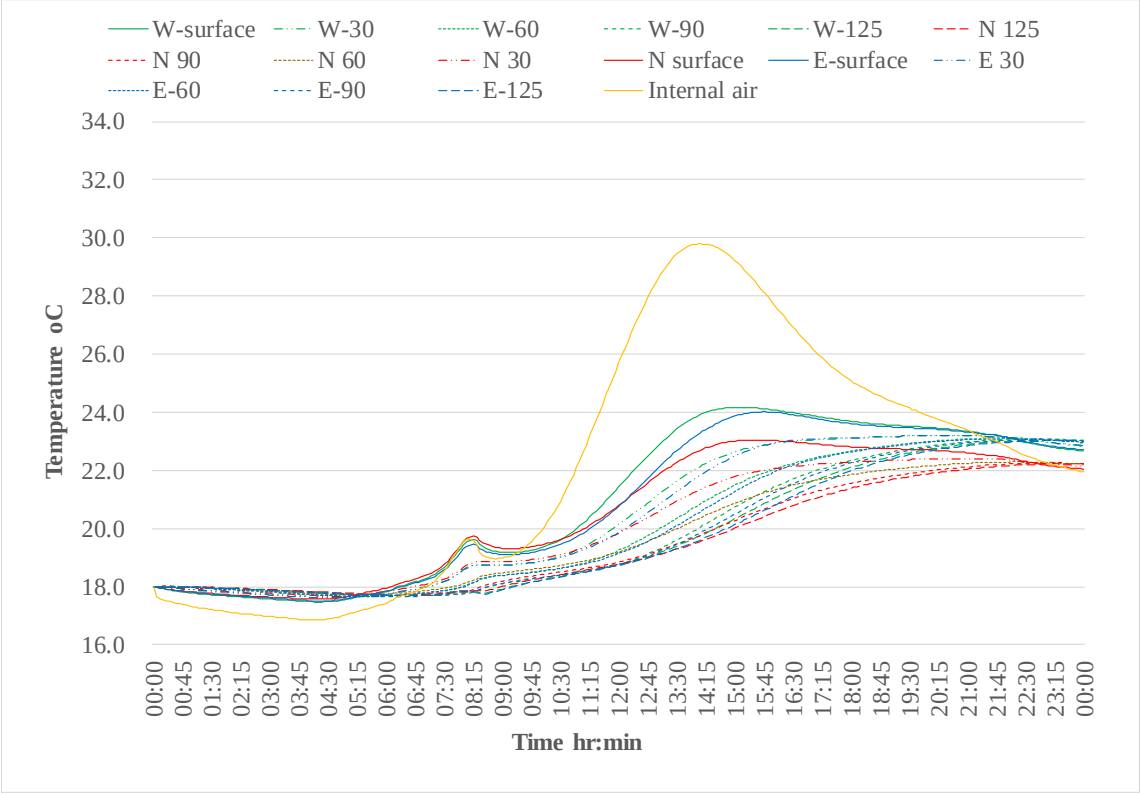


**Figure U-3 Oslo 20th June Full PCM**

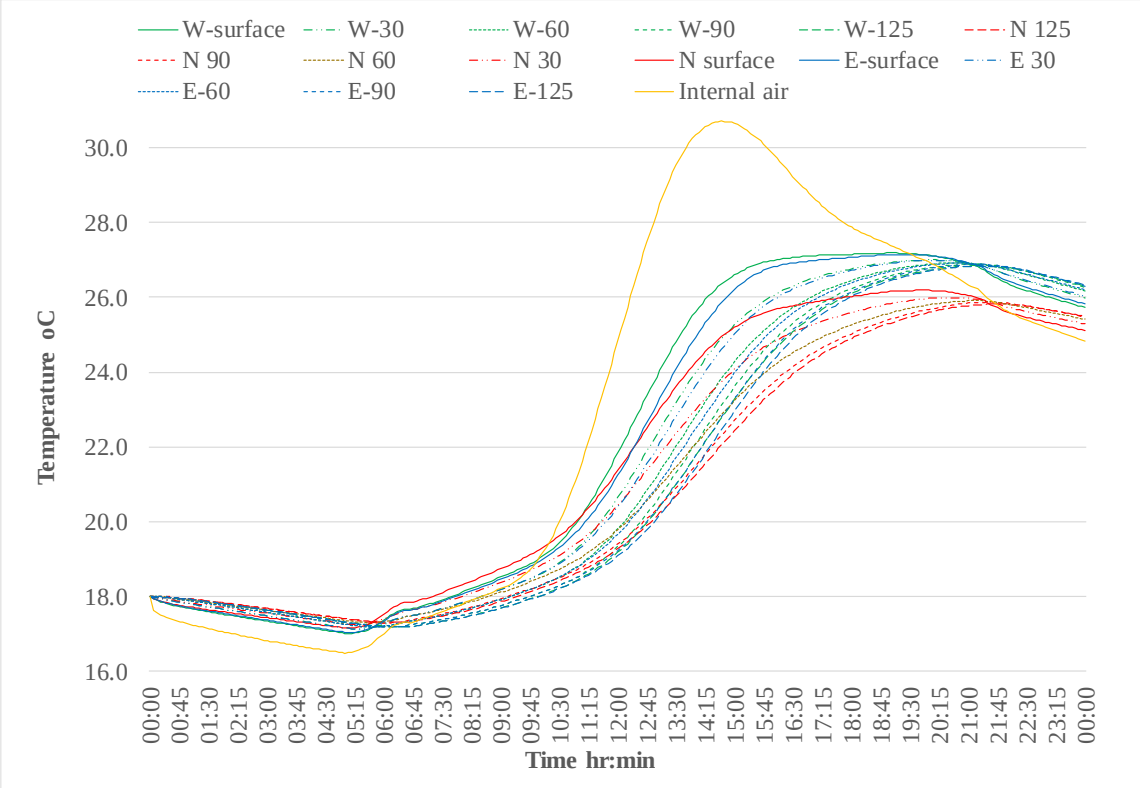


**Figure U-4 Dublin 20th June No PCM**

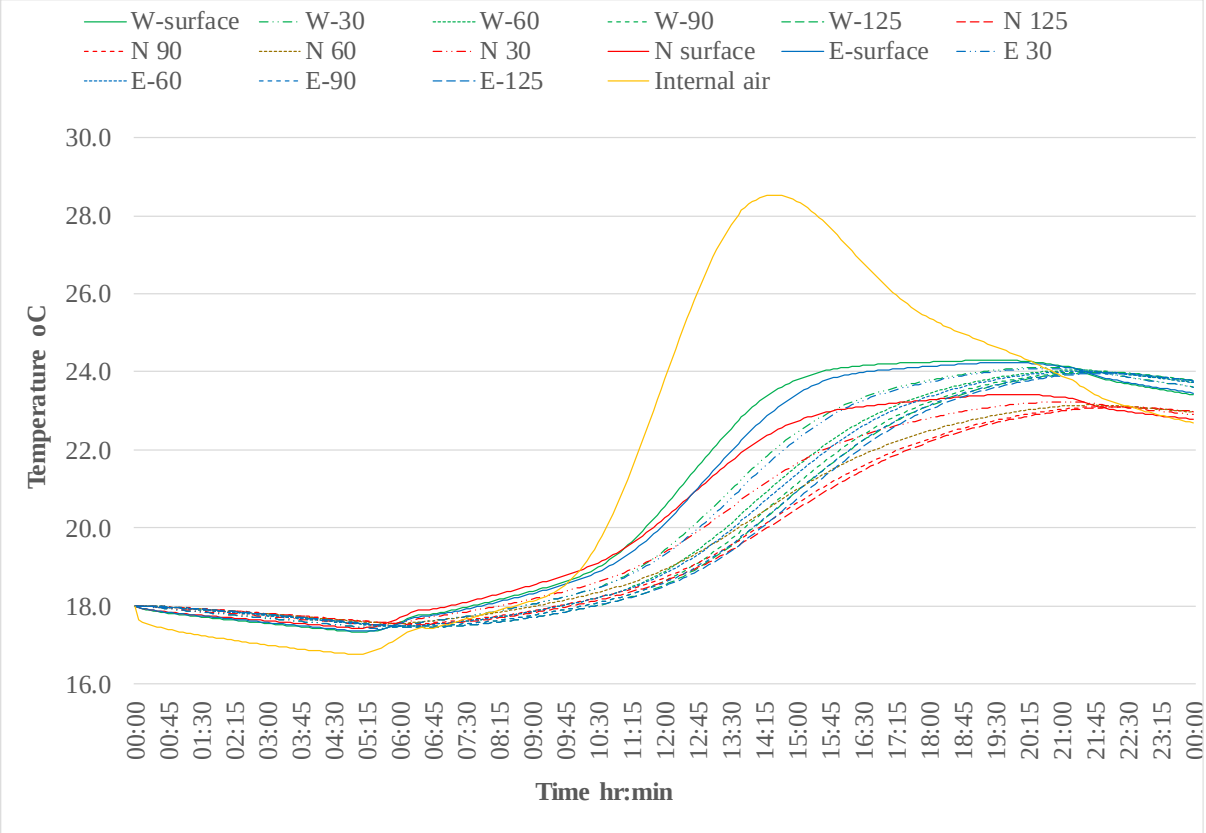


**Figure U-5 Dublin 20th June 60 PCM**

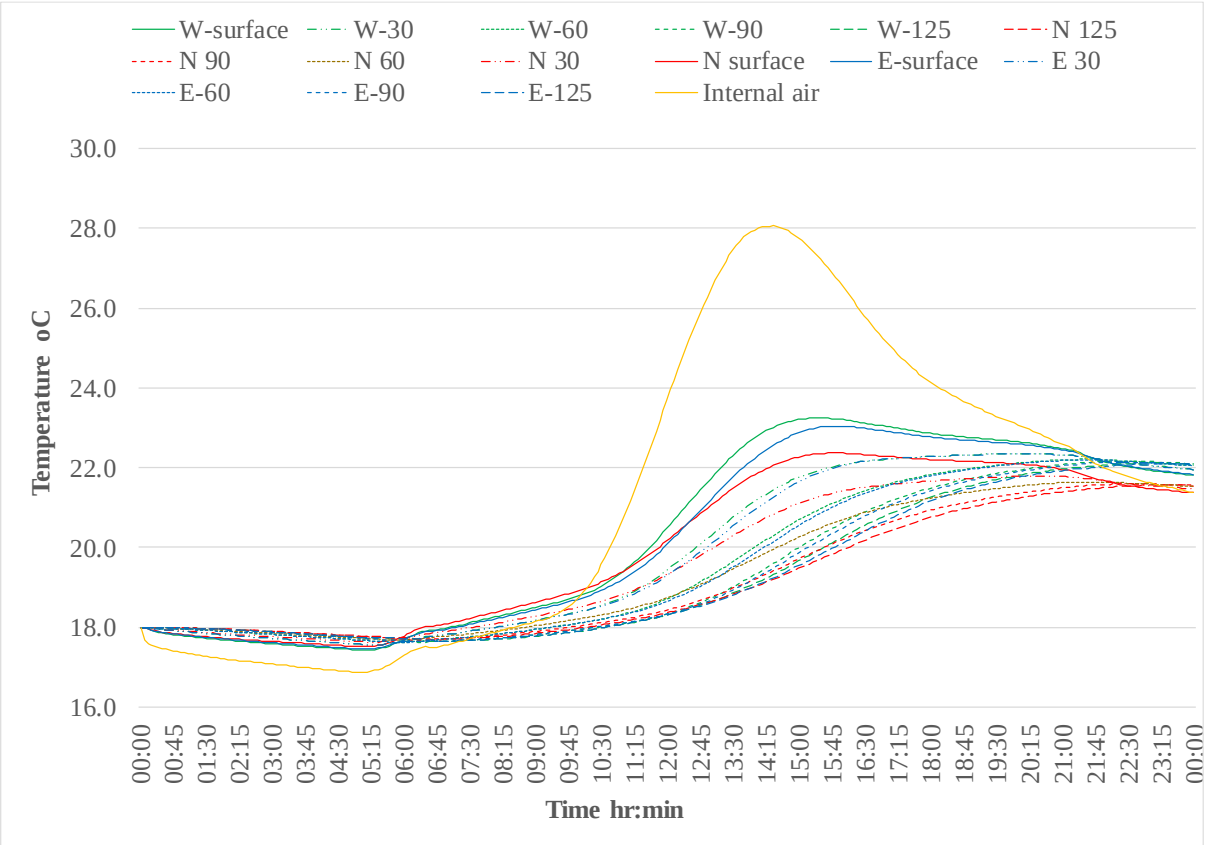


**Figure U-6 Dublin 20th June Full PCM**

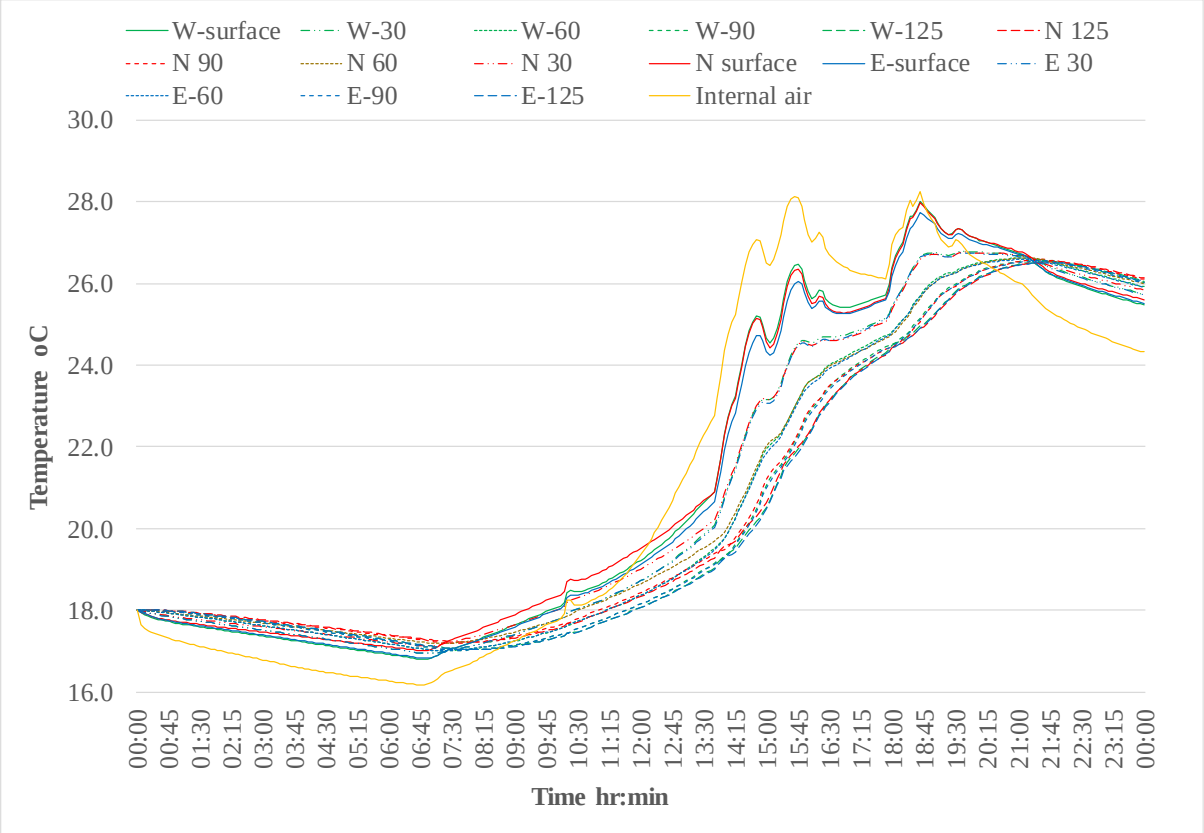


**Figure U-7 Madrid 22nd June No PCM**

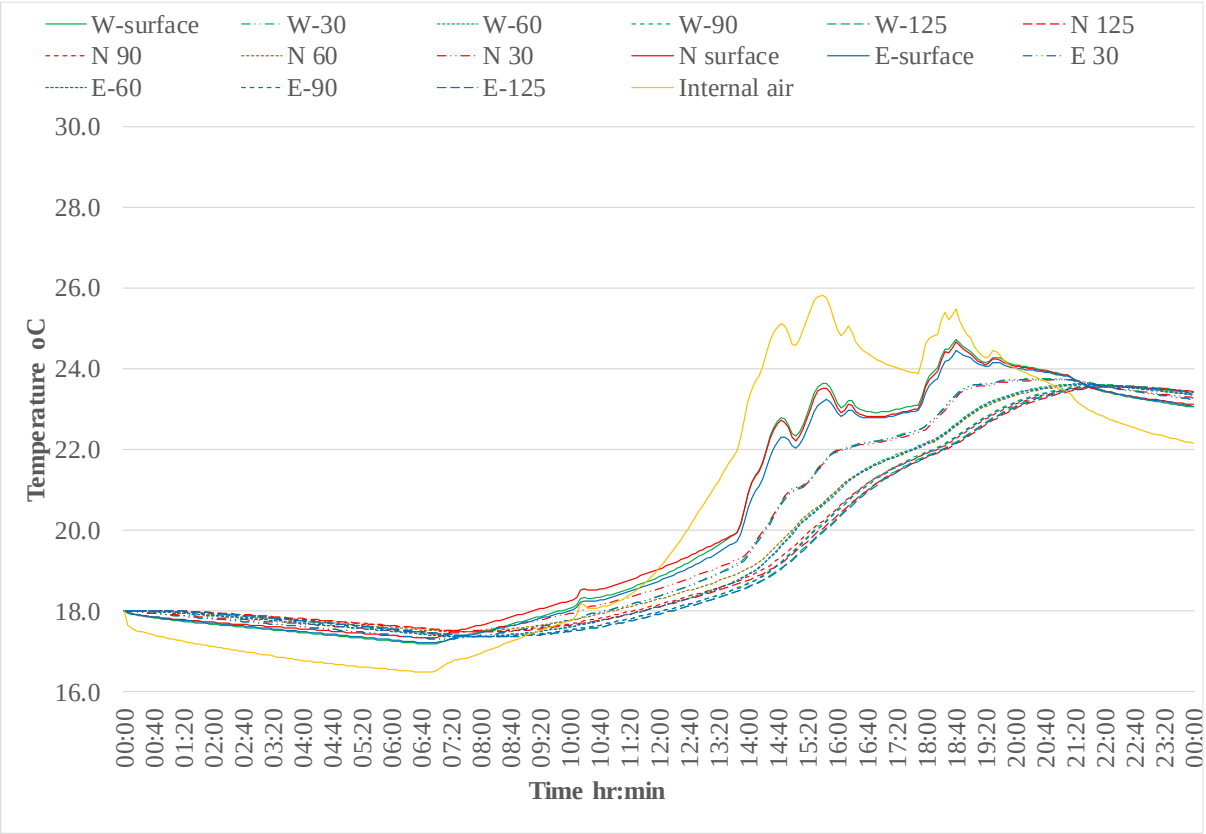


**Figure U-8 Madrid 22nd June 60 PCM**

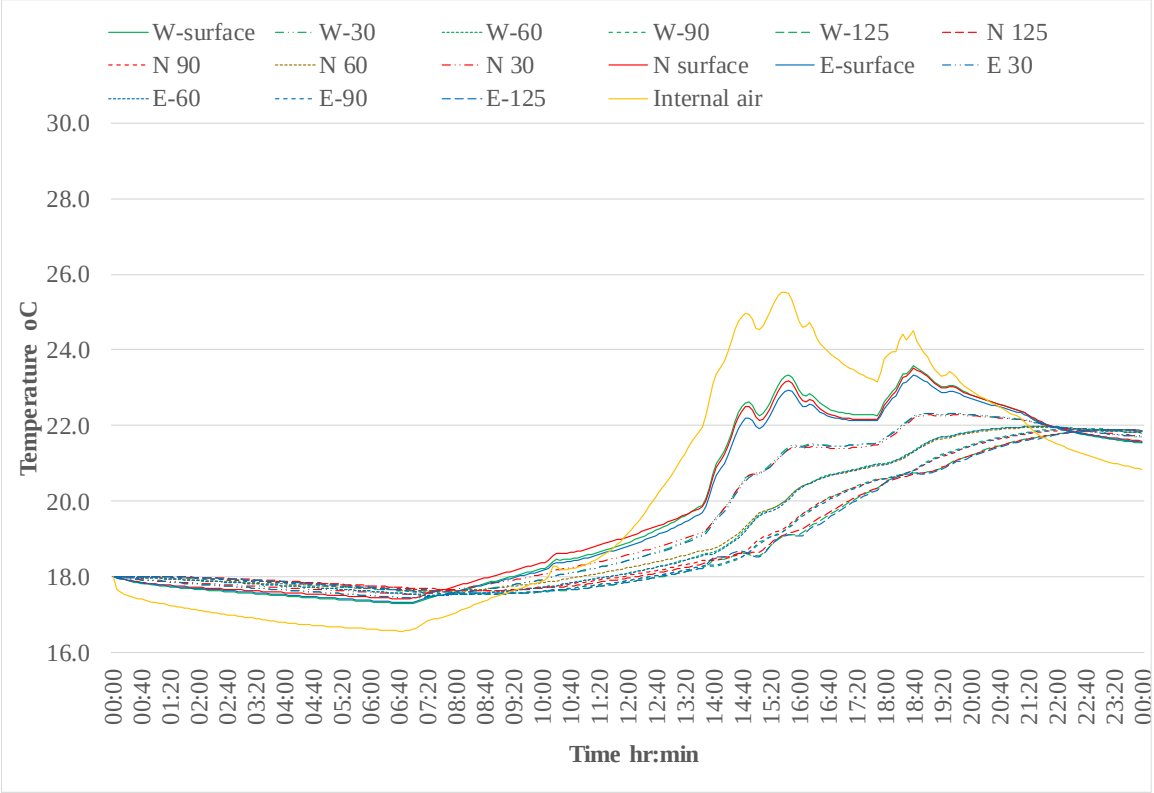


**Figure U-9 Madrid 22nd June Full PCM**

## B. Winter:

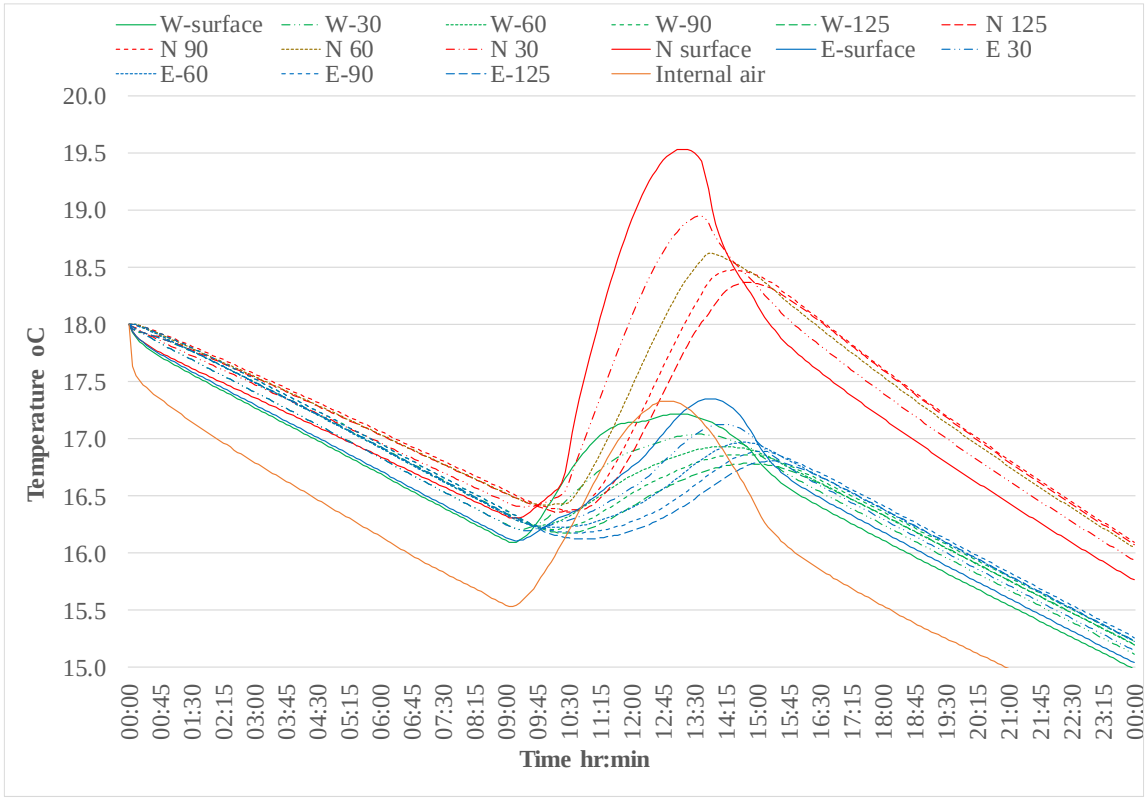


**Figure U-10 Oslo 5th December No PCM**

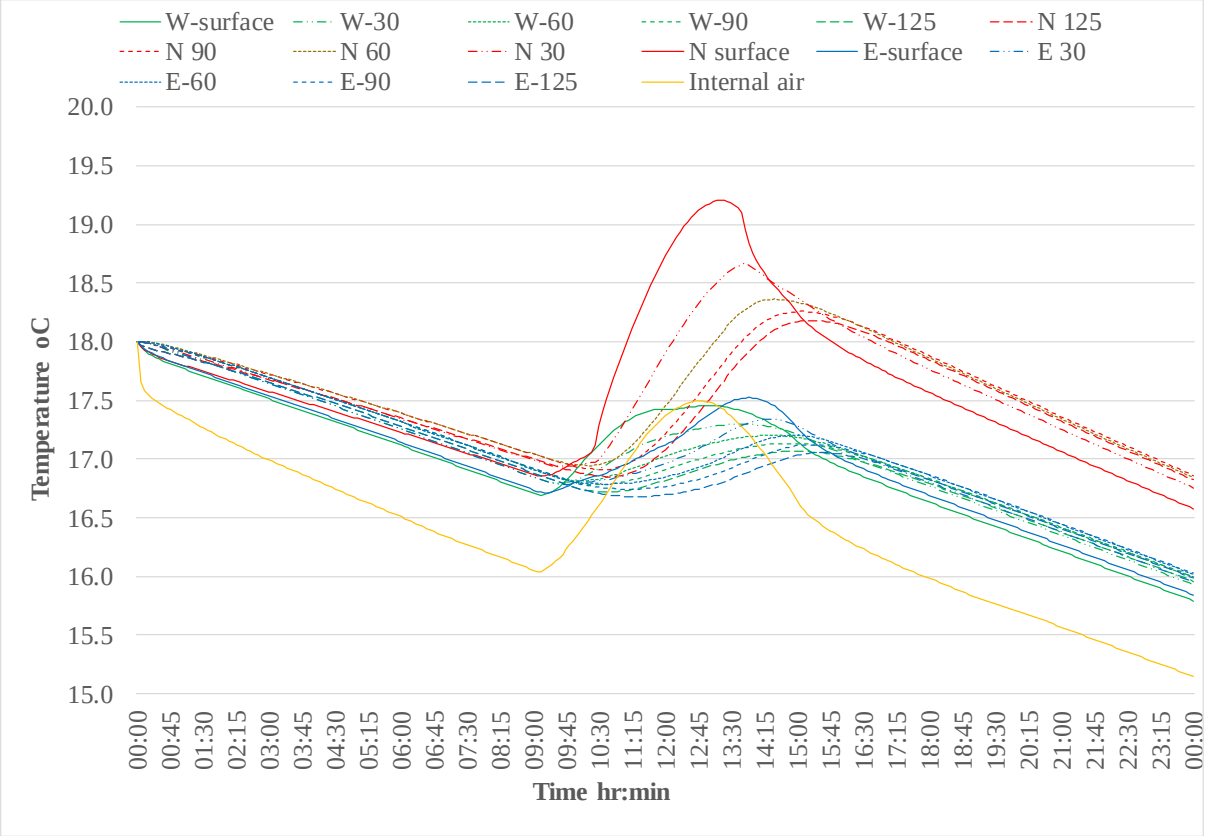


**Figure U-11 Oslo 5th December Partial PCM**

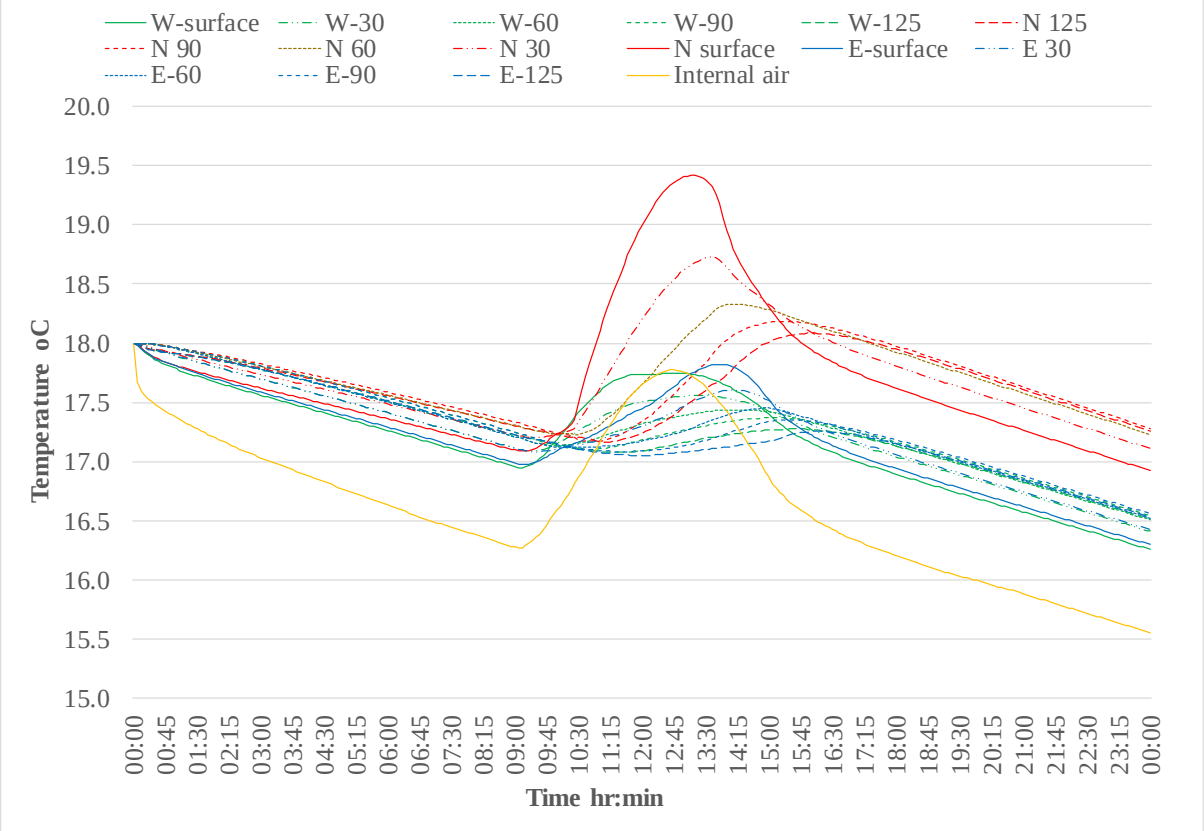


**Figure U-12 Oslo 5th December Full PCM**

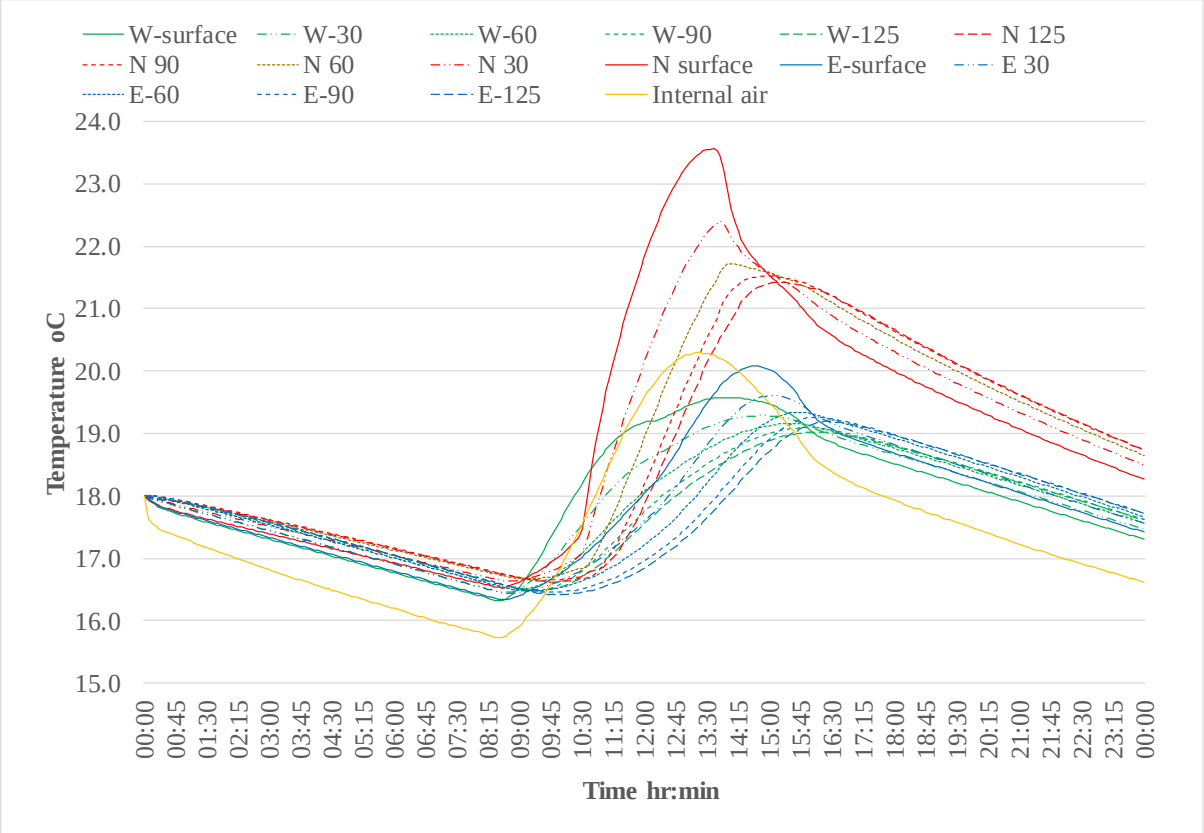


**Figure U-13 Dublin 7th December No PCM**

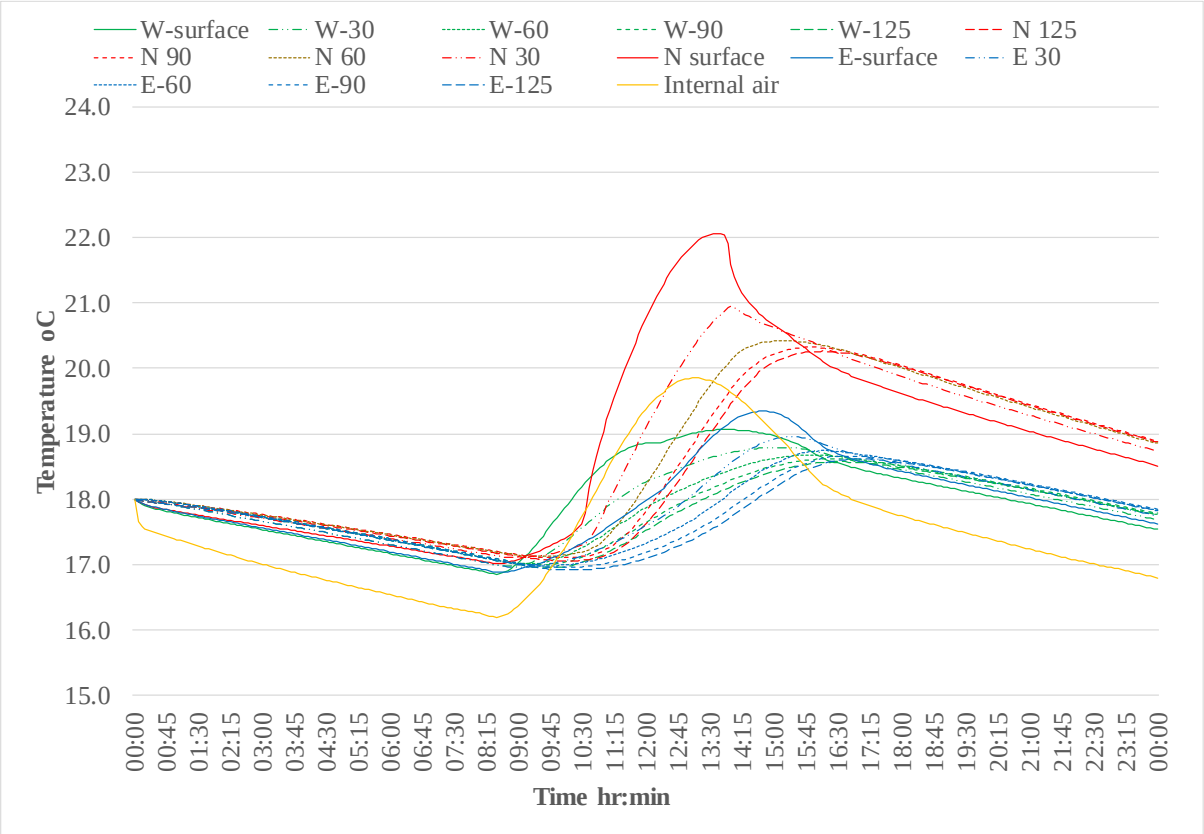


**Figure U-14 Dublin 7th December Partial PCM**

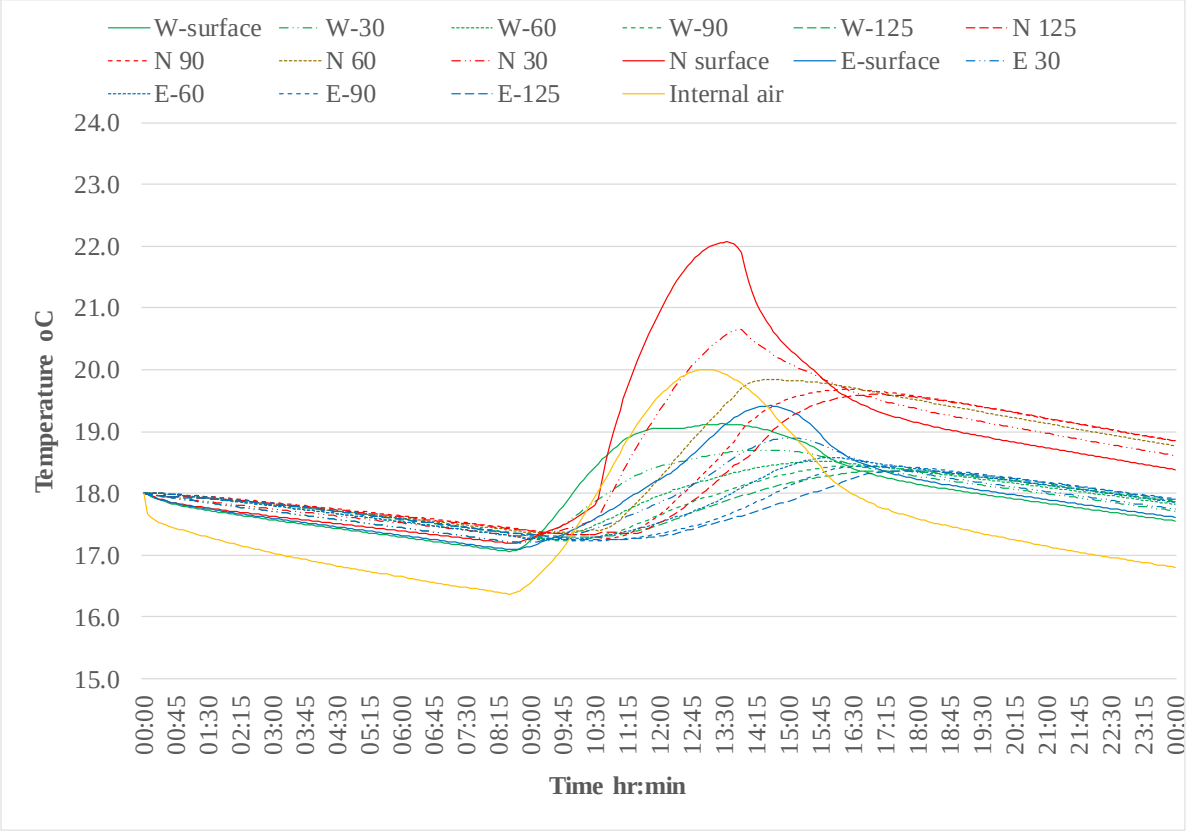


**Figure U-15 Dublin 7th December Full PCM**

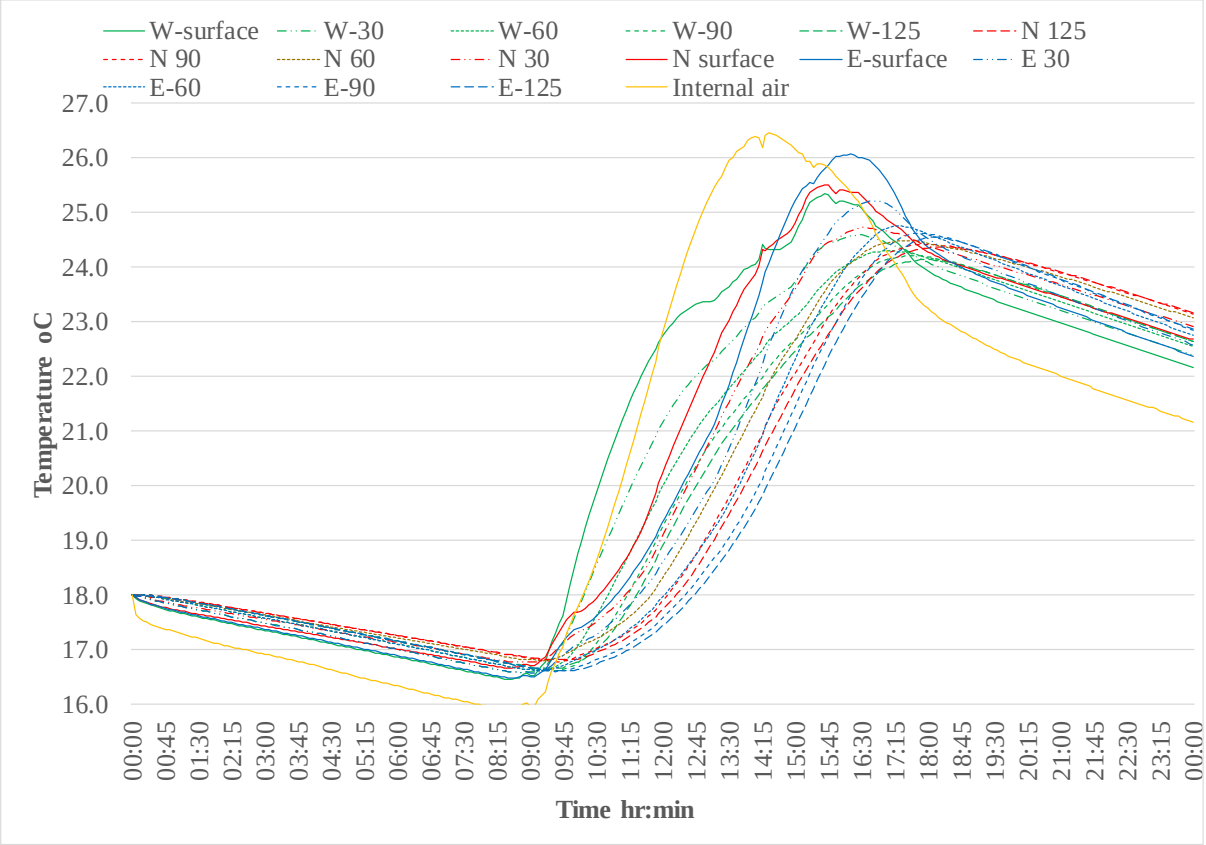


**Figure U-16 Madrid 10th December 2022 No PCM**

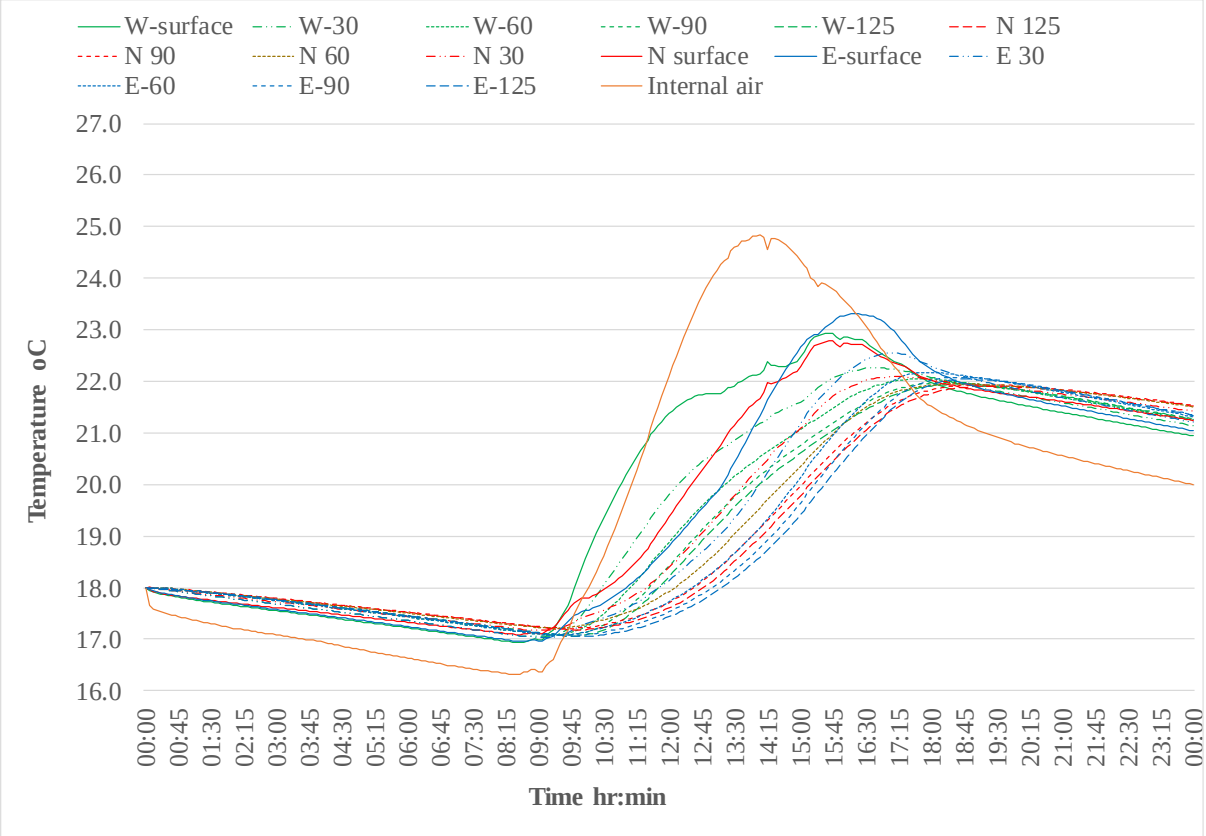


**Figure U-17 Madrid 10th December 2022 Partial PCM**

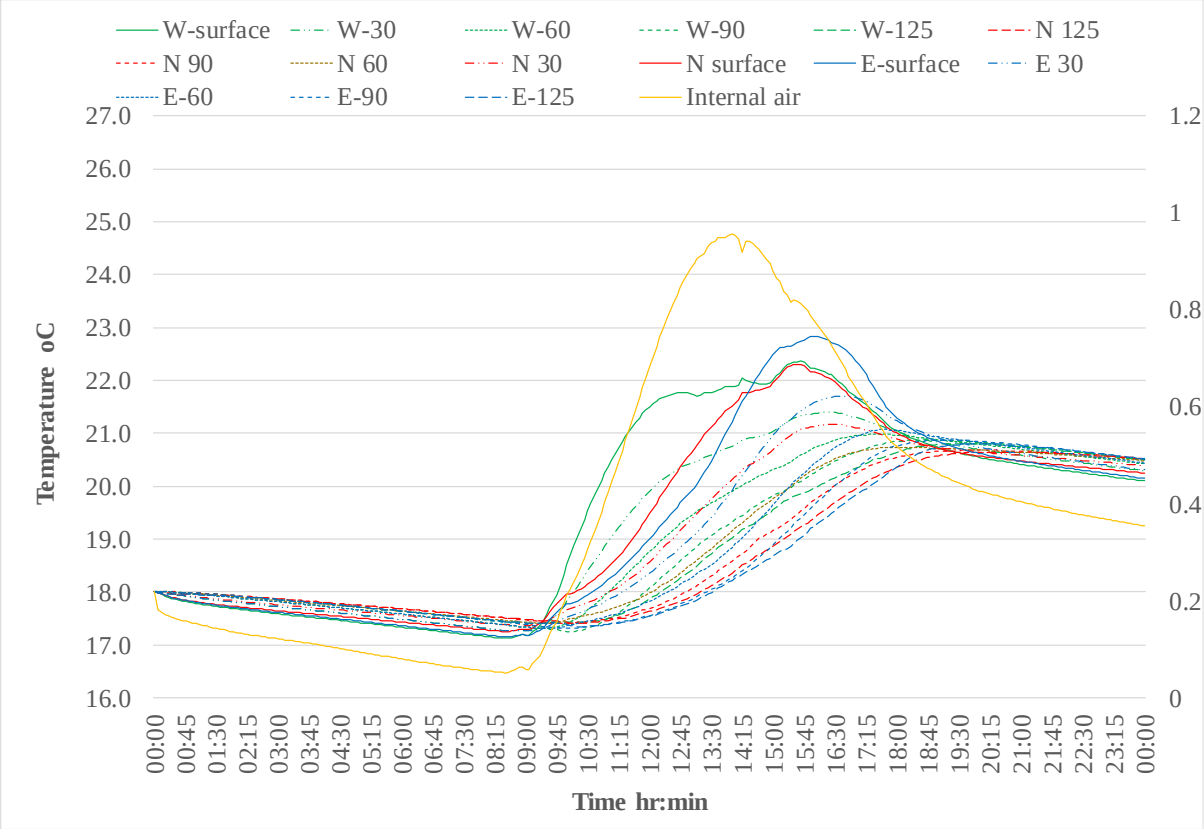


**Figure U-18 Madrid 10th December 2022 Full PCM**

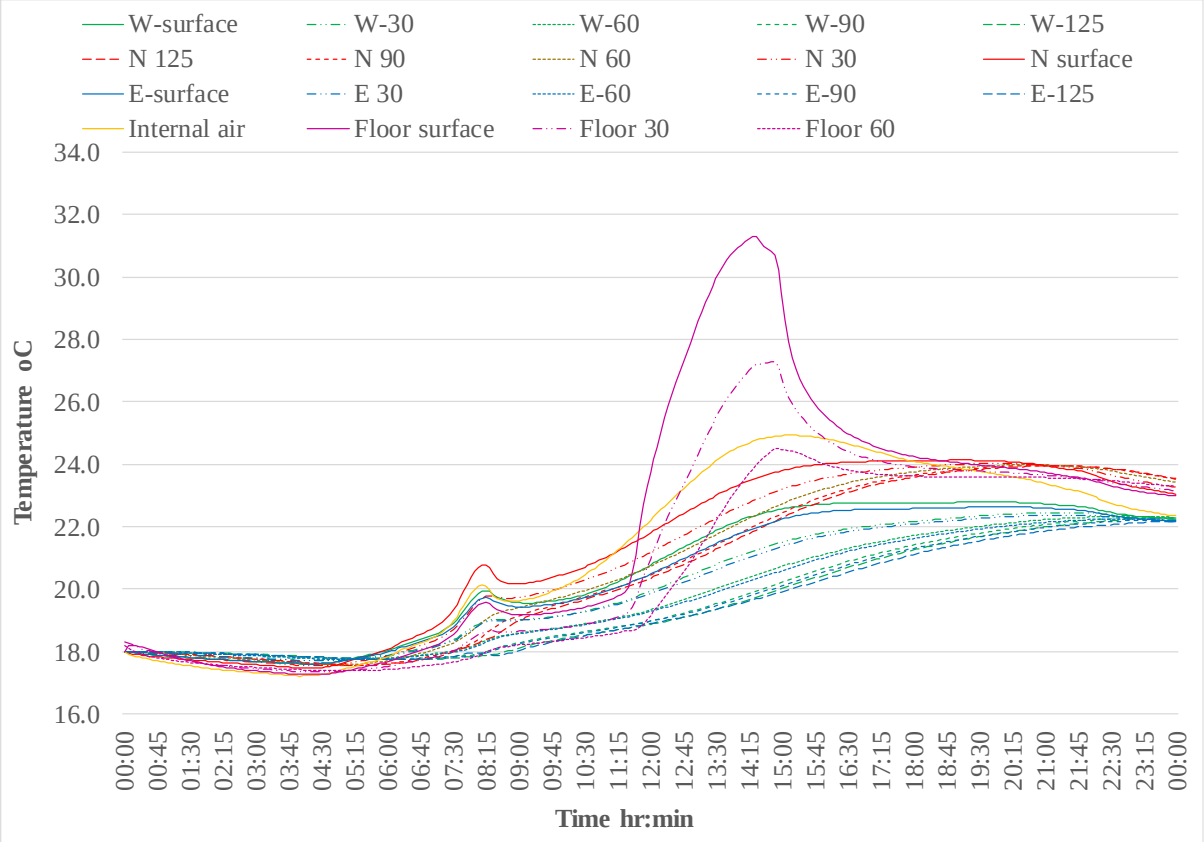


**Figure U-19 Oslo 20th June Full PCM hut with PCM in all East and West walls and floor, no PCM in North wall**

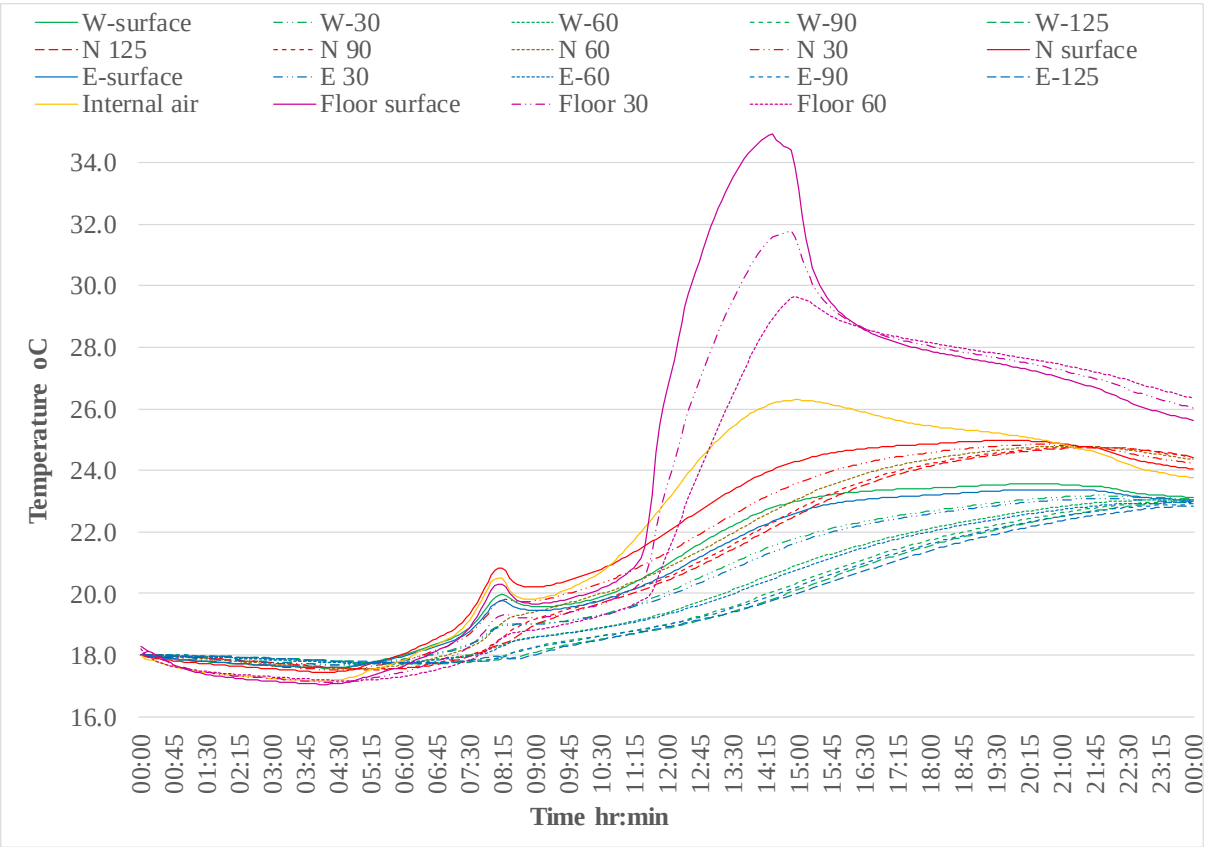


**Figure U-20 Oslo 20th June Full PCM hut with PCM in all walls and Control concrete floor**

## Appendix V Published papers and 10 ECTS credits completed

### Papers published

The following papers have been published on the research work carried out as part of this project:

**Journal Papers:**

1. Niall, D., West, R., McCormack, S. 2016. Assessment of two methods of enhancing thermal mass performance of concrete through the incorporation of phase change materials. *Sustainable Design and Applied Research, Volume 4, Issue 1 November 2016, pp. 30 -37.*

2. Niall, D., Kinnane, O., West, R., McCormack, S. 2017. Mechanical and thermal evaluation of different types of PCM-concrete composite panels. *Journal of Structural Integrity and Maintenance, Vol. 2, Iss. 2, pp 100 – 108.*

**Conference papers:**

1. Niall, D., Kinnane, O., West, R., McCormack, S. 2016. Thermal mass behaviour of concrete panels incorporating phase change materials presented and published at the *International Conference on Sustainable Built Environment (SBE)* in Hamburg, Germany, 8th – 11th March 2016, pp1276 - 1285.

2. Niall, D., Kinnane, O., West, R., McCormack, S. 2016. Mechanical and thermal evaluation of different types of PCM-concrete composite panels presented and published at the *Civil Engineering Research Ireland* conference in Galway, 29th – 30th August 2016, pp 353-358.

3. Niall, D., Kinnane, O., West, R., McCormack, S. 2016. Influence of Ground Granulated Blastfurnace Slag on the thermal properties of PCM-concrete composite panels presented and published at the *Advanced Building Skins* conference in Bern, Switzerland, October 2016, pp 963 -973.

4. Niall, D., Kinnane, O., West, R.. 2018. Design and manufacture of a precast PCM enhanced concrete cladding panel for full scale performance monitoring presented and published at the *Civil Engineering Research Ireland* conference in Dublin, 29th – 30th August 2018

5. Niall, D., West, R.., Kinnane, O., O'Hegarty, R., 2020. Modelling the thermal behaviour of a precast PCM enhanced concrete cladding panel presented and published at the *Civil Engineering Research Ireland* conference, on-line 27th – 28th August 2020

**10 ECTS, level 9 Module on nZEB buildings**

In 2016 the author completed a 10 ECTS credit, level 9 module entitled Professional Energy Skills in nZEB (near Zero Energy Buildings). This module was funded by the European Union under EU Horizon 2020.

This module introduced European and national policies in building energy efficiency and nZEB. It explored the use of materials and installations suitable for nZEB in the design of retrofit building solutions, and the incorporation of renewable energy sources in existing residential building stock. It investigated life cycle cost analysis and explored the management and financial issues necessary for professionals to be able to influence the shift to nZEB design and construction. It explored calculation theories and methodologies used in energy modelling to achieve compliance with the nZEB performance standard.

The module also developed skills in the application of advanced tools in modelling existing residential buildings using national and international energy performance metrics, and techniques for upgrading geometry, fabric and services installations to achieve the nZEB design performance standard in residential buildings.

The author graduated with a distinction.